Pan-African magmatism and regional tectonics of South Brazil

Thesis

Pan-African Magmatism and Regional Tectonics of South Brazil.

A thesis submitted for the degree of Doctor of Philosophy

by

Sian Elizabeth May B.A.

Department of Earth Sciences
The Open University

July, 1990

ABSTRACT

The Dom Feliciano Belt is a Pan-African mobile belt from the Ribeira orogen of southern Brazil. A detailed field and geochemical traverse along the BR392 road section between Pelotas and Caçapava do Sul identifies two major tectonic domains; the Pelotas Batholith and the Santana Metamorphic Belt, striking NNE-SSW parallel to the major foliation of the belts. The two belts are separated by a Triassic basin with flat lying red beds and interbedded andesites and rhyolites.

The Santana Metamorphic Belt is a NW-verging fold belt with a metamorphosed shelf sequence of quartzites, marbles and graphitic schists and a polydeformed Lower Proterozic gneissic basement deformed during the Pan-African orogeny. Detailed mapping recognized four phases of deformation in the basement gneisses, three of which are recorded in the basement schists and cover sequence. There is also evidence of late NE-verging thrusting post-dating the formation unmetamorphosed Paleozoic sediments. Late extension caused NW-SE and NE-SW normal faulting. Metamorphism occurred contemporaneously with D2 and D3, and PT conditions for peak metamorphism have been calculated as 8.6Kb and 600°C within the basement schists corresponding to garnet growth during D3 deformation.

Three phases of granite intrusion are recognized in the Santana Metamorphic Belt. The Santana Granite (800m.y.) represents the first phase intruding the basement and it is folded by D2 and D3. The Campinas Granite (500m.y.) has a D3 foliation and the Caçapava Granite (474m.y.) is post-tectonic and intrudes the NW portion of the Santana Metamorphic Belt.

The Pelotas Batholith is almost entirely composed of granitoids of Pan-African age (600-450m.y.). Both D2 and D3 are recognized in the batholith. A two fold subdivision based on geochemical and field criteria distinguishes the following categories of granitoid; foliated granitoids and unfoliated granites.

Geochemically all granitoids of the two belts have a stong crustal signature. The foliated granitoids of the Pelotas Batholith (600-550m.y.) are metaluminous, calkalkaline granodiorites, and have volcanic arc characteristics with Sr initial ratios between 0.708 and 0.710 and model ages in the range of 1.6-1.4b.y. The unfoliated granites (500-450m.y.) of the Pelotas Batholith are slightly peraluminous and their field relations, trace element and isotopic data suggest a post-collision setting for their formation. Their higher Sr initial ratios (0.710-0.770), Nd model ages of 1.2-1.1b.y. and high source Rb/Sr, support the proposal that they are melts of the migmatized granodiorites. The Canguçu Red Granite and the Capao do Leao Granite are also unfoliated but appear to be geochemically distinct from the other unfoliated granites. They have high Fe/Mg, Rb/Sr and Rb/Ba ratios, flat rare earth element patterns and negative europium anomalies, all suggestive of A-type granites. From isotopic studies, the Canguçu Granite has very high Sr initial ratios of 0.750 to 0.81 and old model ages of 2.0-3.0b.y.

In the Santana Metamorphic Belt, the foliated Santana Granite has a more depleted trace element chemistry than foliated granites of the Pelotas Batholith and an earlier emplacement age of 800m.y. Trace element and isotope modelling suggest it to be a melt of the basement gneisses. The Campinas Granite is strongly peraluminous with high Rb/Sr, Rb/Ba and Sm/Nd and initial ratios between 0.780 and 0.820 and model ages of 2.0 b.y. suggesting that it is a crustal melt from a pelitic source. The unfoliated Caçapava Granite of the Santana Metamorphic Belt has low Rb/Ba, a low Sr initial ratio (0.705) and high model age (2.5b.y.) suggesting it is a lower crustal melt. The unfoliated Encruzilhada Granite is fault bounded and outcrops between the two belts. It is distinctive from granitoids of both belts in terms of its trace element and isotopic characteristics which suggest that it formed from a basaltic source in a within plate tectonic setting.

There appears to be no systematic change in geochemistry with distance along the cross-section and any changes appear to be temporal. Combined Sr and Nd isotope studies suggest that the Pan-African Ribeira orogen represents a period of crustal reworking rather than crustal growth and in this respect resembles the Damara orogen of Namibia which is dominated by crustal reworking, in contrast to the rapid crustal growth observed in the Arabian shield.

ACKNOWLEDGEMENTS

This project would not have been possible without the help of Dr Marta Mantovani who organized the barmy Brazilian bureaucracy and dealt with the 1000% inflation and crazy Sao Paulo traffic to enable us to undertake field work. I owe her deep appreciation for all this and her hospitality and to Miguel Basei who started me off in the field and engaged in fruitful discussion of the Santa Catarina portion of the Dom Feliciano Belt. I am extremely grateful to Elio, my driver who had to spend 5 weeks looking at road and river sections in the "jungle"who taught me the rudiments of Portuguese by sign language which enabled me to survive, since no-one speaks English in the South. I am also grateful to his family for their hospitality.

My thanks must also go to my supervisors Chris Hawkesworth, who set up the Brazilian connection and started me off in the field collecting geochemical granite samples almost as big as me!, and to Nigel Harris for advice on mapping and metamorphic sampling and for the fireworks he smuggled out to Brazil for my birthday on Bonfire night. I am also grateful to them both for the speedy return of my chapters. I am grateful to Dave Peate for his company in Sao Paulo (someone who spoke English). I am also grateful to NERC for providing the grant for this research.

I should also like to thank everyone in the labs at the Open University including Mabsie Kunka for her patience, for making the lab a cheerful place and for being an ace friend, P.V.C for teaching me about mass-specs, Nick Rodgers for REE data, Ian Chaplin, Brian and Mitch for endless sections and rock splitting. I should also like to thank Keith Parish and Steve from the Oxford labs for their patience in recalibrating the machine to run granites for me. I should also like to thank Keith Cox for arranging for me to use Oxford facilities and for accepting me to do geology as an undergraduate, stimulating my interest in the subject and his faith in my ability to undertake research.

I am indebted to Fiona Mc Gibbon for her advice and friendship throughout my stay here and also to my various room mates Cherry Lewis, Seife Berhe, Frank for discussion and to Chukka for proof reading. A big thanks to me ol'gossip mate Tim Elliot who has coped with my manic singing, and to Melchie and Lynne for lending their ears, to Sarah, Maddog O Rough, Jeer and everyone else for happy hour drinking company and to Rachel and Becka for their long-suffering company at lunchtimes. Thanks also goes to Jon Maynard for driving me to visit my sister and family in a bout of homesickness when my car broke and to Min for watching Prisoner with me. I would also like to thank Monty Crear Clarke for being an ace spech matey for the last six years, letting me stay in the CMK flat when I was homeless, making me realize its O.K to loose your cool occasionally, and for taking me wind surfing.

I also owe a special thanks to all my friends at Spencer St NewBradwell especially Alison, Will, Fern and Jay who have been like family to me and for their support and encouragement "Sian's got a degree but she's as thick as two short planks" and hospitality when I lived there. There ain't many people in the world like them. Thanks also to Kate, my first landlady, to Dave, Holly, Evie, Tommo, Olly for making my stay in Milton Keynes unexpectedly ace and to the Galactic Groover for selling me the boat. My thanks also to the team at the marina for letting me live there.
My thanks also goes to Wanda Woo and Clare n Jake, my life-supports and cosmic singing buddys and to the Ox and MK-sabs especially Joe and Maggot who have kept Saturdays exciting.

Finally I would like to thank my parents for their encouragement over the years: "education is the most important thing" , and my lovely sisters who write and phone keeping me up to date and providing endless support.

TABLE OF CONTENTS

1. Introduction	**1**
1.1 The significance of the Pan African/Brasiliano orogenic event	1
1.2 Location and geological framework of study area	2
1.3 Previous work	5
1.3.1 Structural studies	7
1.3.2 Metamorphic studies	7
1.3.3 Igneous studies	8
1.3.4 Tectonic studies	9
1.4 Objectives of study	10
1.4.1 Field objectives	11
1.4.2 Laboratory objectives	11
2. Study of field relations in the Santana Metamorphic Belt	**13**
2.1 Introduction	13
2.1.1 Location	13
2.1.2 Previous work	15
2.1.3 Geological mapping	18
2.2 Field relations	19
2.2.1 Methodology	19
2.2.2 Field relations and lithologies	23
2.2.2.1 Encantada Gneisses	23
2.2.2.2 Encantada Schists	26
2.2.2.3 Arroio Arreiao formation	30
2.2.2.4 Cerro dos Bicudos formation	35
2.2.2.5 Cerro da Canberra formation	37
2.2.2.6 Arroio dos Nobres formation	43
2.2.2.7 Red beds	46
3 Deformational history of the Santana Metamorphic Belt	**47**
3.1 Introduction	47
3.2 Previous work	49
3.3 Deformational phases	53
3.3.1 The first phase of deformation	53
3.3.2 The second phase of deformation	56
3.3.3 The third phase of deformation	63
3.3.4 The fourth phase of deformation	69
3.3.5 Post-D4 extension	75
3.4 Summary and discussion	79
4. Metamorphism and P-T studies of the Santana map area	**85**
4.1. Introduction	85
4.2 Metamorphic assemblages and facies	86
4.2.1 Previous work	86
4.2.2 This study	86
4.2.3 Assemblages of stratigraphic units	90
4.3 Relationship between deformation and metamorphism	95
4.3.1 Introduction	95
4.3.2 Metamorphic events	96
4.4. P-T studies	110
4.5 Conclusions	115

5. A study of field relations, deformation and petrology of igneous rocks between Pelotas and Caçapava do Sul 117
5.1 Introduction 117
5.2 Igneous rocks of the Santana Metamorphic Belt 119
5.2.1 Non-granitic igneous rocks of the Santana Metamorphic Belt 119
5.2.2 Granitic rocks of the Santana Metamorphic Belt 123
5.3 Field relations and petrology ofthe Pelotas Batholith 128
5.3.1 Foliated granites 131
5.3.2 Unfoliated granites 137
5.4 Deformational history of the Pelotas Batholith 146
5.4.1 Introduction 146
5.4.2 Dlg Compressional event 149
5.4.3 D2g Mylonitization and Shear zones 149
5.4.4 D3g Extensional faulting 152
5.4.5 Summary of deformation in the Pelotas Batholith 155
5.5 Conclusions 156

6.Geochemistry of the Dom Feliciano belt 161
6.1 Introduction 161
6.1.1 Objectives 162
6.1.2 Granitoid Geochemistry and Petrogenesis 163
6.1.3 Classification 164
6.1.3.2 CLASSIFICATION OF GRANITOIDS 165
6.2 Geochemistry of the Pelotas Batholith 171
6.2.1 Introduction 171
6.2.3 Major element variation 173
6.2.4 Trace element variation 177
6.2.5. Rare Earth Element variation 181
6.2.6 Spidergrams and tectonic setting for the Pelotas Batholith 182

6.3 Geochemistry of the Santana Metamorphic Belt 188
6.3.1 Geochemistry of the non-granitic rocks 188
6.3.2 Granitoids of the Santana Metamorphic Belt 194
6.3.4 Summary 207
6.4 Conclusions and Discussion 207

7 Isotopic studies of the Dom Feliciano Belt 215
7.1 Introduction 215
7.2 Geochronolgy 215
7.2.1 Introduction 215
7.2.2 Geochronology of the Pelotas Batholith 217
7.2.4 Geochronology of the Santana Metamorphic Belt 221
7.2.5 Summary 223

7.3 Isotope geochemistry and petrogenesis 224
7.3.1 Introduction 224
7.3.2 Nd isotope Geochemistry 226
7.3.3 Sr isotope Geochemistry 232
7.3.3.1 SR EVOLUTION 234
7.3.4 Investigation of possible sources of granite magmas 236
7.3.5 Combined Nd and Sr isotope studies 240
7.4 Summary and discussion 242

8.Conclusions 245
8.1 Introduction 245
8.2 Conclusions from field based studies 245
8.3 Structural and Metamorphic History 248
8.4 Geochemistry 250
8.5 Isotopic conclusions 255
8.6 Geological History andtectonic Model 258
8.7 Regional summary of Eastern Brazil 266
8.8 Implications for Precambrian Tectonics 268

References 271

Appendix 281

A. Analytical Techniques for Geochemistry 281
A.1 Sampling and crushing 281
A.2 XRF Determination 281
A.3 Intrumental Neutron Activation Analysis (INNA) 283
A.4 Radiogenic Isotope Analysis 284
A.5 Mass-Spectrometry 285
B. Analytical techniques for metamorphic and structural. studies 287
B. 1 Microprobe Studies 287
B.2 Thermocalc 292
B.3 Stereographic projection 296
C.Geochemical data 298
D. Calculations and Isotope Data 319
E. Geological map of the Santana Metamorphic BELT (FOLD OUT)

List of Figures and Plates

Volume 1

1.1 Location of the Ribeira Belt 2
1.2 Location of the Dom Feliciano Belt 4
1.3 Location of the BR392 road section 6
2.1 Geological units of the Ribeira Belt 14
2.2a Geological Map of the Santana Metamorphic Belt 20
2.2b Legend to map 21
2.3 Geological cross section 22
2.4 Photo of F2 folds in Encantada Gneiss formation 25
2.5 Contact of gneisses with metagabbro 25
2.6 Photos of handspecimens of the Encantada Gneisses 27
2.7 Type section of the Encantada Schist formation 28
2.8 Handspecimen of chlorite schist from the Encantada Schist formation 28
2.9 Conformable relationship of pink mylonite and muscovite schist 32

2.10 Sketch of conformable relationship of Pink Mylonite and muscovite schists 32
2.11 Cleavage of the pink mylonite of the Arroio Arreiao formation 34
2.12 Sketch of 2.11 34
2.13 Topography of the Cerro dos Bicudos quartzite 36
2.14 Outcrops of the Cerro dos Bicudos quartzite 38
2.15a Isoclinal folding in the Cerro da Canberra formation 40
2.15b Sketch of 2.15a 40
2.16 Hand specimens of the Cerro da Canberra formation 42
2.17 The Arroio dos Nobres formation 44
2.18a Cross bedding in the red beds 45
2.18b Pillow Andesites 45

3.1 Structural features of the mapped area 51
3.2 Legend for structural map 52
3.3 Major fold axes in the area 54
3.4 Interpretative cross-sections for folding 55
3.5 Photos of F2 folds 57
3.6 Photos of F2 folds 59
3.7 Phtomicrographs of F2 folds 61
3.8 Equal area plots for S2 62
3.9 F3 folds 64
3.10 Photographs of topography and features of antiform 64
3.11a Photomicrograph of S3 biotite growth 66
3.11b Photomicrograph of S3 amphibole growth 66
3.12 Equal area plot of Arroio Arreiao formation 68
3.13 Photomicrograph of quartz mylonite 68
3.14a Thrusting of quartzite onto breccia 70
3.14b Sketch of thrusting relations 70
3.15a Thrusting in Arroio dos Nobres formation 71
3.15b F4 Interference folds in graphite schists 71
3.16 Photomicrographs of D4 deformation 73
3.17 Equal area plots of the Cerro da Canberra formation 74
3.18 Major normal faults of the Santana Metamorphic Belt 76
3.19 Equal area plot for S3 foliations 77
3.20 Topographic features of fault scarps 78
3.21 Comparison of cross-sections through the Dom Feliciano Belt 80
3.22 Continuation of the Dom Feliciano Belt in Santa Catarina 81
3:23 Fyson's structural model 82

4.1 Isograds of the Santana area (Jost) 87
4.2 Location of metamorphic samples..... 89
4.3a,b. AFM projections for Encantada Schists and Gneisses 91
4.3c AFM projection for Arroio Arreiao formation 93
4.3d,e AFM projection Cerro da Canberra formation 94
4.4 Photomicrograph of Ml garnet growth 100
4.4b Photomicrograph of Ml clinozoisite growth 101
4.5 Photomicrograph of isoclinal F2 folds in granitic gneiss 102
4.6 Photomicrograph of M2 garnet growth in amphibolite 104
4.7 Photomicrograph of M2 garnet growth in Encantada schist 105
4.8 Photomicrograph of M2 amphibole growth 106
4.9a Photomicrograph of D4 shear zones in graphitic schists 108
4.9b Photomicrograph of Ml clinozoisite growth 108
4.10 P-T graphs of metamorphic facies and reaction 109
4.11 Shreinemaker bundle for sample 119 111
4.12 Shreinemaker bundle for sample 134 113
4.13 Model for metamorphism 114

Volume 2

5.1 Igneous rocks of the Dom Felicianao Belt 118
5.2a Photomicrograph of Metagabbro 120
5.2b Pillow andesites at locality 113 120
5.3a Field photo of Santana Granite 122
5.3b Intrusion of red into grey Caçapava Granite 122
5.4 Photomicrograph of Caçapava Granite 126
5.5 Photomicrograph of red Caçapava Granite 126
5.6 Myrmekitic texture in red Caçapava Granite 127
5.7 Geological map and cross-section of the Pelotas Batholith 129
5.8 Legend to geological map 130
5.9a Photo of Cascata Orthogneiss with xenoliths 132
5.9b Intrusion of Migmatitic Orthogneiss into Cascata Orthogneiss 132
5.10a Hand specimen of Cascata Orthogneiss 133
5.10b Photomicrograph of Cascata Orthogneiss 133
5.11a Photo of Pink Granite intruding Migmatite 135
5.11b Close up of above contact 135
5.12 Photomicrographs of Migmatitic Orthogneiss 136
5.13 Photo of Canguçu Phenocrystic Granite 138
5.14 Photos of Capao do Leao Graanite 139
5.15 Photomicrographs of Canguçu Red Granite 141
5.16 Photos of the Cascata Leucogranite 142
5.17 Photomicrographs of Cascata Leucogranite and Pink Granite 144
5.18 Photo of Pegmatites 145
5.19 Structural map of the Pelotas Batholith 147
5.20 Equal area plots from the Peloatas Batholith 148
5.21 Photographs of D3 shear zones 150
5.22 Photos of mylonites 151
5.23 Geological cross-section of the Dom Feliciano Belt 153
5.24 Equal area plots of PB shear zones 154

6.1 Sketch geological section 162
6.2 Streckeisen Classification of Pelotas Batholith (PB) 166
6.3 Streckeisen Classification for Santana Metamorphic Belt (SMB) 167
6.4 Shand classification of Granites 169
6.5 Calk-alkaline classification of granites 170
6.6 Major element variation PB foliated granites 174
6.7 Major element variation PB unfoliated granites 176
6.8 Trace element variation PB foliated granites 178
6.9 Trace element variation PB unfoliated granites 180
6.10 REE plots for PB foliated granites 181
6.11REE plots for PB unfoliated granites 182
6.12 Spidergram for PB foliated granites 183
6.13 Spidergram for PB unfoliated granites 184
6.14 Comparative spidergram for foliated PB granites 185
6.15 Comparative spidergram for unfoliated PB granites 185
6.16 Tectonic discrimination diagram for PB granites 187
6.17 Major element variation for SMB basement 189
6.18 Trace element variation or SMB basement 191
6.19 REE plot SMB basement 192
6.20 Spidergram for metagabbro 193
6.21 Major element variation for SMB granites 195
6.22 Trace element variation for SMB granites 197
6.23 REE plots for SMB granites 199
6.24 Spidergram for Santana Granite 200
6.25 Comparative spidergram for Santana Granite 201
6.26 Comparative spidergram for SMB granites 201
6.27 Comparative spidergram for Campinas Granite 203

6.28 Comparative spidergram for Encruzilhada Granite 203
6.29 Comparative spidergram for the Caçapava Granite 204
6.30 Tectonic discrimination diagram for granites of the Santana Belt 205
6 31 Spatial variation of major element geochemistry of the Dom Feliciano Belt 209
6 32 Spatial variation of trace element geochemistry of the Dom Feliciano Belt 210

7.1 Errorchron for the Cascata Orthogneiss 218
7.2 Errorchron for the Migmatitic Orthogneiss 219
7.3 Isochron for the shear zone 219
7.4 Errorchron for the Quarry Pink Granite 220
7.5 Errorchron for the NW and SE Pink Granites 220
7.6 Errorchron for the Encantada Gneisses 222
7.7 Errorchron for the Caçapava Granite 222
7.8 Relationship of Sm/Nd to silica 227
7.9 Spatial variation of Nd data 229
7.10 εNd vs Age plot 232
7.11 Spatial variation of age and Sr isotope data 233
7.12 Sr evolution diagram 234
7.13 εSr plot comparing to granites of known tectonic setting 236
7.14 Rb-Sr source data 240
7.15 Data from Dom Feliciano Belt on εNd vs εSr plot 241
7.16 Comparison of Dom Feliciano Belt to other belts on εNd vs εSr plot 241
7.17 Comparison of Dom Feliciano Belt to other belts on εNd vs Age plot 243

8.1 Structural and metamorphic features of the Dom Feliciano Belt 249
8.2 Spatial distribution of geochemical data 254
8.3 Spatial distribution of isotopic data 256
8.4 Combined Sr-Nd plot for granites of the Dom Feliciano Belt 258
8.5 Tectonic model for the Dom Feliciano Belt 262
8.6 Cross-sections through the Dom Feliciano Belt 267
8.7 Comparison of the Dom Feliciano Belt with other Pan-African Belts 269

List of tables

2.1 Carvalhos stratigraphy 15
2.2 Stratigraphy of this study 16
2.3 Jost's stratigraphy 17
2.4 Stratigraphy of Machado et al 18
2.5 Stratigraphy of this study in detail 23
3.1 Structural history 50
4.1 Mineral abbreviations 88
4.2 Metamorphic assemblages 90
4.2b Metamorphic events 96
4.3 Relationship between metamorphism and deformation for metapelites 97
4.4 Relationship between metamorphism and deformation for metabasites 98
4.5 Relationship between metamorphism and deformation for gneisses 98
4.6 Relationship between metamorphism and deformation for metagranites 99
5.1 Deformation events of the Pelotas Batholith 156
5.2 Petrological features of the Pelotas Batholith 157
6.1 Geological history of granites from the Dom Feliciano Belt 213
7.1 Previous geochronological data 216
7.2 Geochronological data from this study 223
7.3 Least model Nd ages 228
8.1 Established dates from geochronological studies 255
8.2 Geological History of the Dom Feliciano Belt 260
8.3 Model for Granite evolution 258

CHAPTER ONE

1. Introduction

1.1 The significance of the Pan-African/Brasiliano orogenic event

The process of orogeny incorporates a variety of stages such as deformation, metamorphism and magmatism which contribute to the evolution of continental crust. The Pan-African/Brasiliano orogenic event (650-450m.y.) marks a transition period between Archaean intercratonic tectonic processes and recent plate tectonics. The nature of large scale tectonic processes in the Late Precambrian remains poorly understood but it has been argued that they differ significantly from those of the Phanerozoic (Kroner 1979, Hurley 1972).

Pan-African orogenic belts fall into two types ; firstly high-grade intracratonic belts such as the Damara Belt of central Namibia (Miller 1983, Mc Dermott 1986) where the granitoids were derived from reworked crust with little crustal growth and secondly low-grade ophiolite and granite terrains as in NE Africa (Shackleton 1979, Berhe 1988) and in the Arabian shield (Duyverman et al 1982) where many granitoids appear to represent new crust.

It is the intention of this study to establish the proportion of new crust generated in the Pan-African/Brasiliano orogeny of SE Brazil and to establish the PT conditions and tectonic setting of this event. This information is then collated with field observations to propose a tectonic model which can then be compared with those for the Damara and Arabian Shield to give a more global picture of Late Precambrian tectonic processes.

1.2 Location and geological framework of study area

The Pan-African/Brasiliano Ribeira orogen of SE Brazil (Fig 1.1) is a deeply eroded orogenic belt. Pre-drift reconstructions of Africa and South America indicate that the Ribeira orogen of South Brazil is part of the Damara coastal branch and provides an opportunity to study the relationship between deformation, regional metamorphism and magmatism and to compare this with the contemporaneous Damara orogen (Miller 1983, Mc Dermott 1986).

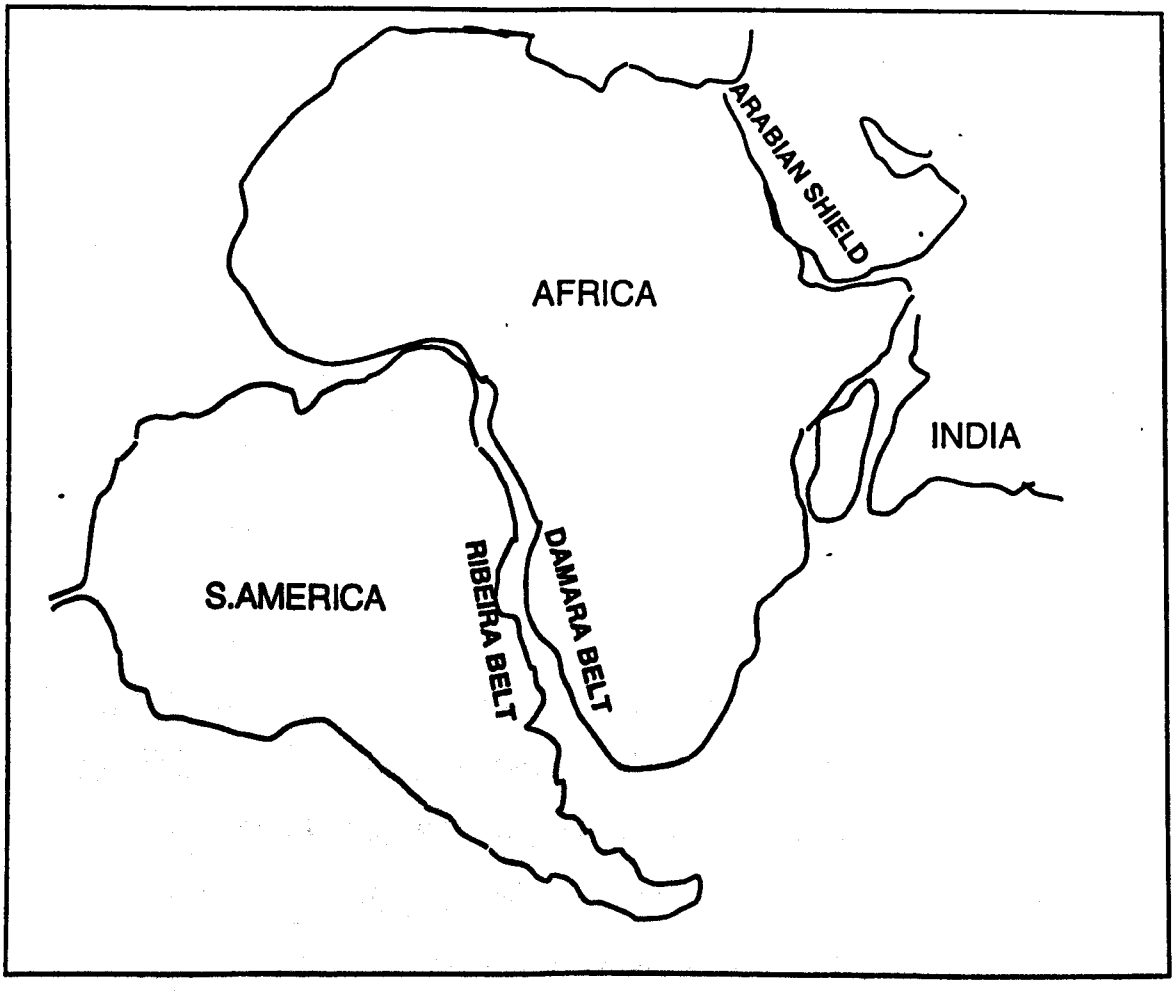

Figure 1.1 Predrift reconstruction showing the location of the Ribeira Belt relative to other Pan-African mobile belts.

The Ribeira Belt is exposed in the SE beneath the late cover of the Parana Basin (fig 1.2) and can be subdivided into two main units; the Rio de la Plata Craton (Almeida et al 1973) and the Dom Feliciano Belt (Fragoso Cesar 1980). The first consists of an old granulite-migmatite terrane of Archaean to Lower Proterozoic age which then acted as a stable foreland in the evolution of the Dom Feliciano mobile belt of Upper Proterozoic age.

The Dom Feliciano Belt belt is 150 km wide, ~1000 km long and stretches from Santa Catarina through Rio Grande Do Sul (this study) to Uruguay (fig. 1.2) and has a main structural fabric oriented NNE-SSW with a dominant vergence to the NW. It can be subdivided into two major units in Rio Grande Do Sul state (fig. 1.3); the Pelotas Batholith, in the SE parallel to the coast line, is a predominantly granitic belt and secondly the Santana Metamorphic Belt which lies to the NW faulted against the Pelotas Batholith and is a greenschist/amphibolite facies metamorphic belt with basement inliers intruded by post-tectonic granites.

The extreme climatic conditions of SE Brazil causes laterization and rapid weathering particularly of pelitic schists and granites and the only exposures are along recent road cuttings, in quarries and river sections. However the BR392 highway, running through the area perpendicular to the main foliation, provides a fresh cross sectional view through this orogenic belt (fig.1.3) and the major study is concentrated along this section.

In the region of the BR392 the faulted contact between these two belts appears to have undergone late extension to form a basin with flat-lying red beds and andesite/rhyolite flows. The relationship between the two belts is explored in terms of their structural, metamorphic, chemical and isotopic evolution in order to propose a tectonic model for the area.

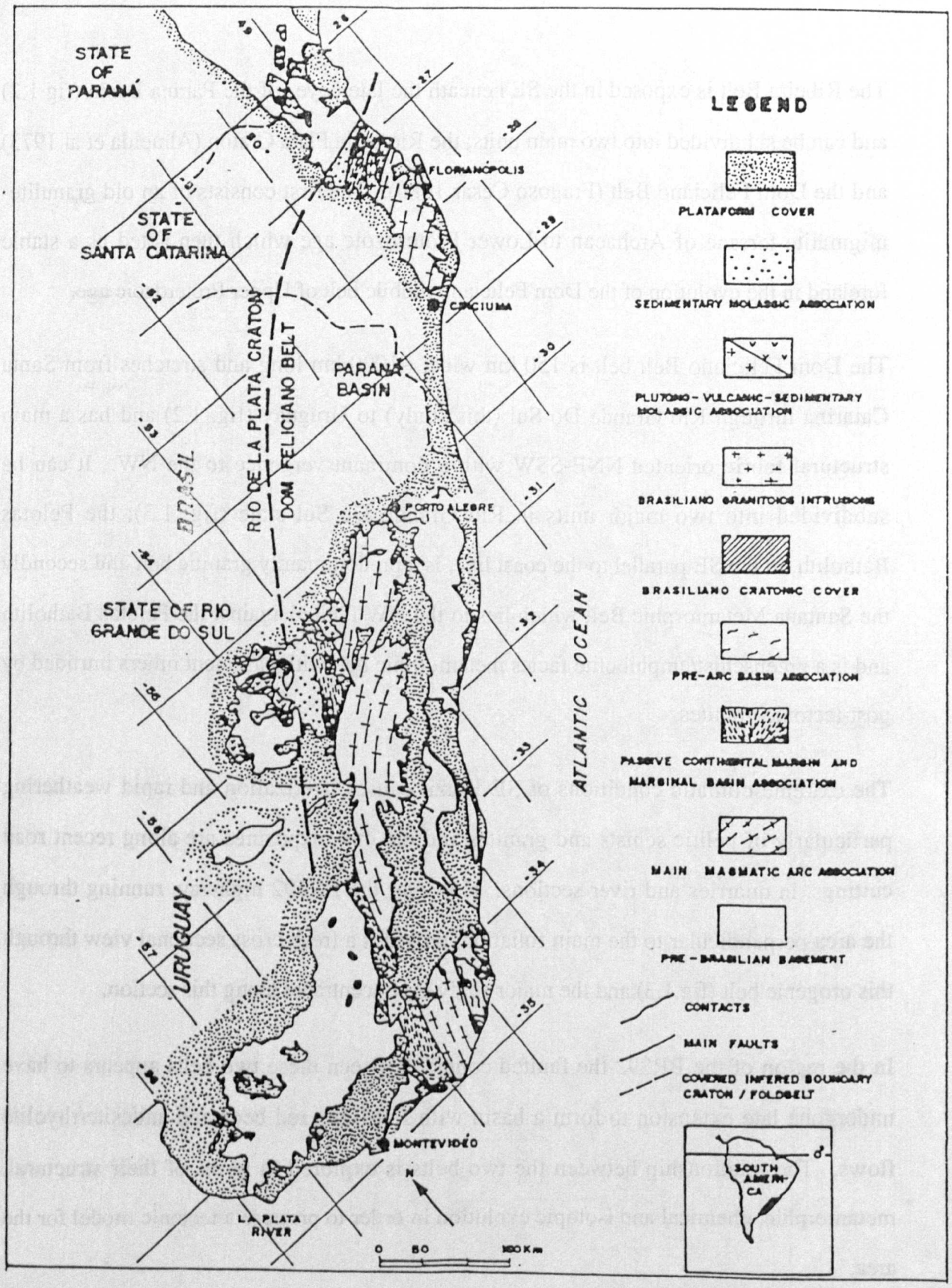

Figure 1.2 Major geological units of Rio Grande Do Sul

The rocks of the Dom Feliciano Belt provide a geological record from the Early Proterozoic (Encantada Gneisses) up until the Early Paleozoic (Triassic red beds). The stratigraphy and field relations of the Santana Metamorphic Belt are discussed in detail in chapter 2 in the context of a detailed geological map and cross section. The field relations of the granitoids intruding both the Pelotas Batholith and the Santana Metamorphic Belt are discussed in chapter 5 along with the structural history of the Pelotas Batholith. The Brasiliano orogeny caused penetrative deformation and metamorphism in the entire Ribeira belt and this was accompanied by voluminous intrusion of syn and post-orogenic granite.

1.3 Previous work

Published geological studies from the Dom Feliciano Belt date from the 1930's (Carvalho 1932) with a geological study of Rio Grande do Sul (Chapter 2). General reconnaissance studies by Ribeira et al (1966), Almeida et al (1973), Fragoso Cesar (1980) and more recently a tectonic comparison with the Damara Belt (Porada 1988) have been undertaken. More detailed studies have been carried out in the Santana Metamorphic Belt by Jost (1981) and geochronological studies of granitoids of the area by Cordani et al (1974) and Soliani (1986). Structural relations have recently been investigated by Machado et al (in press) and Mantovani et al (pers comm) produced a gravimetric survey through the area. Basei (1985) has undertaken detailed research in the Santa Catarina portion of the Dom Feliciano Belt. There have been numerous other workers in the area and these are discussed in the next section and the relevant chapters.

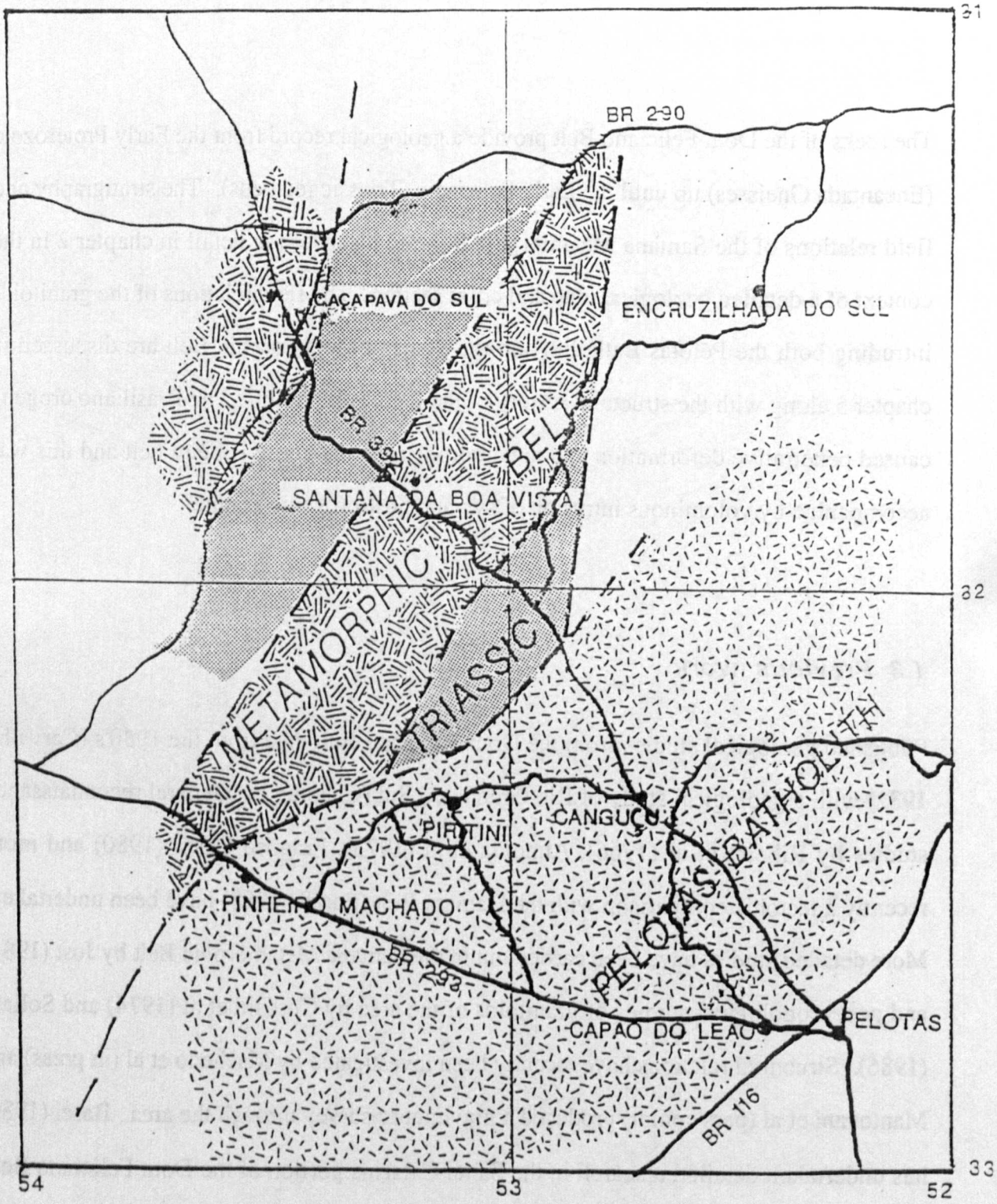

Figure 1.3 Location of study area and road section.

1.3.1 Structural Studies

The structural history of the Dom Feliciano Belt is summarized by Porada (1988) who recognized three major deformational episodes which are generally consistent with this study. In Uruguay, Salda et al (1988) recognized two main tectonic phases the first was NNE-SSW orientated with isoclinal folding and the second produced dome and basin WNW-ESE pattern and strike-slip shearing and thrusting parallel to the first axial planes. Basei (1985) recognized four phases of deformation in the Brusque belt of Santa Catarina to the NE and this belt is also thought to be part of the Dom Feliciano Belt (figure 2.1).

1.3.2 Metamorphism

Previous workers (Tessari and Picada 1966, Ribeiro et al 1966, Picada and Pinto 1966) recorded the metamorphic facies for the schists as greenschist to lower amphibolite facies and sillimanite facies for the Encantada Gneisses. Torquato and Cordani (1981) placed the main period of regional metamorphism of the Ribeira belt at 700-650 m.y. and asssociated it with the D3 collision event. Jost (1981) suggested that metamorphism in the Santana Metamorphic Belt (Tijucas Fold Belt) was low to moderate in the cover units and also proposed that metamorphic pressures increase with the age of the schists indicating there was no inversion of the stratigraphy. Jost and Bittencourt (1980) described an increase in grade from the supracrustals to the basement gneisses with a metamorphic jump betweeen the two. These authors proposed a pressure of 2kb at a temperature of 580°C within the schists. This study, however, disagrees with this pressure (chapter 4) and also found no evidence of a metamorphic jump.

1.3.3 Igneous Studies

Granitoids are by far the most voluminous magma type exposed in the Dom Feliciano Belt and this study concentrates on the origin of granitic magmatism rather than on other less voluminous magma types. Previous studies have been undertaken on the granitoids of the Dom Feliciano Belt by Jost (1981) who undertook some preliminary geochemistry on the Santana Metamorphic Belt granites. Geochronological studies have been undertaken by Cordani et al (1974) and Soliani (1986) and these are discussed in chapter 7. Some preliminary Nd isotope results of Mantovani et al (1987) on composite samples of granites from the Dom Feliciano Belt suggest crustal reworking.

Wernicke et al (1978) noticed that the abundance of granitoids decreases from east to west with the occurrence of large granitic areas in the east (the Pelotas Batholith) where granites form a continuous strip (fig 1.2) whereas in the Santana Metamorphic Belt they only occur as small isolated bodies. The size of the granitic bodies also decreases from east to west. They also suggested that the Encruzilhada Granite has been displaced from a more northerly position along the dextral fault zone separating the two belts which would explain its unique geochemical and isotopic characteristics (chapter 6&7). Detailed major element, trace element and isotopic geochemistry of the granites had however, not been undertaken previous to this study. This aspect of the geology is discussed in detail in chapters 6 and 7.

Studies in the Dom Feliciano Belt in Uruguay by Salda et al (1988) also recognize three phases of magma genesis with pre-orogenic activity occurring at 900m.y., with gneiss and migmatite formation at 675-575m.y., syn-tectonic granites intruded between 590-535m.y. and post-tectonic granites between 550-500m.y.

For the purpose of discussion the granites intruding the Santana Metamorphic Belt are discussed separately from those of the Pelotas Batholith.

1.3.4 Tectonic studies

Shackleton (1969) argued in favour of an essentially "in-situ" evolution of the fold belts of the Damara-Ribeira Pan-African orogen and this view is supported by Martin and Porada (1977), Hasui et al (1975) and Wernick and Hasui (1978). Evidence supporting this conclusion includes the occurrence of older reworked ensialic basement nuclei as domes within the mobile belts, the oblique superposition of late Precambrian belts on older belts and the termination of fold regions against cratonic areas, low to moderate pressure metamorphism, late precambrian granite intrusions and the lack of ophiolites and melanges. This model is supported by Mc Dermott (1986) in his study of the evolution of the Damara Belt who suggested that there is no evidence for subduction in the Damara Belt and that assymetric rifting and asthenopheric upwelling along with subsequent collision provide the mechanism and conditions necessary for metamorphism and magma genesis .

Ribeiro et al (1978) argued in favour of plate movements for the formation of the Ribeira orogen based on the presence of magmatic arcs, the presence of basic rocks and the geometry of the fold belt. Jost (1981) proposed a model for the evolution of the Santana Metamorphic Belt which suggested that it was a deep portion of an orogenic belt eroded to a level where reworked basement has beeen exposed. He proposed that after early rifting of an ensialic basement, thick sedimentation was followed by a compression phase with subduction and underplating, triggering magmatism and culminating in continental collision. A late orogenic phase occured during the Late Precambrian to Early Paleozoic with refolding and shear zones with post-tectonic magmatic activity and deposition of a late molasse.

Soliani (1986), from his study of the geochronology of Rio Grande do Sul, suggested a 1000-850 m.y. pre-orogenic phase with possible back-arc rifting and then extension. He also suggested that initial magma genesis occurred at 800m.y. in response to subduction with contemporaneous back-arc spreading. He then proposed subduction accompanied by felsic volcanic eruption and the intrusion of granodiorites (650-550m.y.). This was followed by collision with D3 syn orogenic granites and thrusting, followed by the intrusion of unfoliated granites between 500-450m.y. Basei (1985) proposed a model for the Santa Catarina portion of the orogen with compression occuring between 700-600m.y. with A-type subduction and intrusion of syn-tectonic granites, then thrusting and underplating between 600-500m.y. accompanied by the intrusion of post-tectonic granites.

In the Porada (1988) model the Upper Proterozoic Pan-African belts of Africa and Southern Brazil are assumed to have evolved from continental rifts formed 1100-1000 m.y. ago forming a proto-Atlantic ocean. Closure was thought to have taken place in two episodes with the ocean closing between 900 and 750m.y.. NW subduction under Brazil was thought to have occurred between 750-500m.y. with SE transport in the Damara Belt. There is a certain degree of conflict between these models which hopefully will be resolved by this study.

1.4 Objectives of study

The main objective of this study was to identify the nature of orogenic processes within Southern Brazil during the Pan-African/Brasiliano event and to interpret the tectonic evolution of the region in the context of Pan-African tectonics in Southern Africa. However, there are several specific field and lab-based objectives that contributed to this end.

1.4.1 Field objectives

The main objectives of the field study were to:

1. Produce a geological map and cross-section for the Santana Metamorphic Belt in the region of Santana Da Boa Vista and thereby establish a stratigraphy, a sequence of structural, metamorphic and magmatic events. From this evidence, a geological history is proposed for this area and a tectonic model is suggested which is consistent with field observations.

2. To map the granites of the Pelotas Batholith (chapter 5), to establish their interrelationship in the field and to construct a basic framework to constrain the geochemical and geochronological data.

2. To collect metamorphic samples for P,T studies from the Santana Metamorphic Belt and to collect granite samples for geochemical analysis along a section from SE to NW through both belts to identify spatial geochemical variation. Samples were also collected for geochronological purposes from quarries.

1.4.2 Laboratory objectives

1. To classify the granitoids geochemically using major, trace and isotope geochemistry and to establish how this relates to time using geochronological studies and tectonic environment.

2. To establish the inter-relationship of the granites in each belt, to suggest a tectonic setting and process of formation and to compare and contrast granitoids of the two belts to establish whether they represent two distinct terranes using geochemical and isotope studies.

3. To use Sr and Nd isotopes combined with trace element geochemistry to establish the possible sources of the granites and to distinguish crustal reworking from crustal growth during this orogenic event.

4. To establish the peak conditons (pressure and temperature) for metamorphism in the Santana Metamorphic Belt using microprobe data and the THERMOCALC program (Chapter 4), to determine the depth of burial and to estimate the amount of thickening of the crust as a result of the Brasiliano orogenic event.

CHAPTER TWO

2. Study of field relations in the Santana Metamorphic Belt.

2.1. Introduction

2.1.1 Location

The Pan-African/Brasiliano terrane in south Brazil is known as the Dom Feliciano Belt (Fragoso Cesar 1980) and is of Upper Proterozoic age. This belt runs through the eastern parts of the states of Santa Catarina and Rio Grande do Sul as well as through Uruguay (see Fig 2.1.). It is approximately 1100 km long, 150 km wide and trends NE-SW parallel to the coast line.

The Dom Feliciano belt is separated from the Atlantic Ocean by Tertiary to Recent sediments. To the west it is bounded by the Rio de la plata Craton (Almeida et al. 1976), which is a granulite migmatite terrane of Archaean to Lower Proterozoic age. This basement formed a foreland to the Dom Feliciano belt during the Brasiliano orogenic event. The continuity of the belt is interrupted by the Parana basin in the northern part of Rio Grande do Sul where it is covered by Jurassic sediments and the Cretaceous basaltic and rhyolitic lavas of the Parana Basin (Wernick et al. 1978). Post orogenic molasse sequences with andesitic and rhyolitic lava flows separate this belt from the Rio de la Plata Craton in the region studied.

The Dom Feliciano Belt of Rio Grande do Sul is composed of two major units; a granite - migmatite belt and a greenschist/amphibolite facies metamorphic belt (Fig 2.1.). The area of the metamorphic belt mapped in detail in this study is referred to as the Santana Metamorphic Belt and the granite belt is known as the Pelotas Batholith (Chapter 5).

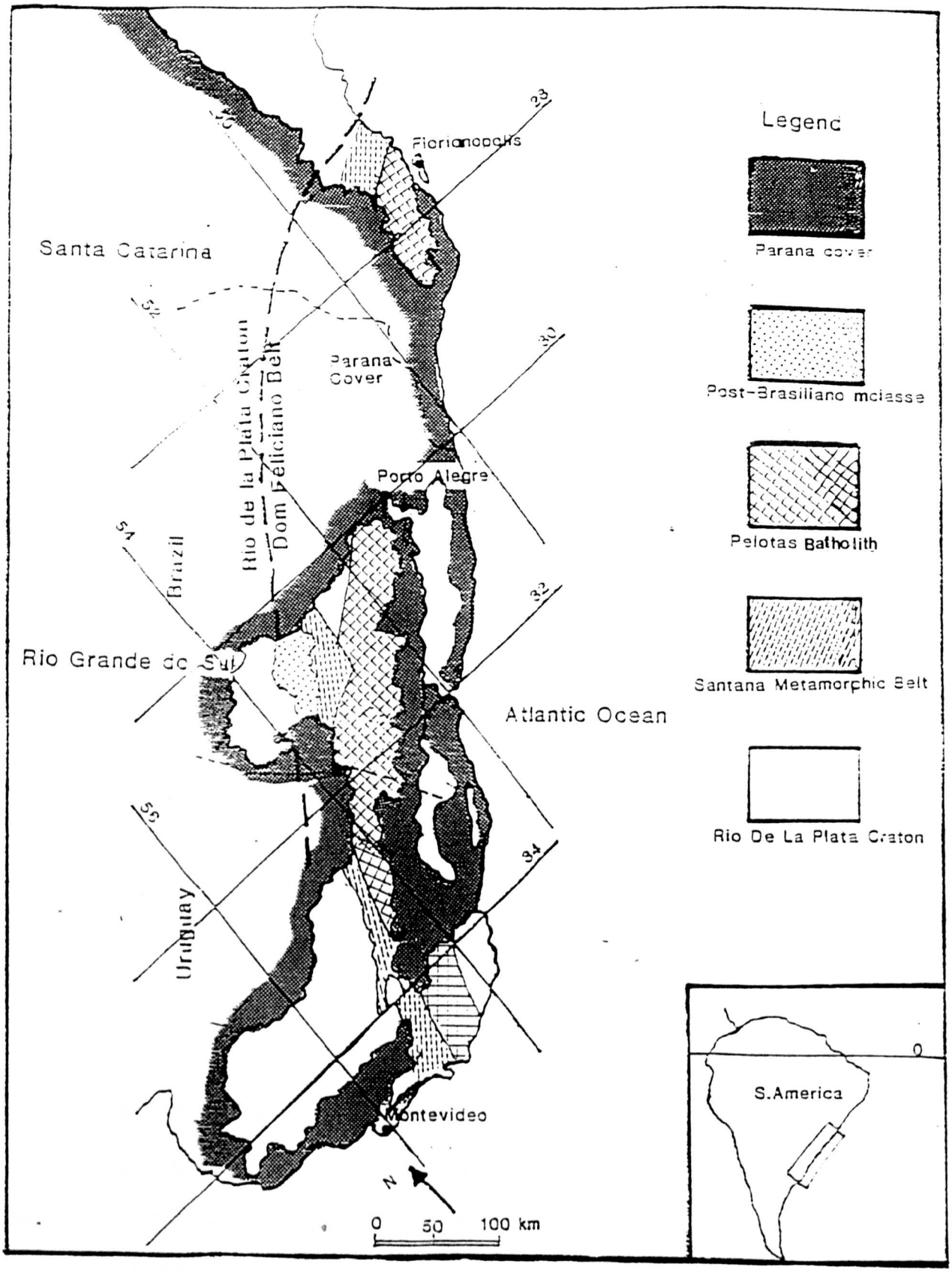

Figure 2.1 Major geological units of Rio Grande Do Sul

The major structural trend within these belts is NNE-SSW which corresponds to the orientation of the contact between the two belts and this stuctural trend is consistent with the axial planes of D3 folding. The dominant vergence of folding is to the northwest. The sequence of structural events is described in detail in chapter 3 and is summarized in table 3.1.

2.1.2 Previous work

The earliest field study made in this area was undertaken by Carvalho in 1932 in his reconnaissance map of the state of Rio Grande do Sul and his stratigraphic column is illustrated in table 2.1.

Carvalho 1932		
Quaternary		
Triassic	volcanics	andesites rhyolites
Permian	Tubarao formation	arenites muds conglomerates
Silurian	Camaquan series	red sandstones mudstones conglomerates
Eo-Paleozoic	Porongos series	marble schist quartzite
Archaean	Crystalline complex	mica schist granite gneiss

Table 2.1

He mapped a crystalline complex which he defined as Archaean, composed of gneiss, muscovite schist and granite, overlain by the Porongos series which he called Eo-Paleozoic, of quartzite, mica schist, marble and phyllite. This is overlain by conglomerates, sandstones and mudstones of Silurian age, and above these are Permian sands and muds and then Triassic volcanics. This study identified a similar sequence of rock types but subdivides the basement and the Porongos group and suggests that the Porongos group is Proterozoic in age as it is deformed by the Brasiliano orogenic event of 750-450 m.y. The stratigraphy used in this study is summarized below in table 2.2 and a more detailed version of this table is given in section 2.2.1 on field relations.

Quaternary		
Permo-Triassic	volcanics red beds	
Eo-Paleozoic	Arroio dos Nobres formatioion	mollasse
Late Proterozoic	Porongos series	metamorphics
Early Proterozoic	Basement	Encantadagneisses

Table 2.2 Stratigraphy established by this study.

The metamorphic schist belt was mapped by Jost (1981), but field data presented here suggests some discrepancy with his mapped units and structural interpretation. He defined three major units ; the Encantada Gneisses which were originally defined by Tessari and Picada in 1966; the Cerro dos Madeiras formation composed of quartzites and arenites and the Cerro da Arvore complex which he subdivided into five tectono-stratigraphic units (see table in fig 2.3) .

Whilst I agree with the definition of the Encantada Gneisses, I disagree with the subdivisions of the Cerro dos Madeiras group and the Cerro da Arvore complex on the grounds that there is no description given of the units in the field and thus it is impossible to find Jost's mappable units for the purpose of more detailed study. I have therefore reconstructed a stratigraphy based on lithologies that were distinctive in the field and correlatable across the area.

Jost 1981		
Paleozoic	Guiritas formation Arroio dos Nobres	fluviatile clastics siltstones arkoses conglomerates
Precambrian Cerro da Arvore complex	CerrodaaAlemao Arroio Arreiao schist Cerro Canberra Rincao do Marahao Cerro do Facao	metapelites, mica schist, graphite schist, quartzite, marble, meta . dacites, carbonates
Cerro dos Madeiras fm	Irapuazinho Arroio Olaria Arroio dos Neves	marbles quartzites meta arkoses,quartzites amphibolites
Encantada Gneisses		quartzofeldspathic gneisses amphibolitesquartzite

Table 2.3 showing Jost's (1981) proposed stratigraphy

A more recent study of the area around Santana da Boa Vista (along the BR392) has been undertaken by Machado et al. (1987) who defined three major units; the Encantada Gneisses, the Porongos suite, thought to be a greenstone belt and a molassic cover. Their stratigraphy along with his correlation of units across the Dom Feliciano belt is shown in fig 2.4.

Machado et al			
	Santa Catarina	Rio grande do Sul	Uruguai
Mollasse	Itajai group	Camaqua group	Barriga Negra fm
Supracrustals	Brusque supergroup	Porongos group	Lavallegasupracrustals
Gneisses	Itapema gneiss	Encantada gneiss	"Basement"gneisses

Table 2.4

2.1.3 Geological mapping

With the continuing advancement of highly technical equipment, it is often easy to forget that geology is ultimately concerned with the interrelationships of naturally formed rocks with the processes that form them, in order to understand how the Earth behaves and whether these processes have changed with time. Often models proposed based on analysis of rock powders are inconsistent with field and structural observations of the rocks in their natural environment. The combination of field studies and laboratory analysis can lead to an overall view with tighter constraints on the proposed geological models.

Geological mapping is the method by which a three dimensional picture of the relationships of rock units can be understood and communicated. By observing the relationship of one unit to another in the Santana Metamorphic Belt, it is possible to construct a geological history with a view to proposing a tectonic model for this complex metamorphic belt. Relationships are studied by observing cross cutting features on an outcrop scale and overstepping relationships on a regional scale. Geological contacts may be the result of an original sedimentary unconformity caused by erosion of underlying deformed rocks, an igneous intusion or a result of faulting superimposing two originally unrelated rock types.

Careful geological mapping and section construction can provide evidence for the causes of such disconformities and thereby provide a framework in which to undertake more detailed studies such as deformation, metamorphism and geochemistry.

2.2 Field relations

2.2.1 Methodology

This section refers to the geological map and cross-sections of figures 2.2 and 2.3. and localities mentioned in the text are also given in figure 2.2 and in appendix E. Geological mapping was undertaken over a period of three months during 1986 and 1987 on a scale of 1:50 000 using base maps produced by a military survey (Minesterio do Agricultura). The squares on the geological map in figure 2.2 and Appendix E represent $4km^2$.

As good exposure is confined to road cuttings and stream sections, studies were concentrated along the recently cut road section of the BR 392 and other roads around the town of Santana Da Boa Vista in the metamorphic belt. Structural data is presented in detail in chapter 3 and Appendix B.

This region has undergone extensive weathering and correlation of mappable units can at times be difficult, although the presence of distinctive marker bands such as quartzite enables structural trends to be mapped out. The spatial location, relative ages and relationship of the map units will be described in the following section. A summary of the stratigraphy is given in table 2.5.

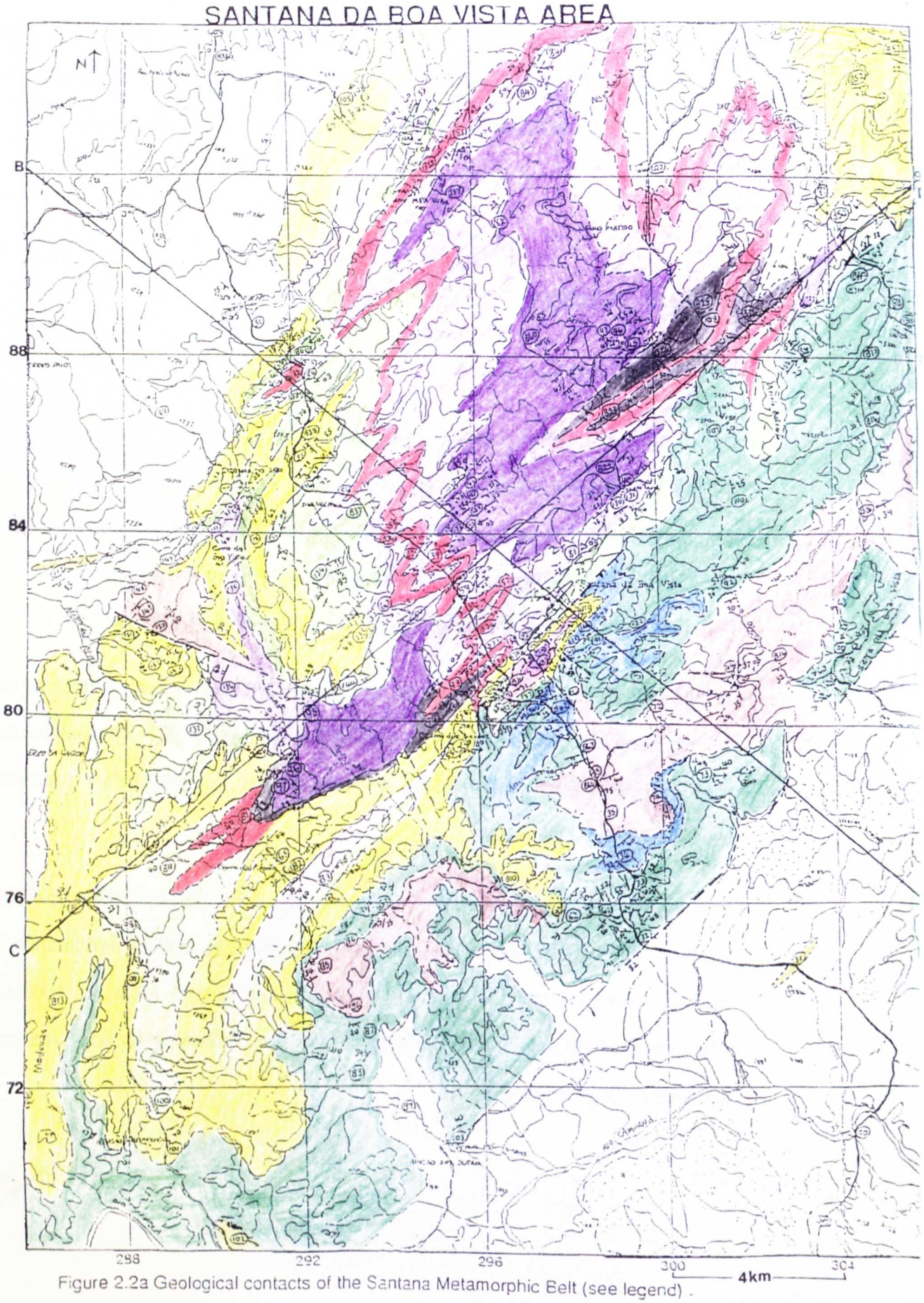

Figure 2.2a Geological contacts of the Santana Metamorphic Belt (see legend) .

SEDIMENTARY ROCKS

Red Beds	Canelarias/Guiritas Formation	Triassic
Red and green conglomerates, sanstones,mudstones	Arroio dos NobresFormation	Early Palaeozoic

METAMORPHIC ROCKS (Early Proterozoic-Brasiliano)

Graphitic schists with rhyolites and marble bands	Cerro da Canberra Formation	PORONGOS SERIES
Thick white pure quartzites	Cerro dos Bicudos Formation	
Muscovite schists with interbanded sandstones from granitic source (g)	Arroio Arreiao Formation	
Chlorite schists, biotite schists, amphibolites and minor quartzites	Encantada Schists	
Biotite quartzofelspathic gneisses, granitic gneisses and amphibolites	Encantada Gneisses	

IGNEOUS ROCKS

Extrusive

Pillow Andesites interbedded with ?Triassic red beds

?Parana Rhyolites

Intrusive Rocks

Santana Granite Pre-Brasiliano~800Ma

Metagabbro (hornblendite)

KEY TO GEOLOGICAL SYMBOLS

- Observed non-tectonic contact (with orientation indicated on down-dip side)
- Inferred non-tectonic contact
- Observed normal fault contact (orientation of fault-plane indicated on down-thrown side)
- Inferred normal fault contact
- Observed thrust fault contact (orientation of fault-plane indicated on up-thrown side)
- Inferred thrust fault contact
- Bedding
- Observed orientation of S2 schistosity in metamorphic rocl (dip and direction of, indicated)
- Observed orientation of S3 cleavage (in fault planes, shear zones etc: dip and direction of, indicated)
- Plunge of fold hinges (dip and direction of, indicated)
- Plunge of lineation (dip and direction of, indicated)
- Younging direction
- Jointing (dip and direction of, indicated)
- Dykes

Figure 2.2b Legend to geological map of the Santana Da Boa Vista map area.

Figure 2.3 Geological cross-sections through the Santana Metamorphic Belt.

This study

Quaternary			
Permo-Triassic		volcanics red beds	andesites rhyolites redarenites red muds conglomerate
Eo-Palaeozoic		Arroio dos Nobres formation	red sandstones mudstones conglomerate
Late Proterozoic	Porongos series	Cerro da Canberra formation Cerro dos Bicudos formation Arroio Arreiao formation Encantada Schists	marble graphite schist Quartzite musc schist pink mylonites schists mylonitic granite
Proterozoic	*Basement*	*Encantada Gneisses*	gneisses amphibolite

Table 2.5.

2.2.2 Field relations and lithologies

The locality numbers given in this section refer to the map of figure 2.2 and also represent the sample numbers allocated in the field. Grid references are given when a locality is first mentioned.

2.2.2.1 ENCANTADA GNEISSES

A.Field relations

These are the oldest rocks exposed in the area and have been dated as Proterozoic at ~2000 m.y by Cordani et al (1974) and by this study at 2030±72 m.y. (Chapter 7). These Proterozoic banded gneisses form a complexly folded body in the core of a domal

structure with a NW-SE trend (GR 010920-890780) located to the northwest of Santana da Boa Vista. They show three phases of folding and evidence of cataclastic deformation. Their structural features are described in more detail in chapter 3.

Type sections of this unit are exposed in the river at locality 40, Passo do Olaria (990852) and locality 45, Passo do Moinho (995882) in figure 2.2. At locality 45 the main foliation of the gneisses is cross cut by granitic sheets and quartz veins (see fig.2.4). At locality B27 (022895) gneisses are in contact with a metamorphosed gabbro and the Santana Granite which cross cut the gneisses as sills (fig.2.5). The gneisses are also exposed in the down faulted portion of the same unit SW of Cerro dos Bicudos. At locality 93 (954806), the gneisses are in contact with granitic gneiss and at 146 (920802), quartzites overlie the gneisses. From the map and cross section it can be seen that the gneisses are structurally and stratigraphically at the base of the sequence and thus we have no indication of their thickness. They are thought by Jost 1981 to represent an Archaean craton made up of high grade metamorphic rocks retrograded by cataclastic deformation. However, this study has dated them as Lower Proterozoic and this will be discussed in the light of other evidence in chapter 8.

B. Lithologies

The Encantada Gneisses are mainly quartzofeldspathic gneisses with granitic gneisses and amphibolite lenses. The most common lithology is a dark grey , medium grained gneiss banded on a mm scale. The leucocratic bands are quartzofeldspathic and the melanocratic bands are mainly biotite with occasional boudinaged feldspar porphyroblasts (fig.2.6) .The boudinage may be evidence of cataclastic deformation.

The second most common lithology is granitic gneiss which is more homogeneous in texture and reddish pink in colour. It is represented by samples 59A (946823) and 45B (995882) (figure 2.6). These gneisses probably represent a metamorphosed sedimentary sequence with later acidic intrusions and quartz veining. There are also amphibolitic lenses which may have been basic sills.

Figure 2.4 Isoclinal folds of quartz veins within the Encantada Gneiss formation looking to 140º.

Figure 2.5 The contact of the Encantada Gneisses with the Metagabbro looking to 184º.

Gneiss samples have been studied in thin section and all of them show evidence of refolded folds forming discontinuous lenses spaced at 2-4 mm intervals. Samples 78d (910840) and 142 (950849) are representative of the biotite quartzofeldspathic gneisses. They both have pelitic lenses describing the folds and these are composed of aligned biotite and chlorite with opaques present in sample 142 and muscovite in sample 78d. The micas wrap around boudinaged lenses which are composed of recrystallized quartz and some plagioclase. Photomicrographs are presented in chapter 3.

The granitic gneisses are represented by sample 93 (954806) which has refolded folds and is banded on a 2mm scale. These have lenses of granitic composition composed of plagioclase, alkali feldspar, quartz and slightly aligned biotite and chlorite. These are separated by lenses of recrystallized quartz.

The amphibolitic gneisses are represented by samples 96 (914790) and 120 (976808). The former is dark green in colour showing some evidence of foliation but with some areas retaining their igneous texture. They are coarse grained with two phases of biotite growth; one phase follows the foliation, the second cross cuts it. Garnet is present and post dates the first foliation. Primary feldspars are replaced by biotite. There is also recrystallized quartz present in thin lenses.

2.2.2.2 ENCANTADA SCHISTS

A. Field relations

This unit is structurally above the Encantada Gneisses and is apparently conformable on them. It crops out in a complexly folded pattern related to that of the gneisses in the region NW of Santana . Whether or not this unit is stratigraphically conformable on the gneisses is a matter of debate. Fewer phases of folding are observable in this formation (there is no evidence of D1) which suggests either that the schistose texture has obliterated some of the folds observed in the gneisses, or that the schists may have undergone less phases of deformation than the gneisses.

Figure 2.6a Handspecimen of a biotite gneiss of the Encantada Gneiss formation.

Figure 2.6b Handspecimen of a granitic gneiss from the Encantada Gneiss formation.

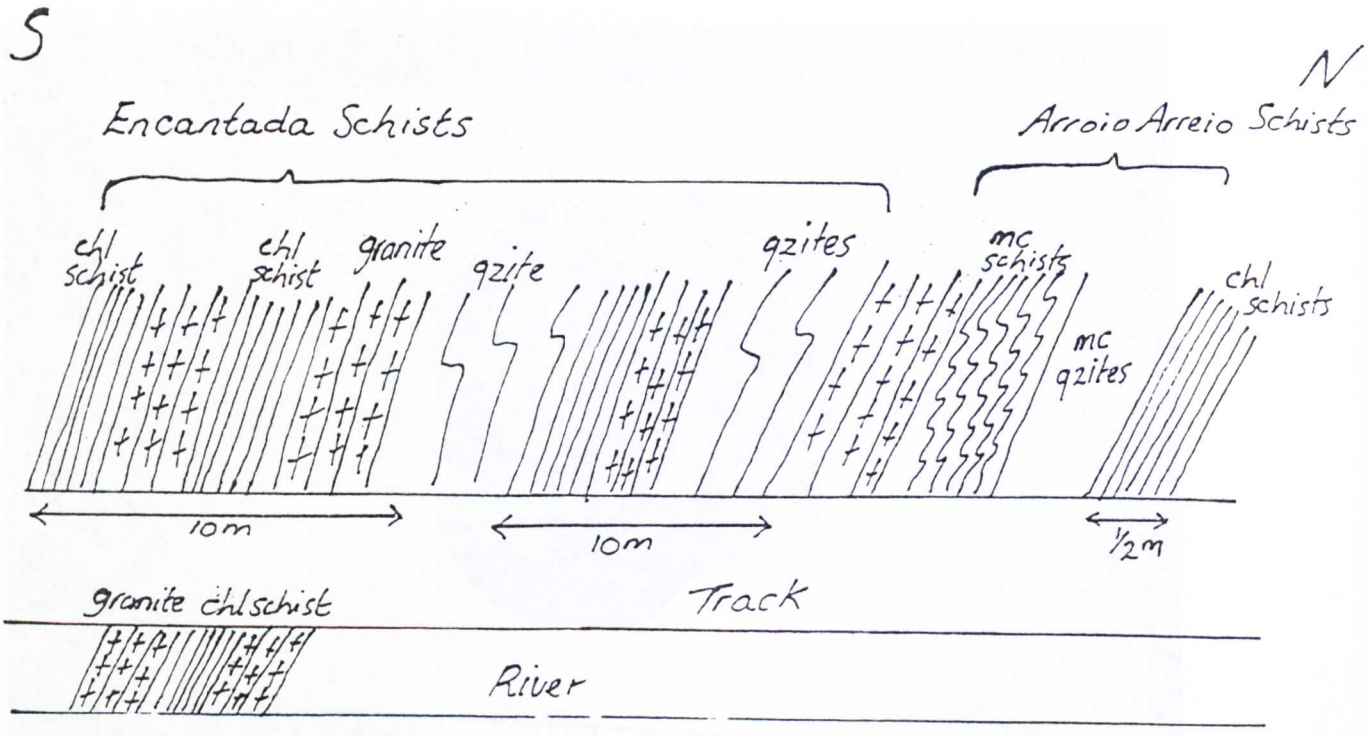

Figure 2.7 Type section of the Encantada Schist formation from locality 117.

Figure 2.8 Hand specimen of a chlorite schist from the Encantada Schist formation.

There are mylonitic granites intruding this formation which have been dated at ~800 m.y by Soliano (1986) (chapter 7) which places a minimum constraint on the age of the schists. On the map this formation is coloured pale purple and type sections occur at localities 117 (970806) below Santana and localites B40 (918879) and 58 (958824) along the BR392 section. The formation is composed of interbanded pale green biotite schists, mylonitic granites and thin quartzite bands. Figure 2.7 shows the interrelationship of the various members of the formation as seen at locality 117. The contact between this unit and the Encantada Gneisses can be observed at this locality where biotite schists are structurally concordant on amphibolites. At other localities the contact is obscured by extensive weathering. At locality 146 , the schists are unconformably overlain by the Cerro dos Bicudos formation (see fig 2.2). The granite and gabbro bands are discordant to the schists and quartzites of the formation and often obscure the contact between this unit and the Arroio Arreiao formation. This is seen at locality 83 (977943). The thickness of the formation is difficult to ascertain since each unit is repeated as a result of tight isoclinal folding.

B. Lithologies

a.Biotite and Chlorite schists

The schists of this formation are quite distinctive in appearance. They are pale green in colour with a marked schistosity regularly interspaced at 2mm intervals with pink feldspathic bands and porphyroblasts (fig.2.8). The schistosity represents an axial plane to a F2 isoclinal folding event (see section 2.3). The green layers are composed of green biotite, some chlorite and muscovite and these wrap around boudins of recrystallized quartz and feldspar. The ratio of biotite to chlorite changes in different samples and epidote is present in the more chlorite rich samples. The metamorphic grade of these schists is upper greenschist facies (see chapter 4).

b.Quartzites

Quartzites associated with this unit are rare and form thin distinctive bands of .5m thickness. A type example of this unit is found at locality 6 (see photos,sample and outcrop).They are rusty brown, homogeneous pure quartz with a sugary texture. There are strong cleavage planes at 3cm intervals.

c. Granites

Both the granites and gabbro will be described in more detail in chapter 5. A representative sample of the granite B36 (939842) still retains some of its granitic texture and is pink in colour and coarse grained but the mafic minerals show some alignment forming a schistosity. In cross section it can be seen that the quartz forms recrystallized rods.

d. Gabbro

Although it retains the texture and dark green colour of a gabbro this rock is in fact an amphibolite in terms of its mineralogy. It is represented by sample 94 (953800) and its spatial distribution is described in chapter 5.

2.2.2.3. ARROIO ARREIAO FORMATION

A.Field relations

This formation is composed of distinctive crenulated muscovite schists with thin quartzite bands, a pink mylonitic rock and thin bands of biotitic schist. It lies structurally above the Encantada Schists but its precise relationship to them is not established from field relations. Metamorphism and deformation have obscured the original stratigraphic relationships.

The complex tight fold patterns affecting the rocks makes unconformities difficult to recognize at some localities. From the map and cross-section it can be observed that this formation follows the same structural patterns as the Encantada Schists and was probably deformed during the same orogenic event. The Arroio Arreiao formation crops out as the cores of synclinal structures within the Encantada Dome NW of Santana. It is coloured pale green and pale pink on the map denoting the muscovite schists and pink mylonite respectively. At locality 106 (942926) the relationship of the two members of this formation can be observed with the pink mylonite younger than and conformable on the muscovite schists (figure 2.9,10).

Type sections occur at localities B32 (973799) and 106 (942926) in the NW of the Santana Metamorphic Belt where it is in contact with the Cerro dos Bicudos quartzite and granitic gneiss, and locality B3 (923763) where pink mylonites grade up into quartzites. At locality B32 on the road the complicated interfolding of this unit can be observed making the apparent thickness much greater than the true thickness.

B.Lithologies

a.Crenulated mica schists

The most distinctive lithology of this formation is a strongly crenulated muscovite schist, pinky white in colour composed of mainly muscovite, some quartz and biotite and rare garnets, depending on the metamorphic grade. This unit is interbanded with 0.5m thick distinctive laminated brown and white quartzite bands with a marked cleavage (figs 2.10).

Figure 2.9. Conformable relationship of the Pink Mylonite and Muscovite Schists of the Arroio Arreiao formation. Photo taken looking to the west at (942926).

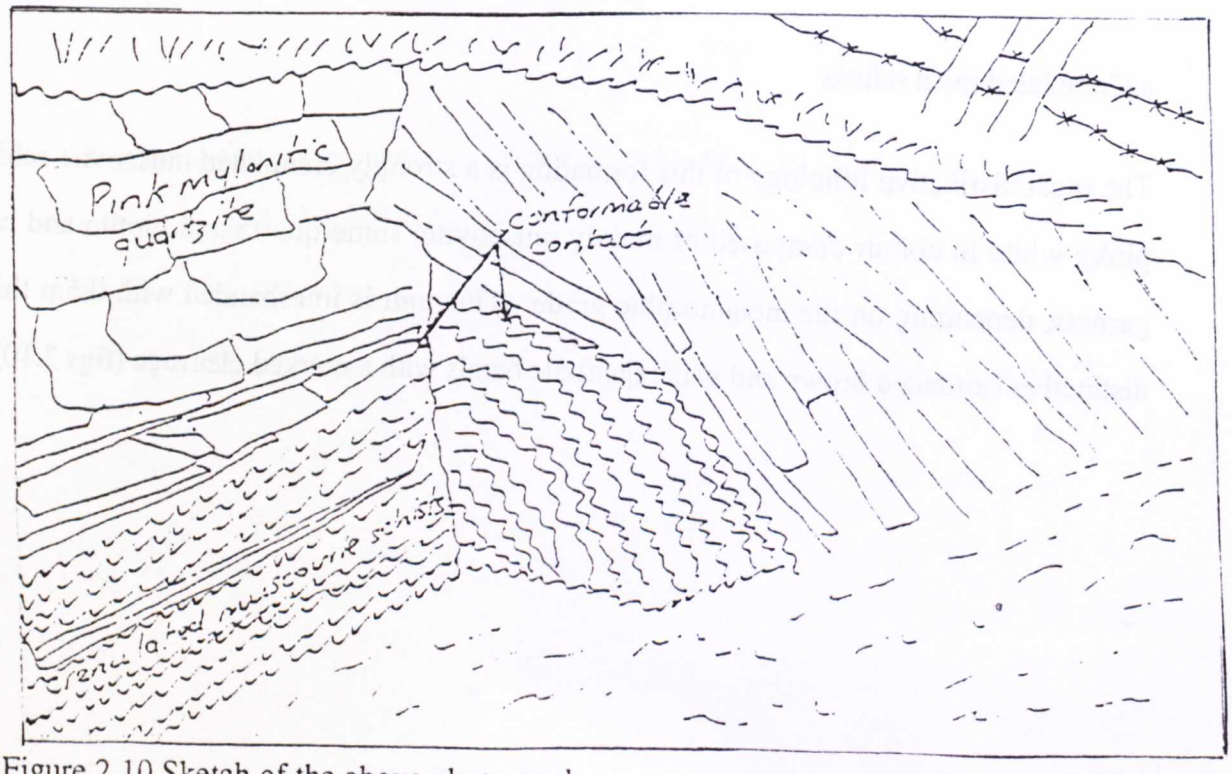

Figure 2.10 Sketch of the above photograph.

In thin section the schists are seen to be composed of muscovite, quartz, some garnet, epidote, biotite and feldspars in sample 134 (926828). This assemblage is studied in greater detail in chapter 4. The muscovite is aligned forming a crenulated schistosity along with biotite. The micas wrap around boudinaged porphyroblasts of recrystallized quartz. The garnets appear to cross-cut the S2 foliation indicating post-tectonic growth.

b.Pink mylonite

This lithology is pale pink in colour with a marked pervasive set of cleavages.The main cleavage is the equivalent of the S3 schistosity of the mica schists and is spaced at 2mm intervals and also shows some crenulation. Another spaced cleavage is perpendicular to this and these two cleavages cause the blocky weathering distinctive of this unit (see fig 2.12). This unit is represented by samples B2 (917767) and B12 (872757) shown in the photos of this figure and has a chalk-like appearance and texture particularly on the schistosity surface.

The mylonite is composed of quartz, feldspar and muscovite and is fine grained with the muscovite aligned to form the pervasive cleavage. In thin section it can be seen that feldspar porphyroblasts cause the crenulation effect with the schistosity wrapping around them. The porphyroblasts are composed of recrystallized quartz and both plagioclase and alkali feldspar. The microstructure of mylonites is discussed and illustrated in further detail in chapter 3.

Figure 2.11 Cleavage in the Pink Mylonite of the Arroio Arreiao formation at 872757 looking NW.

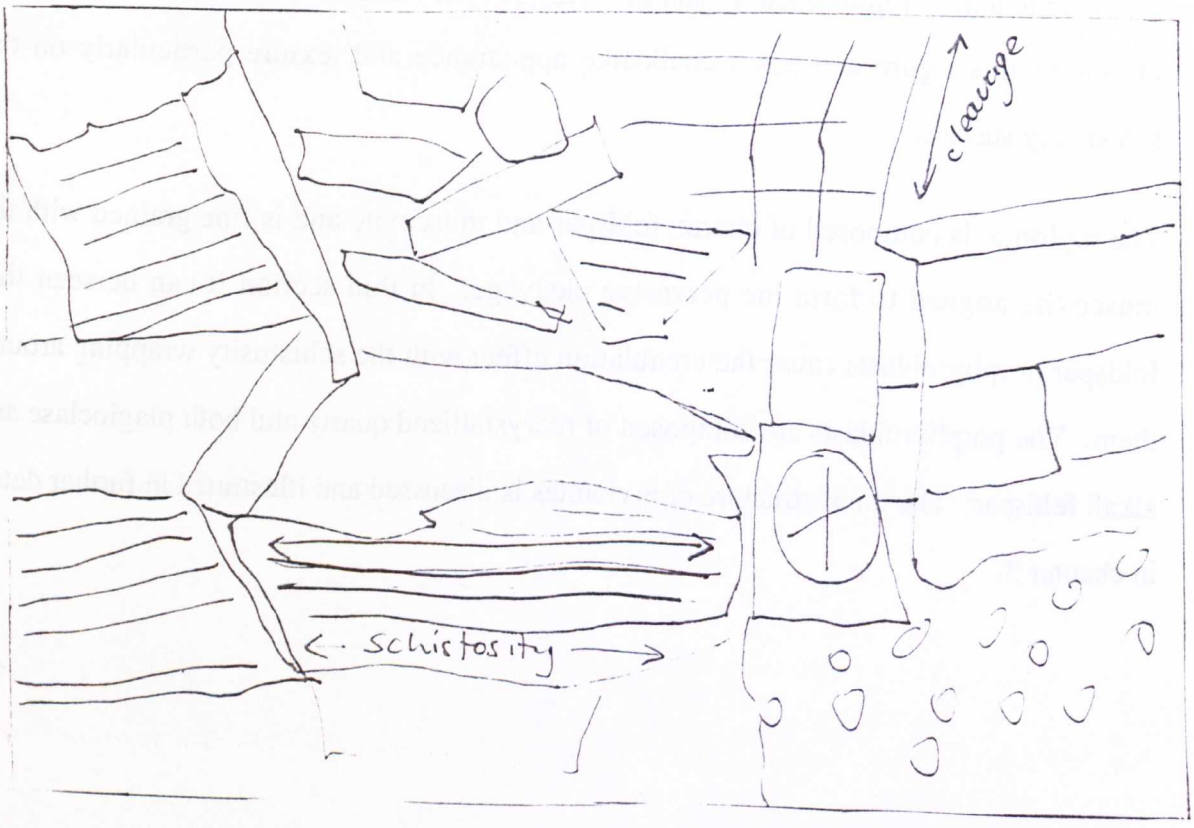

Figure 2.12 Sketch of the above photograph illustrating schistosity and cleavage positions.

2.2.2.4. CERRO DOS BICUDOS QUARTZITE

A.Field relations

This unit is composed of thick, white pure quartzites which overstep the Encantada Schists and the Arroio Arreiao formation (see map) and represent a structural break in the sequence. They are post-D1, since they do not show evidence of the first deformation of the Encantada Gneisses and are pre-Brasiliano in age since they are folded and metamorphosed by D2 and D3. In contrast to the underlying pink mylonites, these quartzites are very mature, composed of 90% quartz and therefore the source was extensively reworked. They may have been deposited in a shelf environment since they are stratigraphically overlain by marble and graphitic schist.

This unit forms the topographic highs of the area such as Cerro dos Bicudos marked as locality 94 (958794), Cerro da Picada, locality 65 (912771) and localites 152 (890817) and B13 (875713) which both form long ridges composed of this formation. These topographic features can be observed on the geological map (fig 2.2 and appendix E) and in the following photographs (fig 2.13). The outcrop pattern of the formation as seen from the geological map and cross-section is a result of folding, thrusting and relative resistance to erosion. Type exposures occur at the above localities and further exposures occur at localities B52 (058917) and 55 (924863) (see figure 2.14).

The Cerro dos Bicudos quartzite has been mylonitized by D2 and folded by the F3 folding event. At locality 94 the quartzite is in contact with gabbro and gneiss which may be a fault contact. At locality 152 (890817) the quartzite is thrust over a breccia containing clasts of the quartzite within it. This breccia post-dates the quartzite at other localities and this is strong evidence for a thrusting event post-dating the deposition of the breccia. The structural relationships are further discussed in chapter 3.

Figure 2.13a Topography of the Cerro dos Bicudos quartzite looking SW at locality 39.

Figure 2.13b The Cerro dos Bicudos quartzite at locality 99 looking south along the ridge.

B.Lithology

The quartzite has a preserved bedding of 0.5m thickness which has been folded with a well developed axial planar cleavage. It has also been extensively jointed. These three features combine to form the distinctive blocky weathering associated with this unit. It is a distinctive milky white in colour due to its purity of composition. From the cross-section the formation appears to be 150m thick along fold limbs with the nose of the folds being considerably thicker.

In thin section (sample 101 (890710)), the quartzite is seen to be composed of recrystallized quartz grains of less than 1mm diameter and is homogeneous in texture although there is some alignment of the few muscovite grains. Quartz grains are extended with the long axis parallel to the alignment and this forms a stretching lineation in hand specimen. There are a few feldspars present but the rock is at least 95% quartz.

2.2.2.5. CERRO DA CANBERRA FORMATION

A.Field relations

This formation is composed of graphitic schists with associated felsic volcanics and marbles. It probably represents a deepening shelf sequence with pure sands grading up through limestone to organic graphitic shists. The felsic volcanics were probably extrusive and are interfolded with the graphitic schists. The marbles are coloured blue on the map and the graphitic schists and volcanics dark green. This formation oversteps the Cerro dos Bicudos quartzites and locally the older gneisses. The formation shows two phases of folding on a map scale, the first being isoclinal with the axes plunging gently to the SW and the second being more open and upright. This is well illustrated on the map and cross-sections.

Figure 2.14a Type section (looking E) of the Cerro dos Bicudos quartzite at locality 116 (970815). The outcrop is 2m high.

Figure 2.14b Photograph (looking E) of the Cerro dos Bicudos quartzite at (921859).

The marble crops out in a synclinal structure just SE of Santana and it is exposed at locality B61 (974798) on the main road, where it is exposed isoclinally folded with quartzites and mica schists (fig.2.15). It also outcrops at locality 124 (980812) where it is complexly interfolded with graphitic schists and along the track from this locality to the SE. At locality 74 (002780), the marble is unconformably overlain by breccia of the Arroio dos Nobres formation which contains clasts of the local schists. The marble may have formed as a reef in a lagoon separated from the ocean by a sand barrier as can be seen on the east coast of Brazil today at Lagoa dos Patos, or alternatively could have been formed in a shelf environment (see section on tectonics).The metamorphism has destroyed many sedimentary clues to the origin of these marbles.

The graphitic schists overstep the marbles onto the Cerro dos Bicudos Quartzites. They crop out in the same synclinal structure as the marbles but are much more extensive covering a large area SE of Santana. Type sections occur at localities 33 (993758) and B17 (048883) where the graphitic schists are in contact with the sandstones and conglomerates of the Arroio dos Nobres formation, and further outcrops occur at B53 (062948) where they are in contact with quartzites. In some areas they are interfolded with felsic fine-grained blue-grey volcanics particularly in the SW portion of the map. These have been described in more detail by Jost (1981) and can be seen at localities 102 (901692) and 103 (950710).

Figure 2.15a Isoclinal folding of the Cerro da Canberra marble and the Cerro dos Bicudos quartzite. Photo taken looking SE at (967803).

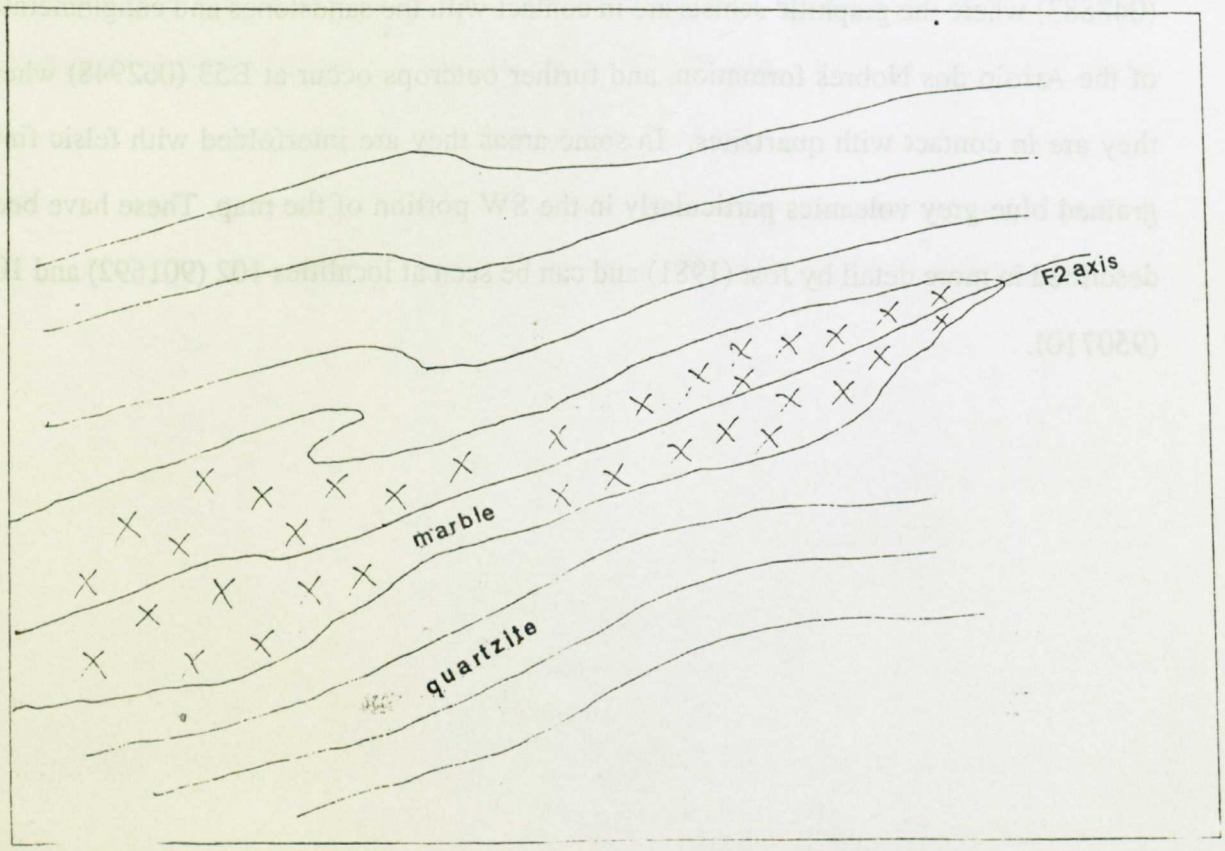

Figure 2.15b Sketch of the above photograph illustrating lithologies.

B.Lithologies

a. Marble

Two types of marble occur in the Santana Metamorphic Belt. The first is almost pure calcite and varies in colour from, pale green to white and has a coarse grained sugary texture. This occurs in the northwestern limb of the syncline e.g. localities B62 (972799) and 124 (980812). The other is less pure in composition, fine grained and dark blue-grey in colour with en-echelon calcite gashes suggesting some sort of extension and occurs at locality 34 (985770). It is very homogeneous in texture but shows some evidence of bedding. Photos of these rock types are shown in fig 2.16. In thin section it is evident that the marbles have a crenulated schistosity and are composed of calcite bands and boudinaged pods separated by fine grained calcite, muscovite and quartz and some graphite. Some of the calcite has large apatite inclusions. The calcite twins are folded which is evidence of strain within these rocks.

b. Graphitic schist

This lithology is distinctive in appearance and is dark grey in colour with a marked S2 schistosity (see chapter 3). It is composed of 2mm quartz laminations separated by graphitic layers of 1mm thickness. A typical representative of this unit in the field and in hand specimen is shown in the photo of fig 2.16. In some areas the graphitic schists contain considerably less quartz .

In thin section the primary schistosity is formed by graphite and muscovite in response to isoclinal F2 folding. This schistosity is then refolded around recrystallized quartz grains. These F3 folds have been broken up by shearzones causing cataclastic deformation destroying the structures produced by ductile deformation. Other minerals present include calcite and apatite.

Figure 2.16a Handspecimens of the various Cerro da Canberra marbles.

Figure 2.16b The graphitic schists of the Cerro da Canberra formation.

In some sections graphite is interfolded with finer grained quartz and muscovite (sample 109 (010865)), and widespread iron staining suggests oxidation of iron sulphide. Sample 91a (990814) shows some classic boudinage structures in the recrystallized quartz suggesting late stage extension. The volcanics are discussed in Chapter 5.

2.2.2.6 ARROIO DOS NOBRES FORMATION

A.Field relations

This unit is unconformable on the Cerro da Canberra formation overstepping marbles and graphitic schists and in some places the quartzites of the unit below (see cross section fig. 2.3). It crops out in a synclinal structure, the axis of which runs SW-NE with the vergence to the SW (see cross section fig 2.3). It shows one phase of folding ; upright open F3 folds of the bedding planes, and no evidence of isoclinal folding or metamorphism. This suggests that this unit post dates the D2 deformation event (see chapter 3). The formation has been affected by D4 thrusts and by late normal faults (chapter 3).

B.Lithology.

The Arroio dos Nobres formation is composed of sands overlain by muds and then conglomerates. Examples of this fomation occur at localities B5 (930742) and B14 (025810) where the green conglomerate has occasional red horizons. Both red and green conglomerates are coarse grained and immature with angular clasts of quartzite, biotite schist and graphitic schist. The difference in colour is a result of different oxidizing conditions .

Figure 2.17a Breccia of the Arroio dos Nobres formation (locality 35). Photo taken looking NE.

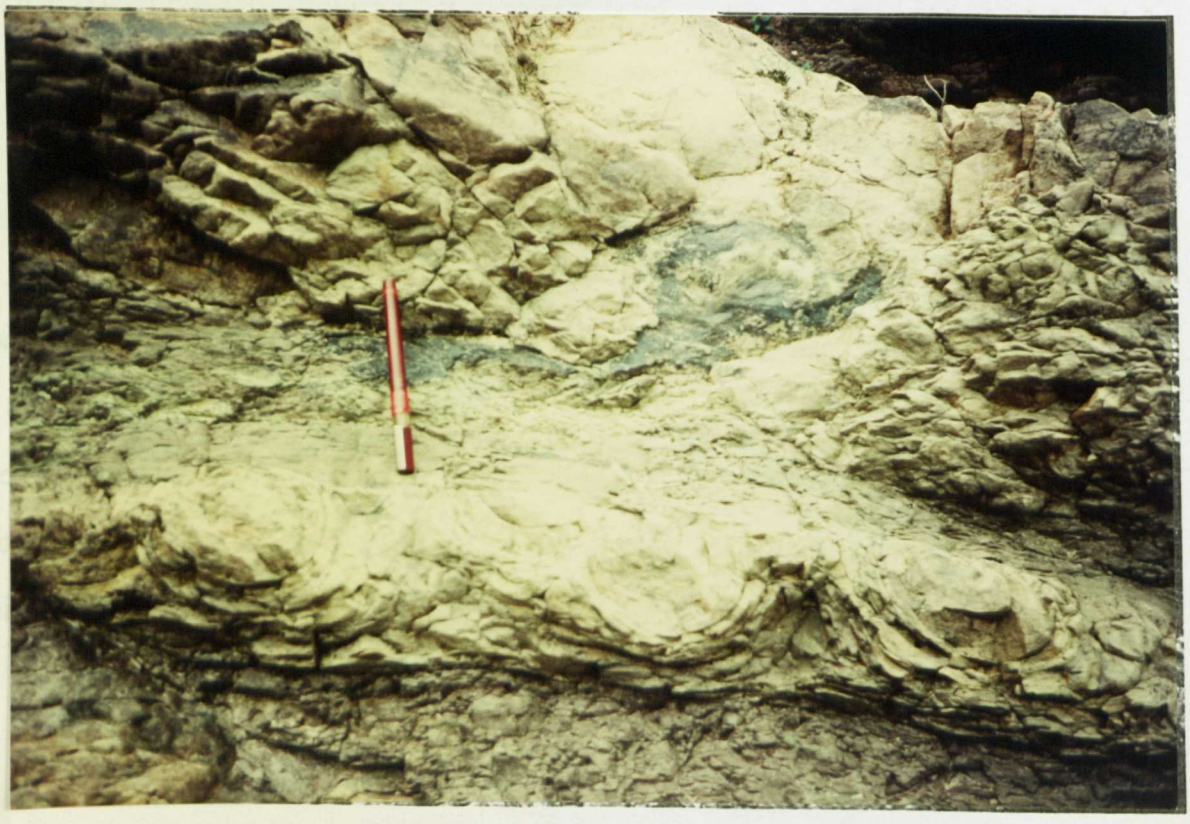

Figure 2.17b Truncated load structures in muds of the Arroio dos Nobres formation at locality 44 indicating that the beds are the correct way up. Photo taken looking NE.

Figure 2.18a Cross bedding in Triassic red beds at locality 104 looking to 100°.

Figure 2.18b Pillow andesite at locality 113 (864830) looking north.

The sandstones are red and micaceous with a slight alignment of the micas forming a parting.These are interbedded with red and green mudstones. At locality 44 (014806), the formation can be seen to be the correct way up with load casts of muds truncated by the next bed (fig 2.17). This formation is thus younger than the graphitic schists and possibly deposited as river or flood deposits. The change from sandstones to conglomerates may represent a change in the rate of uplift and/or a change in the climate.

2.2.2.7. POST-TECTONIC RED BEDS

The red beds were not studied in detail but are discussed in relation to the Santana Metamorphic Belt. Previous authors (Jost 1981, geological map) have described these rocks as molasse which may be Permo-Triassic in age (Carvalho 1932) although the geological survey have called it late Precambrian. In the SE this "mollasse" which separates two portions of the schist belt (see map and section) is known as the Canelarias formation and lies in a fault-bounded basin. It is composed of fine grained cross-bedded siltstones and sandstones (locality 31 (041713)) with interbedded andesite and rhyolite flows. They probably formed in some sort of extensional basin. The Canelarias formation shows some evidence of folding and outcrops in a slight synclinal structure.

In the NW, the red beds are described as the Guiritas formation (Jost 1981) and lie unconformably on the Cerro dos Bicudos quartzite . These are flat lying cross bedded red sandstones, siltstones and conglomerates forming a flat lying basin in the NE with desert like features (figure 2.18). Interbedded pillow andesites (fig 2.18) suggest an underwater formation (chapter 5). This unit can be seen at locality 51 (916890) but its great thickness (~1km) is apparent at Minas do Camaqua to the SW of the area. The red beds have also undergone normal faulting which indicates that extension post dates the formation of this unit which may be associated with the opening of the Atlantic.

CHAPTER THREE

3. Deformational history of the Santana Metamorphic Belt.

3.1 Introduction

Four major episodes of compressional deformation have been recognized in the Santana region of the Dom Feliciano Belt (fig 3.1), with periods of relaxation and sometimes extension, occurring between them. The precise timing of the older compressional events is uncertain although later events are constrained by dating igneous intrusions which cross cut structural features. Careful structural mapping can determine the sequence of structural events and the style and nature of folding and faulting.

Table 3.1 shows the sequence of structural events and defines the terminology used to describe structural features. A more comprehensive geological history integrating both structure and stratigraphy is given in chapter 8.

Structural information is illustrated by means of structural maps and by the use of stereographic projections of data onto Schmidt equal area plots. Structural events are described in chronological order starting with the first recognizable fabric in the oldest rocks. For example D1 represents the first deformational event, S1 the first recognizable schistosity and T1 the first thrust. There may well have been earlier events that are not recorded.

In the structural map of figure 3.1 all the measurements recorded in the field are illustrated. Stratigraphic units below the Cerro dos Bicudos formation are considered to be Basement and the Cerro dos Bicudos formation and those above it are considered to be Cover. The outcrop patterns have been simplified from the geological map to this structural map.

Bedding was only observed in the unmetamorphosed sediments of the Arroio dos Nobres formation and in the Triassic red beds (see legend fig 3.2). The major foliation plane measured in the metamorphic rocks is the S2 schistosity. From figure 3.1 and the geological map of fig 2.2. a map of the axial traces of F2 and F3 folds has been constructed and this is illustrated in fig 3.3. These figures will be referred to throughout this section.

Thin sections from the Santana area have been studied with a view to identifying and understanding structural deformation in the area and to correlating macroscopic features with microscopic features. This work is illustrated using photomicrographs in the relevant sections. Microstructural deformation can be subdivided into three styles depending on the amount of stress and the nature of the material being deformed.

Dislocation deformation occurs where crystals show a plastic rheology in wet rocks under low stress and there are three associated processes. Firstly, a build up of dislocations in the crystal lattice with work hardening, results in kinking and deformation lamellae. Secondly, reorganization of the dislocation into regular arrays (recovery) results in the development of subgrains and thirdly, the migration of grain boundaries reduces strain energy which leads to the formation of sutured grain boundaries and areas of recrystallization.

At higher stresses intracrystalline deformation becomes important with a distinct microstructure resulting in a foliation which is defined by flattened elongated grains. The strain-induced primary recrystallization causes overall grain size reduction and this process competes with secondary recrystallization and grain growth. If grain size reduction is dominant then the texture is described as mylonitic. Cataclastic deformation is a disruptive highly inhomogeneous deformation with no foliation produced and results from brittle fracture across of fault zones. Examples of the various microstructures will be illustrated in section 3.3.

3.2 Previous work

Previous work on the structure of the Santana portion of the Dom Feliciano Belt was undertaken by Ribeiro et al (1966), who first identified a predominance of NNE-SSW lineaments. More recently Jost (1981) and Machado et al (in press) undertook more detailed studies in the area.

Jost used the Turner and Weiss (1963) method of describing the structural features of different tectonic units separately. He recognized the area NW of Santana da Boa Vista as a domal foreland and the area to the SE as a nappe and defined the structural features of each area separately, but he made no attempt to define deformational events or a sequence of events. Machado et al (in press) proposed a more comprehensive study of the structural evolution of the area. Both approaches will be discussed and compared with the approach used in this study.

In the NW region of the mapped area within the Encantada Gneisses, Jost defined S1 to be the metamorphic compositional banding of the gneisses and suggested that F1 folds were not evident since bedding was destroyed in the formation of the gneisses. He proposed that F2 folds were isoclinal and that the F3 folds were open and upright and could only be observed in cross-section. In the SE portion of the area Jost described the cover as a nappe with thrusts but he did not attempt to correlate this with the basement.

Machado et al (in press) recognized four Brasiliano (800-450m.y.) deformations. They also suggested that the Encantada Gneisses have undergone a previous deformation. They recognized the first three compressional events to be practically homoaxial trending NNE-SSW to NE-SW and the fourth D4 to be orthogonal to this.

In the Brusque belt of Santa Catarina,which is thought to be the continuation of the Dom Feliciano Belt under the Parana basalts (fig 2.1), Basei (1985) recognized four phases of deformation. The first phase produced the banding and schistosity, the second isoclinal folds and the third phase folded these isoclinal folds into open upright folds. The second and third phases have NE striking foliations and NW vergence. The fourth phase produces a tight kinking and is related to transcurrent movements along ancient lineaments. Table 3.1 gives the sequence of structural events used in this study.

Deformation	Folding	Foliation	Faulting	Lineation
Extension			normal NW-SE normal NE-SW	
D4	F4 NE verging assymetric folds	S4 NW-SE	Thrusting NE verging	L2
D3	F3 NW verging assymetric open	S3 NE-SW axial trace		L1 crenulation
D2	F2 isoclinal folds recumbant	S2 schistosity		
D1	F1 not observed	S1 gneiss band		

Table 3.1

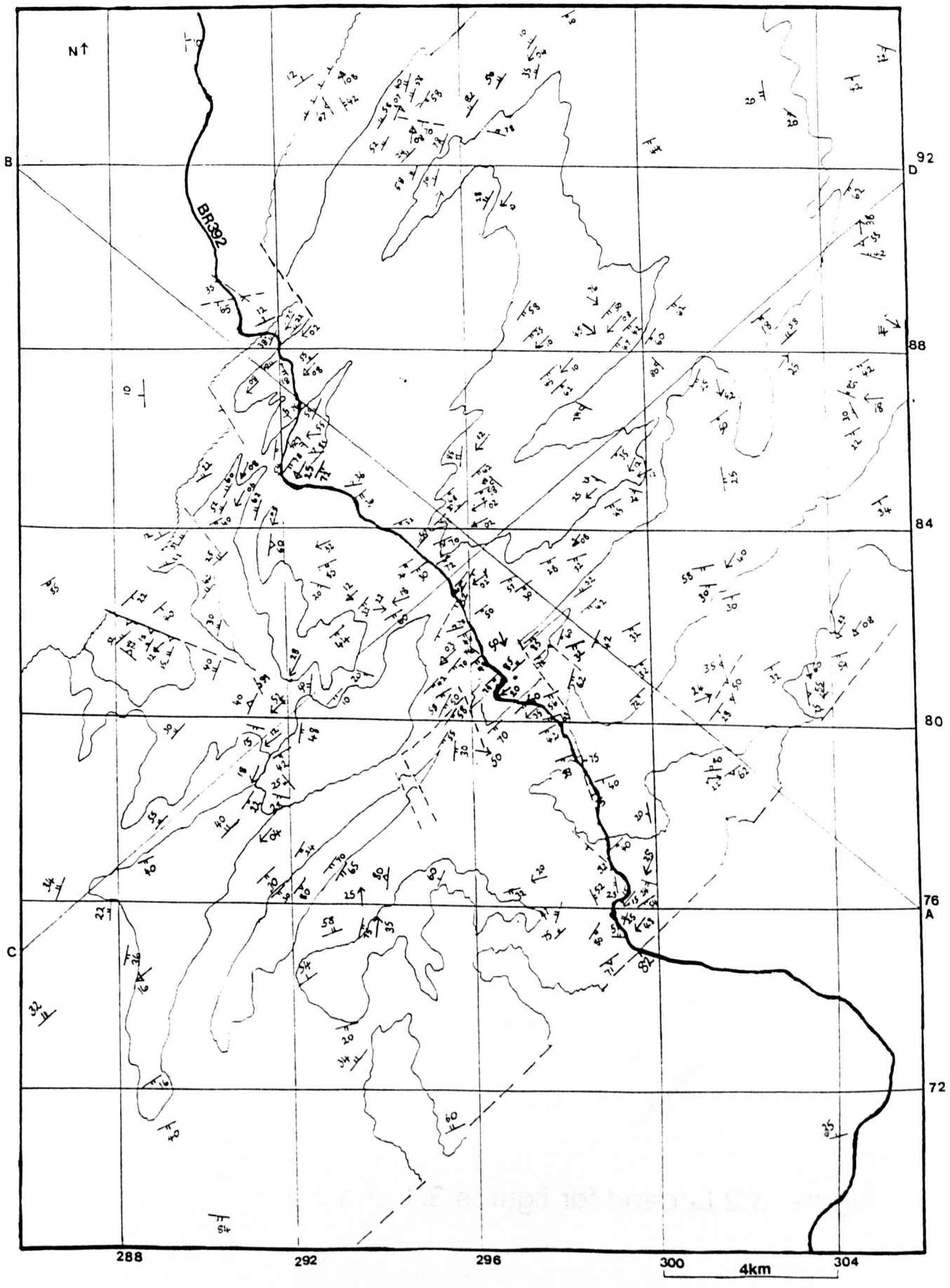

Figure 3.1 Structural map of the Santana Metamorphic Belt showing all field measurements.

KEY TO GEOLOGICAL SYMBOLS

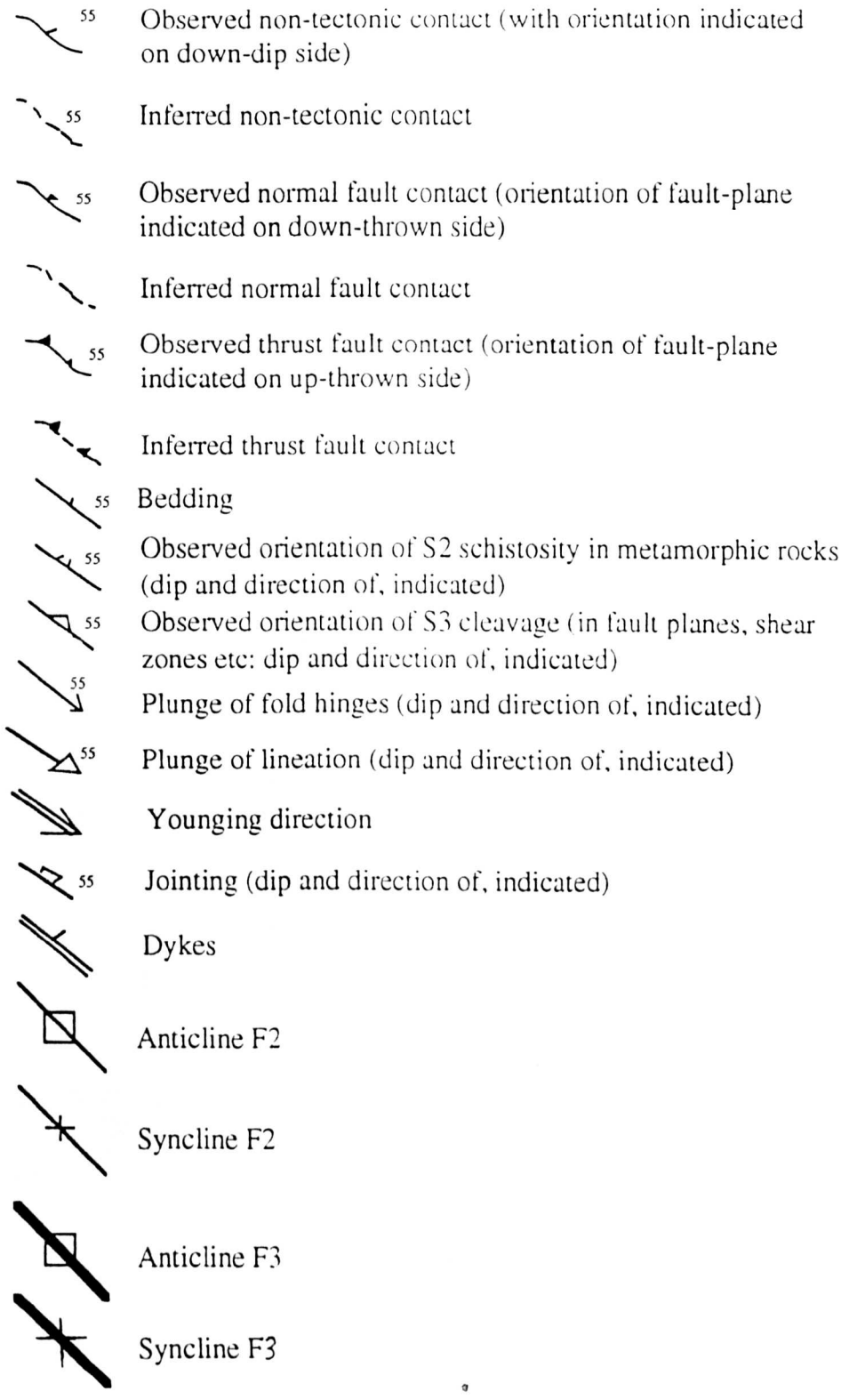

Figure 3.2 Legend for figures 3.1 and 3.3.

3.3 Deformational phases

3.3.1 The first phase of deformation D1

This phase of deformation was responsible for the compositional banding of the Encantada Gneisses which is described as S1 for the purpose of this study. Evidence of F1 folds associated with this banding are not seen on a macroscopic scale due to the obliteration of the bedding within these rocks.

The origin of compositional layering in gneisses is a matter of much debate. Several processes are involved. Many gneisses with layered or lensoid structure (augen gneisses) clearly originated as plutonic rocks, often with cross-cutting veins. Under high strains, such rocks become layered partly due to flattening and elongation of large crystals and partly due to rotation of veins and other heterogeneities into the plane of flattening.

Metamorphic segregation is also important in the development of gneissose banding either by enhancing deformational layering by chemical differentiation, and/or by pressure solution and recrystallization in response to strain. Intensely deformed gneisses of igneous origin are often difficult to distinguish from those of sedimentary origin when they are derived from sediments of mixed composition like greywackes (Park 1983).

The S1 fabric can only be identified as gneissic compositional banding. Therefore S2 is the major fabric measured in the structural study of the Encantada Gneisses. This phase of deformation affects the Encantada Gneisses but not the overlying rocks, so it may represent deformation during the Trans-Amazonian orogeny (Marshak et al 1989)

After the D1 compression and the development of S1 compositional banding, there was a period of relaxation and possibly extension with intrusion of granite and quartz veins which cross-cut the gneissose fabric.

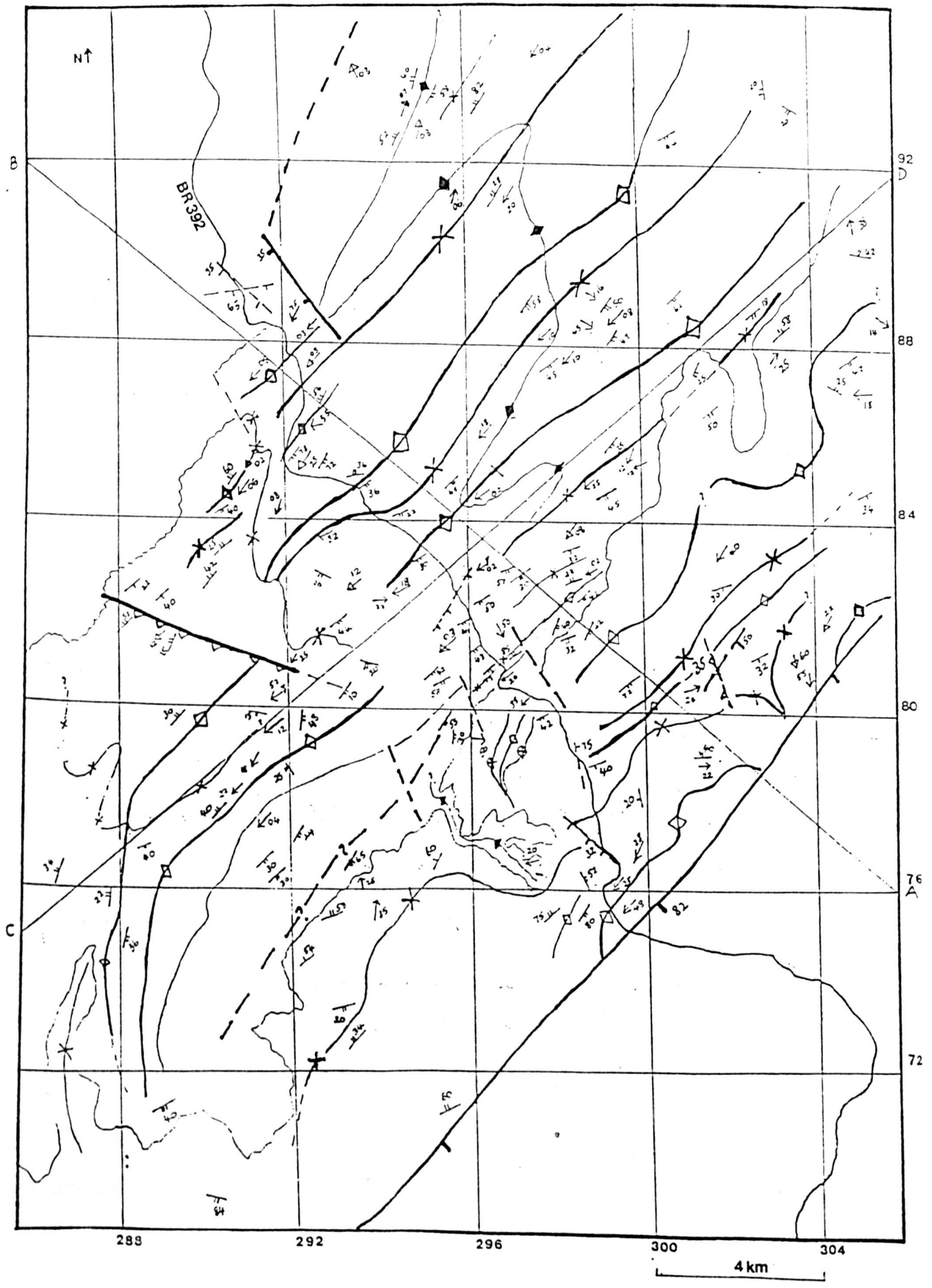

Figure 3.3 Interpretative map of F2 and F3 fold axes in the Santana da Boa Vista mapped area.

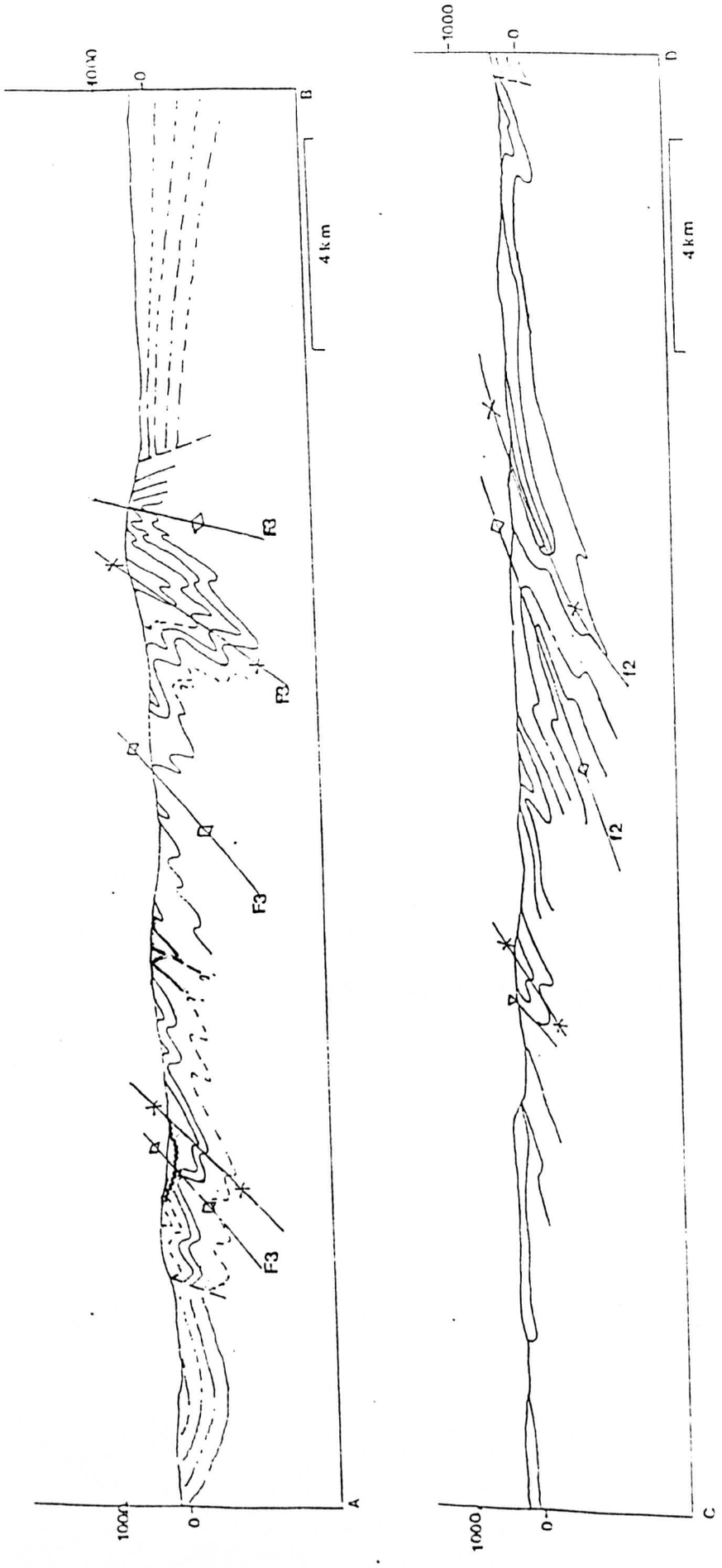

Figure 3.4 Interpretative cross sections for F2 and F3 folding.

3.3.2 The second phase of deformation D2

The second phase of deformation produced tight to isoclinal recumbent symmetrical F2 folds with a NNE-SSW trend with a strong axial planar S2 schistosity defined predominantly by the alignment of micas. This phase of folding also deformed quartz veins and granites intruding the Encantada Gneisses and thus post-dates them and produced the S2 schistosity shown in fig 3.1. F2 folding strongly affected the Encantada Gneisses and schists in addition to the granites which intrude them. This is shown in the photo of fig 3.5. This figure also shows the sequence of deformational events including D2 and its effect on the gneisses.

The S2 schistosity is very marked within the Encantada Schists, the Arroio Arreiao mica schists, the Cerro da Canberra formation and in the Cerro dos Bicudos quartzites although in the latter it occurs as a non-pervasive cleavage defined by the alignment of muscovite. This may be the result of the difference in competence and composition of the different rock types.

Overall, the S2 schistosity is recognized by its pervasiveness and its consistently NE-SW strike, particularly in the basement rocks. This deformational event may also have been responsible for the isoclinal folding within the Cerro da Canberra graphitic schists. In this study area , the dominant planar fabric is the S2 schistosity.

Figure 3.5a Interference pattern of F2+ F3 folding in the Encantada Gneisses at locality 45.

Figure 3.5b F2 isoclinal folds in augen gneiss of the Encantada Gneisses (locality 93).

3.3.2.1 F2 FOLDING

In the map shown in figure 3.3, the axial traces of F2 folds are illustrated in the Encantada Gneisses and the Cerro dos Bicudos Quartzite. Fig 3.3 shows both the axial traces of recumbent F2 folds and upright F3 folds.

Mesoscopic features of F2 folding can be observed at an outcrop scale and in hand specimen, and then are observed to be tight isoclinal folds, symmetrical in nature and with a maximum interlimb separation of 0.5m. Excellent river exposures of F2 folds can be seen at localities B45 and B27 (fig 3.5). In the Encantada Schists the F2 folds are much tighter producing a marked 2mm spaced S2 schistosity (see photos of section 2.2.).

The S2 schistosity is seen as an alignment of micas within the gneisses, and since it is sub-parallel to the compositional banding,it is often difficult to distinguish the effects of S1 from those of S2. Within the mylonitic granites F2 folds can be seen to be folded by F3 (fig.3.6). Also in this figure it can be seen that the quartz veins in the graphitic schists are deformed by F2 folds.

Figure 3.6a F2 folds in quartz veins of the graphitic schists of the Cerro da Canberra Formation at pocality 61. The strike of the f2 axis is 240º and the dip 80º SE.

Figure 3.6b F2 isoclinal folds in the Santana Granite at locality 39 looking to 235º.

In thin section three phases of deformation can be identified in the gneisses and amphibolites, with the S2 micaceous fabric and S3 foliation being particularly well developed. The gneissic banding S1 was formed by chemical differentiation during high grade metamorphism and recrystallization which is the result of intracrystalline plasticity under high strain. This resulted in the orientation of micas and the recrystallization of quartz (see photomicrograph fig 3.7).

The photos of figure 3.7 also illustrate that F2 folds isoclinally fold the S1 fabric resulting in a new S2 schistosity with micas are reorientated to parallel the limbs of the isoclinal folds. Therefore, the S1 foliation can only be clearly observed at fold hinges.

The S2 schistosity in the amphibolites was caused by the rotation of predeformational grains or by preferred nucleation or preferred growth in the direction of extension. The S2 schistosity is the first observable foliation within the Encantada Gneisses and the Arroio Arreiao formation.

A Schmidt equal area plot of the poles to the S2 foliation within the Encantada Gneisses and schists is shown in fig 3.8 as well as a contoured map of these data The major concentration of poles fall in the NW quadrant which demonstrates that the predominant dip is to the SE and a with general NE-SW strike. The observed trend of poles is the result of later folding of the S2 schistosity planes, but it is impossible to distinguish whether this represents F3 or F4 by this technique. Nonetheless, the dominant SE dip of the S2 fabric suggests that the effects of later folding were localized. This is discussed further in section 3.4.

3.3.2.2. POST-D2 EXTENSION

The Arroio dos Nobres formation was unaffected by the D2 deformation event and shows no evidence of metamorphism. It was presumably deposited after the D2 deformation in an extensional basin, comprising sands, muds and thick conglomerates containing clasts of the schists and quartzites.

a)

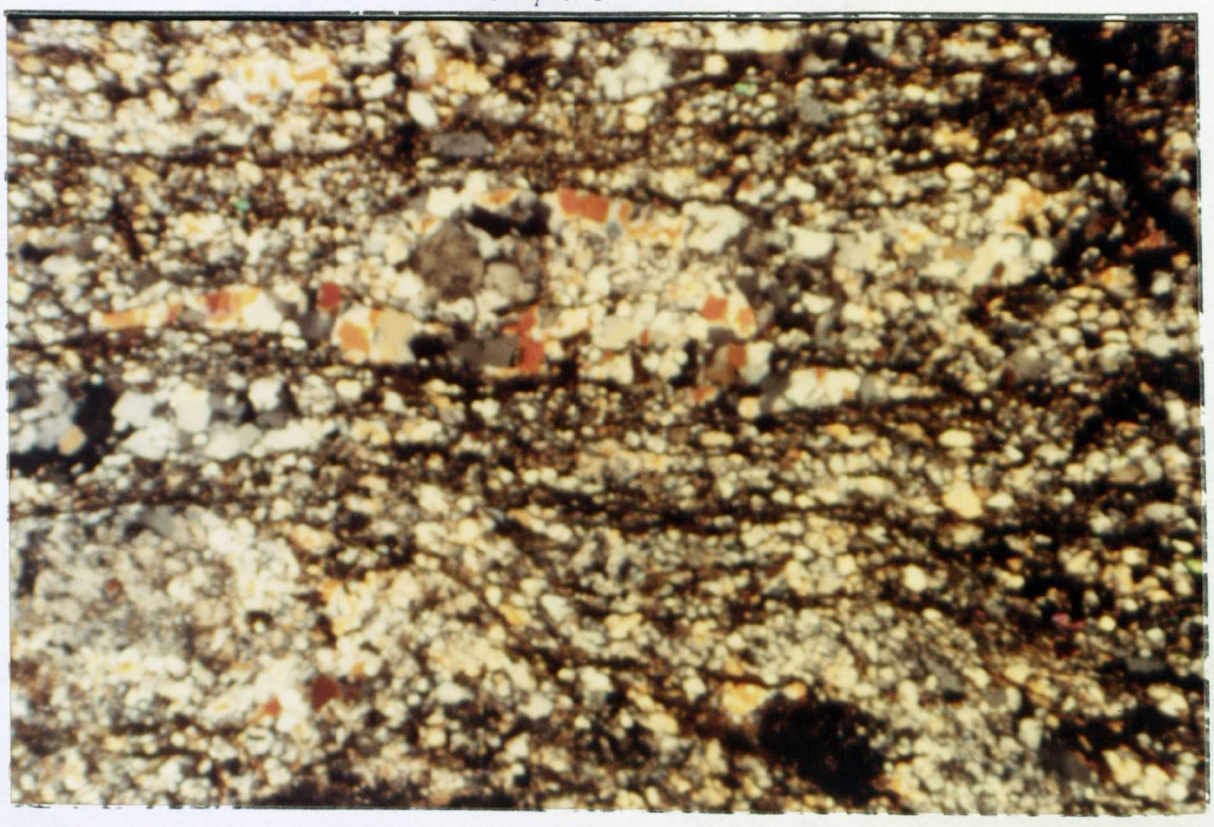

b)

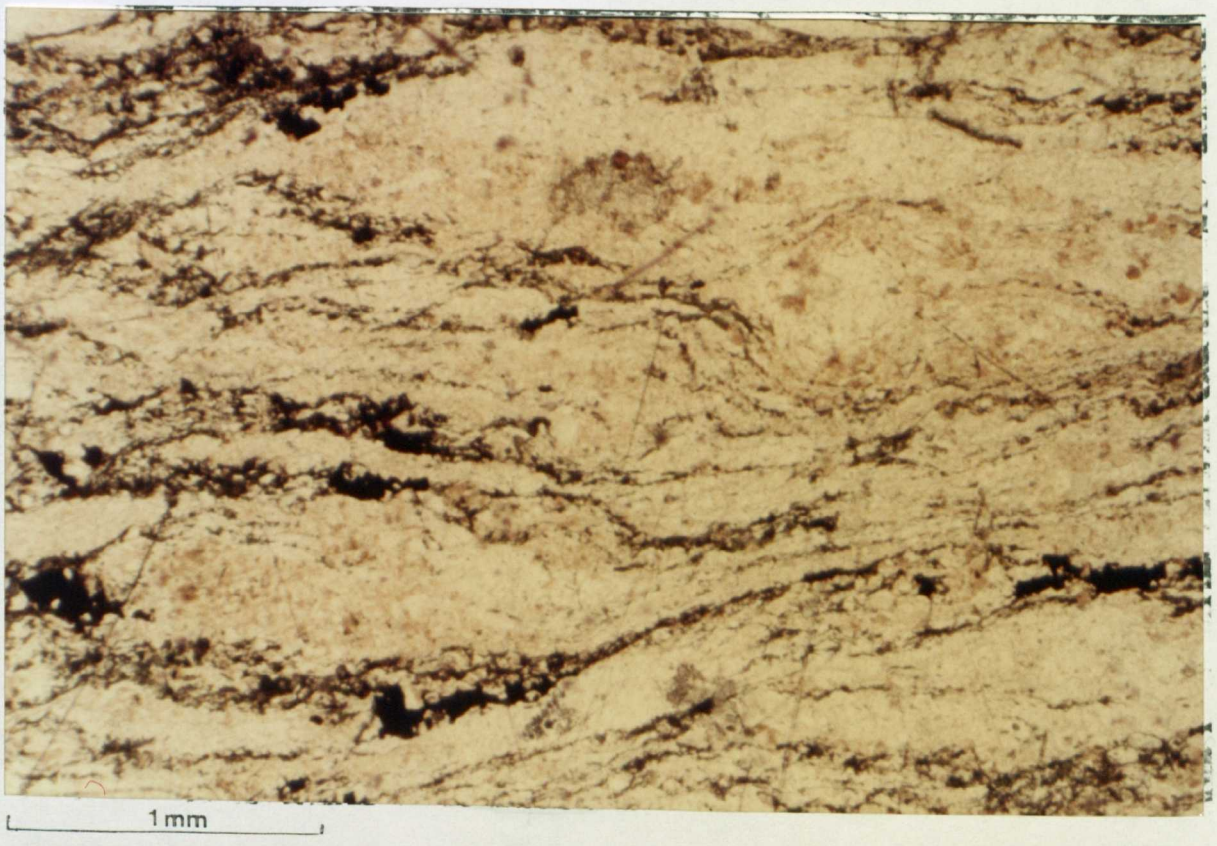

Figure 3.7 Photomicrographs of F2 isoclinal folding in the Encantada Gneisses (x5) (a) (X polars), (b) (plane polarized light) from locality 139

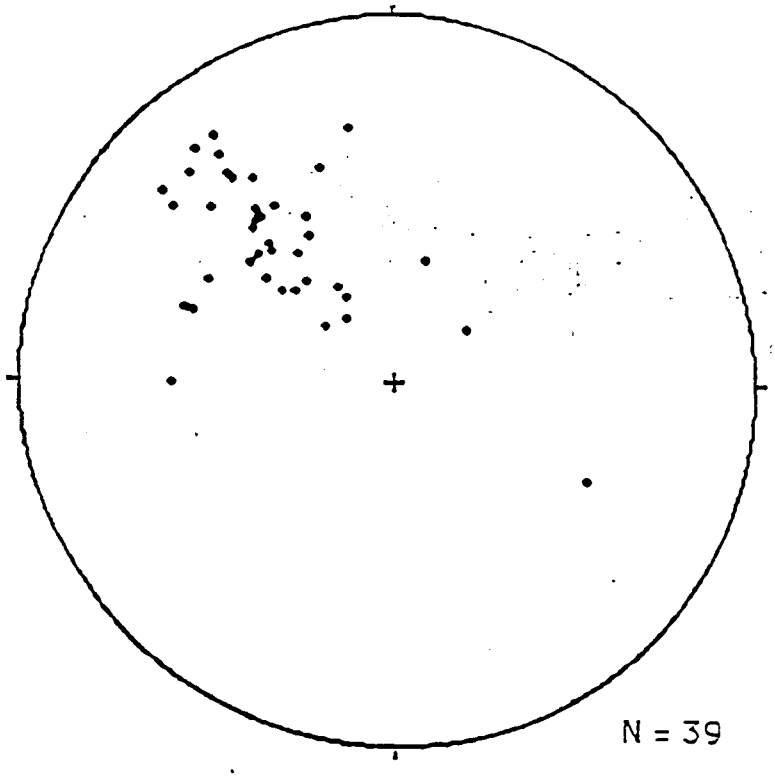

Figure 3.8a Equal area net of poles to S2 foliation within the basement Encantada Gneiss and Encantada Schist formations.

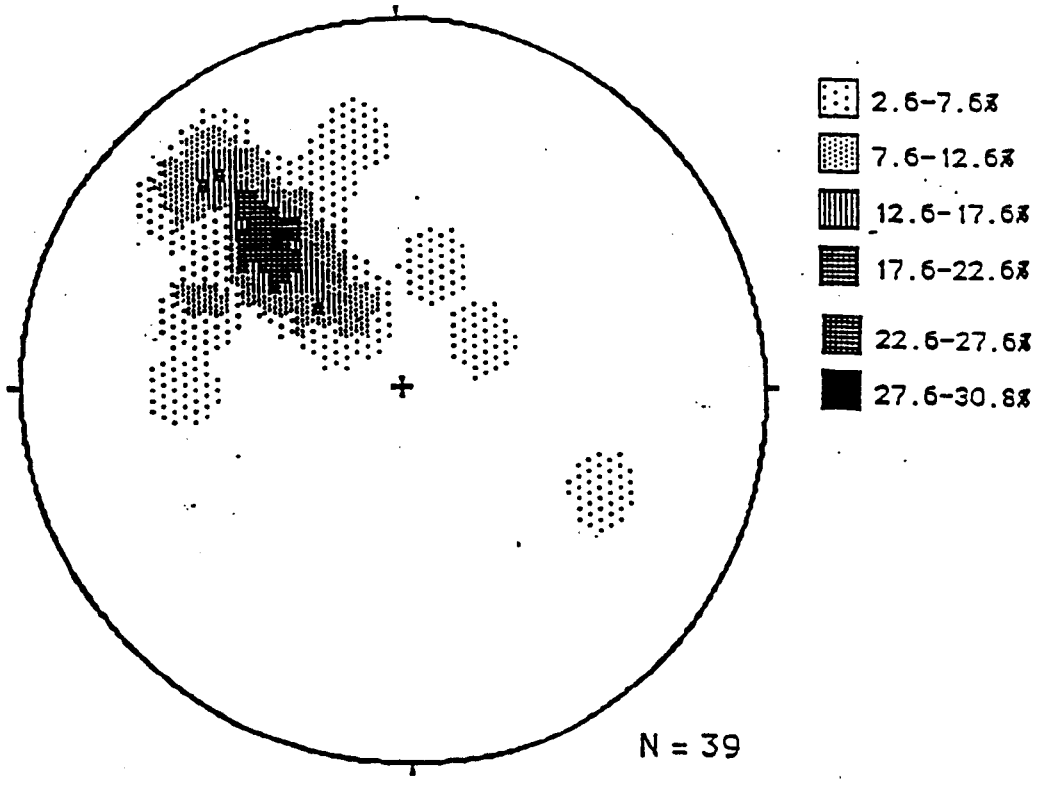

Figure 3.8b Contoured equal area projection poles to S2 in basement rocks suggesting the main dip to be to the southeast.

3.3.3 The third phase of deformation D3

The major event associated with the third phase of deformation was the juxtaposition of a sedimentary shelf sequence and the polydeformed and metamorphosed basement with syntectonic folding of both the cover and to a lesser degree the basement. Associated with D3 was metamorphism of the upper sequences of the basement to amphibolite facies (this is discussed in chapter 4).

The F3 folds associated with this phase of deformation are open asymmetrical and NW verging (section 3.3.3.1) and they are accompanied by a SE plunging L1 lineation and an S3 schistosity. The folds, foliations and lineaments associated with this most recognizable phase of deformation are discussed further below.

3.3.3.1 F3 FOLDING

This phase of folding can only be observed in cross sectional view in road cuttings perpendicular to the main foliation, for example, along the BR392. F3 folds are upright and open with a distance of between 25-75m between the limbs. Their axial planes dip steeply to the SE in the south of the area, and to the NW in the north, and in general they strike NNE-SSW.

Figure 3.3. shows the axial traces of the F3 antiforms and synforms in the map area and comparison with figure 3.1 illustrates that the strike of these axes parallels the trace of major faults and also the S2 schistosity (which is axial planar to F2). This series of parallel structures is responsible for the general tectonic fabric observed by Riberio et al (1966). F3 folds are well displayed in the NW-SE cross section (Fig 3.4).

Figure 3.9 F3 folding of F2 Isoclinal folds with the formation of an upright S3 cleavage at locality 39 looking to 235º.

Figure 3.10 Topographic features of the Cerro dos Bicudos quartzite showing an antiformal structure looking to 156º at locality 94

A classic example of F3 folding can be seen north of locality 39 on the BR392 on the west side of the road (fig 3.9) where it can be seen that isoclinal F2 folds are folded into upright open folds with a SE dipping axial plane. S2 and S3 are also illustrated in this figure.

Other examples of F3 folds can be seen at locality 55, and also between localities 39 and 53 (Fig 2.2), and they are particularly well preserved in the pink mylonites and the quartzites. At locality 94, there is an excellent example of an F3 NW verging antiform in the Cerro dos Bicudos Quartzite (see figure 3.10).

The Cerro dos Bicudos quartzites also display a strong S3 cleavage perpendicular to the S2 cleavage. Within the graphitic schists F3 folding produced refolded folds and in the Arroio dos Nobres formation it produced open folds of bedding planes with the same orientation as in the older units. Thus D3 post dated the formation of the Arroio dos Nobres formation.

In thin section S3 can be seen to have developed at a high angle to S2, and to have caused a realignment of a few micas as a result of parasitic folds to the large open F3 folds. This fabric is only weakly developed in the basement rocks and it is not pervasive. It can be observed in the photomicrographs of samples 116 and 118, and locally it has porphyroblast growth associated with it (figure 3.11a and 11b). This is further discussed in chapter 4.

In the Schmidt net projection (fig 3.12a) data from both the Arroio Arreiao and Cerro dos Bicudos units have been plotted, and the poles to the S2 schistosity lie along a great circle of orientation S314 D82 NE. The general trend of points is similar to that of the underlying gneisses suggesting that all units have been affected by the same D2 deformation events, even though there are very few north dipping rocks within the gneisses, whereas there are many in the quartzites.

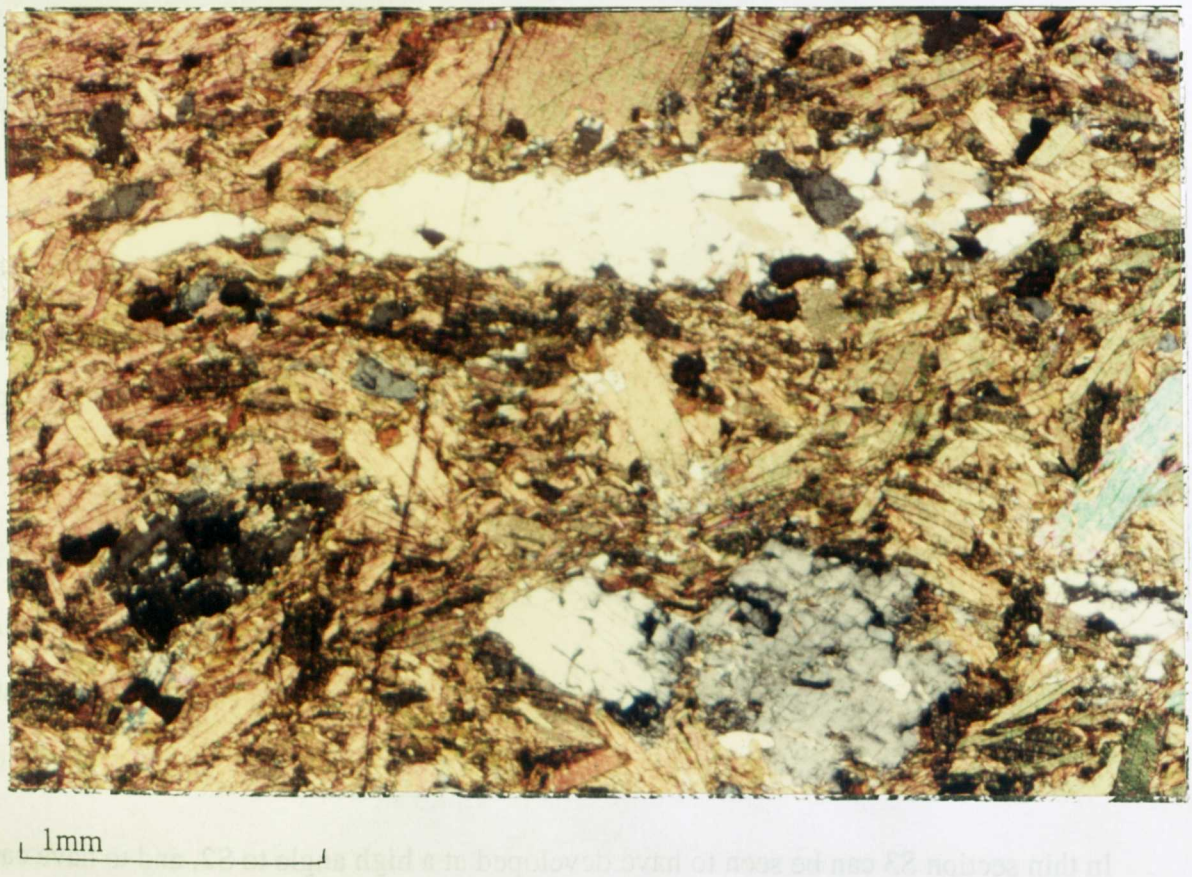

Figure 3.11a Photomicrograph (x5) of S3 biotite growth cross cutting the S2 foliation in the Encantada Schist from locality 96.

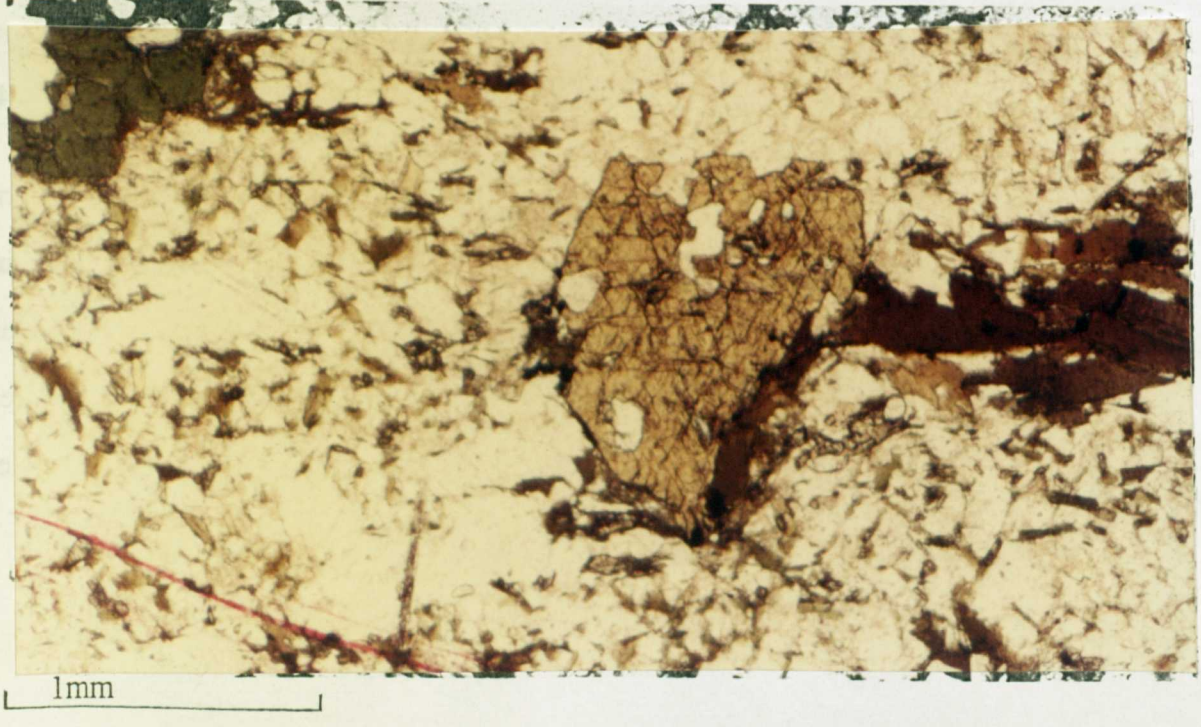

Figure 3.11b Amphibole growth along S3 cross-cutting the S2 biotite foliation in sample 95 from the Encantada Schists (x5).

This suggests that the quartzites have been more affected by post F2 folding than the gneisses. The NE dipping foliations are much steeper than the SE dipping foliations, further suggesting asymmetric folds.

3.3.3.2 THRUSTING

Previous authors (e.g. Jost 1981) have suggested NW thrusting of a shelf sequence onto a polydeformed and metamorphosed basement. Moerover, Basei (1985) argued that there had also been significant thrusting in the Santa Catarina area. There is however little substantial evidence in the field to support D3, NW verging thrusts in the Santana da Boa Vista area. The marked NE-SW fault separating the basement from the cover (which Jost suggested to be a thrust fault) appears to be an extensional fault, as stratigraphic units are missing rather than repeated.

Mylonitic rocks form as a result of intracrystal deformational processes. They occur in the regions adjacent to NE-SW faults in the map area and examples are illustrated below in photomicrographs with total recrystalliztion occuring in sample 79. There was no convincing evidence for D3 thrusting observed in the study area. However, there is strong evidence for NE thrusting post dating the formation of the Arroio dos Nobres formation (section 3.3.4.1).

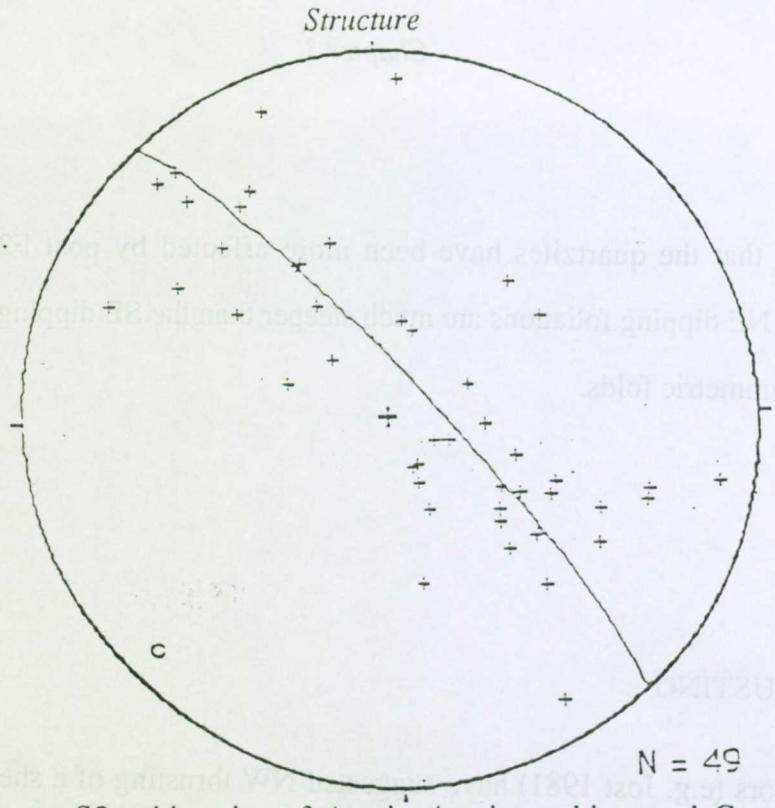

Figure 3.12 Poles to S2 schistosity of Arroio Arreiao schists and Cerro dos Bicudos quartzite fall on a great circle which illustrates F3 folding.

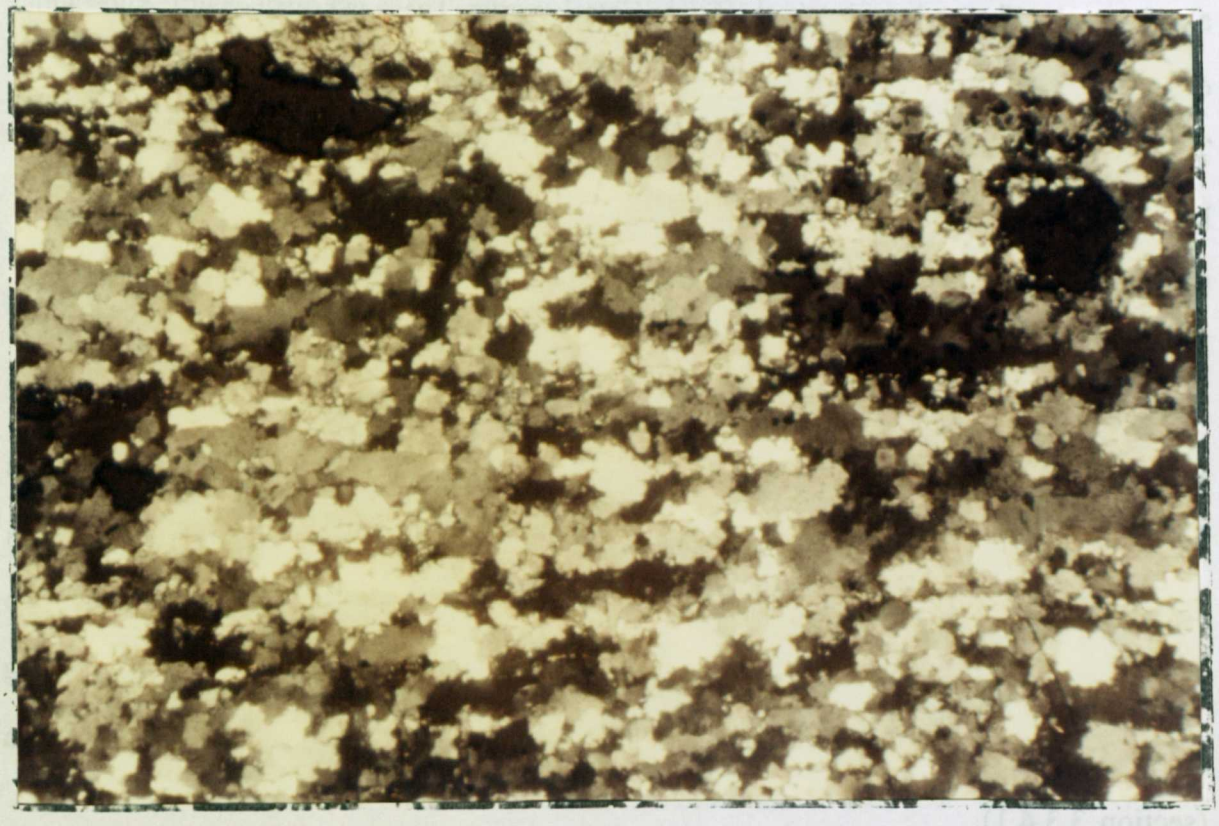

Figure 3.13Photomicrograph of a quartz mylonite showing total recrystallization.

3.3.4 The fourth phase of deformation D4.

This phase of deformation differs from the older events in that the general strike of deformational features is NW-SE which is orthogonal to the earlier events. It was a compressional event characterized by low angle thrusting, and it post-dated the formation of the Arroio dos Nobres unit since the Cerro dos Bicudos quartzites are thrust over the Arroio dos Nobres formation in the west, and graphitic schists in the east. The thrusting appears to be NE-verging (figure 3.1).

3.3.4.1 THRUSTING

The major event associated with D4 deformation is thrusting to the NE. This phase of thrusting emplaced the metamorphic deformed Cerro dos Bicudos metaquartzites onto the unmetamorphosed sediments of the Arroio dos Nobres formation which contain clasts of the metaquartzite.

This relationship can be seen at locality 152, and it is illustrated by the photo in fig 3.14. Small scale reverse faults occur at locality 44 in the Arroio dos Nobres formation (fig 3.15a). Evidence for thrusting also comes from geological mapping which recognizes that stratigraphic units are missing and structural features cross-cut by this thrust (figure 2.2).

Figure 3.14a Thrusting of Cerro dos Bicudos quartzite onto the unmetamorphosed Arroio dos Nobres formation at locality 152 looking to 50°

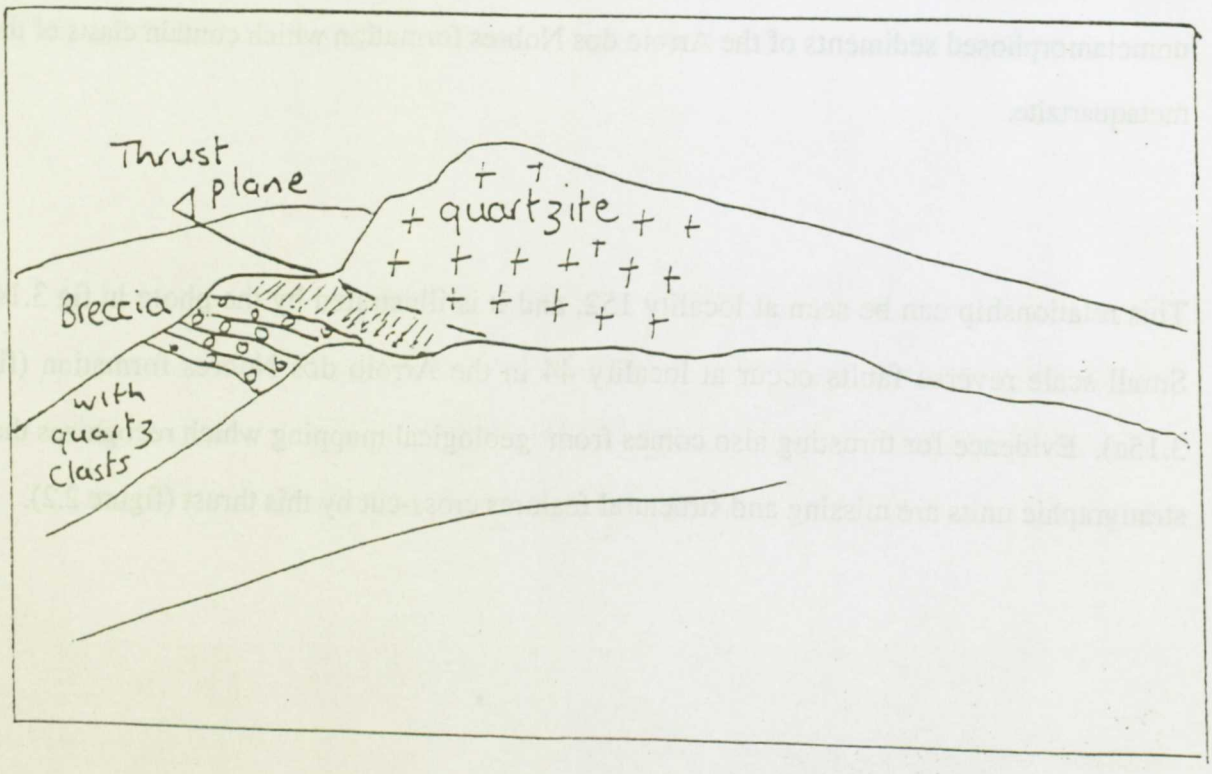

Figure 3.14b Sketch of the above photograph illustrating structural relationships.

Figure 3.15a Thrusting in the Arroio dos Nobres formation at locality 44 looking to 240º.

Figure 3.15b F4 folds in the Cerro da Canberra graphitic schists at locality 58 looking to 240º.

3.3.4.2 F4 FOLDING

There is some evidence of F4 folding of the Cerro da Canberra formation from its overall outcrop pattern (fig 2.2) with graphitic schists showing F4 folds with a NNW striking axial trace. This phase of folding is orthogonal to F3 folding and it can be observed in the structural map of figure 3.3.

The axial trace of these folds is seen to parallel closely the late NNW faulting described below, which suggests that the F4 folding produced the weaknesses which were utilized in the development of normal faults and joints in the subsequent extensional period.

In thin section a S4 schistosity can be observed cross cutting the S2 schistosity at an oblique angle, and it is typically a crenulation cleavage resulting from kinking. The kinking and development of subgrains show that there was intracrystal plasticity, and this is well illustrated within the graphitic schists and the muscovite schists (see photomicrographs in fig 3.16). The kinking was in response to D4 deformation and it is orthogonal to the main S2 schistosity. Also illustrated in these rocks is evidence for extension with the shear zones being opened and infilled and boudinage within the quartzite (fig 3.16).

The Schmidt net projection for the results from the Cerro Da Canberra formation (fig 3.17) shows that the poles to S2 schistosity are more scattered than in other units. However, there is a concentration of poles in the NE quadrant, some in the SW suggesting NE dipping schistosities, and a few poles indicating east and west dipping planes. Such scatter is probably the result of interference folding between F3 and F4. The general plunge of F2 fold hinges can be seen to be dipping shallowly to the SW (fig 3.17).

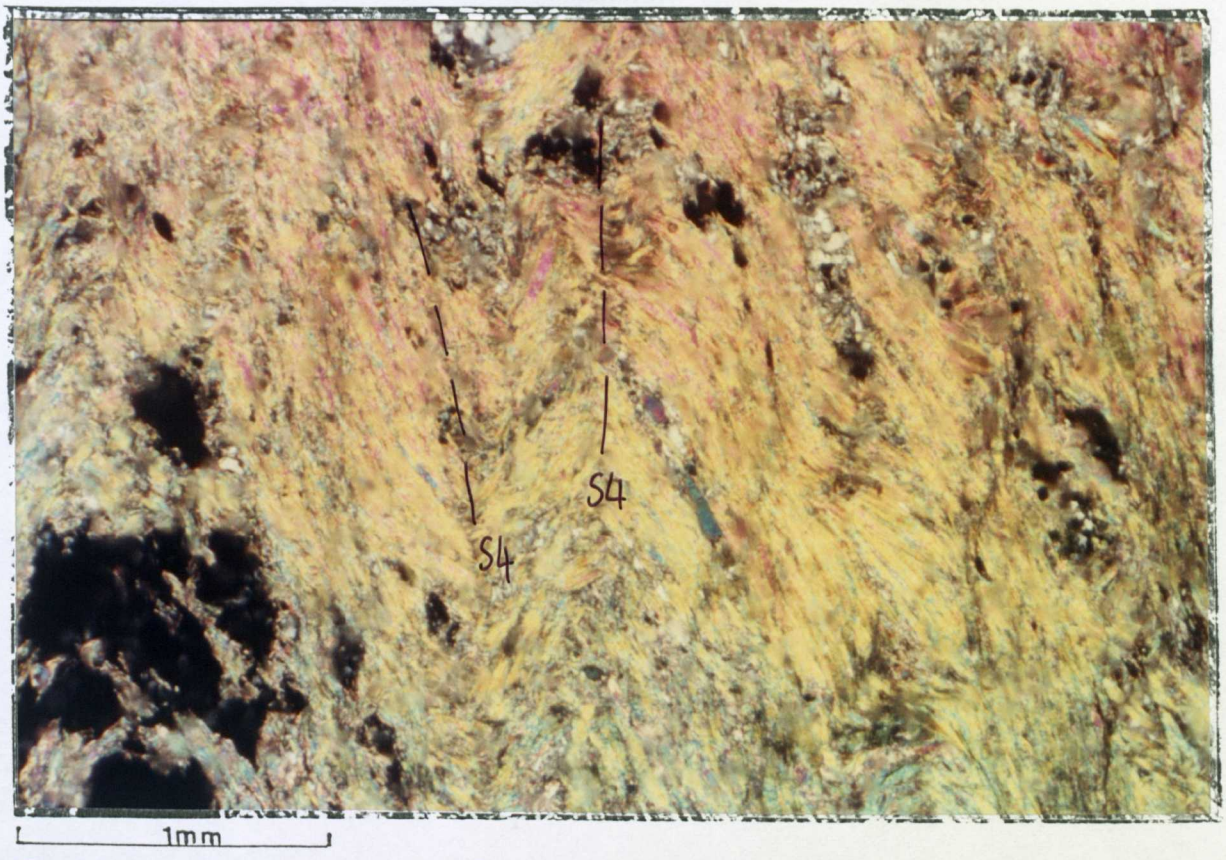

Figure 3.16a Photomicrograph (x5).of the development of S4 kink banding crenulating S2 isoclinal folds at locality 83.

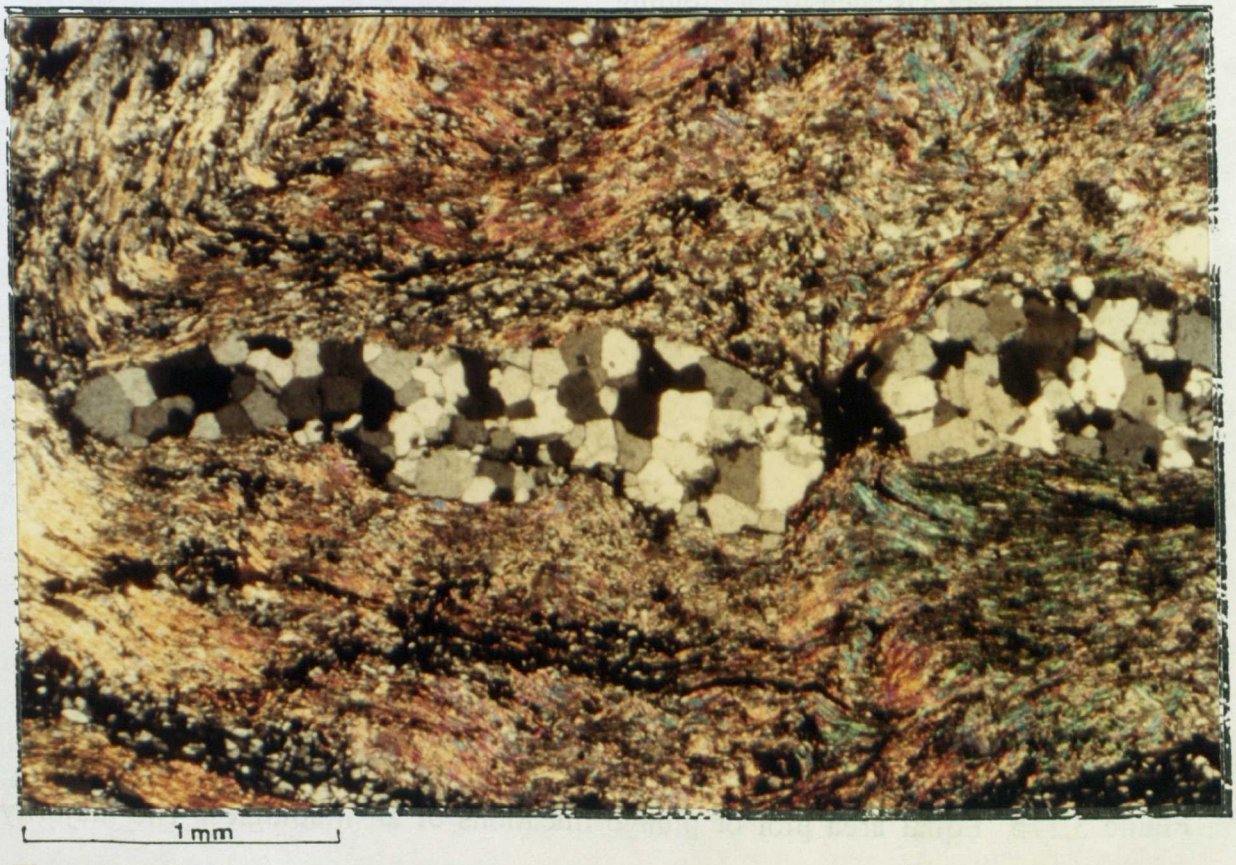

Figure 3.16b Photomicrograph (x5) of the development of boudinage structures (D4) at locality 91.

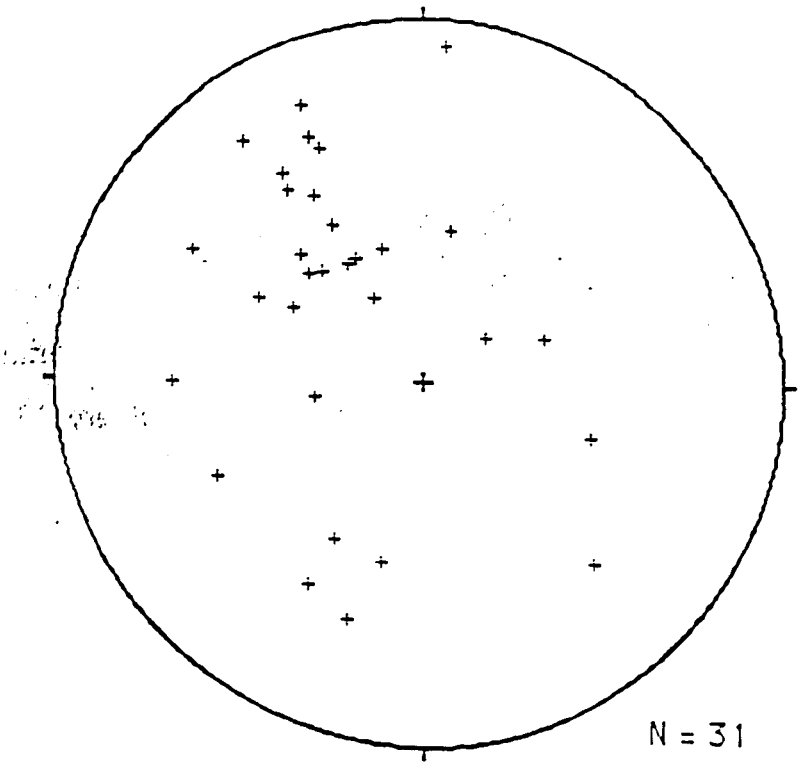

Figure 3.17a Equal area net for poles to S2 foliation in the Cerro da Canberra formation showing that there has been further folding.

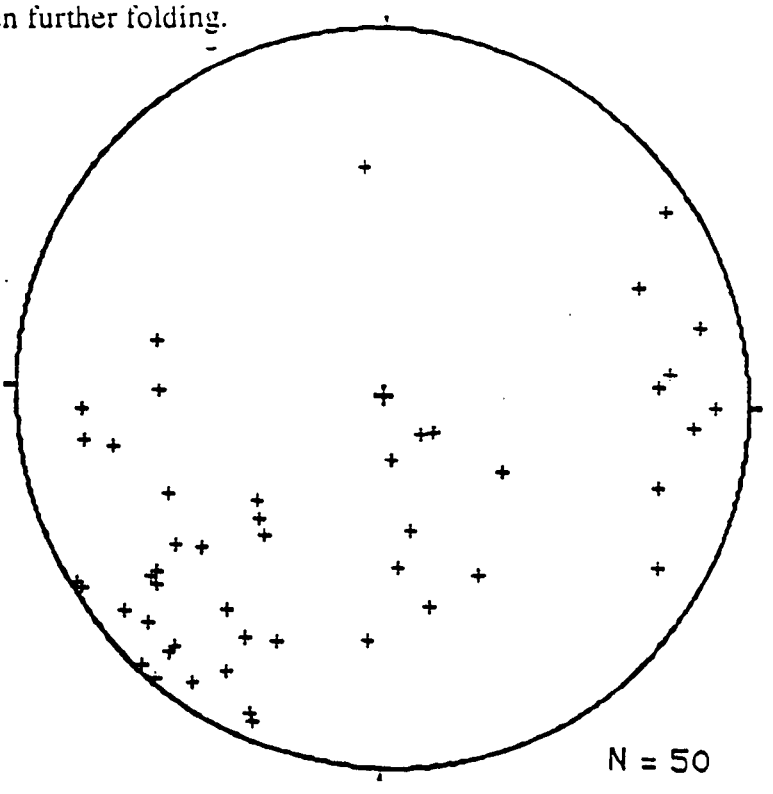

Figure 3.17b Equal area plot of plunge lineations of all lithologies. The majority of measured plunges are to the SW.

3.3.5 Post D4 extension

Major extensional features observed in the area can be divided into two orientations of extensional faulting and these features cross-cut all the phases of folding in the area.

3.3.5.1 NE-SW FAULTING

From the map (fig. 3.1) and figure 3.20a it can be seen that a major faulted basin, with flat lying Triassic red beds and volcanic flows, separates the metamorphic rocks in the SE portion of the area from the Pelotas Batholith to the SE. This is also illustrated in the geological map and cross-sections (chapter 2). The associated faults are oriented NE-SW , they are extensional in nature and parallel to the major tectonic fabric of the area and they may represent the reopening of originally compressional faults or of the S3 fabric. With relaxation and isostatic uplift often comes extension and erosion.

Extension appears to have been greater in the NW region of the area with over 1km of sediment deposited in fault bounded basins. Parallel smaller faults can be observed in the field at various localities e.g. at locality 35 within the Arroio dos Nobres formation, at locality 58 and at locality 106 in the Encanatada Schists (see section 2.2). The low lying topography which is illustrated in figure 3.20a suggests the presence of a fault basin.

3.3.5.2 NNW-SSE FAULTING

This phase of normal faulting is orthogonal to the NE-SW sets described above and it is illustrated in fig 3.18. Figure 3.20b also shows the topographic break associated with the major NE-SW fault of this deformation phase which occurs just east of the BR392 road with down throw on the SW side.

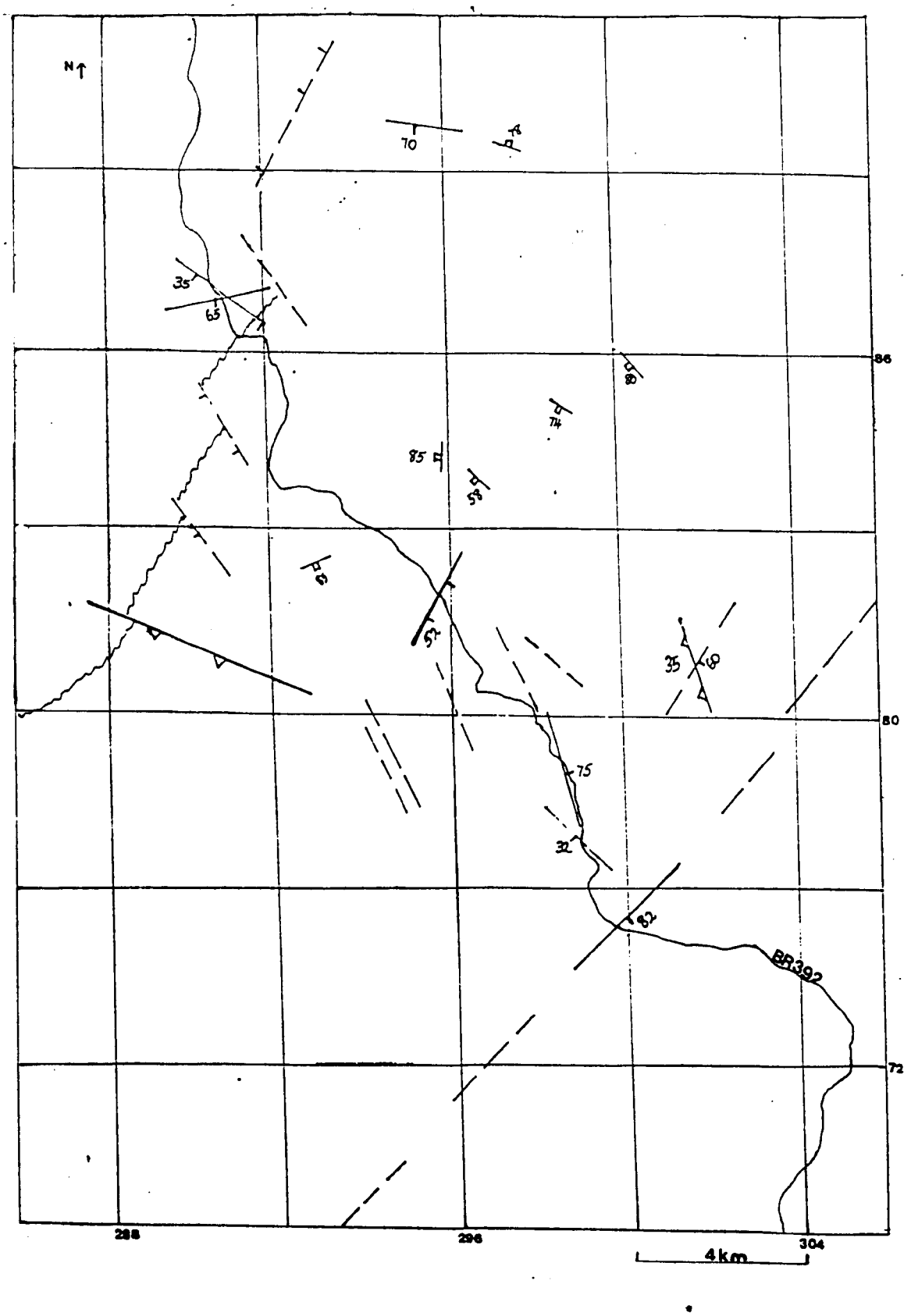

Figure 3.18 Major normal faults and joints of the Santana Metamorphic Belt.

Jointing within the gneisses parallels NNW-SSE faults suggesting that the S4 schistosity was the weakness plane along which joints opened and faulting occurred (fig 3.18). Many smaller faults parallel the major fault described above particularly in the NW of the area. Examples of this type of faulting can be seen at locality 44, locality 51 and just past locality 75 at the turning for Santana. Another major fault of this orientation occurs in the SE portion of the area, and it appears to cross cut the NE-SW extensional faulting.

Fig 3.19 illustrates that S3 foliations are predominantly steeply dipping with two main strike directions of NE-SW and NW-SE which correspond to the two major extensional fault orientations (fig 3.18).

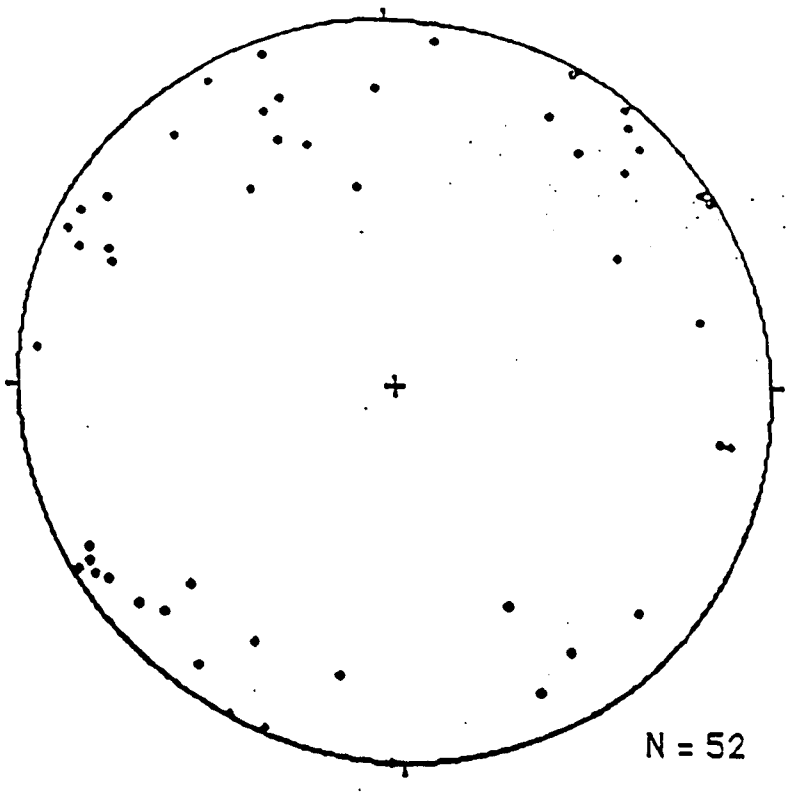

Figure 3.19 Equal area plot for S3 foliations within the mapped area.

Figure 3.20a Topographic break indicating NE-SW faulting between the Santana Metamorphic Belt and the Triassic Basin at locality 33.

Figure 3.20b Topographic break indicating NNW-SSE normal faulting at locality B62.

3.4 Summary and Discussion

3.4.1 Summary

Four phases of deformation have been recognized in the Santana Metamorphic Belt confirming the observations of Machado et al (in press).The dominant fabric is orientated NNE-SSW as recognized by Ribeiro et al (1966). From this study it has been established that D1 produced the banding in the gneisses, and that D2 was responsible for isoclinal folding. D3 resulted in open upright folds and D4 produced kinking and NE verging thrusts.

If this study is compared with that of Jost (1981) it is noted that he attributes F2 isoclinal folding to buoyancy whereas I would attribute it to a tightening during the subsequent D3 compressional event. He interprets the SE part of the area mapped, as a nappe with D3 NW-verging thrusts, whereas I found no evidence of this and thrusting occurs as a D4 event with NE vergence. My structural sequence of events closely resembles that of Machado et al (in press).

Comparison of the Santana Metamorphic Belt with the Brusque Belt of Santa Catarina (Basei 1985) suggests that the two belts are continuous (fig 3.21). In the Brusque Belt D2 is responsible for isoclinal folding and D3 for open upright folds. However NW-verging thrusts (D3) are recognized in the Brusque Belt, and they have not been recognized in this study. Thrusting does not appear to have occured in the Santana Metamorphic Belt until D4 and it is NE-verging. Figure 3.21 compares cross sections from the two belts and figure 3.22 illustrates a regional map of SE Brazil. A regional summary of the tectonic evolution of Eastern Brazil is given in Chapter 8.

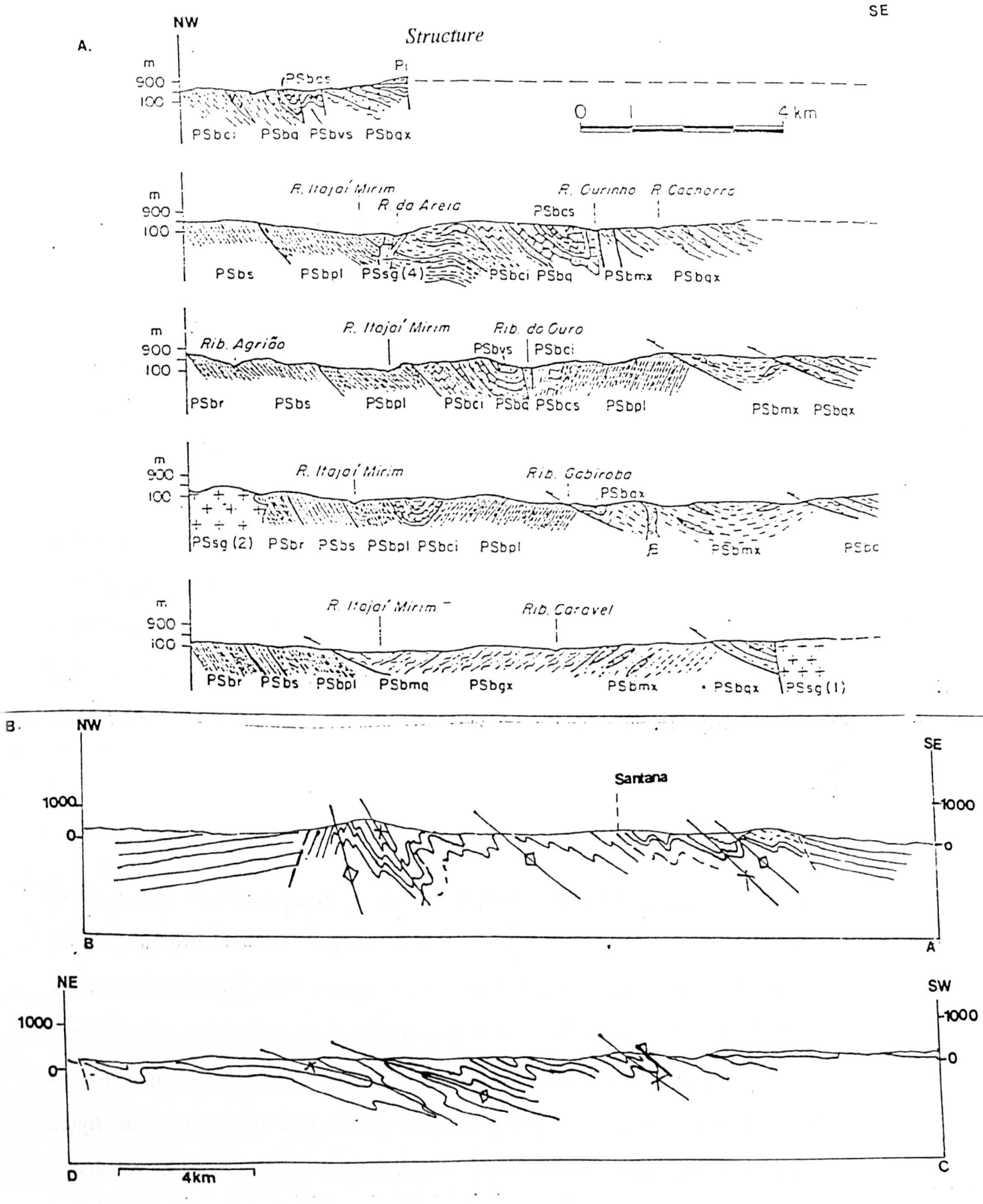

Figure 3.21 compares cross-sections through the Dom Feliciano Belt in a) Santa Catarina and b) Rio Grande do Sul and shows that both have predominantly NW vergence.

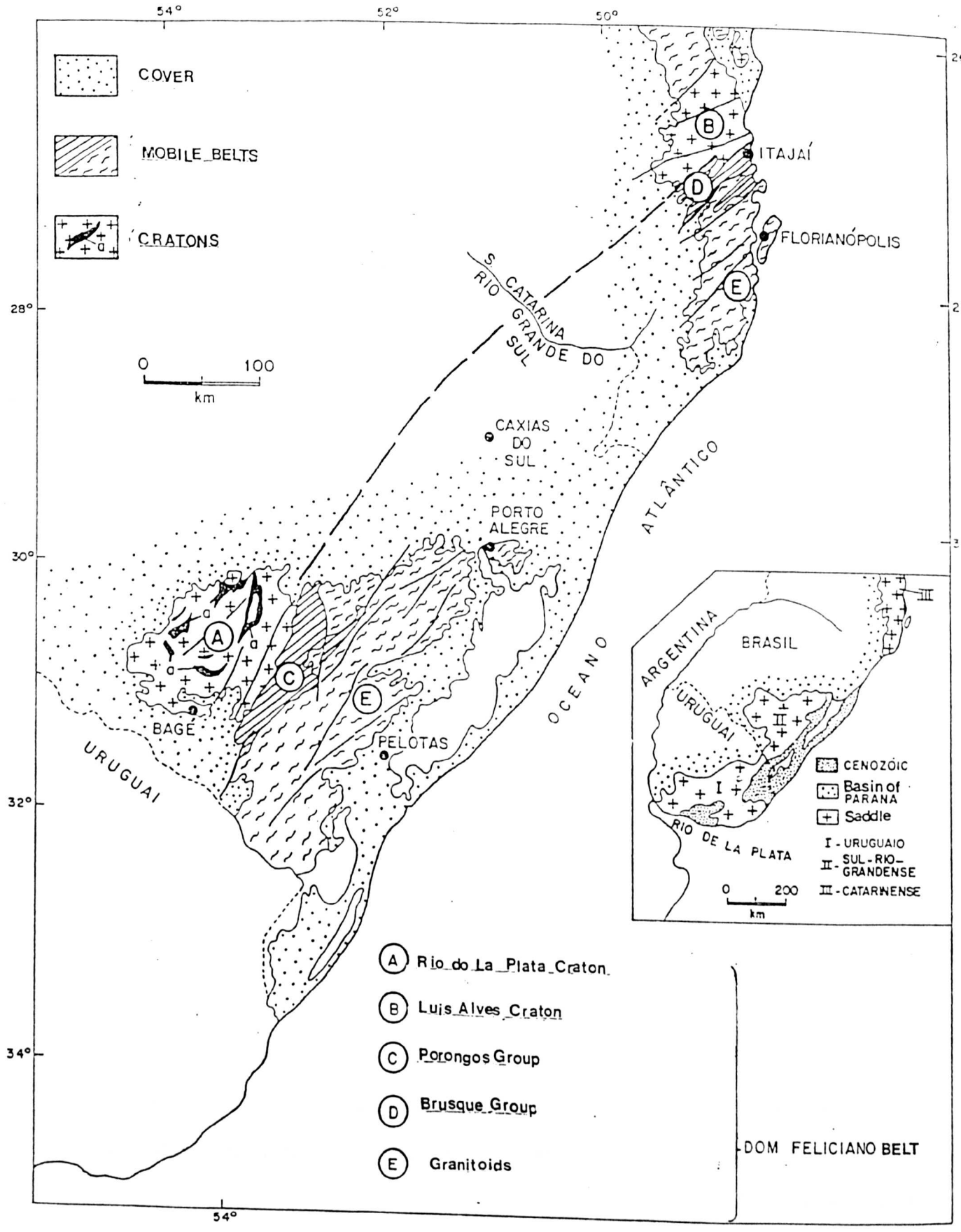

Figure 3.22 shows the conjectured continuation of the Dom Feliciano Belt from Santa Catarina to Rio Grande do Sul.

3.4.2 Discussion

A structural pattern commonly found in metamorphic rocks is the tendency for a temporal change from early recumbent to later upright folding (Fyson 1971). The change in temperature recorded by metamorphic grade seems to have no bearing on this temporal relationship. On the other hand, lithostatic pressure may be a controlling factor in the ability of a rock to form upright folds.

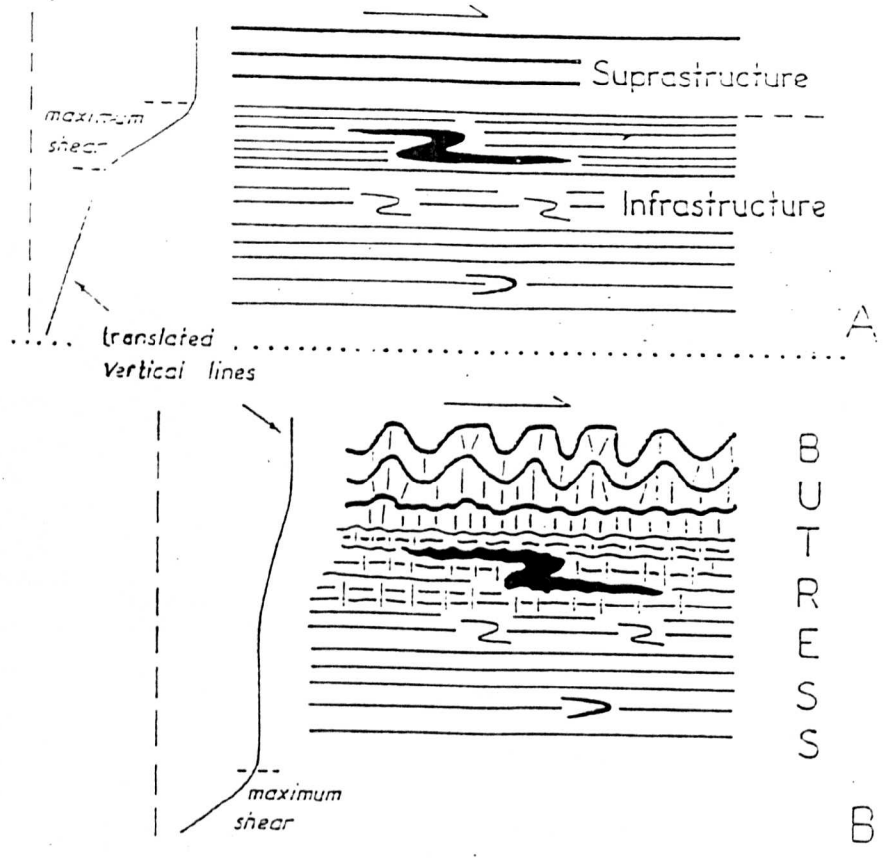

Figure 3.23 Fyson's 1971 crustal model illustrating migration upward of the locus of maximum folding and change in fold attitiude. Vertical lines translated horizontally during unspecified time periods.

A. Early recumbent folds confined to infrastructure. Suprastructure is translated but undeformed.

B. Later upright folds dominant in suprastructure. The zone of maximum shear is displaced downward.

Fyson's model suggests that penetrative and recumbent folding is restricted to the infrastructure beneath the overriding undeformed cover which is translated and undeformed (fig 3.23). The inferred horizontal displacement continued until the cover rocks were obstructed by a buttress. This compression folds the cover, but the basement acts as a homgeneous mass having been welded together by the recumbent folding and recrystallization, and so the zone of maximum shear is displaced downwards. Further movement resulted in horizontal compression in prefolded rocks and upright folding about axes parallel to those of the earlier recumbent folds . In this study F2 folds are isoclinal and recumbent and F3 folds are more open and upright which supports the model.

BLANK PAGE
IN
ORIGINAL

CHAPTER FOUR

4. Metamorphism and P-T studies of the Santana area.

4.1. Introduction

Metamorphic studies have been undertaken in the mapped area around Santana da Boa Vista to determine the number of metamorphic events and their relationship to deformation. A number of approaches have been used including field observations, petrographic studies and analysis of minerals using the wavelength dispersive electron microprobe at the Open University. Equilibrium assemblages have been studied to try and determine the conditions of pressure and temperatures associated with the deformation events.

Metamorphic conditions have been estimated by calculations based on extensions to the data set of Holland and Powell (1985) using the program Thermocalc by Holland and Powell (1988). These extensions involve the addition of the phases almandine, annite and celadonite white mica which have been made consistent with several experimental phase equilibria including Ferry and Spear (1978) and Bohlen et al (1983). Celadonite data has been incorporated following Powell and Evans (1983).

Activities for solid phase components in minerals were calculated by assuming ideal mixing on site (phlogopite, chlinochlore, annite), the Newton Haselton (1981) formulation for garnet activities (pyrope,almandine,grossular) and the Price (1985) and Newton Haselton (1981) activities for sanidine and anorthite. For muscovite and celadonite ideal mixing on site activities was used but non-ideal ion site was introduced using mixing parameters from Chatterjee and Flux (1986). The advantages of using Holland and Powell is that equilibria are self consistent and the uncertainties can be realistically assessed (Harris et al 1988).

4.2 Metamorphic assemblages and facies

4.2.1 Previous work

Picada and Tessari (1970) suggested that the schists in this area have undergone greenschist to lower amphibolite facies metamorphism and that the Encantada Gneisses underwent sillimanite zone prograde metamorphism and then retrogression (Goni 1962). Jost (1981) undertook a more detailed petrological study of metamorphism and pointed out the limitation of metamorphic study in the area, as the bulk composition of the rocks imposed severe restrictions on the sequence of prograde reactions. The absence of unweathered pelitic rocks and the rarity of garnet-bearing assemblages in the area maked the mapping of isograds very difficult. Jost (1981) mapped five major assemblages in the Santana area and produced an isograd map which is shown in fig 4.1. The assemblages that he found were:

quartz-muscovite-chlorite; quartz-muscovite-biotite-chlorite; quartz-muscovite-biotite-garnet; quartz-muscovite-biotite-garnet-staurolite-chlorite-andalusite; quartz-muscovite-biotite-chloritoid-chlorite-kyanite-garnet.

Other minerals present included epidote, sphene, haematite, apatite, albite, pyrite and chalcopyrite. Kyanite was observed in the Cerro da Canberra formation and andalusite and staurolite were rare. He does not discuss the metamorphism of the Encantada Gneisses. Symbols used for minerals in this study are given in table 4.1.

4.2.2 This study

Assemblages found in each of the stratigraphic units of chapter 2 are summarized in the following table 4.2. Approximately fifty thin sections have been studied from the area of mainly pelites, with some metagranites and metabasites. From this study it became apparent that there is no kyanite, andalusite, sillimanite or chloritoid found in any of the pelites collected from a large number of different localities in the area. This absence of aluminous phases may be the result of the extensive weathering of pelite horizons, but more likely it is a function of the rock composition.

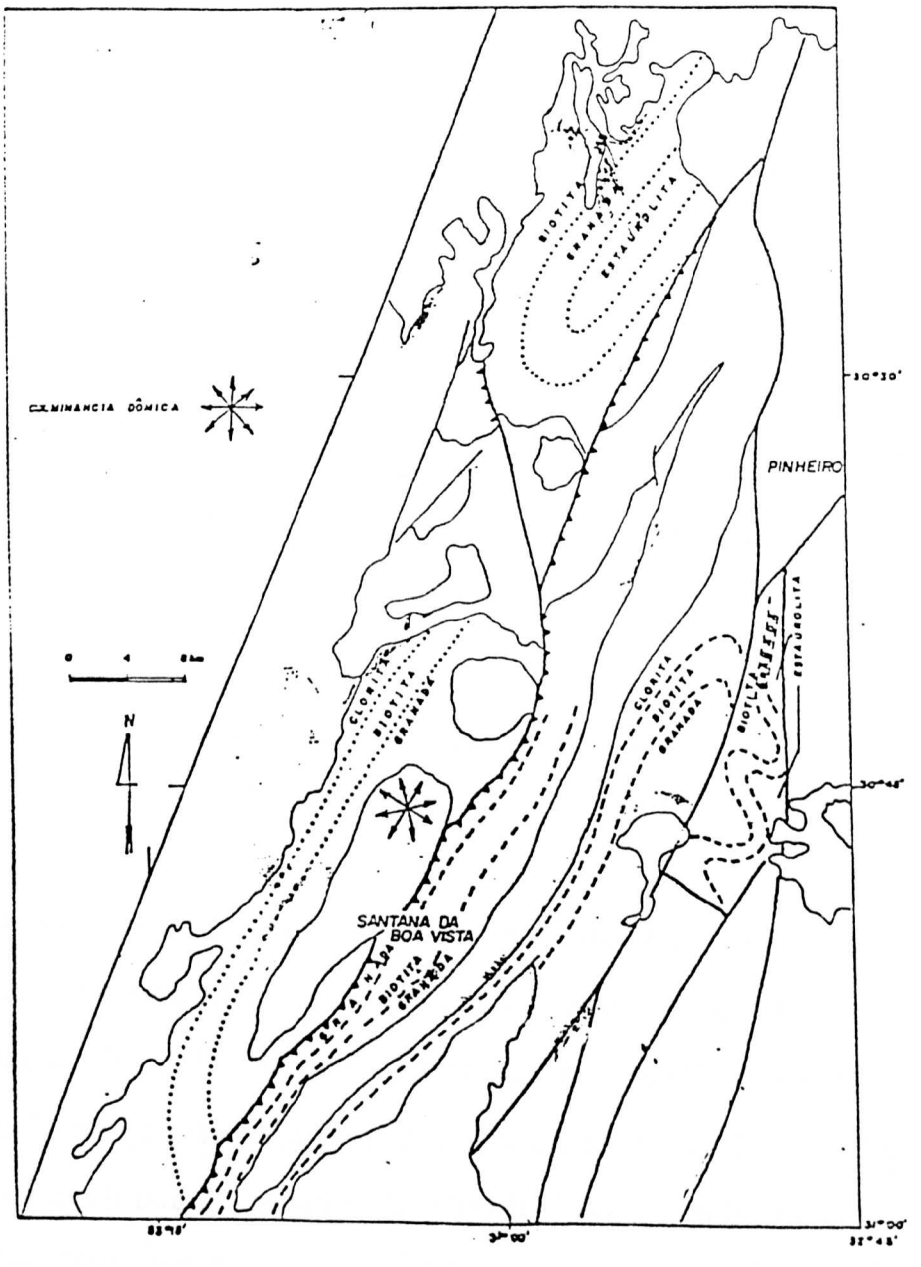

Figure 4.1 Metamorphic isograds mapped by Jost (1981) in the Santana da Boa Vista area.

ALBITE	AB	HORNBLENDE	HBL
ALMANDINE	ALM	K-FELDSPAR	KSPAR
ANNITE	ANN	KYANITE	KY
ANORTHITE	AN	MUSCOVITE	MUSC
BIOTITE	BI	ORTHOPYROXENE	OPX
CALCITE	CALC	OLIVINE	OL
CELADONITE	CEL	PHLOGOPITE	PHL
CHLORITE	CHL	PLAGIOCLASE	PLAG
CLINOPYROXENE	CPX	PYROPE	PY
CLINOZOISITE	CZ	STAUROLITE	ST
EASTONITE	EAST	TOURMALINE	TOURM
EPIDOTE	EP	GRAPHITE	GPT
GROSSULAR	GR	QUARTZ	QZ
GARNET	GT	APATITE	AP

TABLE 4.1 Abbreviations used in this chapter and figure 4.2.

Fortunately a few samples containing garnet were found and these have been used to constrain pressures and temperatures (section 4.4). Other minerals found include biotite, plagioclase, muscovite, clinozoisite, hornblende (see table 4.1). Common accessory minerals include tourmaline, magnetite, apatite, zircon, sphene and pyrite. The location of the samples studied in thin section is illustrated in figure 4.2 and the assemblages are illustrated in fig 4.3 using AFC, AKF and AFM projections (Eskola 1932 and Thompson 1956) are discussed below. Microprobe data is summarized for 6 samples in appendix B.

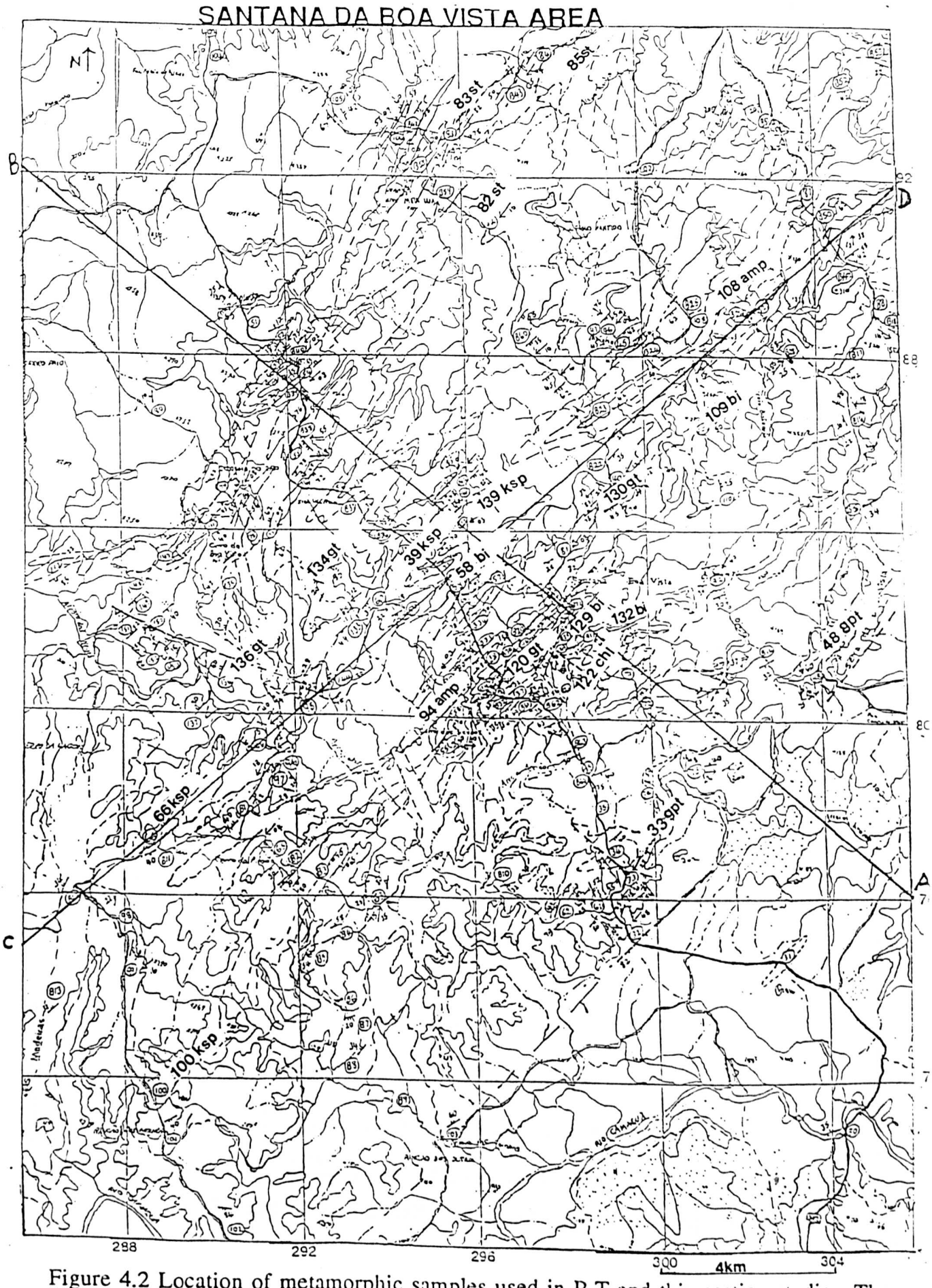

Figure 4.2 Location of metamorphic samples used in P-T and thin section studies. The abbreviations used are given in Table 4.1.

4.2.3 Assemblages of stratigraphic units

4.2.3.1.ENCANTADA GNEISSES

These are represented by the assemblage in sample 139 and the composition of the biotite is illustrated in the AFM projection of figure 4.3.a based on microprobe analysis of the mineral.

UNIT	LITHOLOGY	(sample)	ASSEMBLAGE
Encantada	Biotite gneiss	(142,139)	Qz+bi+ksp+plag±ep,chl
Gneiss	Granitic gneiss	(130,93)	Qz+bi+ksp+chl+musc±ep
	Amphibolitic gneiss	(95)	Qz+bi+ksp+hbl±ep
Encantada	Biotite schist	(58)	Bi+qz+kspar
Schists	Biotite Schist	(85b)	Qz+bi+cz+st
	Biotite Schist	(119,118A)	Qz+musc+bi+gt+pl±ep,chl
Arroio Arreiao	Muscovite schists	(134,136)	Qz+musc+bi+pl+gt+ep
formation	Muscovite schist	(83)	Qz+musc+tourm+cz
	Pink mylonite	(66,100)	Qz+musc+kspar
		(77B)	Qz+musc+kspar+plag
Cerro Dos Bicudos	Quartzite	(99)	Qz+musc
Cerro da Canberra	Marble	(126)	Calc+olivine
	Marble	(34)	Calc+qz+musc
	Graphitic schist	(90,48,33)	Qz+gpt+musc+qz±calc
	Graphitic schist	(132,129)	Qz+gpt+bi+chl+pl
Metabasite	Gabbro	(108)	Qz+hbl+ep

Table 4.2 Metamorphic assemblages found in the Santana Metamorphic Belt.

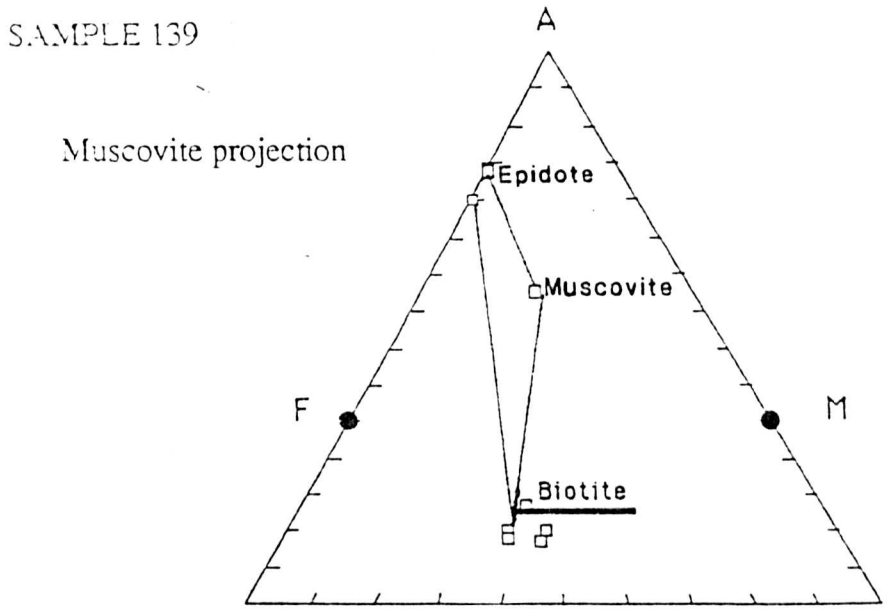

Figure 4.3a Thompson AFM projection for the Encantada Gneiss formation.

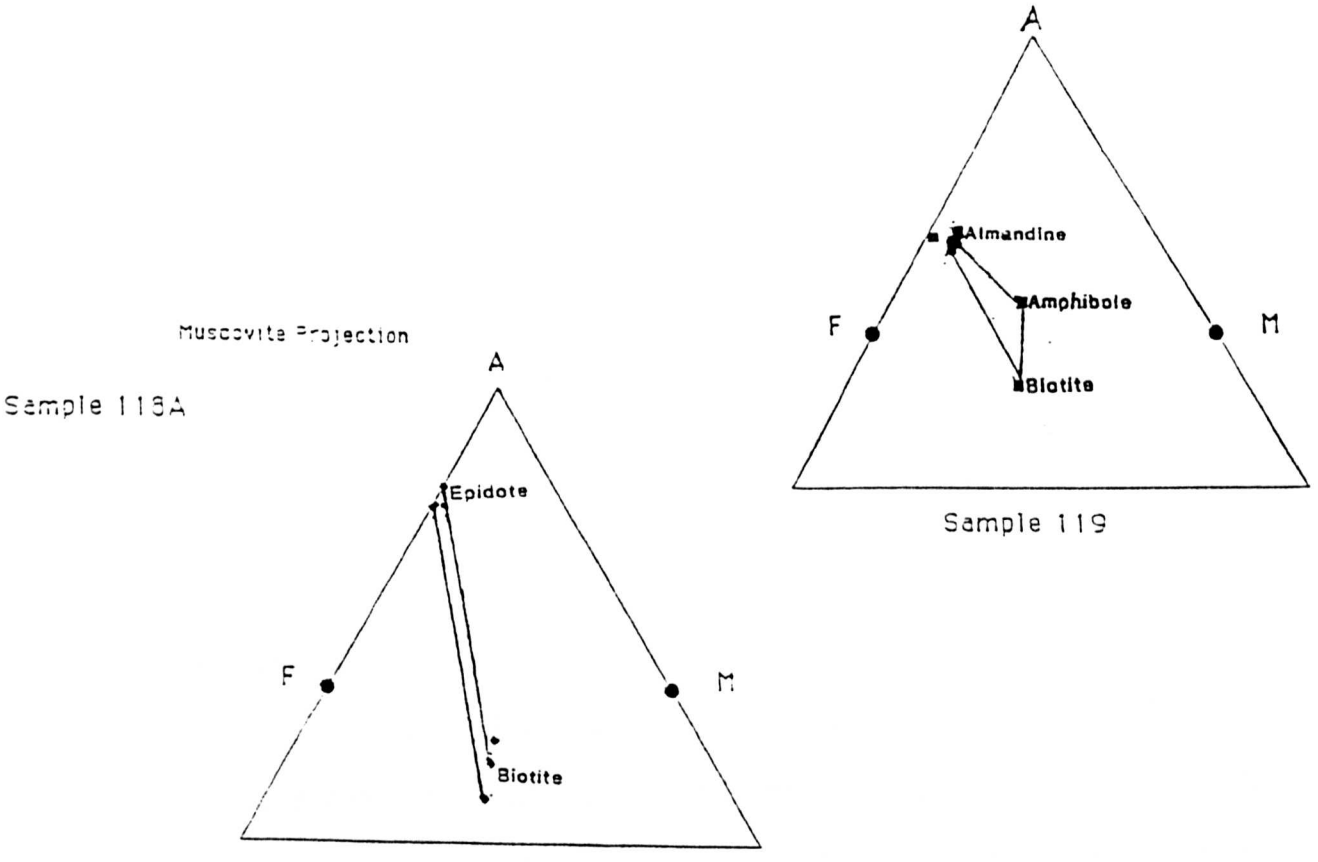

Figure 4.3b Muscovite Thompson AFM projections for the Encantada Schists.

4.2.3.2 ENCANTADA SCHISTS

This unit is represented by sampless 118A and 119 and illustrated in figure 4.3b based on microprobe analyses. These samples contain garnet, although it is rare in sample 118 and there is no microprobe analysis of this mineral for this sample. It does contain muscovite which is absent in 119. These two samples contain garnet-bearing equilibrium assemblages and are used in P-T determinations in section 4.4.

4.2.3.3 ARROIO ARREIAO SCHISTS

Samples 134 represents a garnet-biotite-muscovite pelite from this formation and it contains small garnets along with biotite and muscovite which represents an equilibrium assemblage associated with the main metamorphic event M2 (section 4.3). This assemblage is illustrated in figure 4.3c along with sample 136 which contains no garnet. Secondary epidote appears in both rocks but is not included in the equilibrium assemblage used to constrain pressure and temperature in section 4.4.

4.3.2.4.CERRO DA CANBERRA

This unit is illustrated using sample 132 in figure 4.3d and contains qz-bi-chl-plag and graphite. It has been analysed using the microprobe but assemblages do not constrain a pressure and temperature of equilibration.

4.3.2.5. METAGABBROS

This unit is represented by sample 108 which contains the assemblage hornblende epidote and quartz and is illustrated in the figure 4.3e, along with sample 95 which also contains biotite and alkali feldspar. No pressure and temperaure can be established between phases of known thermodynamic properties using Thermocalc for these samples because end member reactions cannot be constructed from these phases.

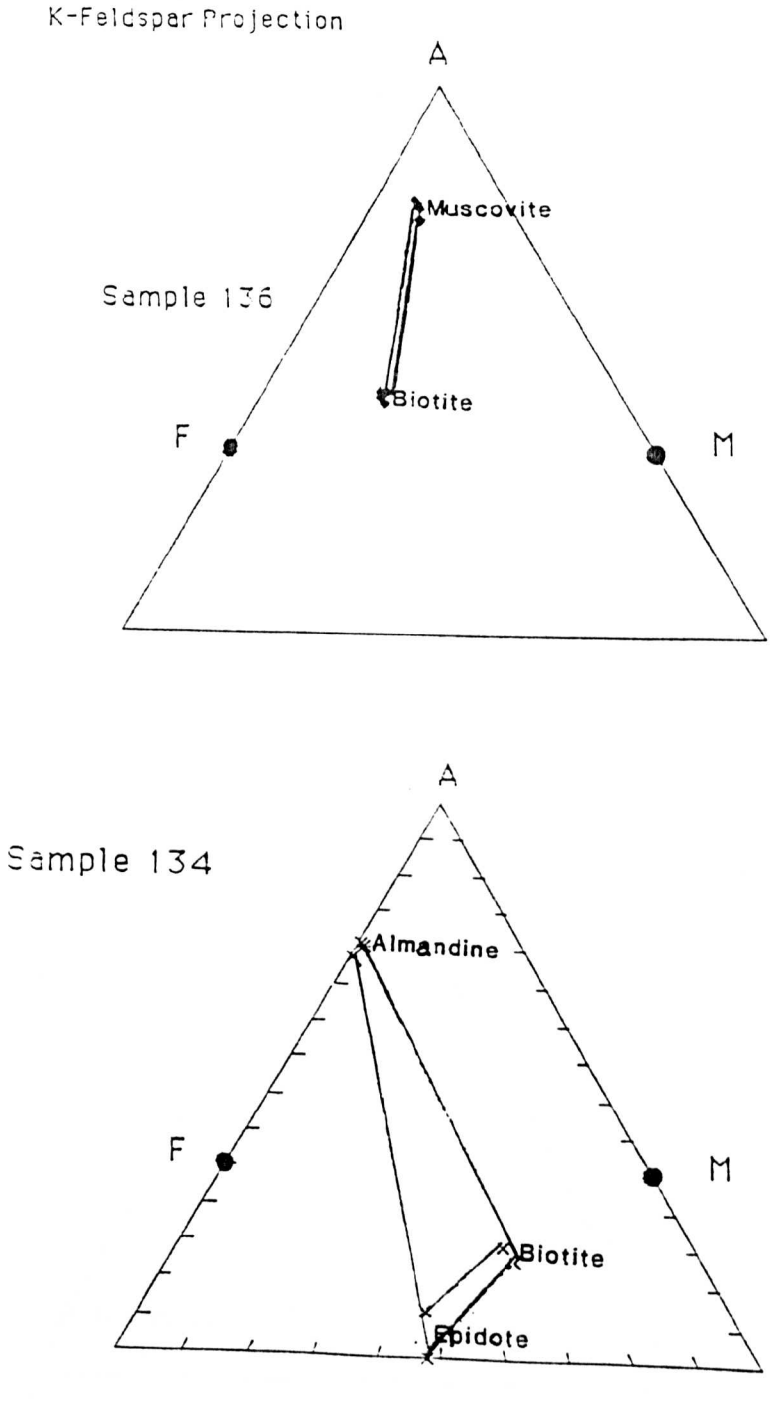

Figure 4.3c Muscovite Thompson AFM projections for the Arroio Arreiao formation.

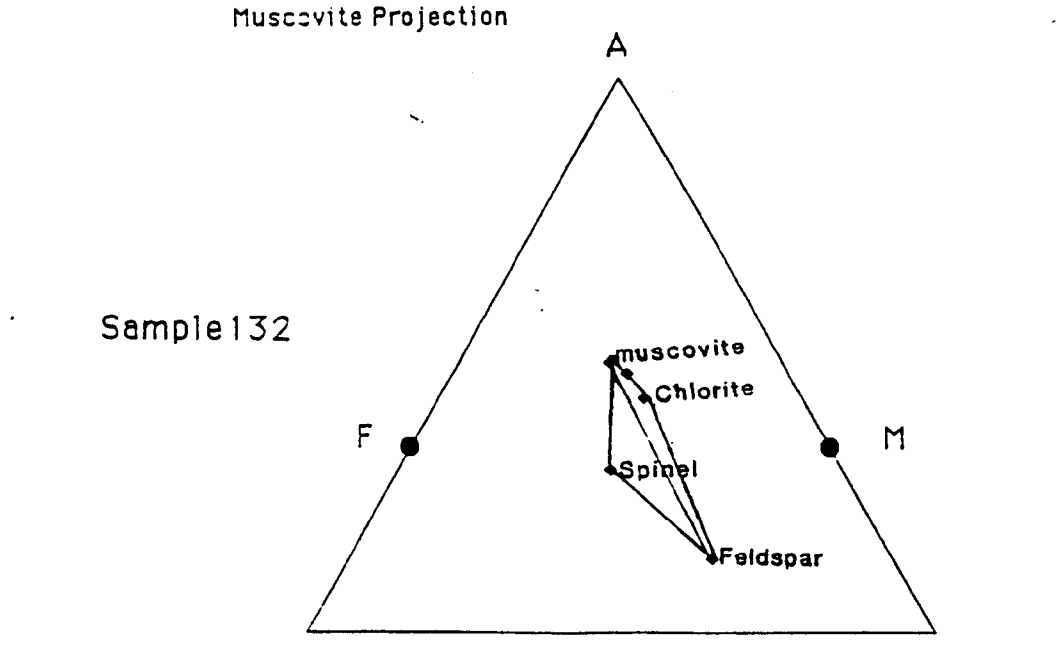

Figure 4.3d Thompson AFM projection for the Cerro da Canberra formation.

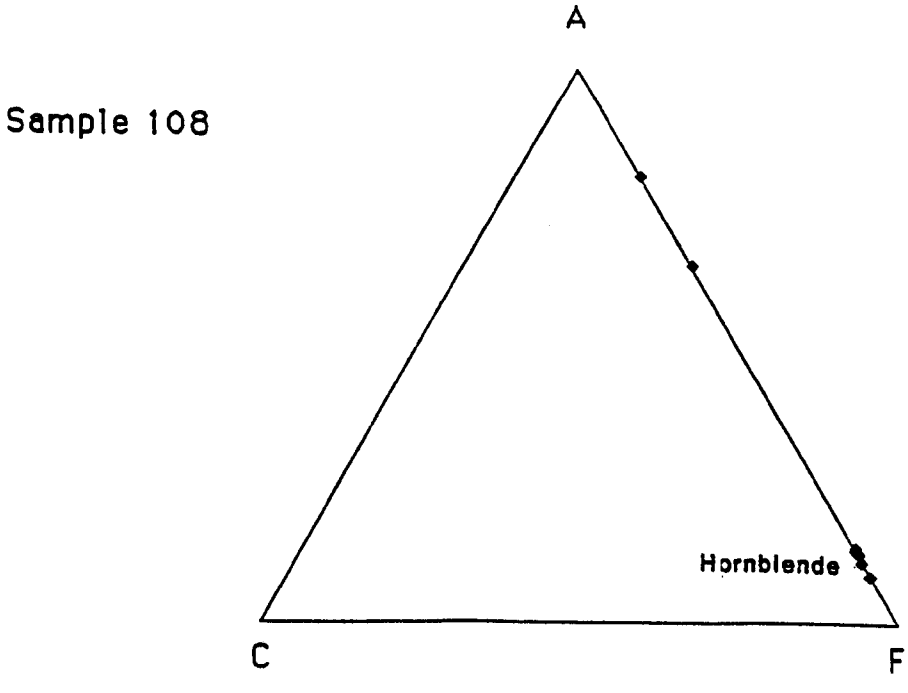

Figure 4.3e Muscovite Thompson AFM projections for the metagabbro.

4.3 Relationship between deformation and metamorphism

4.3.1 Introduction

Studies on the relationship between deformation and metamorphism have been undertaken by Jamieson and Vernon (1987) who analysed the interaction between a growing porphyroblast and a developing crenulation foliation. They concluded that porphyroblasts grow by replacing the matrix in zones of progressive shortening and that inclusion trails within porphyroblasts can therefore give an important indication of the relationship of the growth of metamorphic porphyroblasts to the matrix foliation.

Little is understood about the mechanisms by which porphyroblasts replace existing matrix and there is a controversy over whether a growing porphyroblast can push aside a pre-existing schistosity (Harker 1932), or whether deflection of schistosity has resulted from flattening around the porphyroblasts (Vernon 1978).

Similar work has been undertaken by Bell et al (1986), who advocate that sites of porphyroblast nucleation are controlled by deformation partitioning during deformation and metamorphism. Rubenach and Bell (1988) suggest that porphyroblast growth occurred during the formation of crenulations superimposed on a mylonitic fabric. They conclude that porphyroblasts growing within a matrix do not push aside a pre-existing foliation and that metamorphic reactions may proceed via a complex pattern of sites of dissolution and growth with many minerals acting as catalysts. Strain energy is an important factor as strained minerals are dissolved in preference to unstrained grains.

It is important to discuss metamorphism in the context of the recognized structural events affecting the area (Chapter 3). This is most effectively undertaken by studying thin sections which are illustrated using photomicrographs and annotated sketches. The relative chronology of porphyroblast growth and matrix crystallization provides a firm basis on which to identify equilibrium assemblages, to relate these to regional deformation episodes and to determine P-T constraints for equilibrium during these episodes.

4.3.2 Metamorphic events

Three major metamorphic events have been recognized in this study (table 4.2b). The first event M1, was responsible for the formation of the micas within the Encantada Gneisses, forming the dominant compositional banding in response to D2 isoclinal folding. This event was also responsible for the micaceous minerals within the other schists of the basement.

The second event was responsible for the growth of the garnet and amphibole porphyroblasts in the amphibolites and schists, and this growth post-dated S2 and occurred in response to the strain along crenulations produced in response to S3 (see figure 4.8). The third produced greenschist facies metamorphism causing retrogression of garnet and the growth of clinozoisite and this was related to D4. Each of these events will be discussed in relation to the stratigraphic units they affect, and to the structural fabrics and events.

Event	Matrix	Porphyroblasts	Facies	Schistosity
M1	Muscovite Biotite	Garnet	Upper amphibolite	S2
M2	Muscovite Biotite	Garnet,Hornblende Biotite, Plagioclase	Amphibolite	S3
M3	Graphite Musc.Chlorite	Epidote,Tourmaline	Greenschist	S4

Table 4.2b

The relationship of the appearance of critical minerals to deformational phases is illustrated in the tables 4.3-4.5 for a range of protolith compositions, in order to evaluate the timing and concentration of mineral growth. This is undertaken by studying porphyroblast/matrix relationships in thin sections. From these tables it can be established how mineral growth related to deformation and to changes in P-T conditions.

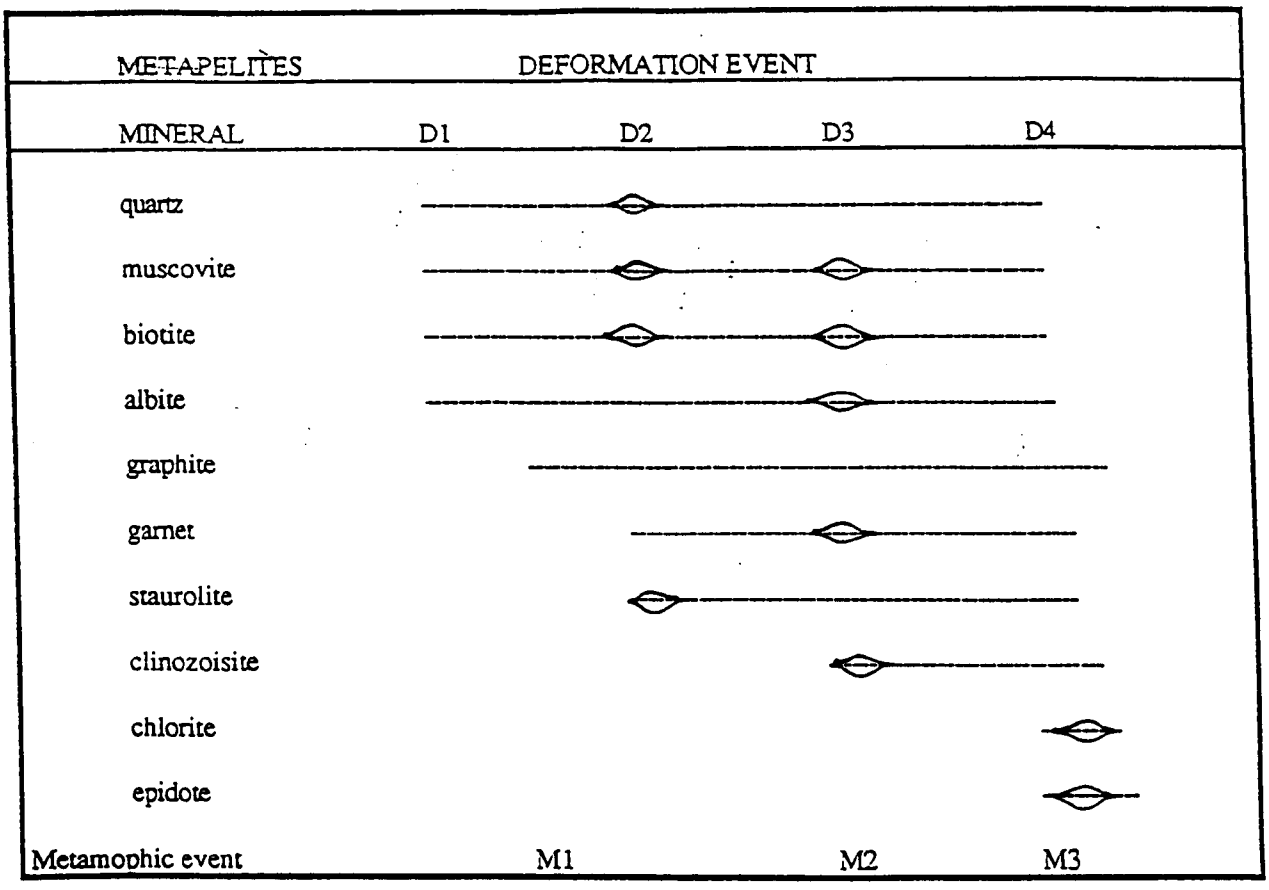

Table 4.3

In the tables shown above, the thickness of the lenses qualitively represents the growth of porphyroblasts. The dotted line represents the continued presence of a mineral from a previous event, or from the original protolith.

It is apparent from the tables that three periods of porphyroblast growth can be recognized in the Santana portion of the Dom Feliciano belt. The relationship of the porphyroblast growth to deformation will be discussed for each event and illustrated using photomicrographs and annotated sketches. The relationship between the matrix and porphyroblasts is also discussed.

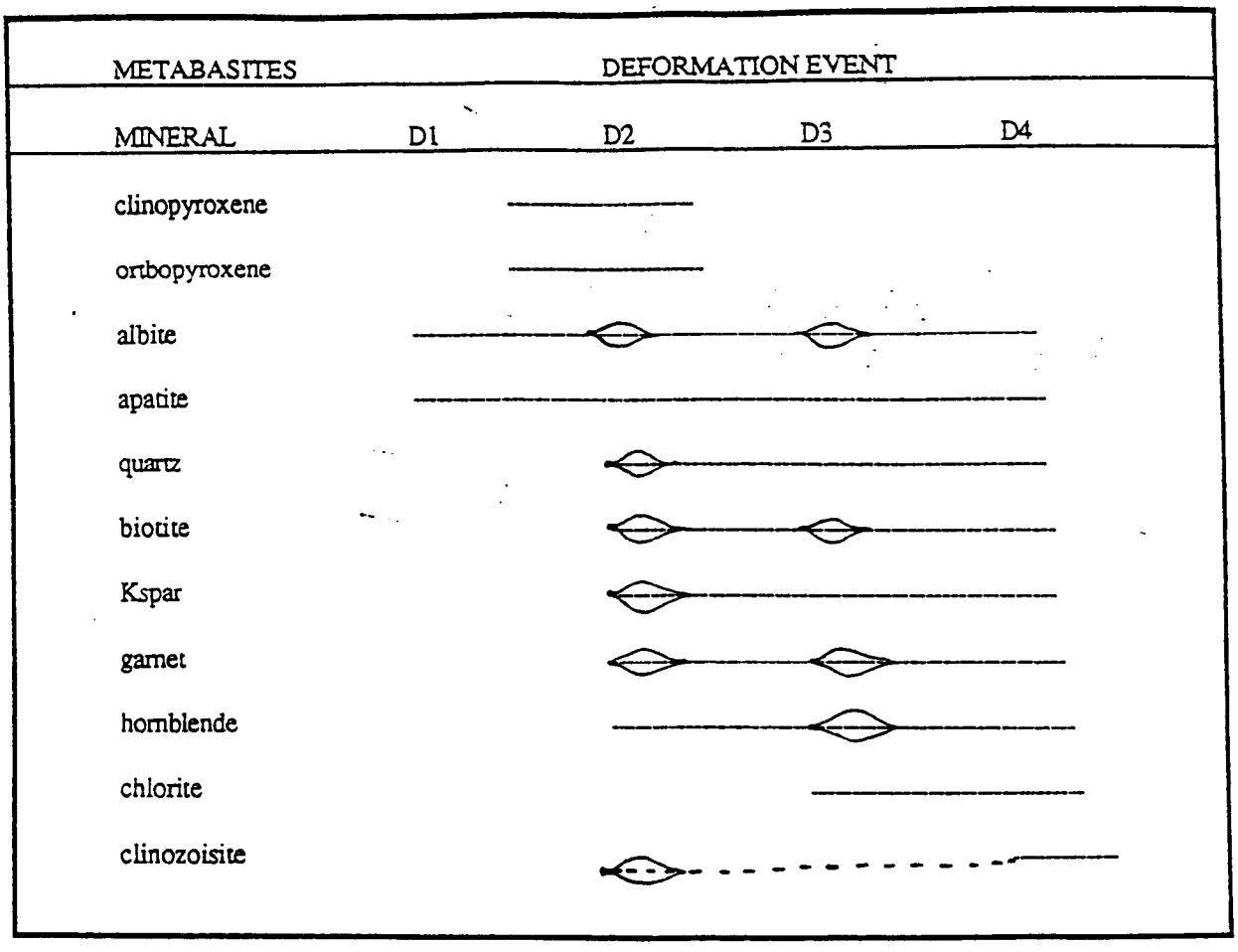

Table 4.4

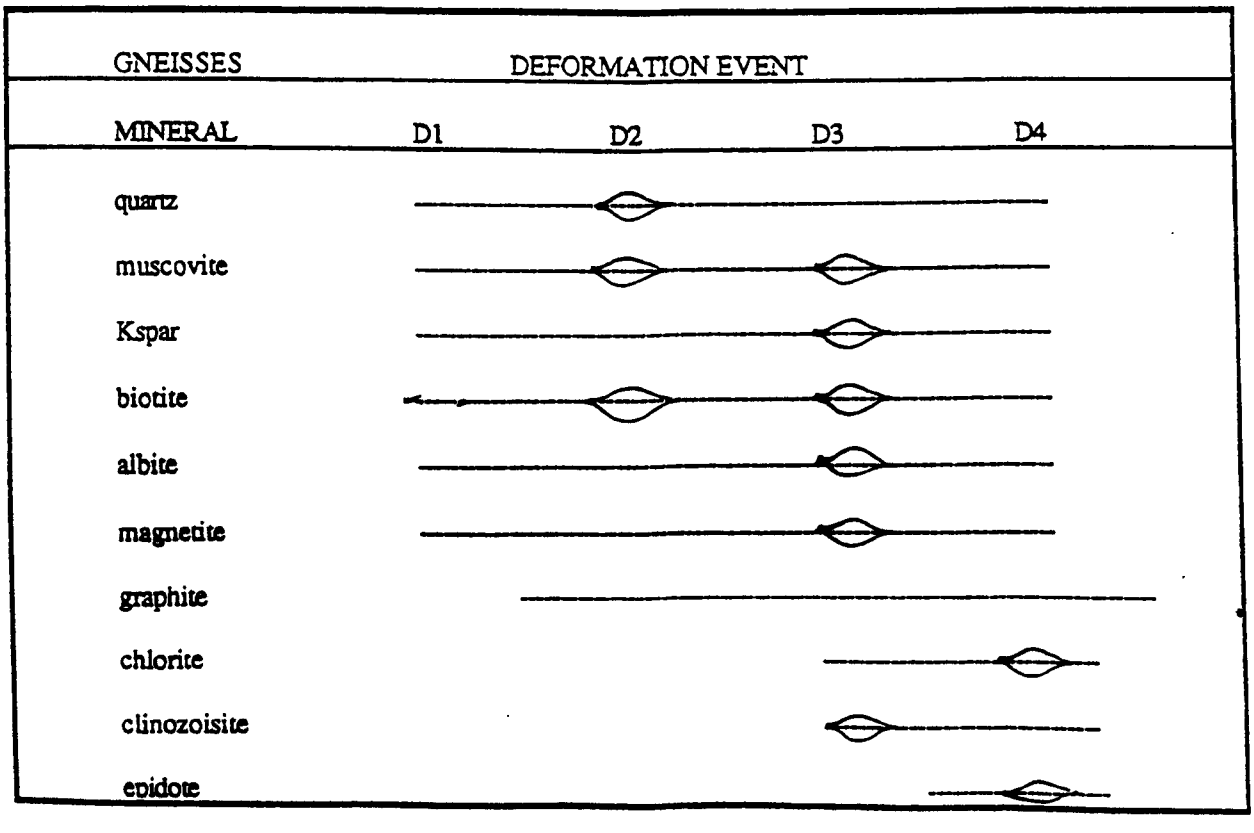

Table 4.5

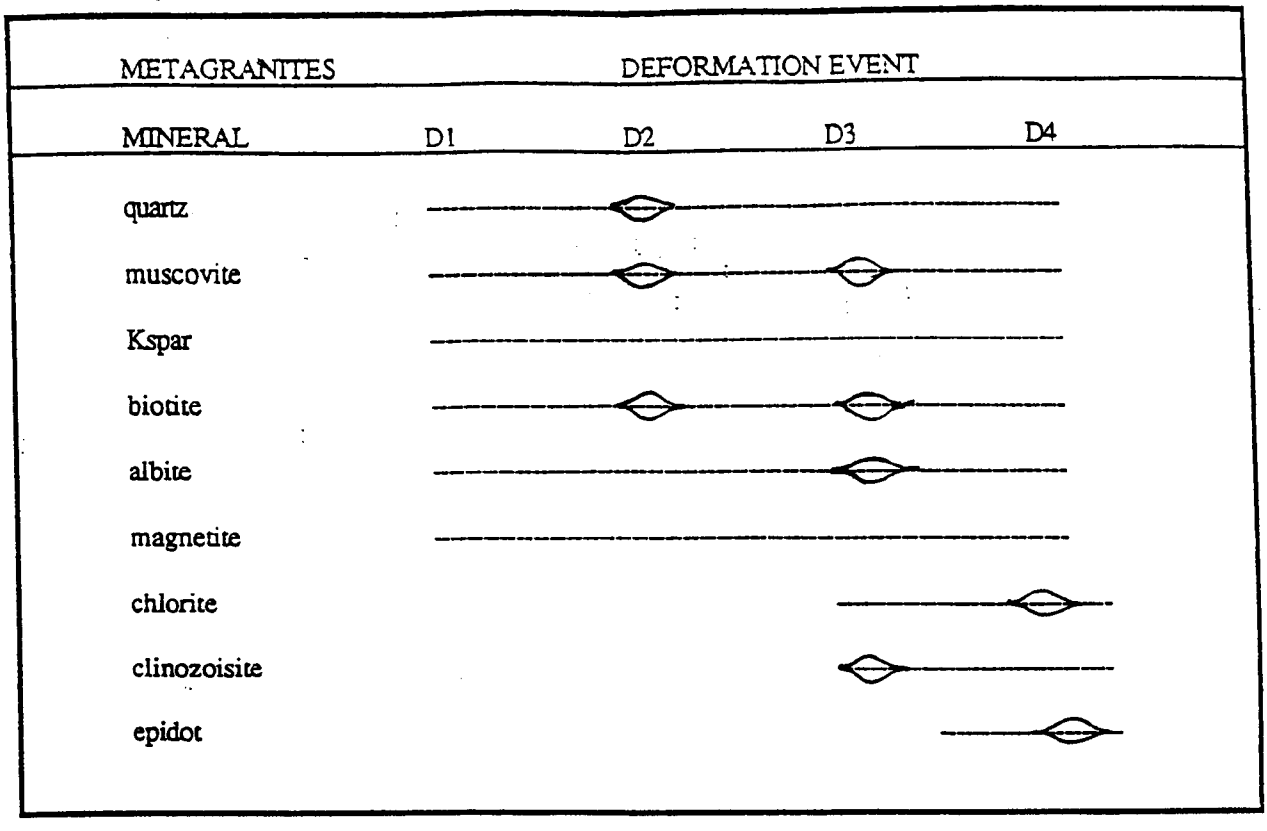

Table 4.6

4.3.2.1 M1 EVENT

This phase of metamorphism is characterized by the growth of muscovite and biotite and the recrystallization of quartz within the Encantada basement gneisses and schists resulting in the marked compositional banding in the gneisses. Garnet growth occurs in some of the amphibolite gneisses along the S2 fabric (fig 4.4). This metamorphism is most likely the result of burial in response to D2 deformation which folds the S1 fabric into isoclinal folds with the re-orienation of the micas at the isoclinal fold hinges. This is illustrated in figure 4.5 where isoclinal hinges are the only illustration of a S1 schistosity since F2 folds are isoclinal.

The timing of this metamorphic event presents a bit of a problem as S1 may have originally been a slaty cleavage within mudstones and only been converted to micas during F2 folding. Alternatively the gneisses may have been retrogressed from granulite facies although there is little evidence to support this apart from their model ages of 3.5 G.a. (chapter 7) and the presence of granulites in the Rio de la Plata craton (chapter 1).

a)

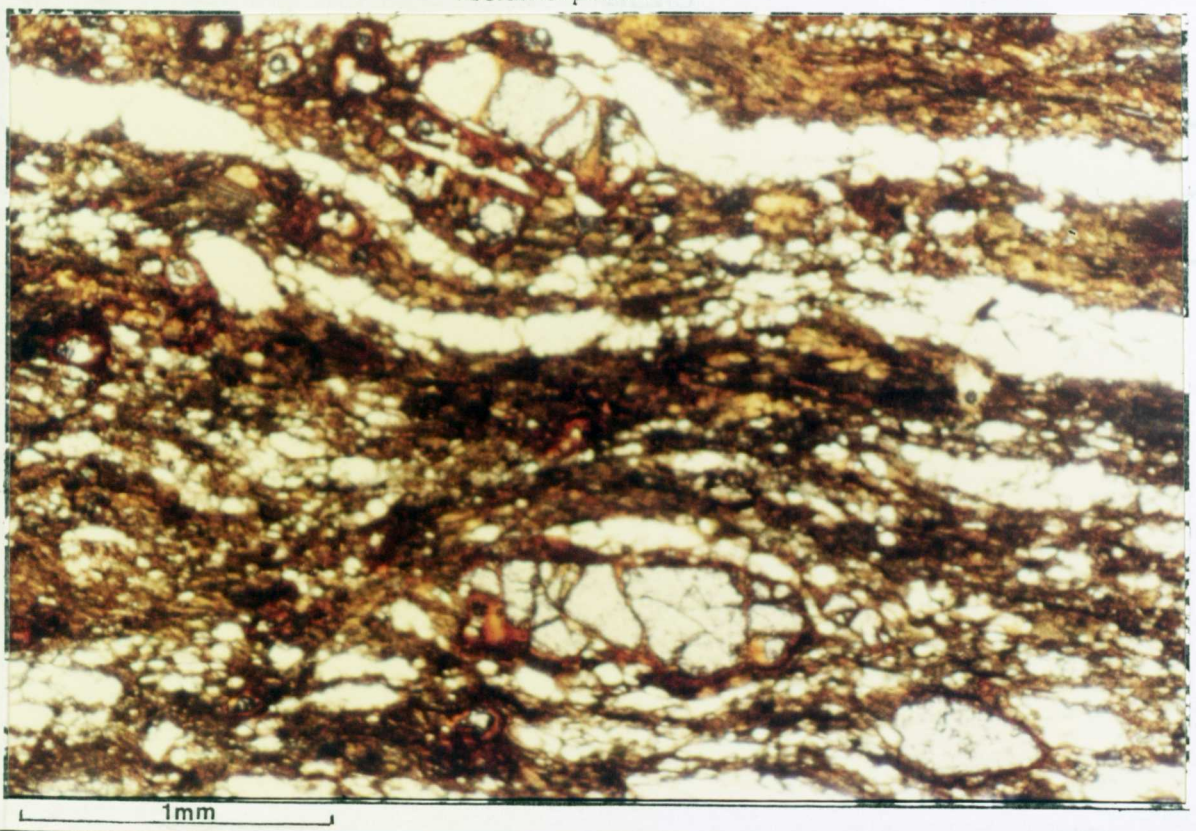

b)

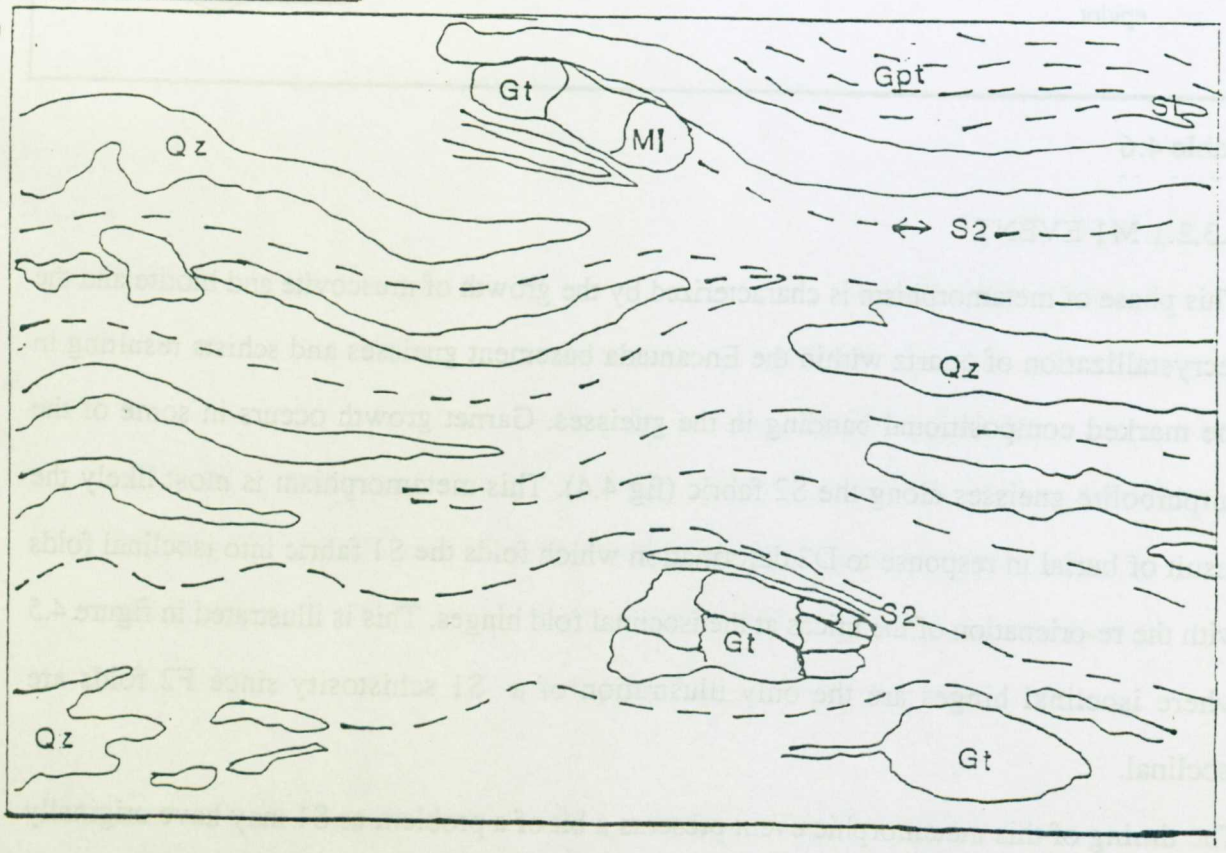

Figure 4.4 Photomicrograph (x5) of sample 120 (a) of an amphibolite band in the Encantada Gneisses with a sketch (b) showing M1 metamorphism and garnet growth along the S2 foliation.

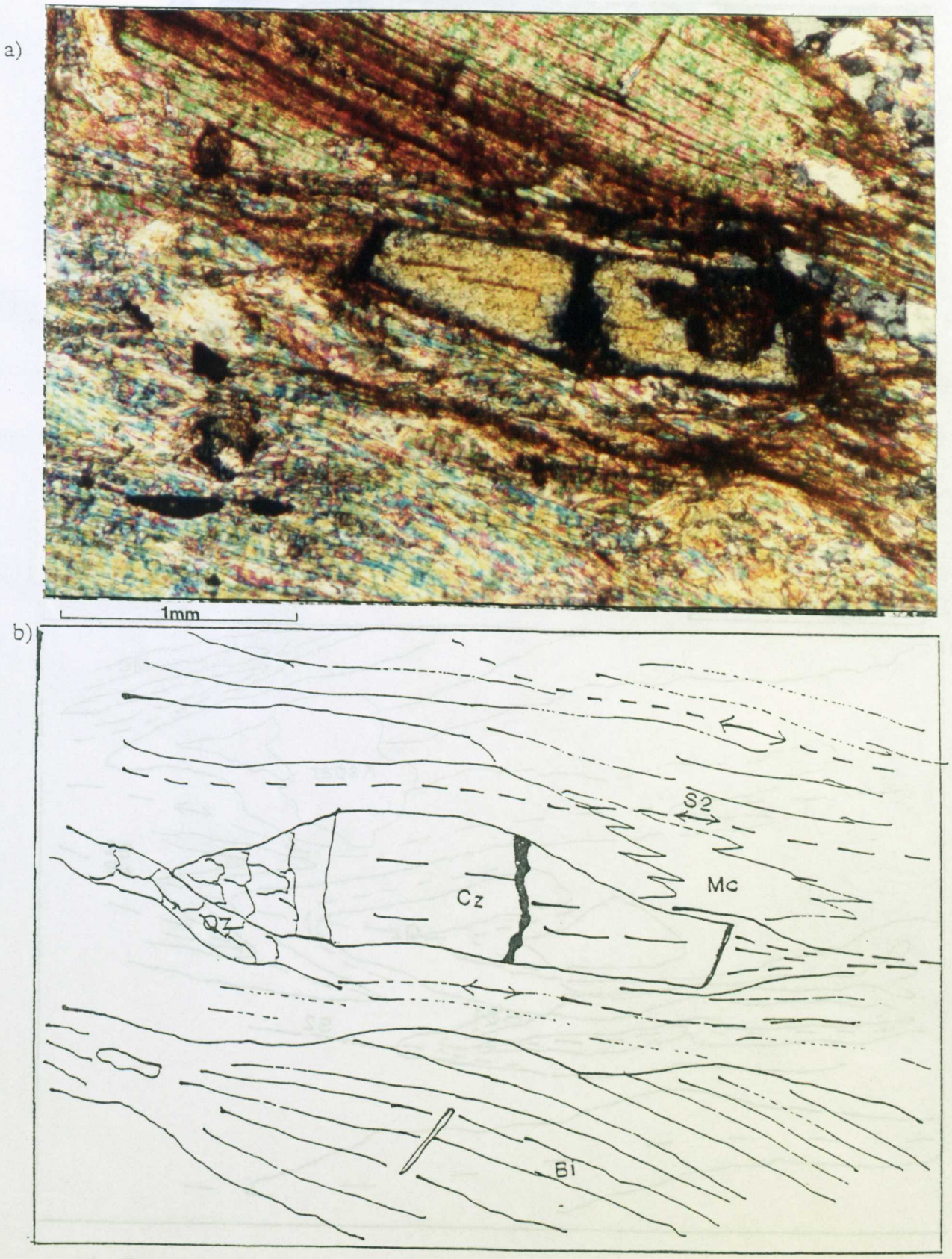

Figure 4.4b Photomicrograph (x5) of sample 82A (a) of a muscovite schist of the Arroio Arreiao formation with a sketch (b) showing M1 metamorphism and clinozoisite growth along the S2 foliation.

a)

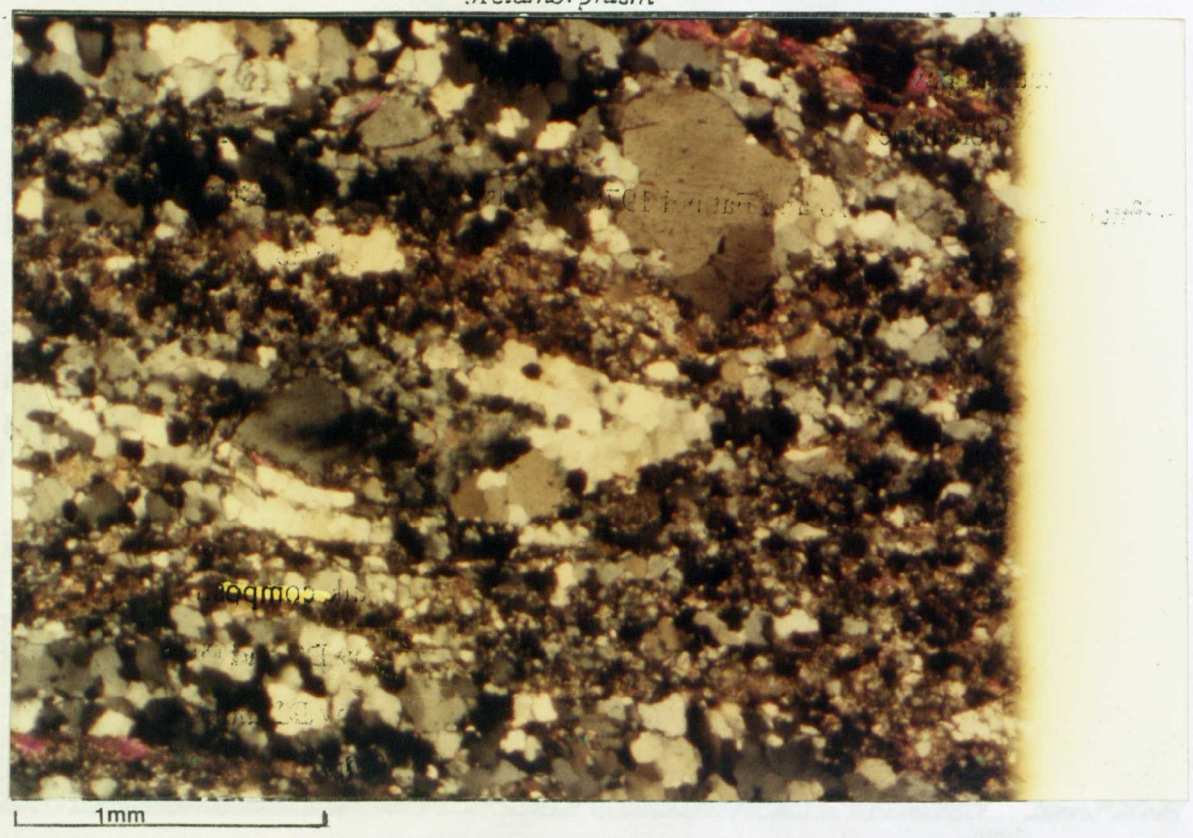

b)

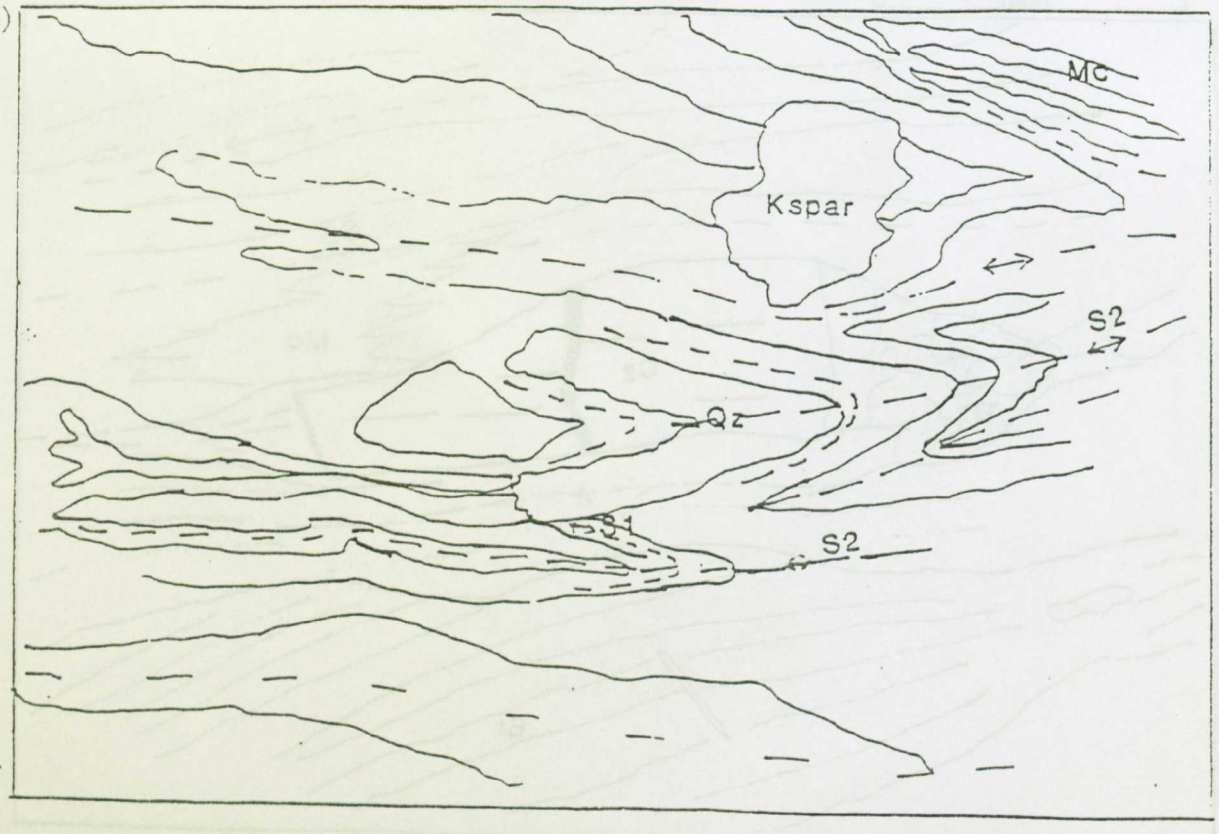

Figure 4.5 Photomicrograph of sample 93 (a) of granitic gneiss of the Encantada Gneisses with a sketch (b) showing the development of the S2 foliation.

Previous authors have suggested that M1 metamorphism reaches sillimanite grade in the Encantada Gneisses (Ribeiro and Fatinel 1978) and assemblages suggest that they reached upper amphibolite facies. Within the Arroio Arreiao schists there is no evidence of S1, and consequently S2 is the first recognizable metamorphic event. It is associated with D2 deformation. and is characterized by the presence of muscovite and recrystallized quartz. Within the Cerro dos Bicudos quartzites D2 causes recrystalliztion of the quartz, but its bulk composition restricts the growth of other minerals. The graphitic schists are deformed by D2 and there is muscovite and biotite associated with the graphite possibly formed by the M1 event. The photomicrographs of figure 4.4 and 4.5 illustrate this.

4.3.2.2 M2 EVENT

This phase of metamorphism predates D3 deformation. It is particularly associated with the formation of the S3 crenulation. Porphyroblast growth of garnet, rare staurolite and plagioclase in the pelites and of amphibole in the metabasites occurs along stressed crenulated micas of the folded S2 foliation. This relationship with respect to garnet is well illustrated in the photomicrograph of figure 4.6a (120) and the annotated sketch illustrates the position of the fabrics. Figure 4.7 illustrates a pelitic assemblage that has equilibrated during M2 metamorphism. Figure 4.8 illustrates the growth of amphibole along the S3 foliation cross cutting the S2 fabric.

Also associated with M2 is the recrystallization of biotite, muscovite, and magnetite along the S3 fabric. Secondary biotite is seen to crystallize along the faces of the garnet that grew along S3 (figure 4.7), which illustrates that the porphyroblasts have not undergone rotation during D3, and that both garnet and secondary micas grew in response to D3 .

a)

b)

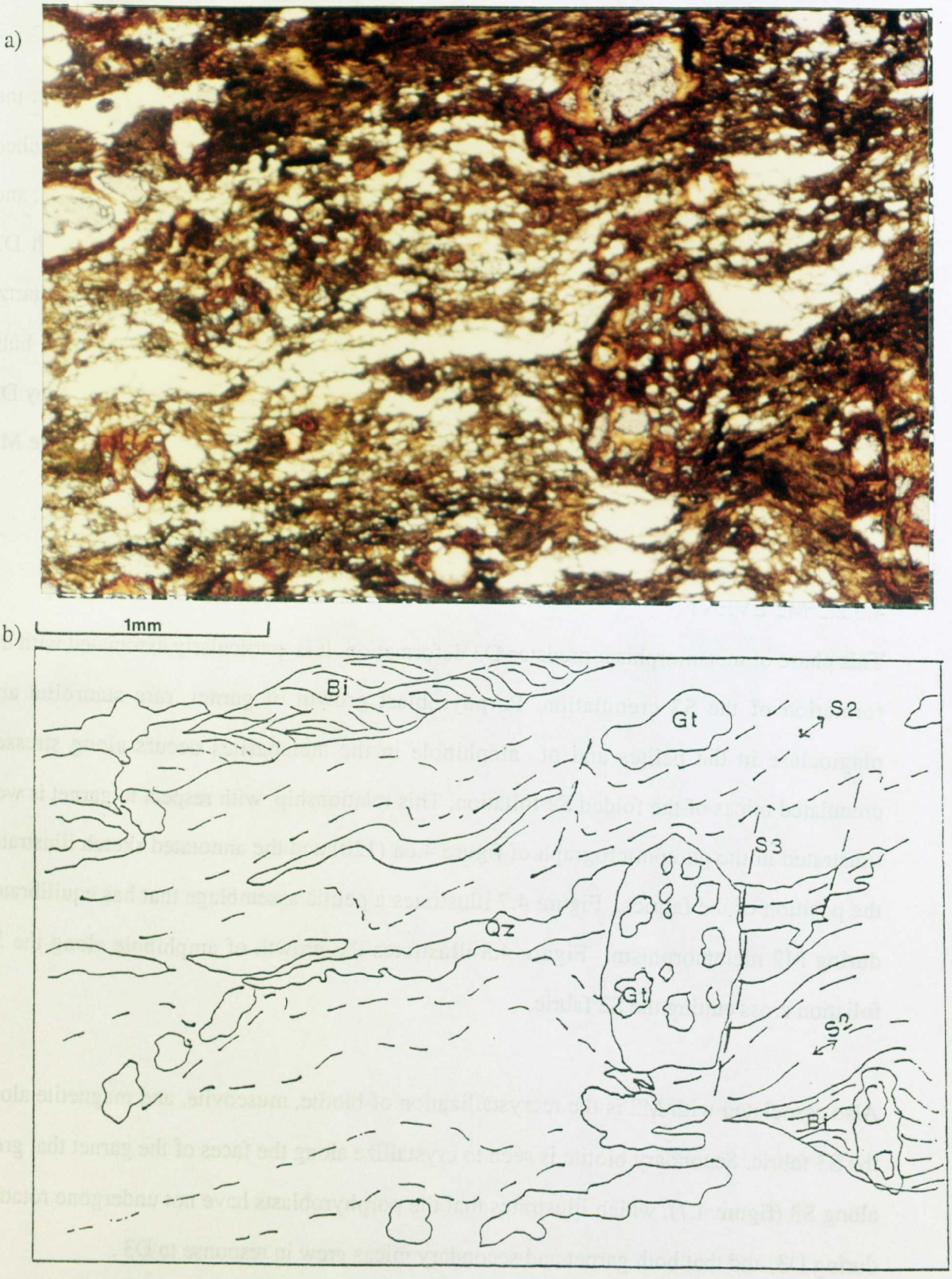

Figure 4.6 Photomicrograph of sample 120 (a) of an amphibolite band in the Encantada Gneisses with a sketch (b) showing M2 metamorphism and garnet growth cross-cutting S2 and forming the S3 foliation.

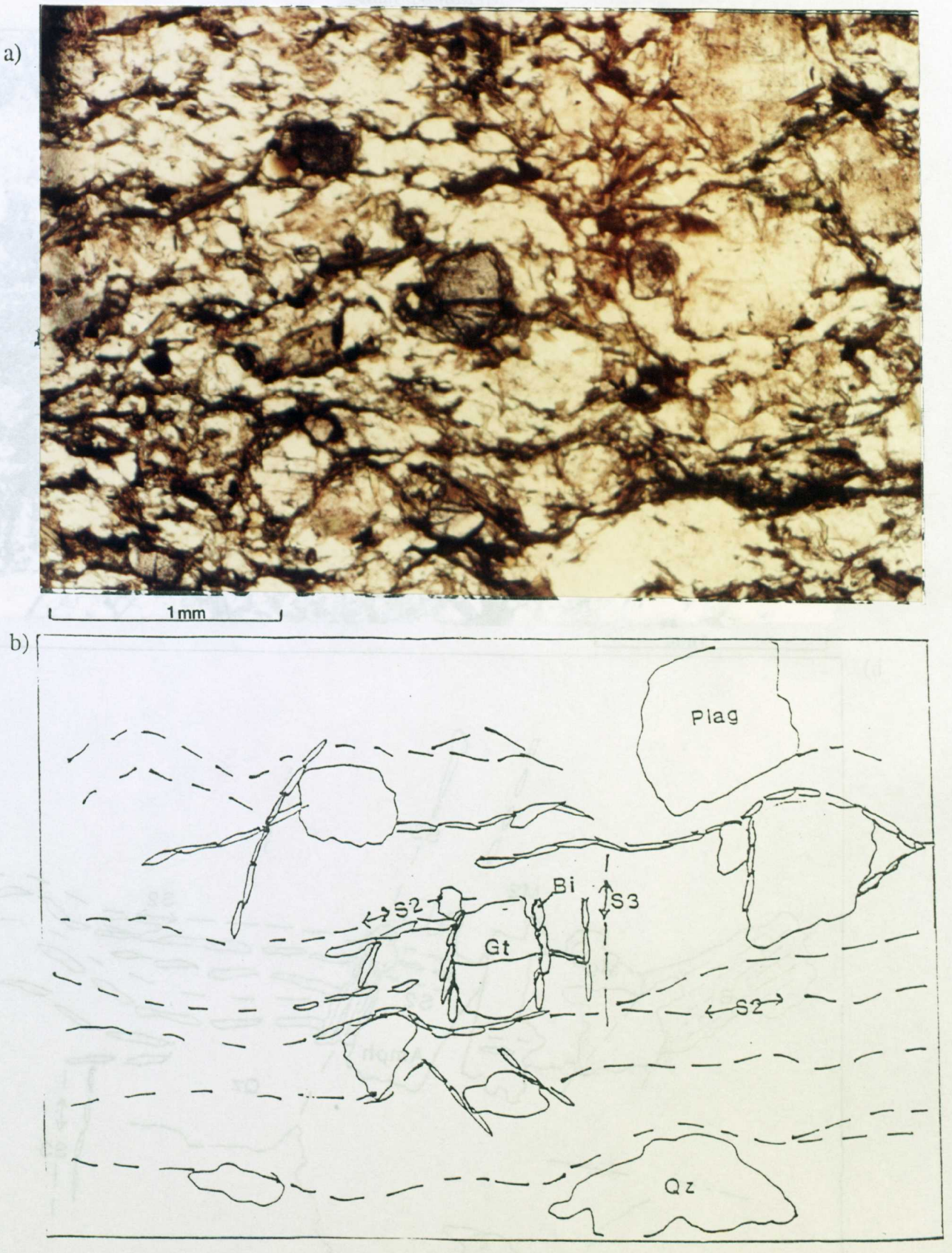

Figure 4.7 Photomicrograph of sample 119 (a) of a biotite schist in the Encantada Schist formation with a sketch (b) showing M2 metamorphism and garnet growth along the S3 foliation.

a)

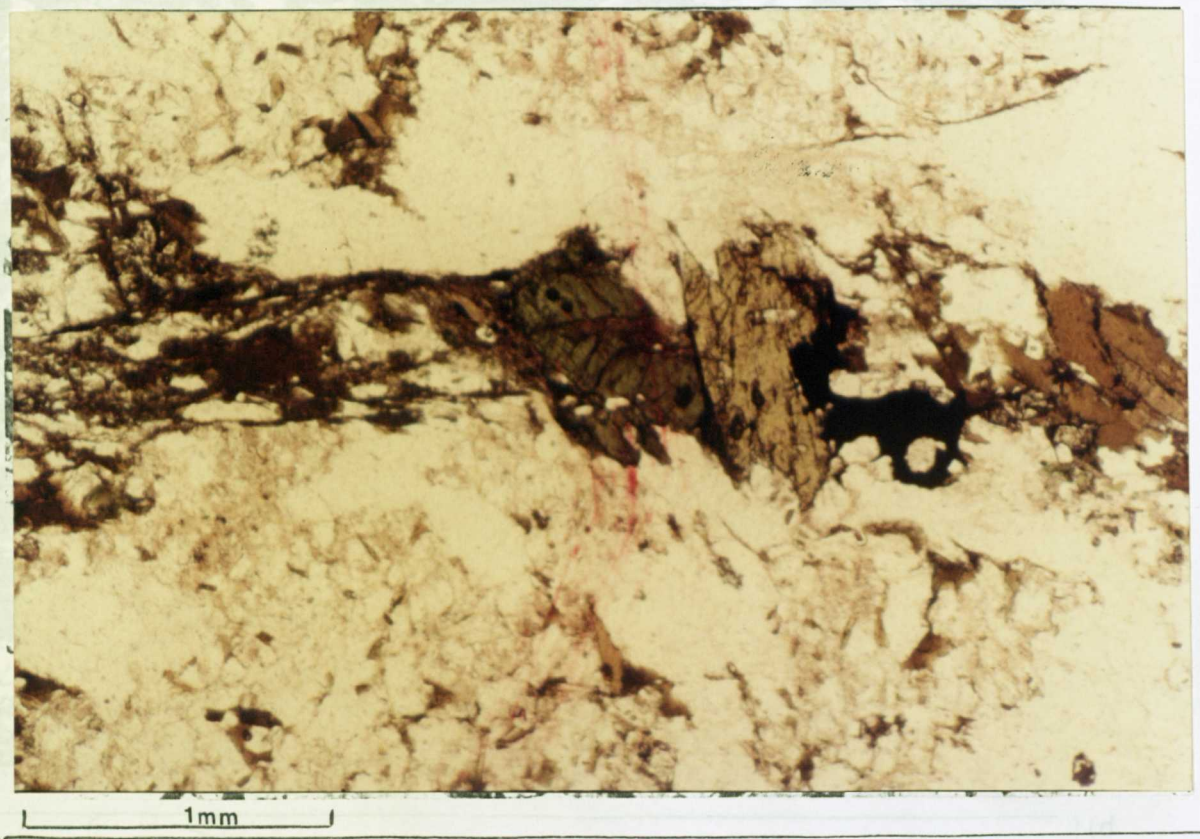

b)

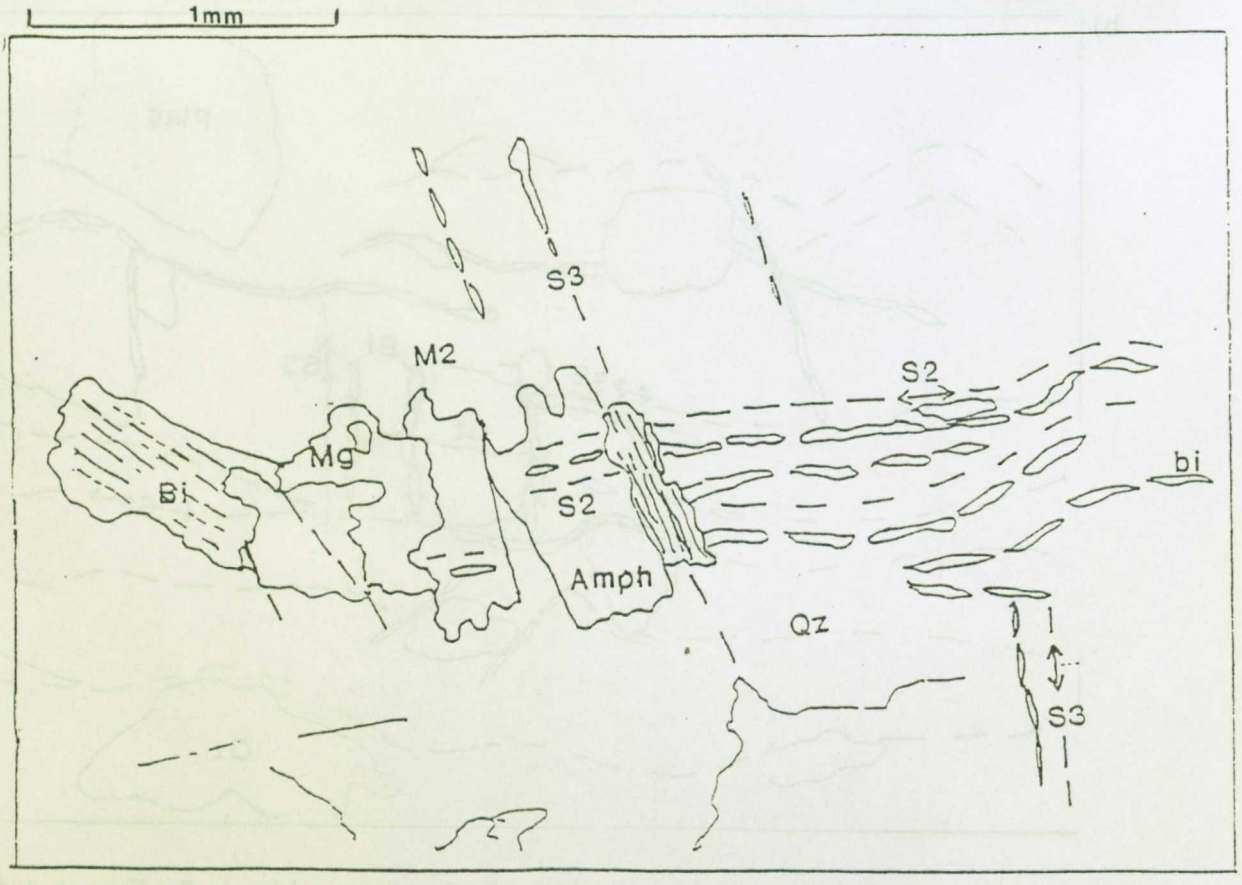

Figure 4.8 Photomicrograph of sample 95 (a) of an amphibolite band in the Encantada Gneisses with a sketch (b) showing M2 metamorphism and amphibole growth along the S3 foliation.

This phase of metamorphism is particularly well-developed in the river section between localities 116 and 120 (see figure 4.2) where garnets appear in the Encantada Schist formation and amphibole and garnet in the amphibolites. Staurolite appears in the mica schists of the Arroio Arreiao formation in the north east of the area at locality 83 (fig 4.1), and this may indicate that the quartzites were thrust over the Arroio Arreiao formation at this locality during D2 (see chapter 3).

The mylonitized granites of the Encantada Schist formation are folded by F3 and may have undergone recrystallization as a result of this metamorphic event. Rb-Sr dating of these granites by Soliano suggests an age of ~800 m.y.and D3 folds these granites. Therefore M2 can be constrained to be younger than 800 m.y . The pressures and temperatures associated with this phase of metamorphism fall in the epidote-amphibolite facies and this is discussed in detail in section 4.4.

4.3.2.3 M3 EVENT

This metamorphic event is retrogressive in nature and results in the replacement of garnet porphyroblasts with epidote and plagioclase, of biotite by chlorite, and the growth of tourmaline. Garnet crystals are sheared by S4 fabrics and graphite grows along the shear zones. This event occurs in response to F4 folding. The growth of graphite and tourmaline is illustrated in the photomicrographs of figure 4.9. This retrogression may be the result of thrusting which post-dates the formation of the Arroio dos Nobres formation (chapter 2 and 3).

Figure 4.9a Photomicrograph (x5) of sample 109 of the Cerro da Canberra formation showing M3 recrystallization of graphite along S4 shear zones.

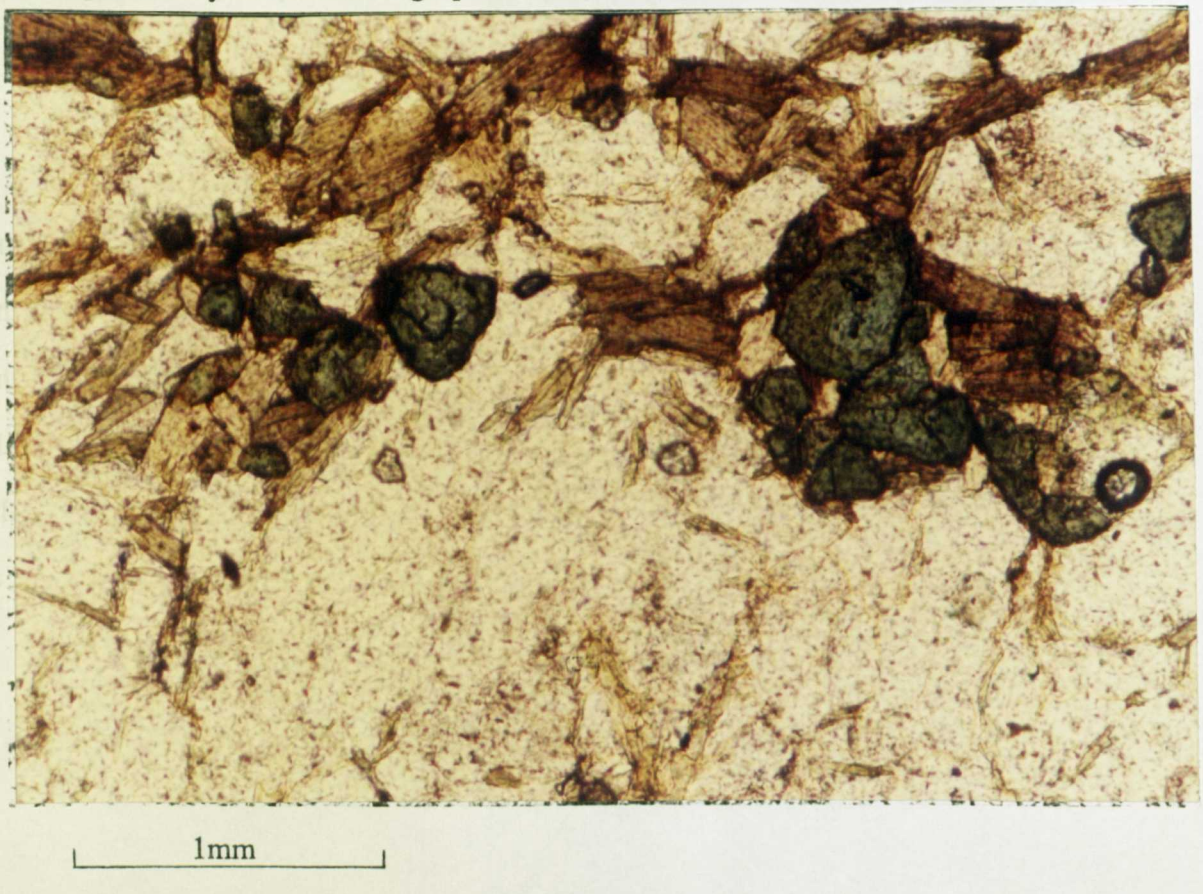

Figure 4.9b Photomicrograph of sample 116 showing tourmilinization in response to M3 retrogression.

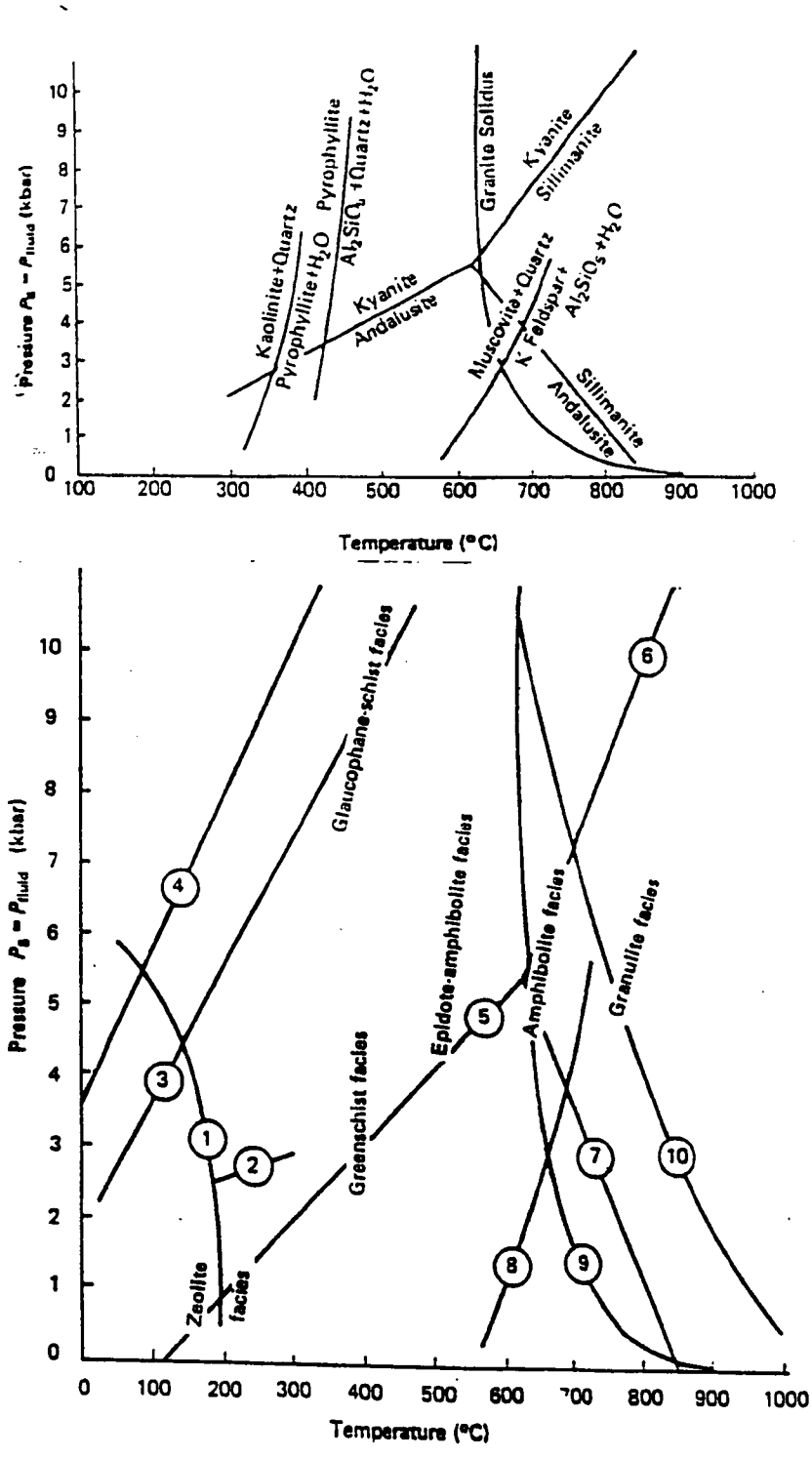

Figure 4.10 Metamorphic facies and geologically significant reactions illustrated in P-T space.

4.4. P-T studies

P-T studies have been undertaken on a pelite from the Arroio Arreiao formation, (sample 134), and one from the Encantada Schist formation , (sample 119). Phases from five other samples have been analysed on the microprobe and evaluated by the Thermocalc program, but only these two samples have provided geologically significant P-T constraints due to the coexistence of critical assemblages. P-T definitions of metamorphic facies and experimentally determined reactions are illustrated in figure 4.10. Microprobe analyses from analysed sections are given in appendix B.

The assemblages studied were formed during the M2 metamorphic event and they are therefore associated with D3 (section 4.3). Equilibrium conditions for both samples will be discussed using the self-consistent data set of Holland and Powell cited in the introduction to this chapter and illustrated using the Shreinemaker projection (Zen 1966). Details of calculated activities and computer read outs are given in appendix B.

Sample 119 contains the asssemblage quartz-plagioclase-biotite-garnet. Activities of end-member phases in the SiO_2-Al_2O_3-FeO-MgO-CaO-K_2O-H_2O system provides a degenerate invariant point from the intersection of the following equilibria in P-T space:

1. py+ann = alm + phl
2. 2py + 6an + 3ann = 6q + 2gr +3alm + 3east
3. 6an + 3phl = 6q + 2gr + 3alm + 3east
4. 6an + 2phl + ann = 6q + 2gr + alm + 3east

The temperature is constrained by the biotite-garnet Fe/Mg exchange (reaction 2) at 564± 129 °C. The calculated pressure, which is independent of water activity, is 8.6 ± 2.8 kbars. From reaction 2 it can be established that the M1 pyrope garnet reacted with biotite and anorthite to produce (Ca,Fe) garnet, Mg-biotite and quartz. This is consistent with the reaction recognized in thin section and identified with M2 metamorphism (section 4.3).

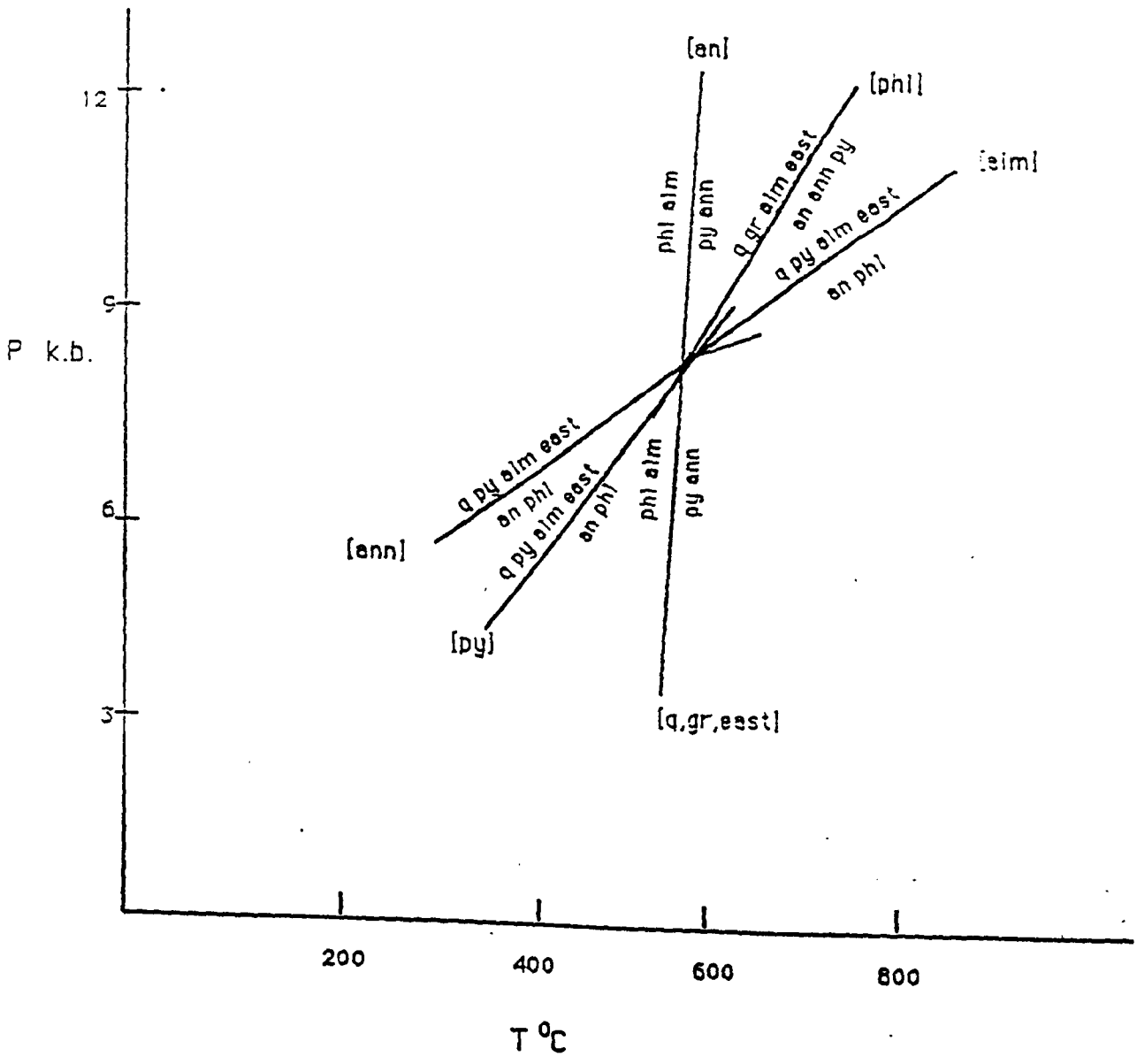

P= 8.6 ± 2.8Kb T= 564 ± 129°C

Figure 4.11 Shreinemaker bundle for sample 119 of the Encantada Schist formation.

The spatial relationship of these four reactions is illustrated in the Shreinemaker bundle of figure 4.11. Although both P and T have large uncertainties, conditions are basically consistent with the epidote-amphibolite facies.

Sample 134 contains the assemblage quartz-muscovite-biotite-garnet-plagioclase-clinozoisite with garnet porphyroblasts. Unfortunately the pyrope content of garnet is too low for pyrope activities to be estimated; hence the Schreinemaker plot for sample 119 cannot be used. However, the presence of white mica allows a second intersection to be used in the SiO_2-Al_2O_3-FeO-MgO-CaO-K_2O-H_2O system:

1. 6q+phl+ann+mu = 3cel +alm
2. 6q+phl+2ann +3an = 3cel+gr+2alm
3. ann+3an = gr+alm+mu
4. 3cel+3an = 6q+phl+gr+2mu

These reactions are consistent with the reactions and relationships recognized from thin section in section 4.3 with garnet , muscovite and biotite porphyroblasts overprinting the S2 schistosity. The above degenerate reactions intersect at an invariant point, independent of water activity at a pressure of 8.6$\pm$1.8k.bars and a temperature of 603$\pm$93°C calculated by Thermocalc (figure 4.12). This sample gives a consistent result with sample 119 which suggests M2 metamorphism took place under similar conditions of temperature and pressure within the Epidote-Amphibolite facies in the Arroio Arreiao formation and in the Encantada Schists. Although the temperature is reasonable for garnet-facies metamorphism in pelites, the pressure is high suggesting that these rocks were buried to a minimum depth of 20 km and possibly as deep as 30km during the D3 deformation event.

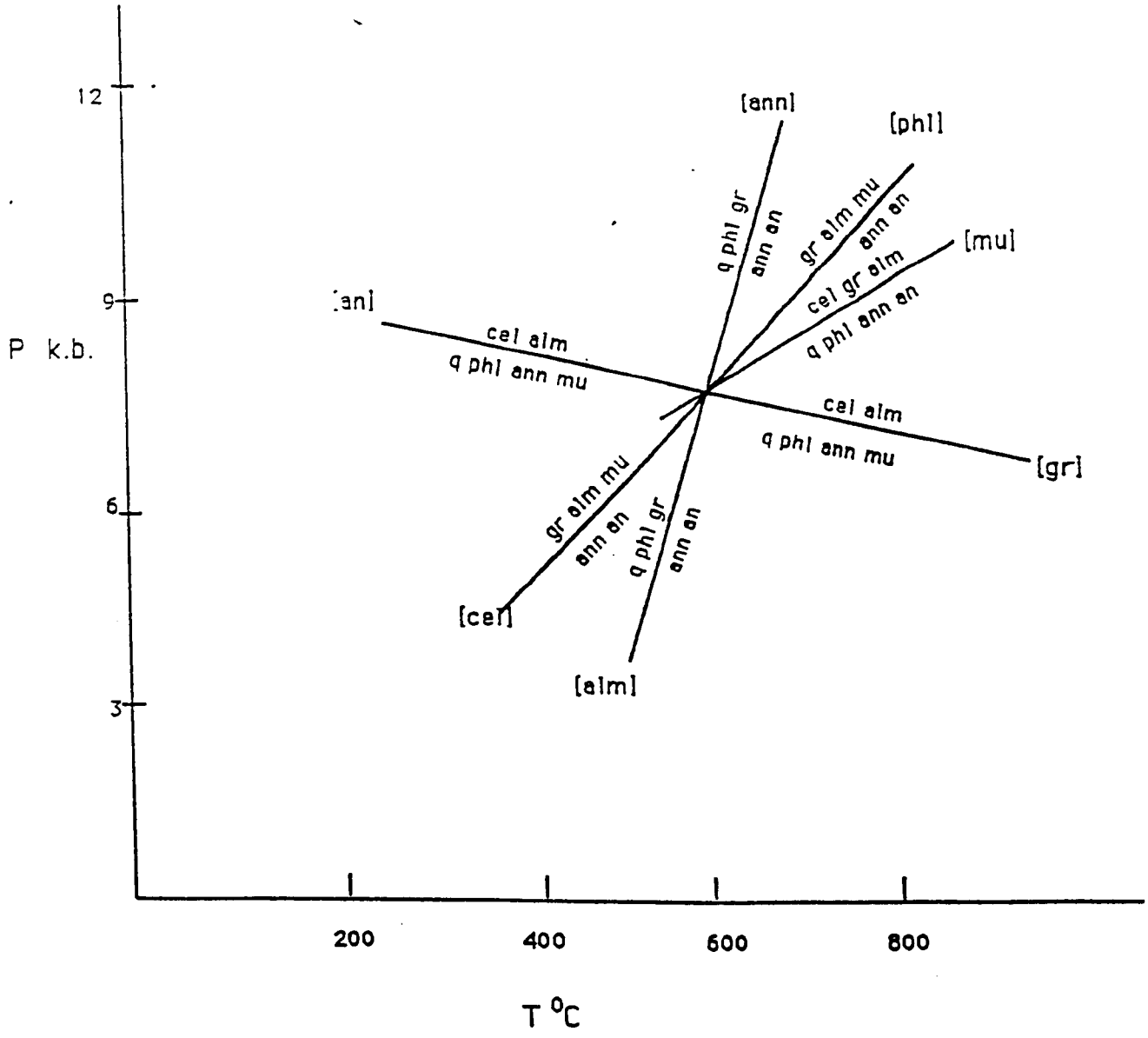

P=. 8.6 ± 1.8Kb T= 603 ± 93°C
at intersection

Figure 4.12 Shreinemaker bundle for sample 134 of the Arroio Arreiao formation.

1.

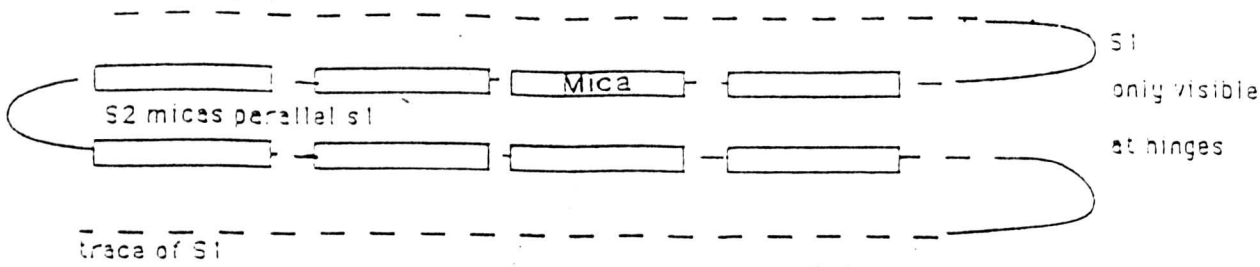

M1 Development of S2 schistoisity in response to isoclinal folding

2. a.

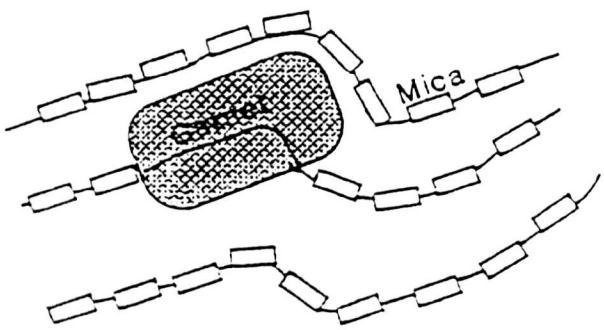

Growth of garnet porphyroblasts during development of F3 folding during D3

b. M2 metamorphism with the development of S3

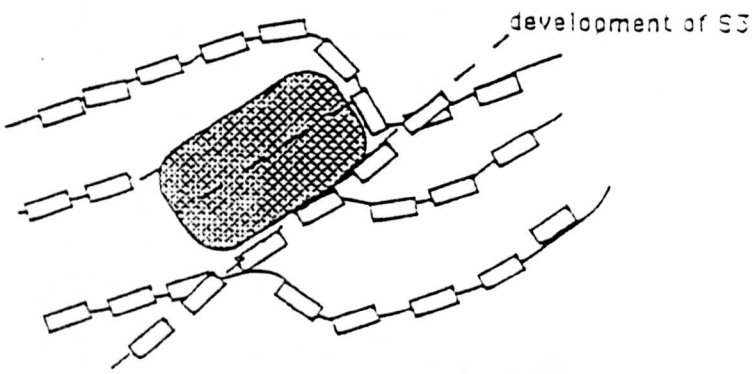

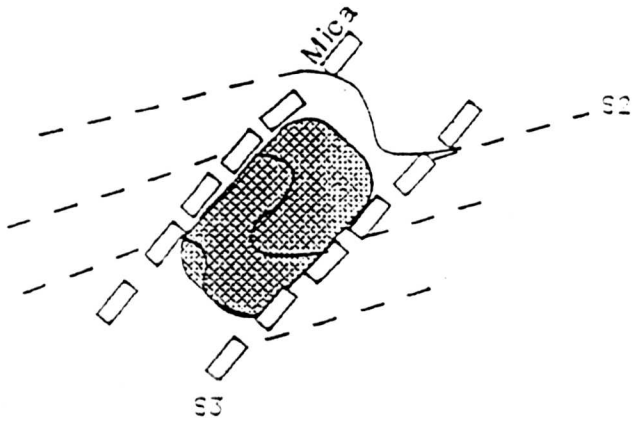

M3 Retrogression of garnet to epidote and biotite to chlorite with the growth of tourmaline.

Figure 4.13 A model for the relationship of metamorphism to deformation in the Santana Metamorphic Belt.

4.5 Conclusions

Three metamorphic events can be recognized from exposures around the Santana da Boa Vista area (figure 4.10). The first event was probably the result of D2 deformation producing porphyroblasts of clinozoisite and garnet and a matrix of biotite and muscovite.

This event has been overprinted by a second metamorphic event associated with D3 deformation (chapter 3) with the growth of garnet and plagioclase porphyroblasts in pelites and amphibole in the metabasites forming the S3 fabric. This phase of metamorphism produced peak P-T conditions within the epidote-amphibolite facies metamorphism in both the Encantada Schists and in the Arroio Arreiao formation, with the pressure at 8.6±2kb and temperature at 600±100°C and an approximate depth of burial of 20-30km.

The assemblages studied provided no evidence of systematic variations in P/T across the area although local increase in T (to above 600°C) allowed straurolite to stabilize in the Arroio Arreiao schists. The presence of muscovite and quartz in all the lithologies of the "cover" units suggests that temperatures have not exceeded the muscovite-quartz breakdown at ~650°C. Muscovite is absent in the Encantada Schists and Encantada Gneisses and so temperatures could have been higher in these units.

Finally retrogression occurs in some rocks, possibly associated with fluid access during thrusting. Post-tectonic granitoids (chapters 5 and 6) may also have increased fluid-circulation locally resulting in the growth of epidote and tourmaline. Tourmalinization is particularly common in the region close to the muscovite-bearing Campinas Granite.

BLANK PAGE
IN
ORIGINAL

CHAPTER FIVE

5. A study of field relations, deformation and petrology of igneous rocks between Pelotas and Caçapava do Sul.

5.1 Introduction

Magmatic activity within the Dom Feliciano Belt occurred sporadically between the early Proterozoic up until the Cretaceous eruptions of the Parana basaltic province. The igneous rocks resulting from these events were studied along the BR392 road section perpendicular to the major tectonic fabric of the area (chapter 3) between Pelotas and Caçapava do Sul (see figure 5.1). The field relations of the igneous rocks of the Santana Metamorphic Belt have already been discussed in chapter 2 but the petrology will be discussed here. However, the bulk of this chapter will concentrate on the field relations, structure and petrology of granitoids found in the granite-migmatite belt known as the Pelotas Batholith (Soliano1986) located in the SE portion of the study area (figure 5.1). A few post-tectonic granitoids intrude both the Santana Metamorphic Belt and the Pelotas Batholith and these will also be discussed in this chapter.

The Pelotas Batholith is separated from the Santana Metamorphic Belt along the road section by flat lying Triassic red beds with associated magmatics. In other areas there is a faulted contact between the two belts. Both the relationship between the two belts and the deformation history of the granite belt will be evaluated. The igneous rocks from the Santana Metamorphic Belt, granitoids of the Pelotas Batholith and late volcanics will be discussed in terms of their field relations and petrology. The interrelationships between these different igneous rocks will also be discussed. An attempt will be made to develop a relative chronology illustrating the sequence of deformational and magmatic events. A brief study of the structural features of the granite belt will be undertaken to see how the structural evolution of the Pelotas Batholith compares with that of the Santana Metamorphic Belt.

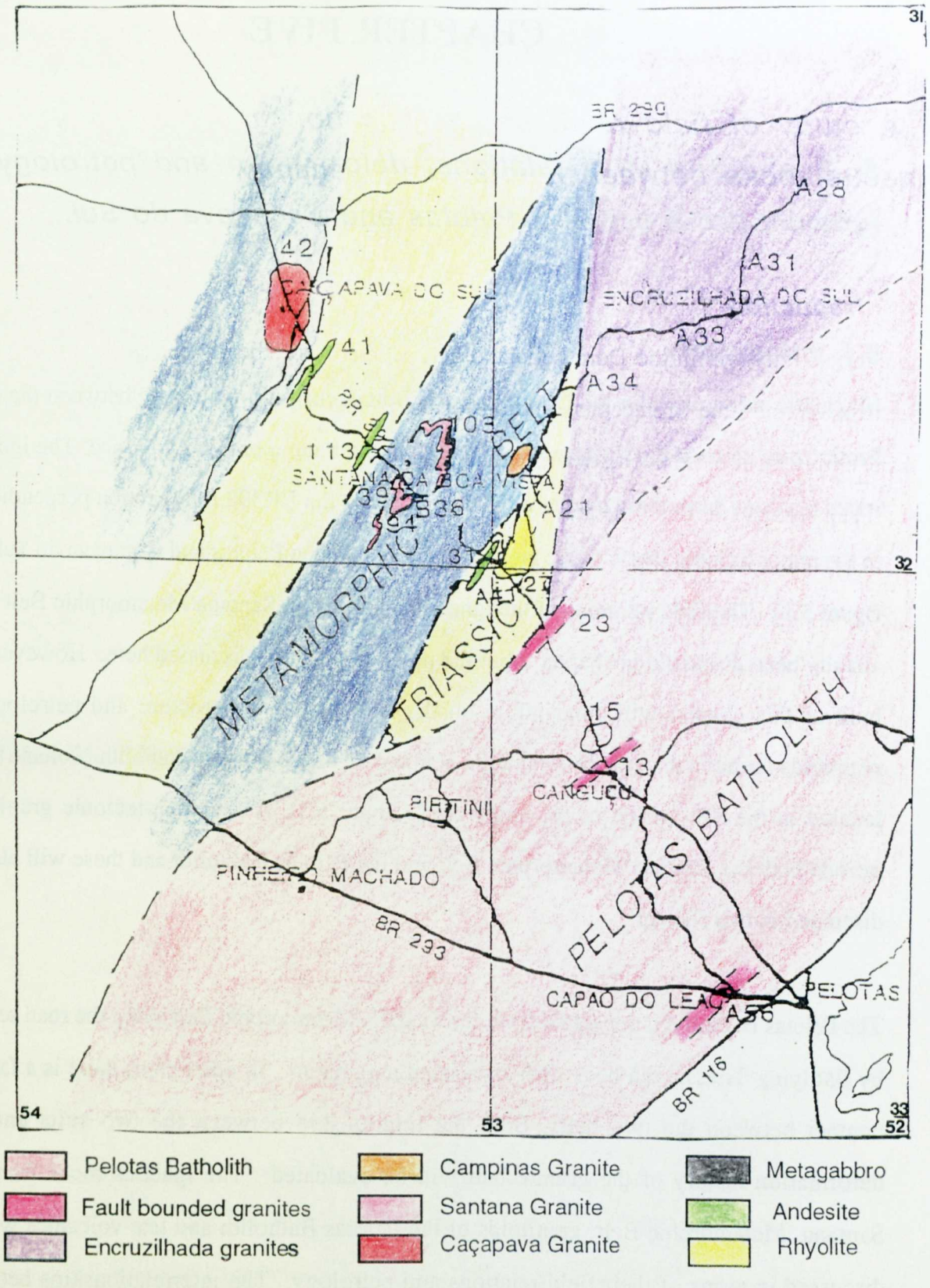

Figure 5.1 Igneous rocks of the Dom Feliciano Belt particularly the Santana Metamorphic Belt showing sample numbers. The granites of the Pelotas Batholith are illustrated in figure 5.7.

5.2 Igneous rocks of the Santana Metamorphic Belt.

5.2.1 Non-granitic igneous rocks

This section describes both foliated and post-tectonic igneous rocks intruding the Santana Metamorphic Belt and includes pre-tectonic amphibolites, metagabbros, felsic volcanics and post-tectonic andesites and rhyolites.

5.2.1.1 METAGABBROS AND AMPHIBOLITES

The location of the main metagabbroic body and amphibolites in the Santana Metamorphic Belt is illustrated in figure 5.1. From this figure and with reference to chapter 2, it can be seen that both units have been affected by D3 deformation and at outcrop it can be observed that while the amphibolites have in fact been deformed by D2 andD3, the metagabbro only shows evidence of D3 deformation. The metagabbro cross cuts the Encantada Gneisses as a sill, and its coarse-grained texture of interlocking crystals is reminiscent of a cumulate texture.

The dark green metagabbros are coarse grained and almost monomineralic hornblendite with occasional quartz which tends to occur as small veins. In thin section the metagabbro can be seen to be composed of large interlocking crystals of euhedral hornblende with distinct 60% cleavage intersections with occasional interstitial quartz and plagioclase grains (figure 5.2a). The hornblende shows local retrogression to biotite.

The protolith of this rock type was most probably a pyroxenite (clinopyroxene and plagioclase) cumulate with some more gabbroic layers. Its relationship to some of the volcanics in the area may be evaluated using geochemical and isotopic studies.

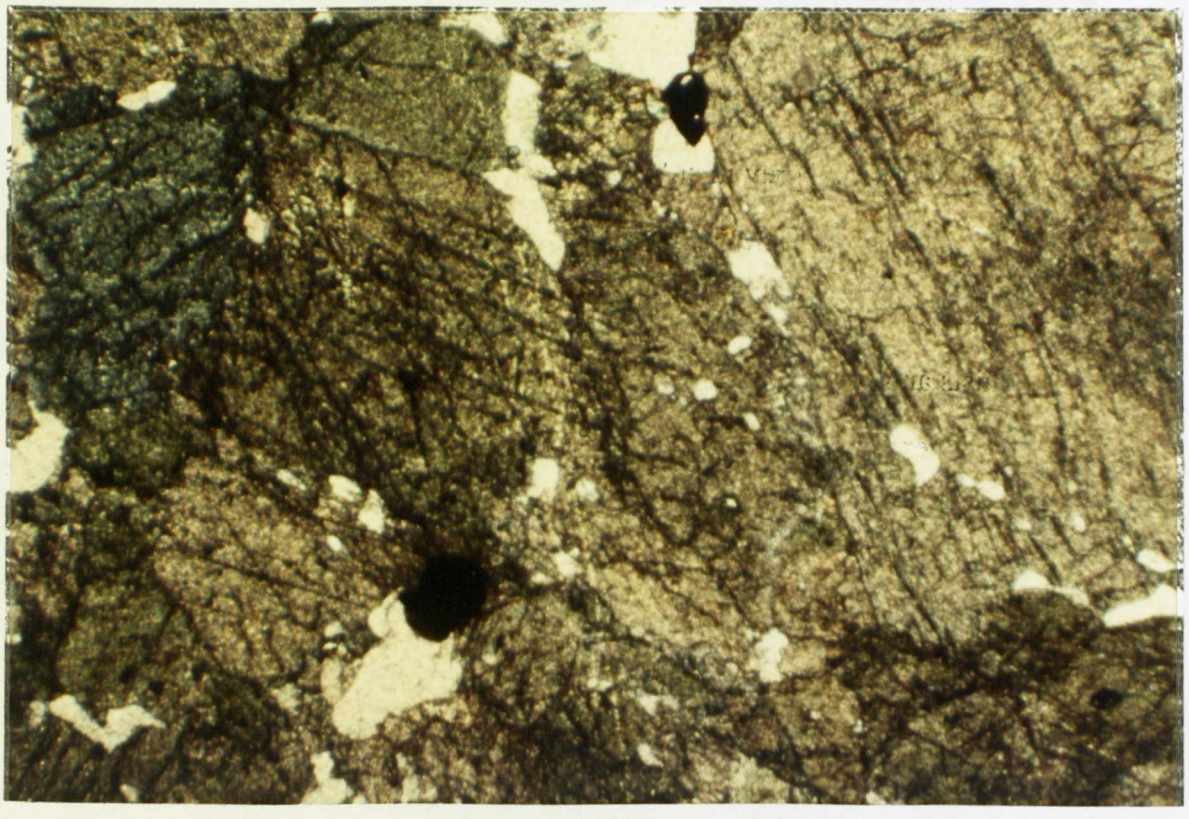

Figure 5.2a Photomicrograph of metagabbro (hornblende and quartz) at locality 94.

Figure 5.2b. Pillow andesites showing good pillow structures at locality 113.

5.2.1.2 FELSIC VOLCANICS

Felsic volcanics are found interfolded with the graphitic schists of the Cerro da Canberra formation and are blueish grey in colour and fine-grained in texture and may represent the extrusive counterpart of the granite intrusions described above. Unfortunately no work has been undertaken in dating these volcanics. This would have constrained the formation of the graphitic schists and possibly dated an episode of extensional tectonics pre-dating the major Proterozoic orogenic event. In thin section the felsic volcanics are composed of elongated alkali feldspar crystals and small quartz grains with a number of flattened vesicles aligned with the schistosity indicative of their volcanic nature.

5.2.1.3 ANDESITES

Pillow andesites (figure 5.2b), outcropping to the NE of the Santana region, are interbedded with the red beds of the Guiritas formation and indicate an underwater crystallization (chapter 2). Other andesites occur within the Triassic red beds of the Canelarias formation outcropping to the SE of Santana at locality 31 and also outcrop in the area SE of Caçapava do Sul at locality 41 (figure 5.1). These andesites are dark reddish brown in colour with small vesicles and they are flat lying, jointed and interbedded with red beds. They may indicate a Triassic subduction environment. The isotopic age of the flows is unknown.

5.2.1.4 RHYOLITES

Rhyolites outcrop along the BR392 at locality 27 interbedded with the Canelarias formation red beds. The outcrop is about 10m in thickness and 100m in length and is columnarly jointed. Rhyolite volcanism may be related to the Parana basaltic province associated with the opening of the Atlantic. Rhyolitic volcanic breccias also crop out in a few areas in the granite belt.

Figure 5.3a Field photograph of the Santana Granite at loclity 39 looking to 235°.

Figure 5.3b Intrusion of the red into the grey facies of the Caçapava Granite at locality 42.

5.2.2 Granites of the Santana Metamorphic Belt.

There are four granites which intrude the Santana Metamorphic Belt two of which are foliated by the Brasiliano Orogenic event. They will be discussed in geochronological order.

5.2.2.1 THE SANTANA GRANITE (foliated)

Mylonized sheets of granites and granodiorites dated at 805±55 m.y. by Soliano (1986) form a major part of the "Porongos metamorphic suite" of the Santana Metamorphic Belt. They intrude as sills at various levels in the sequence and are although they are common in the Encantada Schists, they also intrude the Encantada Gneisses. Granite fabrics indicate that they pre-date the deformation of the Encantada Schist formation (chapter 3) see figure 5.1. If the above age is correct for this formation then this constrains the Brasiliano orogenic event (D2 and D3) to younger than 805 ±55 m.y.

The Santana Granite (fig.5.3a) is pink in colour, medium-grained with a slightly crenulated foliation resulting from the alignment of mica. The granite is composed of approximately 30% quartz,40% K-feldspar, 20% plagioclase and 10% muscovite and biotite and would plot as monzogranite on the Streckeisen plot. These granites are similar in appearance to the late red granites of the Pelotas Batholith and their chemistry is compared with granites from this area in chapter 6.

5.2.2.2 CAMPINAS GRANITE (foliated)

The Campinas Granite is a two mica granite and has been studied by Tessari and Picada (1966) and by Jost (1981) who classified it as a quartz monzonite. It crops out in the region around Campinas in the area SE of Santana da Boa Vista (fig. 5.1) where the Pelotas Batholith and Santana Metamorphic Belt are in contact at a shear zone (locality A21). The emplacement of the Campinas Granite was apparently controlled by the intersection of two shear zones (Jost 1981), but only very weathered outcrops were found and its contacts with other rock types were not exposed and there are few constraints on its age of emplacement. It however is sheared by D3 and is therefore thought to be older than 500m.y. (Chapter 7).

The most distinctive feature of this granite is the presence of large silvery muscovite flakes. The granite is kaolinized, and contains about 40% quartz, 30% plagioclase feldspar and 5% alkali feldspar, and it is foliated with 5% biotite forming the foliation and 5% muscovite flakes oblique to this. Veins of tourmaline and fluorite occur at the borders of the granite.

5.2.2.3 ENCRUZILHADA GRANITE (unfoliated)

The Encruzilhada Granite is a hornblende bearing granite and outcrops over a wide area between Dom Feliciano and Encruzilhada do Sul (figure 5.1). The granite, transversed between A28 and A33 forms rounded hummocks in the field with large alkali feldspars standing out from the rusty brown weathered surface.

This granite is coarse grained, pink and homogeneous composed of interlocking subhedral crystals of pink feldspar making up 35% of the rock and 20% black hornblende separated by 30% interstitial, rounded smoky quartz and 15% plagioclase feldspar (figure 5.3a). The relationship of this granite to the other granitoids of the Pelotas Batholith is not apparent from field studies.

5.2.2.4. CAÇAPAVA GRANITE (unfoliated)

The Caçapava Granite intrudes marbles as an oval shaped body in the northwest part of the Santana Metamorphic Belt in the region of Caçapava (fig 5.1). A quarry into this intrusion occurs on the BR392 just south of Caçapava do Sul at locality 42. Two granite types occur, a grey fine-grained homogeneous granite with a slight foliation intruded by a younger fine-grained red granite (figure 5.3b).

The grey facies of the Caçapava Granite (5.4a) is medium-grained, dark grey and homogeneous with a weak foliation developed. It is composed of about 20% biotite interstitial to 25% red alkali feldspar and 25% large plagioclase crystals with rounded quartz crystals making up about 15-20% of the rock. There are a few thin alkali feldspar veins running through the rock.

In thin section (5.4a) the alkali feldspar is found to be large orthoclase crystals with biotite and magnetite inclusions, suggesting that these feldspars are a secondary growth. There is also microcline present. The plagioclase crystals show multiple twinning and also show two phases of growth. The biotite is well formed but smaller than the other minerals and appears to be in equilibrium. The quartz is rounded, irregular and possibly recrystallized. Accessory minerals include apatite and magnetite.

The red facies of this granite (fig. 5.4b) is fine-grained and homogeneous composed of red alkali feldspar crystals making up 30% of the rock, interlocked with larger white plagioclase crystals making up 30%, and a similar proportion of smoky quartz with about 10% interstitial fine-grained biotite. It is quite similar in appearance to the Canguçu Red Granite although it is finer-grained and less weathered.

In thin section (fig.5.5, 5.6), the alkali feldspar is subhedral fresh orthoclase with occasional myrmekitic texture and some altered microcline. The plagioclase is large and multiply twinned, and the quartz is recrystallized to form small interlocking grains whilst the biotite grains are euhedral. Accessory magnetite and chlorite are present.

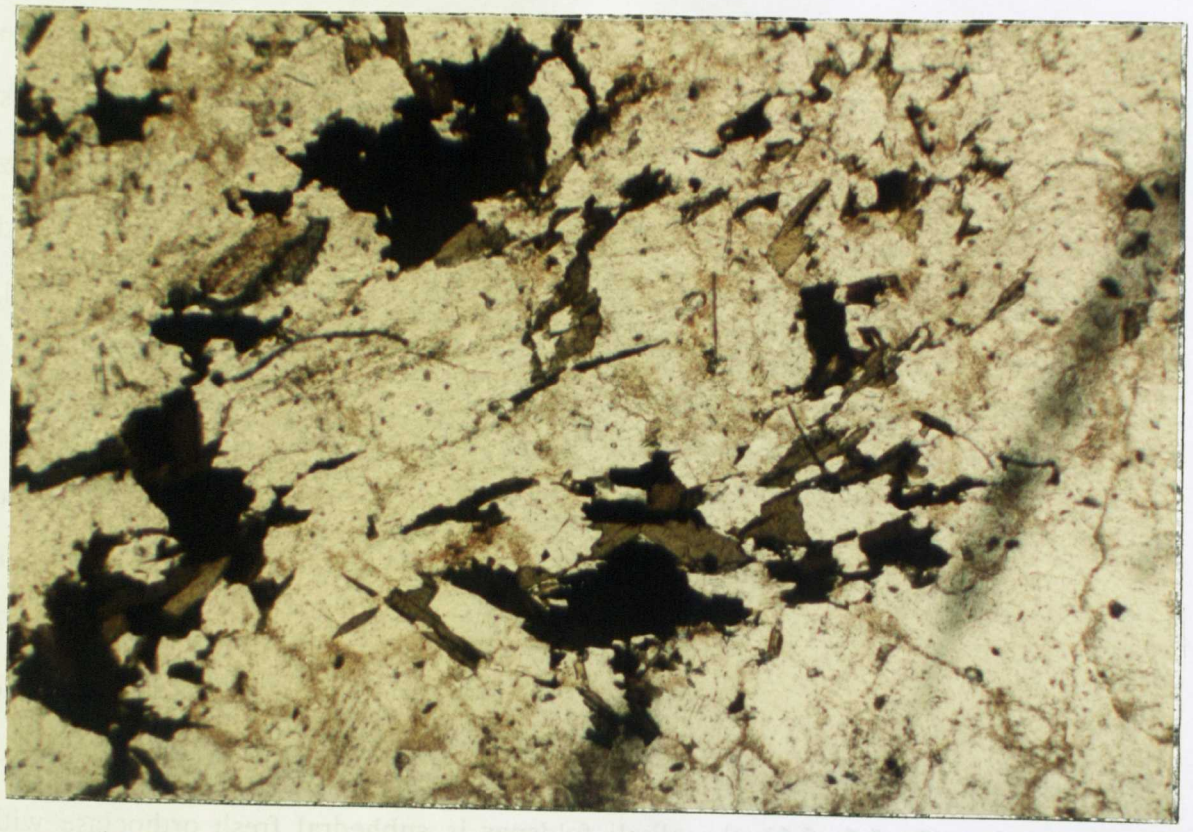

Figure 5.4a Photomicrograph of the grey facies of the Caçapava Granite at locality 42.

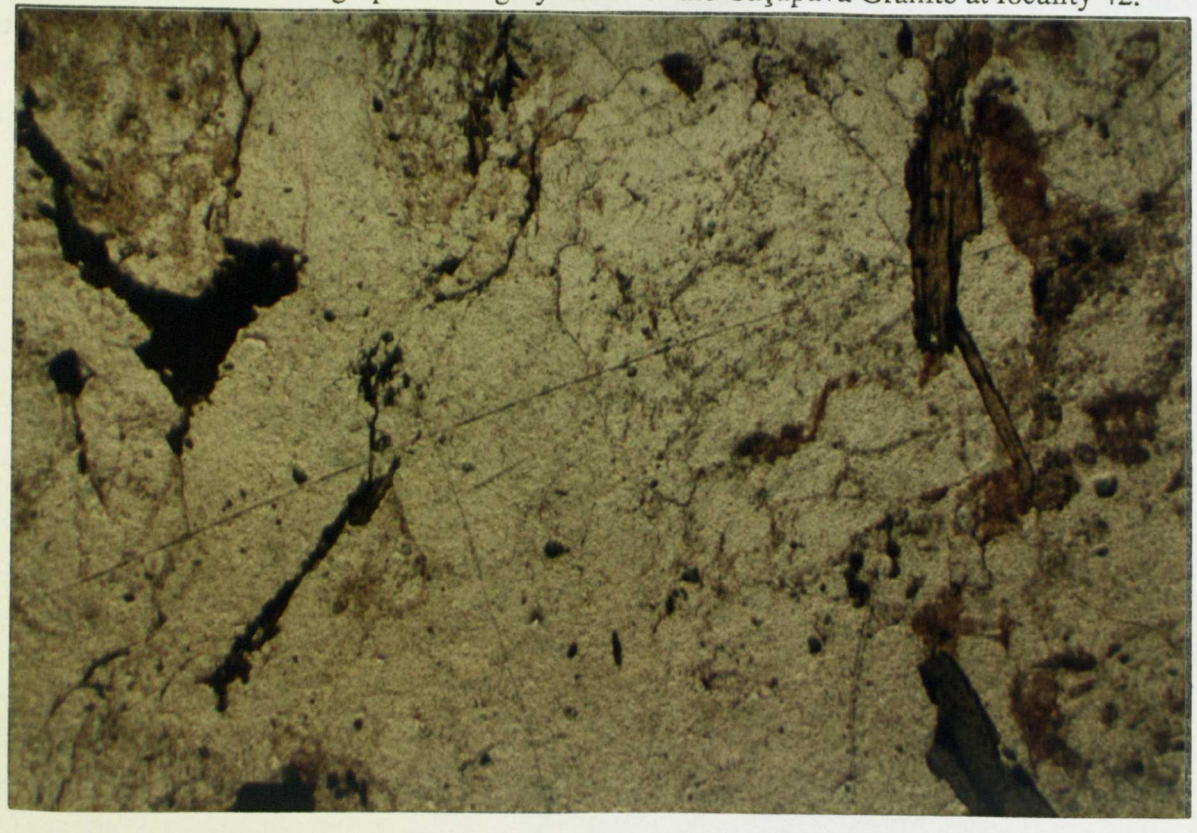

Figure 5.4b Photomicrograph (x5) of the red facies of the Caçapava Granite.

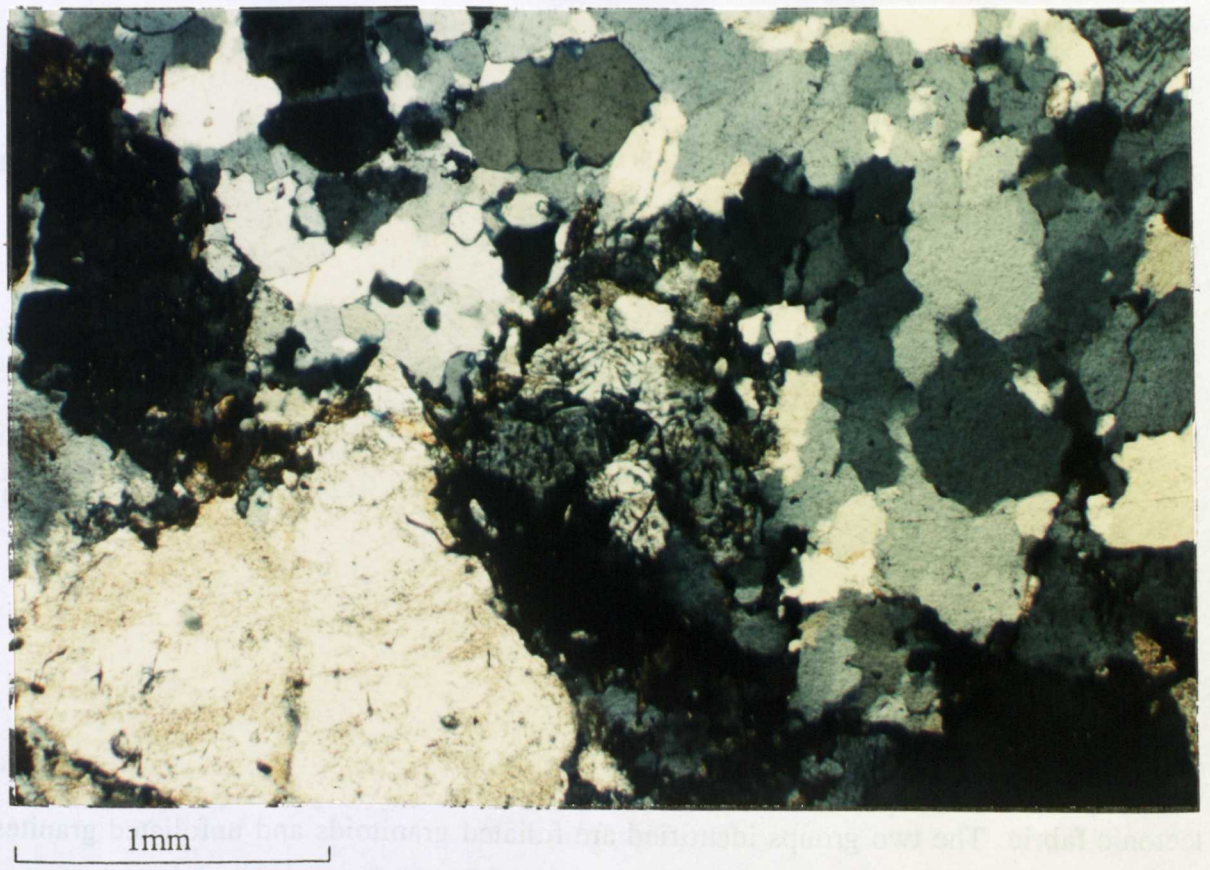

Figure 5.5 Photomicrograph (x5) of the red facies of the Caçapava Granite at locality 42.

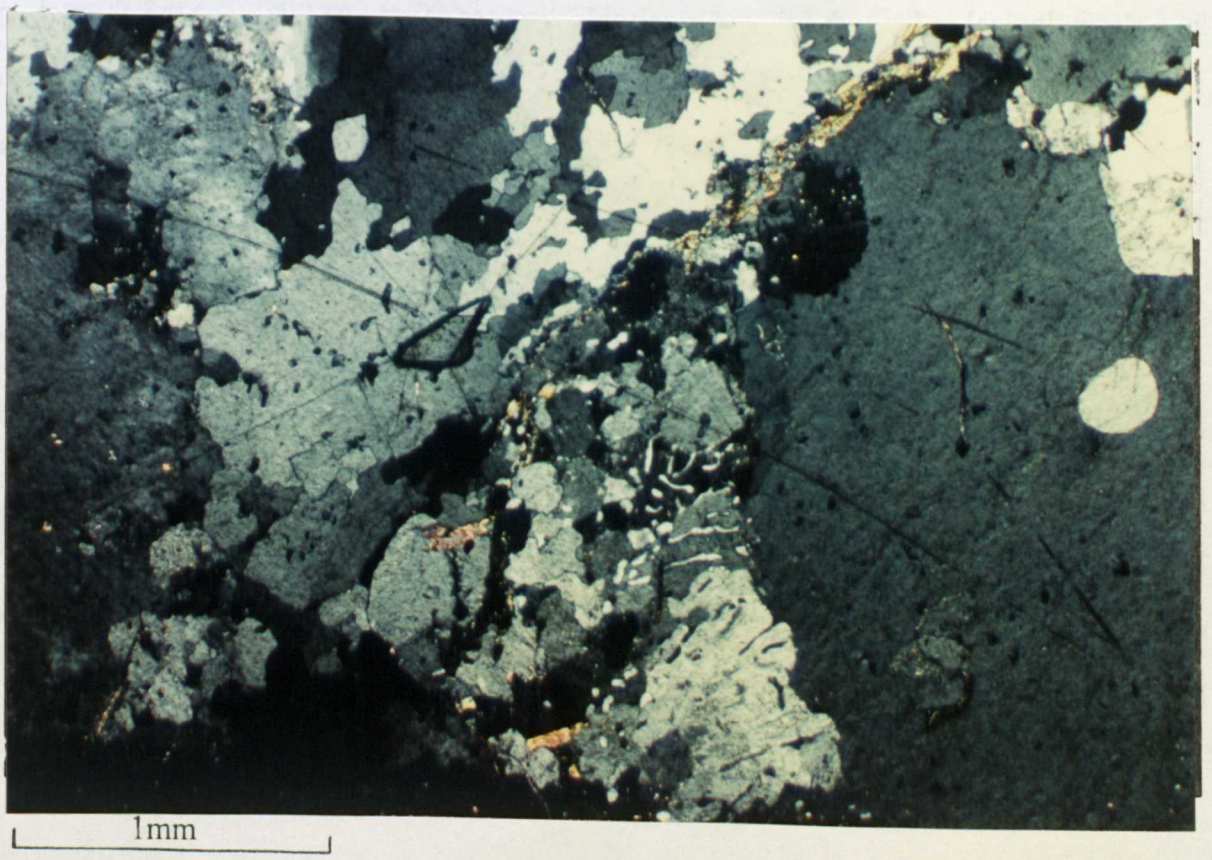

Figure 5.6 Photomicrograph of myrmekitic texture within the red Caçapava Granite

5.3 Field relations and petrology of igneous rocks of the Pelotas Batholith granite belt.

The Pelotas Batholith is almost totally composed of granitoids. However a few basaltic dykes intrude the Pelotas Batholith and there are also outcrops of pillow basalts and felsic pyroclastic rocks within the batholith. There is no evidence of country rock apart from slivers of metasediment associated with the dykes.

Two major granite types have been recognized from field studies based on the presence of a tectonic fabric The two groups identified are foliated granitoids and unfoliated granites although some individual outcrops are difficult to classify. The granitoids will be described in a chronological order with foliated granitoids discussed first. At this stage the chronology is based on established field relations. The different granite types encountered within the Pelotas Batholith are illustrated in the map of figure 5.7a and the schematic cross-section of figure 5.7b. A legend for this map is presented in figure 5.8.

Section 5.3.1 describes the field relations and petrology of the foliated granitoids and includes orthogneisses and granodiorites with two foliations, and granites.with one foliation Section 5.3.2 discusses unfoliated granites.some of which are obviously post-tectonic and others which are fault-bounded and also discusses late pegmatites. Section 5.3.3 describes basaltic flows and dykes intruding the Pelotas Batholith.

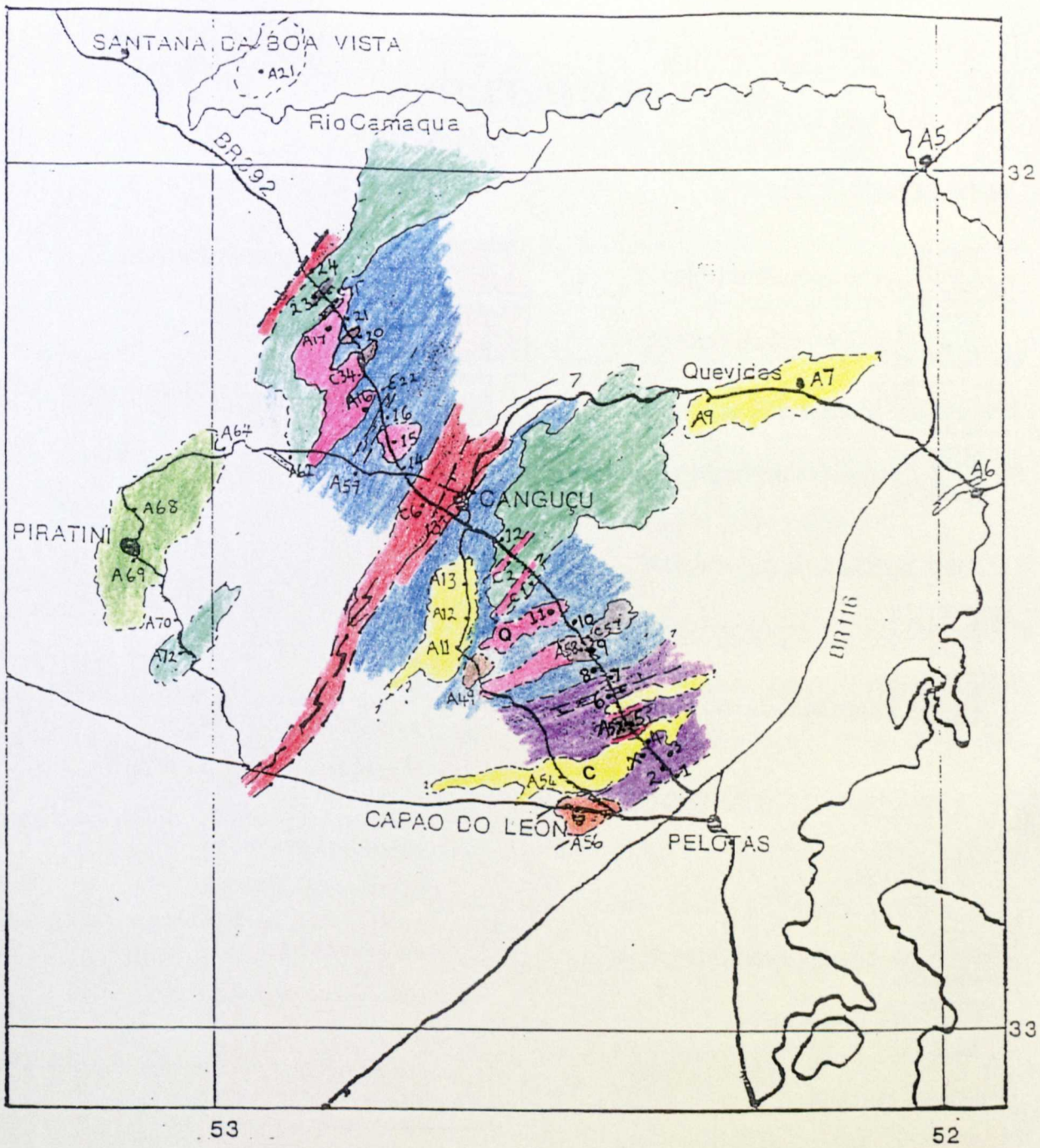

Figure 5.7a Geological map of the various granitoids of the Pelotas Batholith.

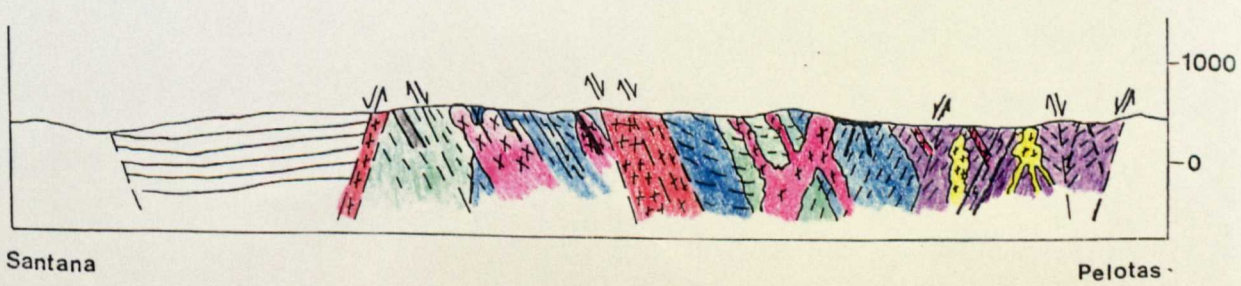

Figure 5.7 Cross-section through the Pelotas Batholith along the BR392 road section

GRANITOIDS

FOLIATED (Pre D3)

- Cascata Orthogneiss
- Migmatitic Orthogneiss
- Piritini Granite
- Cangucu Porphyritic Granite

UNFOLIATED (Post-tectonic)

- Q — Quarry Pink Granite SE
- Pink Granite NW
- C — Cascata Leucogranite
- Cidade dos Piegos Granite

UNFOLIATED (fault bounded)

- Cangucu Red Granite
- Capao do Leao Granite

OTHER IGNEOUS ROCKS

EXTRUSIVE

- Basalt dykes and flows
- Ignimbrites

INTRUSIVE

- Pegmatites
- Aplite dykes

KEY TO GEOLOGICAL SYMBOLS

- Observed non-tectonic contact (with orientation indicated on down-dip side)
- Inferred non-tectonic contact
- Observed normal fault contact (orientation of fault-plane indicated on down-thrown side)
- Inferred normal fault contact
- Observed thrust fault contact (orientation of fault-plane indicated on up-thrown side)
- Inferred thrust fault contact
- Bedding
- Observed orientation of S2 schistisity in metamorphic rocks (dip and direction of, indicated)
- Observed orientation of S3 cleavage (in fault planes, shear zones etc: dip and direction of, indicated)
- Plunge of fold hinges (dip and direction of, indicated)
- Dykes

Fig 5.8 Legend for the geological map of figure 5.7 also illustrating the structural symbols used in section 5.4.

5.3.1 Foliated granitoids

5.3.1.1 CASCATA ORTHOGNEISS

The Cascata Orthogneiss is a foliated biotite-rich granodioritic gneiss and is cross cut by a leucogranite and pegmatites (figure 5.9). This gneiss is best exposed in large quarries e.g the Cascata quarry (locality X) and in road cuttings along the BR392 (localities 3-7 of fig 5.7). It is medium to coarse-grained, dark grey in colour, inhomogeneous with large pink phenocrysts and with a discontinuous segregation into mafic and leucocratic bands. A common feature of this rock type is the presence of mafic blebs (figure 5.9a).

In thin section the major mafic mineral is green biotite making up about 10% of the rock and forms the main NNW-SSW foliation. Hornblende is also present and comprises about 5% (fig5.10b). The leucocratic minerals are interlocking crystals of 10% microcline, 20%, large altered orthoclase, 30% multiple twinned plagioclase and 25% recrystallized quartz. Accessory minerals are magnetite, secondary chlorite, euhedral sphene (which is characteristic of this rock type), zircon and apatite inclusions in the sphene and biotite (fig 5.10). The Cascata Orthogneiss falls in the quartzdiorite to granodiorite fields of the Streckeisen plot (Chapter 6).

5.3.1.2 MIGMATITIC ORTHOGNEISS

The Migmatitic Orthogneiss is foliated, dark grey and finer grained than the Cascata Orthogneiss and shows segregations into mafic and leucocratic portions on a cm scale (figure 5.11). The relationship of this rock to the Cascata Orthogneiss is not clear from field evidence alone. This relationship is investigated further by geochronological methods in chapter 7.

Figure 5.9a The Cascata Orthogneiss (locality 3) illustrating the presence of mafic xenoliths.

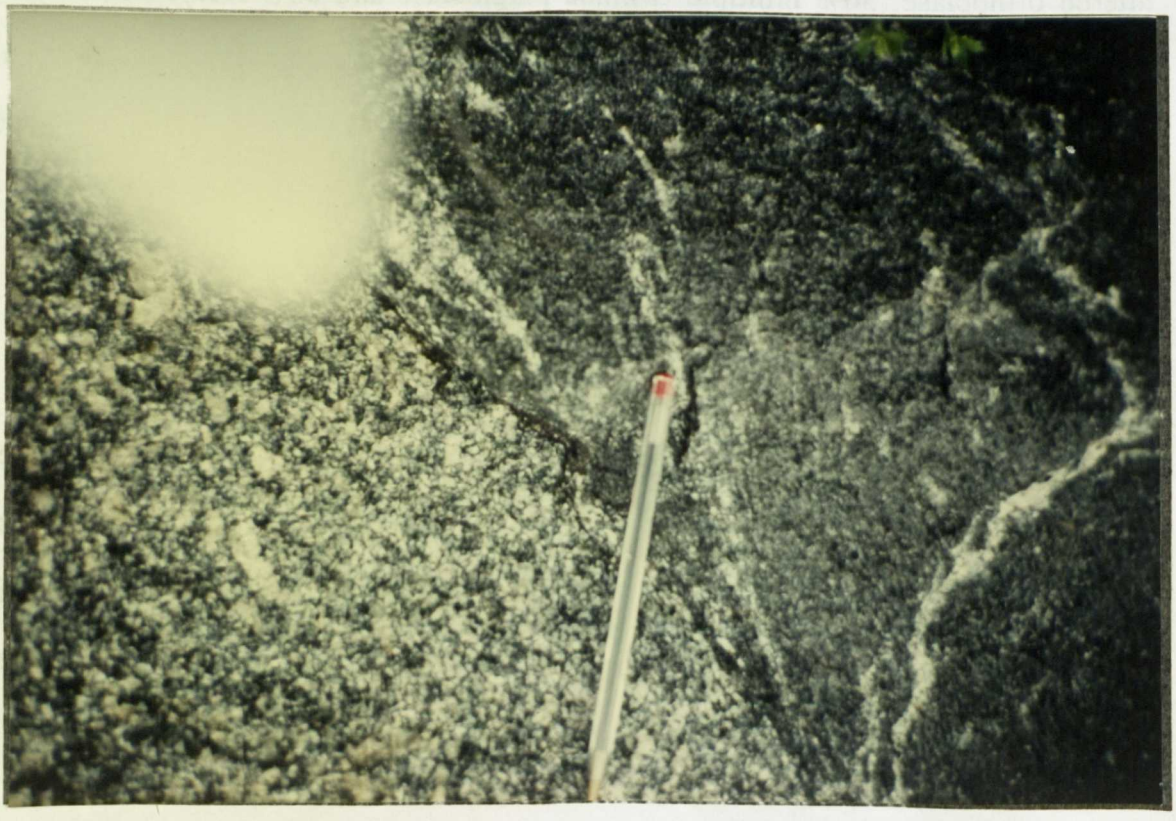

Figure 5.9b.Intrusion of the Migmatitic Orthogneiss into the Cascata Orthogneiss (locality 7).

Figure 5.10a Hand Specimen of the Cascata Orthogneiss showing marked biotite foliation.

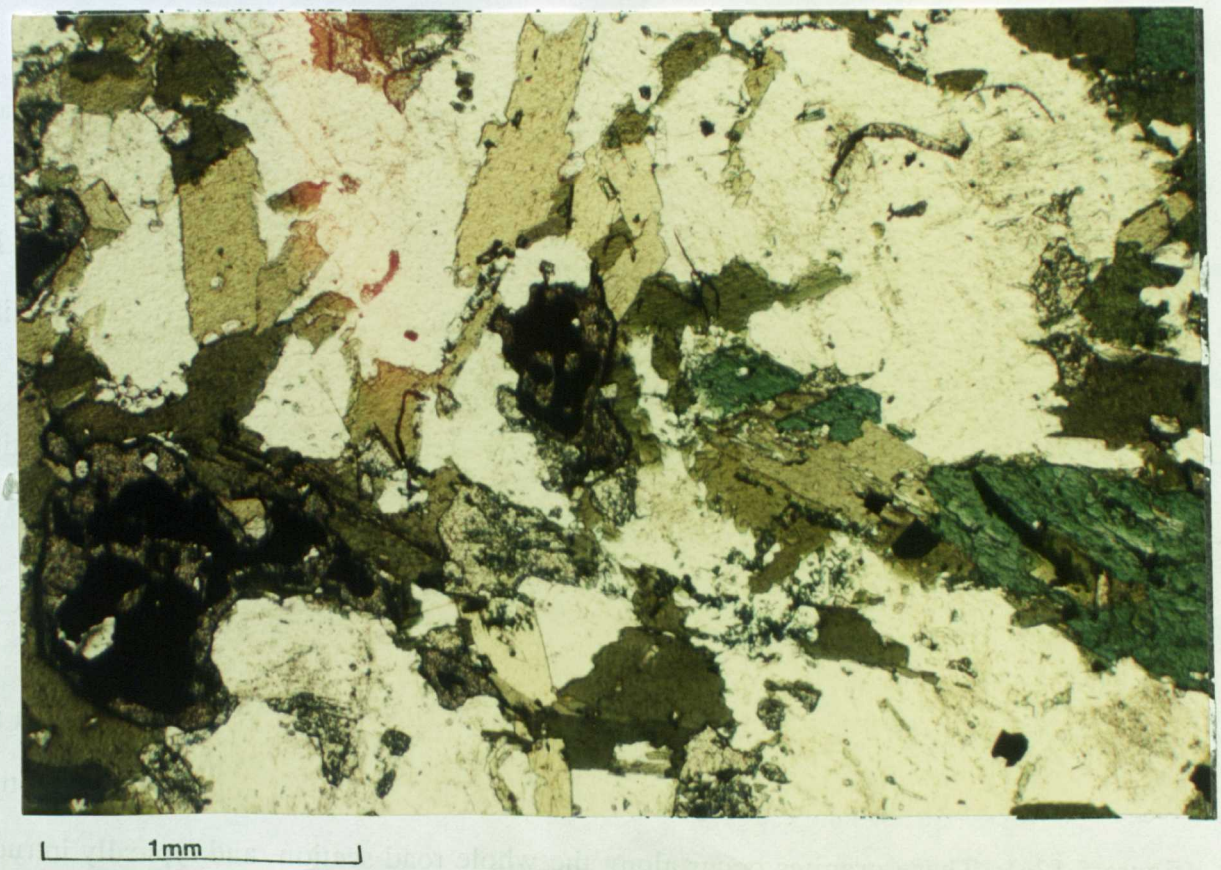

Figure 5.10b Photomicrograph (x5) of the Cascata Orthogneiss illustrating biotite, hornblende, sphene and magnetite as the mafic minerals.

The Migmatitic Orthogneiss is intruded by a number of unfoliated granite types. The most clearly observed example occurs at locality 11, in a quarry where an unfoliated coarse pink granite intrudes the foliated migmatite. This relationship is illustrated in the photographs of figure 5.11a and in more detail in figure 5.11b. The Pink Granite appears to have segregated from the Migmatitic Orthogneiss. In thin section (fig. 5.12) the mafic layers are composed of 10% small green euhedral biotites and magnetite; the leucocratic portions contain 30% subhedral multiply twinned plagioclase, 25% fresh orthoclase and microcline, and 30% recrystallized quartz. Some of the minerals show pressure shadows and other deformational effects which tends to suggest the segregation is a result of deformation.

The minerals are fresher in this rock than in the Cascata Orthogneiss and a noticeable difference between the two is the absence of sphene in this rock (figure 5.12). This rock type also plots in the granodiorite field of the Streckeisen plot (chapter 6), but is more quartz-rich than the Cascata Orthogneiss.

5.3.1.3. PIRITINI GRANITE

This granite is dark in colour, very inhomogeneous with a marked foliation and large alkali feldspar phenocrysts of up to 3cm in length separated by fine greenish biotite, plagioclase and quartz . It plots as a monzogranite on the Streckeisen plot. This granite type is found in the area around Piritini between localities A64 and A69. Its field relations to other granite types is unclear but it does appear to be intruded by pegmatites and late basalts. It is distinguished by its speckly appearance resulting from the dissemination of small biotite flecks.

5.3.1.4. CANGUÇU PHENOCRYSTIC GRANITE

This granite type is characterized by very large pink feldspar phenocrysts (up to 5cm in length) and much smaller smoky quartz grains separated by plagioclase and clots of biotite (figure 5.13a). These granites occur along the whole road section and typically intrude along the main S2 foliation. This unit has been mapped on the basis of the presence of the large feldspar phenocrysts.

Figure 5.11a Intrusion of the Quarry Pink Granite into the Migmatitic Orthogneiss at locality 11 looking to 225°.

Figure 5.11b Close up of the contact of 5.11a with evidence of migmatization and possible segregation of the Pink Granite from the Migmatitic Orthogneiss.

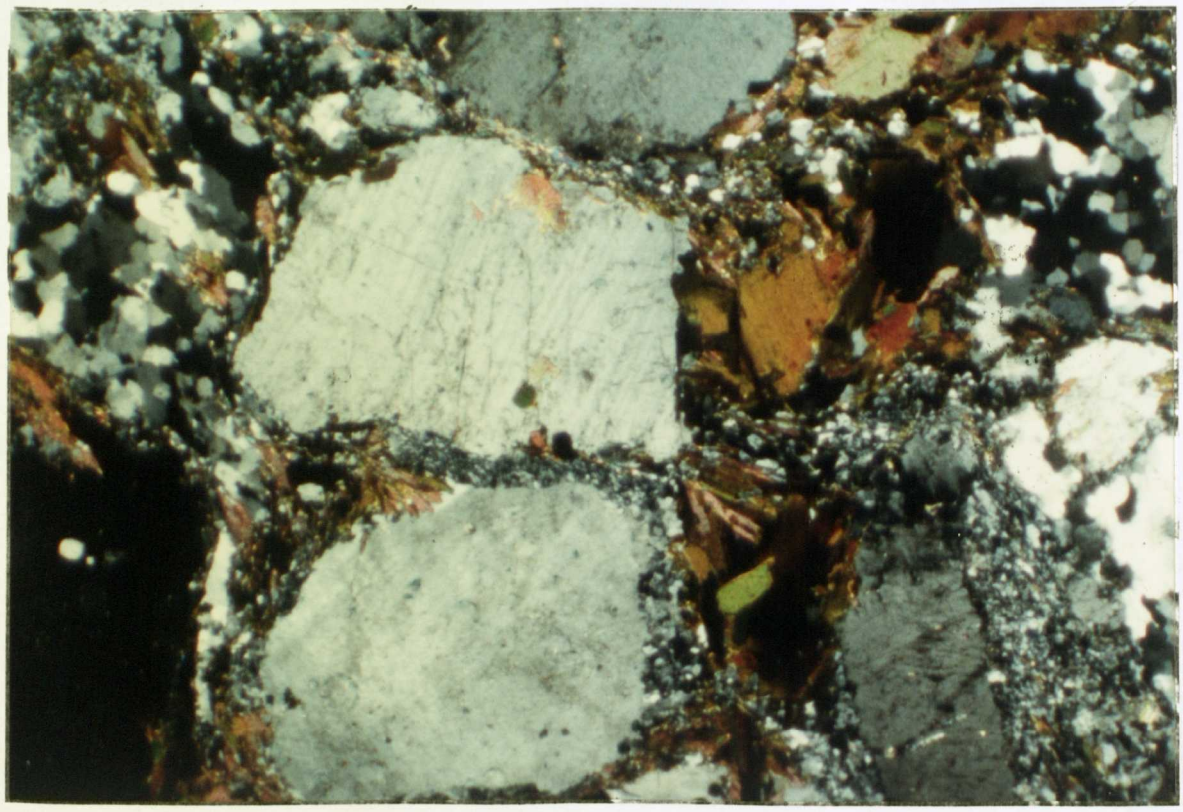

1mm

Figure 5.12a Photomicrograph (x5) of the Migmatitic Orthogneiss from quarry 11.

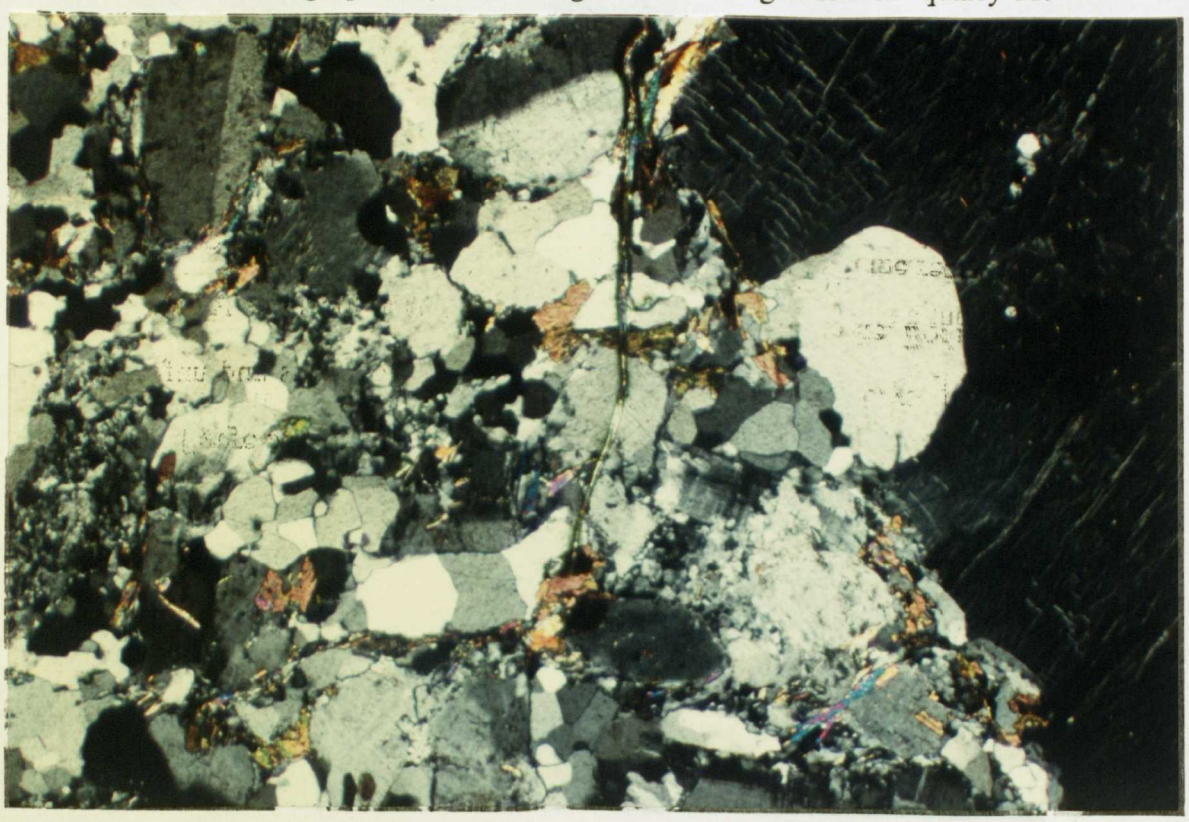

1mm

Figure 5.12b Photomicrograph (x5) of Migmatitic Orthogneiss illustrating its inhomogeneous nature and recrystallization.

This granite type occupies a large area on the map; it forms the hills to the NE of Canguçu and it is also exposed in the quarry at locality A16 where it is intruded by the Pink Granite and at localities 12,C1 (fig 5.7).

In thin section (figure 5.13b) the Canguçu Phenocrystic Granite is seen to be composed of large perthitic alkali feldspars and plagioclase crystals with interstitial recrystallized quartz and small mafic areas of biotite, sphene and secondary epidote and chlorite. Both the plagioclase twins and the biotite cleavage are deformed, and this together with the recrystallization of quartz, indicates that this rock has undergone strain. There is also myrmekitic texture in some of the alkali feldspars megacrysts which may suggest eutectic conditions. Plagioclase and quartz occurs as inclusions within the megacrysts suggesting that they are late or post-crystallization.

5.3.2 Unfoliated granites

There are five unfoliated granites discussed in this section. The Capao do Leao Granite and the Canguçu Granite appear to form a distinct geochemical group (Chapter 6).

5.3.2.1 CAPAO DO LEAO GRANITE

The main occurrence of this granite type is at locality A56 at Capao do Leao quarry on the Bage road, but a similar granite crops out at Quevidos at localities A7 and A9 (fig.5.14a). This granite type is coarse grained, leucocratic, homogeneous and unfoliated with 30% quartz, 25% white alkali feldspar and 35% plagioclase with about 5% biotite and possibly some garnet (5.14b).

Both a pink and a grey facies are observed but there are no clear contacts visible between them which suggests that the colour contrast relates to weathering or is possibly an alteration feature. There are rare biotite clots within the granite which may result from the digestion of xenolithic material. A biotite-garnet enclave may represent source material for this granite type . This premise will be tested using geochemical and isotopic investigation in chapters 6 and 7.

Figure 5.13a Hand specimen of the Canguçu Phenocrystic Granite from locality 12.

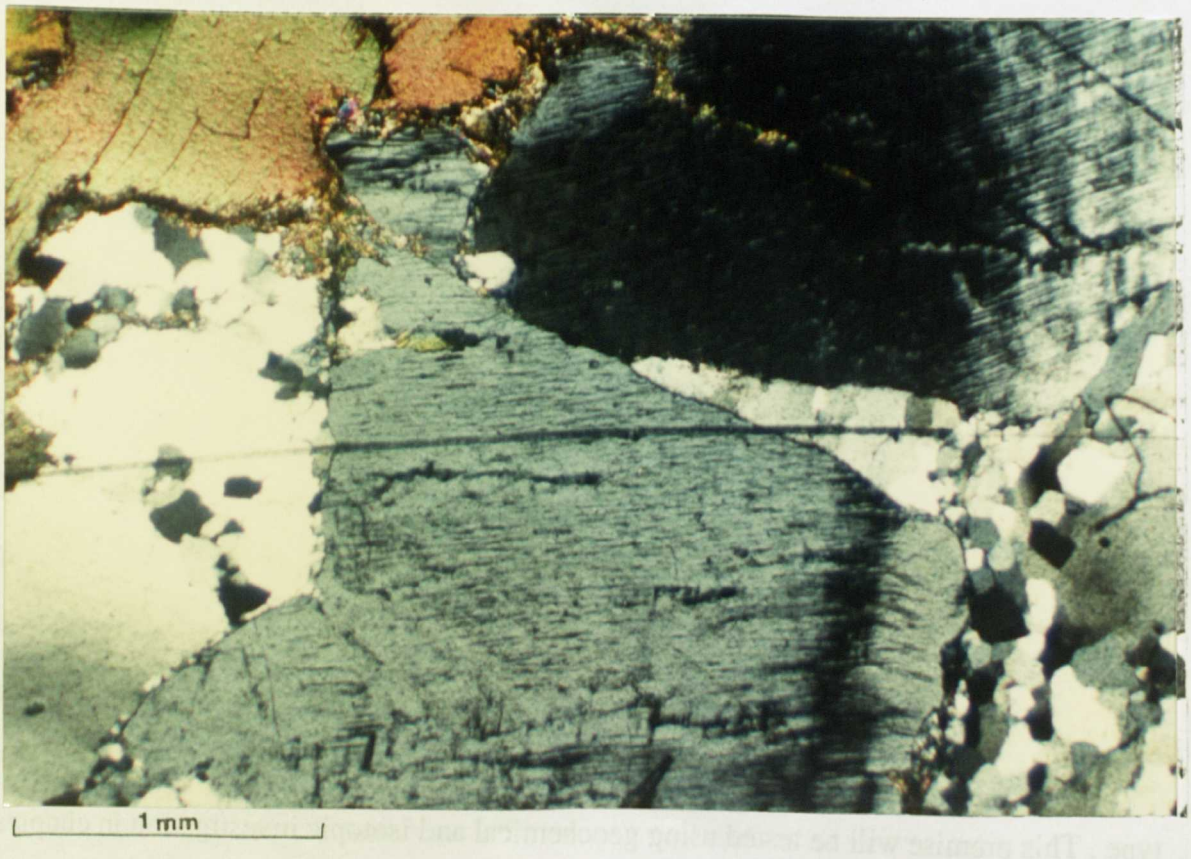

Figure 5.13b Photomicrograph (x5) of the Canguçu Phenocrystic Granite showing strained feldspars suggesting that it has been deformed.

Figure 5.14a Capao do Leao Granite exposed in the quarry at locality A56.

Figure 5.14b Close up of the Capao do Leao Granite.

5.3.2.2 CANGUÇU RED GRANITE

The Canguçu Red Granite is bounded by faults just NW of Canguçu and also crops out just SE of the fault marking the end of the granite belt (see fig 5.7). These are unfoliated, homogeneous, fine-grained and red in colour with 30% smokey quartz, 40% K-spar, 20% plagioclase and have biotite as a mafic mineral making up 5% of the rock (figure 5.15a). Its relationship to the other granites of the Pelotas Batholith is uncertain.

In thin section (5.15b) this granite is composed of equigranular interlocking subhedral crystals of microcline, orthoclase, quartz and plagioclase. Some larger alkali feldspar crystals overgrow the plagioclase in places. The only mafic mineral present is altered dark green-brown biotite altered to chlorite. There are inclusion trails across the feldspars which suggest the involvement of late fluids. This may contribute to the high Rb content of this granite (chapter 6) This rock plots as a granite on the Streckeisen plot.

5.3.2.3 CASCATA LEUCOGRANITE.

The Cascata Leucogranite is an unfoliated fine-grained white, magnetite-bearing granite, forming both dykes and larger sill-like bodies in the south eastern portion of the traverse. It is particularly well exposed in the quarries of localities 3 and X where it intrudes the Cascata Orthogneiss (figure 5.16 and 5.7). This granite type is also found between localities A10-13. A coarser grained leucocratic facies occurs at locality A54 (figure 5.7).

In thin section (5.17a) this leucogranite granite is characterized by less than 5% mafic minerals and by the presence of euhedral sphene associated with biotite and magnetite. The rock is predominantly composed of 35% interlocking altered orthoclase and microperthite with 20% plagioclase and 40% recrystallized quartz making the rock a granite on the Streckeisen plot. Secondary muscovite results from alkali feldspar alteration. Other minerals present are accessory chlorite and apatite.

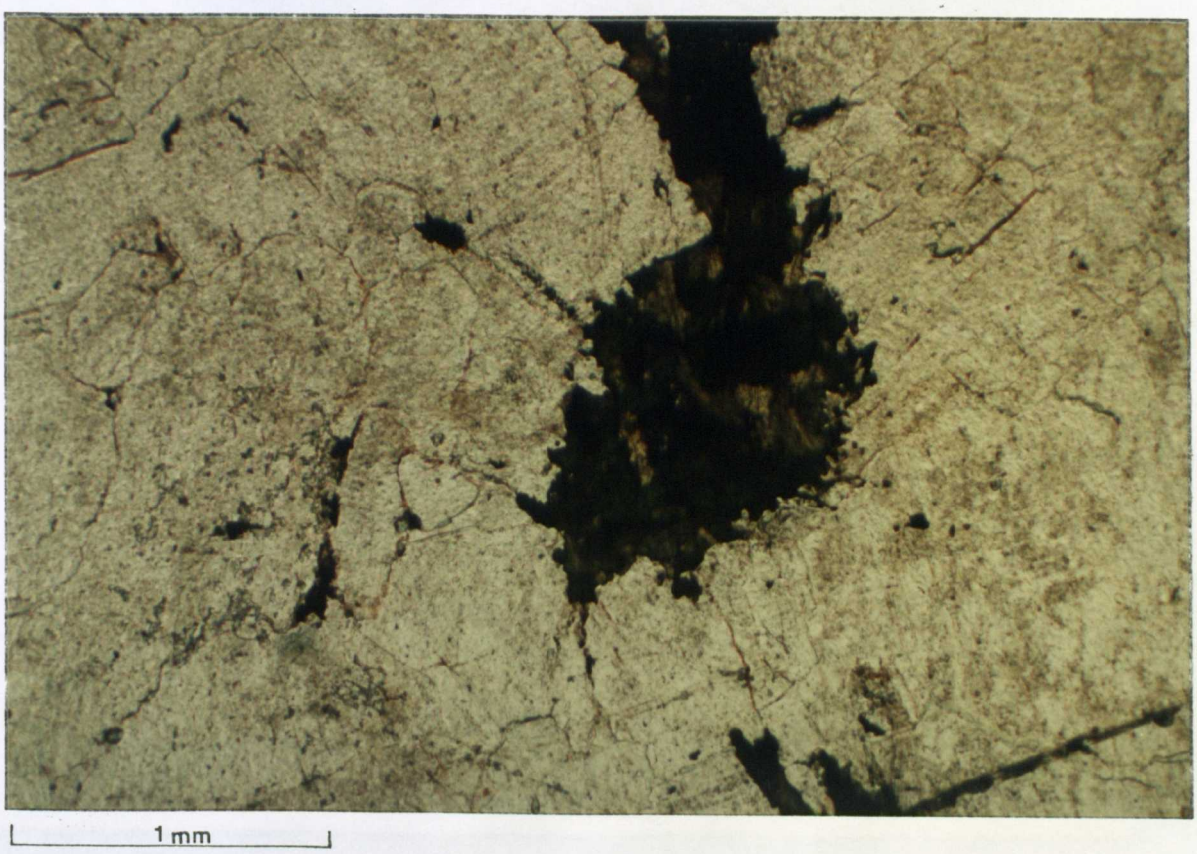

Figure 5.15a Photomicrograph (x5) of the Canguçu Red Granite.

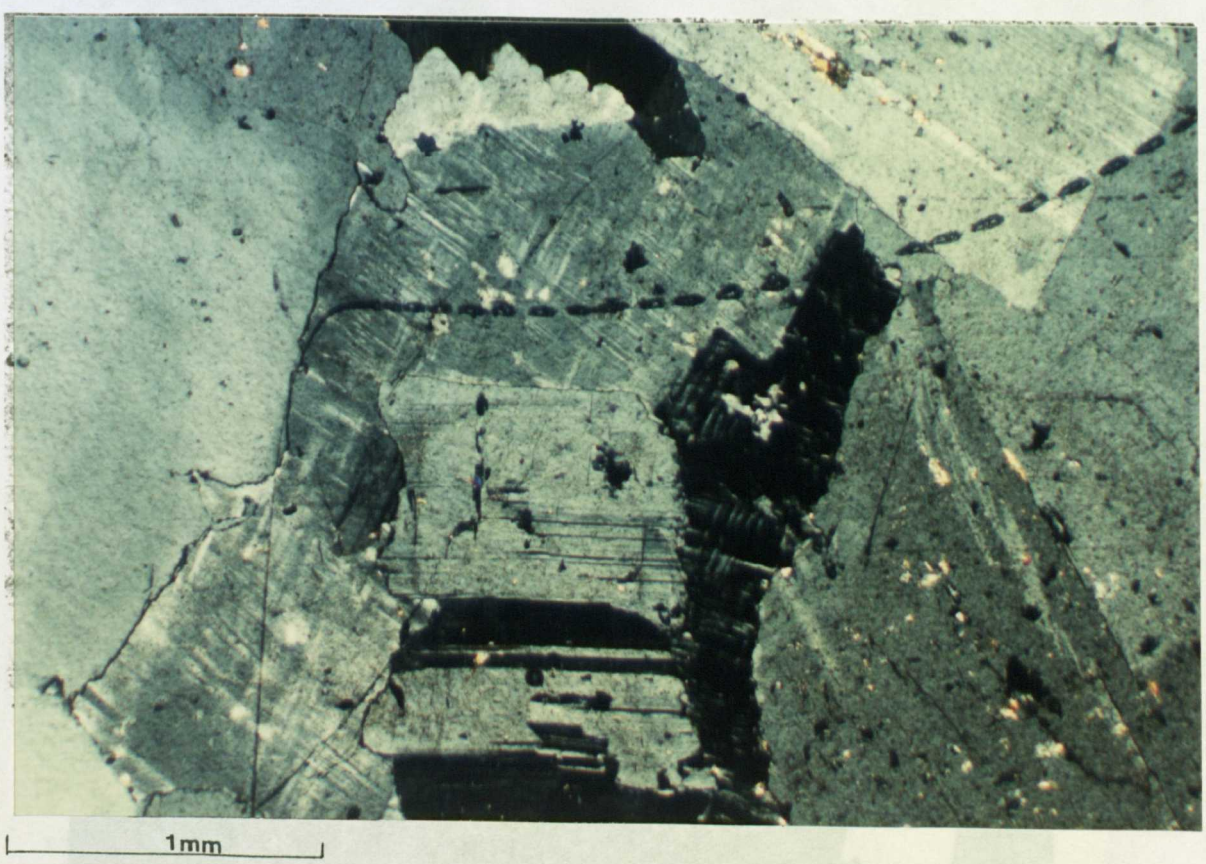

Figure 5.15b Photomicrograph (x5) of the Red Canguçu Granite showing inclusion trail.

Figure 5.16a Field relationship of Cascata Leucogranite intruding the Cascata Orthogneiss as dykes and sills at locality 3.

Figure 5.16b Intrusion of Cascata Leucogranite into Cascata Orthogneiss at locality X.

5.3.2.4 PINK GRANITE

This granite is coarse-grained, pink and homogeneous post-dating the foliated granitoids described above. The Pink Granite intrudes the Migmatitic Orthogneiss along joints and this relationship is best seen at locality 11 in a roadside quarry (see fig 5.7). At locality A16 the granite intrudes the Canguçu Phenocrystic Granite. Correlation between the Pink Granite that outcrops north and south of Canguçu is arguable but hopefully this question may be addressed using geochemical methods.

In thin section (fig.5.17b) the Pink Granite is composed of 30% large orthoclase and microcline crystals with 20% plagioclase and 40% recrystallized quartz. The main mafic mineral is a green mica which makes up less than 5% of the rock and forms a weak foliation and occurs in clusters together with 5% muscovite and magnetite. Chlorite locally replaces biotite. It lies in the monzogranite field of the Streckeisen plot.

5.3.2.5 PEGMATITES AND APLITE VEINS

Pegmatites are common throughout the section and are seen to crosscut both the Cascata Orthogneiss and the Migmatitic Orthogneiss. They intrude as steeply dipping E-W trending dykes of about 1m thickness and have sharp contacts. They are very coarse-grained and composed of large alkali feldspars, quartz, biotite and some muscovite. Good examples can be seen at locality 3,7 and A57 (figure 5.18). Aplite veins cross cut the orthogneisses and are similar in mineralogy to the leucogranites.

Pegmatite textures are variable and in thin section the remarkably fresh pegmatite of locality 3 is composed of occasional large green-brown biotite crystals, quartz and perthitic alkali feldspar.

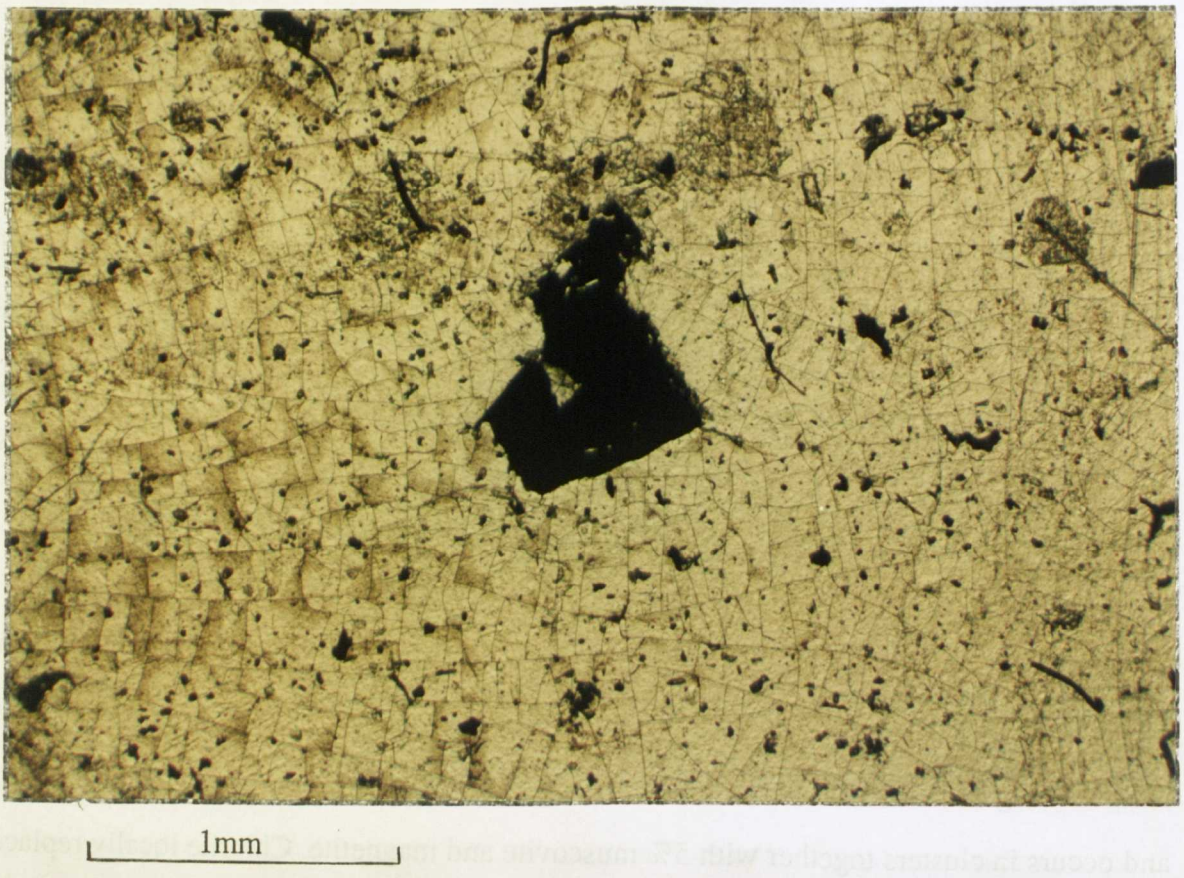

Figure 5.17a Photomicrograph (x5) of the Cascata Leucogranite from locality 3.

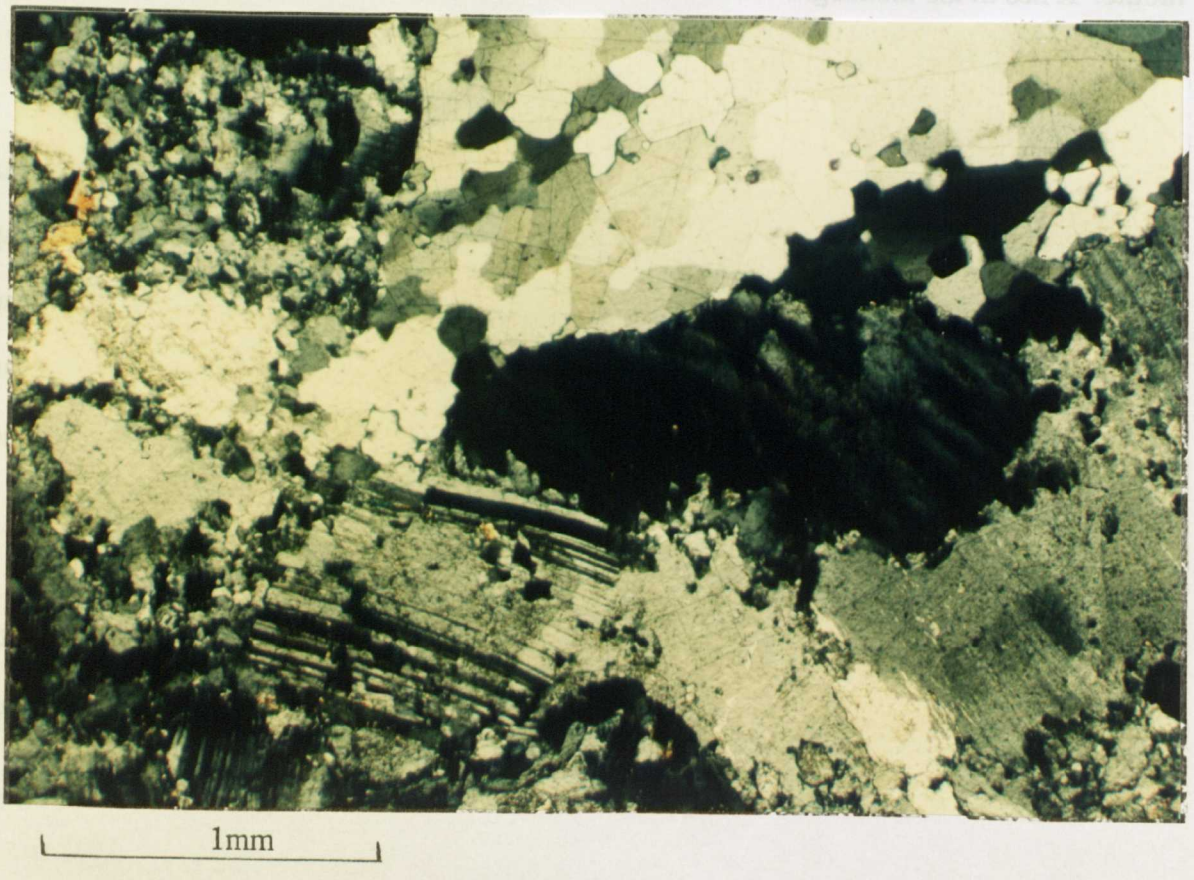

Figure 5.17b Photomicrograph (x5) of the Pink Granite of quarry 11.

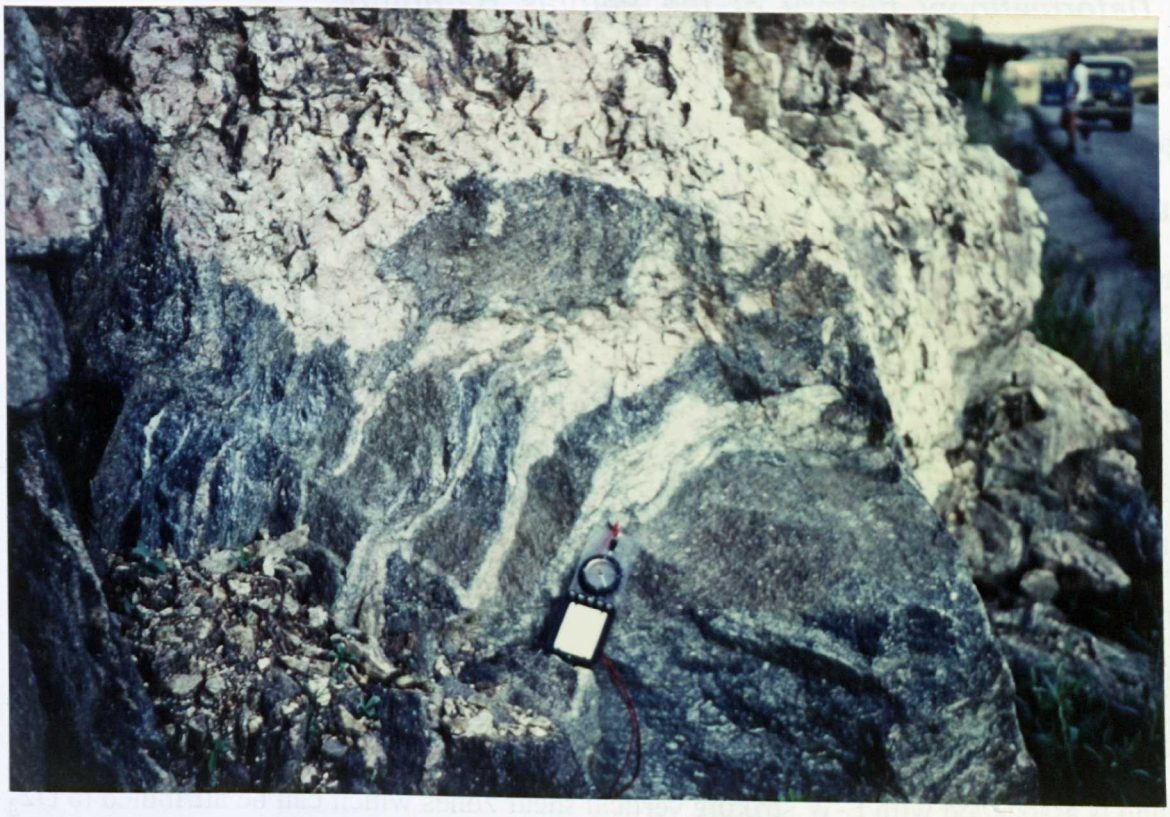

Figure 5.18 Intrusion of pegmatites into the Migmatitic Orthogneiss.

5.3.3. Basalts of the Pelotas Batholith

Vertical basalt dykes striking roughly NE-SW intrude the granite belt possibly along old joint planes. They are common near areas of intense shearing or faulting and a number of dykes occur at locality 23 and at locality A70 (see figure 5.7). Associated with these dykes are spotted schists which contain chlorite pseudomorphs after cordierite.

Basaltic flows outcrop at localities 20, 21 and C57 and often show good aqueous pillow structures suggesting an underwater deposition. Submarine eruption indicates that the area has been considerably uplifted since the extrusion of the basalts. The geochemistry and isotopic nature of these basalts and their relationship with the Parana Basalts is discussed in chapters 6 and 7.

5.4 Deformational history of the Pelotas Batholith

5.4.1 Introduction

In general, deformation fabrics of plutonic rocks provide less information than those of pelites. Deformation in granitoids is recorded by the alignment of micas although more intense shearing can cause local mylonitization. The orientation and timing of deformation in the Pelotas Batholith will be contrasted with that of the Santana Metamorphic Belt, (chapter 3) in order to establish whether correlations may be drawn between their deformational histories. This clearly has implications for interpreting the nature of their faulted contact.

The deformation of the Pelotas Batholith can be divided into three stages. An early compressional event $D1_g$ can be recognized by a biotite foliation S1g within the Cascata Orthogneiss and Migmatitic Orthogneiss. A second foliation S2g can be seen to overprint this and is associated with E-W striking vertical shear zones which can be attributed to $D2_g$ and mylonitization overprints the S1g foliation in places. This affects the Canguçu Phenocrystic Granite and Piritini Granite along with the granitoids affected by $D1_g$. Intrusion of the Canguçu Red Granite and the Capao do Leao Granite occurs after D2g as they are unfoliated although their intrusive relationships with the batholith are obscured by faults. The post tectonic unfoliated granites (Cascata Leucogranite and Pink Granites) are intruded after D2g and this relationship can be observed in the field. Finally the massif is affected by NE-SW extensional faulting $D3_g$ with the associated intrusion of pegmatites and basaltic dykes.

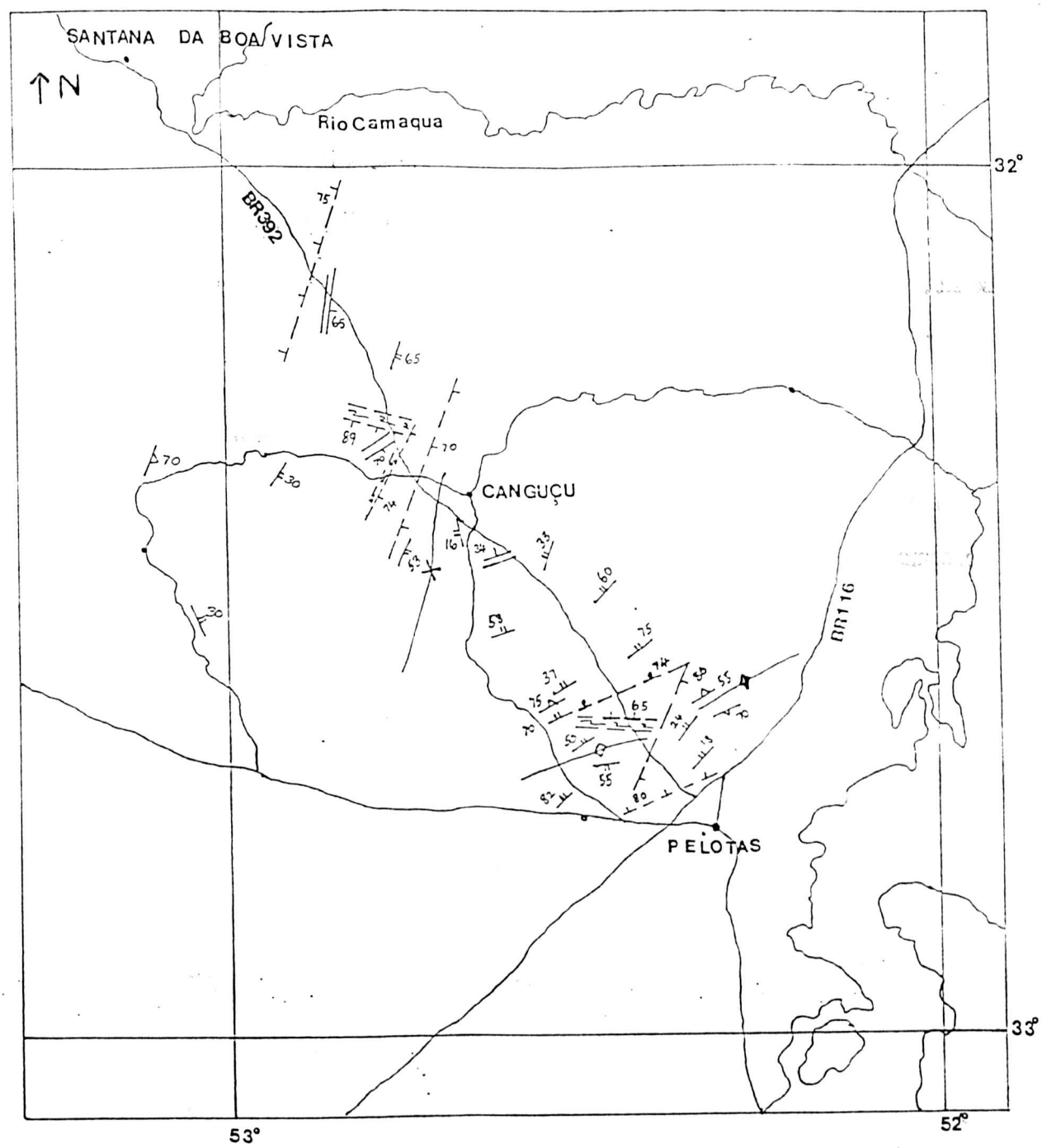

Observed normal fault contact (orientation of fault-plane indicated on down-thrown side)

Inferred normal fault contact

Bedding

Observed orientation of St_g schistosity in granitic rocks (dip and direction of, indicated)

Observed orientation of $S2_g$ cleavage (in fault planes, shear zones etc: dip and direction of, indicated)

Plunge of fold hinges (dip and direction of, indicated)

Dykes

Anticline

Syncline

Figure 5.19 Structural map of the Pelotas Batholith.

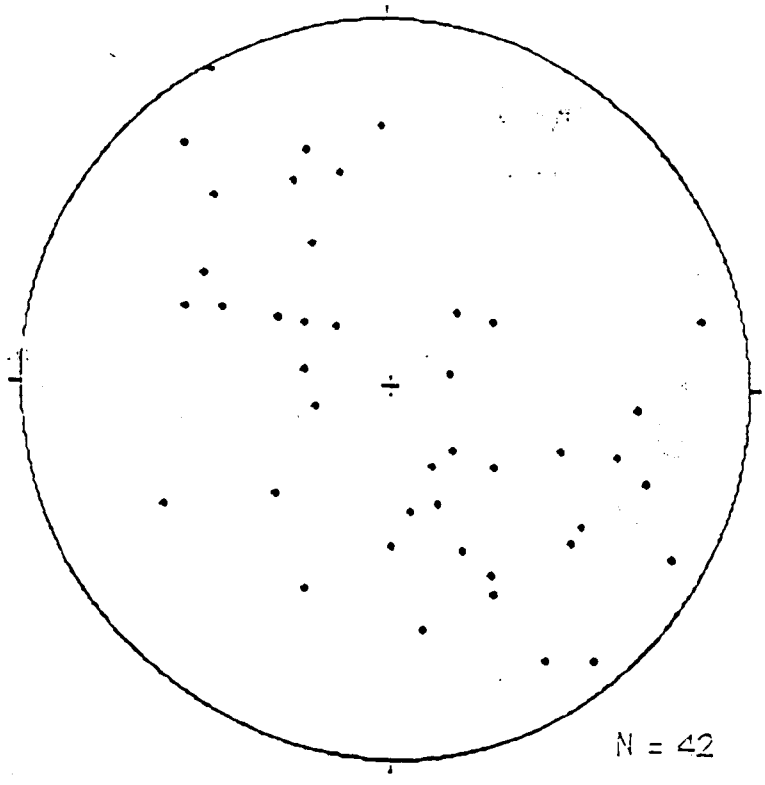

Figure 5.20a Equal area projection of the S1 biotite foliation of the foliated granodiorites.

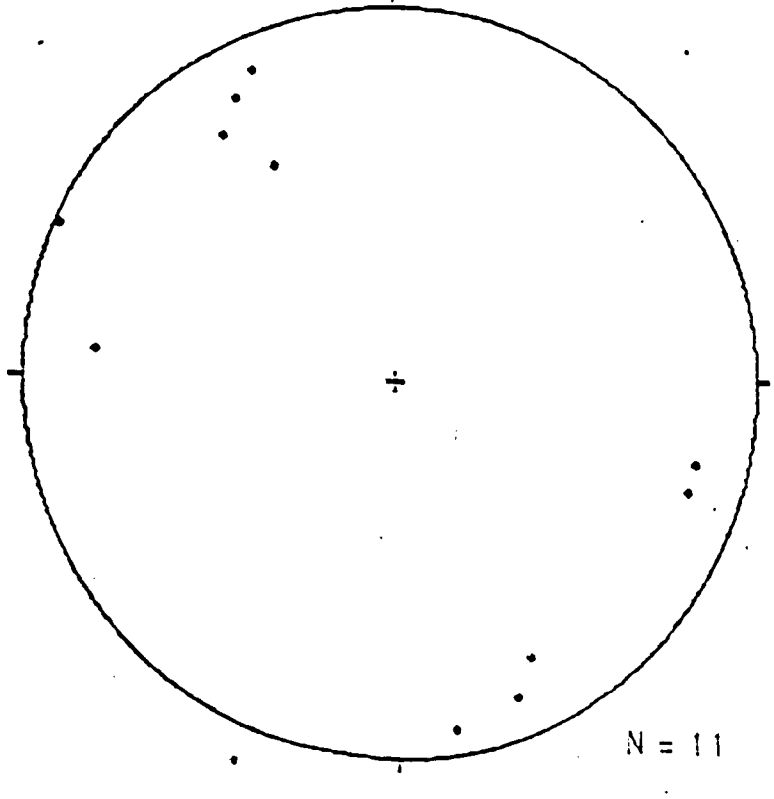

Figure 5.20b Equal area projection for the S2 foliation associated with shear zones affecting the foliated granitoids.

5.4.2. $D1_g$ Compressional event

This event is recognized by a strong gneissic foliation within the Cascata Orthogneiss and the Migmatitic Orthogneiss and the $S1_g$ foliation is illustrated on the map of figure 5.19. This foliation bears no relation to the margins of the igneous intrusions and cuts across igneous boundaries. The strike of this foliation is NE-SW corresponding to the strike of the S2 foliation in the Santana Metamorphic Belt and this foliation may well be formed in response to this D2 event which involved NW-SE compression (chapter 3). If this is the case, then the D2 event can be constrained to be younger than the Cascata Orthogneiss.

5.4.3 D2g Mylonitization and Shearzones

Continued compression resulted in zones of mylonitization and shearing within the Pelotas Batholith. Mylonites occur at two main localities along the BR392 section. At locality 5 (figure 5.21) a vertical shear zone cross-cuts the low-lying biotite foliation within the Cascata gneiss. This shear zone strikes E-W (272°) and mylonitized the granitoid to give a very sheared fine-grained rock.

A vertical E-W (104°) striking intensely mylonitized band approximately 250 m wide occurs at locality 16 (fig 5.22). The resulting mylonite is totally recrystallized and is dark grey finely laminated and quartz rich. This vertical E-W shearing is possibly related to the D3 compressional event of the Santana Metamorphic Belt . This foliation affects the Piritini Granite and the Canguçu Phenocrystic Granite as well as the Cascata Orthogneiss.

Figure 5.21a Vertical shear zone (S3) striking 260 at locality 5 affecting the Cascata Orthogneiss.

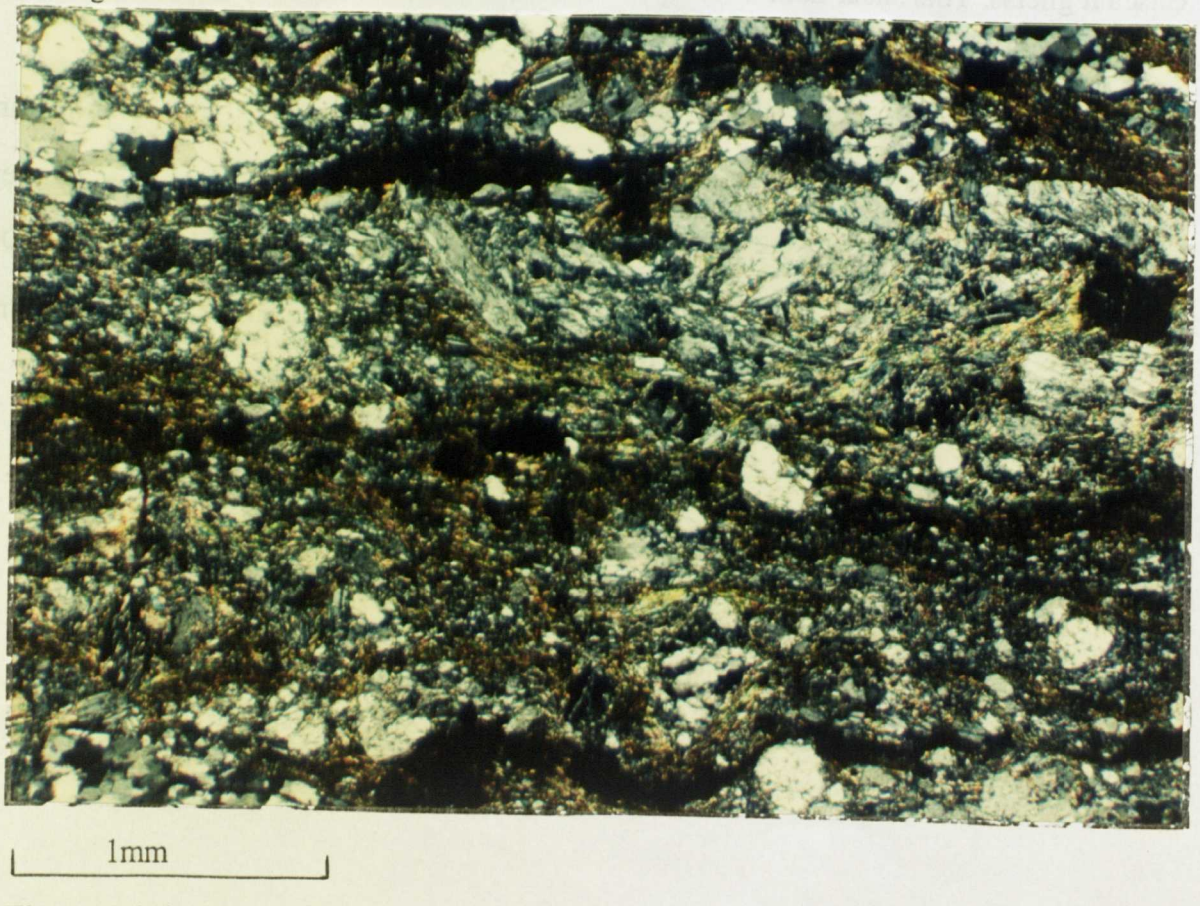

Figure 5.21b Photomicrograph (x5) of the sheared Cascata Orthogneiss at locality 5.

Figure 5.22a Vertical mylonite zone striking E-W at locality 16.

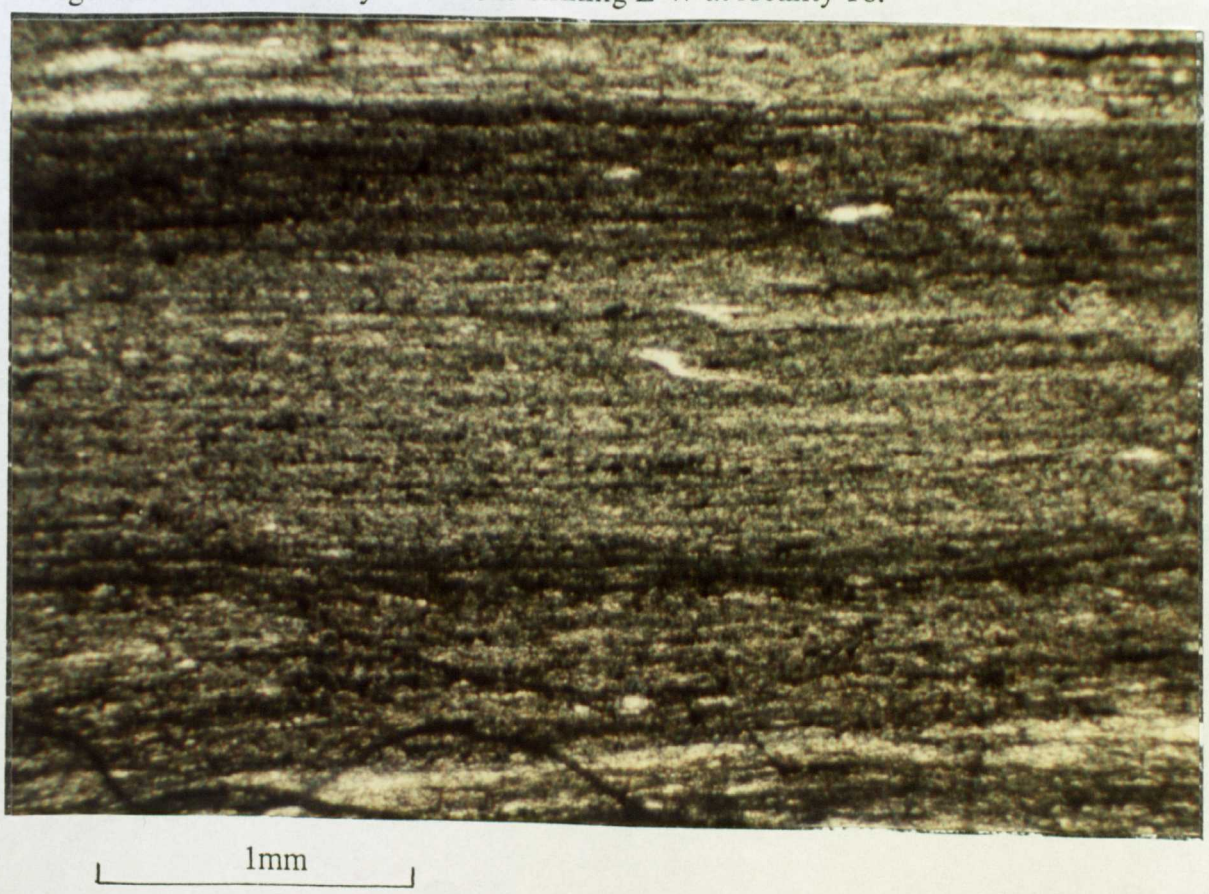

Figure 5.22b Photomicrograph (x5) of a mylonite from the shear zone at locality 16.

The mylonite zones may separate different terranes within the granite belt and this hypothesis is evaluated further using geochemical and isotopic data (chapter 8). The shear zone at locality 5 has been dated using Rb-Sr methods (chapter 7) at 508Ma which, if the above premise is correct, dates the $D2_g$ deformation event and makes it part of the Brasiliano orogenic event. The orientation of the shear zones and the vertical foliation associated with it is illustrated in the map of figure 5.19, which indicates that the shear zones are close to vertical striking 240-260.

5.4.4 D3g Extensional faulting

Extensional faulting occurs in a number of places along the BR392 within the Pelotas Batholith. To the SE this massif is separated from Quaternary sediment and underlying schists by a NE-SW striking fault that parallels the present coast line. At locality 1 the downthrown side is to the SE.

A minor fault of similar orientation occurs at locality 4 (figure 5.7). Two major extensional faults occur just NW of Canguçu which are both down-faulted to the SE on either side of the Canguçu Red Granite. The granite was probably emplaced in its present position as a result of extension and it only occurs in the region of extensional faults at localities 13 and 24. It may have been originally emplaced much higher in the crust. A parallel fault marks the end of the granite belt in the NW and down-faulting was to the NE forming a basin infilled with Triassic red beds interlayered with volcanics and this suggests that these faults were active at least until the Triassic period.

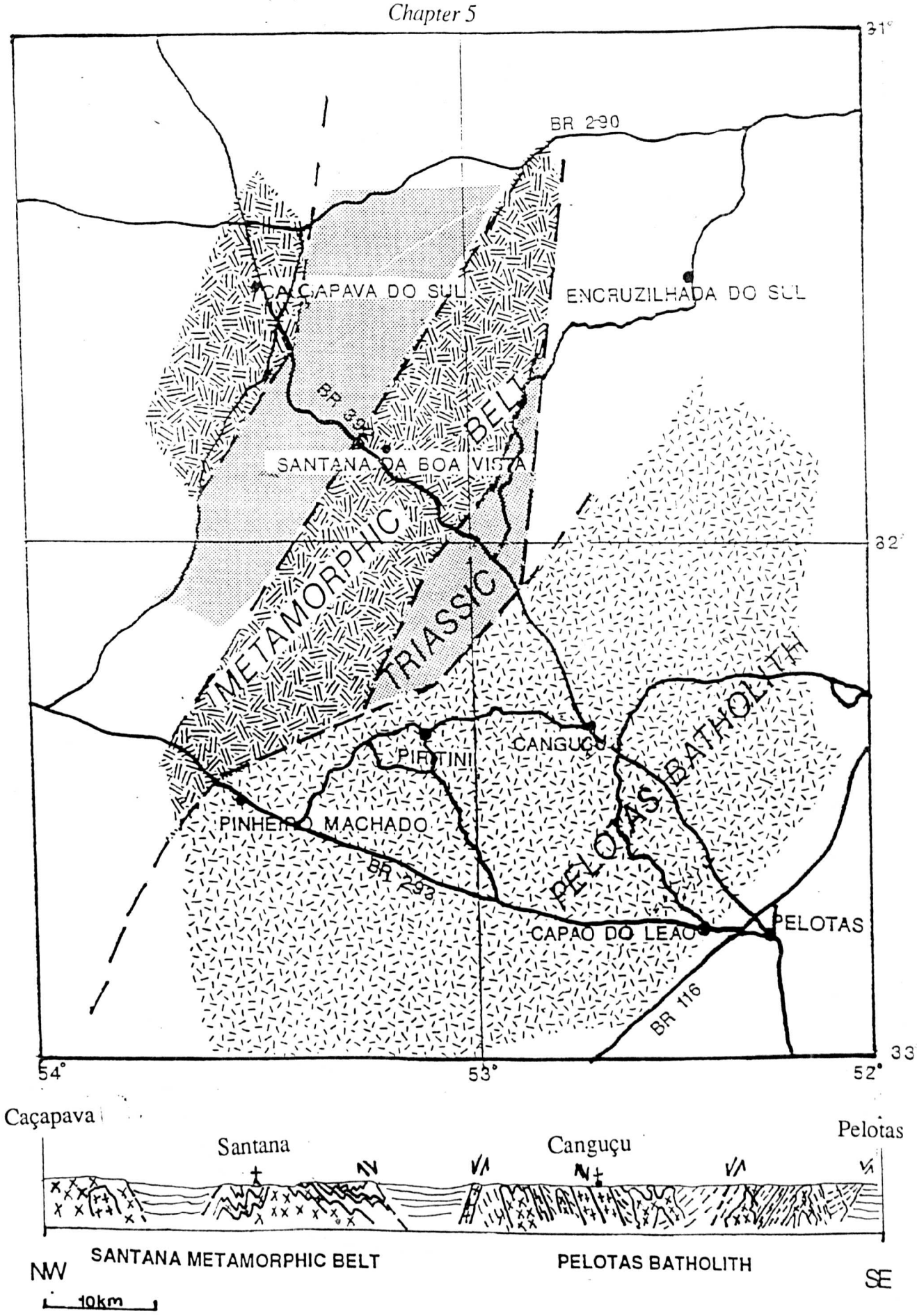

Fig 5.23 Cross section of the Dom Feliciano Belt in Rio Grande do Sul.

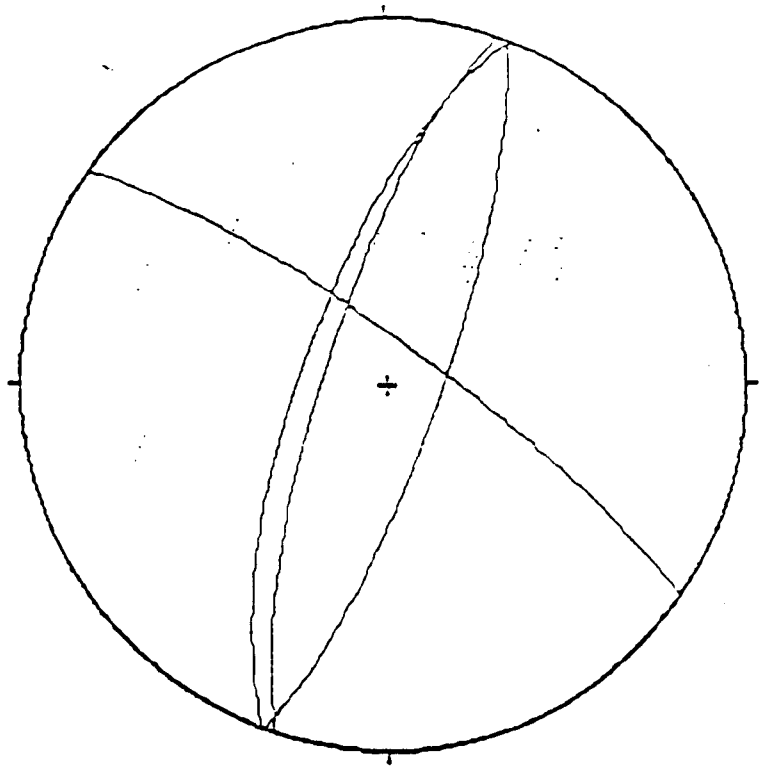

Figure 5.24a Equal area plot of fault planes which plot as great circles.

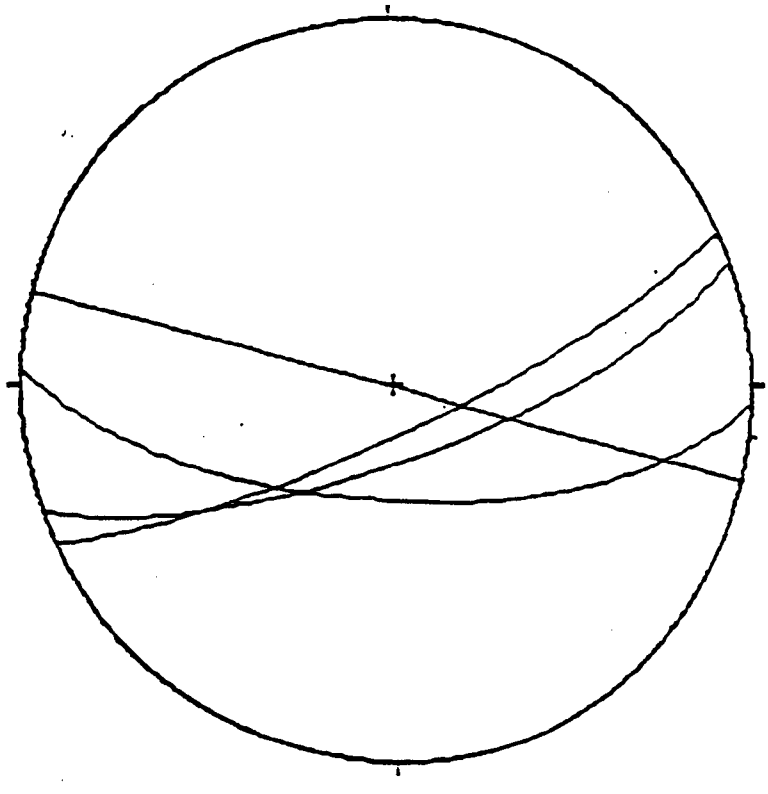

Figure 5.24b Equal area plot of shear zone planes of the Pelotas Batholith

Present data does not exclude association between extensional faulting and the opening of the South Atlantic. These faults have a NNE-SSW orientation closely paralleling the present coastline. When compared with the stereonets (fig 5.24) from the Santana Metamorphic Belt it appears that the two areas have undergone deformational events with the same orientation although the Pelotas Batholith has responded more competently than the Santana Metamorphic Belt.

5.4.5 Summary of deformation in the Pelotas Batholith

Three main deformational styles have been recognized in the Pelotas Batholith granite belt. Development of a biotite foliation within the Cascata Orthogneiss, and Migmatitic Orthogneiss resulting from a NE-SW compressional event D1g which may correspond to the D2 event defined in chapter 3 (table 5.2).

This foliation was then overprinted in certain areas by mylonitic shear zones designated as D2g which may correspond to D3 in the Santana Metamorphic Belt. The Cascata Leucogranite and Pink Granite show no evidence of foliation and were intruded post-D2g deformation. Finally NE-SW extensional faulting occurred parallel to the coast with the associated intrusion of basaltic dykes.Table 5.1 summarizes the geological history deduced from studies so far.

Figure 5.23 presents a cross-section through the Dom Feliciano Belt in Rio Grande do Sul and shows that the orientation of the deformational structures in the Pelotas Batholith is consistent with those observed in the Santana Metamorphic Belt. This suggests that the areas were affected by the same deformational events. It appears that D1 of the Santana Metamorphic Belt did not affect the Pelotas Batholith. Therefore D2 (SMB) was responsible for the first biotite foliation in the orthogneisses and D3 (SMB) for the second foliation. In the following chapters the structural terminology from the Santana Metamorphic Belt will be applied to the Pelotas Batholith in order to set up a systematic classification for granites of the Dom Feliciano Belt (Table 5.2).

Pelotas Batholith	Santana Metamorphic Belt
	D1 Gneissic Fabric
Intrusion of Santana Granite, Cascata Orthogneiss, Migmatitic Orthogneiss	
D1g Formation of S1 bi foliation	**D2** Isoclinal folding of basement
Intrusion of Piritini Granite, Canguçu Phenocrystic Granite, Campinas granite	
D2g Mylonitic shearzones S2	**D3** Open folding
Intrusion of Canguçu Granite, Capao do Leao Granite, Cascata Leucogranite, PinkGranite	
	D4 NE Thrusting
D3g Extensional faulting	Extensional faulting
Intrusion of pegmatites, basalts	Extrusion of andesites, rhyolites, basalt flows/dykes,
Deposition of red beds	

Table 5.1

5.5 Conclusions

From the petrological studies of the igneous rocks of the area table 5.2 has been constructed to illustrate the major similarities and differences observed between the different igneous rocks and their relationship to deformational events. For example, the Santana Granite has a similar mineralogy (table 5.3) to the Pink Granite intruding the Pelotas Batholith. The field relations however illustrate that the Santana Granite is considerably older and affected by two phases of deformation whereas the Pink Granite is unaffected by deformation. This illustrates that the relationship of a granite to the regional deformation is an important factor

MINERALOGY OF ROCK TYPES			
SANTANA METAMORPHIC BELT			
Rock type	Mineralogy	Accessory minerals	Texture
Metagabbros	Hornblende, quartz	Green hornblende	Cumulate
Felsic volcanics	Kspar, quartz, glass	Sanidine	Volcanic
Santana Granite	Ksp,plag,quartz, biotite	Muscovite	Weak foliation
Encruzilhada Granite	Alkali-feldspar, plagioclase,quartz, hornblende	No thin section	coarse grained homogeneous
Campinas Granite	Muscovite, biotite, quartz, plagioclase, weathered K-spar	No thin section	Medium-grained foliated by shear zone
Caçapava Granite	Orthoclase,quartz, microcline,plagioclase, biotite	Apatite, magnetite, chlorite	Grey facies foliated Red facies unfoliated homogeneous.
PELOTAS BATHOLITH			
FOLIATED GRANITOIDS			
Cascata Orthogneiss	Orthoclase, plag microcline,quartz, green biotite,hornblende	Magnetite,sphene, apatite,zircon	Foliated, gneissose, inhomogeneous, mafic enclaves of hornblendite
Migmatitic Orthogneiss	Orthoclase,biotite plagioclase,quartz	Magnetite	Foliated,grey,fine migmatitic
Piritini Granite	Kfeldspar,biotite, plagioclase,quartz		Speckly, foliated, inhomogeneous
Canguçu Phenocrystic Granite	Orthoclase phenocrysts, quartz,plagioclase, biotite	Magnetite,sphene, epidote,chlorite	Phenocrysts k-feldspar, foliatiated,coarsegrained
UNFOLIATED GRANITES			
Canguçu Red Granite	Quartz,orthoclase, plagioclase,biotite	Magnetite	Red,homogeneous, fine grained
Capao do Leao Granite	Orthoclase,quartz, plagioclase,biotite	Garnet	Coarse,white,bi-gt enclaves,homo-geneous,unfoliated

Leucogranite	Orthoclase,quartz, microperthite,biotite	Magnetite,apatite, secondary musc	Unfoliated,white, homogeneous
Pink Granite	Orthoclase,quartz, plagioclase,biotite	Muscovite,epidote,magnetite,chlorite	Coarsepink,homogeneous, unfoliated
Pegmatite	Quartz,perthitic alkali-feldspar, green biotite		Very coarse grained interlocking euhedral crystals

Table 5.2

A similar mineralogy may however suggest that the two granites were produced by a similar process or from a similar source. This premise has been explored by various researchers e.g.Chappell and White (1974). Mineralogical similarities and differences may form a basis on which to establish interrelationships between rocks which can be further explored geochemically and isotopically.

The mineralogical similarities and differences between igneous rocks illustrated in the table allows one to evaluate the interrelationship between mineralogy, deformation, spatial location and age. The mineralogy of most of the granitoids in the Pelotas Batholith is very similar with green biotite as the main mafic mineral and magnetite as the main accesory with the proportion of mafic minerals decreasing progressively within the younger unfoliated granitoids (table 5.2).

There seems to be a positive correlation between the age and the proportion of leucocratic minerals. This suggests progressive evolution of the granitoids of the Pelotas Batholith with time. Certain granitoids are distinguishable in terms of their mineralogy for example the Cascata Orthogneiss can be distingushed from the Migmatitic Orthogneiss by the presence of sphene in the former suggesting a more titanium rich source. The phenocrystic granite also contains sphene and it may possibly be related to the Cascata Orthogneiss with the intrusion of pegmatites causing the growth of feldspar phenocrysts being the sole

difference. Of the unfoliated granites the Pink Granite can be distinguished from the Leucogranite by the presence of muscovite.

The Encruzilhada Granite has a predominance of hornblende as a mafic mineral making it distinctive from all the other granitoids which have biotite as the dominant mafic mineral. (The Cascata Orthogneiss contains some hornblende). This granitoid may also be related to the hornblendite (metagabbro) of the Santana Metamorphic Belt. The Campinas Granite is distinctive by the presence of large muscovite flakes. There appears to be no obvious distinction between the Caçapava Granite and the Pelotas Batholith granitoids in terms of mineralogy although their spatial distribution may suggest that they have different sources since the Caçapava Granite intrudes the Santana Metamorphic Belt. This may be resolved using isotopic methods in chapter 7.

Enclaves within the Cascata Orthogneiss are rich in hornblende and show a striking resemblance to the hornblendite cumulate intruding the Santana Metamorphic Belt. This suggests that there may be a similar hornblendite deep in the Pelotas Batholith through which the Cascata Orthogneiss intruded picking up enclaves as it rose through the crust. The Capao do Leao Granite contains biotite-garnet-Kfeldspar enclaves suggesting a different cumulate deep in the crust and this may account for the presence of garnet as an accessory mineral.

From the structural studies undertaken in the Pelotas Batholith granite belt, it has been established that the Santana Metamorphic Belt underwent at least one more deformational event than the granite belt but that both belts experienced the D2 and D3 events. The former produced isoclinal folds in this metamorphic belt and a biotite foliation in the orthogneisses of the Pelotas Batholith. The D3 event caused an upright foliation in the Pelotas Batholith and upright open folding in the Santana Metamorphic Belt. There is no evidence of D4 thrusting in the Pelotas Batholith. Extensional events affected both areas. The orientation of the structures produced by this deformation is predominantly NNE-SSW in both areas and

this is illustrated in figure 5.23 This correlation is explored further in Chapter 8. Table 5.1 summarized the sequence of structural and magmatitic events in the Dom Feliciano Belt.

Many of the late volcanics are intruded in an underwater environment since they show pillow structures. The andesites are thought to be Triassic in age and the rhyolites somewhat later. The basaltic dykes are obviously an extensional feature associated with extensional faults and are possibly related to the opening of the Atlantic. The tectonic setting of the andesites poses a greater problem which may be resolved by geochemical methods.

CHAPTER SIX

6. Geochemistry of the Dom Feliciano Belt.

6.1 Introduction

The geochemistry of the Dom Feliciano Belt between Pelotas and Caçapava do Sul is discussed in this chapter. The main purpose of this geochemical study is to compare and contrast the granites of the Pelotas Batholith with those intruding the Santana Metamorphic Belt, and to compare both types with granites elsewhere, whose petrogenesis has been modelled in more detail and where the tectonic settings are known. It is also intended to establish whether there is any gradual change in geochemistry from SE to NW through the Dom Feliciano Belt which might relate to changing source regions and/or changing tectonic regimes. Geochemical variations along the traverse across the Dom Feliciano Belt will be investigated in section 6.4, and figure 6.1 illustrates the spatial distribution of the analysed granite bodies.

This section gives a general introduction to the problems involved in granitoid geochemistry, the objectives of this study and a geochemical classification of the sampled rocks. Section 6.2 will be concerned with the geochemistry and petrogenesis of the granitoids of the Pelotas Batholith (chapter 5), and the geochemistry and petrogenesis of selected rocks of the Santana Metamorphic Belt are then discussed in section 6.3.

Basement gneisses, schists and syntectonic igneous intrusions (chapter 2) are discussed in section 6.3.1, along with the andesite volcanics interbedded with red beds in the extensional basins both separating the Pelotas Batholith from the Santana Metamorphic Belt, and also within the latter belt. The granites intruding the Santana Metamorphic Belt are discussed in section 6.3.2. Major, trace and rare earth element data are given in Appendix C and presented here on Harker silica plots and spider diagrams that provide the basis for petrogenetic models.

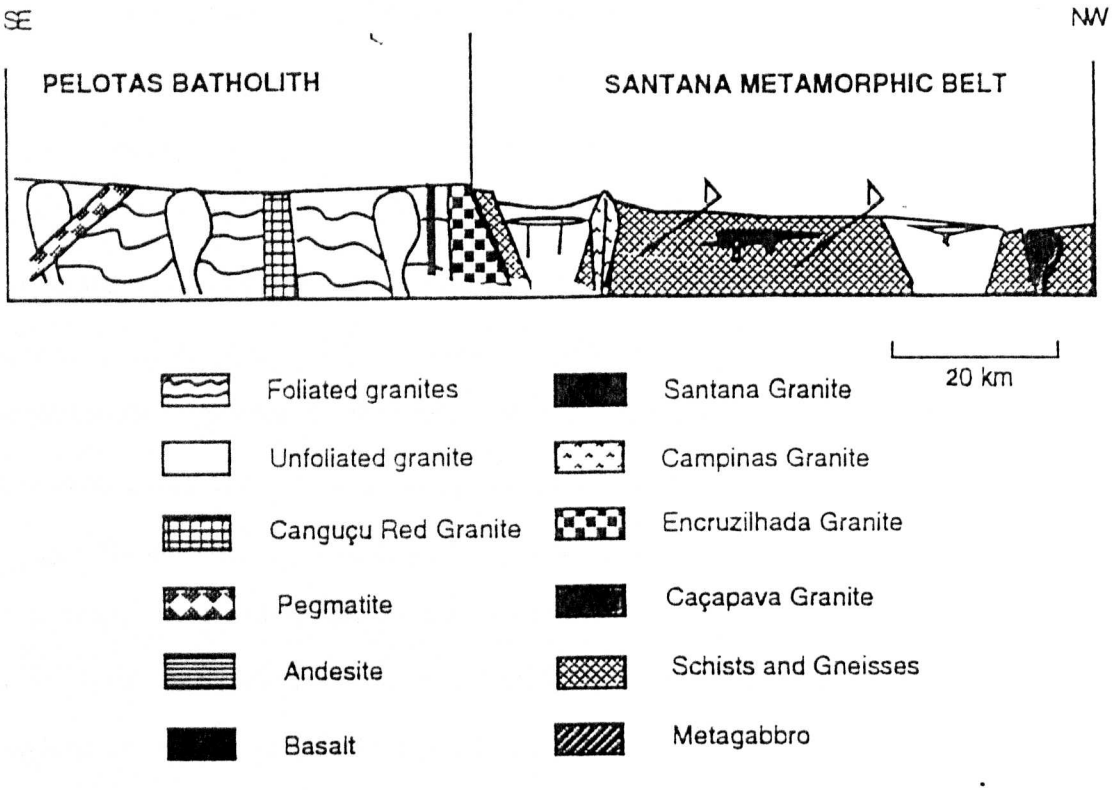

Figure 6.1 Sketch geological section illustrating the location of the granitoids and other igneous intrusions studied for geochemistry.

6.1.1 Objectives

The main purpose of the geochemical study is to compare and contrast the granites of the Pelotas Batholith and the Santana Metamorphic Belt and to see how geochemistry varies along a SE-NW section through the area. Detailed petrogenetic modelling is beyond the scope of this study but the following objectives are identified:

1. To establish the inter-relationships of the basement gneisses, granites, gabbros and schists in the Santana Metamorphic Belt.

2. To establish the inter-relationships between the Pelotas Batholith granitoids and the Santana Metamorphic Belt granites .

3. To establish whether the Pelotas Batholith is a coherent tectonic unit or several units welded together along shear zones.

4. To examine whether there is a gradual change in granite geochemistry from SE to NW across the Pelotas Batholith.

5. To evaluate whether the granitoids of each belt may be related in terms of source rocks and conditions of magmatism.

6. To establish whether the granitoids are derived from the mantle, the lower crust or the upper crust and the nature of their tectonic setting.

6.1.2 Granitoid Geochemistry and Petrogenesis

The origins of granitic melts have been debated by a considerable number of workers and three main processes have been proposed; partial melting of pre-existing crustal rocks, fractional crystallization of basic and/or intermediate magmas, and a mixture of these two processes. Allegre and Ben Othman (1980), Hamilton et al (1980), Farmer and De Paolo (1983), Frost and O'Nions (1985) have suggested that crustal anatexis and the recycling of pre-existing crustal material have played a dominant role in the petrogenesis of leucogranites (see also, Wickham 1988), and that liquids of granitic composition may be obtained from varying amounts of fusion of a range of crustal materials. It is the intention of this section to evaluate qualitatively the dominant processes responsible for the major granitoid types recognized in the field. It is important and necessary to integrate theoretical studies (McKenzie 1984) with field studies, and this is undertaken using a schematic cross-section (figure 6.1) in section 6.4.

Geochemical data are conventionally represented using Harker plots of major and trace elements against silica. Correlations on Harker plots can develop in a number of different ways. Since major elements make up nearly 100% of a rock, some negative correlation with silica, the most abundant element, is to be expected from simple dilution, but significant trends are usually the result of an evolutionary process such as fractional crystallization of a parent magma and/or progressive contamination of a magma by high silica material. It has been argued that curved trends are probably the result of fractional crystallization whereas

linear trends may result from various degrees of separation of the melt and restite during partial melting (Chappell and White1987).

In basaltic melts, trace elements appear to be largely controlled by the major mineral phases, but for granites only Ba, Rb and Sr consistently provide any useful information on the major phases (feldspar, biotite) with the other trace elements often being controlled by accessory phases which cannot be easily modelled. In general, certain trace element patterns may be assigned to particular processes, for example, a negative europium anomaly suggests feldspar fractionation or residual feldspar during partial melting, low Zr and Hf suggest that zircon is residual, and low Ta,Nb and REE may indicate that sphene, apatite and minor phases are residual.

Rare earth element data are conventionally normalized to chondrite and plotted in a spider format. Spider plots are also used to represent trace element data relative to primitive mantle and these are compared with typical lower and upper crustal melts from Idaho and the Andes respectively, and a volcanic arc granite from Chile. Rb-Y-Nb diagrams are used to try and propose a tectonic setting for the different major granites types. Finally elemental ratios are plotted against distance and compared to the schematic cross section in section 6.4.

6.1.3. Classification

6.1.3.1 GENERAL CLASSIFICATION

There are four major rock types studied for geochemistry along the section between Pelotas and Caçapava do Sul, namely granites, basement metamorphics, recent sediments and volcanics (figure 6.1). The latter three were not studied in as much detail as the granites. The Pelotas Batholith can be broadly classified into foliated and unfoliated granitoids, and it also has a few basaltic dykes and flows. The granitoids will be classified in more detail in section 6.1.3.2. The Pelotas Batholith is separated from the Santana Metamorphic Belt by a basin with unmetamorphosed red beds interbedded with andesites. The geochemistry of the

andesites is considered in relation to the Santana Metamorphic Belt purely for convenience. The rocks of the Santana Metamorphic Belt can be classified into two groups: non granitic rocks including metamorphic rocks such as basement gneisses and schists and igneous rocks such as andesites and a metagabbro (chapter 2), and secondly granites including foliated and unfoliated granites. The granites from both belts will be classified in detail.

6.1.3.2 CLASSIFICATION OF GRANITOIDS

A first order petrological classification of granitoids was proposed by Streckeisen (1976) who plotted the relative modal proportions of the three major minerals, quartz, plagioclase and alkali feldspar on a triangular diagram. In this study, modal compositions are replaced by recalculations of the major element analyses, in terms of mineral phases stable on the granite solidus using a GRANNORM program described in Harris and Marriner (1980). This approach reduces the uncertainty of mineral identification and point counting of coarse grained samples. For fresh samples with <20% mafic phases it is accurate to ±2%.

Figure 6.2 shows all the analysed granitoids from the Pelotas Batholith on the Streckeisen plot. It illustrates the large range of granite types from quartz diorite through to syenogranite present in this complex belt. There appears to be a distinction between the foliated and unfoliated granitoids of the Pelotas Batholith although the fields overlap with the Piritini Granite and leucogranites lying in the monzogranite field. The foliated orthogneisses and migmatites fall between the quartzdiorite and monzogranite fields and there appears to be a trend for the Cascata Orthogneiss (foliated biotite granite gneiss), which falls mainly in the granodiorite field, away from the plagioclase apex, suggesting a strong plagioclase control. Some of the Migmatitic Orthogneisses (fine grained segregated biotite granite with pink leucosome) are enriched in quartz relative to the main trend. These also lie mainly in the granodiorite field. There are a couple of xenoliths associated with these foliated rocks and these plot on the Qz-absent line indicating they are not granitic. All samples of the Piritini Granite (speckly green biotite granite) lie in the monzogranite field.

FOLIATED GRANITOIDS

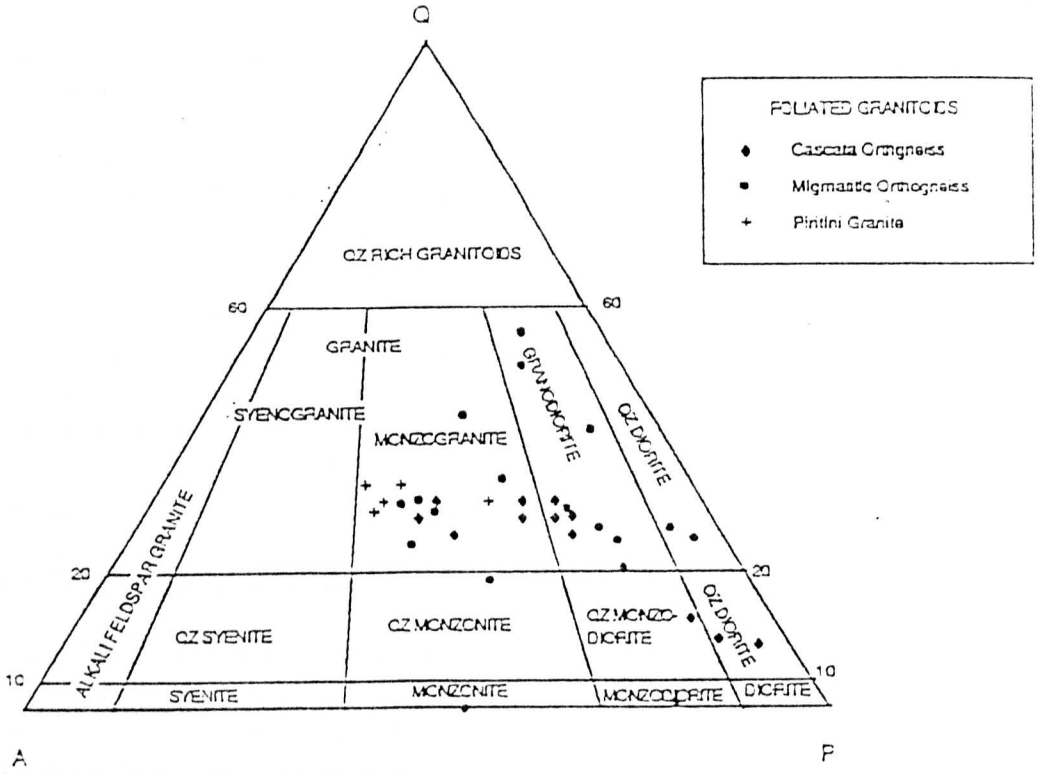

UNFOLIATED GRANITOIDS

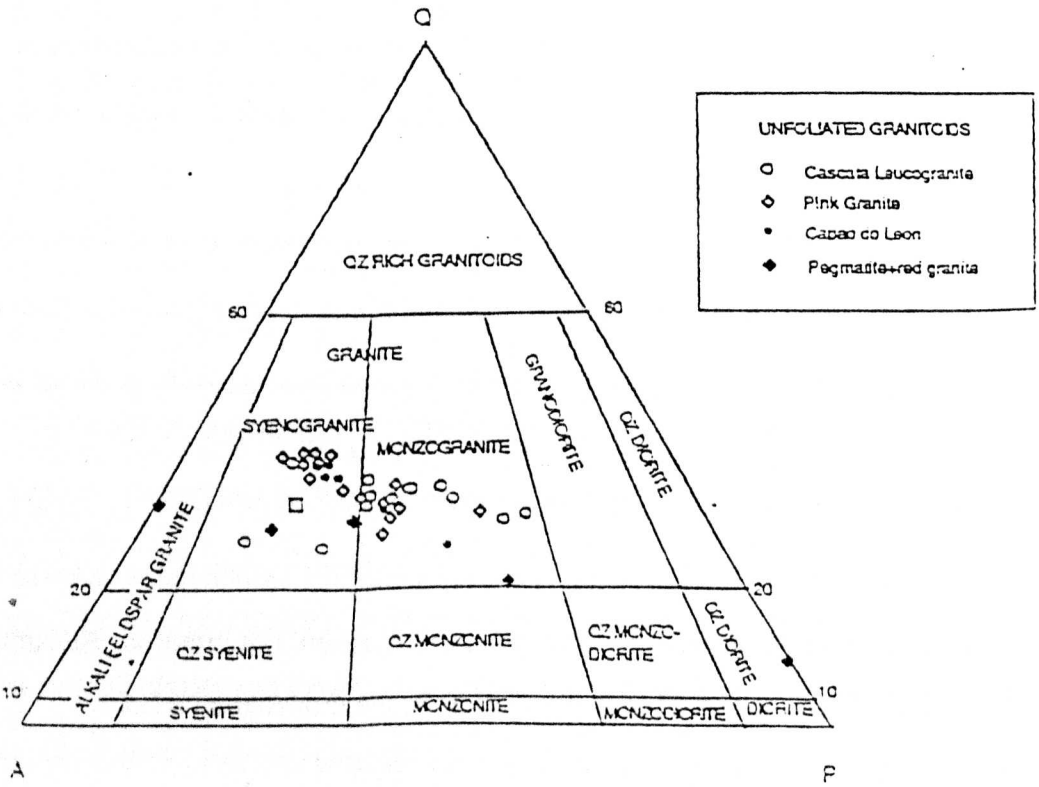

Figure 6.2 Streckeisen plot of Granitoids from the Pelotas Batholith.

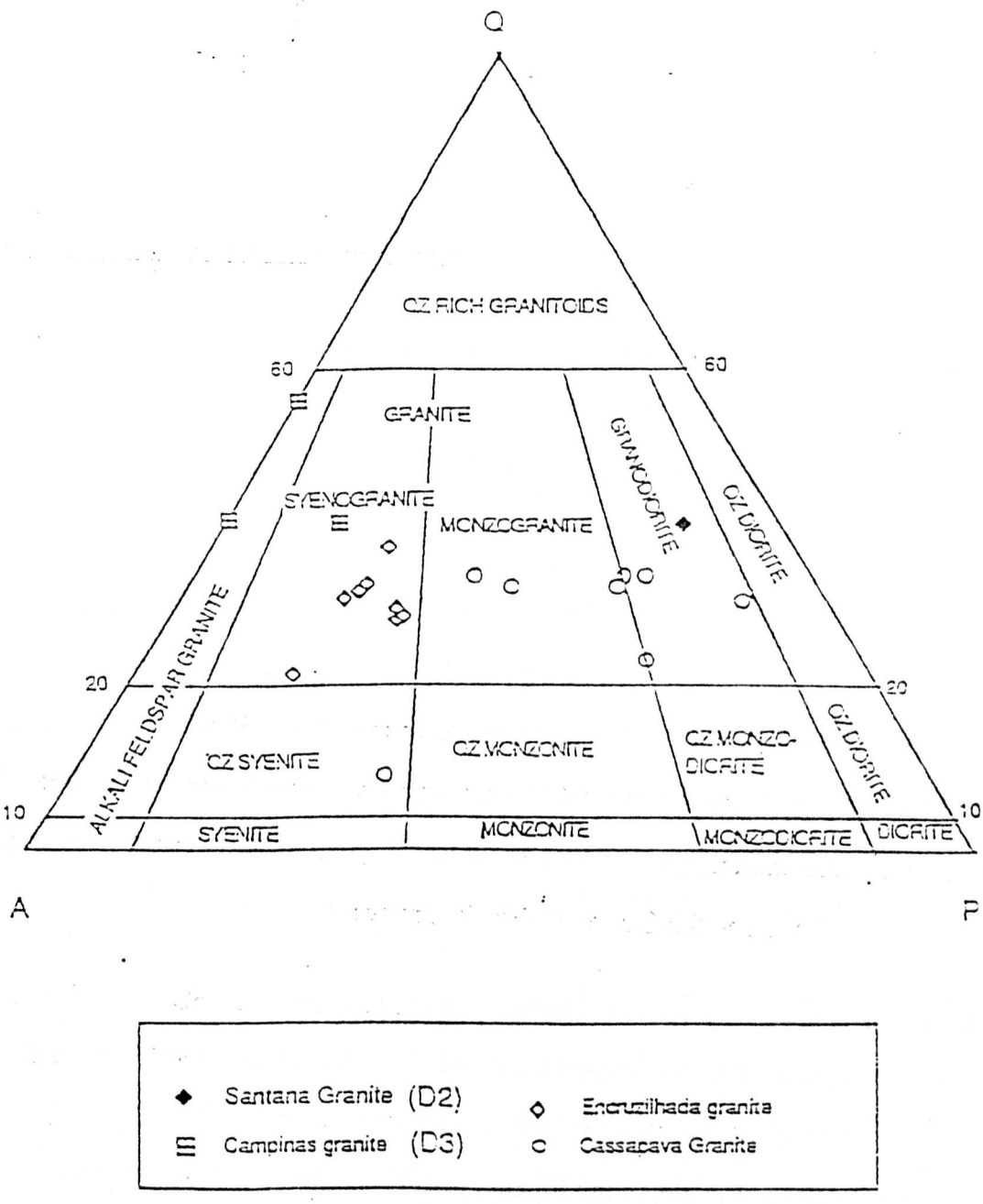

Figure 6.3 Granites intruding the Santana Metamorphic Belt. The Santana Granite is affected by D2 and D3, the Campinas granite is sheared by D3 and the Encruzilhada and Caçapava granites are post tectonic.

The unfoliated granitoids fall in the monzogranite to syenogranite fields. The unfoliated Capao do Leao Granite and Canguçu Granite (Chapter 5) are included in the unfoliated granites for the purpose of general geochemical discussion. The Pink Granite separates into two groups with the SE pink granites lying in the Syenogranite field and the NW pink granites in the Monzogranite field. The trend of these granites again suggests strong plagioclase control. The Capao do Leao Granite is a syenogranite and seems to be very similar to the Pink Granite although the enclave lies in the monzogranite field. The Canguçu Red Granite and Pegmatites appear to be related and are relatively quartz poor. The two leucocratic dykes appear to be related to this trend rather than to that of the leucogranites. The Canguçu Red Granite defines a much flatter trend which suggests it may have formed by a different process. This is borne out by its extremely high $^{87}Sr/^{86}Sr_i$ ratio of 0.8 (chapter 7).

The granites intruding the Santana Metamorphic Belt are plotted on the Streckeisen diagram of figure 6.3. The Santana Granite plots as a granodiorite and in this sense shows a geochemical similarity to the Foliated Granites of the Pelotas Batholith. This comparison will be taken further in section 6.2. The Caçapava Granite exhibits a range between granodiorite and monzogranite with the enclave lying in the quartz syenite field. The Encruzilhada Granite and the Campinas Granite are syenogranites.

Shand (1927) used the degree of alumina saturation molecular ($Al_2O_3/CaO+Na_2O+K_2O$) to classify the major oxides as peraluminous ($Al_2O_3 > Na_2O+K_2O+CaO$), metaluminous ($Na_2O+K_2O < Al_2O_3 < Na_2O+K_2O+CaO$) or peralkaline ($Al_2O_3 < Na_2O+K_2O+CaO$). This is illustrated in figure 6.4 where the foliated granitoids form a trend from strongly calcic and metaluminous to peraluminous. The unfoliated granitoids are more alkalic and straddle the metaluminous-peraluminous boundary with the Campinas Granite being the most peraluminous granite in the area.

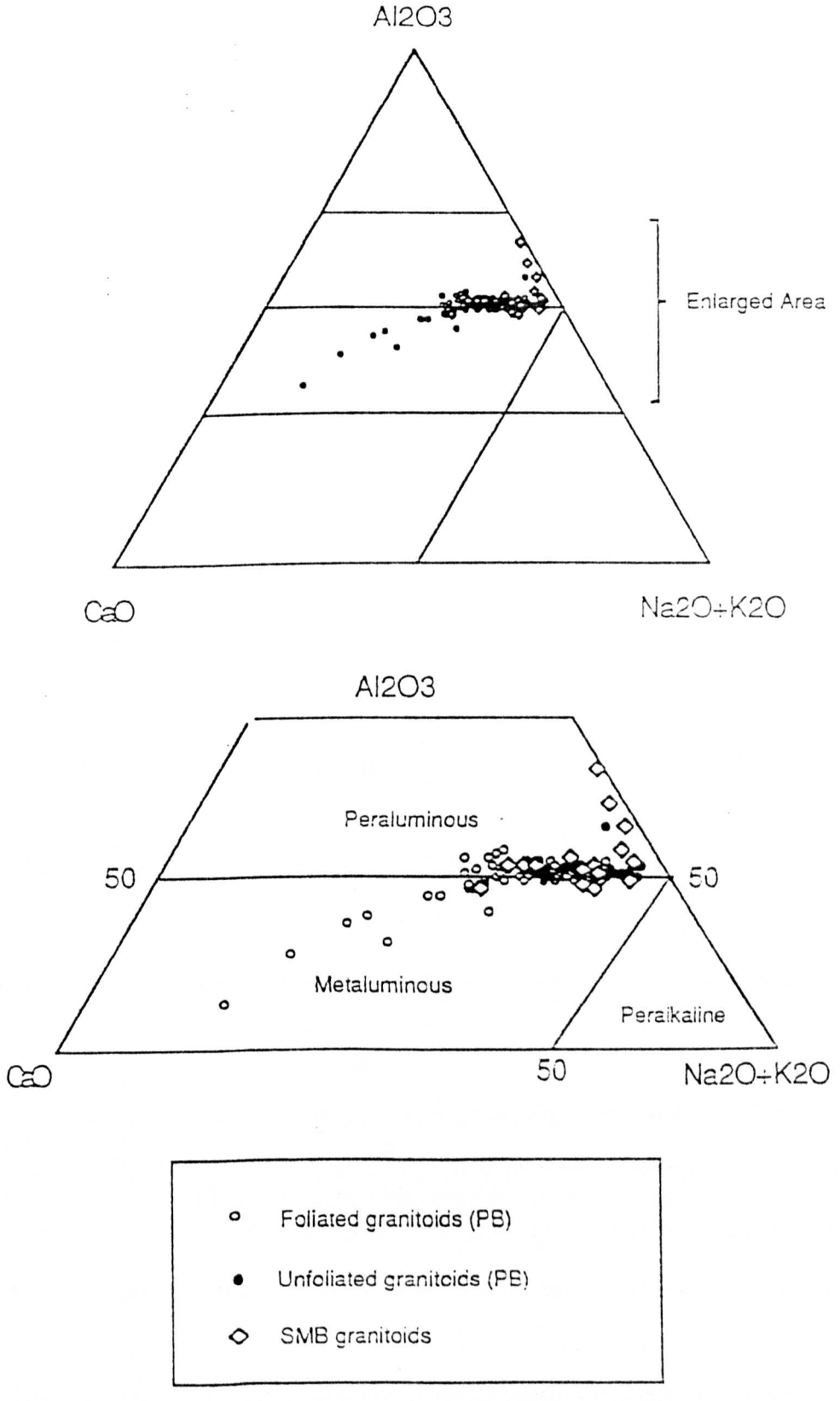

Figure 6.4 The Shand plot of all analysed granitoids

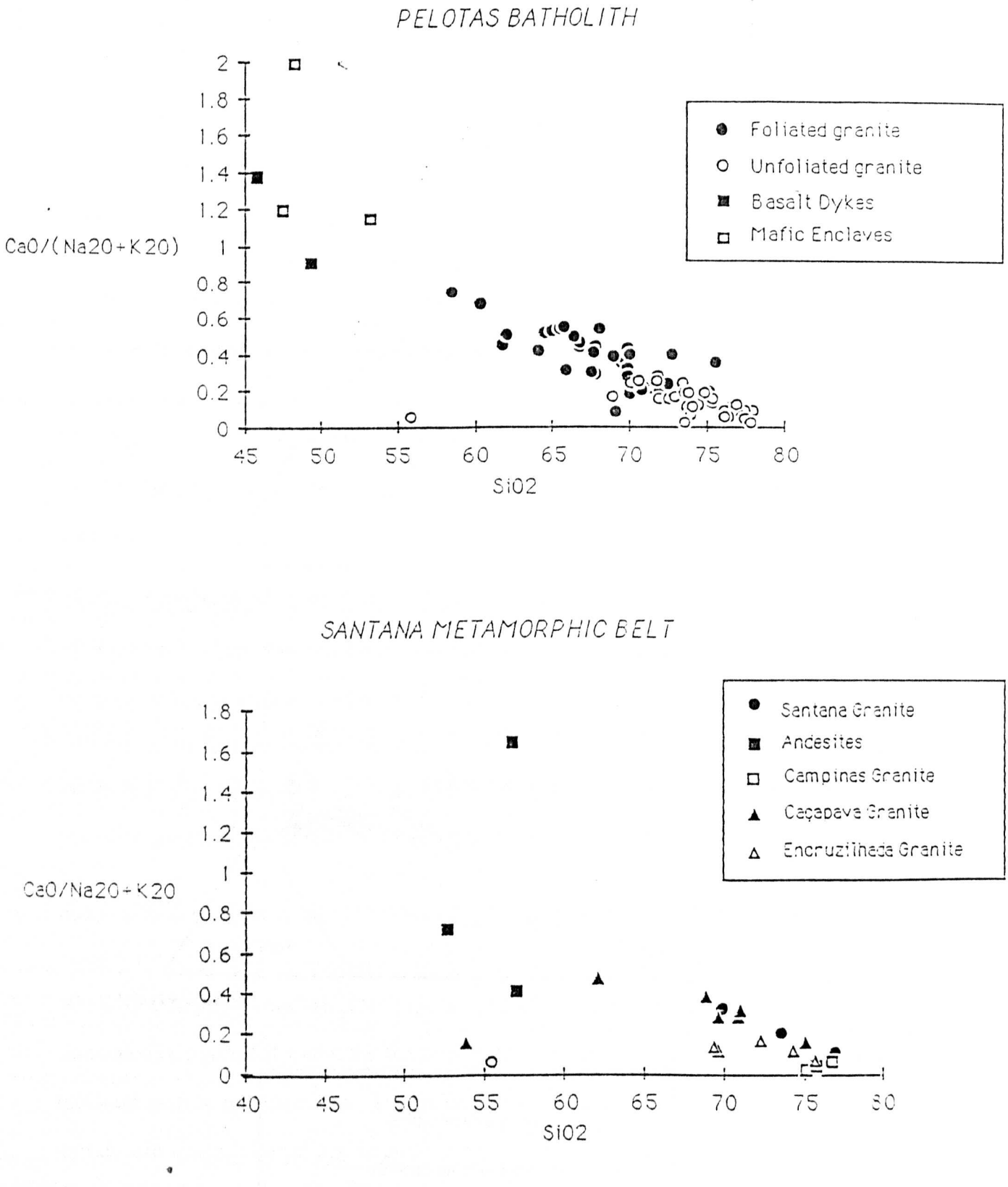

Figure 6.5 Foliated and unfoliated granites from the Pelotas Batholith show a trend becoming less calkalkaline with increasing silica. The granites intruding the Santana Metamorphic Belt lie on a similar trend with the Santana Granite and the Campinas Granite (crustal melts) having the highest silica and alkali contents. The basalts appear to be similar to the mafic enclaves (PB) and andesites do not lie on the trend.

One of the main criteria from the Chappell and White (1974) classification to identify S-type granites is a A/CNK ratio of greater than 1.1, which is taken as evidence for a totally sedimentary source and again only the Campinas Granite would qualify for this. Peacock (1931) used the ratio of calcium to alkaline oxides to determine the calc-alkaline series where the boundary between calcic and calc-alkaline was at 65% CaO on the Shand plot, and on this basis almost all the granitoids from this area are calc-alkaline. Figure 6.5 shows that the unfoliated granites become more alkalic and less calcic with increasing silica.

6.2 Geochemistry of the Pelotas Batholith

6.2.1. Introduction

This section will describe the geochemistry of the granitoids forming the Pelotas Batholith (chapter 5). Geochemical analyses of samples from this area are given in Appendix C. The majority of samples were collected from quarries where several granite types are exposed together (chapter 5). The mapping of lithological units is based on mineralogical and textural differences recognized in the field, and these features are clearly a function of chemical composition. Chappell and White (1983) defined a mappable intrusion as one with a distinctive chemical composition sometimes homogeneous and sometimes displaying a systematic variation throughout the intrusion.

An igneous suite (Bayly 1968) is a group of rocks whose field relations and compositional characteristics make it apppear to have a common source. In a batholith, suites are mostly in linear belts parallel to the trend of a batholith. Chappell (1984) defined a suite as a group of rocks with strong petrographic, chemical and isotopic similarities, even though they were not necessarily from the same pluton. For the purpose of this study a suite will be assumed to be a group of spatially related granitoids intruding one another.

For example, at Cascata quarry 3 (chapter 5), leucogranites and pegmatites intrude the Cascata Orthogneiss which contains mafic enclaves. These four rock types are considered to be a suite. A second suite can be identified between locality 7 and Canguçu, and this includes the Migmatitic Orthogneiss, the Canguçu Porphyritic Granite and the Pink Granite. For the purpose of this study a third suite is proposed for rocks NW of the Canguçu shear zone including the Piritini Granite, Migmatitic Orthogneiss and Pink Granite although these may prove to be quite similar geochemically to the second suite.

Walls and Clemens (1987) question whether suites are a good unit to work with when investigating granitoid formation, since there is no need for the rocks grouped as a suite to be comagmatic, and the only feature that granitoids in a suite need to have in common is that they are emplaced in close proximity. They suggest that suites should not be used to discuss differentiation processes, since they may contain rocks which crystallized from several separate magmas, and that it is important to study chemical variations within individual plutons or to group comagmatic lineages.

An alternative way therefore, to approach the geochemistry of this batholith is in a chronological sequence based on field relations with two major groups recognized; foliated granitoids and unfoliated granitoids. For the purpose of classification this chronological subdivision will be used but the "suite" grouping will also be considered when discussing interrelationships between the granitoids and their sources. The major and trace element geochemistry of the Pelotas Batholith will be discussed first for the foliated, and then for the unfoliated granites. The tectonic setting of the granites will be explored in section 6.4.

6.2.3 Major element variation

6.2.3.1 FOLIATED GRANITOIDS

Harker major element variation diagrams have been plotted for the foliated granitoids of the Pelotas Batholith, specifically the Cascata Orthogneiss, Migmatitic Orthogneiss, Piritini Granite and the Canguçu Phenocrystic Granite (figure 6.6). Also included on these plots are the more mafic xenoliths from these granitoids to investigate their relationship to their host, the Santana Granite and two samples of Encantada Gneiss to allow a comparison between the foliated granitoids of the Pelotas Batholith and those of the Santana Metamorphic Belt.

SiO_2 variation in the foliated granitoids is between 55% and 78% with mafic enclaves lying between 45-47%. Linear trends which are consistent with primary igneous processes are observed for the major elements (except K_2O) of most foliated granitoids. The negative correlation for TiO_2, MgO, MnO and MgO suggests that there has been fractionation of the more mafic and titaniferous phases with increasing silica, and/or such phases were residual in the source regions. The positive correlation of K_2O with SiO_2 suggests plagioclase control rather than alkali feldspar and this is supported by the correlation between CaO and SiO_2. The Migmatitic Orthogneiss provides poor correlations for the alkali elements which may be the result of the inhomogeneous nature of the rock, and a large variation in the leucosome content in the samples. Three of the migmatitic rocks are depleted in Al and K and enriched in Ti, Fe and Mg suggesting that alkali feldspar has been fractionated.

The Piritini Granite also lies on the trend of the other intrusions and is notably enriched in K which is a distinguishing feature. The Encantada Gneisses appear to lie on the same trend as the Pelotas Batholith Granitoids which suggests that the two may be related. The Santana Granite is the most evolved sample of foliated granite analysed and is relatively depleted in all the major elements relative to foliated granites of the Pelotas Batholith except for an anomalously high Na reflected by its plagioclase rich composition.

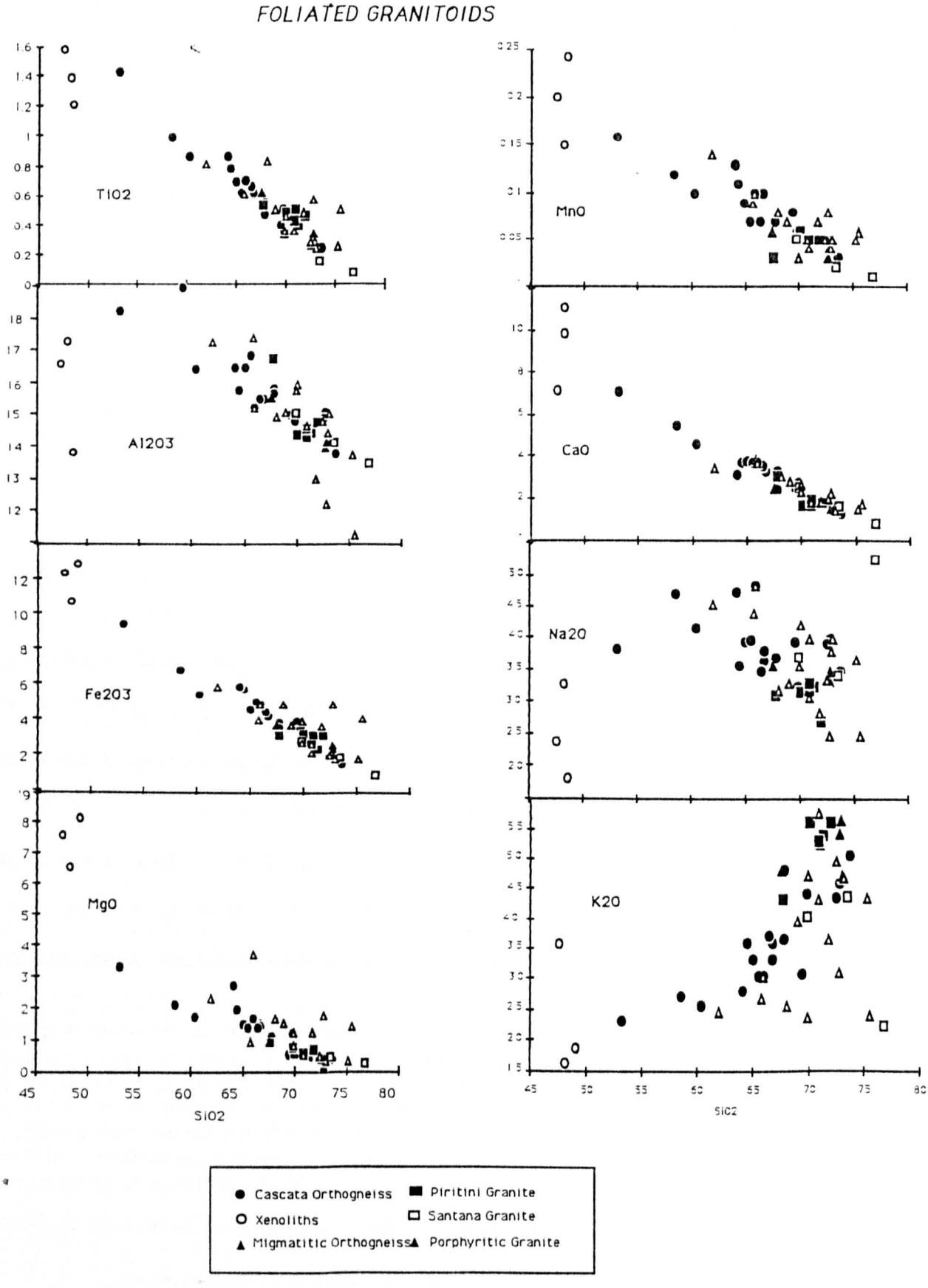

Figure 6.6 Major elements plotted against silica for the foliated granitoids of the Pelotas Batholith with the Santana Granite and xenoliths plotted for comparison.

The xenoliths from the orthogneisses fall on the extrapolation of the major element trends, except for Al, Na and K (which is probably related to feldspar crystallization), and this correlation suggests that the enclaves may represent an earlier, less evolved fraction of the granite, and be related to the orthogneisses by fractionation.

6.2.3.2 UNFOLIATED GRANITOIDS

SiO_2 variation for the unfoliated granitoids ranges between 70% and 77% with a mafic enclave from the Capao do Leao Granite plotted at 55% SiO_2 for comparison (figure 6.7). There appears to be no particular segregation in the geochemistry of the different granite types, although the Pink Granite from quarry 11 appears to form a cluster on its own for most elements and with the Canguçu Red Granite and the Capao do Leao granite for TiO_2, MgO and P_2O_5.

The Pink Granite SE of Canguçu appear to be geochemically distinct from those found to the NW. The leucogranites and pegmatites are geochemically similar to the NW Pink Granite. The P_2O_5 plot shows the separation into two groups quite well and this may be related to processes dependent on tectonic setting since the three above-mentioned intrusions are the youngest in the batholith.

Major elements form a negative correlation, which can be extrapolated back to the enclave, for TiO_2 and Fe_2O_3 suggesting that the enclave could represent a possible source or residue for these unfoliated granitoids. The TiO_2 trend closely resembles that of the foliated granitoids whereas for Fe_2O_3 the trend is much less steep for the unfoliated granitoids. For Al_2O_3, CaO, MgO and P_2O_5, the unfoliated granitoids define a much steeper negative correlation than for the foliated granitoids.

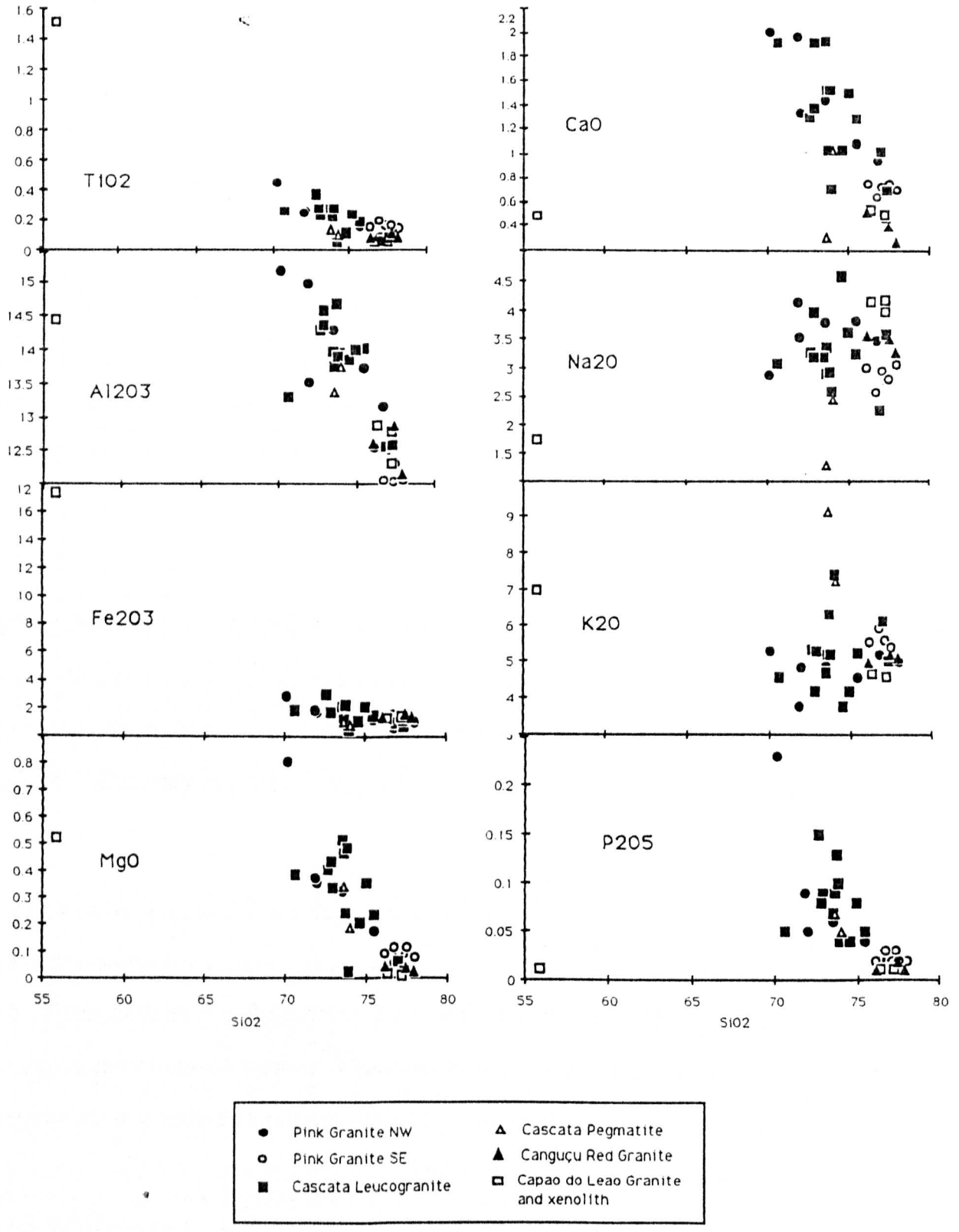

Figure 6.7 Major elements plotted against silica for the unfoliated granitoids of the Pelotas Batholith with a mafic biotite garnet enclave from the Capao do Leao Granite plotted for comparison.

Na_2O shows no particular trend and closely resembles the field shown by the foliated granites. K_2O roughly increases with SiO_2 with two parallel trends, one culminating in the pegmatites, the other culminating in the pink and red granites. The pegmatites are particularly low in Na_2O and CaO and enriched in K_2O relative to the granites suggesting they are plagioclase free. The enclave is depleted in Na_2O, CaO and P_2O_5 suggesting it is poor in plagioclase and enriched in K_2O. This is supported by petrographic studies which show that the enclave is composed of garnet, biotite and alkali feldspar. The enclave is depleted in Al_2O_3, CaO, MgO and P_2O_5 relative to the extrapolated trend and is depleted in MgO and CaO relative to other enclaves from the foliated granites, which suggests that the enclave may in fact be a restite after melting with the above elements concentrated in the granites.

6.2.4 Trace element variation

6.2.4.1 FOLIATED GRANITOIDS

Of the trace elements Zn, Co, V and possibly Rb and Sr form strong negative correlations with SiO2 (figure 6.8). Rb and Sr data suggest that the xenoliths and orthogneiss are not comagmatic. The Migmatitic Orthogneiss follows the general trend defined by the Cascata Orthogneiss but it is generally more depleted in Rb, Sr, Y, Zr and Nb possibly resulting from migmatization processes.

The Piritini Granite and Porphyritic Granite follow the main trends shown by the other foliated granites.The minor phases of zircon, apatite and sphene may cause some of the scatter in many of the trace elements. The Santana Granite from the Santana Metamorphic Belt, is compared to the foliated granitoids and is relatively depleted in all trace elements suggesting it may be a late stage melt of a depleted source. It is also particularly depleted in Zr. The Encantada Gneisses and Santana Granite form a parallel trend to the Cascata Orthogneiss for Sr but at a higher SiO_2 content than the Pelotas Batholith granitoids .

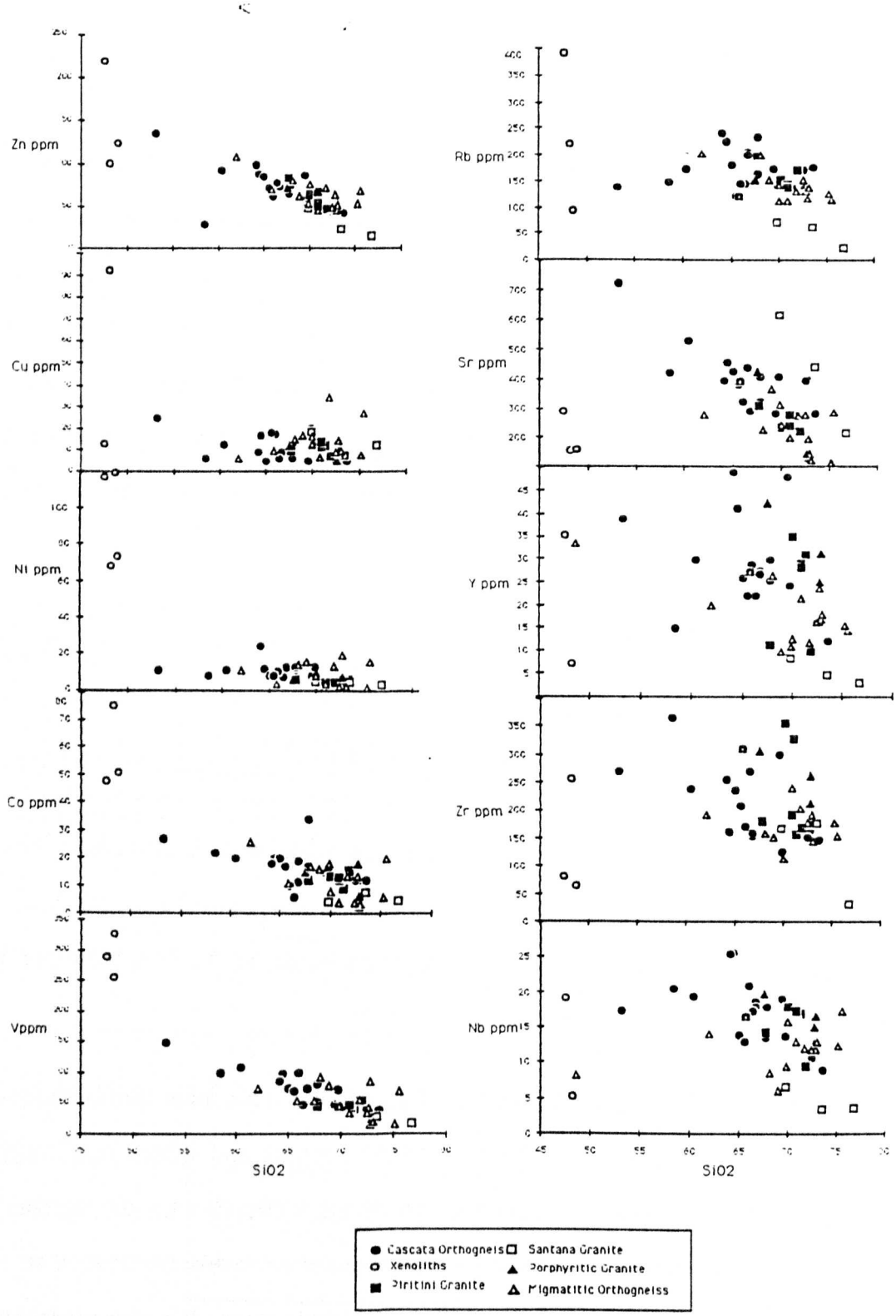

Figure 6.8 Harker diagrams for trace elements for the foliated granites of the Pelotas Batholith

6.2.4.2 UNFOLIATED GRANITOIDS

Of the trace elements, Zn, Ni, Sr and Zr seem to form strong negative trends with increasing silica. Cu and Nb form slightly scattered positive trends. Rb has an inflexion point at about 73% SiO_2 (figure 6.9). The enclave appears not to lie on any of the trends apart from possibly Zn in which it is considerably enriched. The enclave is also enriched in Nb, Rb and U relative to the trend and to the other enclaves from the foliated granitoids . It is depleted in Ni, Y and Zr and extremely depleted in Cu, Ba and Sr.

The pink granites from the NW of Canguçu have a wide range in SiO_2 from 70-75% and are enriched in Cu, Ni, Ba, Sr, Zr and U relative to the Pink Granite from quarry 11 in the SE and depleted only in Rb. They are quite scattered in their composition and this may be because they come from different localities.

The samples from the SE Pink Granite all come from the same quarry and form a cluster with low Zn, Y, Nb, Ba, Rb, Sr and U with slightly enriched Cu, Ni and Zr relative to the general trend. The leucogranites form a trend for Nb, Sr, Zr and U and show a great variation in trace element content for a relatively small range of silica (70-76%). This group includes both dykes and sills of fine-grained leucogranite from a variety of localities which may account for some of the spread. The most silicic sample is a dyke which clusters with the Pink Granite for Nb and U and probably represents a late stage melt.

The Capao do Leao Granite (Figure 6.9) is rich in Cu, especially relative to the enclave which suggests that either the enclave is depleted or that the magma has been enriched by contamination. The granite is also enriched in Y which may be indicative of the garnet present as an accessory phase in this rock having been assimilated from a restite similar to the enclave. It is also enriched in Rb and Zr which might be due to contamination, and the extremely low Sr content suggests that contamination is not by plagioclase-bearing crust.

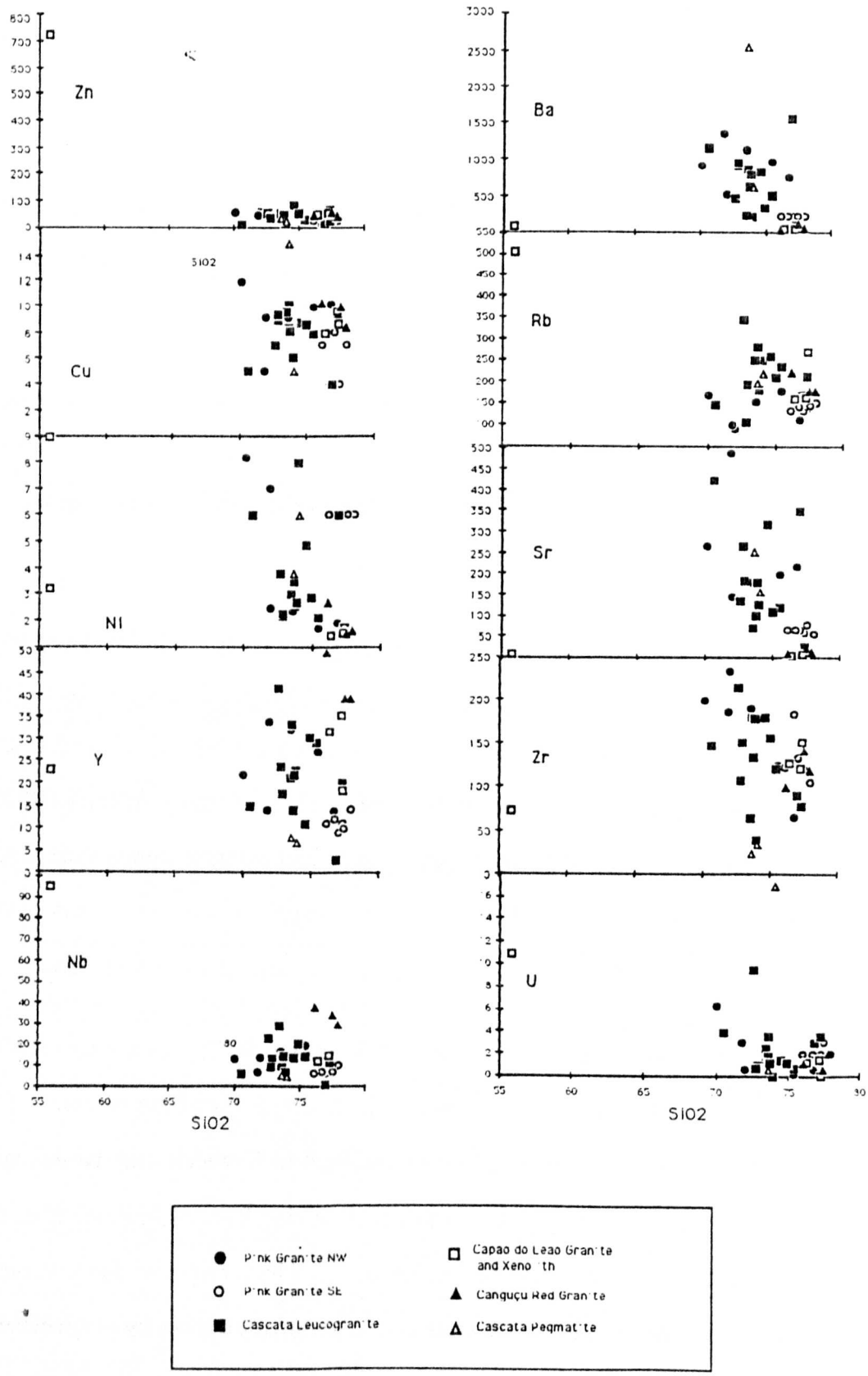

Figure 6.9 Harker diagrams for trace elements for the unfoliated granites of Pelotas Batholith.

The Canguçu Red Granite is depleted in Ni, Sr, Ba and U and enriched in Cu, Nb, Zr and very enriched in Y relative to the other granites on this plot. The pegmatites are depleted in Y, Nb, and Zr and enriched in Ba, U, Sr and Cu.

6.2.5. Rare Earth Element variation

The rare earth element plot of figure 6.10 illustrates the similarity in the REE patterns between all the foliated rocks of the Pelotas Batholith, although the orthogneisses have a slight negative Eu anomaly which is not observed in the Piritini Granite. Relative to Chondrite, these rocks are more enriched in LREE elements than HREE which is common in many granites.

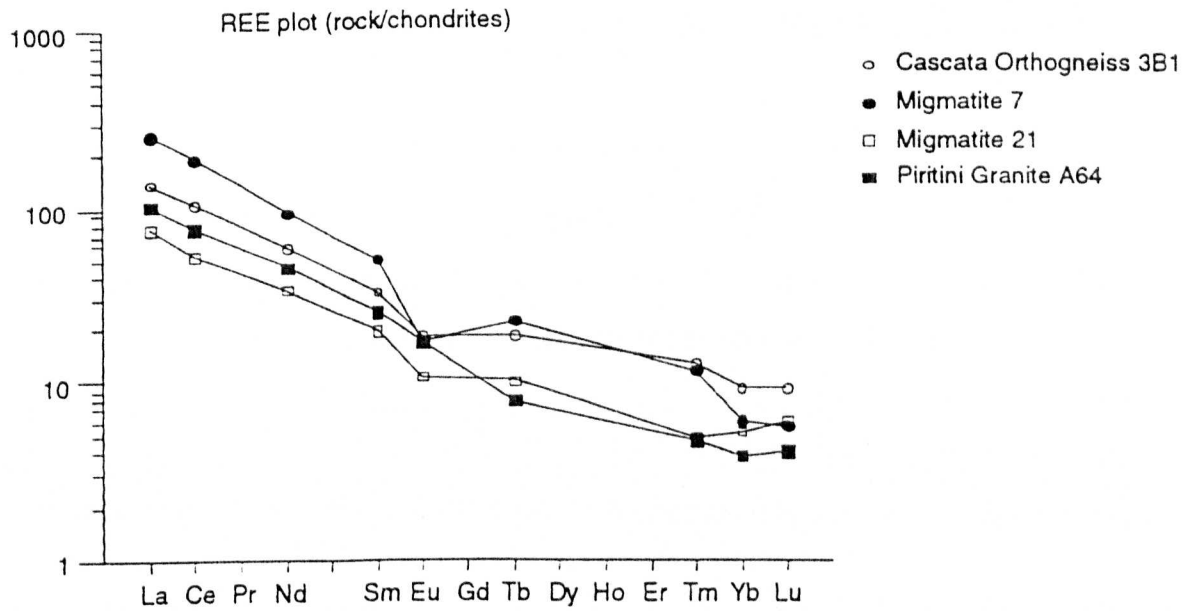

Figure 6.10 Rare Earth Element plot for foliated granites

Unfoliated granites (figure 6.11) show a variety of different patterns, with the Pink Granite having a pattern similar to that of the foliated granites, albeit with a slight Eu anomaly. The Cascata Leucogranite has a slight Eu anomaly, and very low Yb and Lu, and its pattern is subparallel to that of the Pink Granite. The Capao do Leao Granite and Canguçu Red Granite have a pronounced Eu anomaly and an overall flat pattern with the Canguçu Red Granite slightly more enriched in REE.

A negative europium anomaly comes either from feldspar control during partial melting or fractional crystallization, or from fluid interaction. This flat pattern may be associated with the tectonic environment of these granites which intrude at fault zones and may be syn-collision crustal melts with relative LREE depletion and HREE enrichment.

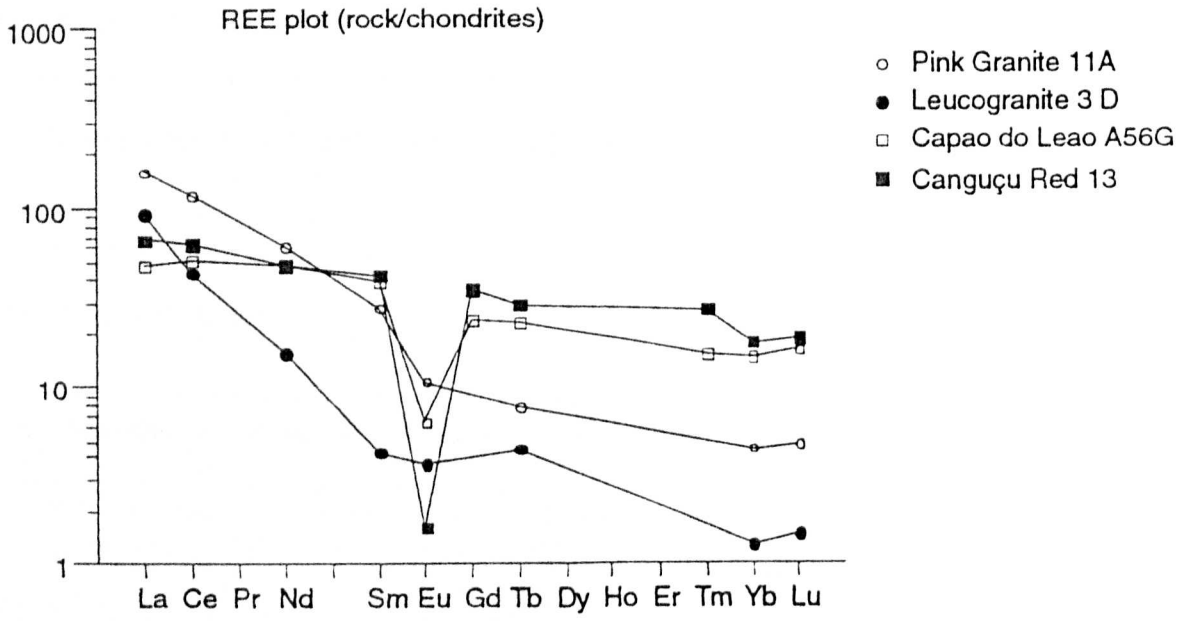

Figure 6.11 Rare Earth Element pattern for unfoliated granites illustrating two distinct patterns, perhaps indicative of relating to different tectonic environment and/or sources.

6.2.6 Spidergrams for the Pelotas Batholith

The relationships between the foliated granitoids of the Pelotas Batholith is better illustrated using a spider diagram (fig 6.12) which illustrates the trace element compositions normalized against primitive mantle. All samples of foliated granite are from the Pelotas Batholith (except for the Santana Granite) and they show similar trace element patterns. The similarity in patterns suggests that they either are cogenetic, or that at least they formed by similar processes.

Isotope studies (chapter 7) disprove the first proposition since the initial Sr ratios are 0.708 for the Cascata Orthogneiss and 0.710 for the Migmatitic Orthogneiss which suggests they come from different sources. The Piritini Granite is markedly depleted in K relative to the other foliated granitoids, and this suggests it may have undergone weathering which is supported by field evidence. The Santana Granite has a distinctively different pattern with a low Rb/Sr ratio and is generally more depleted in HFS elements.

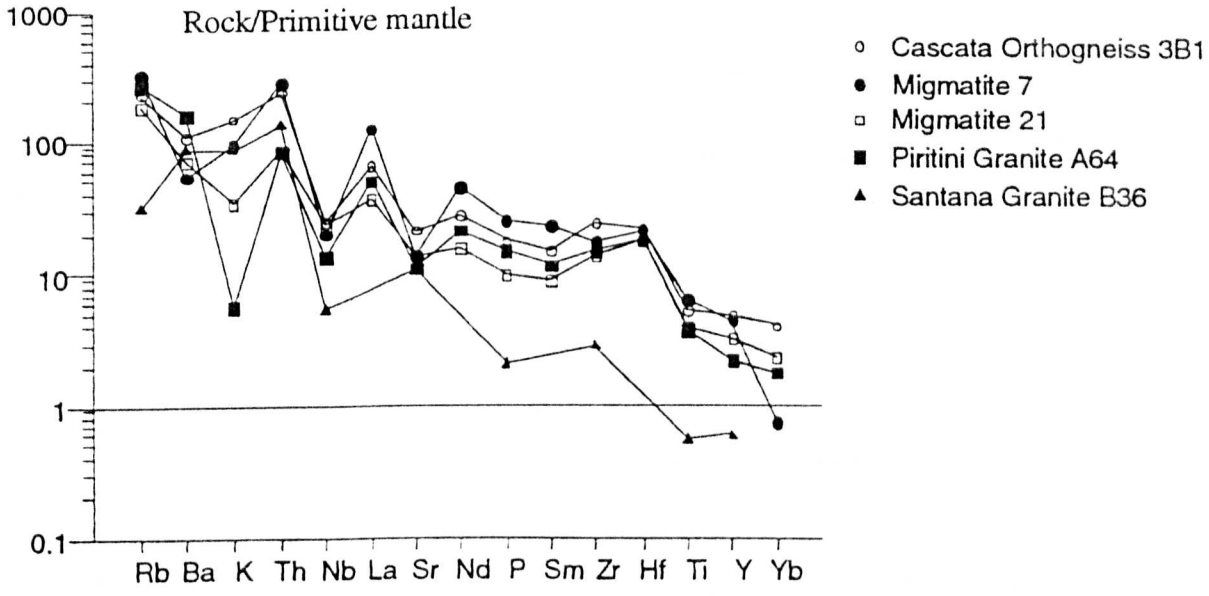

Figure 6.12 Spider plot for foliated granitoids of the Pelotas Batholith with the Santana Granite plotted for comparison.

The unfoliated granites are illustrated in figure 6.13. The leucogranite is depleted in Sr, Nb and Sm and enriched in Y and Zr. The two Pink Granites both show similar patterns with the sample from the SE showing more fractionation with depleted Ba, Nb, Sr, P and Ti and peaks for La, Sm and Y. The Pink Granite from the NW is depleted in Yb relative to that of the SE. The unfoliated granites are most likely upper crustal melts from their trace element patterns (Figure 6.15). Spider plots for the Capao do Leao Granite and the Canguçu Red Granite are similar suggesting a similar process of formation and/or similar source. They differ however in their Sm/Nd ratio which is higher for the Canguçu Red Granite which also

is much more enriched in Ba, Nb and Sm (figure 6.13) Comparison with granites from the Lachlan belt suggest these granites to be A-type granites (Collins et al 1980).

In summary the Quarry 11 Pink Granite and the Migmatitic Orthogneiss may be cogenetic (figure 6.13). The Capao do Leao Granite and the mafic enclave appear cogenetic although the enclave is enriched in Sm. The Piritini Granite and the Cascata Orthogneiss are basically cogenetic although the K depletion is possibly the result of the weathered nature of the Piritini Granite. The Cascata Leucogranite may be related to the Cascata Orthogneiss but the Canguçu Red Granite appears to be unrelated to the Santana Granite inspite of the similarity in appearance and their mineralogy. The Canguçu Red Granite could be a more fractionated version of the Quarry 11 Pink Granite although it has enriched Th, Nb, Y and Yb.

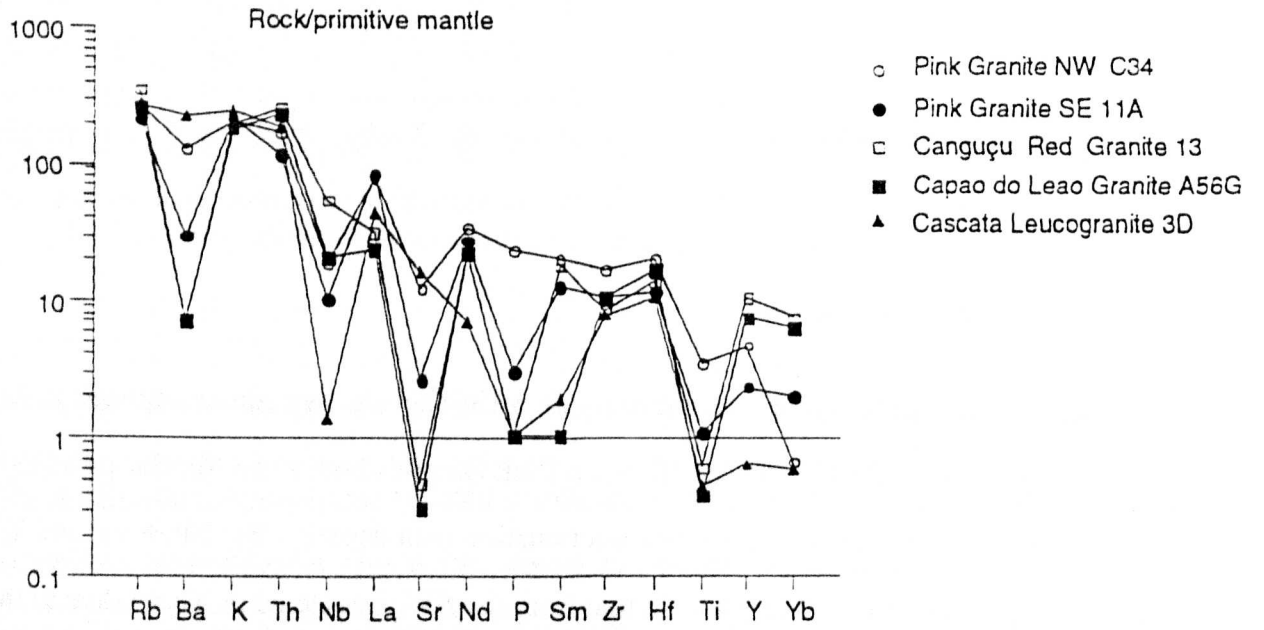

Figure 6.13 Spider Plot of unfoliated granitoids of the Pelotas Batholith

Granites from the Pelotas Batholith are compared with an upper crustal melt from the Andes, a lower crustal melt from the Idaho Batholith, and a volcanic arc granite from Chile in figure 6.14 and 6.15. The Cascata Orthogneiss, a typical foliated granite, shows a greater similarity to the upper crustal melt with a low Ba/Rb and Sr/Nd ratios. It also however shows some similarity to the volcanic arc granite with high Th and Y. In constrast, lower crustal melts have high Ba/Rb and Sr/Nd.

The Cascata Orthogneiss, however, has high Th, Zr and Ti relative to the upper crustal melt which may indicate the presence of zircon and sphene in this rock. The unfoliated Pink Granite shows a similar pattern to the Chilean volcanic arc magma with very low Ba, Sr and Ti but its field relations illustrate that it is a post-tectonic intrusion. It is strongly depleted in Ba, Nb, Sr and P relative to the upper crustal ignimbrite and enriched in K, La and Nd. Isotope studies (chapter 7) may establish more precisely the nature of the sources.

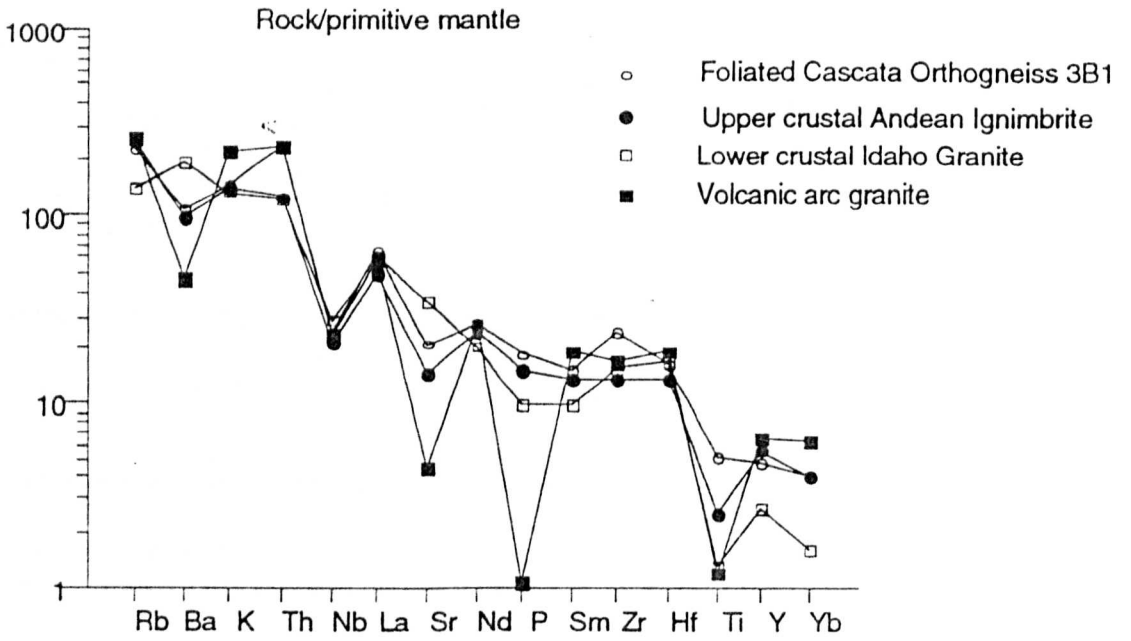

Figure 6.14 Comparative plots of foliated Pelotas Batholith granitoids with typical crustal melts and a volcanic arc granite

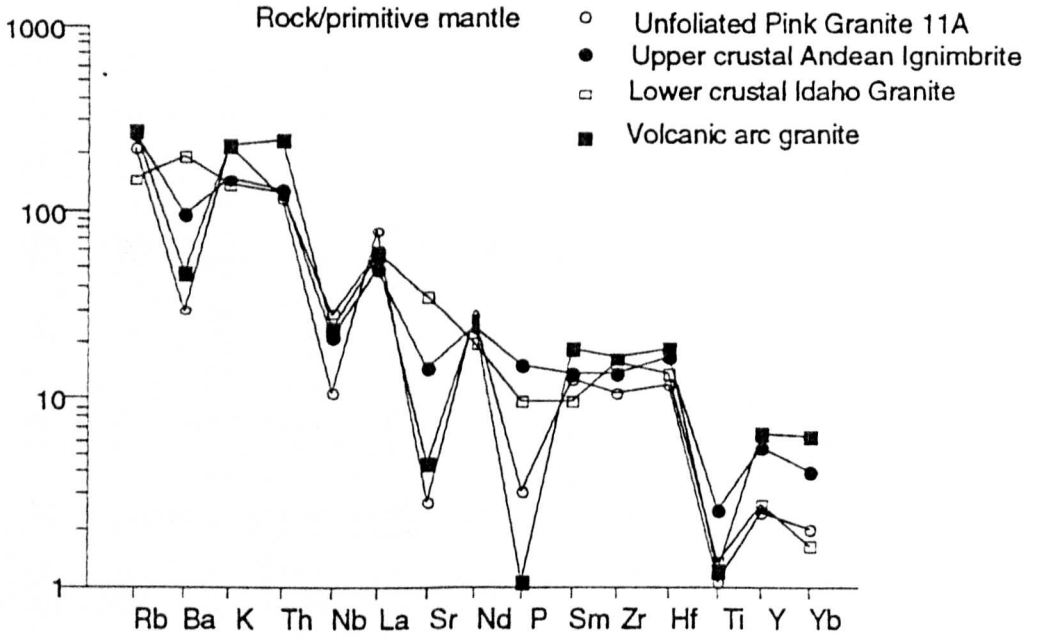

Figure 6.15 Comparative plots of unfoliated Pelotas Batholith granitoids with typical crustal melts and a volcanic arc granite

Pearce et al (1984) proposed a classification of granites based on their tectonic setting and the compositions of the Pelotas Batholith granitoids are illustrated on the Rb vs Y+Nb discrminant plot of figure 6.16. This illustrates that all the foliated granites lie within the volcanic arc field, the majority of unfoliated granites from the Pelotas Batholith also lie in this field although a few samples of leucogranite straddle the syn-collision field. This suggests, along with field evidence, that the foliated granites were formed in a volcanic arc environment and then foliated as a result of a collision event during, or soon after which the leucogranites were intruded.

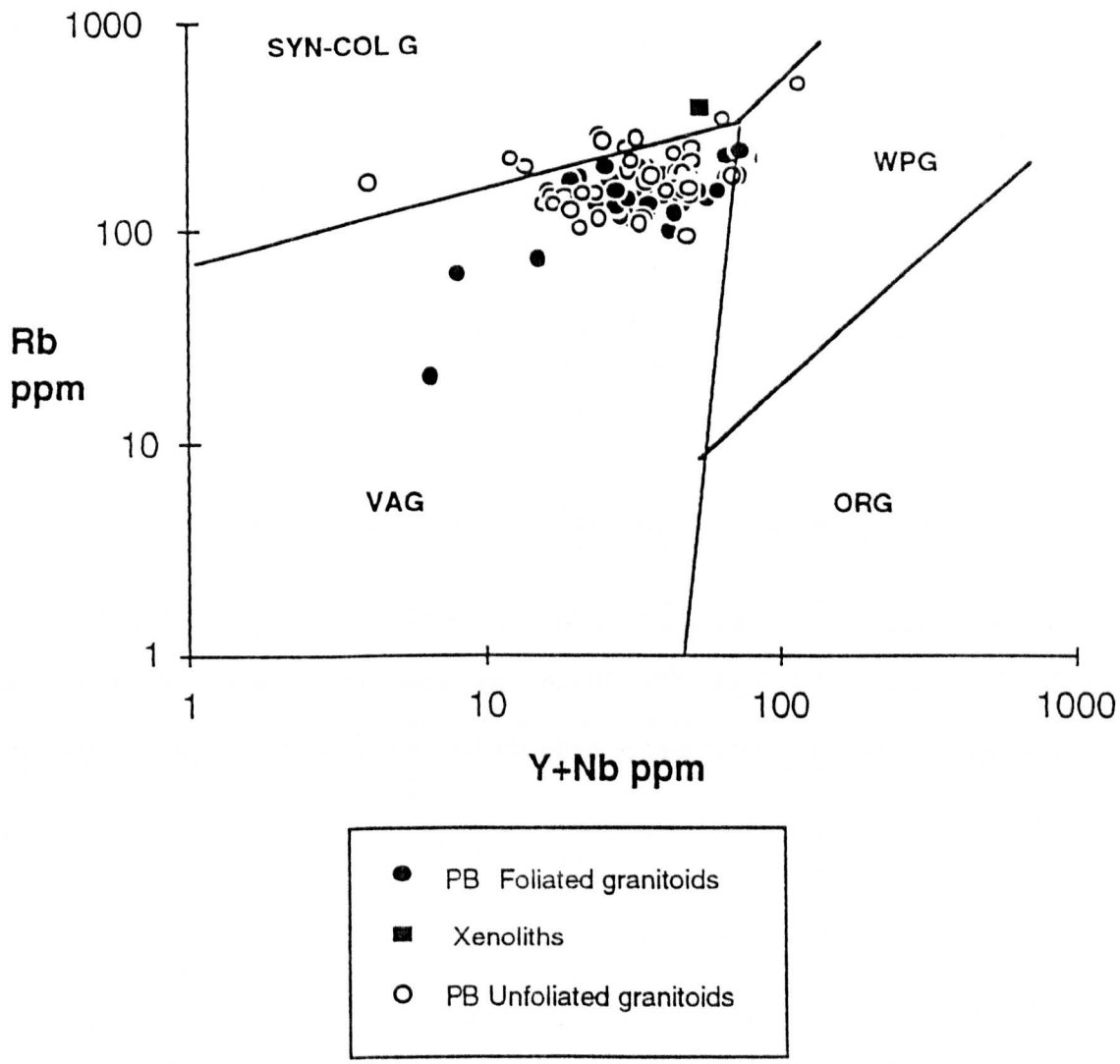

Figure 6.16 Tectonic discrimination diagram for granitoids of the Pelotas Batholith

The foliated Pelotas Batholith granodiorites seem to show features similar to a volcanic arc granite with some indication of the involvement of upper crust. The Capao do Leao Granite and Canguçu Granite are unfoliated and they appear to be A-type granites. The unfoliated Pink Granites and Cascata Leucogranite are post-tectonic granites. The nature of the sources will be further explored in the Chapter 7. A reasonable shift in geochemistry with time from older foliated volcanic-arc granodiorites through to younger unfoliated post-collision granites (Figure 6.2) is observed in the Pelotas Batholith This is discussed further in section 6.4.

6.3 Geochemistry of the Santana Metamorphic Belt

For the purpose of geochemical study the rocks of the Santana Metamorphic Belt will be divided into two groups; firstly the non granitic rocks are discussed in section 6.3.1 where they are also compared with the Encantada Gneisses and pelitic schists, and secondly the granites intruding this belt are discussed in section 6.3.

6.3.1 Geochemistry of the non-granitic rocks compared to the basement.

The igneous intrusions discussed are the metagabbro which is folded by D3 and unfoliated andesites from the red bed basin. The Encantada Gneisses and pelitic schists were also studied along with andesites from the red bed basins (Chapter 5) for comparative purposes.

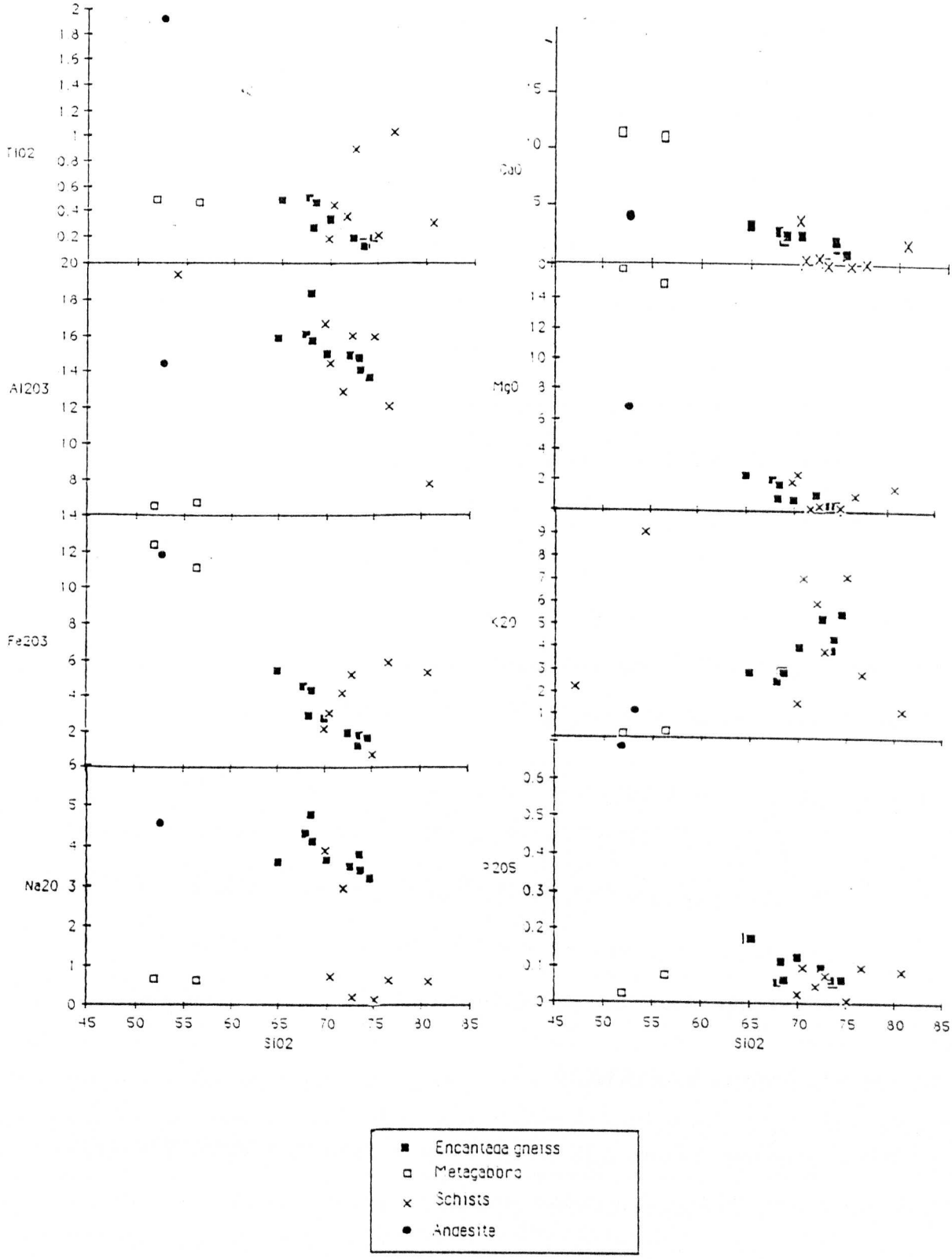

Figure 6.17 Major element variation for the Santana MetamorphicBelt namely the Encantada Gneisses, igneous intrusions and schists.

6.3.1.1 MAJOR ELEMENT VARIATION

The Harker variation diagrams of figure 6.17 illustrate the relationship of various major elements to silica for the Encantada Gneisses, two metagabbros, various schists and an andesite from the extensional red bed basin. The metagabbros have 51% and 56% SiO_2, the andesite 52%. The analyses are given in appendix C. The Encantada Gneisses range between 65% and 75% SiO_2 and define a negative trend for TiO_2, CaO, Al_2O_3, MgO, Fe_2O_3, Na_2O and P_2O_5, and a positive correlation for K_2O versus SiO_2.
The gneisses have an increasing proportion of quartzofeldspathic material with increasing silica content, consistent with some segregation of granitic material within the gneisses. The metagabbros are not on the same trend as the gneisses with respect to TiO_2, Al_2O_3 and P_2O_5 but they are with respect to K_2O, Fe_2O_3 and CaO suggesting they could be cumulates. The schists are different from the gneisses and this is well illustrated by the Fe plot.

The andesite is unlikely to be related to the gneisses, but it is enriched TiO_2 and P_2O_5 relative to this trend and depleted in CaO, Al_2O_3 and Na_2O and appears to lie on the trend for MgO and Fe_2O_3. With respect to TiO_2, Al_2O_3, Na_2O and P_2O_5 the gabbros are depleted relative to the extrapolated trend of the gneisses and they are enriched in CaO and MgO. The overall picture tends to suggest that the gabbros are unrelated to the gneisses and granite.

6.3.1.2 TRACE ELEMENT VARIATION

From the Harker diagrams of figure 6.18, it can be observed that the trace elements do not show such clearly defined trends as the major elements.

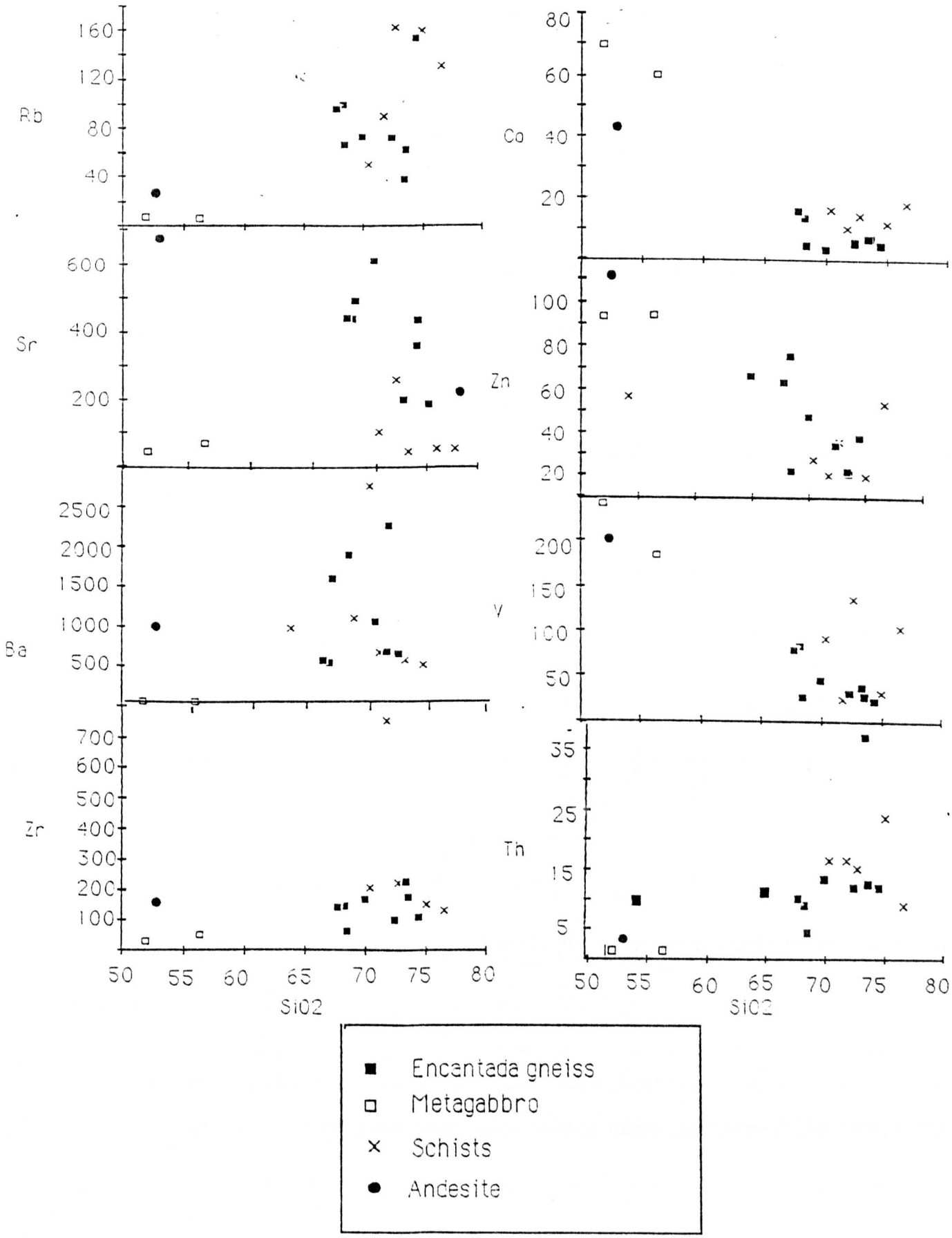

Figure 6.18 Trace element variation in the Santana Metamorphic Belt.

The elements Zn, Co and V seem to show a relationship with silica for the metagabbros, gneisses and granite. The metagabbros are enriched in Co, Zn and V (and also Cu,Ni and Cr not illustrated) relative to the schists, gneisses they are depleted in Ba, Rb, Sr and Zr.

6.3.1.3 RARE EARTH ELEMENT DATA

Rare earth element data been obtained for the Encantada Gneisses in the Santana Metamorphic Belt. These are compared with schists from this Belt and the red beds from the basin between this belt and the Pelotas Batholith. Figure 6.19 illustrates that there is a similarity in the pattern of rare earth elements for gneisses, metasediments and undeformed red beds all samples showing a slight negative Eu anomaly. The red beds, have lower rare earth elements abundances than the Proterozoic gneisses. The gneiss 45A is depleted in Yb and Lu relative to the other samples.

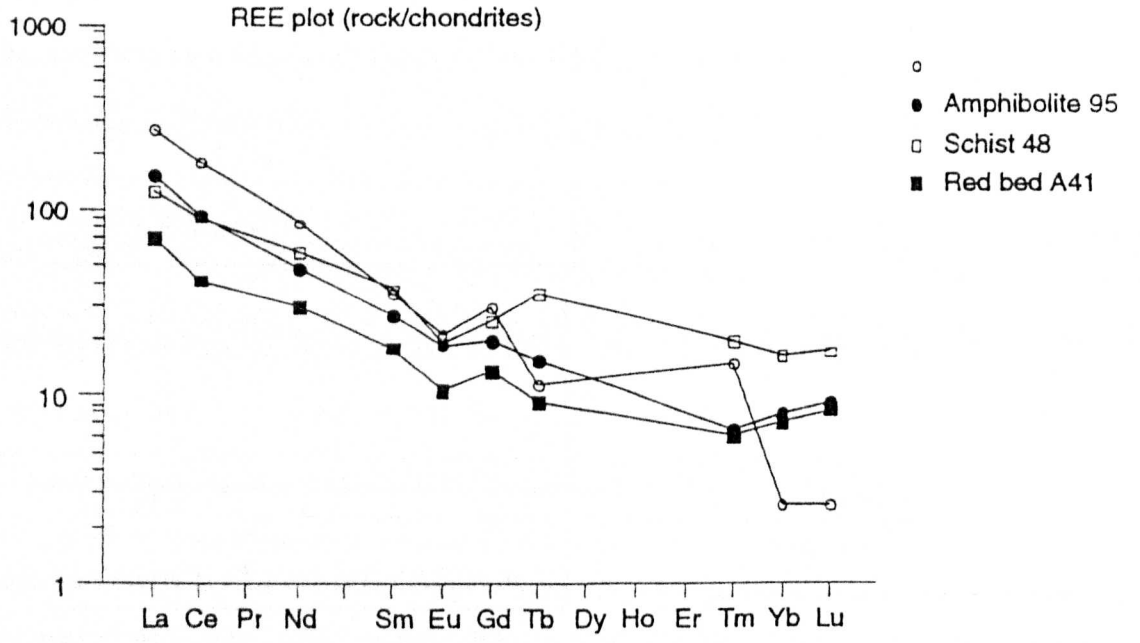

Figure 6.19 REE plot for Encantada Gneisses and schists compared to red beds from the Triassic basin between the Pelotas Batholith and Santana Metamorphic Belt.

6.3.1.4 SPIDERGRAMS

Figure 6.20 compares the metagabbro to primitive mantle and MORB and it can be seen that it is depleted in HFS elements relative to MORB, and enriched in LIL elements. It is generally trace element enriched relative to mantle and appears to be unrelated to the andesite from the basin. It shows a similar but more depleted pattern to the basaltic dykes intruding the Pelotas Batholith suggesting that the source may be similar for these two basic rocks.

The gabbro appears to be unrelated to the gneisses or granites. Schists from the cover unit do not lie on the gneiss trend and are geochemically unrelated to them.

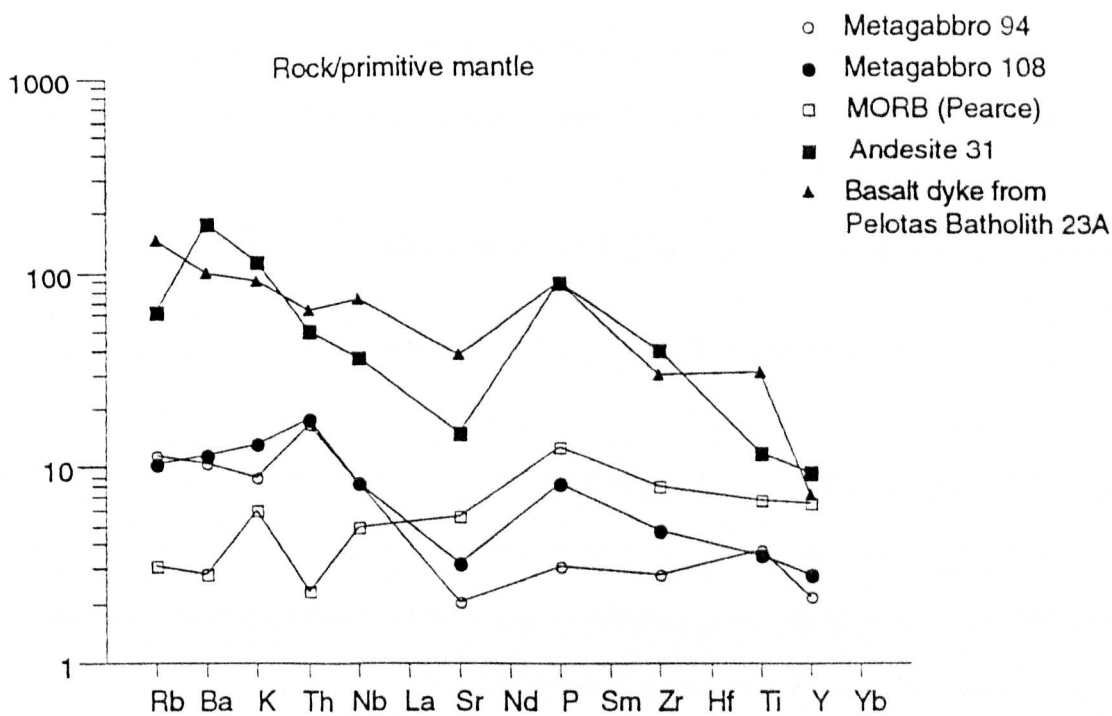

Figure 6.20 Metagabbro compared with MORB,andesites and basaltic dykes.

6.3.2 Granitoids of the Santana Metamorphic Belt.

Four main granitoid bodies intrude the Santana Metamorphic Belt and they will be discussed in chronological order. The Santana Granite is folded by D2 and D3 and intrudes the Encantada Gneisses. The Campinas Granite is foliated by the D3 shear zone separating the two belts. The Encruzilhada Granite lies east of the shear zone and it is fault bounded and separate from the Pelotas Batholith, and may represent a different tectonic domain. The Caçapava Granite intrudes schists of the Santana Metamorphic Belt to the NW of the study area, the other side of the red bed basin (chapter 5) and its relationship to the Pelotas Batholith is unclear.

6.3.2.1 MAJOR ELEMENT VARIATION

The Harker diagrams of figure 6.21 compare major element data for the four granitoids which intrude the Santana Metamorphic Belt and compare these to the Encantada Gneisses which provide a possible source. Good negative correlations occur for the elements TiO_2, Fe_2O_3, MnO and MgO which suggests an igneous process relating the post-tectonic rocks to the basement gneisses involving residual mafic minerals.

For each of the oxides except Na_2O and K_2O, the Santana Granite sample lies at the end of the trend defined by the gneisses and this suggests that they could be related by a simple process; however the different alkalis suggest that the granite was not formed by simple partial melting, unless micas were residual phases. The gneisses have an increasing proportion off quartzofeldspathic material with increasing silica content, consistent with some segregation of granitic material within the gneisses.

The Campinas Muscovite Granite (chapter 5) is foliated by the shear zone between the Pelotas Batholith and the Santana Metamorphic Belt and it is distinctive in that it contains large primary muscovite flakes which reflect the strongly peraluminous nature of the melt. Its silica composition ranges between 75 and 77%. It is very low in TiO_2, MgO, MnO and

GRANITOIDS OF THE SANTANA METAMORPHIC BELT

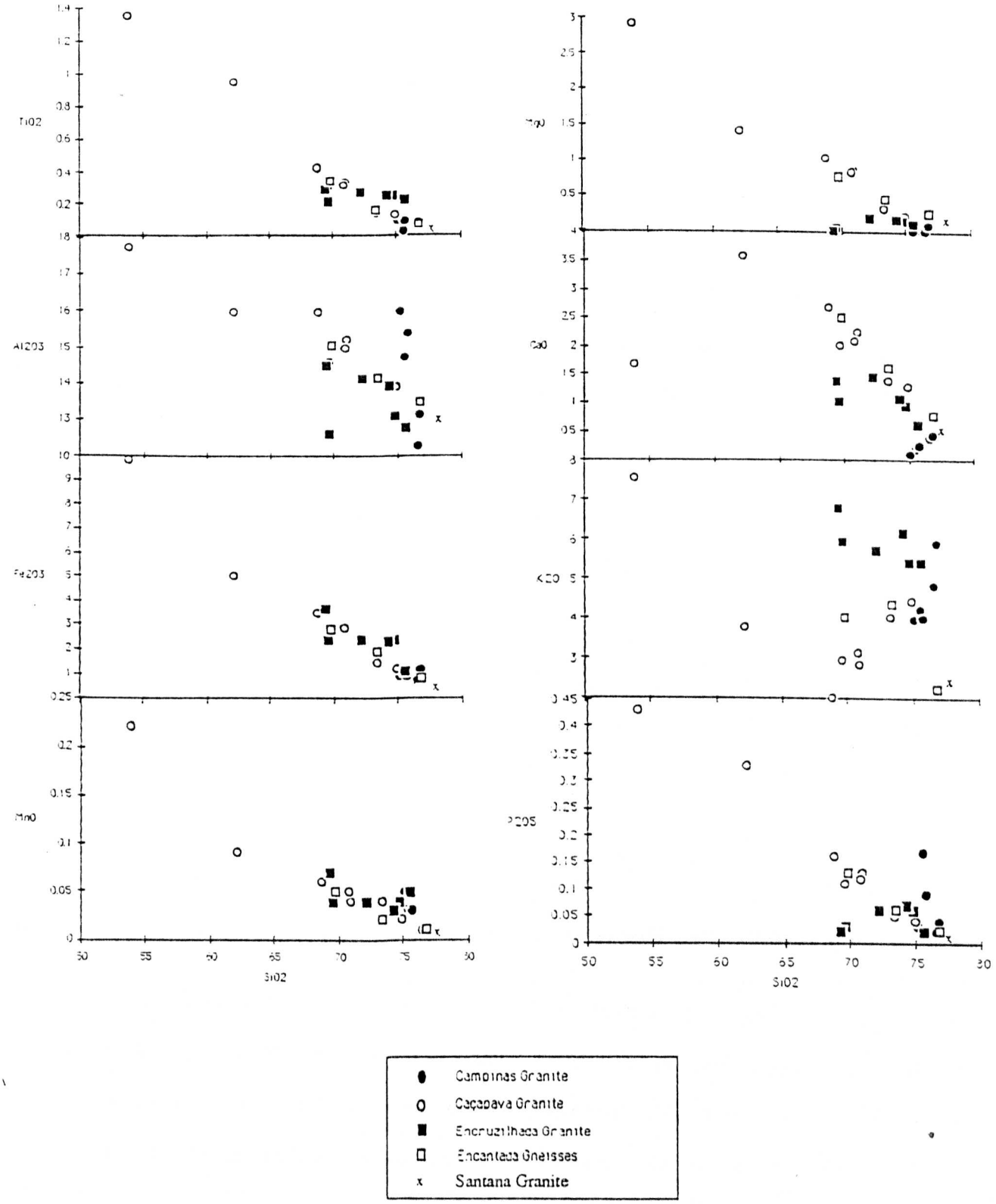

Figure 6.21 Granitoids intruding the Santana Metamorphic Belt with the Encantada Gneisses plotted for comparison.

Fe_2O_3, and falls at the high SiO_2 end of the negative trend shown by the other granitoids and the Encantada Gneisses. The Al_2O_3 content of the granite deviates away from the main trend reflecting its peraluminous composition. Such aluminous compositions are indicative of partial melting of a pelitic sediment.

The Caçapava Granite samples include both the pink and grey facies, and a xenolith, and they define a good negative trend for TiO_2, MgO, MnO and Fe_2O_3 and P_2O_5 which suggests fractionation within the granitoid of mafic phases, and also that the xenolith bears some relation to the granite. For CaO the xenolith lies below the projected negative trend of the suite suggesting that the xenolith is depleted in plagioclase relative to the source. Both Al_2O_3 and CaO form steep negative trends for the Caçapava Granite suggesting plagioclase fractionation.

The Encruzilhada Granite shows very little variation in major elements although there is a slight negative correlation between Al_2O_3 and CaO with increasing silica probably related to plagioclase fractionation. The samples are distinctive in their very low MgO and high K_2O content and do not appear to follow the trends shown by other post-tectonic granites, or by the Pelotas Batholith granitoids.

6.3.2.2 TRACE ELEMENT VARIATION

The available trace element data exhibit few good trends relating the various granites intruding the Santana Metamorphic Belt. These granites are therefore discussed as individual suites and figure 6.22 illustrates the trace element Harker plots for these suites. The Encantada Gneisses are also plotted on the diagram as a possible source for crustal melting.

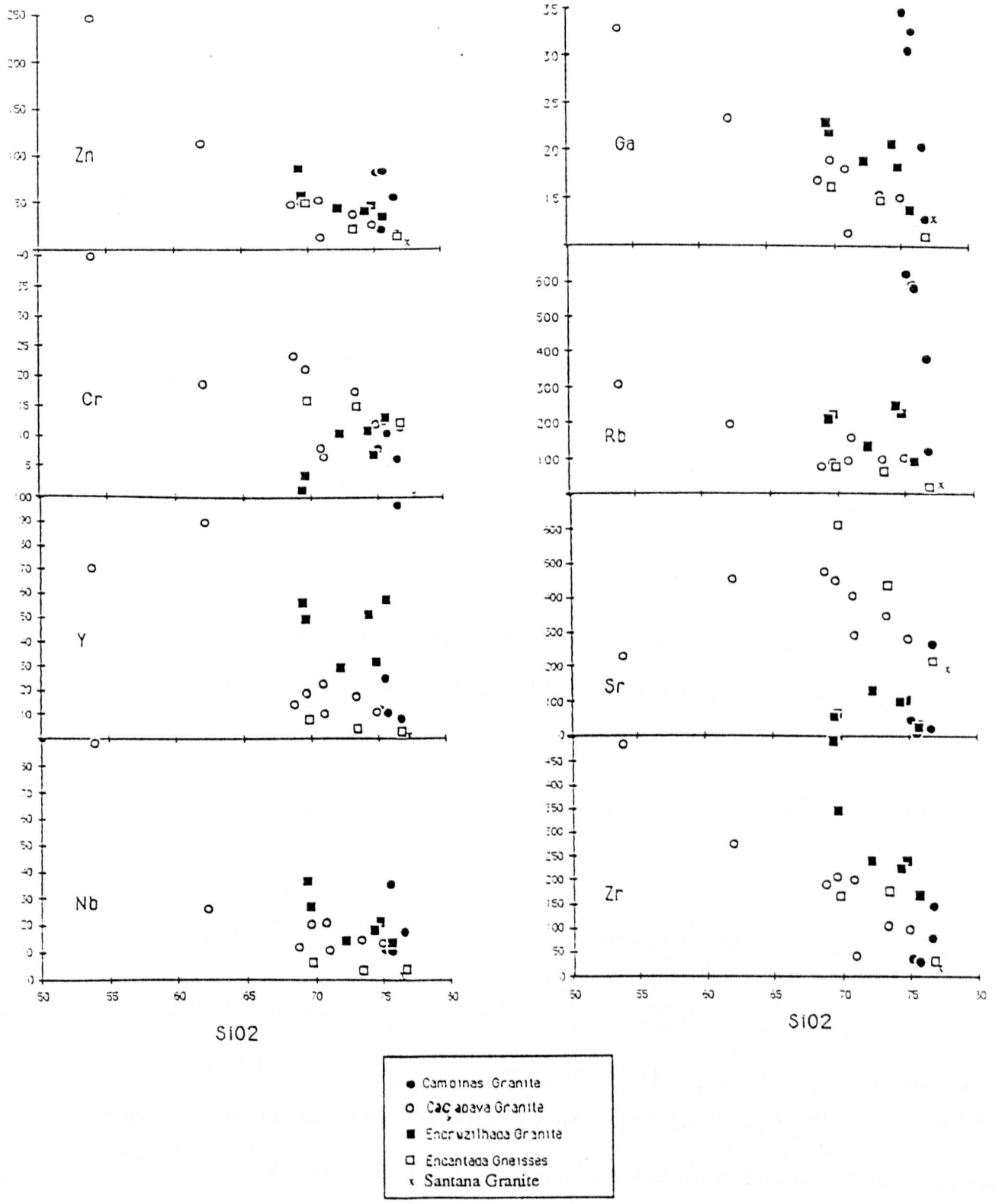

Figure 6.22 Trace element Harker diagrams for granitic rocks intruding the Santana Metamorphic Belt compared with the Encantada Gneisses.

The Santana Granite is a foliated two mica granite falls on the gneiss trend for Rb, Zr, Co, Zn and V reinforcing the view that the granite might be related to the Encantada Gneisses.

The Campinas Granite is a peraluminous two mica granite. Figure 6.22 illustrates that it is relatively enriched in Zn, Ga and Rb compared to the other granites and the Encantada Gneisses, and it shows a steep negative trend for Ga and Rb which is possibly controlled by mica and/or alkali feldspar. The Campinas samples are generally depleted in Sr and Y suggesting that plagioclase and garnet have either remained in the source or subsequently fractionated.

The Caçapava Granite appears to show a negative correlation for Zr with the xenolith particularly rich in it. A similar trend can be observed for Nb, Ga,Rb and Zr, although one sample (72% SiO_2) falls below the trend for Ga and Rb, which overall shows a less steep trend. There appears to be fractionation of Sr with increasing silica within the main suite of the Caçapava Granite. It also illustrates that the Caçapava Granite is depleted in Rb, K, Nb, Sr and Ti relative to the gneisses sugesting residual mica and feldspar during melting.

The Encruzilhada Granite shows a negative correlation for Zn and Nb with silica and it is generally enriched in trace elements relative to the other granites. It is however relatively depleted in Sr which is controlled by feldspar behaviour and suggests that it may have fractionated plagioclase.

6.3.3.3 RARE EARTH ELEMENT DATA

REE plots for these granites are shown in figure 6.23 and they illustrate that the Caçapava Granite has a slight Eu anomaly. The Encruzilhada Granite is enriched in LREE and has a marked negative Europium anomaly consistent with feldspar control. The Campinas Granite is relatively depleted in rare earth elements relative to the other granites and metasediments.

Unfortunately data for Gd was not obtained for this sample and therefore it is not clear whether there is a Eu anomaly, but it seems unlikely. The metasediments show flatter patterns and slight negative Eu anomalies.

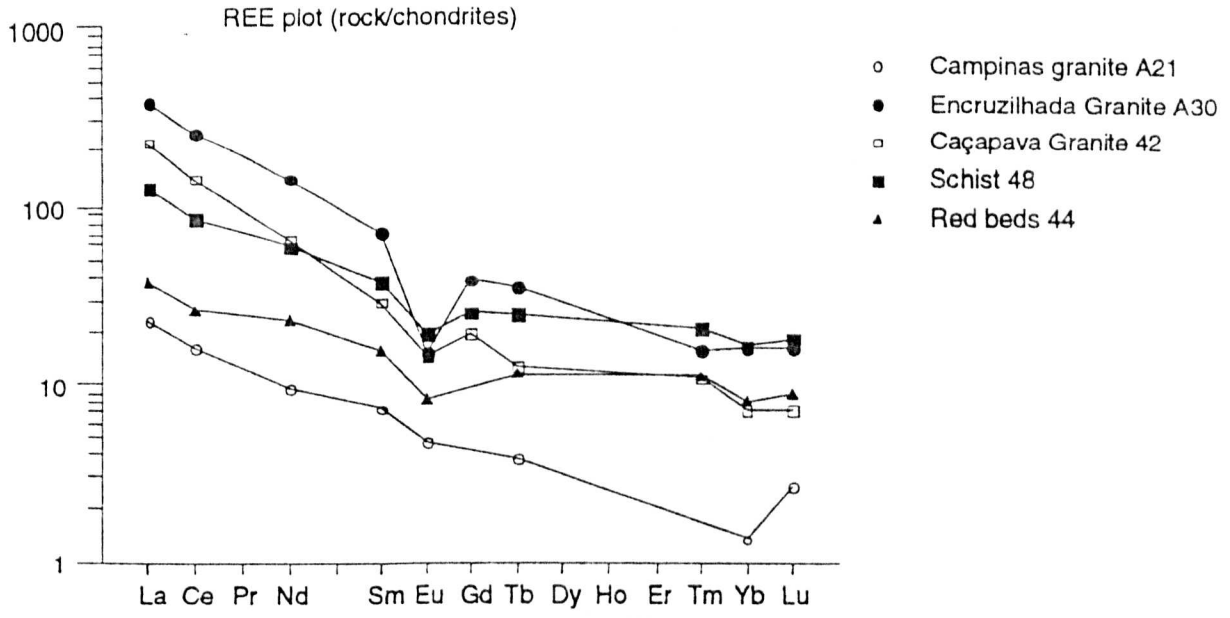

Figure 6.23 Comparison of granites with local metasediments.

6.3.3.4 SPIDERGRAMS

From the spidergram in figure 6.24 it can be seen that the Santana Granite is enriched in LIL elements, particularly barium which shows a positive anomaly, and depleted in HFS elements relative to primitive mantle. When it is compared to the Encantada Gneisses, it can be observed that it shows a similar general pattern to the gneisses which further establishes the interrelationship of the two. It also illustrates the similarities between the gneiss and granite with respect to their Rb/Sr ratios of 0.119 for the Proterozoic Encantada Gneisses and 0.095 for the Santana Granite. Typical crustal material has a Rb/Sr ratio of 0.12. The granite has anomalously high Ba content and low Rb which may reflect the nature of the source and/or the melting process.

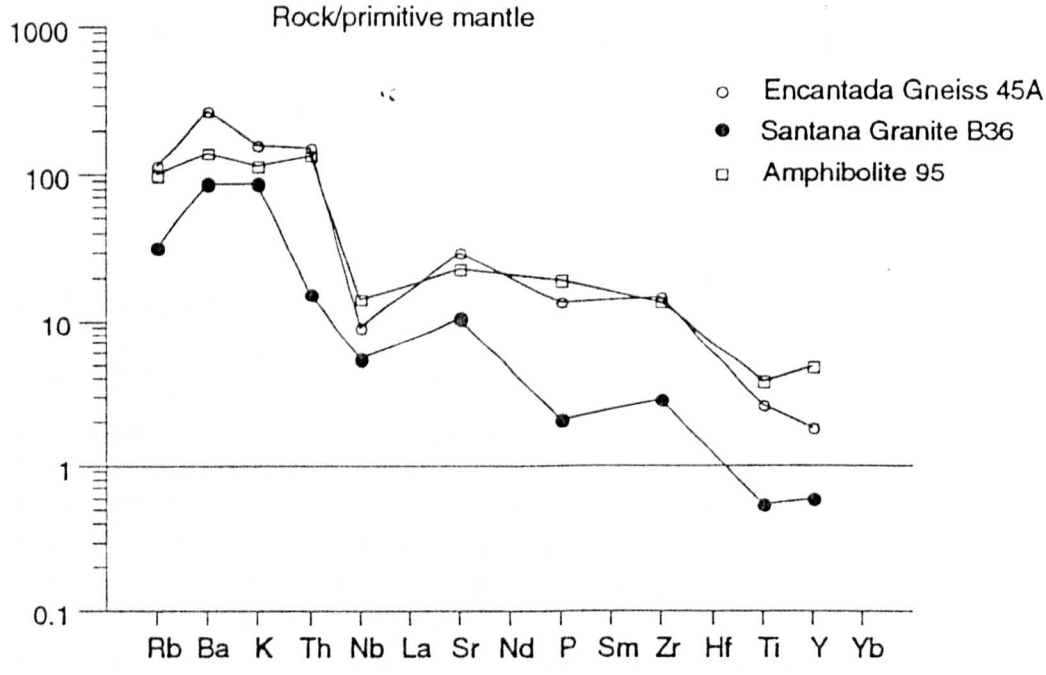

Figure 6.24 Spidergram of Santana Granite compared with the Encantada Gneiss .

The Santana Granite has been compared with selected lower and upper crustal melts and a volcanic arc granite from Chile (figure 6.25), and it shows a stronger resemblence to the lower crustal melt with its high Ba/Rb ratio and no depletion of Sr. The absence of mica and/or alkali feldspar in the source will result in unfractionated Ba/Rb ratios, in sharp contrast to upper crustal melts. Thus the mineralogy of the source is critical in constraining the relative Rb-Sr-Ba contents of the melt. Tectonic discriminant diagrams will be plotted for this and other granites intruding the Santana Metamorphic Belt in section 6.3.3.5

The spider diagram (fig 6.26) of the Campinas Granite shows it to have large Rb/Sr ratio and HREE depletion. It is also depleted in Ti and Yb relative to primitive mantle. This figure also illustrates that the Caçapava Granite is enriched in Ba and depleted in Rb and REE relative to the other post-tectonic granites. The Encruzilhada Granite shows high Rb/Sr ratios.

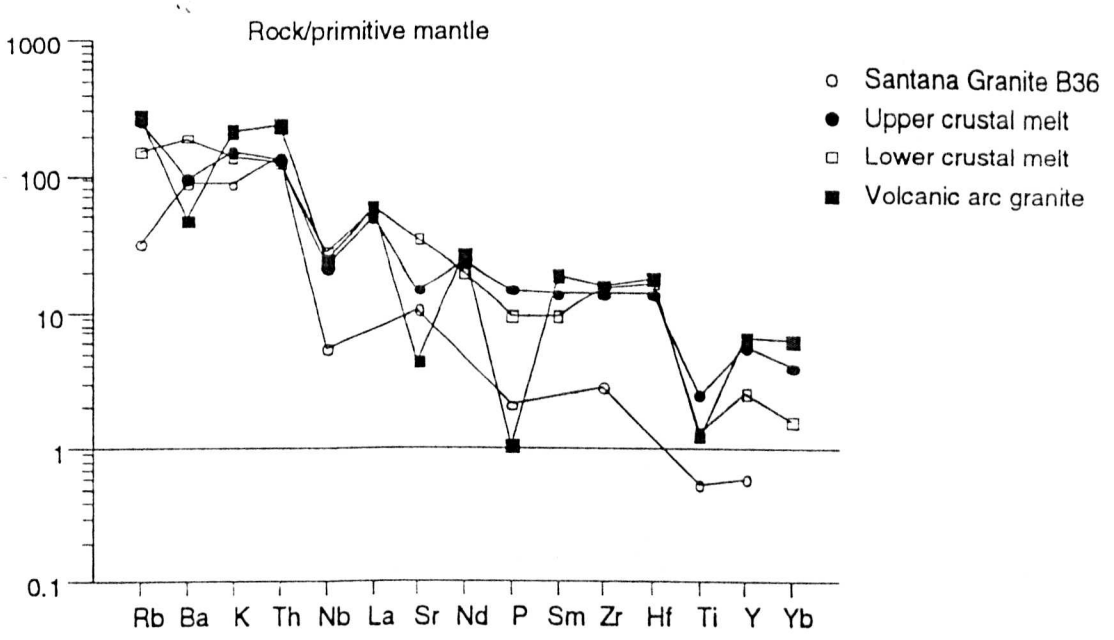

Figure 6.25 Comparison of Santana Granite with an upper crustal melt, a lower crustal melt and a volcanic arc granite.

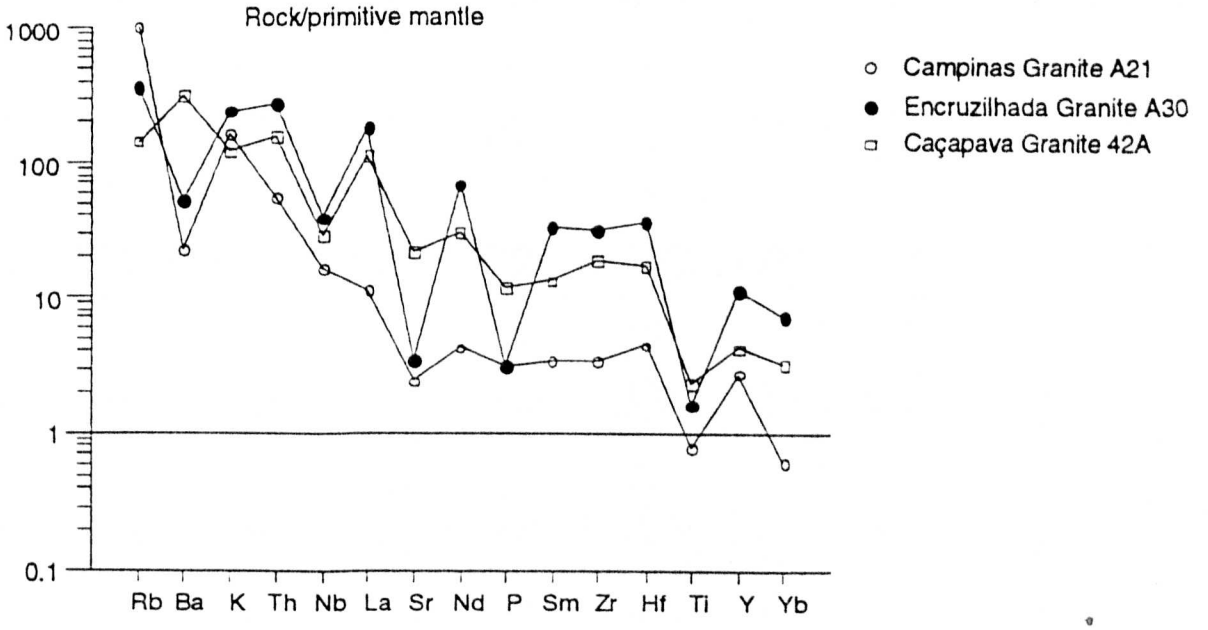

Figure 6.26 Comparison of granites intruding the Santana Metamorphic Belt.

When the spider plot of the Campinas Granite is compared with typical upper and lower crustal melts (figure 6.27) it shows a closer resemblance to the upper crustal melt with high Rb/Ba and Nd/Sr although it is relatively depleted in most elements apart from Rb and K. Ti is particularly depleted suggesting that there was a residual Ti phase. Its high Rb content and high initial Sr ratio suggests that it is a melt of an upper crustal material probably a pelite (chapter 7). Moreover it is unlikely to have been a melt of the Encantada Gneisses as the Rb is too high and also it has a high aluminium content and high $^{87}Sr/^{86}Sr$.

The Encruzilhada Granite is compared to the selected crustal melts in figure 6.28, where it is seen to be most similar to a volcanic arc granite with enrichment in K, Th, La, Nd, Sm, Zr, Y and Yb along with the extreme Sr depletion. Its initial $^{87}Sr/^{86}Sr$ ratio of 0.707 suggests it may be derived from an igneous precursor (chapter 7) and this is consistent with a volcanic arc setting for this granite. This is explored further in the next section.

The geochemistry of the Caçapava Granite is intermediate between the upper and lower crustal melts which suggests it is a lower to middle crustal melt with a low Rb/Ba ratio (figure 6.29). It may have formed from a lower crustal source similar to that proposed for the Idaho Batholith (C.Clarke pers com) which may also be subduction related. The Caçapava Granite may have formed by a similar process to the Pelotas Batholith but certainly involved different source material.

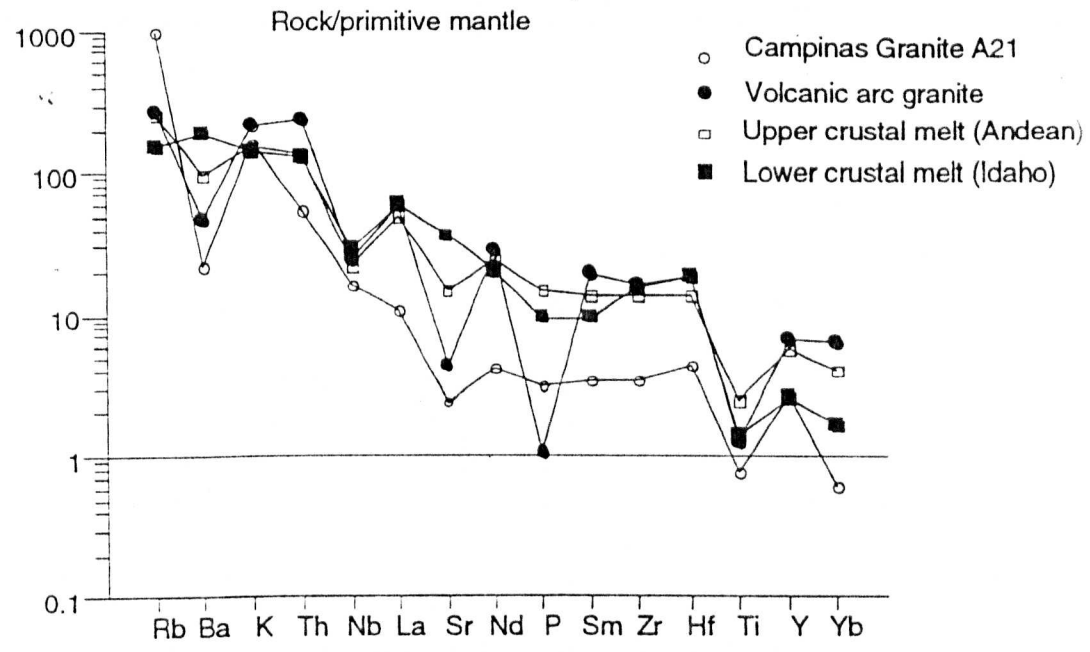

Figure 6.27 Comparison of Campinas Granite with granites from known tectonic setting

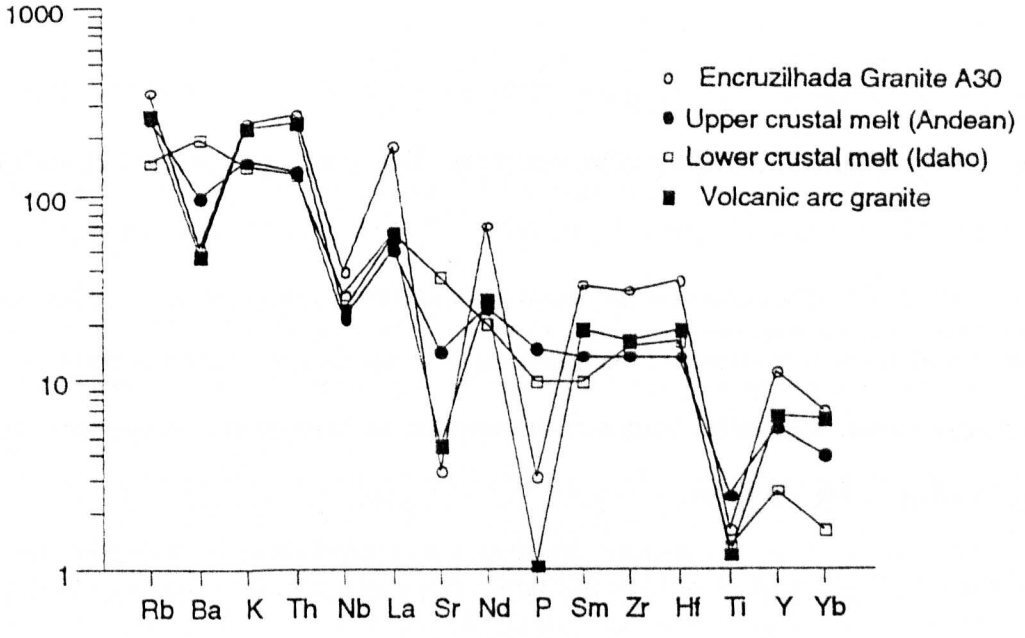

Figure 6.28 Comparison of Encruzilhada Granite with granites from known tectonic setting

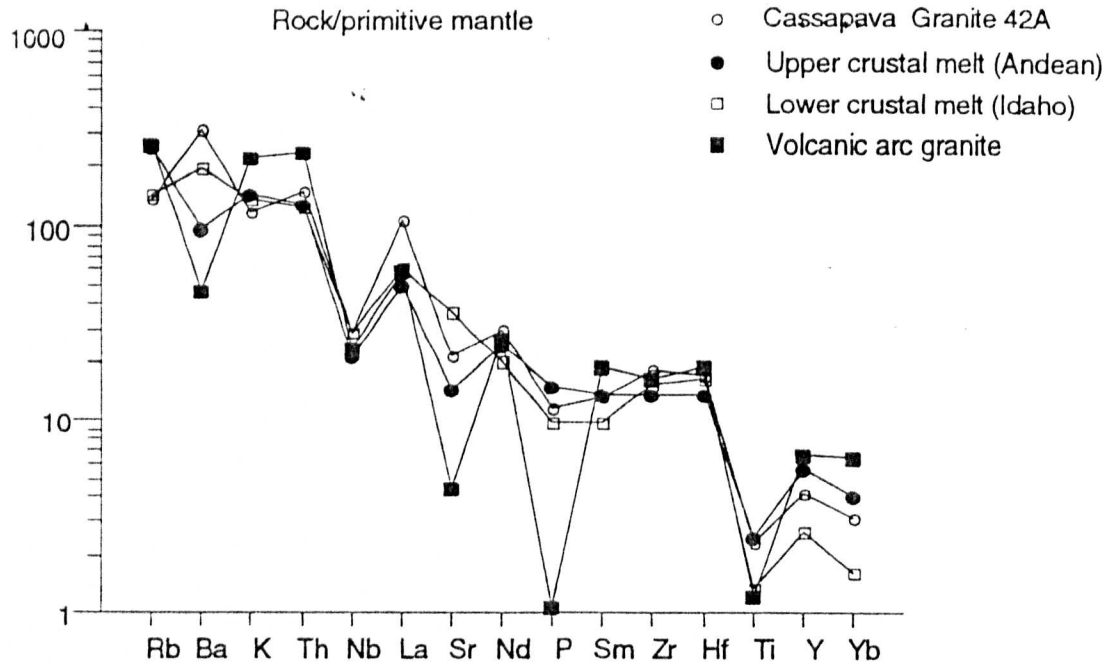

Figure 6.29 Comparison of Caçapava Granite with granites of known tectonic setting

6.3.3.5 DISCUSSION AND TECTONIC SETTING

The granites intruding the Santana Metamorphic Belt are plotted on the tectonic discriminant diagram of Pearce et al (1986) in figure 6.30. The Campinas Granite falls in the syntectonic field of the Pearce plot and is a two mica peraluminous granite with high Rb, low Ba and a high initial Sr ratio (chapter 7) suggesting it is an S-type granite formed by the partial melting of pelitic sediment. This melting appears to have been in response to compression and shearing of the D3 event.

The Encruzilhada Granite falls in the WPG field of the Pearce plot and in this sense it is distinct from the granites from the Pelotas Batholith and may have formed in a within-plate enviroment during a period of lithospheric extension. The Encruzilhada Granite, like many within-plate granites may result from the fractionation of an alkali basalt or syenitic parent or be a melt of an intraplate basalt. It has a Sr initial ratio of 0.707 which supports the suggestion that it comes from a basaltic parent.

The age of this intrusion is not established by this study (chapter 7). It is also much more enriched in rare earth elements than the Pelotas Batholith granitoids.

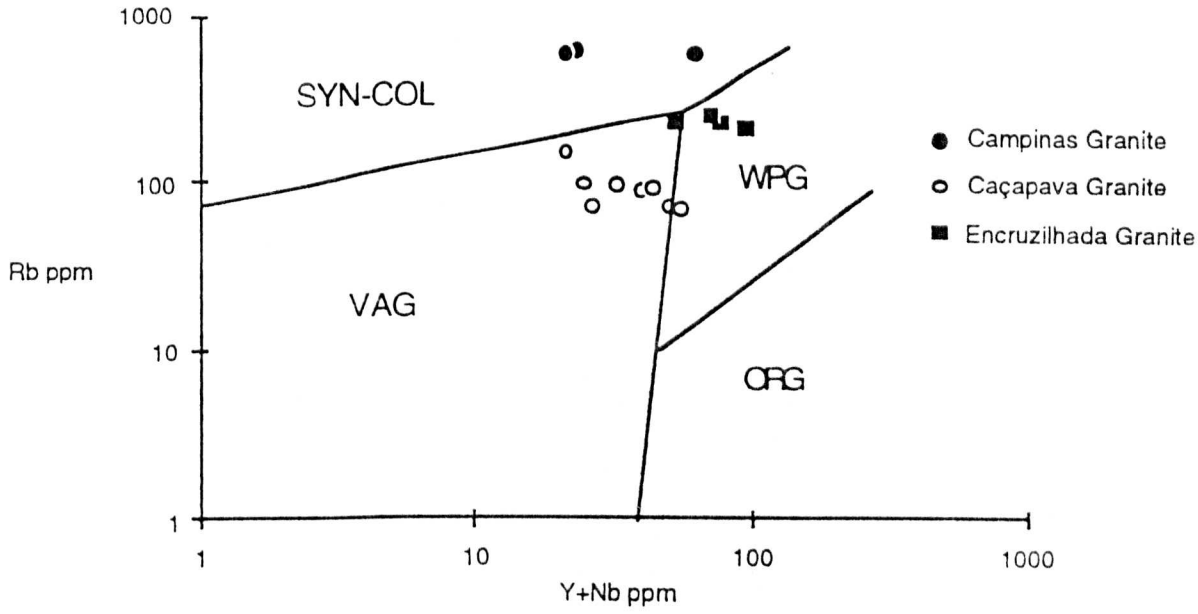

Figure 6.30 Discrimination plot for the granites intruding the Santana Metamorphic Belt.

The Caçapava Granite lies in the VAG field of figure 6.30 although this field also includes post-collision magmas (Pearce et al 1984). The Caçapava Granite may be the result of melting of a lower crustal source, see for example, its low HREE and unfractionated Rb/Ba. This is supported by the combination of its very low Sr initial ratio of 0.705 and its Proterozoic model Nd age (chapter 7).

6.3.3.6 PETROGENESIS OF THE SANTANA GRANITE

It is rarely possible to link a granitoid magma directly to its source, but in the Santana Metamorphic Belt the Santana Granite is exposed intruding the Encantada Gneisses and also at higher levels as a sill intruding the Encantada Schists (chapter 2). The Encantada Gneisses, contains lenses of granite at structurally higher levels. Geochemical variation

patterns suggests that the syntectonic Santana Granite may be related to the Encantada Gneisses by a simple process such as partial melting.

The trace element spidergrams (figure 6.21) show that the granite is relatively depleted in all elements compared with the gneisses which demonstrates that the former can only be a simple melt of the gneisses if most of the minor and trace elements are held back in residual phases such as alkali feldspar. Sr isotope data confirm that the granite could be a melt of these gneisses (chapter 7).

The Santana Granite is rich in quartz and alkali feldspar, poor in mafic phases and peraluminous. These are features common to crustal melts segregated at low melt fractions, which would also be small in size and emplaced close to the site of generation. The Santana Granite appears to obey all of these constraints and it is proposed that it is a partial melt of a source similar to the Encantada Gneisses. The mineralogy of the gneisses is biotite, quartz, plagioclase, alkali feldspar with zircon, apatite and sphene accessories. Experiments have shown that biotite sillimanite schist can generate liquids of leucogranites for all melt fractions up to 40% (Wickham 1987).

Pressures of 8Kb and temperatures of 650°C have been calculated for the Santana Metamorphic Belt (chapter 4) which could be high enough for partial melting given~5% water . The granite body does not travel far because on decompression it rapidly crosses the vapour-present solidus and crystallizes. Experiments have shown that biotite sillimanite schist can generate liquids of leucogranitic compositon for all melt fractions up to 40%, and a suggested model for the petrogenesis of leucogranites in high grade metamorphic belts has been proposed by Wickham (1987). The source melts in response to high temperature and pressures and partial melts segregate into lenses which rise from the source once a critical melt fraction is exceeded.

Field evidence suggests granite melting has occurred within some of the Encantada Gneisses (sample 93). These may have separated and intruded into the Encantada Schist formation (chapter 2). This may occur in response to decompression with the melt filling extensional

cracks, or by the ductile deformation of layers of differing composition causing separation of a low melt fraction (Robin 1979,Fletcher 1982, Van de Molen 1985). The field evidence suggests that the segregation occurred during D2 compression.

The degree of melting and the exact nature of the source is not yet established, although it appears to be a crustal melt with a high Ba/Rb ratio and the pattern resembles a lower crustal melt pattern from Idaho. The gabbro appears not to be directly related to the gneisses, or the granite and a different model needs to be proposed for the formation of this rock. Schists from the cover unit do not lie on the gneiss trend and are geochemically unrelated.

6.3.4 Summary

From the study of the Santana Metamorphic Belt grantoids it appears that there are two likely lower crustal melts, the Santana Granite and the Caçapava Granite. The Encruzilhada Granite and Campinas Granite are both upper crustal melts generated near the boundary of the Pelotas Batholith and the Santana Metamorphic Belt. The Campinas Granite probably formed in response to shearing and collision, and melted upper crustal sediments, whereas the Encruzilhada Granite may have had an igneous precursor and formed during extensional tectonics.

6.4 Conclusions and Discussion

Granitoids of the Dom Feliciano Belt can be divided into two major groups based on their degree of deformation, field relations and tectonic setting into (i) foliated granodiorites and (ii) unfoliated granites (figure 6.31). Two unfoliated granites namely the Canguçu Granite and the Capao do Leao Granite form a distinct geochemical group and appear to be A-type granites. The Encruzilhada Granite lies in a within plate field and is discussed separately.

The main purpose of this section is to compare and contrast the granitoid geochemistry of the granites of the Pelotas Batholith and the Santana Metamorphic Belt, along a schematic cross section (fig 6.31-32) in order to propose a tectonic model.Also plotted for comparison are basement schists and gneisses, Post-Brasiliano igneous rocks and recent sediments. The

geochemical plots directly match the cross section and so individual rock types can be located. Granite types from both belts will be discussed in terms of their geochemistry with respect to these figures (6.31,32) and previous Harker plots and Spider diagrams and then the two belts will be compared.

The Pelotas Batholith granitoids can be subdivided into two types according to their state of deformation; foliated granitoids and unfoliated granites. There appears to be no progressive change in granitoid geochemistry, with distance from Peloltas, through the Pelotas Batholith (figures 6.31,6.32). However there is a distinct geochemical change with time with the two groups having distinctive geochemical characteristics. The Streckeisen classification system (figure 6.2) demonstrates that undeformed rocks (granites) are more chemically evolved than deformed rocks (granodiorites) implying progressive reworking of older crust to form a more sialic crust with time.

The foliated granodiorites are calkalkaline and lie in the VAG field of the Pearce et al (1984) discriminant plot. They are generally metaluminous, although some migmatites are peraluminous; they are enriched in LIL elements and LREE. They are slightly peraluminous with high Rb/Ba and very high Rb/Sr. In terms of their major element geochemistry, the unfoliated granites are, more silicic and more peraluminous with higher Fe/Mg (figure 6.31).

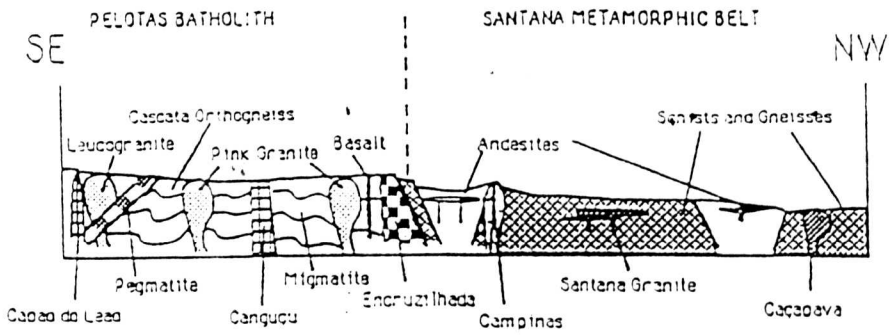

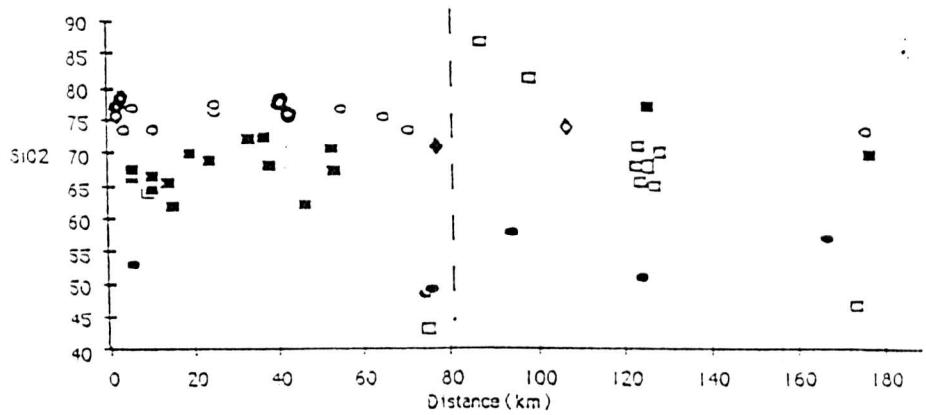

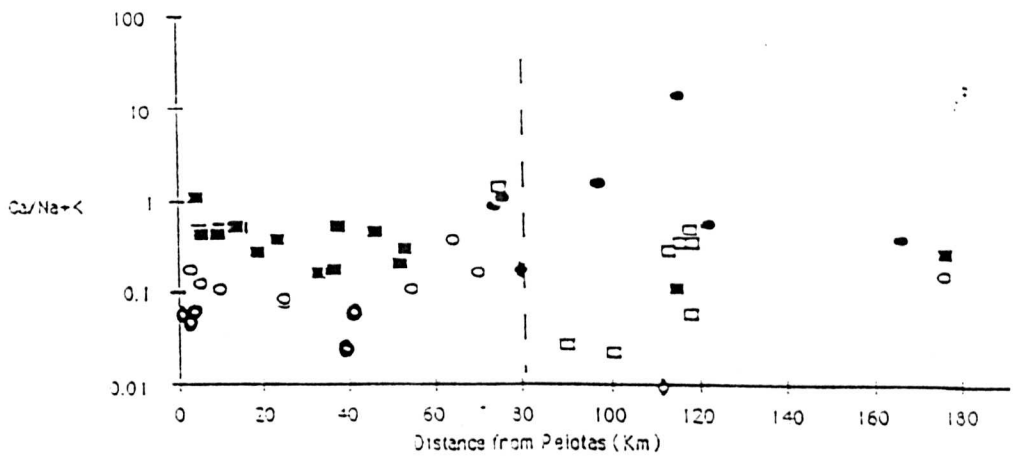

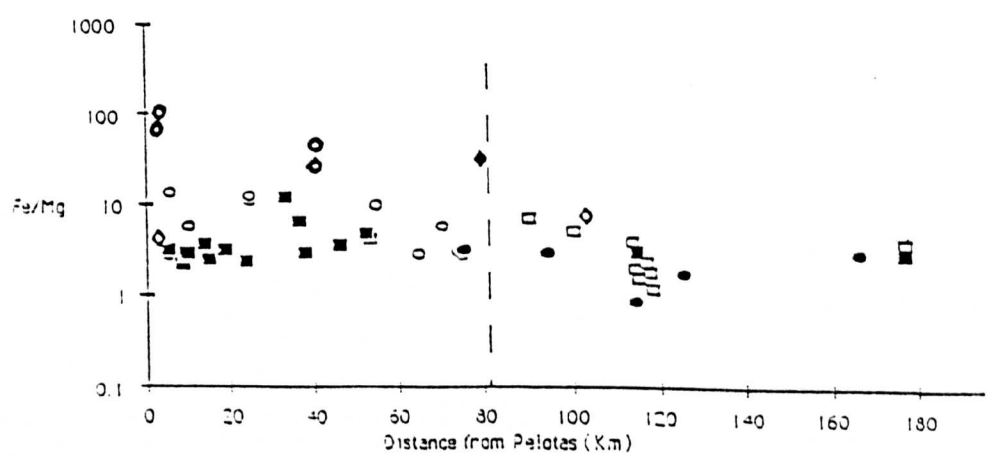

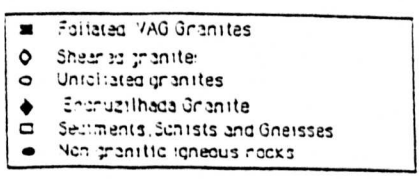

Figure 6.31 Comparative major element geochemistry of the Pelotas Batholith and the Santana Metamorphic Belt along the BR392 road section.

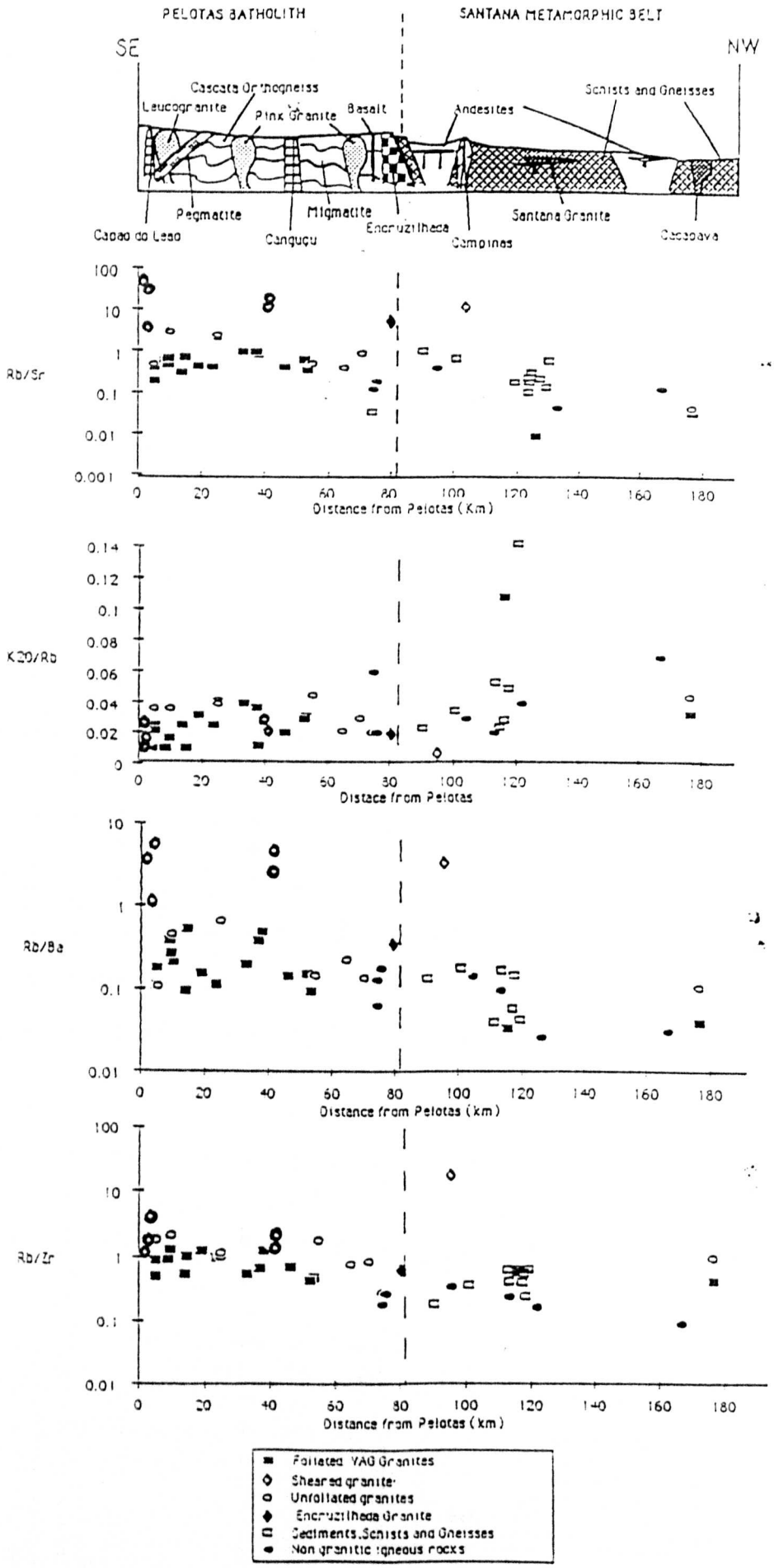

Figure 6.32 Trace element ratios plotted against distance along the studied section.

Two of the unfoliated granites however have very high Rb/Sr, Rb/Zr and Rb/Ba ratios relative to the other unfoliated granites (figure 6.32). The Canguçu Red Granite outcrops between faults and has a high Rb/Sr (figure 6.32) and old Nd model ages (2500) suggesting an Archaean source. The Capao do Leao Granite has similar geochemical characteristics to this red granite with flat rare earth patterns and a marked negative Eu anomaly. These two granites are geochemically associated and may have a similar petrogenetic history and appear to be A-type granites (Collins et al 1980). Their tectonic setting is however,1 not established.

In terms of trace element ratios the unfoliated granites are more enriched in Rb than the foliated granites. The Cascata Leucogranite lies in the syn-collision field (figure 6.16) whereas the later Pink Granite lies in the VAG/post-collision field and are more likely to be post collision since they are unfoliated. The late stage pegmatites contain little plagioclase and are highly enriched in K_2O, Ba, U and Cu and thus they may be similar in these respects to the alaskites of the Damara belt (Mc Dermott 1986).

Comparing the two belts, the granites of the Pelotas Batholith have considerably higher Rb/Sr and Rb/Ba ratios compared to those intruding the Santana Metamorphic Belt with the exception of the Campinas Granite which has very high Rb and is sheared by D3. It is apparent from the cross-section plots that the unfoliated granites have generally higher Si and lower Ca/Na+K than the foliated granites and that the Capao do Leao Granite and Canguçu Red Granite have extremely high Rb/Sr, Fe/Mg and Rb/Ba and low K/Rb and Ca (figure 6.32) consistent with A-type granites.

The foliated Santana Granite has high Si, low Ca , low Rb/Sr and high K relative to the foliated granites of the Pelotas Batholith. The Caçapava Granite, when compared to unfoliated granites of the Pelotas Batholith, has much lower Rb/Sr, and lower Rb/Ba suggesting a different source. The Encruzilhada Granite has high Rb/Sr and high Fe/Mg. The data suggests that there are distinctly different sources for the Santana Metamorphic Belt and the Pelotas Batholith.

The evolution of the Pelotas Batholith appears to fit the model of Harris et al (1986) for collision-zone magmatism in that four groups of intrusions can be recognized each associated with a particular stage in the evolution of a collision zone (table 6.1). The first group are pre-collision calkalkaline (volcanic arc) intrusions characterized by selective enrichment in LIL elements. The foliated granitoids of the Pelotas Batholith appear to fall into this category. The second group in the model are syn-collision peraluminous intrusions (leucogranites), and of the unfoliated granites studied the Cascata Leucogranite, Canguçu Red Granite and Capao do Leao Granite fall into the syn-collision field and so may belong to this group. The Cascata Leucogranite however does not have particularly high Rb/Zr (1.8) or Ta/Nb (0.15) in contrast to known syn-collision crustal melts such as from the High Himalayas (Harris et al 1986) but low K/Rb ratios are characteristic of both this leucogranite and those from collision-related melts. The peraluminous Canguçu Red Granite and the Capao do Leao granite appear to be A-type granites and have high Rb/Zr (2.25), Ta/Nb (0.07) and low K/Rb (0.02) suggesting they also belong to this second group.

The third group recognized in the Harris et al model are late, or post-collision calc-alkaline intrusions (table 6.1) distinguished by high Ta/Hf and Ta/Zr. The Pink Granites may fall into this group with Ta/Hf of 0.2 in contrast to values of 0.15 for the foliated granites, and a higher Ta/Zr value of 0.006 compared to 0.004 for the foliated granites. This granite is thought to be a partial melt of the Migmatitic Orthogneiss based on $^{87}Sr/^{86}Sr$ initial ratios (chapter 7). The fourth group recognized in the model are post-collision alkaline intrusions. Granitic magmas of this type have not been identified although late pegmatites do suggest a late pulse of alkalic magmatism which is also supported by the presence of alkali basalts and phonolites in the Piritini area of the Pelotas Batholith (Barbieri et al,1987). However the Piritini alkalic magmas are Cretaceous in age and therefore not related to the Brasiliano orogenic event.

The granites intruding the Santana Metamorphic Belt have a greater range in age than the Pelotas Batholith. The Santana Granite is pre-D2 and it has granodioritic composition, low

Rb/Ba, low Rb/Sr, it is depleted in trace elements and is peraluminous and falls in the VAG/Post collision field of figure 6.30 because of its low Rb value. However, it is thought to be a partial melt of the Encantada Gneisses based on field evidence, Sr isotope data (Chapter 7) and the similarity in geochemical patterns. Moreover, the melting may be in response to compression and metamorphism(chapter 2). It is distinguished from the foliated granites of the Pelotas Batholith by both source age and composition.

The Encruzilhada Granite is a fault-bounded metaluminous to peraluminous intrusion that lies in the WPG field of figure 6.30 with high Rb/Ba and Rb/Sr. Its low Sr initial ratio (0.707) suggests it may have a basic igneous source consistent with a within-plate setting. It has a marked negative Eu anomaly and is low in CaO, both suggesting plagioclase control, and is generally enriched in Rare Earth Elements.

The Campinas Granite is a strongly peraluminous two mica granite and lies in the syn-tectonic field of the Pearce plot. It appears to be foliated during D3 collision. It is very Rb enriched and thus has high Rb/Zr (16.8) and Ta/Nb (0.33) and low K/Rb (0.006) typical of group 2 syncollision leucogranites. The Campinas Granite also has a high initial Sr ratio and this combined with its A/CNK>1 value and high Rb suggests it is an S-type granite melt of a pelitic source.

The Caçapava Granite intrudes the NW portion of the Santana Metamorphic Belt as a small pluton. There are two facies; pink monzogranite (unfoliated) and grey granodiorite (foliated) and they both lie in the VAG/Post-collision field of the Pearce plot. They have low Rb/Ba and Rb/Sr ratios and are thought to be lower crustal melts. Both the Ta/Hf (0.16) and Ta/Zr (0.004) are low suggesting that this is not a post-collision granite. It has a very low initial Sr ratio of 0.705 and an Archaean Nd model age (chapter 7) which suggests it was derived from an old primitive igneous souce. Melting of the lower crust after crustal thickening, although not considered by Pearce et al (1984) is a predictable consequence of collision tectonics (Deyores 1989).

The granites intruding the Santana Metamorphic Belt appear to represent a range of tectonic environments and processes. The Santana Granite and Campinas Granite appear to be related to the collision event between the Pelotas Batholith and the Santana Metamorphic event and correspond to stages 1 and 2 continent-continent collision. In contrast the Encruzilhada Granite appears to form in an extensional within plate setting. The Caçapava Granite is derived from the lower crust in response to crustal thickening after collision. These conclusions will be integrated with field evidence, metamorphic and isotopic studies in chapter 8 to support a regional tectonic model.

CHAPTER SEVEN

7. Isotopic studies of the Dom Feliciano Belt.

7.1 Introduction

Isotopic studies have been undertaken in the Dom Feliciano Belt for two reasons. The first is to establish the timing of the orogeny, and the second is to establish the relationships between the various granitoids and their sources in order to relate the petrogenetic history of the Pelotas Batholith to the Santana Metamorphic Belt, and hence to develop an overall tectonic model for the Dom Feliciano Belt.

This chapter is subdivided into two sections. The first section discusses the geochronological studies undertaken in the area using Rb-Sr whole rock age determinations. The second section discusses isotope geochemistry and petrogenesis using Sr initial ratios and Nd model ages in the context of geological and geochemical studies undertaken in previous chapters. Analytical techniques are discussed in Appendix A and isotopic data are given in Appendix D.

7.2 Geochronolgy

7.2.1 Introduction

Previous work on the geochronology of the Dom Feliciano Belt has been undertaken by Cordani et al (1974), Texiera (1982), and extensively by Soliano (1986) in his thesis on the geochronology of Rio Grande Do Sul. Table 7.1 gives the ages and $^{87}Sr/^{86}Sr$ initial ratios of various granitoids dated by previous studies. Samples from four granitoids and from the Encantada Gneiss formation were collected in this study for Rb-Sr isotopic analysis. Where possible, discrete granitoid types have been identified petrologically and sampled from single or closely spaced quarries for whole rock Rb-Sr analysis.

This approach makes it more likely that comagmatic suites have been sampled and it supports and constrains the field studies which have already established inter-relationships between various intrusions (chapter 5). The geochronology undertaken in this context places an absolute time scale on the established relative chronology.

SANTANA METAMORPHIC BELT			
Intrusion	Author	Age (m.y.)	Initial ratio
Encantada Gneisses	Cordani	2270±235	0.703
Santana Granite	Soliani	805±555	0.710
Campinas Granite	Cordani	785±103	0.714
Encruzilhada Granite	Soliani	617±10	0.707
Caçapava Granite	Cordani	552±10	0.705
PELOTAS BATHOLITH			
Intrusion	Author	Age (m.y.)	Initial ratio
Foliated granitoids	Soliani	775±36	0.706
Unfoliated granitoids	Soliani	446±69	0.707

TABLE 7.1

In the following diagrams sample locality numbers refer to those identified on figure 5.2. The Sr isotopic ratios were determined to better than ±0.01%, whilst errors of the Rb-Sr elemental ratios determined by XRF are calculated to be ±2%. All uncertainties are quoted to two standard errors on the mean (±2σ). For all isochron calculations the isochron regression line was calculated using a computer program written by D.W.Wright using the least squares approximation method of York (1969). This defines an isochron as having MSWD<1. If it is greater than 1 the correct definition is an errorchron. All the plots in this study are errorchrons by this definition apart from the shear zone isochron. One of the causes of scatter of data points on Rb-Sr errorchrons may be extensive tectonic activity in

that allows fluids to circulate, particularly in shear zones, mobilizing Rb and consequently opening the system to Sr isotopes.

The inhomogeneous nature of melting in granites may also cause differences in initial Sr between samples on the hand specimen scale which would prevent an isochron being formed. No samples have been dropped from the Rb-Sr plots since all samples collected at the quarries were representative of the granite types analysed. Samples of a particular granitoid collected from other localities than the quarries along the section are plotted as open circles.

7.2.2 Geochronology of the Pelotas Batholith

Two foliated granitoids and one unfoliated granitoid were collected from three available quarries in the Pelotas Batholith for geochronological Rb-Sr isotope analysis. Samples were also collected from a shear zone within the Cascata Orthogneiss in order to date the D3 event. Unfortunately the very low Sr content (6ppm) of the Capao do Leao Granite made it impossible to date using whole rock Rb-Sr methods.

7.2.2.1 CASCATA ORTHOGNEISS

Ten fresh samples from this pluton were collected from recently blasted quarries (3 and X), in close proximity to one another along the main road BR392 (figure 5.2). Samples provided a wide range in both Rb/Sr and $^{87}Sr/^{86}Sr$ and define an errorchron that gives an age of 572±54 m.y. (figure 7.1a). If a wider range of samples from this intrusion, sampled from exposures along the road section rather than quarries, are plotted (figure 7.1b), these also seem to fall close to the errorchron line suggesting they are cogenetic which supports field evidence. The initial $^{87}Sr/^{86}Sr$ ratio of this orthogneiss (0.7089±4) is typical of many Phanerozoic orogenic batholiths. Its implications for the nature of the source and for petrogenesis will be discussed in section 7.3.

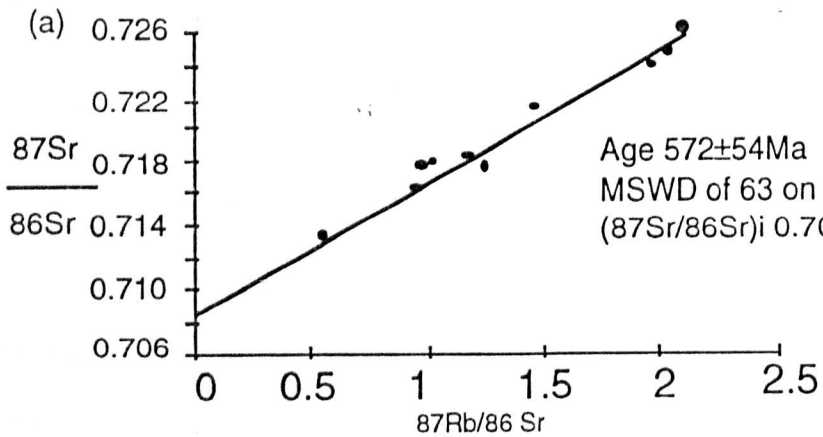

Figure 7.1a shows the errorchron for the Cascata Orthogneiss obtained from plotting the samples from quarries in black circles.

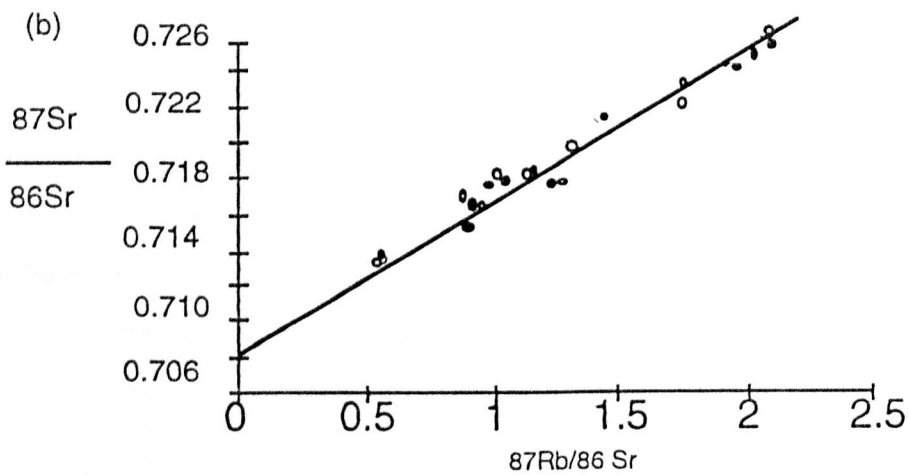

Figure 7.1b also plots samples collected from the intrusion, represented by open circles and these lie on the same line.

7.2.2.2 MIGMATITIC ORTHOGNEISS

Four samples were collected from a freshly blasted quarry at locality 11 along the BR392 section and the age obtained (557±46) is analytically indistinguishable from the Cascata Orthogneiss (fig.7.2) although field relations suggest that the Migmatitic Orthogneiss intrudes the Cascata Orthogneiss. The high MSWD of 13 results from the inhomogeneous nature of the migmatite. Nine samples of migmatite were collected outside the quarry along the road section and are plotted on the second diagram of figure 7.2b four of which lie on the errorchron, but two lie well away from it with significantly higher $^{87}Sr/^{86}Sr$ ratios. The initial $^{87}Sr/^{86}Sr$ ratio of this errorchron is 0.710±7 and the significance of this will be discussed in section 7.3 .

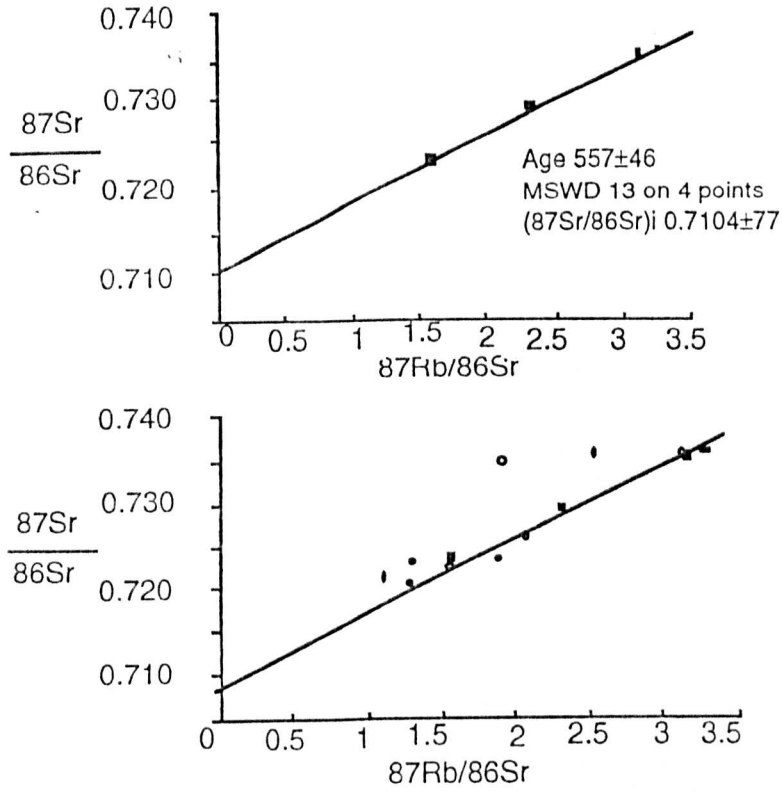

Figure 7.2a. Errorchron for the Migmatitic Orthogneiss based on quarry samples, 7.2b includes migmatite from the road section.

7.2.2.3 PELOTAS BATHOLITH SHEAR ZONE

Four small samples were collected from recrystallized granite within a shear zone at locality 5 (chapter 5). The isochron obtained is therefore interpreted as the age of the shearing event at 508±7 m.y.(figure 7.3) This date is older than the intrusion of the unfoliated pink granite which is consistent with the field evidence.

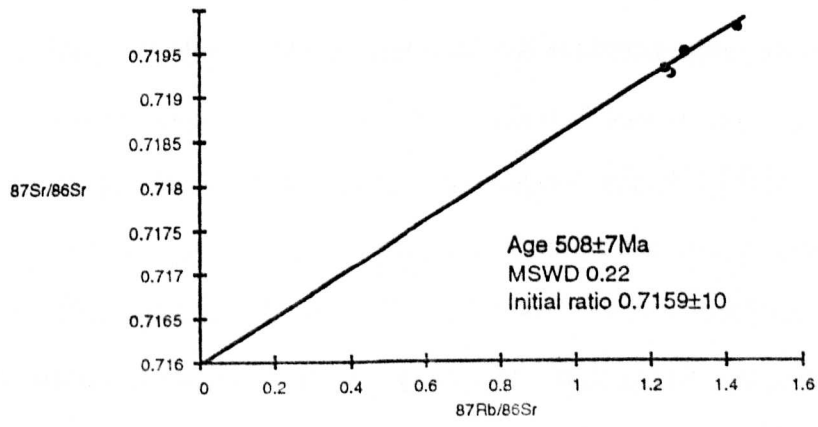

Figure 7.3 Isochron for sheared Cascata Orthogneiss dating the D3 shearing event

7.2.2.4 PINK GRANITE

Figures 7.4 below presents an errorchron from the Pink Granite at quarry 11.

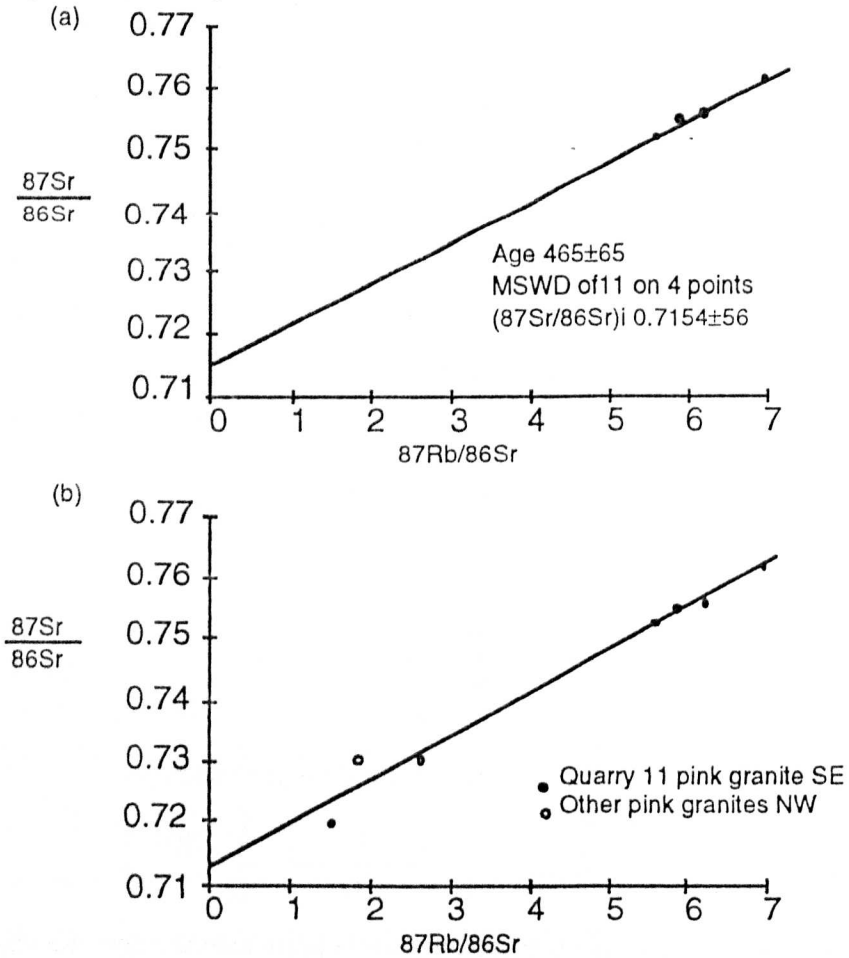

Figure 7.5 presents an errorchron compares the data from figure 7.4 with Pink Granites from other localities. These appear to lie on the same errorchron.

Four samples of pink granite from quarry 11 provide a near linear array on the Rb-Sr plot (fig. 7.4), with a MSWD of 11 and an age of 465±65 m.y., which is consistent with field relations since this Pink Granite intrudes the Migmatitic Orthogneiss at quarry 11 (chapter 5). The interrelationship between the two rock types will be discussed in section 7.3. The initial $^{87}Sr/^{86}Sr$ ratio is high at 0.715±6 and this suggests a high proportion of Sr from older crustal sources. The high Rb/Sr ratio is a significant feature of this granite. Other samples of Pink Granite have been analysed from the NW portion of the section and are represented in figure 7.5. These have lower Rb/Sr than the quarry samples but scatter about the errorchron suggesting a possible comagmatic origin, although some isotopic disturbance is indicated by the data.

7.2.4 Geochronology of the Santana Metamorphic Belt

The Encantada Gneisses and the Caçapava Granite have been dated from the Santana Metamorphic Belt. The Campinas Granite, dated at 785±103 m.y. by Cordani (1974) has not been dated in this study since no fresh samples were found. The Encruzilhada Granite also did not provide suitable samples for dating in this field area, but it has been dated at 617±10 m.y. by Soliani (1986).

7.2.4.1.ENCANTADA GNEISSES

The Encantada Gneisses are composed of a range of lithologies including granitic gneisses, amphibolitic gneisses and sedimentary gneisses. Unfortunately these are only exposed in river sections and large sample suites from any one locality have been impossible to obtain. Therefore samples from a range of localities have been plotted on the same Rb-Sr array (fig. 7.6). Although this technique is unlikely to yield precise geological ages as samples are less likely to have the same initial Sr isotope ratios, it can provide a broad indication of metamorphic age that can be compared with the Pelotas Batholith intrusion ages.

The five sampled gneisses give an age of 2030± 72 m.y. with a MSWD of 100 (fig 7.6) which is comparable to the age of 2000 m.y obtained by Cordani et al (1974). The large MSWD of the errorchron may result from the inhomogeneous nature of the gneisses, combined with partial homogenization during metamorphism. The low initial $^{87}Sr/^{86}Sr$ ratio of 0.705±5 suggests that the source crustal rocks were young at the time of metamorphism and/or that the source was characterized by low Rb/Sr.

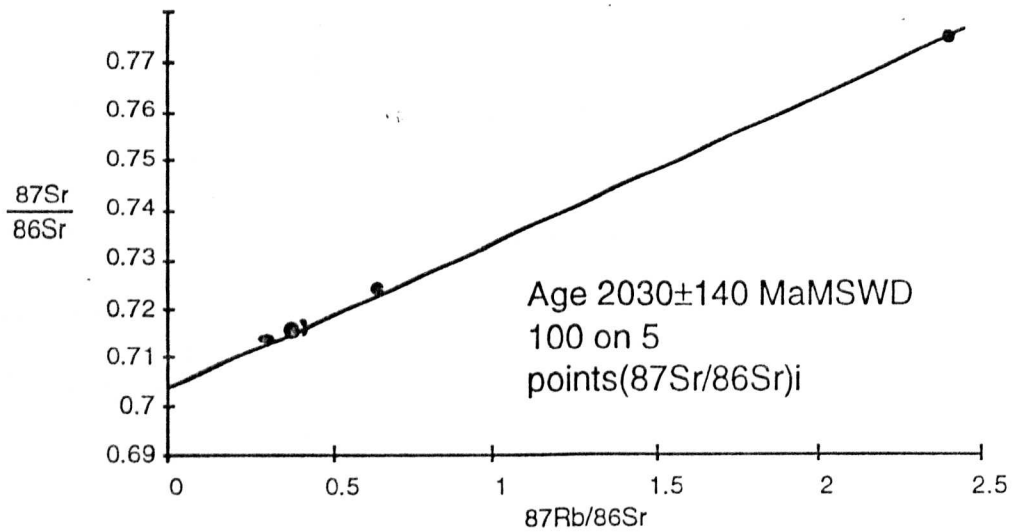

Figure 7.6 Errorchron for the Encantada Gneisses

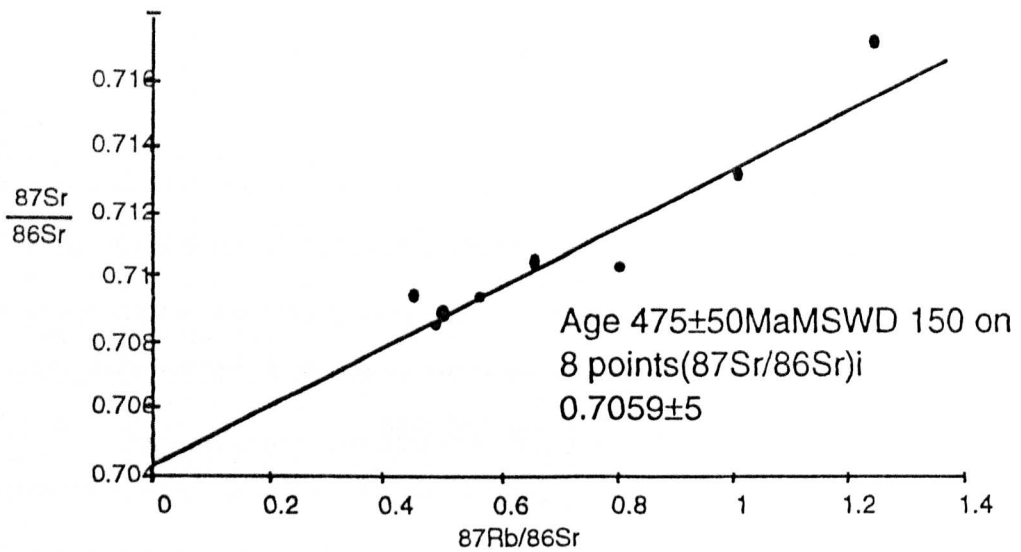

Figure 7.7 Errorchron for the Caçapava Granite.

7.2.4.2 CAÇAPAVA GRANITE

The Caçapava Granite has been dated by this study and gives an errorochron age of 474±50 m.y. with an MSWD of 150 (fig 7.7). Both the pink and grey facies have been plotted on the diagram. This granite intrudes the Santana Metamorphic Belt and the samples were all collected from a quarry at locality 42 opposite Caçapava Do Sul on the BR392 road section. It has a low initial ratio of 0.7059±5 suggesting a mantle or a low Rb/Sr crustal source. This relationship is explored in section 7.3.

7.2.5 Summary

SANTANA METAMORPHIC BELT		
Intrusion	Age (m.y.)	Initial ratio
Encantada Gneisses	2030±72	0.7045±47
Caçapava Granite	474±50	0.7059±5
PELOTAS BATHOLITH		
Intrusion	Age (m.y.)	Initial ratio
Cascata Orthogneiss	572±54	0.7089±1
Migmatitic Orthogneiss	556±46	0.7104±77
Sheared granite	508±7	0.7159±10
Pink Granite	465±65	0.7154±56

Table 7.2 Summary of isochron data from this study.

From table 7.2 it can be seen that the geochronological studies undertaken in this study support the field relations established in chapters 2 and 5 for both the belts. There appears to be two distinct tectonothermal events within the Santana Metamorphic Belt. The Basement records an Early Proterozoic event whereas intrusions into it and the overlying schists are clearly Pan-African, as represented by the Caçapava Granite in this study.

In contrast the Pelotas Batholith has no Early Proterozoic basement and the oldest dated intrusion of this study is the Cascata Orthogneiss which has an intrusion age of 572±54m.y. This is then foliated by a compressional event and sheared at ~508 m.y., with post-tectonic magmatitic activity at least until 465 m.y. which is the age of intrusion of the Pink Granite. These ages therefore suggest that the orogenic event responsible for the formation of the Pelotas Batholith lasted at least 100 m.y. Only a small portion of the batholith has been investigated and more extensive studies may find a wider range in ages. The D3 shearing event resulting from collision between the two belts and probably occurred around 500 m.y.

7.3 Isotope geochemistry and petrogenesis

7.3.1.Introduction

The formation of granites can be described by two end member models, one of which views granite to be the ultimate differentiation product of basaltic magma and the other to be product of crustal anatexis. Most granites are considered to have formed by a process somewhere between these two extreme models. One objective of this isotopic study is to propose a likely model for the genesis of the Pan-African granites of SE Brazil.

Sr isotopes can be used as petrogenetic tracers since rocks derived from a homogeneous source or parent magma should all possess the same initial $^{87}Sr/^{86}Sr$ ratios. Similarly, magma derived from sources with low Rb/Sr (i.e. the mantle) should have low initial Sr ratios whereas those derived from crust which is both old and has high Rb/Sr, should have high initial ratios. Initial $^{87}Sr/^{86}Sr$ ratios of less than 0.704 generally suggest no crustal involvement and that the magma is derived from a mantle source although derivation from a very young crust is also possible. Intermediate initial ratios suggest either fusion of continental crust with a low Rb/Sr ratio, derivation from enriched mantle, or contamination of magmas by assimilation of older crust. High Rb/Sr and initial $^{87}Sr/^{86}Sr$ ratios of greater than 0.712 suggest that a high proportion of the Sr comes from old crustal sources and that the melt is derived entirely from the continental crust.

Nd isotopes can be used as powerful tracers and their usefulness is due to two geochemical properties of the rare earth elements. The first is that they are not very mobile in aqueous fluids and the second is that large geochemical fractionation of the parent/daughter Sm/Nd ratio does not generally result from crustal processes They can therefore be used to see back to major crust-forming events (Hawkesworth 1982), and they can also be used to distinguish mantle-derived rocks from those which have incorporated crustal material.

Combined Nd and Sr isotope determinations are used to constrain the proportion of reworked older crust to juvenile crustal growth. In this study they are used to investigate crustal growth in the Pan-African/Brasiliano Orogenic event.

The main objectives therefore of this chapter are :-

1. To establish possible sources for the various granitoids using Sr isotopes and Rb/Sr source calculations and to test relationships between granitoids proposed in previous chapters.

2. To determine the crustal prehistory of the source material using Nd model ages.

3. To establish whether the Brasiliano granitoids of South Brazil represent a major period of crustal growth or largely reworked crust generated in an earlier orogeny.

The ages of samples used in calculating isotope ratios are presented in appendix D and plotted against a schematic cross-section in figure 7.1. The ages used for the Pelotas Batholith are based on errorchrons from this study, with the exceptions of the Canguçu Red Granite which is assumed to be 500m.y.as is unfoliated (D3 is dated at 508m.y.), and the Cascata Leucogranite which is assumed to be 465m.y., as its field relations suggest it is similar in age to the unfoliated Pink Granite.

The age of the Encantada Gneisses (2030m.y.) is based on the geochronological studies undertaken here but the assumed schist age of 1000m.y. is based on previous work (Soliani 1986). The assumed age of the Campinas Granite and Encruzilhada Granite are also based on Soliani's study but the Caçapava Granite has been dated as 475m.y.by this study.

7.3.2. Nd isotope Geochemistry

Nd isotopic ratios have been determined for selected granitoids, volcanics, sediments and metamorphic rocks from the BR392 section and these are presented in Appendix D. Continental rocks are generally enriched in LREE, with minor variation in Sm/Nd ratio; the resulting narrow range in $^{143}Nd/^{144}Nd$, makes this a poor method for dating continental rocks. However, from the measured $^{143}Nd/^{144}Nd$ and Sm/Nd ratios it is possible to calculate the model Nd age.

7.3.2.1 MODEL ND AGES

The model Nd age represents the time at which a continental rock or its precursor was derived from a model mantle reservoir. The calculation of model age is given in appendix D and based on the parameters given by Ben Othman and Allegre (1984). This is based on the assumption that the upper mantle is LREE depleted and that the process responsible for the major change in Sm/Nd ratio is the formation of new continental crust. It is assumed that Sm/Nd does not fractionate once the source magma has left the mantle to form continental crust.. Figure 7.8 illustrates that Sm/Nd ratios from granites, gneisses and sediments from the Dom Feliciano Belt generally lie between 0.1 and 0.25 with strong fractionation within the unfoliated granites.

The Cascata Leucogranite has an exceptionally low Sm/Nd ratio. The Encantada Gneisses and Caçapava Granite have low Sm/Nd ratios. The Campinas Granite and Canguçu Red Granite have high Sm/Nd ratios. In contrast to that observed by other authors (Lewis, 1988, Deniel et al, 1987), there appears to be no correlation with silica so fractionation of accessory phases in high SiO_2 rocks is probably not a contributory factor to Sm/Nd fractionation in these samples. The lack of correlation allows model Nd ages to be calculated from the measured Sm/Nd ratio.

If the granite is derived from the mantle by a one-stage process then the model Nd age should be the same as the whole rock emplacement age. If the source was of sedimentary composition then the model age will be an average of all the model ages of rocks that contributed to the source at the time of sedimentation. If the rock is formed from part crust and part mantle, then the model age will be a mixture of the two. If there is fractionation of Sm/Nd from crustal processes, whether igneous or sedimentary, this will further complicate the interpretation of the model age with the more fractionated samples with high Sm/Nd giving a higher model age.

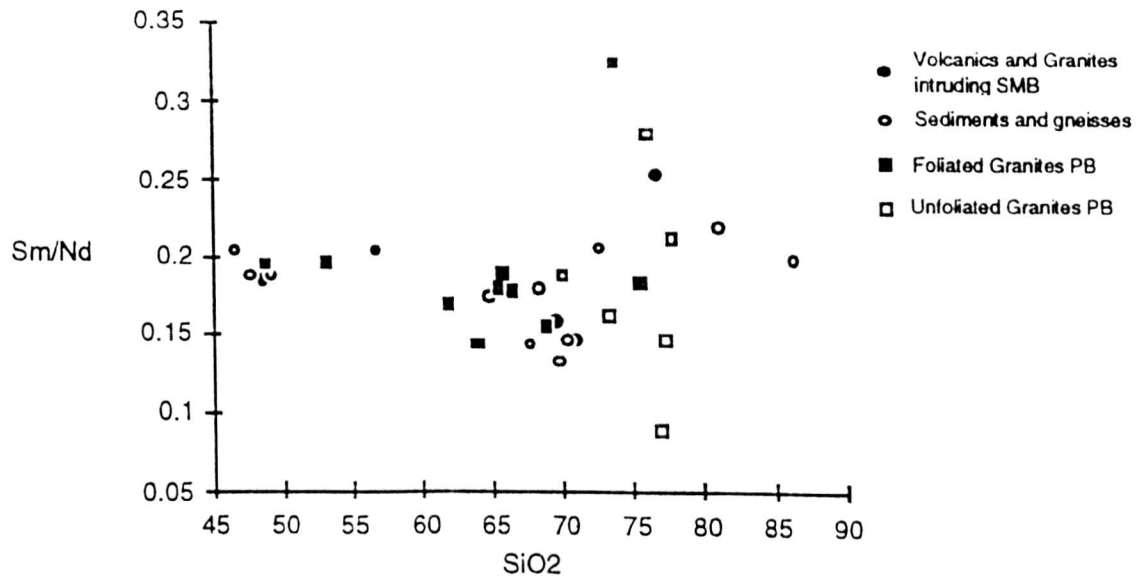

Figure 7.8 Relationship of Sm/Nd to increasing silica fractionation

Figure 7.9(a) illustrates the measured Nd data plotted against distance along the section and illustrates an increase in $^{143}Nd/^{144}Nd$ with distance from Pelotas in the Pelotas Batholith with the unfoliated granites having higher $^{143}Nd/^{144}Nd$ ratios. The Encantada Gneisses have very low ratios. The Caçapava Granite also has low ratios relative to the similar age post-tectonic granites of the Pelotas Batholith. The andesites appear to have similar ratios to the foliated granites of the Pelotas Batholith.

Model ages are calculated relative to depleted mantle for samples from various units using the parameters of Ben Othman and Allegre (1984) (Appendix D). The data are shown in figure 7.9b and compared to a schematic cross section and the least model Nd ages are given in table 7.3 to give a general indication of differences between various rock types of the Dom Feliciano Belt The complete data set of the 44 samples analysed for Nd is given in Appendix D.

Pelotas Batholith	**Least Model Age (TDM)**
Cascata Orthogneiss	1600 m.y.
Migmatitic Orthogneiss	1600 m.y.
Cascata Leucogranite	1200 m.y.
Quarry Pink Granite	1200 m.y.
Canguçu Red Granite	2500 m.y.
Basalt Dyke	650 m.y.
Metasediment	650 m.y.
Santana Metamorphic Belt	
Encantada Gneisses	2500 m.y.
Metagabbro	1400 m.y.
Schist	2000 m.y.
Caçapava Granite	2200 m.y.
Sedimentary Basin	
Andesite	1600 m.y.
Red Bed	1400 m.y.

Table 7.3 Least model Nd ages of all calculated ages from each intrusion

There appears to be a general decrease in model age with distance from Pelotas in the Pelotas Batholith (fig 7.9b) with the unfoliated granites tending to have younger model ages with the exception of the Canguçu Granite which has high Sm/Nd ratio and this may have an older source. This is supported by its high Rb/Sr ratio (fig. 7.11).

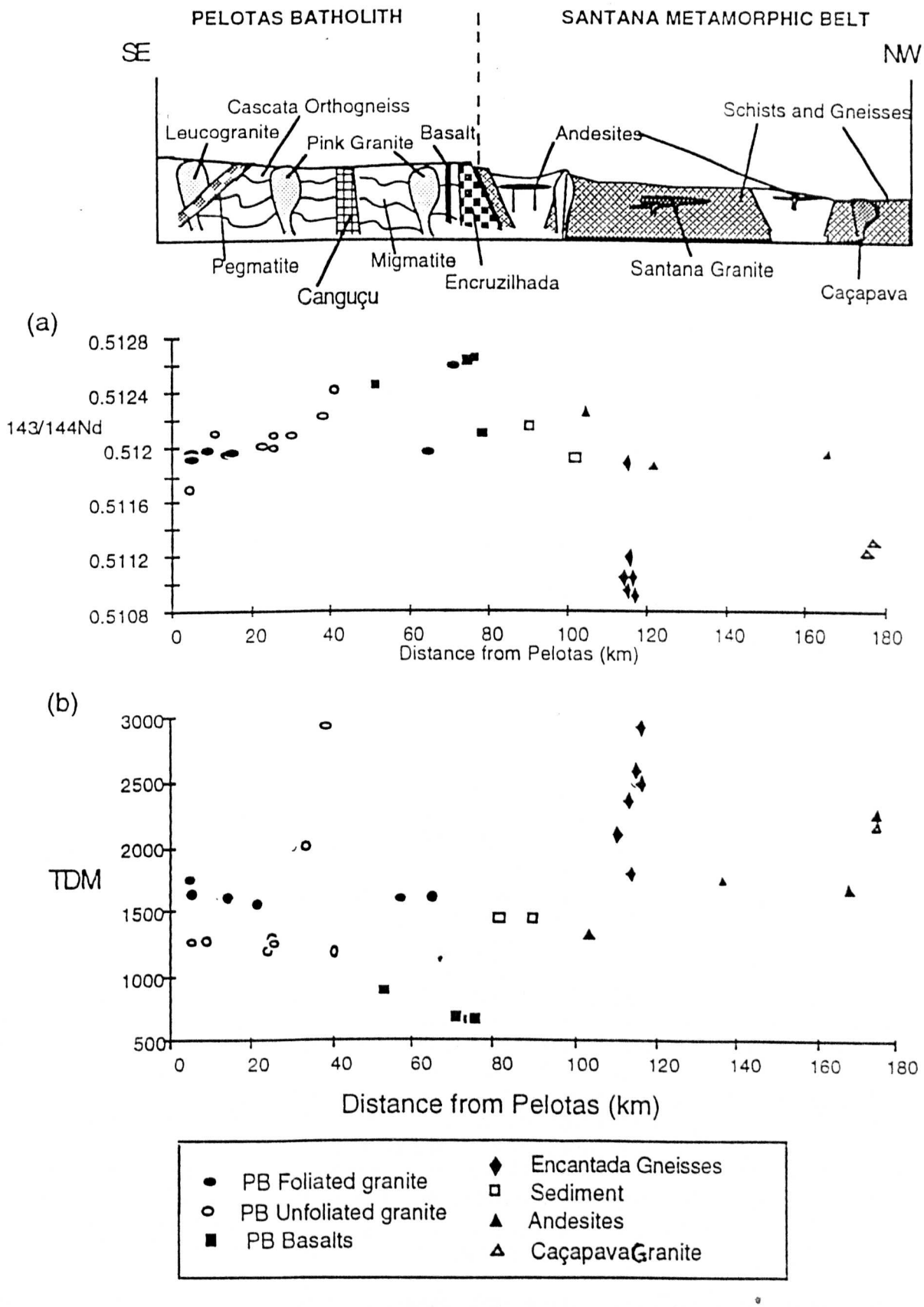

Figure 7.9(a) Measured 143/144Nd and (b) Nd model age (TDm)plotted against distance from Pelotas.

The basalts have low model ages and represent a different tectonic event with different sources. The Santana Metamorphic Belt gneisses and granites have much higher model ages which tends to suggest different source regions.

From table 7.3 it can be observed that the Pelotas Batholith foliated granites have a least model age of 1600 m.y. compared with intrusion ages ranging between 600 and 500 m.y. This therefore implies that these granites represent reworked crust. The unfoliated granites have least model ages of 1200 m.y. which again suggests they formed by the reworking of older crust since the intrusion ages range between 500 and 400 m.y. The Canguçu Red Granite appears to have a more ancient source with its 2000m.y. model age. More recent volcanic activity in the Pelotas Batholith caused the intrusion of basaltic dykes with model ages of 600 m.y. which implies a Proterozoic source for these basalts and associated metasediments.

In contrast, the Santana Metamorphic Belt has much older model ages of 2000-2500 m.y. (figure 7.9). This relationship is explored further in chapter 8. The Caçapava Granite has a least model age of 2200 m.y. suggesting it came from a source similar to that of the Encantada Gneisses. This confirms the relationship established in section 7.3.2.3. The andesites extruded in the basin between the two belts have model ages of 1600 m.y. which suggests they may have a similar source to the foliated granites from the Pelotas Batholith. The red beds interbedded with the andesites have model ages of 1400 m.y. which is an average age of all the potential sources of sedimentation in the basin. None of the granites intruding the Pelotas Batholith or the Santana Metamorphic Belt has been directly evolved from the mantle. The Brasiliano Orogenic event appears to have recycled older crust with no evidence of significant crustal growth within the study area.

7.3.2.2 εND NOTATION

The εNd notation is used by De Paolo and Wasserburg (1976) to enable different rock types to be compared isotopically to bulk earth independent of their age. The calculation of εNd is given in Appendix D and strictly refers to the value at time t by definition. In this instance, the εNd notation refers to the value at the time of intrusion of an igneous rock or formation of a sedimentary rock . Therefore εNd = εNd(t) for the purpose of this study.

Figure 7.10 illustrates εNd plotted against emplacement age for various rocks from the Dom Feliciano Belt. The majority of samples have significantly negative εNd values which suggests they are formed by the reworking of old crust. Previous work undertaken on composite samples from the Pelotas Batholith found the samples to lie between -5 and -15 (Mantovani et al 1988). The majority of granitoids fall between -5 and -10 which is comparible with data from the Damara Belt in Namibia (Mc Dermott 1986).

The andesites from the red bed basin have a significant crustal component along with all the granites intruding the Santana Metamorphic Belt. The Canguçu Red Granite from the shear zone in the Pelotas Batholith has a high negative value between -10 and -15 and the Caçapava Granite intruding the northwest part of the Santana Metamorphic Belt has an exceptionally high negative value of -20 reflecting an ancient source. The only samples to have positive values are the basaltic dykes intruding the Pelotas Batholith and some of the Early Proterozoic Encantada Gneisses from the Santana Metamorphic Belt. This data confirm that the Brasiliano Orogenic event was predominantly a period of crustal reworking rather than of crustal growth.

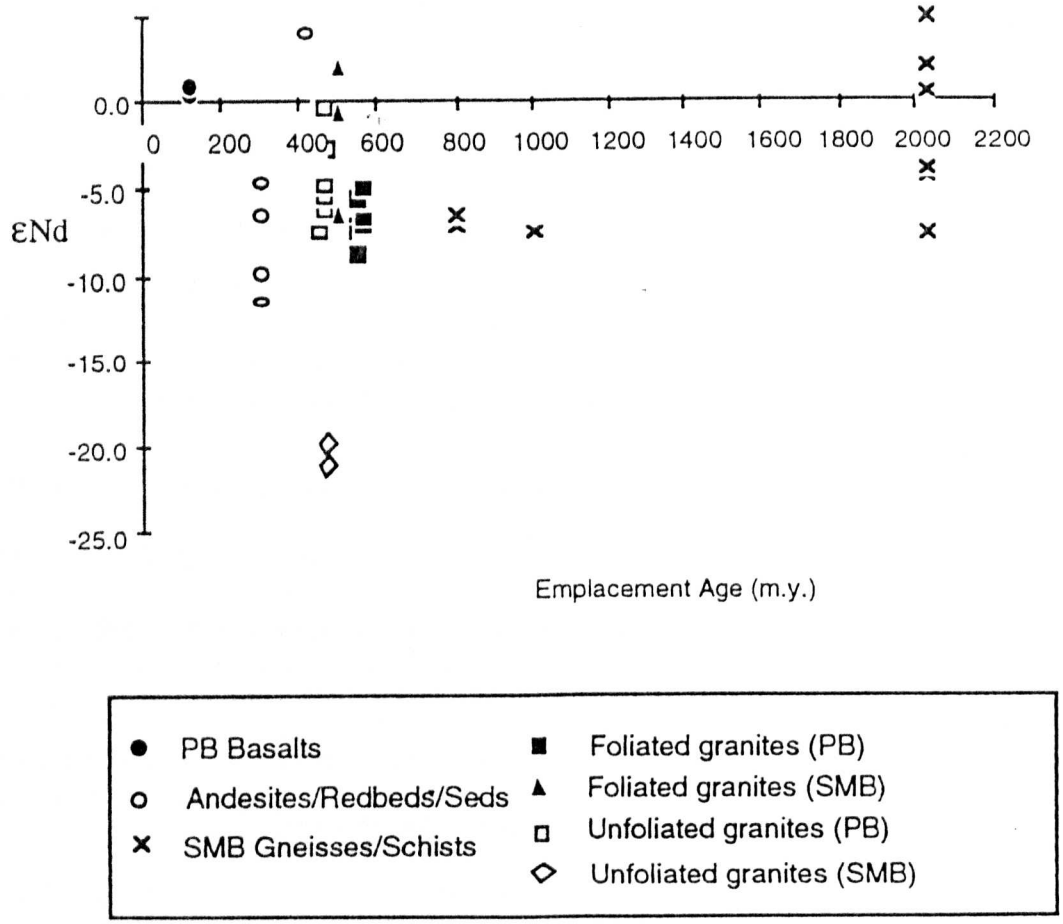

Figure 7.10 εNd plotted against emplacement age for analysed samples from the Dom Feliciano Belt.

7.3.3 Sr Isotope Geochemistry

Measured 87Sr/86Sr ratios and the calculated initial ratios are presented in Appendix D. Samples were collected at regular intervals along the BR392 road section between Pelotas and Caçapava do Sul, and figure 7.11a shows the initial $^{87}Sr/^{86}Sr$ ratios plotted against distance from Pelotas. The intrusion ages are illustrated in figure 7.11b. There appears to be no significant change in initial $^{87}Sr/^{86}Sr$ with distance or between the two belts. However the Canguçu Granite has very high initial Sr. The characteristics of this granite are unusual to the area and need to be investigated further. The basalts and Encantada Gneisses have lower initial ratios possibly suggesting a mantle source. Samples were also collected from individual plutons and the measured 87Sr/86Sr ratios along with the assumed ages are presented in Appendix D for each granitoid type.

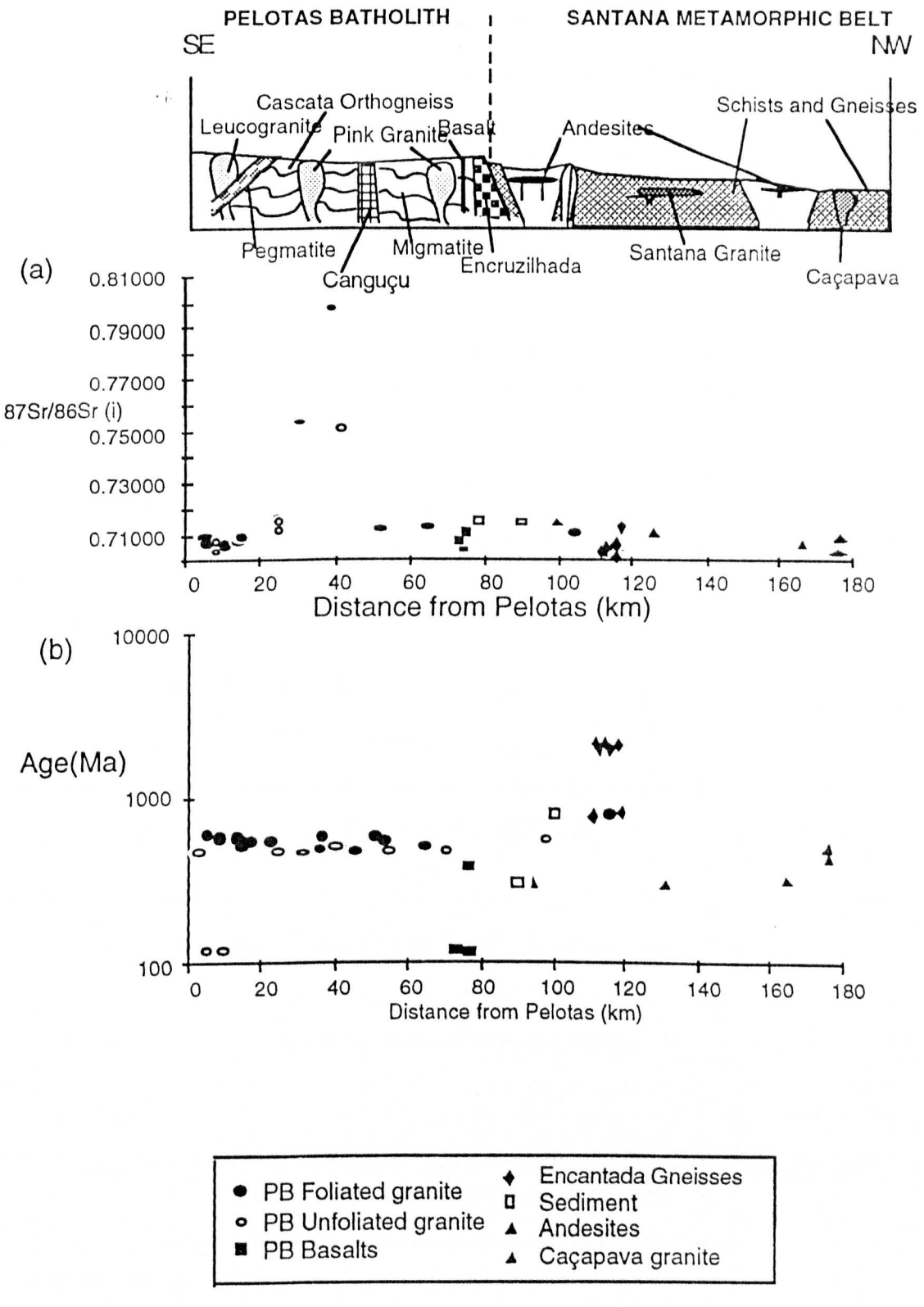

Figure 7.11
(a) Initial 87Sr/86Sr ratio plotted against distance from Pelotas
(b) Emplacement age plotted against distance from Pelotas

7.3.3.1 SR EVOLUTION

Calculated initial ratios are plotted on a Sr evolution diagram in figure 7.12. Initial ratios between 0.708 and 0.710 for the Pelotas Batholith foliated granites suggest some involment of a crustal component.

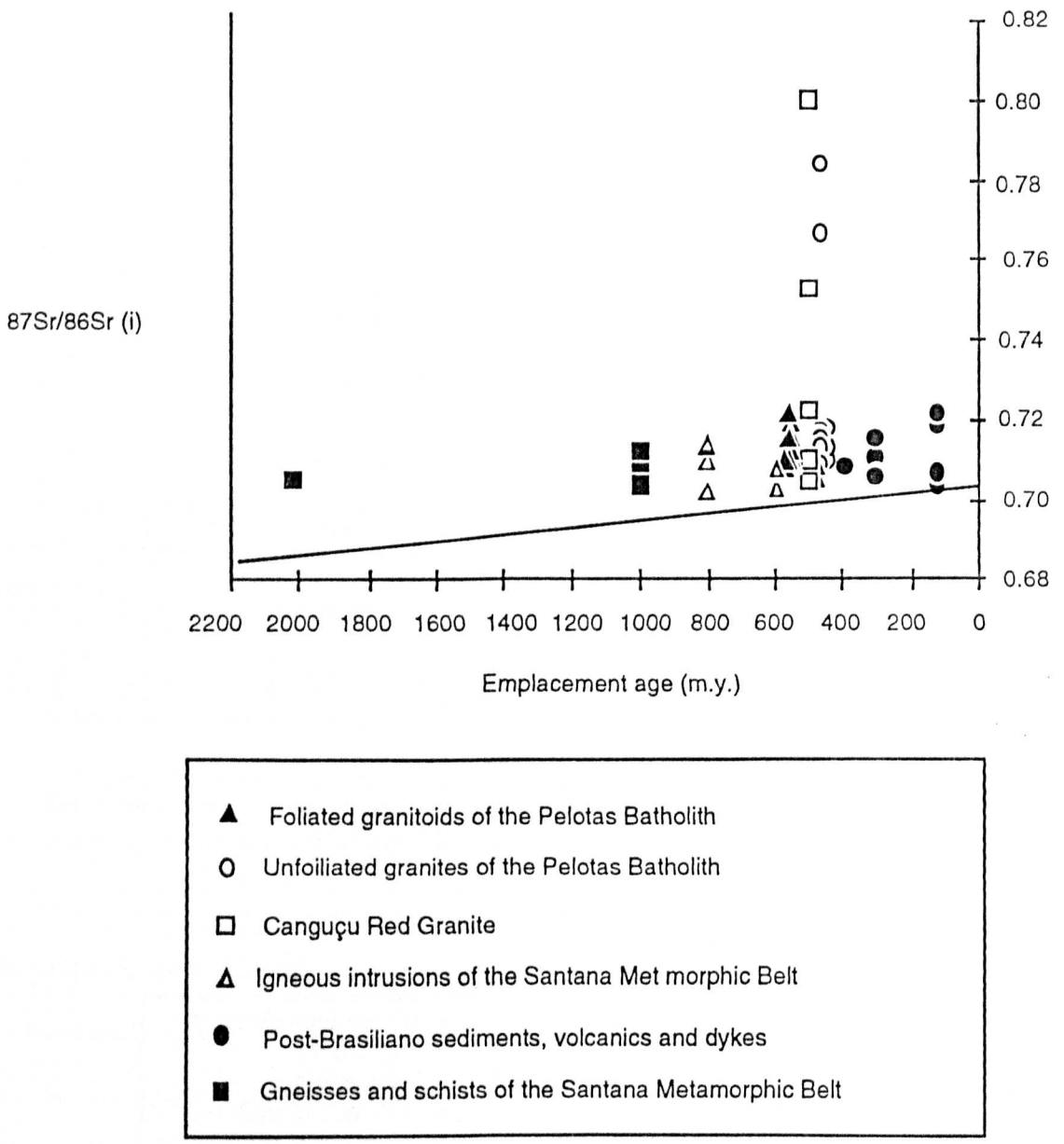

Figure 7.12 87Sr/86 Sr evolution diagram for all the samples analysed in this study.

The unfoliated granites initial ratios between 0.709 and 0.840 suggesting a large component of crustal melting involved in their formation. The basalts intruding the batholith have low initial ratios of 0.703 and 0.705 suggesting that they formed from a mantle source consistent with an extensional setting.

In the Santana Metamorphic Belt the gneisses are plotted at 2000 m.y. and lie quite close to the mantle evolution line with a low initial ratio of 0.7045 suggesting that the sediments from which they were derived had a juvenile crustal source. The schists plot at 1000 m.y. with initial ratios of between 0.707 and 0.712 indicative of variable crustal sources. The Santana Granite has an initial ratio of 0.710 which may indicate crustal melting at 800 m.y. in contrast to the gabbros (800m.y.) that have a low initial ratio of 0.703. The andesites have initial ratios of 0.707-0.715 and are possibly the extrusive equivalents of the Pelotas Batholith granitoids preserved in a down-faulted basin. Unfortunately there is no constraint on their age of extrusion.

The unfoliated granites intruding the Santana Metamorpic Belt have initial ratios ranging between 0.705 for the Caçapava Granite, 0.707 for the Encruzilhada Granite which could be mantle-derived and 0.723 for the Campinas Granite which is certainly a crustal melt from its geochemical properties (Chapter 6).

No analysed granites lie close to the Bulk Earth evolution trend and therefore none is likely to have been derived from a mantle source. Remaining models include a mantle source contaminated with sediment, reworked immature sedimentary crustal source or an igneous source with both crustal and mantle components. It is the object of this section to distinguish which of these models applies to the granites of the Dom Feliciano Belt.

7.3.3.2 εSR NOTATION

The εSr notation is used by De Paolo and Wasserburg (1976) to enable different rock types to be compared isotopically to bulk earth independent of their age. The calculation of εSr is given in Appendix D. Bulk earth has a value of zero. A positive value for a sample indicates a higher $^{87}Sr/^{86}Sr$ ratio at the time of formation and hence a possible crustal component. A negative value suggests a mantle source.

Figure 7.13 compares the εSr of the Dom Feliciano Belt rocks with granites from known tectonic settings (Harris et al 1986) VAG granites plot around εSr=0 and there is some suggestion that the foliated granites of the Pelotas Batholith may be volcanic-arc granites. Syn-collision Himalayan leucogranites plot between 400 and 1000 and the Canguçu Red Granites with high εSr may have formed in a tectonic environment of this nature.

Other unfoliated granites lie between 0 and 400 and the Santana Metamorphic Belt granites have a similar range of εSr values. This comparison is however not comprehensive and only gives an indication of how the Sr isotope data for Brazilian granites compare with the data from granites formed in known collision environments.

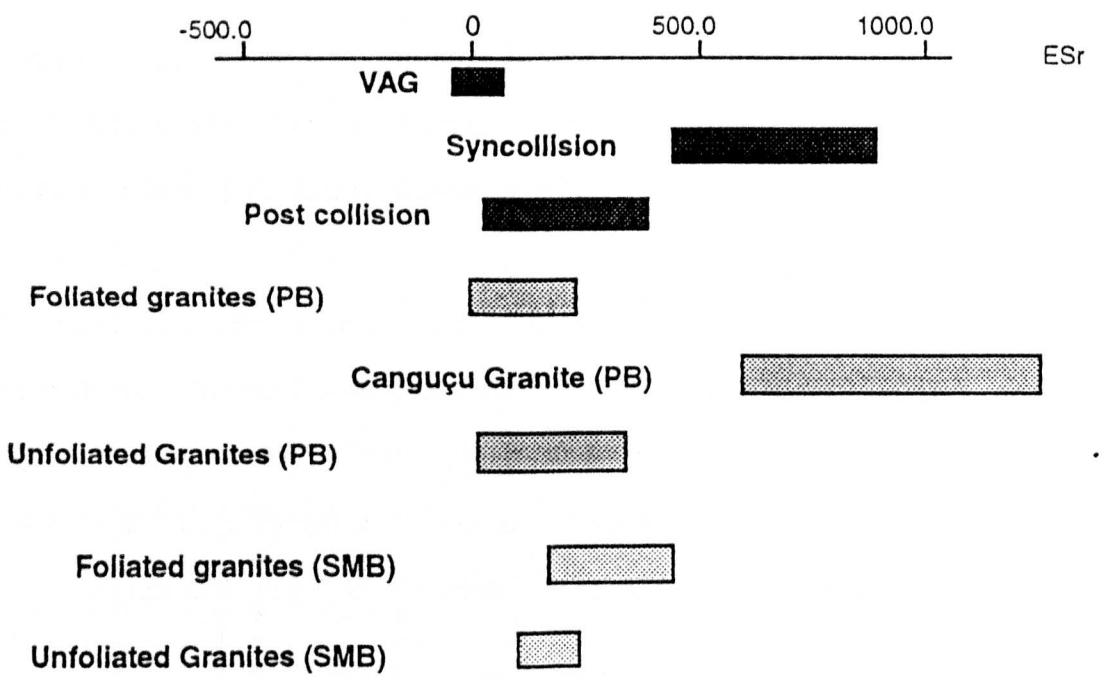

Figure 7.13 E Sr from Dom Feliciano belt compared with data from collision zone magmatism (Harris et al 1986).

7.3.4 Investigation of possible sources of granite magmas.

7.3.4.1 SPECIFIC SOURCES BASED ON FIELD ASSOCIATION

Sr isotope studies may test and constrain the inter-relationships between granitoids that are suggested by the study of their field relations and geochemistry. By calculating and comparing the initial Sr ratio of the suspected source at the time of intrusion of the granite, crustal melt models can be tested.

Similar initial ratios for the granite and source are consistent with the hypothesis that the particular granite was derived from that particular source. The following calculations are used to relate granites with proposed source regions.

$$(^{87}Sr/^{86}Sr)_{ig} = (^{87}Sr/^{86}Sr)_{pg} - (^{87}Rb/^{86}Sr)_{pg}(e^{\lambda t}-1)$$

at time of formation of granite in question

$$(^{87}Sr/^{86}Sr)_{ts} = (^{87}Sr/^{86}Sr)_{ps} - (^{87}Rb/^{86}Sr)_{ps}(e^{\lambda t}-1)$$

at time t of extraction of above granite from the source

Where

$(^{87}Sr/^{86}Sr)_{ig}$ = Initial ratio of granite

$(^{87}Sr/^{86}Sr)_{ts}$ = Sr ratio of the source at the time of formation of the granite

$(^{87}Sr/^{86}Sr)_{pg}$ = Present day Sr ratio of the granite

$(^{87}Sr/^{86}Sr)_{ps}$ = Present day Sr ratio of the source

t = time of formation of the granite $\lambda=1.42 \times 10^{-11}a^{-1}$

If $(^{87}Sr/^{86}Sr)_{ig} = (^{87}Sr/^{86}Sr)_{ts}$ then Sr data are consistent with that the granite in question being derived from the conjectured source. The interrelationships established in previous chapters will be investigated in this way:

A. Santana Metamorphic Belt

In Chapter 6 it was proposed that the Santana Granite was related geochemically to the Encantada Gneisses and that it may be a partial melt of the them. Using the above calculations at 800m.y.

$(^{87}Sr/^{86}Sr)_{ig} = 0.7106\pm4$

$(^{87}Sr/^{86}Sr)_{ts} = 0.7096\pm20$

which are equal within error suggesting that the Encantada gneisses are a likely source for the formation of the Santana Granite. The isotope data is thus consistent with field and geochemical evidence.

The Campinas Granite is a two mica granite and very probably a crustal melt of either sediments or gneisses at the shear zone between the Sanatana Metamorphic Belt and the Pelotas Batholith since its $(^{87}Sr/^{86}Sr)_{ig} = 0.7237\pm25$.

The initial ratio of 0.7059±5 suggests that the Caçapava Granite is derived from a mantle source or from a juvenile crust from the Santana Metamorphic Belt such as would be generated during active subduction under the area.

B. Pelotas Batholith

Field relations and geochemistry have indicated that the Pink Granite may be derived from the melting of the Migmatitic Orthogneiss. Using the above calculation at 465 m.y which is the age of formation of the Pink Granite:

$(^{87}Sr/^{86}Sr)_{ig} = 0.7154\pm5$

$(^{87}Sr/^{86}Sr)_{ts} = 0.7148\pm7$

The similarity in these two ratios support the Migmatitic Orthogneiss as a possible source for the Pink Granite. This calculation however does not constrain the process by which one was formed from the other.

7.3.4.2 RB-SR SOURCE CALCULATIONS

Having calculated model Nd ages for the granites of the Dom Feliciano Belt (table 7.3), it is then possible to estimate the 87Rb/86Sr ratio in the source in an attempt to identify the most probable source region. This can be done using the equation:

$$^{87}Rb/^{86}Sr \text{ source} = \frac{R_s(t1) - R_{Dm}(t2)}{e^{\lambda(t2-t1)} - 1}$$

Where

R_st1 = the initial $^{87}Sr/^{86}Sr$ ratio of the sample at the time of emplacement

$R_{Dm}t2$= the initial 87Sr/86Sr ratio of the depleted mantle at the time given by the model age

$\lambda\,^{87}Rb = 1.42 \times 10^{-11}$

$^{87}Sr/^{86}Sr$ (BE) = 0.7047

$^{87}Rb/^{86}Sr$ (BE) = 0.0847

$^{87}Sr/^{86}Sr$ (Dm) = 0.7026 (Jacobsen and Wasserburg, 1979)

$^{87}Rb/^{86}Sr$ (Dm) = 0.0541 (Goldstein and Jacobsen, 1988)

Figure 7.14 presents the results of this calculation and it can be observed that the calculated $^{87}Rb/^{86}Sr$ for the source of all the foliated granites lie between the values of 0.9 for average continental crust (Taylor and Mc Lennan, 1985) and of 0.35 for Bulk Continental Crust. The implied sources for the unfoliated granites of the Pelotas Batholith have higher $^{87}Rb/^{86}Sr$ ratios than Bulk Continental Crust which supports the hypothesis that all the granites of the Pelotas Batholith are crustal mellts. $^{87}Rb/^{86}Sr$ for the source of the Caçapava, Granite of the Santana Metamorphic Belt lies below the crustal field suggesting a mantle source for this granite.

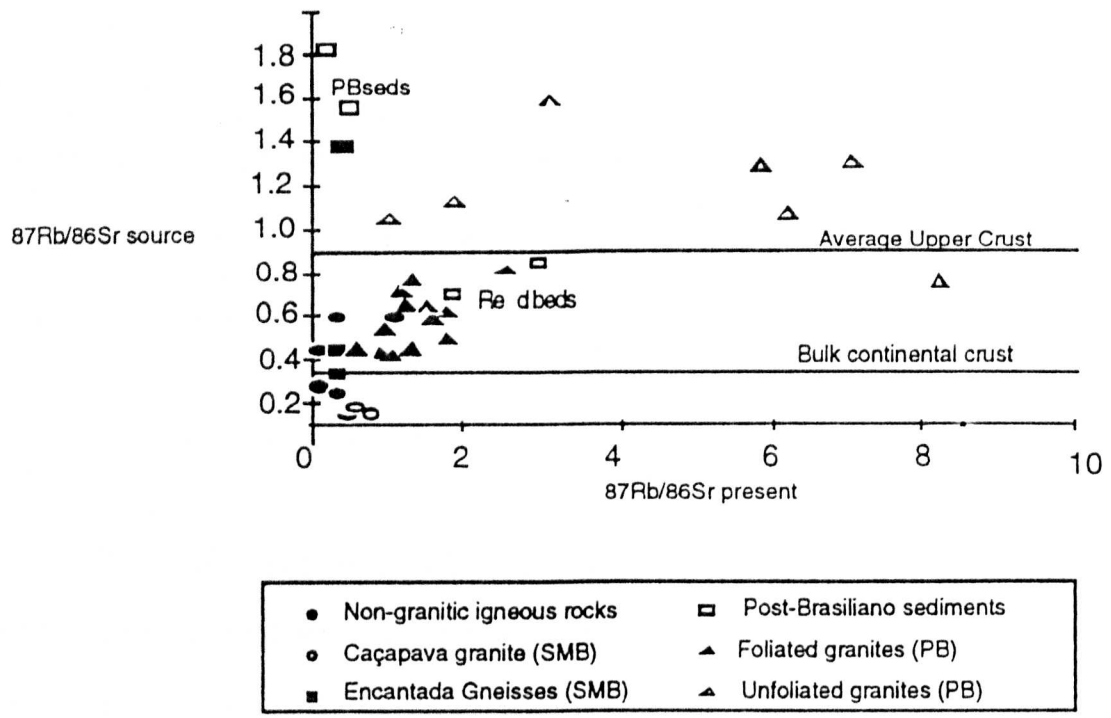

Figure 7.14 Comparison of calculated 87Rb/86Sr in source against present day values for samples.

7.3.5 Combined Nd and Sr isotope studies.

Combined Nd and Sr isotope studies on granitic rock (Allegre and Ben Othman 1980) have concluded that large amounts of recycled crust must be involved in Phanerozoic granitoid genesis. In contrast many Precambrian granitoids >600 m.y. have initial Nd and Sr values close to that of the mantle. Rb-Sr and Sm-Nd isotopic data are presented in figure 7.15 using the ε-notation which enables different rock types to be compared isotopically, independent of age. Fields for these granitoids are given in Fig. 7.16 together with fields for other Pan-African terranes. A "mantle array" is defined in the top left hand quadrant by oceanic basalts. Granites that plot in the lower right hand quadrant may be modelled by mixing lines that combine crustal and depleted mantle sources (De Paolo 1981, Mc Culloch and Chappell 1982).

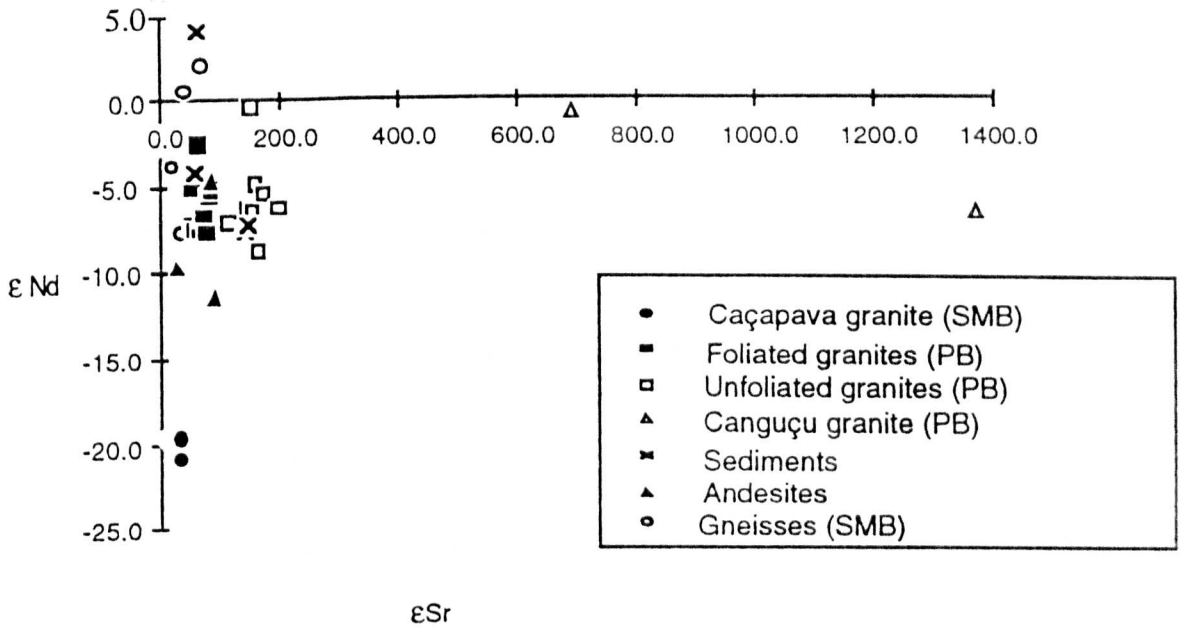

Figure 7.15 εSr vs εNd for all samples analysed in this study. The Canguçu Red Granite has exceptionally high εSr as a result of its high Rb/Sr ratio.

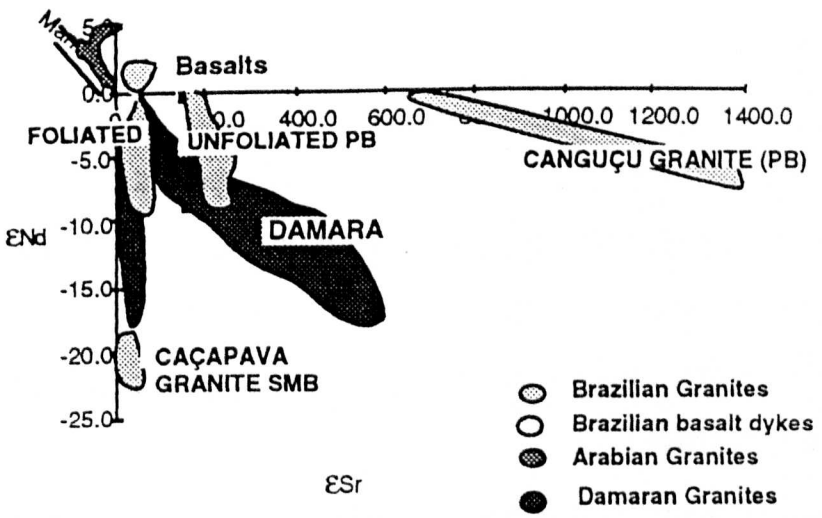

Figure 7.16 Granitoids from the Dom Feliciano belt compared with granitoids from the Damara belt of Namibia (Mc Dermott 1986) and the Arabian Shield (Duyverman et al 1982).

The Pelotas Batholith granitoids have εNd values between -3 and -10 and the majority of εSr values between 0 and 200 with the Canguçu Red Granite having exceptionally high values of 800-1400 due to the high Rb/Sr in their source. Comparing foliated with unfoliated granites, there appears to be an increase in εSr with time indicating an increasing Rb/Sr ratio in the crustal source.

The fields from the Damara Belt in Namibia (Mc Dermott 1986) and the Arabian field of Duyverman et al (1986) are plotted for comparison with the Pelotas Batholith. Although both granitoid suites were formed during the Pan-African Orogeny, the former results from crustal reworking wheras the latter is an example of rapid crustal growth. In general, granitoids from the Dom Feliciano Belt of south Brazil overlap with the Damara rocks confirming a crustal reworking model. The foliated granites have extremely high εSr values suggesting an unusually high Rb/Sr ratio in the source. In the Santana Metamorphic Belt the Caçapava Granite has a strongly negative field which reflects its old primitive crustal source.

7.3.5 Summary and discussion

The Brasiliano granitoids can be classified into 4 groups on the basis of this isotopic study (fig 7.15); foliated granitoids from the Pelotas Batholith (εNd ratios between -5 and -10), εSr between 50 and 150, unfoliated granitoids from the Pelotas Batholith with similar Nd values and εSr values between 100 and 200, the Canguçu Red Granite within the Pelotas Batholith (extremely high εSr), and the Caçapava Granite intruding the Santana Metamorphic Belt (extremely negative εNd)

Harris et al (1986) collated available Nd data from sediments and granitoids in southern Africa that are compared with the data from southern Brazil.(Fig 7.17) Both subcontinents have Archaean cratonic blocks and Brasiliano/Pan-African age mobile belts. There are clearly recognized mid-Proterozoic mobile belts in both terranes. Orogenic events in southern Africa have been recognized at about 500-800 m.y., 1.4b.y. and 2b.y.. This compares with the Orogenic events recognized in Southern Brazil at 2b.y. for the Encantada

Gneisses, 1.6-1.2 for the source of the Pelotas Batholith, 800m.y. for the Santana Granite and 650-450m.y. for the intrusion of the granitoids of the Pelotas Batholith.

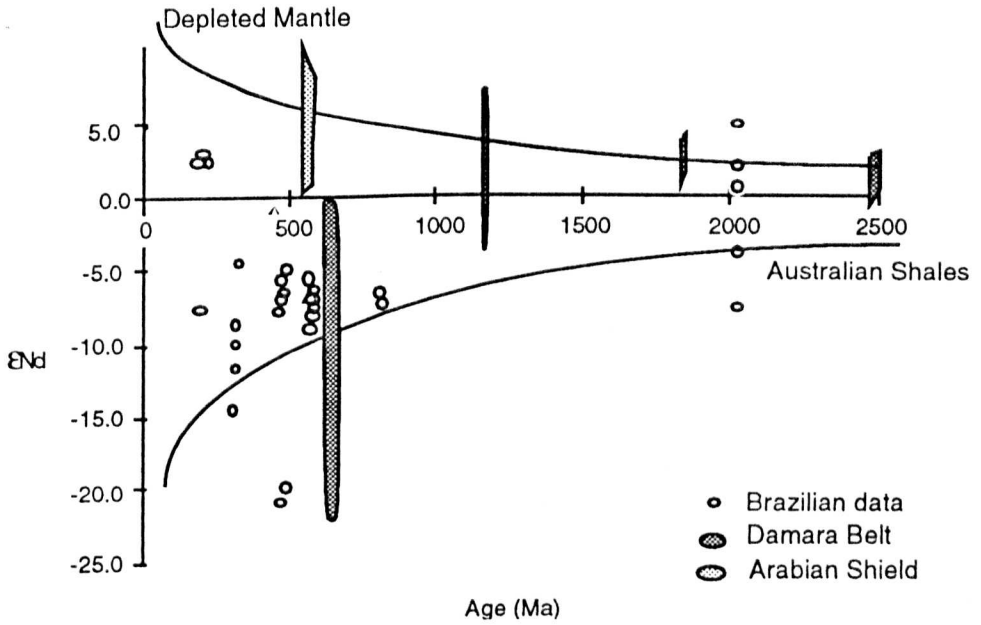

Figure 7.17 Comparison of Brazilian Samples with the Damara Belt of Namibia, Arabian shieldGranites and the growth curves for the Australian shales and depleted mantle.

The similarity of the variation of εNd in rocks of different ages from southern Africa and Brazil is striking. (figure 7.17). The Brasiliano event produces little new crust and reworks crust of 2.2-1.2 b.y.. In terms of African orogenic events, the Pan-African orogeny of Southern Brazil was essentially a reworking event that remobilized Proterozoic crust of Eburnian (~2.0b.y.) and Kibaran (~1.4b.y.) age.

However the period of extension following this event resulted in some new crust in the form of basaltic dykes and leucocratic aplite veins. The Dom Feliciano Belt is analogous to the Damara Belt in Namibia in that it is dominated by crustal reworking in contrast to the similar age belt in the Arabian Shield where crustal growth is the dominant process.

BLANK PAGE
IN
ORIGINAL

CHAPTER EIGHT

8. Conclusions

8.1 Introduction

The main objective of this thesis was to establish a cross section through the Dom Feliciano Belt along the recently constructed BR392 road that runs perpendicular to the main strike of the structural trend, in order to unravel the tectonic history of this Late Proterozoic Brasiliano orogenic belt. The geological field relations and stratigraphy, together with the sequence of structural and metamorphic events, provide a geological context for laboratory studies. These have included major and trace element geochemistry, isotope analysis and thermobarometric analysis. The aim of this concluding chapter is to summarize the conclusions drawn from previous chapters and to synthesize these into a tectonic model, which is evaluated in the context of other contemporaneous Pan-African orogenic belts such as the Dom Feliciano Belt in Santa Catarina (Basei 1985), the Damaran Belt in Namibia (McDermott 1986), and the Arabian Belt (Duyverman 1986).

8.2 Conclusions from field based studies.

8.2.1. STRATIGRAPHY OF THE SANTANA METAMORPHIC BELT

From Chapter 2, it has been concluded that the stratigraphy of the Santana Metamorphic Belt can be subdivided into basement and cover units. The basement is composed of the Early Proterozoic Encantada Gneiss formation overlain by the chlorite and biotite schists of the Encantada Schist formation. Intruded into these are the Santana Granite and a gabbroic body. These are then overlain by the pelites and immature granite-rich arenites of the Arroio Arreiao formation. These units comprise the basement rocks of the Santana Metamorphic Belt.

The cover units form a synclinal structure in the SE of the area (fig 2.2a) and are composed of an upper greenschist facies metamorphosed lagoonal sequence of quartzites (Cerro dos Bicudos formation), marbles and graphitic schists (Cerro da Canberra formation). There is however no good evidence for thrusting at the basement-cover interface and the relationship between the cover and basement is not clear. All the stratigraphic units described have been affected by D2 isoclinal folds, and D3 open upright folding. The Arroio dos Nobres formation was deposited after D2. It is unmetamorphosed and deformed only by D3 and younger events. During D4 the Cerro dos Bicudos quartzite was thrust in a NE direction onto the sandstones and conglomerates of the Arroio dos Nobres formation. Undeformed red beds outcrop in extensional basins to the SE and NW of the Santana Metamorphic Belt. The stratigraphy of the Santana Metamorphic Belt is best summarized by referring to a schematic geological cross-section through the area (fig. 8.1).

8.2.2 GRANITOID INTRUSIVE RELATIONS AND PETROGRAPHY

In Chapter 5, it was demonstrated that the granites of the Dom Feliciano Belt can usefully be subdivided into two major groups; foliated granitoids and unfoliated granites. These two groups can be found in both the Pelotas Batholith and intruding the Santana Metamorphic Belt. The Encruzilhada Granite is fault-bounded at the boundary between the two belts and does not fit into this two fold classification. Figure 8.1 illustrates the intrusive relationships of the granitoids of the Dom Feliciano Belt.

Petrographically, the foliated granitoids of the Pelotas Batholith (PB) have a common mineralogy of green biotite, orthoclase, plagioclase and quartz, with accessory minerals distinguishing the different intrusions. The Cascata Orthogneiss and Canguçu Porphyritic Granite have magnetite and sphene as their main accessory minerals whereas the Migmatitic Orthogneiss only has magnetite. The Cascata Orthogneiss has hornblende rich mafic enclaves. The Porphyritic Granite has distinctive large orthoclase phenocrysts.

Of the foliated granites from the Santana Metamorphic Belt (SMB), the Santana Granite has muscovite as an accessory mineral which distinguishes it from the foliated granites of the Pelotas Batholith. The Campinas Granite (SMB) has distinctive large muscovite crystals as a major mineral phase along with biotite, orthoclase and plagioclase.

The unfoliated granites of the Pelotas Batholith are leucocratic with 5% mafic minerals. The Canguçu Granite is red in colour, and it has accessory magnetite whereas the Capao do Leao Granite is distinctive with garnet as an accessory mineral. Both the Pink Granite and Cascata Leucogranite of the Pelotas Batholith have a two feldspar, quartz, biotite mineralogy with accessory muscovite.

The Encruzilhada Granite is fault bounded and outcrops in the fault-zone between both belts. It is distinctive in terms of its mineralogy with hornblende as a major mafic mineral in contrast to the green biotite found in the granites of the Pelotas Batholith and Santana Metamorphic Belt. This supports the view that it formed in a differnt tectonic setting and was then faulted into place (section 8.4). The Caçapava Granite of the Santana Metamorphic Belt is leucocratic and has accessory chlorite and magnetite.

8.2.3 NON-GRANITIC MAGMATISM

Both pre and post-Brasiliano magmatic rocks have been recognized in the Dom Feliciano Belt and these are briefly discussed in this section. The presence of folded amphibolite bands within the Encantada Gneisses of the Santana Metamorphic Belt suggests an early phase of basic magmatism before D2 deformation. There is also evidence of rhyolitic magmatism contemporaneous with the formation of the graphitic schists of the Cerro da Canberra formation, these are also pre-D2 in age and may be related to the intrusion of the Santana Granite. The metagabbro was intruded post-D2 and pre-D3, and subsequently metamorphosed to a hornblendite during the M2 metamorphism event.

Late stage magmatism has been recognized in both the Pelotas Batholith and the Triassic basins. There are late basaltic dykes intruding the Pelotas Batholith and associated flows

which may be Parana (Cretaceous) in age. There are also late aplite veins intruding the Cascata Leucogranite which may also be post-Triassic in age. There are rhyolitic and andesitic flows interbedded with the Triassic red beds suggesting a Triassic age for their extrusion and their location in a down-faulted basin may suggest an extensional setting for their formation.

8.3 Structural and Metamorphic History

8.3.1 DEFORMATION EVENTS

Four phases of deformation have been recognized in the Santana Metamorphic Belt. The first, D1 is only recognized in the Encantada Gneisses of the basement complex. D2-D4 events are identified in the metamorphic rocks of both the basement and cover units, whereas only D3 and D4 have been recognized in the unmetamorphosed Arroio dos Nobres formation. D2 compression was expressed as recumbent isoclinal folding resulting in a pervasive S2 schistosity affecting all units except the Arroio dos Nobres formation. The D3 event resulted in upright open folds with the local development of a vertical NE-SW striking axial planar S3 schistosity. D4 was marked by NE thrusting which emplaced the metamorphosed quartzites onto the unmetamorphosed Arroio dos Nobres formation. Late extension caused reactivation of S3 and S4 fabrics forming NE-SW and NW-SE normal faults.

In the Pelotas Batholith two phases of deformation are recognized; D1g is represented by a biotite foliation in the foliated granodiorites and this corresponds to the D2 deformation of the Santana Metamorphic Belt. D2g is expressed as a vertical E-W striking biotite foliation, and a mylonite fabric in shear zones affecting the foliated granites of the Pelotas Batholith, and this may corresponds to D3 of the Santana Metamorphic Belt. There is some evidence of late extensional faulting in the batholith associated with the emplacement of basaltic dykes.

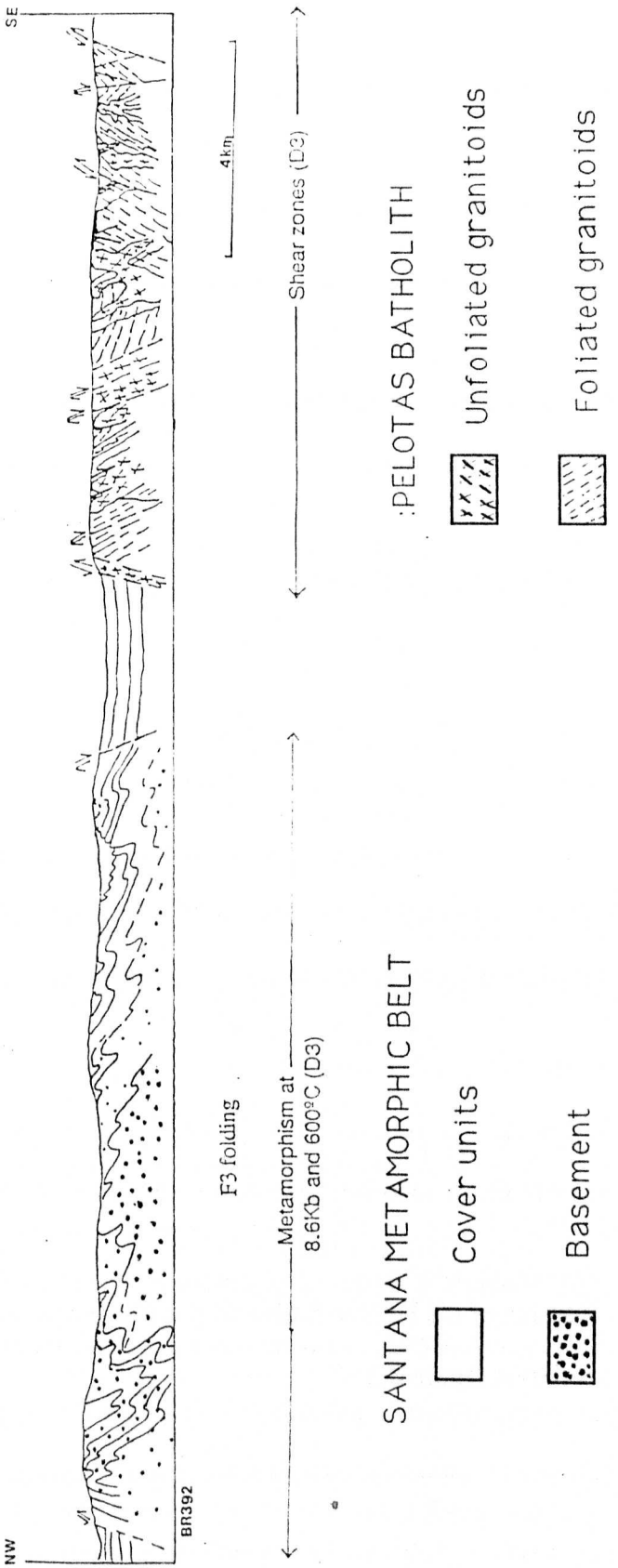

Figure 8.1 illustrating the main structural and metamorphic features of the Dom Feliciano Belt in Rio Grande do Sul (this study).

8.3.2 METAMORPISM

Metamorphism has been studied in the Santana Metamorphic Belt and three phases of metamorphism have been recognized. The first, M1 is associated with the D2 deformation and resulted in mica and garnet growth along the S2 schistosity in the basement gneisses and schists. This is overprinted by M2 metamorphism which reached its peak before F3 folding forming garnet, biotite, muscovite plagioclase and amphibole porphyroblasts in the basement schists. This phase of metamorphism has been studied in detail and peak metamorphic conditions have been established at 8.6 Kb and 600°C for two selected pelites from the basement sequence. Late stage M3 retrogression is recognized by chloritization and tourmalinization. Figure 8.1 presents a cross section through the whole area and compares the structural and metamorphic data of the Santana Metamorphic Belt and the Pelotas Batholith.

8.4 Geochemistry

8.4.1 PELOTAS BATHOLITH

Geochemical studies in the Pelotas Batholith support the field based two fold classification of granitoids, with unfoliated granitoids intruded into foliated granites. Two of the unfoliated granites namely the Capao do Leao and Cangução Granites appear to form a distinct geochemical group and have the characteristics of A-type granites (Collins et al 1980). Geochemical features of the Pelotas Batholith granitoids are presented plotted along the geological cross section in figure 8.2.

The foliated granitoids (Cascata,Migmatitic Orthogneiss, Porphyritic and Piritini Granites) have silica contents of less than 72%, they are calc-alkaline, metaluminous and fall in the VAG field of the Pearce et al (1986) plot. The various foliated granitoids of the Pelotas Batholith show good trends for both major and trace elements elements within and between the different intrusions. Rare earth element data show negative Eu anomalies suggesting plagioclase control. The trace element spidergrams have high Rb/Ba and Nd/Sr ratios, but when compared with melts from known tectonic regimes, do not distinguish between an upper crustal melts and volcanic arc granites.

The unfoliated granites (Pink Granite, Cascata Leucogranite) also fall in the VAG field of the Pearce plot, but from their field relations and geochemistry they are more likely to be post-collision granites. They are more silicic (>72%) and more peraluminous than the foliated granitoids with higher Fe/Mg and K_2O/Rb ratios (fig 8.2). Their rare earth element patterns are similar to those of the foliated granitoids, although there is no Eu anomaly which suggests there is no feldspar fractionation. Their trace element patterns lies between that of an upper crustal melt and a volcanic arc granite, and field relations suggest that they are a crustal melts of the foliated Migmatitic Orthogneiss.

The geochemically distinct Canguçu Granite and Capao do Leao Granite are strongly peraluminous and have an exceptionally high Na content which is distinctive. They are extremely depleted in Sr and enriched in Y and Zr with distinctive high Rb/Sr and Rb/Ba (fig 8.2) compared with the other two groups. They have flat rare earth element patterns with a marked negative Eu anomaly which may suggests feldspar control. These granites fall within the syn-collision field of the Pearce plot and seem to fit the characteristics of A-type granites.

From this summary of the geochemistry of the Pelotas Batholith, it can be observed that there is a geochemical shift with time from metaluminous calc-alkaline granodiorites through to peraluminous granites. There does not appear to be a significant change in geochemistry with distance across the belt (figue 8.2). The evolution of the Pelotas Batholith seems to fit the model of collision zone magmatism of Harris et al (1986).

8.4.2 SANTANA METAMORPHIC BELT

The igneous rocks of the Santana Metamorphic Belt can also be subdivided into foliated and unfoliated groups. Geochemical studies concentrated on the granitic magmatism of the belt, although basement gneisses, schists, a metagabbro and andesite from the Triassic basin were analysed for comparative purposes.

Within the foliated rocks, there appears to be a geochemical link between the Santana Granite and the Encantada Gneisses in terms of their major and trace element geochemistry. The schists and metagabbro however appear to be unrelated to this trend. The Santana Granite is a peraluminous leucogranite, particularly depleted in Rb, Ti and Y, and folded by the D2 deformation. Comparison with crustal melts suggests that the Santana Granite, with its low Rb/Ba ratio, is likely to be a lower-middle crustal melt which supports the proposal that it is a melt of the Encantada Gneiss formation.

The foliated Campinas Granite is a strongly peraluminous muscovite bearing syenogranite enriched in Al_2O3, K_2O, P_2O_5, particurlarly enriched in Rb and depleted in Sr. It has similar major and trace element characteristics (e.g high Rb/Sr and Rb/Ba) to the Canguçu Red Granite of the Pelotas Batholith (figure 8.5). However, it has a different (steeper) rare earth element pattern with no negative Eu anomaly. Its trace element pattern shows a striking similarity to an Upper Crustal Melt and it falls in the syn-collision field of the Pearce (1981) plot, consistent with the field evedence. Its mineralogy and isotopic characteristics (section 8.5) suggest it to be a melt of a pelitic source.

The unfoliated red Caçapava Granite lies in the Monzogranite field of the Streckeisen plot in contrast to the unfoliated granites of the Pelotas Batholith. It shows relatively good trends for major and trace elements and a slight Eu anomaly. The Caçapava Granite lies in the VAG/Post-collision field of the Pearce plot. The spidergram for this granite suggests a strong similarity with a lower crustal melt (low Rb/Ba) and isotopic data supports this proposal.

The Encruzilhada Granite is hornblende bearing and it is fault bounded apparently belonging to neither belt. It plots within the WPG field of the Pearce plot and this is a distinctive feature since no other granites from the study area lie in this field. It shows reasonable trends for major and trace elements and its depleted Sr and rare earth element pattern with a strong negative Eu anomaly suggests a strong plagioclase control. Its trace element pattern strongly resembles that of a Volcanic Arc Granite (high Rb/Sr and Rb/Ba) but isotopic considerations suggests it to be a melt of a within plate basalt.

8.4.3 SPATIAL VARIATION OF GEOCHEMISTRY

Comparing the analytical data from the two belts along a cross-section from Pelotas to Caçapava do Sul (fig.8.2) there appears to be no striking relationship between geochemistry and distance across the Dom Feliciano Belt and no noticable change in the geochemistry of granitoids between the Santana Metamorphic Belt and the Pelotas Batholith.

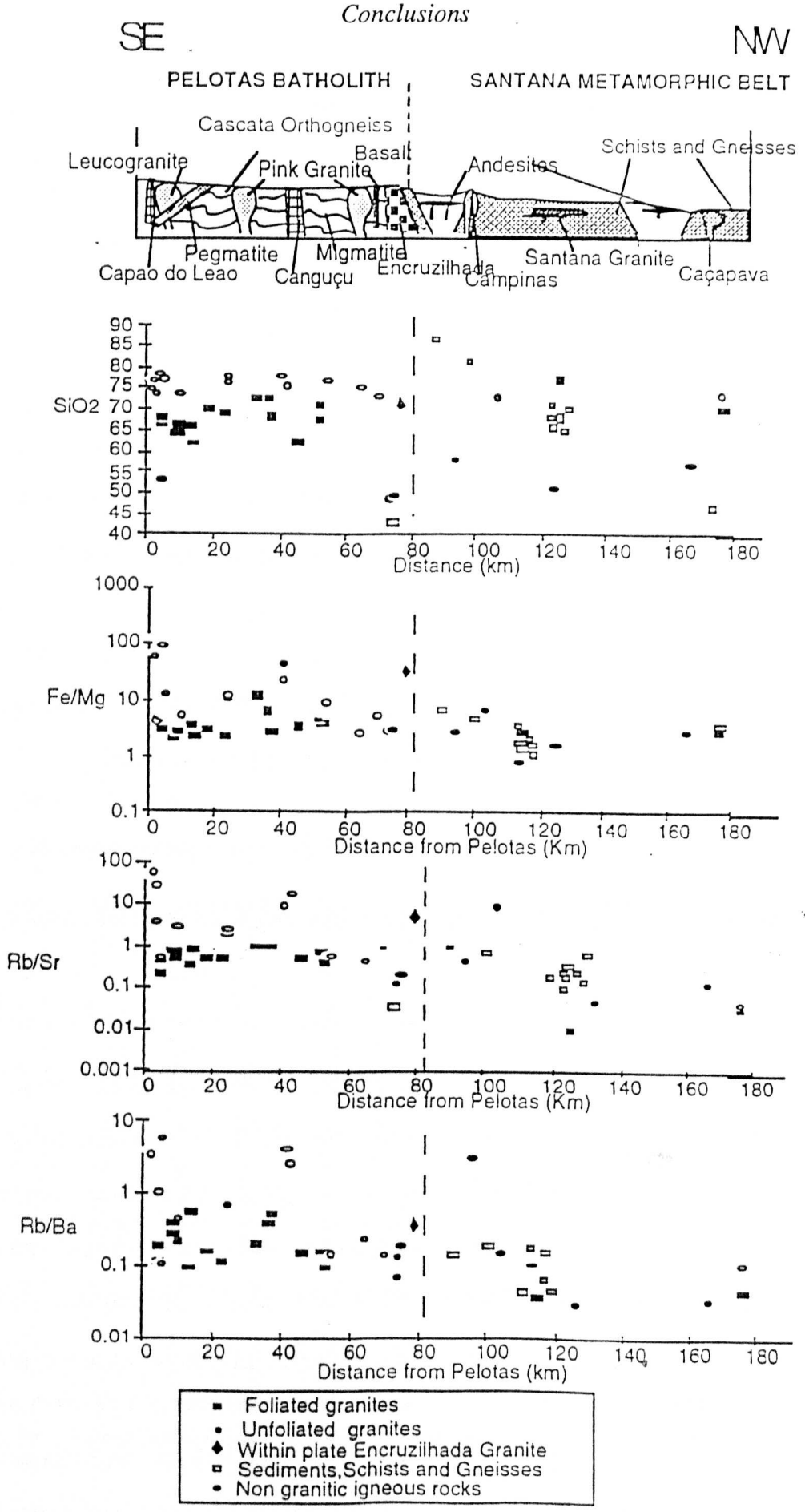

Figure 8.2 Comparative geochemistry of the Pelotas Batholith and the Santana Metamorphic Belt along the BR392 road section.

The geochemical changes appear to be temporal and related to a collision event with foliated and unfoliated granitoids being geochemically distinct and the younger granites more geochemically evolved. The Cangucu and Capao do Leao unfoliated granites have a distinct geochemical signature suggestive of A-type granites.

8.5. Isotopic Conclusions

8.5.1 GEOCHRONOLOGY

Geochronological studies of the Dom Feliciano Belt are best summarized by table 8.1.

SANTANA METAMORPHIC BELT		
Intrusion	Age (m.y.)	Initial ratio
Encantada Gneisses	2030±72	0.7045±47
Caçapava Granite	474±50	0.7059±5
PELOTAS BATHOLITH		
Intrusion	Age (m.y.)	Initial ratio
Cascata Orthogneiss	572±54	0.7089±1
Migmatitic Orthogneiss	556±46	0.7104±77
Sheared granite	508±7	0.7159±10
Pink granite	465±65	0.7154±56

Table 8.1 Established dates from geochronological studies.

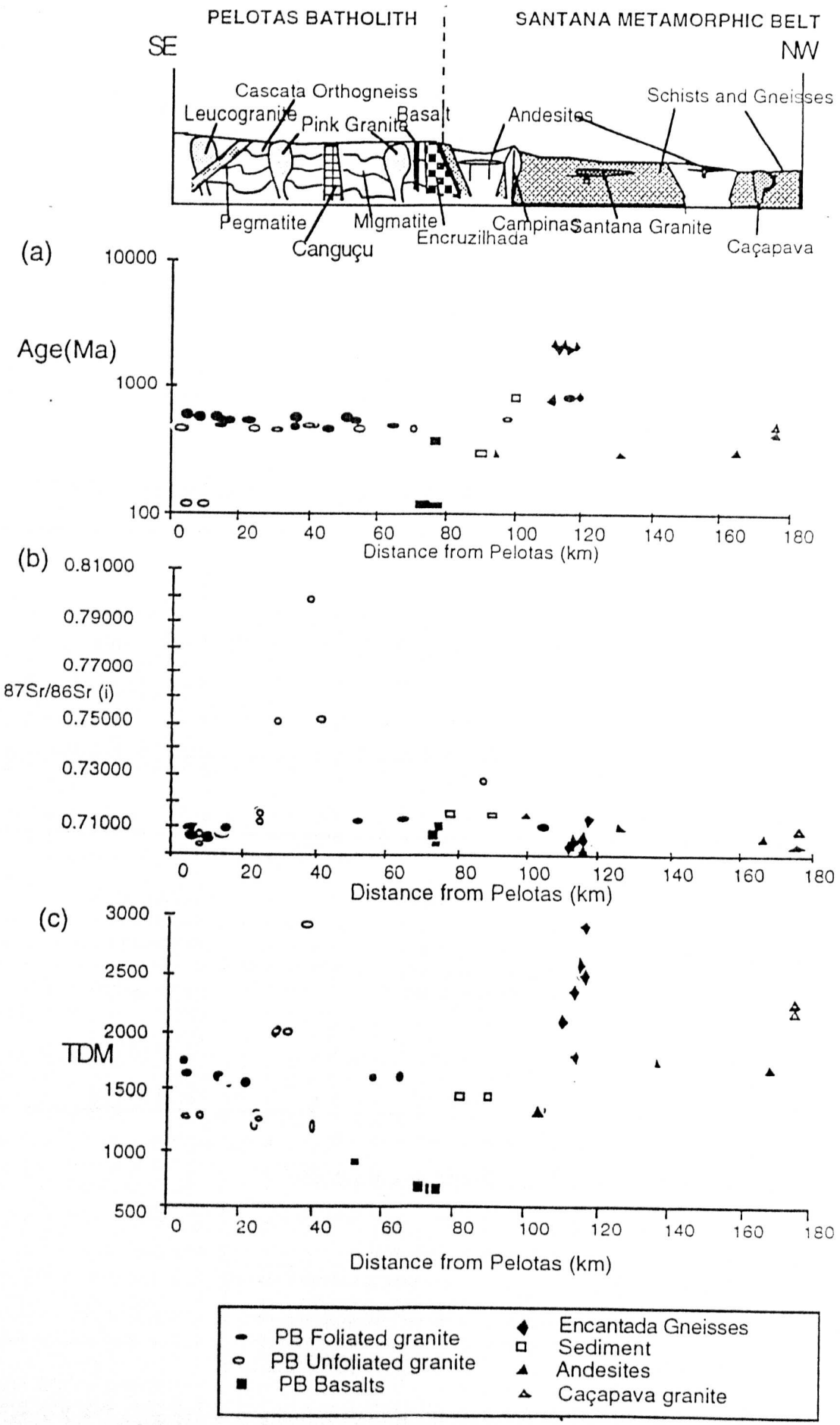

Figure 8.3. Spatial variation of isotopic data between Pelotas and Caçapava do Sul.

8.5.2 RADIOGENIC ISOTOPES

Isotopic studies were undertaken to establish the possible sources for the Brasiliano Granites and to establish whether this orogenic event was dominated by crustal growth or by crustal reworking. Rb/Sr source calculations, initial Sr isotope back calculations, and Nd model age studies (fig 8.3) support a model of crustal reworking in both belts. Figure 8.4 illustrates that the foliated granitoids are isotopically distinct from the unfoliated granites and that the geochemically distinct Canguçu Red Granite also has different isotope ratios.

In the Pelotas Batholith, the foliated granitoids have initial Sr ratios of between 0.708 and 0.710, Rb/Sr source values of 0.4-0.8 and model Nd ages between 1600-1400m.y. suggesting reworking of a crustal igneous precursor. The unfoliated granites of the Pelotas Batholith have Sr initial ratios of 0.715-0.720, Rb/Sr source values of 1-1.4 and Nd model ages of 1100-1200m.y. (fig 8.3). The estimated Rb/Sr source ratios, along with field evidence suggest they are melts of the foliated granodiorites, or of similar upper crustal igneous precursors. The Canguçu Red Granite has Sr initial ratios of 0.720-0.800, Rb/Sr source values of 1.2-1.6 and Nd model ages of 1600-2000m.y. suggesting an upper crustal pelitic source.

In the Santana Metamorphic Belt, the Santana Granite is thought to be a crustal melt of basement gneisses both from Sr isotope back calculations and field relations. The Campinas Granite has a high initial Sr value indicative of a pelitic source. The post-tectonic Caçapava Granite has an initial Sr ratio of 0.705, Rb-Sr source value of 0.1-0.2 and a Nd model age of 2500m.y. which suggests it is a melt of a lower crustal primitive source, possibly granulite. The Encruzilhada Granite which does not fit this classification, and is fault bounded, is a within plate granite with a Sr initial isotope ratio of 0.705: its geochemistry suggests it was a melt of a basaltic precursor.

Combined Sr-Nd studies illustrate that the foliated granites of the Pelotas Batholith have generally lower positive εSr values and a smaller range of εNd values than the unfoliated granites. The Campinas Granite has a distinctively high εSr values indicative of a pelitic source, and the post-tectonic Caçapava Granite of the Santana Metamorphic Belt has extremely negative εNd suggestive of a primitive lower crustal source. The negative values of εNd shown by all the granites of the Dom Feliciano Belt is indicative of dominant crustal reworking processes in the Dom Feliciano Pan-African/Brasiliano orogenic belt.

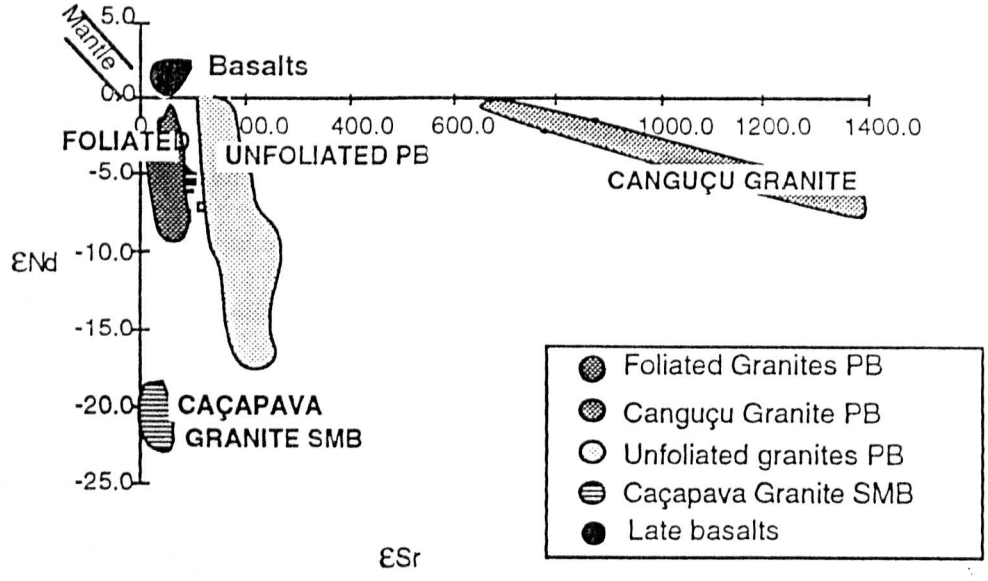

Figure 8.4 illustrating the isotopic distribution of the Dom Feliciano granitoid groups.

8.6 Geological History and Tectonic Model

8.6.1 GEOLOGICAL HISTORY OF THE DOM FELICIANO BELT

From the established field relations and stuctural and metamorphic studies, a geological history of the Dom Feliciano Belt in the studied area has been proposed and is presented in table 8.2.

GEOLOGICAL HISTORY OF THE DOM FELICIANO BELT

Time	Event	Tectonic regime
?Cretaceous	Intrusion of basalt dykes and aplites in Pelotas Batholith	Extensional
?Triassic	Deposition of red beds with contemporaneous sub ariel extrusion of andesites and rhyolites	Extensional
	NE-SW, NW-SE Extensional faulting	
Post-450m.y.	Intrusion of Pegmatites into the Pelotas Batholith	?Extensional
465m.y.	Intrusion of Pink Granites and Cascata Leucogranite into Pelotas Batholith	Post-collision
474m.y.	Intrusion of the Caçapava Granite in the SMB	
	D4 NE-verging thrusting	
	Intrusion of Capao do Leao and Canguçu Red Granites	
500m.y.	**D3** F3 open folding (SMB)/ shearing (PB)	Collision
	Deposition of Arroio dos Nobres formation	
	Intrusion of Campinas Granite	
	M2 metamorphism	
550-500m.y.	Intrusion of Metagabbro, Piritini Granite and Porphyritic Granite	Compression

	D2 isoclinal folding **M1**Metamorphism	
	Migmatization of granodiorites	
600-550m.y.	Intrusion of pre-tectonic	
	granodiorites (Orthogneisses)	?Subduction
750-600m.y.	Deposition of cover lagoonal shelf sequence	
	Extrusion of rhyolites and basic magmas	Extension
	Erosion of granites and basement and	
	Deposition of Arroio Arreiao Fm	
800m.y.	Intrusion of the Santana Granite	
~1000m.y.	Deposition of Encantada Schists	
~2000m.y.	**D1** deformation	Compression
	Formation of Encantada Gneisses	

Table 8.2 Geological History of the Dom Feliciano Belt

8.6.2 TECTONIC MODEL

The proposed tectonic model for the evolution of the Ribeira orogen of South Brazil is constrained by the following critical observations.

1. Four phases of deformation in the Santana Metamorphic Belt, with at least two phases of metamorphic growth with pressures reaching 8kb and temperatures of 600 °C.

2. Two phases of deformation in the Pelotas Batholith which appear to correspond to D2 and D3 of the Santana Metamorphic Belt.

3. Voluminous granite magmatism (600-450m.y.) in the Pelotas Batholith (spanning pre-post tectonic history) with comparatively sparse, predominantly granitic magmatism (800-470m.y.) in the Santana Metamorphic Belt.

4. Geochemical evolution of the Pelotas Batholith from metaluminous, calkalkaline granodiorites to more silicic peraluminous peralkaline granites with time.

5. Isotopic data indicating a major crustal contribution to all magmas with probable sources from the middle and upper crust.

Lower Proterozoic (2000-1000m.y.)

The first recognizable event occurs with the formation of the Encantada Gneisses which have been dated at 2030±72 m.y.(Chapter 7) which is probably a metamorphic age and represents the stabilization of a Lower Proterozoic craton. This event is recorded as D1 in figure 8.5a and table 8.1. Amphibolites intrude the Encantada Gneisses and these were probably intruded as basalts during a rifting event between 2000 and 800 m.y. which may have been the opening of the Proto-Atlantic (8.5b). The Encantada Schists stratigraphically overlie the gneisses and their protoliths were deposited between 2000-1000m.y. perhaps in response to rifting. Model ages of 1600-1200m.y. in the Pelotas Batholith suggest that there was an orogenic event involving significantcrustal growth in the Middle to Late Proterozoic.

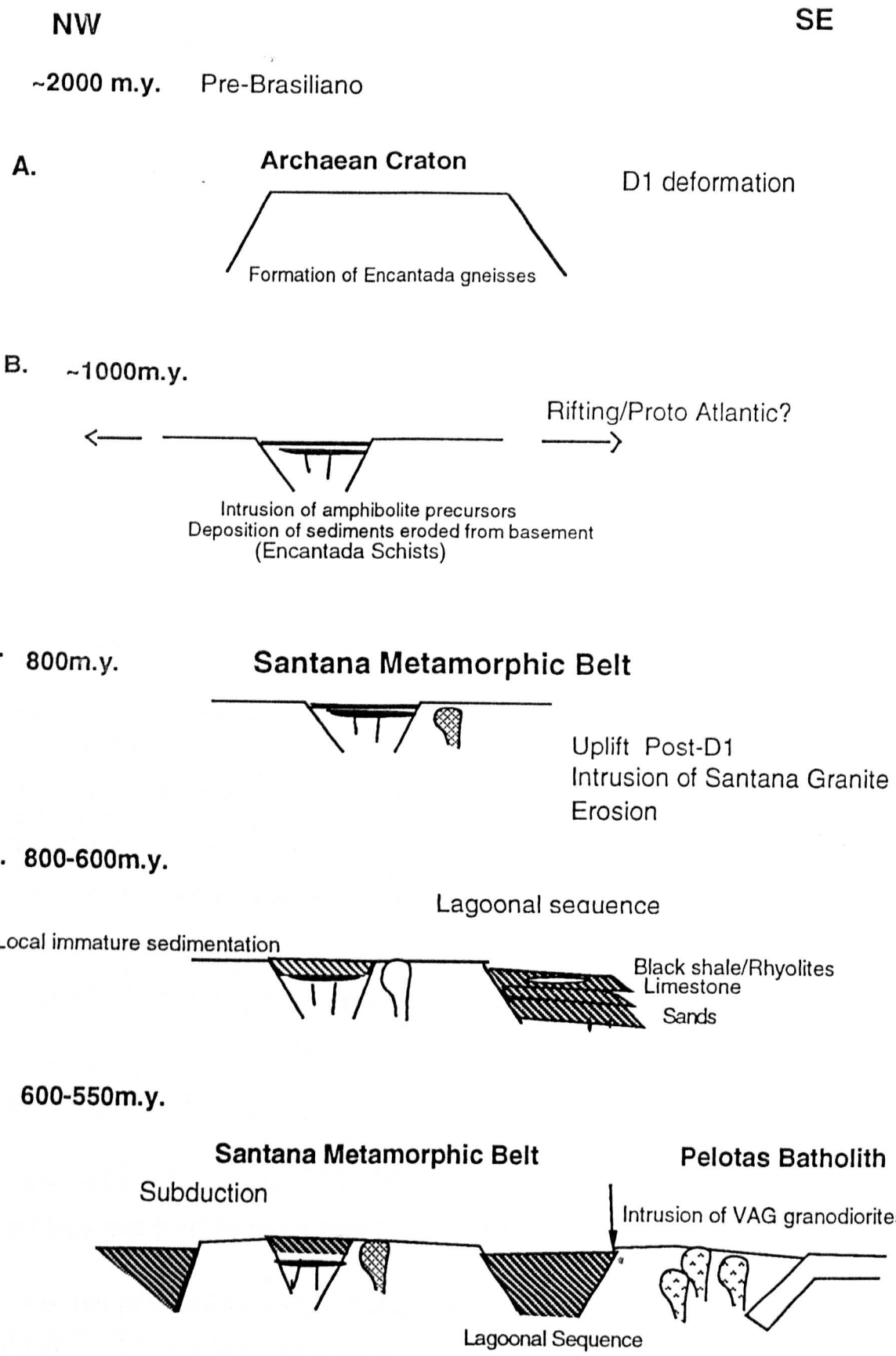

Figure 8.5 A-E of the tectonic model for the evolution of the Dom Feliciano Belt.

NW SE

F. ~550m.y. Brasiliano event D2 deformation Isoclinal NW verging folds

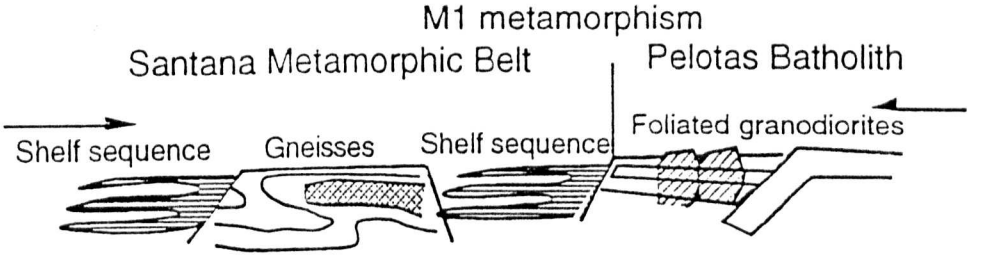

G. ~500m.y. Collision

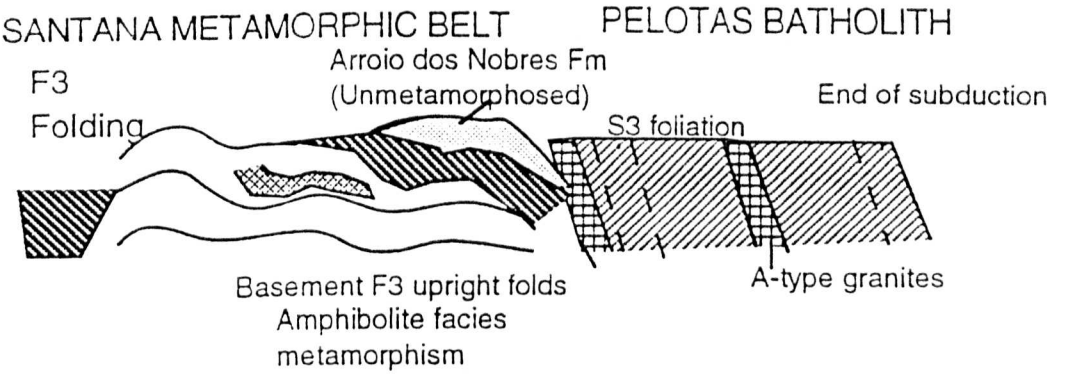

H. 500-450m.y.

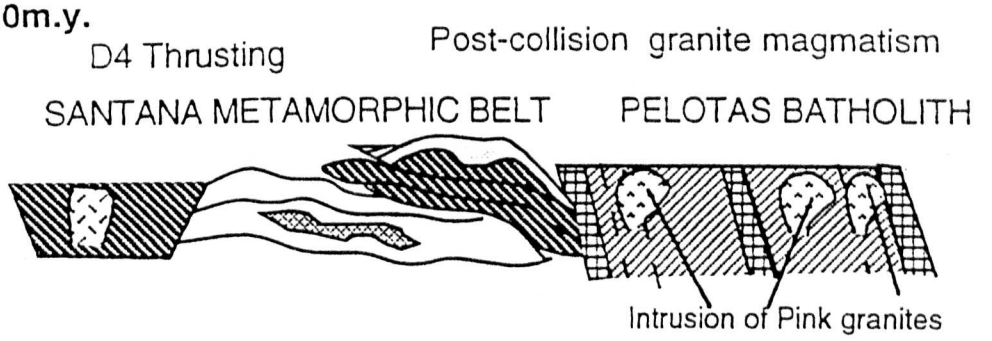

I. Post 450m.y.

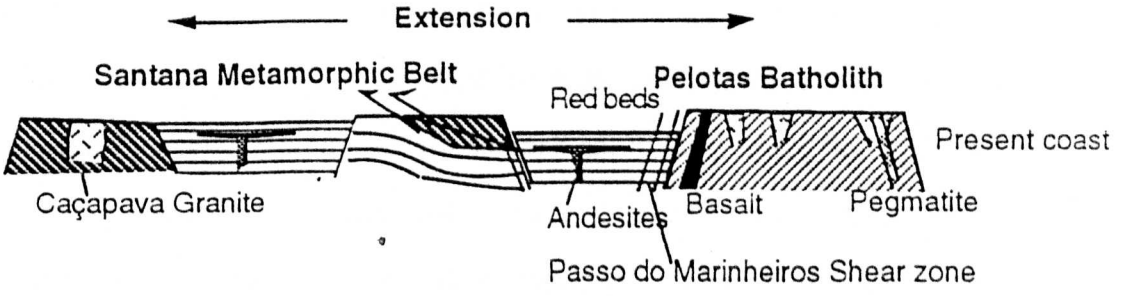

Figure 8.5 F-I of the tectonic model for the evolution of the Dom Feliciano Belt.

Early Brasiliano (800-600m.y.)

The next recognizable event in the Santana Metamorphic Belt was the intrusion of the Santana Granite into the Encantada Gneisses and the Encantada Schist formation and this intrusion has been dated at ~800m.y. (fig.8.5c). The tectonic environment of its formation is uncertain. However, from geochemical and isotopic considerations, it appears to be a melt of the Encantada Gneisses. The arenites of the Arroio Arreiao formation are unconformable on the Encantada Schists, and they are composed of locally derived weathered granite suggesting a period of weathering and uplift and possible extension (fig.8.5d). The lagoonal sequence of the Cerro dos Bicudos quartzites, marbles and graphitic schists was probably deposited in a shelf lagoon as the Proto-Atlantic opened. This suggests that the Santana Granite may have been formed in an extensional setting.

Brasiliano Orogenic Event 600-550m.y. (subduction between 600-500)

The granodiorites of the Pelotas Batholith were intruded between 600-550m.y. and the rhyolites interbedded with the graphitic sediments were extruded. This phase of granodioritic magmatism of a calc-alkaline affinity suggests NW subduction (fig 8.5e) under the old craton, melting crust of 1600-1400m.y. (Nd model ages).

550-500m.y. D2 deformation

Continued compression resulted in D2 deformation and M1 metamorphism with the formation of a biotite fabric in the Pelotas Batholith (D1g) and isoclinal folding in the basement and basins (D2) of the Santana Metamorphic Belt (fig 8.5f). Relaxation resulted in the intrusion of the Piritini Granite into the Pelotas Batholith and gabbro into the Santana Metamorphic Belt, and the deposition of the Arroio dos Nobres formation.

500m.y. Collision (D3)

Continued compression culminated in the collision of the Pelotas Batholith with the Santana Metamorphic Belt basement. In the Santana Metamorphic Belt, the collision resulted in M2 metamorphism of amphibolite facies (8.6kb, 600°C). This was followed by F3 folding of the basement and cover units along with the unmetamorphosed Arroio dos Nobres formation (fig. 8.5g). In the Pelotas Batholith the collision was expressed in the development of the D2g vertical fabric, shear zones and migmatization. This collision appears to have marked the end of subduction in this area.

500-450m.y. Post-collisional granite magmatism

The increased temperatures that developed in response to crustal thickening during the collision event, resulted in post-collision granite magmatism in the Pelotas Batholith and the Santana Metamorphic Belt. In the former, migmatization and melting of pre-tectonic upper crustal granodiorites occurred to form the unfoliated Pink Granite and leucogranites which intruded as dykes and sill like bodies (fig.8.5h). The unfoliated Canguçu Red and Capao do Leao Granites were also probably formed during this period although they are fault bounded, and so their relative ages are difficult to establish. The Caçapava Granite intrudes the NW portion of the Santana Metamorphic Belt and is the only true post-tectonic granite of this belt. It differs from the unfolited granites of the Pelotas Batholith with respect to its source since evidence suggests it to be a melt of lower crustal, relative to primitive rocks. NE thrusting emplaced quartzites from the cover over the Arroio dos Nobres formation and this event characterizes D4.

450-0m.y. Extension

Late pegmatites, aplites and basaltic dykes intrude the Pelotas Batholith (fig.8.5i) in this period and appear to be related to post-orogenic relaxation and then extension. Two

directional extensional faulting open the old S3 (NE-SW) and S4 (NNW-SSE) fabrics and form a horst and graben topography, probably in the Triassic, with the uplift of the horsts and the deposition of red beds in the grabens with associated subaerial andesite extrusion. Basaltic and rhyolitic flows overlie the red beds and are probaly Cretaceous in age. This extension resulted in the opening of the Atlantic and is continuing at present.

8.7 Regional summary of Eastern Brazil

In this section a comparison is made between the Dom Feliciano Belt in Rio Grande do Sul (this study) and in Santa Catarina (Basei 1985) with the aim of providing a regional summary of the tectonic evolution of Eastern Brazil. Two main tectonic units are identified in both belts ; the Rio de la Plata Craton forming the foreland and the Dom Feliciano Belt forming a mobile belt (Almeida et al 1973). Figure 8.6 compares a NW-SE cross sections across the Dom Feliciano Belt in Santa Catarina (Basei 1985) with a NW-SE cross-sections through the same belt in Rio Grande do Sul (this study).

In Santa Catarina the Dom Feliciano Belt can be subdivided into three domains where the internal zone is characterized by migmatites intruded by granites. This appears to correspond to the Pelotas Batholith in Rio Grande do Sul. The intermediate zone of Santa Catarina is characterized by metamorphosed and deformed metasediments of the Brusque Group intruded by several granitoids. This is comparable with the Santana Metamorphic Belt in Rio Grande do Sul (fig 8.6). The external zone in Santa Catarina is a mollassic Basin and that appears to correspond to the Triassic Basin described in this study.

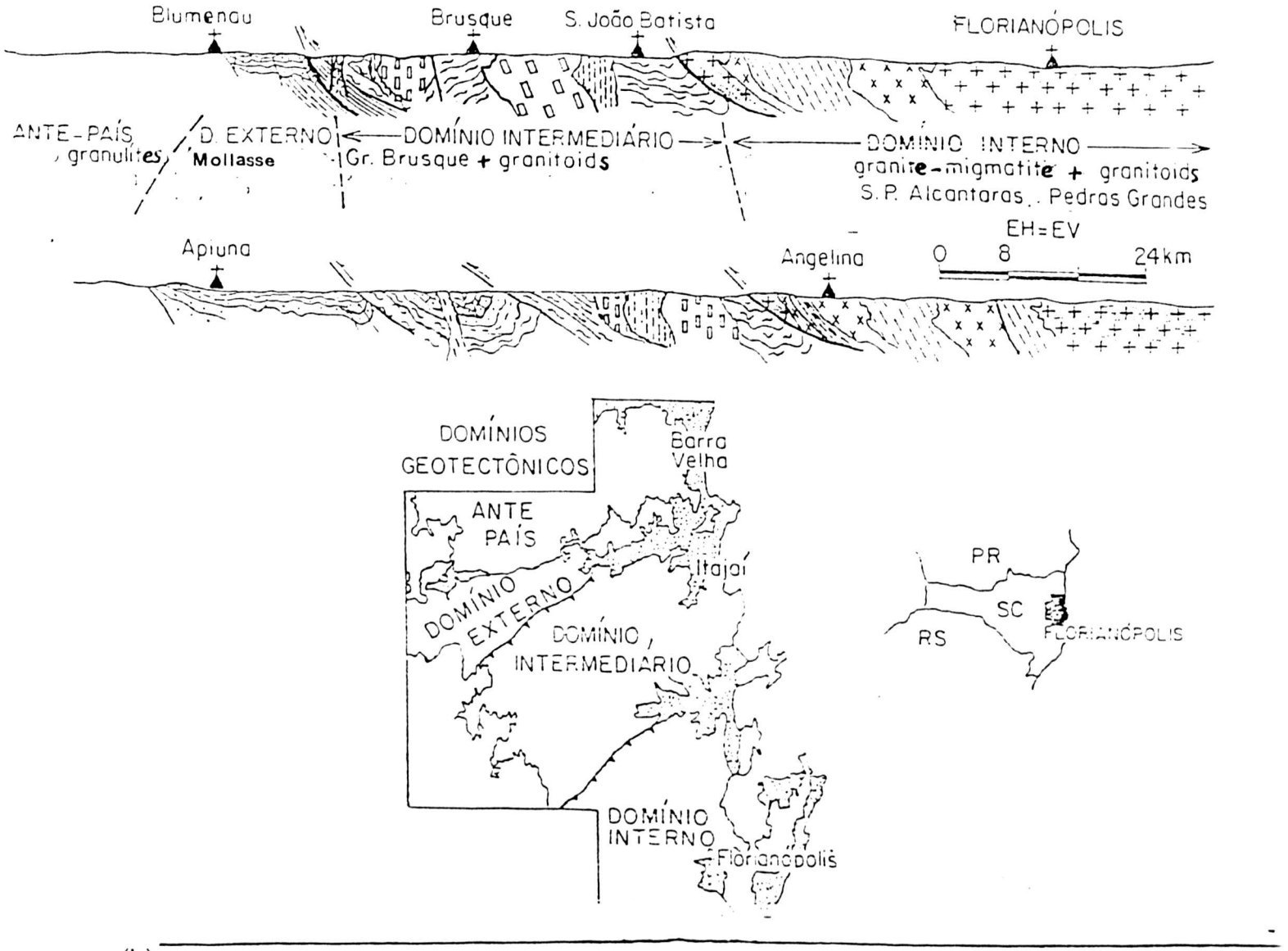

(b)

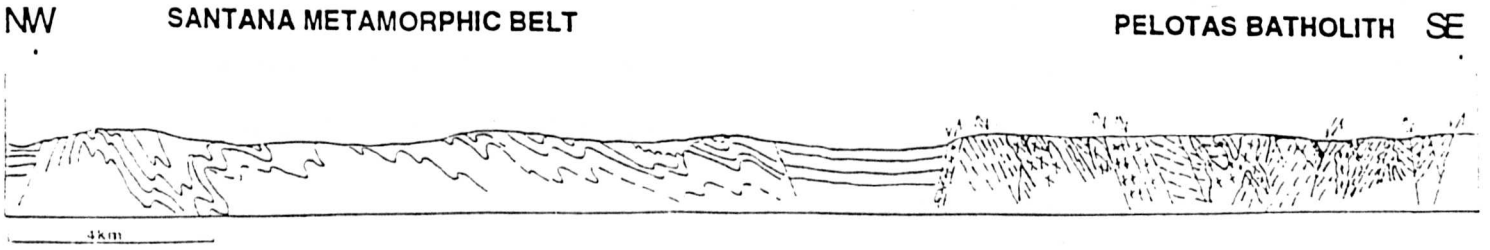

Figure 8.6 compares a NW-SE cross-section of the Dom Feliciano Belt in Santa Catarina (Basei 1985) and in Rio Grande do Sul (this study).

In Santa Catarina four phases of deformation are recognized with the second and third phases having a NE-SW strike and NW vergence. This is consistent with data from Rio Grande do Sul which suggest that the Dom Feliciano Belt is continuous between the two states.

Granite genesis in Santa Catarina is predominantly crustal which also corresponds to the results presented here from Rio Grande do Sul. However, two main magmatic events are recognized by Basei (1985) in Santa Catarina, the first at 650±50m.y. and the second at 560±40m.y. with the cooling age of the belt at 500m.y. In Rio Grande do Sul the first event appears to have been at 550±50m.y. and the second at 450m.y, i.e.younger than those in Santa Catarina.

Basei proposed subduction as an explanation for granitogenesis and deformation and this model is supported by this study. The overall evidence suggests that the Dom Feliciano Belt is continuous between Rio Grande do Sul and Santa Catarina (figure 8.6).

8.8 Implications for Precambrian tectonics

The Dom Feliciano Belt may be compared with the broadly contemporaneous Pan-African orogenic belts of Namibia (Damara Belt) and Arabia. Combined Nd and Sr isotopic studies suggest that the Damara Belt (Mc Dermott, 1986) was dominated by extensive crustal reworking whereas the Pan-African event of the Arabian shield invoved rapid crustal growth (Duyverman et al, 1982), and in this respect the Dom Feliciano Belt of southern Brazil is similar to the Damara Belt (fig 8.7).

Further comparisons can be made with the Damara Belt (Hawkesworth et al, 1986), and it is noted that the Damara also has 2.0-1.0Ga basement inliers underlying continental sediments overlain by molasse sediments, and with voluminous syn and post-tectonic granites intruded between 750-450m.y., which is comparable to the Dom Feliciano Belt.

The above cited study also proposed that at 500m.y. (D3 collision in this study), basement was sanwiched between rocks of younger model ages which supports a model for collision of the Damara and Dom Feliciano Belt at this time.

a.

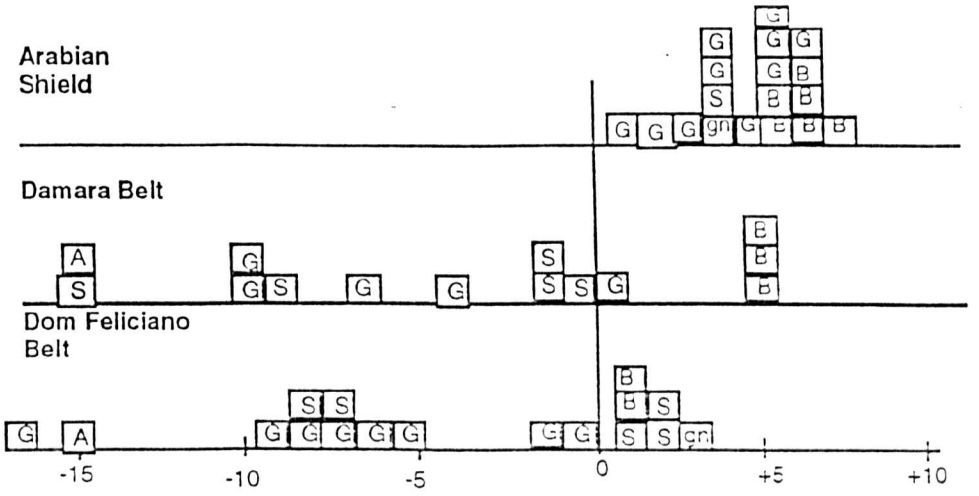

G=granite S=Schist/sediment B=basalt gn=graniticgneiss A=alaskite

b.

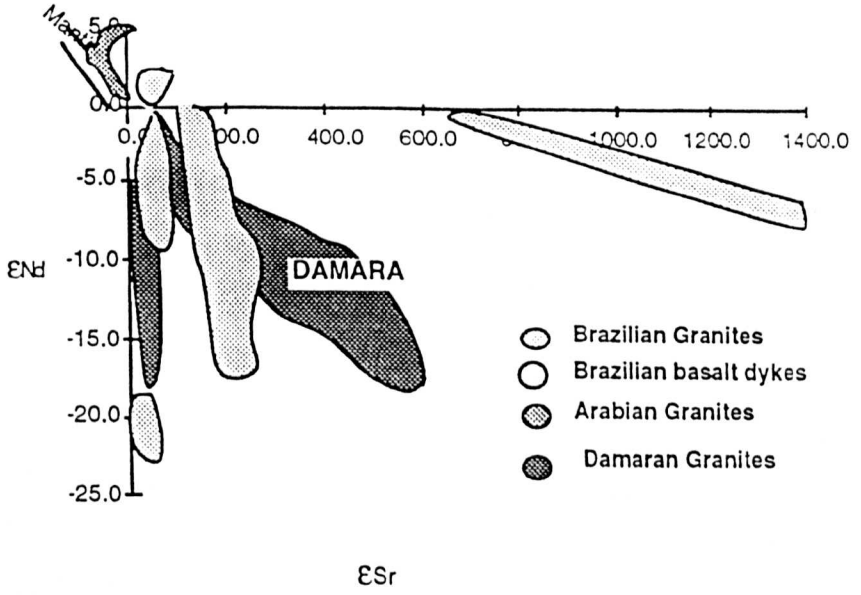

Figure 8.7 a Comparison of the Dom Feliciano Belt with other Pan-African orogenic Belts from isotopic studies a) shows a histogram and b) a εNd vs εSr plot.

Metamorphic temperatures reached 620°C and 7-8kb in the south of the Damara Belt which corresponds to the 600°C and 8.5Kb conditions for M2 metamorphism in the basement of the Dom Feliciano Belt. Mc Dermott (1986) suggested that the Damara evolved in an extensional intracontinental basin and Hawkesworth et al (1986) suggested that this evolution occured behind a zone of active subduction. Their suggestion is supported by this study which proposes NW subduction under the Dom Feliciano Belt between 600 and 500m.y. culminating in a collision event.

BIBLIOGRAPHY

ALLEGRE.,C.J and BEN OTHMAN, D. (1980). Nd-Sr isotopic relationships in granitoid rocks and continental crust development: a chemical approach to orogenesis. *Nature* **286**, 335-41.

ALLEGRE, C.J and ROUSSEAU, D., (1985) Nd isotopes in Frech Phanerozoic Shales: external vs. internal aspects of crustal evolution. *Geochim. Cosmochim. Acta*, **49**, 101-610

ALMEIDA. F.F.M; AMARAL. G.; CORDANI U.G. e KAWASHITA, K (1973) The Precambrian evolution of the South American cratonic margin south of the Amazon river. In: *The Ocean Bassin and Margins (Nairn and Stehli, Eds.)* Plenum P. 1411-1446 New York.

ALMEIDA. F.F.M;.HASUI Y.; BRITO NEVES, B.B. e FUCK R.A. (1977) Provencias estrurais brasileiras. *Atas do VIII Simposio de Geologia do Nordeste* p. 363-391, Campina Grande.

BARBIERE,M et al (1987) Petrological and Geochemical studies of alkaline rocks from continental Brazil. 1. The phonolitic suite from Piritini R.S. *Geochemica Brasiliensis*, 1 (1):109-138

BASEI. M.A.S. (1984) O Cinturao Dom Feliciano em Santa Catarina. Phd Thesis, University of Sao Paulo.*Relatorio de Atividades. Fapesp, Sao Paulo* (inedito).

BASEI, M.A.S. (1985) Cinturao Dom Feliciano em Santa Catarina.Tese de Doutoramento, Curso de Pos Graduacao em Geocienciasdo IG/USP, Sao Paulo (inedito).

BAYLY B. (1968) Introduction to Petrology : Prentice Hall 371p

BELL T.H., FLEMING P.D. and RUBENACH M.J. (1986) Porphyroblast nucleation, growth and dissolution in regional metamorphic rocks as a function of deformation partitioning during foliation development. *Journal of Metamorphic Geology* **4** pp 37-68

BEN OTHMAN D.,POLVE M., ALLEGRE C.J. (1984) Nd-Sr isotopic composition of granulites and constraints on the evolution of the lower continental crust. *Nature* Vol **307** pp 501-515

BERNASCONI (1983) Geological comparison between precambrian and early Paleozoic terranes of SE S.America. *Precambrian Res* **23**, 9-31

BITENCOURT. M.F.(1983) Metamrfitos da regiao de Cacapava do Sul. RS. Geologia e relacoes com o corpo granitico. *Atas do I⁰ Simp. Sul—bras. Geol.*, p. 37-48, Porto Alegre.

BITENCOURT, M.F. e HARTMANN, L.A. (1984) Reconhecimento geoquimico dos xistos magnesianos da regio do Passo Feio, Cacapava do Sul, R.S. *An. XXXIII Congr. Bras. Geol.*, 6: 2607-2614, Rio de Janeiro.

BONHOMME, M.G. e RIBEIRO, M.J. (1983) Datacoes K-Ar das argilas associadas a mineralizacoes de cobre da Mina Camaqua e de suas encaixantes. *Atas do I⁰ Simp. Sul-bras. Geol.*, p 82-88, Porto Alegre.

BOHLEN S.R., WALL V.J. and BOETHCHER A.L. (1983) Experimental investigations and geological applications of equilibria in the system FeO-TiO2-Al2O3-SiO2-H2O. Am. Mineral. 68 pp 1049-1058

BRITO NEVES, B.B; BEURLEN, H. e SANTOS, E.J. (1982) Characteristics and mineralizations of the Archaean and Early Proterorozoic of the Borborema Province, Brazil. *Rev. Bras. Geoc.* 12 (1-3): 234-239-(Anais do ISaP) Sao Paulo.

CARMICHAEL, D.M.(1969). On the mechanisms of prograde metamorphic reactions in quartz bearing pelitic rocks. *Contributions to Mineralogy and petrology*, **20**, 244-269.

CARVALHO P. F. (1932) Reconhecimento geologico no Estado do Rio Grande do Sul. *Bol. Inst. Geol. Mim. do Brasil*, 66: 1-72 Rio de Janeiro.

CHATTERJEE, N.D. and FLUX, S (1986). Thermodynamic mixing properties of muscovite-paragonite crystalline solutions at high temperatures and pressures, and their geological applications. *J. petrol.* **27**, 677-693.

CHAPPELL B.W .(1984) Source rocks of I- and S-type granites in the Lachlan Fold Belt, south eastern Australia. *Royal Soceity of London Philosophical Transactions. Series* A, **310**, 693-704

CHAPPELL B.W. and WHITE, A.J.R. (1984) Two contrasting granite types. *Pacific Geol* 8 173-4

CLEMENS J.D. and WALL, V.J. (1981). Origin and crystallization of some peraluminous (S-Type) granitic magmas. *Can. Miner.* **19,** 111-31

COLLINS W.J., BEAMS S.D., WHITE A.J.R. and CHAPPELL B.W. Nature and Origin of A-type Granites with particular reference to Southeastern Australia. *Contrib Mineral Petrol* (1982) **80**: 189-200

CORDANI. U.G. (19BO) Fundamentos do Interpretacao geocronologica. *Bol. no 6 do XXXI Congr. Bras. Geol., Camboriu.*

CORDANI U.G., HALPERN. M. e BERENHOLC. M (1974) Comentarios sobre as determinacoes geochronologicas na Folha Porto Alegre. In: *Carta Geologica do Brasil ao Milonesimo, texto explicativo das folha Porto Alegre e Lagoa Mirim, DNPM*, p.70-84 Brasilia

CORDANI, U.G. e BRITO NEVES, B.B (1982) The geological evolution of South America during the Archaean and Early Proterozoic. *Rev.Bras.Geoc.*,12 (1-3):78-58 (Anais do ISAP), Sao Paulo.

CORDANI, U.G. e BRITO NEVES, B.B; FUCK, R.A; THOMAS FILHO, A.e CUNHA. F.M.B. (1984) Estudo preliminar de integracao do Pre-Cambriano com os eventos tectonicos das bacias sedimentares brasileiras *Ciencia-Tecnica -Petroleo*, 15:1-70, Petrobras CENPES-DIVEX), Rio de Janeiro.

CORDANI, U.G.; SATO, K. e MARINHO, M.M (198S) The geologic evolution of the ancient granite-greenstone terrane of central southern Bahia, *Brazil Precambr. Res.*, 27 1—3):187-213 Amsterdam.

COX, BELL AND PANKHURST The Interpretation of igneous rocks. *George, Allen and Unwin Ltd* London. 450 pp

DE YOREO, J.J.; LUX, D.R. and GUIDOTTI, C.V. The role of crustal anatexis and magma migration in the thermal evolution of regions of thickened continental crust. *Daly, J.S.,Cliff R.A. and Yardley B.W.D (eds), Evolution of metamorphic belts, Geol. Soc. Special Publication* no.**43**, pp 187-202

DRESCH, R.A.C.; FIGUEIREDO F^0, P.M.; FORMOSO, M.L.L. (1973) Comentarios sobre algumas datacoes radiometricas de rochas precambrianas do Rio Grande do Sul. *II Congr. Latino-amer. de Geol.*, p. 1617-1623, Caracas.

DUTROW, B.L. and HOLDAWAY, M.J. (1986). Upper thermal stability of Staurolite+ Quartz at medium pressures:a reinvestigation. *Terra Cogn.* **6**,24 (abstract).

DUYVERMAN, H.J, HARRIS,N.B.W and HAWKESWORTH, C.J (1982). Crustal accretion in the Pan-African: Nd and Sr isotope evidence from the Arabian Shield. *Earth Planet. Sci Lett.*, 5995-326

FARMER, G.L. and DE PAULO, D.J. (1983) Origin of Mesozoic and Tertiary granite in the Western United States and implications for pre-Mesozoic crustal structure. (1) Nd and sr isotopic tudies in the geocline of the Northern Great Basin. *J. geophys. Res* **88**, 3379-401

FAURE, G. (1977) Princlples of Isotope Geology. *John Wiley and Sons,* 464 p., New York.

FAURE G. and POWELL, J.L. (1972) Strontium Isotope Geology. *Springer-Verlag*, 188p, New York.

FERRY, J.H. and SPEAR, F.S (1978). Experimental calibration of the partitioning of Fe and Mg between biotite and garnet. *Contr. Mineral. Petrol.* **66**,113-117

FORMOSO, M.L.L. e CARRARO, C.C. (1968) Anortosito de Capivarita, Rio Pardo, R.S. *An. Acad. Bras. Cienc.*, 40 (3):361-372, Rio de Janeiro.

FRAGOSO CESAR, A.R.S. (1980) 0 Craton do Rio de La Plata e o Cinturao Dom Feliciano no Escudo Uruguaio-Sul-riograndense. *An. XXXI Congr. Bras. Geol.* 5: 2879-2892, Camboriu.

FRAGOSO CESAR, A.R.S.; WERNICK, E. e SOLIANI JR., E. (1982a) , Associacoes Petrotectonicas do Cinturao Dom Feliciano (SE de Plataforma Sul-americana) *An. XXXII Congr. Bras. Geol* , 1: 1-12, Salvador

FRAGOSO CESAR, A.R.S.; WERNICK, E. e SOLIANI JR., E. (1982b) , Evolucao Geotectonica do Cinturao Dom Feliciano - Uma contribuicao atraves da aplicacao do Modelo de tectonica de Placas. *An. XXXII Congr. Bras. Geol.,1*: 13-23, Salvador

FRAGOSO CESAR, A.R.S. e SOLIANI JR, E (1984). Compartimentacao tectonica do Craton do Rio de La Plata. *An. XXXIII Congr. Bras. Geol.* 5 : 2426-2434 Rio de Janeiro

FRAGOSO CESAR, A.R.S.; LAVINA, E.L.: PAIM, P.S.G. e FACCINI, U.F. (1984) A Antefossa Molassica do Cinturgo Dom Feliciano no Escudo do Rio Grande do Sul. *An. XXXIII Congr. Bras. Geol.*, 7: 3272-3283, Rio de Janeiro.

FRAGOSO CESAR, A.R.S.; LAVINA, E.L.: PAIM, P.S.G. e FACCINI, U.F. e ALTAMIRANO, J.R.F. (1985). Revisao da Estratigrafia das Molassas do Ciclo Brasiliano no Rio Grande do Sul *Atas II^o Simp. Sul—bras. Geol.*, p. 477-491, Florianopolis.

FRAG0S0 CESAR, A.R.S.; FIGUEIREDO, M.C.H. SOLIANI JR., E. e FACCINI, U.F. (em prep). 0 Batolito Pelotas (Proterozoico Superior/Eo—paleozico) no Escudo do Rio Grande do Sul .

FRANTZ, J.C. e JOST H. (1983). Petrologia dos granitos estaniferos do Rio Grande do Sul. *Atas I⁰ Simp. Sul-bras.* Geol. p. 49-67 Porto Alegre

FRANTZ, J.C.; LIMA, E.F.; MACHADO, R.P. e NAUMANN, M.P (1984) Contribuicao a geolagia da regiao de Encruzilhada do Sul RS. *An. XXXIII Congr. Bras. Geol.*, 5: 2407-2416, Rio de Janeiro.

FROST ,C.D and O'NIONS,R.K (1985). Caledonian magma genesis and crustal recycling. *Journal of Petrology*, **26,** 515-44

FYSON, W.K. (1971) Fold Attitudes in metamorphic rocks.*American Journal of science,* **vol.270**, 373-382.

GEOSTANDARDS NEWSLETTER VOL X111 Special issue July 1989.

GIRADI. V.A.V.(1973) Descriao petrografica das rochas do Embasamento do Rio Grande do Sul. CPGeo - IG/USP, S. Paulo (rel.int., inedito)

GONI, J.C (1962) Origine das roches ultrabasiques et serpentinues du Pre-Cambrian du Rio Grande do Sul (Bresil). Mode de gisement et mineralisation. *Bol Esc. Geol., UFRGS.* **12:** 1-89,
Porto Alegre.

GONI, J.C.;G0S0, H. e ISSLER, R.S. (1962) Estratigrafia e Geologia Economica do Pre-Cambriano e Eo-Paleozoico Uruguaio e Sul rio-grandese. *Avulso da Esc. Geol., UFRGS.* **3**: 1-105, Porto Alegre

GREEN, N.L. and USDANSKY, S.I. (1986) Toward a practical plagioclase-muscovite thermometer. *Am. Mineral. 71.1109-1117.*

HALPERN M.; CORDANI, U.G. e BERENHOLC. M. (1974) Geochronology of Rio Grande do Sul State. Southeastern Brazil . CPGeo - IG/USP, Sao Paulo rel. int., inedito).

HAMILTON,P.J, O 'NIONS, R.K., and PANKHURST, R.J.,(1980). Isotopic evidence for the provenance of some Caledonian granites. *Nature,* **287**, 279-84.

HARKER, A. (1932) *Metamorphism. A study of the transformation of rock masses.*Methuen. London

HARRIS, N.B.W., HOLLAND, T.J.B. and TINDLE, A.G (1988). Metamorphic rocks of the 1985 Tibet Geotraverse, Lhasa to Golmud. *Phil. Trans. R.Soc. Lond.* **A 327**, 203-213.

HARRIS, N.B.W, HAWKESWORTH, C.J. and RIES, A.C., (1984). Crustal evidence in NE and E Africa from model neodymium ages. *Nature*, **309**, 773-776.

HARRIS, N.B.W, HAWKESWORTH, C.J, VAN CALSTEREN, P and MC DERMOTT, F (1988). Evolution of continental crust in southern Africa. *Earth Planet Sci Lett. Pages??*

HARRIS, N.B.W., PEARCE, A.J. and TINDLE, A.G.(1986) Geochemical characteristics of collision zone magmatism. From COWARD, M.P & RIES, A.C. (eds) *Collision Tectonics, Geological Soceity Special Publication* **No 19**, pp 67-81

HART, S. (1966). Radiometric ages in Uruguay and Argentina and their implications concerning Continental Drift. *Geol. Soc Am., Annual Meeting, San Francisco.*

HARTMANN. L.A e NARDI, L.V.S. (1983). Contribuicao a Geologia da regiao oeste do Escudo Sul-rio grandense. *Atas do I^o. Simp.Sul—bras. Geol.*, p. 9- 18, Porto Alegre

HARTNADY, C; JOUBERT, P and STOWE:, C. (1985)) Proterozoic crustal evolution in Southwestern Africa. *Episodes.* 8 (4) :236-244 Ontario .

HASUI Y.; CARNEIRO, C.D.R e COIMBRA, A.M. (1975) The Ribeira Folded Belt *Rev. Bras. Geoc.*, 5 (4) 257-266. Sao Paulo.

HAWKESWORTH, C.J and MARLOW, A.G., (1983). Isotopic evolution of the Damara Orogenic Belt. In: *Spec Publ geol Soc. S. Afr.*, **11** 397-407

HAWKESWORTH, C.J.and VAN CALSTERN, P (1984) Radiogenic Isotopes-some geological applications. In: *Rare Earth Geochemistry Developments in geochemistry* **2**, Ed. P. Henderson. Elsevier Publishers B,V., Amsterdam. 375-421.

HAWKESWORTH, C.J., KRAMERS,J.D. and MC G MILLER, R, (1981) Old Model Nd Ages in Namibian Pan-African rocks, *Nature* **289** 278.

HOESHEK,G. (1967) Untersuchungen zum stabilitats bereich von chloritoid und staurolith. *Contr. Mineral. Petrol.* **14**,123-162.

HOLDAWAY, M.J. (1971) Stability of Andalusite and the aluminium silicate phase dagram *Amer. J. Sci.* **271**,97-131.

HOLLAND, J.T.B. and POWELL,R. (1985) An internally consistent thermodynamic data-set with uncertainties and correlations: 2: Data and results. *J.metamorphic Geol.*, **3**, 343-

HURLEY, P.M. Can the subduction of mountain building be extended to Pan African and similar orogenic belts? *Earth Planet Sci lett* **15** (1972) 305.

ISSLER, R.S.(1982) Evento geodynamico Brasiliano-Fechemanto de oceano e coliasao continental dos cratons Rio de la Plata e Dom Feliciano: granitos a duas micas e ophoiolites. *An XXXII Congres. Bras. Geol.* 1:24-38, Salvador.

ISSLER, R.S. (1983). Evolucao crustal da faixa arco-fossa Tijucas e faixa magmatica Pedras Grande: Craton Dom Feliciano. *Atas do I^0 Simp. Sul—bras. Geol.*, p19-36, Porto Alegre.

ISSLER, R.S.(1984) Granitos e granitoides da Regiao Sul. Projeto RADAMBRASIL, 54 p., Florianopolis (rel int, inedito)

ISSLER R S.; JOST H. e VILLWOCK. J.A (1965). Esboco preliminar da geoteconica no Escudo Rio—grandense. *Conferencia proferida no nucleo rio-grandense da SBG* . Porto Alegre.

ISSLER R.S; DRESCH, A.C. e ROISEMBERG, A (1973) Geocronologia do Gabro de Mata Grande, Municipo de Sao Sepe, Estado do Rio Grande do Sul. *Rev. Bras. Geoc.*, 3 (2) : 124-127,Sao Paulo.

JÅGER E.(1979) Introduction to geochronology. In: Lectures in isotope geology, *E Jåger and J.C. Hinzicker eds, Springer Verlag*, Berlin 1-12

JACOBSEN, S.B.and WASSERBURG, G.H.(1979). The mean age of mantle and crustal reservoirs. *Jour. Geophys. Res.* **84** 7411-7426

JAMIESON, R.A and VERNON, R.H (1987) Timing of porphyroblast growth in the Fleur de Lys Supergroup Newfoundland. *J. metamorphic Geol.* 1987, **5**, 273-288.

JOST, H. (1981). Geology and metallogeny of the Santana da Boa Vista Region, South Brasil. The University of Georgia (Ph.D.Thesis) Athens.

JOST H. (1984) Sedimentacao e vulcanismo durante o Ciclo Brasiliano no Rio Grande do Sul: uma revisiao. *An XXIII Congr. Bras. Geol.*, : 3241-3257, Rio de Janeiro.

JOST H. e VILLWOCK, J.A. (1966) Contribucao a estratigrafia do Pre-Cambriano no Rio Grande do Sul *Notas e Estudos da Esc. Geol., UFRGS*, **1** (l): 13-26, Porto Alegre.

JOST H. e BITTENCOURT, M.F. (1980) Estratigrafia e tectonica de uma fracao da faixa de dobramentos Tijucas no Rio Grantde do Sul. *Acta Geol. Leop.*, **11** (7): 27—59, Sao Leopoldo.

JOST, H; FRANTZ, J.C e WERNICKE , E> (1984). Impicacacoes geotectonicas da variacao composional temporal e regional dos granitoids do ciclo Brasiliano no Escudo Sul-rio-grandense. *An XXXIII Congr. Bras.Geol.*, **6** : 2978-3000, Rio do Janeiro.

JOST, H; .FRANTZ , J.C. e BROD, J.A. (1984). Revisao da tipologia, cronologia e significado geotectonico das falhamentos do Escudo Sul-rio-grandense *An. XXXIII Congr. Bras. Geol .*, **4**: 1707-1720, Rio de Janeiro .

KAUL, P.F.T. e TEXEIRA, W. (1982) Archaean and Proterozoic complexes of Santa Catarina, South-south eastern Brazil: an outline of their structural evolution. *Rev. Bras. Geoc.*,**12** (1-3) : 172-182 (Anais do ISAP), Sao Paulo.

KERRICH, D.M (1972). Experimental determination of muscovite + quartz stability with $P_{H2O} < P_{total}$.*Am.J.Sci.* **272**, 946-958.

KRONER, A, (1979) Pan African plate tectonics and its repurcussions on the crust of NE Africa. *Geol Rundsch,* **68**, 565.

MANTOVANI, M.S.M., HAWKESWORTH, C.J (1988) Crustal contamination inverted: Some preliminary results. *Brazil. Rev. Bras. Geoc.*, **18**, 27-32.

MANTOVANI, M.S.M., HAWKESWORTH, C.J and BASEI, M.A.S. (1987) Nd and Pb isotope studies bearing on the crustal evolution of S.E. Brazil. *Rev. Bras. Geoc.*, **17**, 263-268.

MCCULLOCH, M.T. and WASSERBURG, G.J., (1978) Sm-Nd and Rb-Sr chronology of continental crust formation.

MC DERMOTT, F., GLEDHILL,A.R., HARRIS, NBW and HAWKESWORTH, C.J. (1986). Crustal remobilisation in the Damara High Belt, Namibia. *Terra Cognita*, **6**, 236.

MC KENZIE, D.P. (1984). The generation and compaction of partially melted rock. *J. Petrology*, **25**, 713-65.

MC G. MILLER, R.(1983) The Pan-African Damara Orogen of S.W.Africa/Namibia. *Spec. Publ. Geol. Soc. S.Afr.*, **11** 431-515.

MILLER C.F. (1985) Are strongly peraluminous magmas derived from pelitic sedimentary sources? Jour. of Geol. **93**. 673-689.

MOREIRA , M.L.O. e MARIMON,M.P.C.(1982) Estudo petrographico e litoquimico das rochas graniticas do Escudo Sul -rio-grandense. *An. XXXII Congr. Bras. Geol.*, **2:** 566-576, Salvador.

MOREIRA, M.L.O e MARIMON, M.P.C. (1984) Petrografia dos granulitos do leste do Escudo Sul-rio-grandense. *An. XXXIII Congr. Bras. Geol.*, 9: 4463-4471, Rio de Janeiro.

NARDI , L.V.S. (1984) Geochemistry and Petrolology of the Lavras Granite Complex, RS, Brazil. .Iniv. de Londres, 268p, Tese de Doutermeento (inedito).

NAUMANN, M.P.(1984) 0 Complexo vulcano-Sedimentar ultramafico e granitoides da regiao de Ibare. R.S. Dissertacao de Mestrado, Curso de Pos-Graduacao em Geociencias,UFPGS, Porto Alegre (inedito)

NAUMANN, M.P.; HARTMANN, L.A.; KOPPE, J.C. e CHEMALE JR.F. (1984) Sequencias supracrustais, gnaisses graniticos, granulitos e granitos intrusivos da regiao de Ibare - Palma, RS.- Geologia aspectos. estratigraphicos e consideracoes geotectonicas. *An . XXXIII Congr Bras. Geol.*, **5**: 2417-2425, Rio de Janeiro.

NEWTON, R.C. and HASELTON, H.T. (1981). Thermodynamics of the Garnet-Plagioclase-Al_2SiO_5-Quartz geobarometer.In *Thermodynamics of minerals and melts* (ed R.C.Newton, A. Narrotsky and B.J. Wood),pp.129-145. New York:Springer-Verlag.

PEARCE,J.A., HARRIS N.B.W and TINDLE A.G> (1984) Trace element discrimination diagrams for the tectonic interpretation of igneous rocks. *J. Petrology.* **25** 956-983

PICADA, R.S.(i965) Ocorrencia de migmatos, granitos e greisens controlados por fraturas regionais, Encruzilhada do Sul, RS *Bol . Esc. Geol ., UFRGS.* **14**: 7-59, Porto Alegre.

PICADA, R S. (1967) Estudos Preliminares sobre a evolucao geoquimica e mineralogica do Macio granitico Encruzilhada. *Publ. Esp. Esc. Geol. UFRGS*, **14**: 1-87, Porto Alegre

PICADA, R.S. (1971) Ensaio sobre a tectonica do Escudo Sul-rio-grandense . Caracterizacao dos sistemas de falhas. *An XXV Congr. Bras. Geol* ,: **1:** 167-191, Sao Paulo.

PITCHER, W.S. (1978) The anatomy of a batholith. *Jour. Geol. Soc. Lond .*, 135: 157-182, London .

PITCHER, W S (1982) Granite type and tectonic environment In: Mountain Building Processes. (K.J. Hsu, Ed), *Academic press*, p.18-40 New York.

PORADA, H. (1979) The Damara-Ribeira Orogen of the Pan-African-Brasiliallo Cycle in Namibia and Brazil as interpreted in terms of continental collision. *Tectonophysics.* **57**: 237-265, Amsterdam.

POWELL, R. and EVANS, J. (1983). A new geobarometer for the assemblage biotite-muscovite-chlorite-quartz. *J metamorphic. Geol.* 1,331-336.

POWELL, R. and HOLLAND, T.J.B.(1987). An internally consistent data set with uncertainties and correlations. 3: application methods, worked examples and a computer program. *J. Mm. Geol.* (in press).

POUPEAU, G.; SOLIANI JR., E.; KAWASHITA, K.; BAITELLI, R; BERBERT, M. e CESAR, M.F. (1985) Um Perfil geocronologico (K-Ar/Tracos de Fissao) leste-oeste no Escudo Sul-rio-grandense. *Atas II°Simp. Sul-bras. Geol.*, p.308-321, Florianopolis.

PRICE, J.G. (1985). Ideal site mixing in solid solutions with an application to two feldspar geothermometry. *Am. Mineral.* **70**, 696-701.

RIBEIRO, M (1977). Mapa Geologico da Quadricula de Piratini. RS. *Fund. Zoobot. Est R.G. Sul. Pulbl. Esp nº 2, Esc. 1:50000 Porto Alegre.*

RIBEIRO, M. (1981) ()correncia de komatiitos no Escudo do Rio Grande do Sul. *Iheringia, Ser. Geol.*, **6:** 79-82, Porto Alegre.

RIBEIRO e TEIXEIRA C.A.S. (1970) Datacoes de rochas do Rio Grande do Sul e sua influencia nos; conceitos estratigraphicos e geotectonicos locais. *Iheringia, Ser. Geol.*, **3**: 109-120 Porto Alegre.

RIBERIO, M. e FATINEL, L.M. (1978). Associacoes petrotectonicas do Escudo Sul-rio-grandense: Tabulacao e distribution das associacaoes petrotectonicas do Escudo do Rio Grande do Sul. *Iheringia, Ser. Geol.*,5: 19-54, Porto Alegre

RIBEIRO, M e LICHTENBERG, E.(1978) Sintese da geologia do Escudo do Rio Grande do Sul. *An XXX Congr. Bras. Geol.* ,**6**: 2451-2463, Recife.

RICHARDSON, S.W. (1968) Staurolite stability in a part of the system Fe-Al-Si-O-H. *J.Petrol.* **9**, 467-488

ROBIN, P.Y.F. (1979). Theory of Metamorphic segregation and related processes. *Geochemica et Cosmochemica Acta,* **43**, 1587-600.

ROBERTSON J.F. (1966) Revision of the stratigraphy and nomenclature of rock units in the Cacapava-Lavras region, State of Rio Grande do Sul, Brazil. *Notas e Estudos da Esc. Geol.. UFRGS.* 1 (2) :41-54, Porto Alegre.

ROISENBERG, A.; LOSS, E.L; ALTAMIRANDO,J.A.F e FERREIRA, A.C. (1983). Aspectss petrologicos e geochemicos do vulcanismo pre-cambriano/eo-paleozoic do R.G.S,com base nos elementos maiores. *Atas Iº Simp. Sul-Bras. Geol.*, p.273-285, Porto Alegre

RUBENACH, M.J. and BELL,T.H. (1988). Microstructural controls and the role of graphite in matrix/porphyroblast exchange during synkinematic andalusite growth in a granitoid aureole. *J. metamorphic geology 1988 ,6,* 651-666.

SALDA, L.D; BOSSI,J. and CINGOLANI, C. (1988). The Rio de la Plata Cratonic Region of S.W. Gondwanaland. *Episodes volume 11*, no **4** 263-269

SANTOS, E.L.; BECKEL, J.; MACEDO, P.M ; GONZALES Fº, F. e CHABAN, M. (1978). Divisao lito-estratigrafica do Eo-cambriano -PreCambriano Superior do Escudo Sul-rio-grandense *An. XXX Congr.Bras. Geol.*, **2:** 670-684, Recife.

SARTORI, P.L.P. Petrologia do Complexo Granitico de Sao Sepe. R.S. Modelo Evolucional de Granitos do Sul do Brasil. *Tese de Doutoramento, Curso de Pos-graduacao em Geociencia do IG/USP,Sao Paulo (inedito).*

SARTORI, P L.P.e KAWASHITA. K (1985) Petrologia e geocronologia do Batholito Granitico de Cacapava do Sul, RS. *Atas IIº Simp. Sul—bras. Geol.*, p. 102-115, Florianopolis.

SCHNEIDER,.W.; LOSS, E.L e PINTO, J.F. (1974) Mapa Geoloqico da Folha de Porto Alegre, RS. IG/UFRGS, Mapa no 7, Porto Alegre.

SHACKLETON, R.M.(1977) Possible late-Precambrian ophiolites in Africa and Brazil. *Ann. Rep. Res. Inst. Afric.Geol. Univ. Leeds* **20** 3-7

SHACKLETON, R.M.(1979), Precambrian tectonics of NE Africa. *Inst. App. Geol. Bull.* **3, vol 2,** 1

SILVA , B.C. (1984) Geology of the polyphase deformed precambrian terrane of thc Vila Nova region, State of Rio Grande do Sul,Southern Brasil. Part 1: Petrogenesis. *Acta Geol. Leop.* **27** (17):35-152, Sao Leopold.

SOARES, P.C; LANDIM, P.M.B e FULFARO , V.J. (1974) Avaliacao preliminar da evolucao geotectonica das bacias intracratonicas brasileiras. *An. XXXIII Congr. Bras. Geol* **4**: 61-84, Porto Alegre

SOLIANI. JR, E (1986) Os Dados geochronologicos do Escudo Sul-Rio-Grandesnse e suas implications de ordem geotectonica. *Tese de docutoramento USP Sao Paulo*

SOLIANI JR, E; FRAGOSO CESAR,A.R.S; TE1XEIRA, W e KAWASHITA K(1984). Panorama geocronologico da Porcao meridional do Escudo Atlantico. *An. XXXIII Congr. Bras. Geol.*,5: 2435-2449, Rio de Janeiro.

STEIGER and JAGER (1977). *Earth and Planetary Science Letters*, **36** 359-362

STRECKEISEN A. (1975) To each plutonic rock its proper name. *Earth-Sci. Rev.* **12** 1-33.

TAYLOR R.P and MC CLENNAN S.M. (1985) The continental crust: it's composition and evolution. *Geoscience Texts, Blackwell Scientific Publications.*

TESSARI, R.I. e PICADA, R.S. (1966) Geologia da Quadricula de Encruzilhada do Sul R.S. *Bol. Div. Fom. Prod. Min. DNPM*, 124: 147, Rio de Janeiro .

TORQUATA, J.R. and CORDANI, U.G. (1981) Brazil-Africa Geological links, *Earth-Sci Rev.* **17** 155-176

TUTTLE O.F.(1955) The origin of granite. *Reprint from Scientific American.*

UNISINOS (1982) Projeto Encruzilhado do Sul .Depto. Geoc, Centro Tecnologico, *Trabalho de Graduacao Sao Leopoldo* (inedito).

UNISINOS (1984) Projeto Cangucu .Depto. Geoc, Centro Tecnologico, *Trabalho de Graduacao Sao Leopoldo* (inedito).

UNISINOS (1985) Projeto Piratini. Depto. Geoc, Centro Tecnologico, *Trabalho de Graduacao Sao Leopoldo* (inedito).

UPPIERE, M. and HALPERN, M.(1971) Edados estroncio-rubidio en rocas cristalinas del sul de la Republica Oriental del Uruguay, *Revista de la Associacion Geologia Argentina vol 26*, **no 2** 133-151

VILLWOCK, J.A. e LOSS E.L.(1970) Um novo tipo de complexo basico-ultrabasico na faixa serpentintica do Pre-Cambriano do Rio Grande do Sul. *Notas e Estudos da Esc. Geol , UFRGS,* **2** (1): 15-22 Porto Alegre.

WATSON, E.B. and HARRISON,T.M. (1984) Accessory minerals and the geochemical evolution of crustal magmatic systems: a summary and prospectus of experimental approaches. *Physics of the Earth and Planetary Interiors*, **35,** 19-30.

WERNICK, E. e PENALVA, F. (1978) Contribuicao ao conhecimento das rochas granitoides do Sul do Brasil. *Rev. Bras. Geoc.*, 8 (2): 113-133, Sao Paulo

WICKHAM, STEPHEN. M (1986) Crustal anatexis and granite petrogenesis during low-pressure regional metamorphism: The Trois Seigneirs Massif, Pyrenees, France. (1987) *Journal of Petrology.* **Vol 28** Part 1 127-169

WICKHAM, STEPHEN. M (1987) The segregation and emplacement of granitic magmas. *Journal of the Geological Soceity, London*, Vol **144,** !987, pp. 281-297.

APPENDIX

A. Analytical Techniques for Geochemistry

A.1 Sampling and crushing

Granite and gneiss samples were typically 1-2kg in weight when collected. Smaller samples of schists and volcanics of 1kg were collected. All samples were cleared of weathered surfaces and markings using a hydraulic splitter. Each sample was split into small cubes which were washed in order to remove any dust contaminant. The cubes were then crushed in a hardened steel jaw and crushed to less than 0.5cm fragments. A representative sample of about 100g of this crushite material was sampled by cone and quatering techniques to obtain a representative sub-sample. The sub-sample was then placed in an agate lined tema barrell and ground for 15-20 minutes until the powder was less than 200 mesh size.

A2 XRF Determination

A.2.1.Sample preparation

Trace elements were determined on pressed powder pellets while major elements were analysed on glass beads. For pressed about 7g of rock powder were mixed with movil binder and preesed into a 5cm diameter pellet using a hydraulic press. Pellets were dried and hardened overnight in an oven at 110°C

To make glass beads, rock powder was weighed into crucibles and heated overnight at 110°C. The resulting weight loss is H_20-. The crucibles were then placed in a furnace at 1000°C and left overnight. Weight loss is H_2O+ and includes structurally bound Cl, F, CO_3, SO_4, and OH^- and is offset by FeO conversion to Fe_2O_3. Powders were allowed to cool in dessicators and were mixed with a 4:1 lithium metaborate:tetraborate mixture (Spectraflux 100B) in the ratio 5:1. The flux had been dried for one hour at 600°C and cooled in a dessicator. 5.0000gof flux and 1.0000g of sample were weighed into a

platinum$^{95\%}$-gold$^{5\%}$ alloy crucible which had been cleaned in boiling 50% HCL between samples, and thoroughly stirres. The mixture was then fused in a muffle furnace at 1200°C for 15 minutes and swirled every 5 minutes to ensure dissolution. The mixture was then poured into a platinum mould and cooled instanly on a blast of cold air. If the bead showed even colour then it was labbled and analysed , if not it was remade.

A.2.2 Sample analysis

Samples were analysed at Oxford University (the XRF at the Open University was broken) using standard tecniques and calibrated using 48 international rock standards which are listed in appendix C. Other standards are only occasionally run to monitor the calibration and only for major elements in the period of this study. The machine used for analysis of both pressed pellets and glass beads was a Phillips PW1400 X-ray flourescence (XRF) spectrometer, with data processing using theX14 package on a PDP11 minicomputer. A Rh-tube was used to generate the X-rays for both the major and trace element analysis. Analysing crystals used were LiF 220, LiF 200, PE and PX1. At least 25 U.S.G.S standards were used to calibrate the machine on a regular basis finding a best fit calibration line for each run and bracketing the specimen unknowns in composition.

For major element analysis no heavy absorber is added to the flux and so the X14 package makes a correction using α–values (or absorbance factors) for mass absorbtion, using De Jongh's formula. For traces, the elements are analysed in two groups. The first are Nb, Zr, Y, Sr, Rb, Pb, U, Th, Zn, Cu, Ni and Ga and these have mass absorption determined using the Rh Compton scatter peak. The second group is Co, Cr, V and Ba , and in addition to the Compton scatter peak, these have mass absorption corrected for the Fe, Mn and Ti absorption edges and line overlaps.

A.3 Intrumental Neutron Activation Analysis (INNA)

A.3.1 Sample preparation

INAA was carried out to determine the concentrations of REE as well as the abundances of Cs, h, Ta,Hf,U,Co and Sc. Rock powders were dried overnight at 110°C. Approximately 0.3g of each powder was accurately weighed in plythene capsules. The capsule lids were sealed to prevent leakage of radioactive powder. The irradiation capsules were then stacked in a polythene tube, and a pre-weighed laquered iron foil was placed between each irradiation capsule to monitor neutron flux variations along the length of the tube. Each irradiation capsule to monitor neutron flux variations along the length of the tube. Each irradiation package contained nine samples and two standards which were the irradiation standard AC (OURS), and a sample of the Whin Sill which is used as an internal standard.

A.3.2 Sample analysis

Samples were irradiated in a core tube at the Imperial College reactor centre, Silwood Park, Ascot in a thermal flux of $5x10^{12}$ n cm^2 s^{-1} for 24-30 hours. Following irradiation, the samples were "counted" at the Open University using two detectors on either side of the sample capsule- aplanar low energy photon spectrometer (LEPS) and a coaxial Ge (Li) detector. Each sample was counted for 800 seconds on the LEPS`detector for Sm, and on the coaxial detector for La, Co and Sc. The other elements were determined by counting each sample for 2.5×10^4 to $5x10^4$ seconds using the LEPS detector. The iron foils were "counted" using the coaxial detector for 300 seconds each, to assess variations in the neutron flux. Data was processed using spectroscopy amplifiers and a multichannel anayser. Photopeak data were corrected for neutron flux variations calculated using the iron foil data. Details of counting conditions, peak fitting, calibration and corrections are given in Potts et al (1980 and 1985).

A.4 Radiogenic Isotope Analysis

All isotopic analysis and sample preparations were carried out in a clean-air laboratory in which a positive air pressure is maintained. Sample dissolutions and beaker handling are carried out in laminar flow units. All dissolutions were carried out in PTFE bombs to ensure complete dissolution of all accessory phases, and aliquots were collected off the ion exchange columns in teflon beakers. Bombs and beakers are thoroughly cleaned between sample batches to prevent cross contamination.

The teflon beakers are cleaned by rinsing in quartz distilles (QD) H_2O; soaking for at least 24 hours in conc. HNO_3 at 80°C and finally soaking in QD H_2O for a further 24 hours. They are then rinsed and allowed to dry under the evaporation lamps. The PTFE bombs are cleaned by filling them with 6M HCl and placing them in monel jackets in the oven at 180°C for 24 hours, before soaking them in QD H_2O for a further 24 hours.

All H2O is distilled by a two-stage quartz still, or produced by a Milli-Q reverse osmosis wwater purification system. HCl and HNO3 are doubly distilled in quartz still and finally purufied in ssub-boiling teflon still. HF is also purified in sub-boiling stills. Total procedural blanks for Sm and Nd are >1ng and 8ng for Sr.

A.4.1 Sr Whole rock chemistry

About 100-150Mg of rock powder is weighed into a teflon bomb to which a couple of drops of QD H_2O are added to avoid splattering when the acid is added. About 5ml of 40% HF and 2ml of concentrated HNO3 is then added to the water/powder mixture. The PTFE bomb is then placed in a polythene slleve which holds the top of the bomb in position. This asembly is then placed in a monel jacket and allowed to stand overnight in an oven at 180°C. When the bomb is removed from the oven, The solution is evaporated down under the evaporating lamps to near dryness. 6ml of 6M QD HCl are then added, and when complete dissolution has been acheived the solution is evaporated to near dryness and the residue is redissolved in 1ml of QD 2.5M HCl for loading on to the cation exchange

columns. Any residue is centrifuged off, and the clear solution is carefully pipetted onto preconditioned cation exchange columns. The sample is slowly washed into the column using two 1ml aliquots of 2.5M HCl. A further 40ml of 2.5M HCl is then allowed to perculate through the columns and the Sr fraction is collected with 10ml of QD 2.5M HCl. The solution containing the Sr fraction is evaporated to dryness and the beakers are sealed with parafilm and stored for isotopic analysis.

A.4.3 Nd whole rock chemistry

The procedure for dissolving samples for Nd chemistry is identical to that for Sr and usually done on the same aliquot. After the Sr fraction has been collected, the columns are washed with 1ml of QD H_2O and eluted with 6ml of 3M HNO_3, after which 4ml of 3M HNO_3 are collected. This fraction is evaporated to dryness.

A.5 Mass-Spectrometry

Sr and Nd are analysed on, respectively, outgassed single Ta and triple Re/Ta filaments (with Re in the centre). The Sr fraction is redissolved in about 0.5ml QD H_2O and loaded into a drop of H_3PO_4 on th centre of a single Ta filament using a micropipette. A current is passed through the filament and gradually increased until the phosphoric acid fumes off, then it is further increased until a dull red glow is observed and the sample has dried.

Loaded filaments are carefully positioned in a clean sample turret. Electrical connectors are checked and the turret is allowed to stand in a vacuum oven until ready for loading into the mass-spectrometer. All Sr radiogenic isotope mass spectrometry was carried out on a MAT Finigan 261 mass spectrometer which runs the analyses automatically using software developed by D.W.Wright and P.W.C.Van Calsteren and Nd spectrometry was also carried out on a MAT Finigan 261. Standards run over the period of this study are given in Appendix D.

A.5.1 Sr isotopic Measurements

The computer adjusts the filament current until a beam intensity of 15pA is obtained. the measuring cycle is mass 88,87,86.5,86 and 84. When the Rb contribution to the 87 peak is>0.01% the 85 peak is no longer counted. The intensities are calculated using a double interpolation algorithm (Dodson, 1978). Corrections are applied for zero,dynamic memory and Rb interference. The $^{87}Sr/^{86}Rb$ ratio is corrected for mass fractionation assuming that the fractionation is linearly dependent on mass difference, and that $^{87}Sr/^{88}Sr = 0.1194$. as an analysis proceeds ratios are stored by the computer in sets of 10. Means and errors are calculated, and the ratios are rejected if Chauvenets criterion is not satisfied. If the total error for the set is greater or equal to 100 then the whole set is rejected. If the total error is greater than 500 the whole set is ignored. The run for an individual sample is terminated when at least 100 ratios have been accumulated and the 87Sr/86Sr ratio error is better than 0.00002 at the one sigma level.

A.5.2. Nd isotopic measurement

Nd beams are run at an intensity of about 7pA. The MAT Finigan 261 has an 8Kv accelerating potential and has a 7 cup multicollector and Nd is run statically. The measuring cycle is mass 146,144,142.5,142,147. The 147 peak is eliminated when the Sm contribution to the 144 peak is <0.01%. The $^{143}Nd/^{144}Nd$ ratio is corrected for mass-fractionation assuming 146Nd/144Nd=0.7219. a run is terminated when at least 200 ratios are accumulated and the error is better than 0.00001 at the one sigma level.

B. Analytical tecniques for metamorphic and structural. studies.

B.1 Microprobe Studies

B.1.1 Wavelength dispersive electron microprobe analysis

Microprobe mineral analysis were carried out on polished carbon-coated thin sections using a Cambridge intruments Microscan (M9) microprobe. The M9 incorporates a fully automated computerised system which automatically controls spectrometer angles, count times, crystal selection and specimin position. In addition on-line ZAF corrections are performed automatically.

Element	Mineral	Concentration %	Crystal	Peak angles	Std	Unk
Si	Wollastonite	2.05	TAP	16.04	20	30
Ti	Rutile	5.95	PET	18.232	15	30
Al	Jadeite	3.28	TAP	18.851	30	30
Cr	Metal	100.00	LiF	34.639	20	50
Fe	Fayalite	52.95	LiF	28.72	30	50
Mn	Metal	100.00	LiF	31.45	20	50
Mg	Forsterite	25.52	TAP	22.58	30	30
Ca	Wollastonite	34.16	PET	22.49	20	20
Na	Jadeite	11.2	TAP	27.57	40	30
K	KCl	52.45	PET	25.24	15	30
Ba	Barite	57.11	PET	18.413	20	50
F	LiF	73.25	TAP	45.36	80	100
Cl	KCl	47.55	PET	32.64	20	30

Table B1 Calibration standards and operating conditions for microprobe analyses

An accelerating potential of 20kV and a probe current of 30nA were used for all wavelength dispersive analyses using a defocussed 15 micron diameter electron beam. The instrument was calibrated daily using the mineral standards and operating conditions listed in table B1. An "in-house" standard (ABG-a basaltic glass) was analysed several times each day to monitor instrument precision.

B.1.2 Data

A.Samples used for thermocalc

SAMPLE 119 (Encantada Schists)

	SiO2	TiO2	Al2O3	Cr2O3	Fe2O	FeO	MnO	MgO	CaO	Na2O	K2O
Gt1	36.05	0.03	21.06	0.00	0.00	32.14	1.84	2.53	4.99	0.02	0.02
Gt2	39.31	0.05	20.63	0.00	0.00	31.48	1.65	2.32	4.91	0.07	0.07
Gt3	37.82	0.61	20.84	0.00	0.00	30.84	1.68	2.36	3.67	0.04	0.08
Gt4	38.43	0.07	21.13	0.00	0.00	31.66	1.83	2.16	4.90	0.02	0.20
Gt5	38.06	0.05	21.84	0.02	0.00	29.07	1.73	2.10	5.51	0.61	0.44
Gt6	38.11	0.03	21.80	0.02	0.00	28.65	1.67	2.11	5.26	0.67	0.35
Gt7	36.73	0.04	21.32	0.03	0.00	29.41	1.53	2.25	7.00	0.02	0.06
Gt8	37.62	0.03	21.37	0.00	0.00	31.45	2.60	2.26	5.00	0.02	0.05
Fpar1	38.19	0.05	21.69	0.00	0.00	30.43	2.01	2.33	6.01	0.04	0.01
Fpar2	62.11	0.02	23.63	0.00	0.00	0.06	0.00	0.00	4.90	9.34	0.13
Fpar3	59.25	0.02	25.24	0.00	0.00	0.06	0.02	0.00	6.98	7.61	0.09
Fpar4	57.80	0.04	24.46	0.00	0.00	0.03	0.00	0.00	5.80	7.93	0.11
Bi 1	36.05	0.88	21.60	0.00	0.00	24.54	0.20	10.21	0.23	0.07	4.41
Bi 2	37.95	1.98	19.95	0.00	0.00	16.91	0.11	7.01	0.94	1.44	7.95
Amp1	38.18	0.03	21.70	0.00	0.00	30.33	3.02	0.48	4.33	0.01	0.18

Sample 134(Arroio Arreiao formation)

Mc1	SiO2	TiO2	Al2O3	Cr2O3	Fe2O3	FeO	MnO	MgO	CaO	Na2O	K2O
Mc2	48.86	0.88	32.39	0.00	0.00	3.62	0.01	1.80	0.01	0.15	10.79
Mc3	48.92	0.54	29.42	0.00	0.00	3.05	0.02	2.00	0.01	0.12	10.26
Bi 1	48.67	1.47	31.16	0.00	0.00	3.81	0.02	1.94	0.00	0.14	10.66
Bi 2	40.33	2.15	18.07	0.00	0.00	13.28	0.22	13.29	0.13	0.05	8.64
Gt1	39.30	1.81	17.65	0.00	0.00	14.14	0.29	13.15	0.20	0.03	8.19
Gt2	47.02	0.06	23.29	0.00	0.00	10.35	0.16	0.21	21.03	0.00	1.01
Ep 1	37.79	0.07	22.79	0.00	0.00	12.03	0.28	0.02	23.60	0.02	0.00
Ep 2	38.03	0.09	24.08	0.00	0.00	10.73	0.00	0.00	24.06	0.01	0.02

B. Other probe analyses

Sample 139 (Encantada Gneisses)

	SiO2	TiO	Al2O3	Cr2O3	Fe2O3	FeO	MnO	MgO	CaO	Na2O	K2O
Bi 1	35.93	2.61	17.88	0.00	0.00	22.06	0.37	8.19	0.01	0.11	9.20
Bi 2	35.58	3.03	17.24	0.00	0.00	19.85	0.37	9.46	0.03	0.09	9.30
Bi 3	35.63	2.80	16.80	0.00	0.00	19.99	0.37	9.77	0.01	0.09	8.92
Bi 4	35.97	2.30	16.42	0.00	0.00	21.78	0.47	9.25	0.04	0.06	8.19
Bi 5	36.10	3.09	16.39	0.00	0.00	22.08	0.40	8.21	0.79	0.06	8.93
Mu 1	48.20	0.00	23.83	0.02	0.00	8.97	0.17	3.56	3.27	3.98	3.60
Ep 1	38.08	0.00	24.99	0.00	0.00	11.52	0.26	0.02	23.82	0.02	0.01
Ep 2	38.73	0.00	27.45	0.00	0.00	8.83	0.25	0.02	23.92	0.02	0.01
Ep 3	38.37	0.00	27.12	0.00	0.00	8.97	0.30	0.03	23.85	0.02	0.00
Fsp 1	64.49	0.02	22.50	0.00	0.00	0.04	0.00	0.00	4.30	9.14	0.17
Fsp 2	65.25	0.00	25.80	0.00	0.00	0.00	0.00	0.00	5.22	7.73	0.14
Fsp 3	62.52	0.00	26.08	0.00	0.00	0.00	0.00	0.00	5.81	7.55	0.13
Fsp 4	63.98	0.00	25.04	0.00	0.00	0.00	0.00	0.00	1.74	3.93	5.19

Sample 118 (Encantada Schists)

	SiO2	TiO2	Al2O3	Cr2O3	Fe2O3	FeO	MnO	MgO	CaO	Na2O	K2O
Fsp1	65.62	0.02	25.86	0.00	0.00	0.11	0.00	0.00	5.15	8.17	0.12
Fsp 2	63.45	0.02	25.93	0.00	0.00	0.08	0.00	0.00	5.71	7.85	0.13
Fsp 3	66.07	0.02	26.43	0.00	0.00	0.14	0.00	0.00	5.66	7.47	0.13
Fsp 4	62.23	0.02	28.70	0.00	0.00	0.25	0.00	0.00	2.76	4.47	2.43
Fsp 5	65.35	0.04	24.70	0.00	0.00	0.48	0.00	0.00	1.71	5.25	5.46
Fsp 6	64.73	0.02	24.97	0.00	0.00	0.20	0.00	0.00	5.02	7.40	1.04
Bi 1	35.91	2.11	17.01	0.00	0.00	19.39	0.56	10.11	0.17	0.05	7.62
Bi 2	36.43	2.64	17.74	0.00	0.00	19.53	0.45	9.82	0.04	0.14	8.65
Bi 3	37.00	2.74	16.65	0.00	0.00	20.09	0.37	9.65	0.02	0.11	9.39
Ep 1	37.74	2.31	26.50	0.00	0.00	9.24	0.27	0.03	23.47	0.00	0.01
Ep 2	37.93	2.24	25.07	0.02	0.00	11.44	0.26	0.02	23.00	0.00	0.02
Ep 3	39.00	2.04	24.74	0.00	0.00	11.09	0.00	0.02	23.92	0.02	0.00

Sample 136(Arroio Arreiao schists)

	SiO2	TiO2	Al2O3	Cr2O3	Fe2O3	FeO	MnO	MgO	CaO	Na2O	K2O
Mu 1	44.84	0.43	28.09	0.00	0.00	4.75	0.02	1.43	0.00	0.25	9.73
Mu 2	44.36	0.46	29.52	0.00	0.00	4.54	0.00	0.99	0.01	0.28	9.34
Mu 3	45.40	0.41	29.56	0.00	0.00	4.44	0.02	1.28	0.01	0.26	10.07
Mu 4	44.56	0.43	29.56	0.00	0.00	4.46	0.02	1.08	0.01	0.25	9.99
Bi 1	36.34	2.80	16.39	0.00	0.00	23.60	0.15	6.59	0.07	0.06	8.28
Bi 2	37.24	2.76	17.71	0.00	0.00	21.95	0.14	5.80	0.04	0.06	8.52
Bi 3	35.35	3.02	17.33	0.00	0.00	22.99	0.20	6.51	0.10	0.08	7.32
Bi 4	36.39	2.82	16.88	0.00	0.00	23.29	0.17	5.92	0.10	0.04	7.90

Sample 129 (graphitic schists)

	SiO2	TiO2	Al2O3	Cr2O3	Fe2O3	FeO	MnO	MgO	CaO	Na2O	K2O
Mu a	46.09	1.21	34.97	0.00	0.00	1.05	0.02	0.61	0.01	1.02	8.64
Mu b	47.04	0.67	35.01	0.00	0.00	1.11	0.03	0.82	0.48	0.82	7.97
Mu c	63.60	0.00	23.06	0.00	0.00	0.07	0.00	0.00	4.15	9.25	4.15
Mu 4	64.05	0.00	22.61	0.00	0.00	0.03	0.00	0.00	3.82	9.46	0.10
Mu 5	63.45	0.00	23.14	0.00	0.00	0.06	0.00	0.00	4.36	8.95	0.13
Fsp 1	46.67	0.00	35.35	0.00	0.00	1.02	0.00	0.57	0.01	1.26	8.75
Fsp 2	46.08	0.00	34.95	0.00	0.00	1.22	0.00	0.60	0.01	1.24	9.31

SAMPLE 132 (Graphite schists)

	SiO2	TiO2	Al2O3	Cr2O3	Fe2O3	FeO	MnO	MgO	CaO	Na2O	K2O
Mu 1	43.42	0.32	31.31	0.00	0.00	1.82	0.02	1.29	0.01	0.52	9.36
Mu 2	47.42	0.34	31.05	0.00	0.00	2.87	0.03	1.69	0.01	0.60	8.91
Mu 3	50.30	0.26	28.06	0.00	0.00	2.27	0.03	2.45	0.00	0.37	9.31
Chl 1	24.63	0.09	21.73	0.00	0.00	26.64	0.55	12.99	0.01	0.00	0.03
Fsp1	65.97	0.07	18.34	0.00	0.00	0.06	0.02	0.00	0.07	12.20	0.05
Fsp2	69.10	0.02	19.09	0.00	0.00	0.03	0.02	0.00	0.06	11.41	0.05
Fsp3	70.10	0.00	19.35	0.00	0.00	0.07	0.02	0.00	0.07	11.00	0.06
Fsp4	69.33	0.02	19.11	0.00	0.00	0.04	0.02	0.00	0.03	11.53	0.06
Sp	46.05	37.11	13.17	0.00	0.00	0.67	0.02	0.34	0.01	0.25	4.09

Sample 108a (metagabbro/hornblendite)

	SiO2	TiO2	Al2O3	Cr2O3	Fe2O3	FeO	MnO	MgO	CaO	Na2O	K2O
Amp1	48.67	0.59	8.78	0.00	0.00	10.94	0.23	14.71	11.83	0.96	0.62
Amp2	49.02	0.52	8.08	0.00	0.00	10.38	0.25	15.06	11.87	1.00	0.53
Amp3	50.42	0.24	6.79	0.00	0.00	10.21	0.20	15.43	12.31	0.69	0.22
Amp4	52.69	0.17	5.37	0.00	0.00	9.63	0.23	16.44	12.24	0.57	0.08
Amp5	48.50	0.42	8.40	0.00	0.00	11.33	0.22	14.19	11.92	0.80	0.55
Ep 1	38.32	0.07	25.22	0.00	0.00	9.63	0.14	0.03	22.73	0.05	0.00
Ep2	48.77	0.06	25.25	0.00	0.00	4.09	0.06	0.10	14.32	3.41	0.14

B.2 Thermocalc

B.2.1 Program

Metamorphic conditions have been estimated by calculations based on extensions to the data set of Holland and Powell (1985) using the program Thermocalc by Holland and Powell (1988). These extensions involve the addition of the phases almandine, annite and celadonite white mica which have been made consistent with several experimental phase equilibria including Ferry and Spear (1978) and Bohlen et al (1983). Celadonite data has been incorporated follwing Powell and Evans (1983).

Activities for solid phase components in minerals were calculated by assuming ideal mixing on site (phlogopite, chlinochlore, annite), the Newton Haselton (1981) formulation for garnet activities (pyrope,almandine,grossular) and the Price (1985) and Newton Haselton (1981) activities for sanidine and anorthite. For muscovite and celadonite ideal mixing on site activities were used but non-ideal ion site was introduced using mixing parameters from Chatterjee and Flux (1986). The advantages of using Holland and Powell is that equilibria are self consistent and the uncertainties can be realistically assessed (Harris et al 1988).

B.2.2.Program output

Sample 119 (Encantada schists) M2 metamorphism

	an	q	ab	py	gr	alm	phl	ann	east	naph
activity	0.353	1.00	0.717	1.0e-3	0.003	0.296	0.015	0.019	0.025	0.003
sd(ln a)	0.125	0	0.024	0.729	0.659	0.101	0.462	0.484	0.425	3.333

no excluded assemblages

no of reactions = 4, no of intersections = 1,

1) 6an + 3phl = 6q + py + 2gr + 3east

2) alm + phl = py + ann

3) 6q + 2gr + 3alm + 3east = 6an + 2py + 3ann

4) 6an + 2phl + ann = 6q + 2gr + alm + 3east

Temperatures for in the range 100 <-> 900°C; uncertainties at or near 6.5 kbars

T°C	1.0	3.0	5.0	7.0	9.0	11.0	12.0	sdT	sdP
1	199	199	244	428	608	781	864	134	1.5
2	521	531	543	555	567	581	588	114	18
3	266	346	426	505	584	662	701	65	1.6
4	199	219	346	471	594	715	775	84	1.4

P-T of intersections for

window : P 1.0 <-> 12.0 kbars; T 100 <-> 900°C

• stable intersection 1 involving an,q,py,gr,alm,phl,ann,east or [ab,naph]

		LowT	HighT	dP/dT
1) 6q + py + 2gr + 3east = 6an + 3phl	[alm,ann]	stable	stable	0.0112
4) 6q + 2gr + alm + 3east = 6an + 2phl + ann	[py]	stable		0.0163
3) 6q + 2gr + 3alm + 3east = 6an + 2py + 3ann	[phl]		stable	0.0254
2) alm + phl = py + ann	[an,q,gr,east]	stable	stable	0.156

P = 8.5 kbar (sd = 2.8), T = 564°C (sd = 130), (cor = 0.845)

Sample 134 (muscovite schist of the Arroio Arreiao formation)

	q	pa	cel	phl	ann	east	naph	gr
activity(a)	1.0	0.140	0.082	0.084	0.015	0.049	7.0e-4	0.297
sd(ln a)	0	0.221	0.305	0.302	0.511	0.364	1.4e+1	0.09968

	alm	an	ab	mu
activity	0.018	0.76	0.543	0.554
sd(ln a)	0.49	0.017	0.062	0.03923

excluded assemblages | pa phl | pa cel east | pa cel alm | q pa ann east |

no of reactions = 14, no of intersections = 7,

1) phl + mu = cel + east
2) 6q + 2east + gr = cel + phl + 3an
3) 3cel + 3an = 6q + phl + gr + 2mu
4) 2cel + 3an = 6q + east + gr + mu
5) 6q + 3east + gr = 2phl + 3an + mu
6) gr + alm + mu = ann + 3an
7) 2cel + alm = 6q + ann + east
8) 3cel + alm = 6q + phl + ann + mu
9) 2phl + alm + 2mu = 6q + ann + 3east
10) 6q + phl + 2ann + 3an = 3cel + gr + 2alm
11) 6q + 3east + 2gr + alm = 2phl + ann + 6an
12) cel + east + gr + alm = phl + ann + 3an
13) 6q + naph + gr + 3mu = pa + 3cel + 3an
14) 2naph + 3an + 3mu = 6q + 2pa + 3east + gr

Temperatures for in the range 200 <-> 800°C;

uncertainties at or near 6.0 kbars

T°C	2.0	4.0	6.0	8.0	10.0	sdT	sdP
1	+	+	+	+	767	284	15
2	250	336	419	500	578	73	1.8
3	458	502	547	590	634	57	2.6
4	374	435	494	553	611	50	1.7
5	-	-	298	416	528	126	2.1
6	-	316	441	567	693	38	0.61
7	-	-	-	*	*		
8			-	-	786	622	2.4
9	342	482	637	+	+	278	3.4
10	-	-	328	539	771	78	0.77
11	-	267	390	511	631	54	0.88
12	-	213	366	522	679	54	0.70
13	660	709	757	+	+	1285	54
14	-	-	-	-	269	996	28

P-T of intersections for

window : P 2.0 <-> 10.0 kbars; T 200 <-> 800°C

metastable intersection 3 involving q,cel,phl,ann,east,gr,alm,an or [pa,naph,ab,mu]

P = 7.4 kbar (sd = 2.0), T = 477°C (sd = 141), (cor = 0.914)

• stable intersection 4 involving q,cel,phl,ann,gr,alm,an,mu or [pa,east,naph,ab]

		low T	high T	dp/dt
8) 6q + phl + ann + mu = 3cel + alm	[gr,an]	stable	stable	-0.00241
10) 3cel + gr + 2alm = 6q + phl + 2ann + 3an	[mu]		stable	0.00881
6) gr + alm + mu = ann + 3an	[q,cel,phl]	stable	stable	0.0158
3) 6q + phl + gr + 2mu = 3cel + 3an	[ann,alm]	stable	stable	0.0461

P = 8.6 kbar (sd = 1.8), T = 603°C (sd = 93), (cor = 0.914)

metastable intersection 5 involving q,cel,ann,east,gr,alm,an,mu or [pa,phl,naph,ab]

P = 7.6 kbar (sd = 2.0), T = 542°C (sd = 102), (cor = 0.942)

Stability of reactions not involved in intersections :

<= stable => 1) phl + mu = cel + east

<= stable => 5) 6q + 3east + gr = 2phl + 3an + mu

<= stable => 9) 2phl + alm + 2mu = 6q + ann + 3east

<= stable => 13) 6q + naph + gr + 3mu = pa + 3cel + 3an

<= stable => 14) 6q + 2pa + 3east + gr = 2naph + 3an + 3mu

B.3 Stereographic projection

B.3.1 Use of the projection

The stereographic projection (Phillips 1971,Ragan 1973) is a method for interpreting the orientation of three dimensional structures in two dimensions. For structural data an equal area Schmitt net is used. All measurements are plotted using the right hand rule. All lineations plot as points and planes may be plotted either as great circles or as points representing the normals to the planes.The intersection of two planes, which might appear as a lineation in the field, plots as a point so if the orientation of two planes is known then lineation orientations can be calculated using the projection.

B.3.2 Data

Stereo data

Santana Metamorphic Belt

S2 Cz/Mc schist	S2 graphite schist	S2 Gneisses	S3	Plunge of F2 folds	Thrusts	Faults
74 42		164 28	292 88	354 38	50 35	45 82
100 22	30 62	145 20	330 88	120 14	30 50	130 82
240 78	284 42	52 42	72 58	256 18	60 30	50 35
267 89	300 54	20 48	30 84	270 38	36 32	160 35
196 62	300 42	20 50	24 70	76 12	260 35	30 50
160 20	360 58	56 48	316 66		238 60	80 65
56 60	160 30	56 57	66 62	166 42	20 52	310 35
224 34	60 22	40 42	190 79	90 10	68 62	120 65
46 79	145 18	80 60	55 54	282 36	130 32	82 65
35 42	288 58	40 32	272 90	230 35	130 35	36 32
50 78	60 42	360 50	320 80	68 24	144 25	156 42
20 24	226 58	44 42	50 78	175 52	50 40	340 75
192 80	60 50	40 70	24 80	84 22	156 42	260 38
48 70	352 25	54 36	26 72	220 48		238 60
246 16	62 32	62 22	150 58	204 28		324 25
60 40	388 42	54 72	34 80	210 25		359 30
94 82	58 32	206 50	98 85	225 50		270 12
220 32	56 58	50 30	26 85	202 20		50 40
210 34	44 36	50 72	298 89	94 16		20 80
185 22	100 36	52 50	306 82	056 8		21 52
23 72	65 63	50 48	330 84	230 20		296 74
212 55	48 40	44 58	70 85	86 25		86 62
62 40	53 71	48 42	120 89	20 50		60 78
60 30	55 54	52 48	81 45	210 6		
48 18	335 52	43 30	70 72	184 35		
32 58	198 41	60 25	190 76	168 60		
260 38	73 32	30 48	136 82	232 22		
46 55	48 34	48 47	316 76	230 52		
260 38	66 60	47 40	300 68	222 2		
202 40	94 82	39 65	238 72	245 35		
228 52	30 34	71 52	282 68	203 8		
207 12		52 60	120 88	210 15		
109 20		40 20	244 55	230 8		
200 15		54 18	68 70	219 2		
219 42		46 68	224 75	202 6		
202 40		60 38	246 78	226 12		
212 30		40 37	137 74	216 28		
198 62		53 67	130 68	238 2		
204 52		52 62	128 70	260 18		
246 22			168 72	106 22		
244 12			6 85	234 30		
228 40			66 62	237 2		
134 42			88 70	220 12		
197 30			332 82	150 45		
148 42			132 84	122 76		
69 79			30 84	258 25		
60 62			120 74	134 78		
238 12			326 82	076 12		
206 40			148 87	220 10		
			150 88	214 8		
			328 85	172 76		
			60 85	120 58		

Pelotas Batholith

S1g PB granites	S2 PB granite
045 18	065 80
010 20	243 70
035 24	060 55
134 23	060 75
318 36	005 70
049 75	195 75
060 37	248 78
047 60	054 68
332 60	024 89
239 74	200 75
200 65	260 82
215 55	
148 28	
224 20	
245 40	
240 20	
294 50	
219 55	
232 82	
210 80	
168 14	
030 30	
345 18	
260 28	
024 42	
185 59	
270 35	
240 48	
242 52	
106 56	
030 50	
168 78	
262 55	
070 58	
200 42	
020 50	
060 89	
064 52	
076 50	
246 28	
216 30	
088 60	

C.Geochemical data

C.1 Major and trace element data

Samples analysed for trace elements at Oxford University were calibrated using the following international rock standards for each batch run:

1. G-1	2. W-1	3. AGV-1
4.BCR-1	5.DTS-1	6 G -2
7.GSP-1	8.PCC-1	9.BHVO-1
10.SY-1	11.SY-3	12.MRG-1
13.GR	14.GA	15.GH
16.BR	17.MICA-FE	18.MICA-MG
19.DR-N	20.UB-N	21.DT-N
22.GS-N	23.FK-N	24.AN-G
25.BE-N	26.MA-N	27.IF-G
28.T-1	29.NIM-D	30.NIM-G
31.NIM-L	32.NIM-N	33.NIM-P
34.NIM-S	35.SIO2	36.JB-2
37.JB-3	38.JGB-1	39.JR-1
40.JR-2	41.AL-1	42.MAG-1
43.QLO-1	44.RGM-1	45.SCO-1
46.SDC-1	47.SGR-1	48.STM-1

For major elements some standards were run along with the samples and these are included in the data tables and also compared with accepted values.

Spider diagrams for Trace elements are normalized to primitive mantle using the Thompson plot and the normalizing values are as follows:

Ba 6.900	Rb 0.350	Th 0.042	K 0.014	Nb 0.350	Ta 0.020
La 0.328	Ce 0.865	Sr 11.800	Nd 0.630	P 0.010	Sm 0.203
Zr 6.840	Hf 0.200	Ti 0.103	Tb 0.052	Y 2.000	Tm 0.034
Yb 0.220					

The accepted values for standards in terms of major elements are:

AGV-1

Si 58.79	Al 17.14	FeT 6.76	Mn 0.092	Mg 1.53	Ca 4.94
Na 4.26	K 2.91	Ti 1.05	P 0.49		

G-2

Si 69.08	Al 15.38	FeT 2.66	Mn 0.032	Mg 0.75	Ca 1.96
Na 4.08	K4.48	Ti 0.48	P 0.14		

GH

Si 75.8	Al 12.5	FeT 1.34	Mn 0.05	Mg 0.03	Ca 0.69
Na 3.8	K 4.50	Ti 0.08	P 0.01		

GSP-1

Si 67.15	Al 15.10	FeT 4.29	Mn 0.04	Mg 0.96	Ca 2.07
Na 2.8	K 5.51	Ti 0.65	P 0.28		

Comparison with standards run

	Accepted AGV 1	Run AGV 1	Accepted GSP 1	Run GSP 1	Accepted GH	Run GH
Si	58.79	60.00	67.15	68.13	76.99	75.8
Al	17.14	17.45	15.10	15.37	12.84	12.5
FeT	6.76	6.94	4.29	4.38	1.36	1.34
Mn	0.092	0.100	0.04	0.04	0.05	0.05
Mg	1.53	1.57	0.96	0.99	0.07	0.03
Ca	4.94	4.98	2.07	2.02	0.74	0.69
Na	4.26	4.52	2.80	2.83	3.95	3.80
K	2.91	2.97	5.51	5.51	4.82	4.5
Ti	1.05	1.07	0.65	0.65	0.08	0.08
P	0.49	0.50	0.28	0.28	0.01	0.01

Major and trace element data tables for all samples analyzed are given on pages 300-313.

FOLIATED GRANITES

	Standard	Cascata Gneiss									
MAJORS	AGV 1	RSMX1	RSMX2	RSMX3	RSMX7	RS SM 3A	RS SM 3B1	RS SM 3B2	RS SM 3B3	RS SM 3C	RS SM 3C2
SiO2	60.24	66.65	66.68	67.74	64.38	53.09	66.35	60.3	67.7	64.94	58.41
TiO2	1.06	0.62	0.63	0.48	0.79	1.43	0.67	0.87	0.56	0.7	0.99
Al2O3	17.68	15.49	15.49	15.84	15.78	18.24	15.5	16.42	15.67	16.48	18.97
Fe2O3T	6.91	4.3	4.17	3.83	5.67	9.42	4.41	5.38	3.55	4.53	6.77
MnO	0.1	0.1	0.1	0.07	0.11	0.16	0.07	0.1	0.07	0.09	0.12
MgO	1.57	1.51	1.47	0.85	2.02	3.33	1.38	1.77	1.12	1.5	2.16
CaO	4.96	3.26	3.34	2.48	3.76	7.14	3.59	4.61	3.32	3.85	5.5
Na2O	4.33	3.65	3.81	3.71	3.55	3.82	3.49	4.16	3.7	3.94	4.69
K2O	2.96	3.62	3.32	4.82	3.62	2.31	3.73	2.57	3.68	3.34	2.73
P2O5	0.51	0.18	0.17	0.15	0.19	0.44	0.17	0.25	0.15	0.2	0.32
Total	100.32	99.39	99.17	99.97	99.86	99.38	99.37	96.43	99.52	99.57	100.67

	Cascata Gneiss									
TRACES	RSMX1	RSMX2	RSMX3	RSMX7	RS SM 3A	RS SM 3B1	RS SM 3B2	RS SM 3B3	RS SM 3C	RS SM 3C
Zn ppm	72.5	72.7	72.3	87.1	136	77	92	65	84	27
Cu ppm	9.7	9	12.4	16.9	25	6	13	6	5	6
Ni ppm	12.5	12.4	12.6	11.4	11	7	11	7	8	8
Co ppm	10.1	11.6	34.2	20.2	27	6	20	17	20	22
Cr ppm	24.8	20.8	21.1	18.2	62	62	70	53	52	56
V ppm	76	75.9	82	98.7	150	48	108	53	75	99
Ba ppm	762.8	686.9	1064.7	1012	1228	755	961	884	802	706
Ga ppm	20.1	19.9	19.6	20.4	136	19	24	17	22	23
Rb ppm	207.4	200.2	233.7	225.9	140	148	174	165	181	150
Sr ppm	297	296.6	325	456	722	438	531	411	426	422
Y ppm	27.4	26.9	25.5	41.2	39	22	30	30	26	15
Zr ppm	155.2	161.4	177.1	162.5	270	270	239	178	238	366
Nb ppm	18.6	17.9	18	25.7	17.4	17.4	19.4	13.5	14	20.6
Pb ppm	27.4	26.4	36.1	28.2	23	26	23	28	28	18
Th ppm	18.6	14.9	17.7	25.9	12	20	12	17	18	22
U ppm	6.2	7	6.2	5.5	4	8	4	5	5	5

FOLIATED GRANITES

	Standard	Cascata Gneiss									
MAJORS	AGV I	RSMX1	RSMX2	RSMX3	RSMX7	RS SM 3A	RS SM 3B1	RS SM 3B2	RS SM 3B3	RS SM 3C	RS SM 3C2
SiO2	60.24	66.65	66.68	67.74	64.38	53.09	66.35	60.3	67.7	64.94	58.41
TiO2	1.06	0.62	0.63	0.48	0.79	1.43	0.67	0.87	0.56	0.7	0.99
Al2O3	17.68	15.49	15.49	15.84	15.78	18.24	15.5	16.42	15.67	16.48	18.97
Fe2O3T	6.91	4.3	4.17	3.83	5.67	9.42	4.41	5.38	3.55	4.53	6.77
MnO	0.1	0.1	0.1	0.07	0.11	0.16	0.07	0.1	0.07	0.09	0.12
MgO	1.57	1.51	1.47	0.85	2.02	3.33	1.38	1.77	1.12	1.5	2.16
CaO	4.96	3.26	3.34	2.48	3.76	7.14	3.59	4.61	3.32	3.85	5.5
Na2O	4.33	3.65	3.81	3.71	3.55	3.82	3.49	4.16	3.7	3.94	4.69
K2O	2.96	3.62	3.32	4.82	3.62	2.31	3.73	2.57	3.68	3.34	2.73
P2O5	0.51	0.18	0.17	0.15	0.19	0.44	0.17	0.25	0.15	0.2	0.32
Total	100.32	99.39	99.17	99.97	99.86	99.38	99.37	96.43	99.52	99.57	100.67

	Cascata Gneiss									
TRACES	RSMX1	RSMX2	RSMX3	RSMX7	RS SM 3A	RS SM 3B1	RS SM 3B2	RS SM 3B3	RS SM 3C	RS SM 3C
Zn ppm	72.5	72.7	72.3	87.1	136	77	92	65	84	27
Cu ppm	9.7	9	12.4	16.9	25	6	13	6	5	6
Ni ppm	12.5	12.4	12.6	11.4	11	7	11	7	8	8
Co ppm	19.1	11.6	34.2	20.2	27	6	20	17	20	22
Cr ppm	24.8	28.8	21.1	18.2	62	62	70	53	52	56
V ppm	76	75.9	82	98.7	150	48	108	53	75	99
Ba ppm	762.8	686.9	1064.7	1012	1228	755	961	884	802	706
Ga ppm	20.1	19.9	19.6	20.4	136	19	24	17	22	23
Rb ppm	207.4	200.2	233.7	225.9	140	148	174	165	181	150
Sr ppm	297	296.6	325	456	722	438	531	411	426	422
Y ppm	27.4	26.9	25.5	41.2	39	22	30	30	26	15
Zr ppm	155.2	161.4	177.1	162.5	270	270	239	178	238	366
Nb ppm	18.6	17.9	18	25.7	17.4	17.4	19.4	13.5	14	20.6
Pb ppm	27.4	26.4	36.1	28.2	23	26	23	28	28	18
Th ppm	18.6	14.9	17.7	25.9	12	20	12	17	18	22
U ppm	6.2	7	6.2	5.5	4	8	4	5	5	5

FOLIATED GRANITES

	Cascata Gneiss									xenolith	
MAJORS	RSM A5A	RSM A5D	RSM A5F	RSMA6B	RSM2A	RSM4A	RSM5	RSM6A	RSM11.5	RSMX12	RSM 3F
SiO2	72.62	72.41	73.55	69.39	69.7	64.01	65.88	65.44	65.7	47.52	48.15
TiO2	0.25	0.26	0.25	0.41	0.51	0.87	0.71	0.63	0.62	1.58	1.39
Al2O3	15.07	14.9	13.77	15.01	14.81	16.48	15.24	16.85	17.42	16.57	17.26
Fe2O3T	1.83	1.89	1.51	3.94	3.53	5.84	4.86	5.02	4.02	12.3	10.72
MnO	0.05	0.05	0.03	0.08	0.06	0.13	0.1	0.07	0.09	0.2	0.15
MgO	0.39	0.41	0.38	0.54	1.2	2.73	1.68	1.38	0.97	7.61	6.55
CaO	1.76	1.71	1.3	2.54	2.8	3.18	3.73	3.77	3.89	7.15	9.81
Na2O	3.99	3.92	3.49	3.93	3.23	4.73	4.85	3.96	4.4	2.36	3.26
K2O	4.62	4.38	5.06	3.1	4.43	2.82	3.07	3.05	2.69	3.58	1.62
P2O5	0.08	0.08	0.07	0.1	0.14	0.43	0.19	0.18	0.14	0.31	0.25
Total	100.67	100.01	99.43	99.05	100.42	101.23	100.32	100.36	99.95	99.23	99.19

TRACES	RSM A5A	RSM A5D	RSM A5F	RSMA6B	RSM2A	RSM 4A	RSM5	RSM 6A	RSM11.5	RSMX12	RSM 3F
Zn ppm	49	47	43	87	58.1	98	62	70	69.3	219.4	101
Cu ppm	7	5	5	5	19.8	9	17.9	18	10	12.9	92
Ni ppm	6	6	6	8	12.5	24	10.5	8	3.7	116.3	68
Co ppm	12	12	12	15	16.3	18	10.1	17	11	47.8	75
Cr ppm	45	46	40	54	34	56	17.5	55	16.4	283	56
V ppm	40	42	40	48	72.6	86	100.6	70	55.2	288.5	255
Ba ppm	941	1096	1035	1431	1024.8	615	597.6	1236	1377.5	797.4	1164
Ga ppm	18	19	16	21	17.7	22	20.1	21	21.7	28.6	21
Rb ppm	175	171	176	174	142.3	240	146.7	122	121.1	392.9	220
Sr ppm	399	395	286	288	411.2	396	324.1	385	396.3	289.6	157
Y ppm	16	16	12	48	24.2	49	28.9	22	27.3	35.4	7
Zr ppm	164	153	148	300	127.4	255	172.7	210	311.7	82.1	255
Nb ppm	11.5	10.7	9.1	19	13.8	25.4	20.9	12.9	16.5	19	5.3
Pb ppm	38	38	32	22	28.9	26	24.4	25	20.5	10.5	28
Th ppm	7	6	5	22	16.5	32	19	15	19	1.7	19
U ppm	9	9	5	1.5	8	17	6.2	4	1.9	4	

FOLIATED GRANITES

Migmatitic Orthogneiss

MAJORS	RSM21	RSM20	RSMC46	RSM11KI	RSM11KII	RSM11L	RSM11M	RSMC35B	RSMC54	RS SM7	RS SM9
SiO2	75.47	72.68	68.03	70.78	72.86	75.14	72.99	71.69	72.38	61.91	69.85
TiO2	0.51	0.58	0.84	0.37	0.29	0.26	0.25	0.49	0.29	0.82	0.37
Al2O3	11.22	12.2	14.96	14.7	14.42	13.73	15.03	13.01	14.83	17.29	15.78
Fe2O3T	4.04	4.82	4.86	2.1	1.89	1.77	1.76	3.66	2.02	5.83	2.72
MnO	0.06	0.08	0.08	0.05	0.04	0.05	0.05	0.07	0.05	0.14	0.03
MgO	1.44	1.8	1.69	0.49	0.38	0.34	0.34	1.26	0.5	2.34	0.83
CaO	1.77	2.26	3.11	1.74	1.52	1.57	1.45	1.85	2.01	3.53	2.33
Na2O	2.49	2.48	3.19	4	3.81	3.67	3.99	2.83	3.34	4.53	3.57
K2O	2.41	3.12	2.57	4.33	4.74	4.38	4.71	3.67	4.99	2.47	4.73
P2O5	0.09	0.12	0.21	0.13	0.1	0.09	0.1	0.1	0.1	0.24	0.13
Total	99.51	100.15	99.52	98.69	100.05	100.99	100.67	98.63	100.51	99.12	100.36

TRACES	RSM21	RSM20	RSMC46	RSM11KI	RSM11KII	RSM11L	RSM11M	RSMC35B	RSMC54	RS SM7	RS SM9
Zn ppm	67.1	62.8	80.7	50.8	45.8	52.9	52.1	70	49.2	108	53
Cu ppm	27.2	14.9	15.2	6.9	8.3	7.8	9.8	34.9	9.1	6	13
Ni ppm	15.3	19	13.8	1.7	2.3	1.1	2.2	13.3	2.5	11	8
Co ppm	20.2	13.6	17	4.2	2.5	6.3	3.8	13.5	4.2	26	18
Cr ppm	52.3	65.3	44.7	15.7	13.3	23.5	9.7	35.7	30.4	30	30
V ppm	70.3	86.5	93.2	36.1	27.4	18.4	21.3	57.5	34.7	76	47
Ba ppm	493.5	653	399.3	1198.8	856.1	526.6	663.8	981.5	1287.6	374	903
Ga ppm	14.9	13.9	20.8	17.1	16.5	17.4	17.5	15.7	17.1	30	19
Rb ppm	114.4	132.7	200.6	112.3	116.5	126.9	140.2	131.7	154.9	203	145
Sr ppm	289.8	201	229.3	203.5	145.2	117.4	123.9	277.3	284.1	282	318
Y ppm	14.5	23.6	26.6	21.5	17	15.5	18	11.9	16.5	20	11
Zr ppm	155.1	176.3	160.3	242.2	193.8	179.3	145.9	204.4	178.5	192	116
Nb ppm	17.3	12.8	8.6	13	11.9	12.4	13	12.1	11.8	14.1	9.5
Pb ppm	13	12	17.4	23.3	21.5	20.9	22.7	16.3	29	35	35
Th ppm	7.5	9.9	9.7	21.9	14.7	5.5	11	5.3	14.6	24	14
U ppm	0	0.5	1.5	0.8	1.4	6.3	4.2	1.2	1.7	4	3

FOLIATED GRANITES

	Pirilini Granite						Cangucu porphyritic			
MAJORS	RSMA68	RSMA69A	RSMA64	RSMA26II	RSMA69B	RSMA68B	RSMA16C	RSM12	RSM12B	RSMC57
SiO2	71.25	70	71.82	67.64	70.86	70.82	67.45	72.63	72.73	69.92
TiO2	0.41	0.49	0.47	0.54	0.51	0.44	0.63	0.35	0.27	0.47
Al2O3	14.42	14.38	14.78	16.75	14.3	14.59	15.55	13.98	14.15	15.97
Fe2O3T	2.32	3.22	3.12	3.16	3.16	2.62	3.69	2.55	2.33	3.89
MnO	0.05	0.06	0.05	0.03	0.05	0.05	0.06	0.03	0.04	0.03
MgO	0.48	0.6	0.7	0.88	0.6	0.59	0.93	0.39	0.2	1.26
CaO	1.86	1.67	1.75	3.07	1.86	1.93	2.55	1.55	1.43	2.67
Na2O	3.23	3.15	2.69	3.11	3.17	3.29	3.56	3.31	3.48	4.2
K2O	5.4	5.61	5.62	4.35	5.26	5.32	4.83	5.45	5.65	2.38
P2O5	0.12	0.16	0.14	0.12	0.15	0.13	0.21	0.08	0.07	0.15
Total	99.54	99.34	101.15	99.65	99.93	99.79	99.46	100.32	100.36	100.94

TRACES	RSMA68	RSMA69A	RSMA64	RSMA26II	RSMA69B	RSMA68B	RSMA16C	RSM12	RSM12B	RSMC57
Zn ppm	46.2	62.2	47.9	83.3	66.7	53.2	69.9	44	47.5	75.3
Cu ppm	12	12.5	7.6	10	11.7	13.8	12.1	5	9.7	16.5
Ni ppm	3.8	4.1	4.7	5.8	2.9	4.2	5.9	7	2.5	9.3
Co ppm	9	13.4	15.5	12	12	13.1	15.1	18	6.6	8.2
Cr ppm	10.8	9.8	22.2	22.4	11.5	9.5	8.5	50	11.4	26.4
V ppm	43.1	44.1	54.5	46.4	44.9	48.5	55.8	44	17.9	45.4
Ba ppm	1109.8	1674.5	1127.6	802.1	1534.6	1137.3	1591.7	374	674.5	288.9
Ga ppm	17.9	18.6	17.1	23.3	18.1	18.1	20.3	18	18.9	21.2
Rb ppm	136.4	155.5	171.7	199.2	145.7	140.7	154.1	145	135.1	112
Sr ppm	278.8	240.9	226.7	314.7	241.4	281.5	425.5	149	133.9	248.3
Y ppm	31.1	34.9	9.8	11.3	29	28.2	42.3	25	31.2	12.6
Zr ppm	158	355.5	168.6	180.5	327.1	192.6	307.5	215	261.8	116.5
Nb ppm	17	17.9	9.6	14.4	17.2	17.3	19.8	15	16.5	15.9
Pb ppm	24.1	25.8	20.3	48.1	24.8	23.7	25.4	21	19.9	17.3
Th ppm	7.8	10.6	7	15.6	9.5	8.7	6.1	16	12.4	3.1
U ppm	0.1	0.7	1.2	0.3	0.2	1.3	0.7	3	0.1	0.3

	Mafic migmatite		Mylonites		
MAJORS	RS SM 10	RSM10B	RSM 16A	RSM 16B	RSM 5
SiO2	68.87	48.43	70.81	48.67	65.88
TiO2	0.51	1.22	0.44	3.08	0.71
Al2O3	15.07	13.9	14.66	14.84	15.24
Fe2O3T	3.73	13.02	2.6	14.59	4.86
MnO	0.07	0.25	0.04	0.38	0.1
MgO	1.53	8.1	0.56	3.74	1.68
CaO	2.82	11.18	1.87	6.22	3.73
Na2O	3.3	1.93	3.08	3.71	4.85
K2O	3.98	2.02	5.77	2.75	3.07
P2O5	0.22	0.11	0.14	1.37	0.19
Total	100.11	100.2	99.98	99.35	100.32

TRACES	RS SM 10	RSM10B	RSM 16A	RSM 16B	RSM 5
Zn ppm	61	125.8	45.9	128.3	62
Cu ppm	17	0.3	12.6	4	17.9
Ni ppm	15	75.4	3.7	2.7	10.5
Co ppm	16	50.8	13.7	38.3	10.1
Cr ppm	54	237.6	13	6.9	17.5
V ppm	79	327.1	42.6	165.5	100.6
Ba ppm	1338	174.6	1310.1	877.7	597.6
Ga ppm	18	19.4	19	26.4	20.1
Rb ppm	155	98.8	186.2	141.7	146.7
Sr ppm	371	167.7	290.6	661.5	324.1
Y ppm	10	33.6	27.9	45.9	28.9
Zr ppm	153	69.6	315.9	310.9	172.7
Nb ppm	6.2	8.3	17.5	46.8	20.9
Pb ppm	25	11	24.5	15.5	24.4
Th ppm	11	0	10.7	5.3	19
U ppm	4	0	1.5	1.7	6.2

TEXT
CUT OFF IN THE
ORIGINAL

			Pink Granite						(Quarry)				
MAJORS	MAJORS	Standard GH	RSM23C	RSMA17A	RSM A17B	RSMA16B1	RSMC34	RSMC12	RSM11A	RSM 11B	RSM11C	RSM 11D	RSM11E
SiO2	SiO2	76.99	70.03	73.47	71.92	76.71	75.42	71.8	77.34	78	77.06	77.5	76.73
TiO2	TiO2	0.08	0.45	0.28	0.26	0.08	0.16	0.25	0.14	0.14	0.16	0.16	0.19
Al2O3	Al2O3	12.84	15.17	14.3	13.54	13.16	13.74	14.97	12.04	12.07	12.51	12.3	12.05
Fe2O3T	Fe2O3T	1.36	2.94	1.86	1.8	0.57	1.27	1.93	1.08	0.97	1.1	1.16	1.47
MnO	MnO	0.05	0.05	0.07	0.06	0.01	0.02	0.05	0.03	0.03	0.03	0.03	0.04
MgO	MgO	0.07	0.81	0.33	0.36	0.06	0.18	0.38	0.09	0.08	0.1	0.12	0.12
CaO	CaO	0.74	2.01	1.45	1.34	0.95	1.09	1.98	0.71	0.7	0.73	0.75	0.64
Na2O	Na2O	3.95	2.91	3.8	3.55	3.5	3.83	4.14	2.77	3.08	2.95	2.81	2.59
K2O	K2O	4.82	5.31	4.89	4.86	5.21	4.59	3.82	5.51	5.01	5.6	5.4	5.89
P2O5	P2O5	0.01	0.23	0.06	0.05	0.02	0.04	0.09	0.03	0.02	0.02	0.02	0.03
Total	Total	100.91	99.9	100.52	97.75	100.27	100.35	99.4	99.74	100.1	100.27	100.25	99.75

TRACES	TRACES		RSM23C	RSMA17A	RSMA17B	RSMA16BI	RSMC34	RSM C12	RSM 11A	RSM 11B	RSM 11C	RSM 11D	RSM 11E
Zn ppm	Zn ppm		56.6	45.4	57.5	11.5	25.9	44	26	25	25	26	33
Cu ppm	Cu ppm		11.8	9.1	9.1	10.2	10	5	4	7	8	4	4
Ni ppm	Ni ppm		8.2	2.4	2.5	1.9	1.7	7	6	6	6	6	6
Co ppm	Co ppm		9.3	4.2	7.5	9.8	5.5	13	17	16	17	17	19
Cr ppm	Cr ppm		18.9	12.5	13.9	19.2	15.5	48	43	42	45	45	46
V ppm	V ppm		52.4	25.4	22.9	15	16.2	43	43	43	43	43	43
Ba ppm	Ba ppm		920.5	1136.8	520.8	751.2	976.8	1344	208	206	209	210	215
Ga ppm	Ga ppm		17.5	16.3	15.3	14.8	17.5	20	13	14	12	14	12
Rb ppm	Rb ppm		171.3	155.9	93.9	114	179.9	102	139	153	134	146	144
Sr ppm	Sr ppm		266	181.2	143.9	219.7	199.7	491	58	56	63	76	64
Y ppm	Y ppm		21.9	32.1	33.9	13.9	27	14	11	14	9	10	12
Zr ppm	Zr ppm		199.7	190.3	232.9	65.3	124.4	186	121	104	132	120	182
Nb ppm	Nb ppm		13.5	16.4	14	10.8	19.6	7	7.6	9.9	6.5	6.7	6.8
Pb ppm	Pb ppm		40.4	29	23.9	25.1	28.4	26	24	10	14	14	15
Th ppm	Th ppm		14.6	15.5	10	5.2	12.2	7	10	10	14	14	15
U ppm	U ppm		6.4	1.5	0.7	0.6	0.3	3	2	2	3	3	2

UNFOLIATED GRANITES

	Pink Granite Quarry		Cascata leucogranite								
MAJORS	RSM11F	RSM 11G	RSMA34	RSM 3D	RSM 3D1	RSMX11	RSMA6A	RSM2B	RSMA54	RSMA47	RSMC62B
SiO2	76.12	68.96	72.58	76.88	70.53	73.65	73.91	73.44	74.52	75.4	72.85
TiO2	0.15	0.3	0.38	0.06	0 26	0.22	0.05	0.29	0.12	0.19	0.23
Al2O3	12.54	13.95	14.29	12.57	13.32	14.68	13.97	13.99	13.86	14.03	14.37
Fe2O3T	1.07	1.82	2.98	0.94	1.84	1.41	0.52	2.18	1.13	1.5	1.64
MnO	0.03	0.04	0.04	0.01	0.03	0.02	0.02	0.02	0.06	0.04	0.03
MgO	0.09	0.36	0.41	0.07	0.39	0.25	0.03	0.52	0.21	0.24	0.34
CaO	0.75	1.43	1.31	1.03	1.93	1.04	0.72	1.94	1.04	1.29	1 39
Na2O	3 01	3.67	3.29	2.26	3.1	3.38	2.61	3.2	4.61	3.27	3.2
K2O	5.53	4.97	5.34	6.14	4.56	6.31	7.41	4.73	3.79	5.27	5.33
P2O5	0.02	0.11	0.15	0.01	0.05	0.13	0.04	0.07	0.04	0.05	0.09
Total	99.31	95.61	100.78	99.98	96.01	101.09	99.28	100.39	99.38	101.28	99.48

TRACES	RSM 11F	RSM 11G	RSMA34	RSM 3D	RSM 3D1	RSMX11	RSM A6A	RSM 2B	RSMA54	RSMA47	RSMC62B
Zn ppm	27	26.5	48.8	14	12	54.5	15	32.1	79.3	31.9	42.2
Cu ppm	7	9.8	7	4	5	8.3	6	9.6	8.7	7.9	8.9
Ni ppm	6	2.8	3.8	6	6	2.6	8	3	4.9	2.1	2.2
Co ppm	16	5.4	40.3	10	21	0.5	8	3	14.3	1.9	4.7
Cr ppm	44	35.8	9.5	45	44	16.1	41	16.2	13.8	9.6	10
V ppm	43	12.9	27.4	40	48	16.7	42	14.8	37.6	22.9	26.5
Ba ppm	208	425	466	1573	1164	624.9	200	219.2	817.1	513.7	916.5
Ga ppm	13	12.6	22.2	12	12	21.1	19	22.3	25.6	17.1	16.8
Rb ppm	133	123.2	346.7	170	150	284.8	252	252.4	262.7	235.8	197.2
Sr ppm	66	61.9	133.7	349	422	101.2	125	72	316.1	117.3	183.3
Y ppm	11	11.5	41.6	3	15	14	23	21.3	11.1	29.3	17.7
Zr ppm	121	120.5	214.8	90	148	132.8	39	63.6	179.4	119.2	150.6
Nb ppm	6.2	7.9	23	1	6.3	10.4	6.9	29.3	14.1	14.9	13.3
Pb ppm	23	19.5	28.4	31	28	42.9	41	32.3	45.7	26.3	28.2
Th ppm	10	8.7	38.8	16	19	15.7	5	9	17.6	21.5	18.2
U ppm	2	1	9.6	3	4	3.6	<4	2.5	1.5	0.8	1

UNFOLIATED GRANITES

	Cascata Leucogranite					Capao do Leao Granite			xenolith
MAJORS	RSMA13	RSMA12	RSMA11	RSMA9AI	RSM A7A	RSMA56A	RSMA56F	RSMA56G	RSMA56H
SiO2	74.91	73.58	73.76	72.79	77.28	76.37	77.32	77.25	55.83
TiO2	0.24	0.28	0.28	0.28	0.09	0.05	0.05	0.05	1.51
Al2O3	14.01	13.78	13.91	14.58	12.59	12.87	12.31	12.79	14.44
Fe2O3T	2.08	2.18	2.26	1.76	0.78	1.27	1.14	1.32	17.86
MnO	0.06	0.04	0.04	0.05	0.04	0.14	0.1	0.14	0.95
MgO	0.36	0.47	0.49	0.44	0.03	0.02	0.01	0.01	0.52
CaO	1.5	1.52	1.53	1.93	0.7	0.54	0.47	0.5	0.49
Na2O	3.64	2.93	2.94	3.97	3.61	4.15	3.97	4.17	1.74
K2O	4.23	5.2	5.23	4.23	5.04	4.67	4.54	4.57	6.98
P2O5	0.08	0.09	0.1	0.08	0.01	0.01	0.01	0.01	0.01
Total	101.1	100.07	100.53	100.1	100.16	100.08	99.9	100.8	100.34

TRACES	RSMA13	RSMA12	RSMA11	RSMA9AI	RSM A7A	RSMA56A	RSMA56F	RSMA56G	RSMA56H
Zn ppm	48.5	49.1	45.2	35.5	23.2	47.7	60.6	50.2	722.3
Cu ppm	8.6	10.4	8.1	9.4	9.4	7.9	8.6	9.6	0
Ni ppm	2.9	3.5	2.7	2.3	1.6	1.4	1.7	1.5	3.2
Co ppm	8.2	14.7	11.6	3.3	3.5	4.2	3.6	5.8	6.5
Cr ppm	10.2	17.7	14.7	10.7	10.6	9.7	6.9	13	9.6
V ppm	24.5	30.5	30.7	30.5	11.2	7.7	9.1	9.4	10.9
Ba ppm	332.2	864.5	788.7	951.5	102.9	42.6	46.2	48.5	74.3
Ga ppm	17.9	16.3	16.6	14.9	15.2	15.5	19.4	15.6	33.8
Rb ppm	211.8	186.2	182.6	106.9	213.4	161	270.5	163.5	504.4
Sr ppm	109.4	180.1	178.4	265.6	27	4.7	6.2	6.5	6
Y ppm	30.3	33.3	22	23.9	20.1	31.7	18.2	35.1	22.8
Zr ppm	156.5	179.3	177.6	106.5	78.1	126	150.8	119.8	71.3
Nb ppm	20.2	14.2	14.9	9.5	11.6	12.3	14.5	14.9	95.3
Pb ppm	26	23.8	26.4	21.4	29	21.4	35	23.8	19.2
Th ppm	32.6	31.4	30.6	8.6	33.4	16.2	19.6	20.3	10.1
U ppm	1.3	1.8	1.2	0.8	3.6	1.2	0.1	1.5	10.9

	anguca Red Granite			Pegmatites		Metasediments		
MAJORS	RSM 13	RSM13B	RSMC6	RSMA57A	RSM3E	RSM 23E	RSM C71	RSM23B
SiO2	76.08	77.43	77.86	73.59	74.01	47.63	49.1	46.52
TiO2	0.08	0.12	0.09	0.14	0.11	3.38	3.16	3.56
Al2O3	12.61	12.88	12.15	13.39	13.78	17.18	17.03	18.78
Fe2O3T	1.39	1.6	1.35	1.12	0.92	13.87	13.43	14.88
MnO	0.03	0.02	0.02	0.03	0.02	0.18	0.16	0.2
MgO	0.05	0.04	0.03	0.35	0.19	4.5	4.22	5.04
CaO	0.52	0.39	0.26	0.3	1.04	6.13	6.29	3.34
Na2O	3.59	3.53	3.28	1.31	2.48	4.73	3.97	5.35
K2O	4.97	5.21	5.12	9.16	7.22	1.03	1.82	0.84
P2O5	0.01	0.02	0.01	0.07	0.05	0.85	0.94	0.01
Total	99.31	101.24	100.17	99.45	99.82	99.49	100.01	99.45

TRACES	RSM13	RSM13B	RSMC6	RSMA57A	RSM 3E	RSM 23E	RSM C71	RSM23B
Zn ppm	47.7	54.1	42.4	35.9	23	126.1	130.3	235
Cu ppm	10.3	10	8.4	14.8	5	10.6	12.6	10.9
Ni ppm	2.7	1.5	1.6	3.8	6	6.7	6.5	6.8
Co ppm	0	3.8	2.5	4.9	10	31.2	28	45.3
Cr ppm	11.1	13.1	15.3	15.1	45	0.9	1.8	0.1
V ppm	10.6	12	9.4	30.3	41	226	223.6	245.7
Ba ppm	48.9	114.8	64.2	2552.3	615	380	487	256
Ga ppm	21.3	20.7	20.1	10.2	16	24.7	24.4	26.8
Rb ppm	223.1	181.1	181.6	200.1	220	44.2	90.5	44
Sr ppm	10.2	24.2	14.6	253.9	157	488	488.3	283.8
Y ppm	49.8	39	39.2	8.2	7	33.1	34.7	37.5
Zr ppm	99.5	140.6	117.7	23.2	34	336.2	339.1	390.9
Nb ppm	38.8	34.5	30.3	5.4	5.3	53	52.2	60.6
Pb ppm	28.5	26.2	23	34.7	26	6.8	18.6	15.9
Th ppm	22	18.2	20.5	8.4	32	5.1	4.6	6.6
U ppm	1.2	0.6	2.1	0.7	17	0.9	3.9	4.9

	Basalts				Andesites			Gabbros	
MAJORS	RSM23D	RSM23A	RSMA70B	RSMA17C	RSM31	RSM113A	RSM41B	RSM94	RSM108A
SiO2	43.21	48.52	55.44		56.67	52.68	56.97	51.82	56.25
TiO2	4.01	3.24	1.51		1.3	1.99	1.54	0.49	0.47
Al2O3	15.62	17.12	14.24		15.27	14.58	15.23	6.59	6.76
Fe2O3T	15.82	13.41	18.1		10.64	12.04	8.97	12.49	11.26
MnO	0.16	0.18	0.99		0.12	0.14	0.11	0.23	0.21
MgO	5.68	4.48	0.52		3.96	6.8	3.1	15.86	14.9
CaO	7.76	6.06	0.49		7.92	4.25	3.61	11.37	11.09
Na2O	3.21	4.28	1.72		2.5	4.62	5.99	0.7	0.66
K2O	2.35	2.21	6.73		2.3	1.27	2.78	0.22	0.33
P2O5	0.97	0.83	0.01		0.21	0.7	0.82	0.03	0.08
Total	98.78	100.32	99.76		100.89	99.11	99.12	99.91	102.15

TRACES	RSM23D	RSM23A	RSMA70B	RSMA17C	RSM31	RSM113A	RSM41B	RSM94	RSM108A
Zn ppm	66.6	125.5	717.5	125.9	91.9	111.8	67.8	93.7	94.1
Cu ppm	21.7	17.2	0	19.5	101.6	9.2	15.6	49.7	32.7
Ni ppm	40.2	7.9	3.5	61.4	64.2	111.2	50.9	330.7	220.3
Co ppm	47.2	43.4	2.7	78.1	41.7	43.9	25.7	70.1	60.6
Cr ppm	4.5	0	7.6	42.5	73.6	151.7	67.9	751.6	1044.4
V ppm	166.8	222.5	9.2	243.9	249.3	200.7	140.5	242.5	185.2
Ba ppm	583.2	687.7	72	347.6	501.9	1032.1	1238	73.2	81.4
Ga ppm	14.2	24.2	33.5	24.7	20.5	17.6	19.1	11.2	9.9
Rb ppm	38.2	93.8	504	66.3	76.6	26.5	40.1	7.4	6.7
Sr ppm	1030.1	776.8	5	551.6	199	681.2	317.7	43	68.2
Y ppm	40	33.2	23.9	29	35.4	29.3	43.8	10.1	12.8
Zr ppm	216	333.7	71.1	207.6	191.6	160.5	440	31.3	53.2
Nb ppm	60.4	51.5	96.7	22.8	15.2	19.4	25.5	6	6
Pb ppm	2.8	9.2	19.4	6.2	14	5.8	6.7	4.3	2.4
Th ppm	2.1	5.3	7.5	1.2	9.3	3.1	4.3	1.4	1.5
U ppm	0	2.5	14	0.8	2	0	0	0.2	0

	Santana granite	Campinas Granite					Cassapava Granite				
MAJORS	RSMB36	RSMA33	RSMA31	RSMA21	RSMC67	RSMA58B	RSM42A	RSM 42B	RSM 42C	RSM 42D	RSM 42F
SiO2	76.78	76.49	75.48	75.06	75.66	76.66	73.36	74.9	69.62	70.81	
TiO2	0.07	0.08	0.03	0.1	0.1	0.09	0.14	0.13	0.3	0.31	
Al2O3	13.47	12.31	14.73	15.98	15.4	13.14	14.12	13.88	14.57	14.97	
Fe2O3T	0.83	0.77	1.08	0.94	0.97	1.22	1.44	1.21	2.61	2.86	
MnO	0.01	0.01	0.03	0.05	0.03	0.01	0.04	0.02	0.04	0.05	
MgO	0.26	0.01	-0.01	0.14	0.14	0.1	0.32	0.22	0.77	0.85	
CaO	0.79	0.39	0.21	0.13	0.26	0.44	1.38	1.29	2.02	2.11	
Na2O	5.25	3.32	4	3.04	3.63	2.6	4.15	3.85	4.23	4.33	
K2O	2.24	4.85	4.25	3.97	4.03	5.89	4.03	4.44	2.94	3.15	
P2O5	0.02	0.02	0.17	0.03	0.09	0.04	0.05	0.04	0.11	0.12	
Total	99.73	98.26	100	99.45	100.3	100.19	99.04	99.98	97.22	99.56	

								pink	grey		
TRACES	RSMB36	RSMA33	RSMA31	RSMA21	RSMC67	RSMA58B	RSM42K	RSM 42B	RSM 42C	RSM 42D	RSM 42 F
Zn ppm	12.8	55.7	20.4	81.2	83	16.9	36	25	48	51	62
Cu ppm	12.3	47.6	11.1	10.6	11.7	31.9	10.8	7	10	8	19
Ni ppm	2.9	3	2.7	4	2.9	1.8	8.1	6	11	11	9
Co ppm	4.6	9.8	3.9	7.8	9.8	6	3.6	18	15	15	16
Cr ppm	12.2	6.4	12.6	8	10.6	11.4	17.4	12	21	8	49
V ppm	17.8	9.7	8.4	12.6	14.9	35.1	20.7	42	80	43	67
Ba ppm	616.1	116.6	62.6	153.5	142.1	1289.1	887.1	1068	2140	2026	643
Ga ppm	11	20.4	30.6	34.7	32.6	12.8	15.4	15	19	18	22
Rb ppm	20.8	382.6	596.8	626.5	586.5	123.4	96.8	99	88	92	71
Sr ppm	218.3	25.3	8.4	49.8	37.7	269.2	348.3	284	448	406	425
Y ppm	2.7	97.6	25.5	12.2	10.9	8.6	17.5	11	19	23	27
Zr ppm	31.6	80.3	27.7	37.2	31.9	148.3	103.2	97	205	198	204
Nb ppm	3.8	18.2	35.6	11.3	10.5	4.3	14.9	13.7	20.5	20.9	23.3
Pb ppm	6.2	40.7	23.1	24.1	27	28	29.4	34	29	30	27
Th ppm	1.3	35	4.9	4.6	2.3	9.2	19.5	8	13	12	16
U ppm	0	6.1	8.7	0.9	2.1	0	1.1	4	3	4	18

	Xenolith				Encruzilhada Granite					
MAJORS	RSM 42M	RSM42N	RSM 42 Q	RSM42G	RSM15A	RSMC31	RSMA30	RSMA28	RSMA19	RSMA72B	RSMC3
SiO2	70.96	68.76		53.83	62.1	74.72	69.56	69.3	74.25	75.58	72.14
TiO2	0.33	0.42		1.35	0.94	0.25	0.21	0.29	0.25	0.22	0.27
Al2O3	15.18	15.95		17.74	15.96	13.08	12.64	14.49	13.93	12.78	14.12
Fe2O3T	2.89	3.51		9.87	5.03	2.4	2.43	3.7	2.33	1.12	2.4
MnO	0.04	0.06		0.22	0.09	0.04	0.04	0.07	0.03	0.05	0.04
MgO	0.87	1.02		2.9	1.41	0.16	0.05	0.01	0.18	0.11	0.2
CaO	2.27	2.68		1.67	3.58	0.96	1.03	1.38	1.09	0.63	1.47
Na2O	4.34	4.96		3.05	3.79	2.87	2.76	3.34	3.01	3.62	3.43
K2O	2.85	2.01		7.55	3.77	5.44	5.95	6.81	6.18	5.41	5.71
P2O5	0.13	0.16		0.43	0.33	0.06	0.03	0.02	0.07	0.02	0.06
Total	99.87	99.52		98.62	97.01	100	94.71	99.41	101.31	99.54	99.84

	Xenolith					Encruzilhada Granite					
TRACES	RSM 42M	RSM42N	RSM42Q	RSM42G	RSM15A	RSMC31	RSMA30	RSMA28	RSMA19	RSMA72B	RSMC3
Zn ppm	11.6	47.2	61.8	246	110.3	46.9	57.1	84.8	40.4	35.1	43.8
Cu ppm	12.7	9.2	17.7	3	57.3	9.1	11.8	13.7	8.5	10.6	7.9
Ni ppm	1.8	6.6	7.1	20.8	8.7	2	3.1	2.7	1.6	2.6	1.6
Co ppm	7.3	14.5	7.3	23.9	16.5	7.1	6.4	12.4	6	3.3	9.6
Cr ppm	6.7	23.1	19.3	39.8	18.6	7	3.6	1.2	10.9	13.1	10.6
V ppm	16.1	42.8	46.6	83.9	96.6	15.5	12.1	9	17.9	13.2	17.5
Ba ppm	3743.1	2117.2	803.6	2320.6	1232.6	637.8	365.2	277.7	587.9	154	660.1
Ga ppm	11.3	16.8	21.2	32.8	23.4	18.4	22	23	20.7	15	19
Rb ppm	154.4	73.3	70.5	306.8	194.4	228.1	224.2	211.1	248.3	90.4	134.6
Sr ppm	289.4	475.2	411.7	231.5	452.2	107.3	69.7	58.2	104.1	28.9	134.5
Y ppm	10.8	14.3	27.2	70.4	90.3	32.1	50.4	57.3	52.3	58.5	29.6
Zr ppm	42.3	188.2	208.7	486.4	275.1	241.3	347.1	493.4	227	171.2	243.5
Nb ppm	10.6	12.1	27.7	88.8	25.9	21.3	27	36.8	18.8	14.1	14.8
Pb ppm	50.3	20.7	21.6	35.4	65.1	21.1	27.8	28.6	25.1	23.9	21
Th ppm	6.1	8.4	13.3	63.3	12.4	11.4	22.6	27.1	11.6	7.7	11.8
U ppm	1	0.5	2.6	1.1	7.7	2.3	0.5	3.2	2.8	0.5	0.5

Encantada Gneisses

MAJORS	RSM45A	RSM45B	RSM54	RSM59A	RSM59B	RSM59C	RSM78D	RSM93	RSM95	RSM40B
SiO2	69.81	73.45	72.28	67.62	68.33	73.31	68.13	74.35	64.74	70.93
TiO2	0.34	0.16	0.2	0.51	0.47	0.14	0.28	0.2	0.49	0.04
Al2O3	15.03	14.12	14.95	16.07	15.73	14.78	18.41	13.69	15.88	13.01
Fe2O3T	2.81	1.88	2.03	4.63	4.38	1.27	2.97	1.71	5.47	0.47
MnO	0.05	0.02	0.02	0.06	0.05	0.02	0.03	0.04	0.11	0.01
MgO	0.77	0.44	1.18	2.14	1.85	0.48	0.89	0.48	2.46	0.09
CaO	2.51	1.62	0.22	2.85	2.58	2.07	2.23	0.93	3.42	1.43
Na2O	3.69	3.41	3.5	4.35	4.13	3.8	4.81	3.22	3.6	4.62
K2O	4.02	4.37	5.26	2.53	2.9	3.91	2.96	5.5	2.89	2.43
P2O5	0.13	0.06	0.1	0.06	0.07	0.07	0.12	0.07	0.18	0.01
Total	99.16	99.53	99.76	100.86	100.51	99.85	100.83	100.19	99.24	93.04

TRACES	RSM45A	RSM45B	RSM54	RSM59A	RSM59B	RSM59C	RSM78D	RSM93	RSM95	RSM40B
Zn ppm	47.3	21.1	34.4	75.7	63.9	22.1	21.9	37.8	66.7	14.7
Cu ppm	18.4	7.2	9.4	24.7	37.5	18.2	15.8	10	7.2	10.6
Ni ppm	4.2	4	5.3	44	34.2	6	5.3	3.3	9.7	2.4
Co ppm	3.9	73.8	6.3	14.2	16.1	5.1	7.5	5.5	16.2	8.1
Cr ppm	15.9	14.9	11.7	129.9	120.7	27.2	12.7	27.6	27	14.9
V ppm	45.2	28.7	31.2	84.4	78.8	26.9	38.5	22.8	96.5	16.7
Ba ppm	1909	2268	1069.6	561.1	582.6	1624.6	698.5	660.3	989.5	1059.6
Ga ppm	16.1	14.7	15.4	18.5	17.8	14.5	20.1	16.8	15.7	11.9
Rb ppm	73.1	61.9	71.6	99.2	95.5	65.8	37.6	154.1	62.2	28.6
Sr ppm	612.4	437.9	200.2	441.2	445.6	492.3	360.6	186.9	482.3	379.9
Y ppm	8.3	4.4	11.1	8.3	9.2	5.1	11.3	13	21.6	1.1
Zr ppm	167.2	176.8	100.8	149.8	143.8	66.2	224.1	111.2	153.4	64
Nb ppm	6.5	3.6	6.9	12.7	10.2	5.2	10.3	13.6	10	3.6
Pb ppm	16.3	13.7	9.4	14.5	15.1	25.8	9	21.9	11.1	14.9
Th ppm	13.4	12.7	12.2	9.2	10.2	4.4	37.6	12.1	11.5	2.7
U ppm	0	0.5	0.2	0.3	0	0.4	0.2	1.6	1.3	-0.8

	Encantada schists								Red beds	
MAJORS	RSM33	RSM34B	RSM85A	RSM100	RSM48	RSM96B	RSM122	RSM66	RSM119B	RSMA41	RSM44
SiO2	80.64	46.92	69.73	54.08	72.62	70.3	76.49	74.92	71.66	86.45	81.1
TiO2	0.31	0.7	0.19	0.19	0.9	0.45	1.02	0.22	0.37	0.33	0.51
Al2O3	7.79	10.91	16.68	19.34	16.02	14.47	12.13	15.92	12.94	9.1	9.6
Fe2O3T	5.39	5.11	2.22	2.98	5.25	3.11	5.91	0.78	4.29	1.03	3.51
MnO	0.06	0.17	0.03	0.03	0.01	0.02	0.04	0.01	0.01	0.04	0.05
MgO	1.53	6.85	1.96	10.13	0.41	2.48	1.09	0.25	0.17	0.15	0.71
CaO	1.9	25.29	3.95	0.41	0.01	0.45	0.16	0	0.55	0.07	0.75
Na2O	0.63	0.7	3.92	0.87	0.22	0.77	0.65	0.15	2.99	0.11	2.18
K2O	1.2	2.27	1.54	9.08	3.84	7.06	2.84	7.15	5.96	2.44	1.86
P2O5	0.09	0.12	0.03	0.06	0.08	0.1	0.1	0.01	0.05	0.01	0.16
Total	99.54	99.04	100.26	97.17	99.37	99.21	100.43	99.41	98.99	99.73	100.44

TRACES	RSM33	RSM34B	RSM85A	RSM100	RSM48	RSM96B	RSM122	RSM66	RSM119B	RSMA41	RSM44
Zn ppm	52.3	64.9	30.2	57.1	36.1	27.6	53.9	19.6	20.5	24.5	48.5
Cu ppm	16.4	23.1	8.4	4.7	52	7.4	10.4	11.4	25.1	14.2	18.4
Ni ppm	16.9	38.4	17.5	12.5	6.1	14.7	24.1	3.3	4.9	10.2	17.2
Co ppm	12.7	21.7	13.1	33.2	15	16.6	18.5	12.4	10.8	10.2	8.2
Cr ppm	35.1	78.8	15.3	9.8	90	38	70.9	9.2	2.6	14.9	45.2
V ppm	50.7	90.6	47.7	31.1	136.6	92.4	103.3	31.4	24	25.7	54.6
Ba ppm	254.8	283.3	322.9	1066.4	680.3	1107.8	527.2	579.8	2759.7	514.9	438.7
Ga ppm	9	12.1	14	19.4	21.3	14.8	16	18.8	15.1	8.3	11.2
Rb ppm	55.8	112.3	20.3	86.9	162.3	50.4	131.6	160	89.1	69.6	82.2
Sr ppm	49.8	106.8	280.8	86.4	43.8	103.8	50.2	51	259.6	68.6	129.6
Y ppm	18	18.5	2.6	3.9	40	12.8	29.1	21.6	22.1	16.8	18.2
Zr ppm	153.7	78.9	181	107.7	223	205.9	131.7	152	755.8	383.1	224.2
Nb ppm	9.2	11.4	5.4	6.5	18	9.3	17.1	17.2	15.7	8.4	13.8
Pb ppm	9.4	8.9	6.9	9.3	16.7	12.4	33.2	24	20.2	13.3	17.8
Th ppm	3.6	4.7	2.3	9.9	15.4	16.7	9.2	24.1	16.8	5	13.9
U ppm	0	0.7	0	0	2.1	0.5	1.9	0.3	0.5	0	1

C.2 Rare Earth Element data

Rare earth element data are normalized by the following chondritic values for the spider diagrams illustrated in chapter 6. The data is given in table C2

La 0.329	Ce 0.865	Pr 0.116	Nd 0.630	Sm 0.203	Eu 0.077
Gd 0.276	Tb 0.048	Dy 0.343	Ho 0.071	Er 0.225	Tm 0.031
Yb 0.220	Lu 0.034				

The accepted values for the standard Whin Sill are listed below where these are compared with the actual values analysed in this study.

	Accepted value	Actual value	Actual value
La	25.0	25.41	25.76
Ce	57.4	57.75	54.96
Nd	33.2	33.62	33.33
Sm	7.27	7.25	7.116
Eu	2.26	2.204	2.239
Tb	1.13	1.155	1.014
Yb	2.5	2.444	2.434
Lu	0.37	0.379	0.394
Th	2.95	2.995	2.894
U	0.7	---	0.8276
Ta	1.29	1.38	1.336
Hf	4.93	4.815	4.796
Cs	1.03	1.042	1.074
Co	48.2	48.97	49.66

Rare earth element data

REE DATA	Standard AC2/1	Cascata Gneiss RS SM A6A	RS SM 2B	RS SM 3A	RS SM 3B1	RS SM 4A	RS SM 6A	Pink Granite RSM 23C	RSM 11A	Leucogranite RS SM 3D	RSM A10	RSM X11
La	59.36	7.162	47.21	59.48	45.14	107.2	37.41	55.21	53.89	30.29	73.24	39.43
Ce	149.6	13.73	86.49	123.8	90.3	189.9	78.68	108.1	103.6	37.92	132.2	77.16
Nd	93.93	7.499	30.65	60.12	37.28	14.44	26.72	48.72	38.66	9.65	49.44	36.71
Sm	25.61	2.434	4.99	11.85	6.64	2.093	4.814	9.201	5.66	0.866	7.804	8.646
Eu	1.992	0.629	0.87	2.66	1.389	11.31	1.05	1.433	0.82	0.28	0.946	0.984
Gd	39.67			13.67		11.37		7.545			6.365	6.62
Tb	4.785	0.413	0.629	1.43	0.875	1.723	0.693	27.3	0.3743	0.218	0.869	0.769
Tm	2.405	0.264	0.3018	0.32	0.398	0.578	0.412	0		0	0.344	0.1599
Yb	16.37	1.811	1.275	2.71	1.99	3.643	2.194	0.337	0.9886	0.29	1.659	0.771
Lu	2.458	0.304	0.209	0.38	0.311	0.603	0.352	0.256	0.166	0.05	0.287	0.123
Th	17.8	3.902	17.86	10.94	18.87	31.7	13.83	18.45	11.4	15.43	34.67	18.68
Ta	6.672	0.5976	0.856	1.083	1.294	1.826	1.158	0.8862	0.8031	0.1517	1.068	0.6937
Hf	26.26	1.765	4.34	6.048	4.917	6.75	6.104	6.44	3.65	3.35	6.035	4.28
Co	20.45	0.598	3.513	22.88	9.339	13.89	10.7	5.251	0.6453	0.6127	3.031	1.495
Sc	0.126	1.802	2	19.64	7.577	18.08	8.904	6.549	1.275	0.3343	4.768	1.876
U	4.873	7.881	2.625	1.936	2.724	12.46	2.356	6.354	2.029	1.606	2.548	5.508
Cs	2.839		4.051	5.142	4.362	16.73	5.67	4.411	2.919	2.084		7.418

	Standard WS	Migmatitic Gneiss RS SM 7	RS SM 8	RS SM 9	RSM 10	RS SM 21	Cangucu Granite RSM 13	RSM C6	RSM C2A	CDLEAO RSM A56G	Xenolith RSM A56H
La	25.42	84.71	23.6	112.34	52.65	25.33	21.76	43.59	68.67	16.03	2.606
Ce	57.75	166.5	44.5	78.79	92.17	45.58	54.92	80.03	129	44.41	8.962
Nd	33.62	58.86	17.28	31.8	34.53	21.33	30.7	50.58	61.26	30.25	6.423
Sm	7.249	9.998	2.661	6.464	5.352	3.93	8.503	10.78	13.1	7.75	1.88
Eu	2.204	1.29	0.723	1.133	1.037	0.8295	0.1245	0.235	1.522	0.49	0.208
Gd	8.586			7.761			9.541	9.972	12.04	6.521	
Tb	1.155	1.056	0.329	12.8	0.525	0.485	1.381	1.385	1.961	1.11	0.561
Tm	0.538	0.359	0.148	0.667	0	0.149	0.843	0.29	0.908	0.46	0
Yb	2.444	1.304	0.776	0.466	0.687	1.149	3.859	3.328	4.3	3.18	2.222
Lu	0.379	0.189	0.137	0.113	0.104	0.202	0.643	0.551	0.685	0.55	0.415
Th	2.995	22.49	6.113	15	11.77	7.243	23.76	24.38	18.71	21.22	8.681
Ta	1.38	0.621	0.3046	0.447	0.3856	0.623	3.059	2.403	2.307	1.052	2.434
Hf	4.815	6.42	3.983	3.842	4.467	5.427	4.466	5.81	7.077	5.324	3.787
Co	48.97	15.85	8.074	5.687	9.693	10.64	0.3049	0.5098	3.818	0.068	0.4088
Sc	29	10.55	4.341	4.766	7.807	9.537	1.988	2.15	9.12	3.44	22.76
U		1.239	0.5889	1.516	0.6804	1.269	1.835	2.566	3.616	1.421	9.874
Cs	1.042	6.555	2.213	2.359	2.926	3.165	1.035	0.9097	2.222		

Rare earth element data

	Standard AC2/1	sheared RS SM 16A	RS SM 16B	Cassapava RS SM 42A	RSM 42C	RSM 15A	Enc gnoisses RSM 96B	RSM 45A	RSM 59A	RSM 59B	RSM 95	Schist RSM 48	Schist RSM 54
La	59.91	57.93	52.95	39.49	73.37	52.77	32.42	88.92	26.85	20.33	50.11	41.08	36.27
Ce	154.3	114.5	120.2	59.88	121.7	120.8	62.57	152.8	51.11	57,47	80.2	72.73	66.46
Nd	93.56	46.81	67.08	20.7	40.18	67.74	21.9	63.15	21.83	15.13	30.77	37.09	27.56
Sm	25.2	8.154	13.12	3.429	5.873	17.29	3.214	7.03	3.58	2.72	5.4	7.669	4.72
Eu	1.987	1.491	4.017	0.761	1.11	2.858	0.93	1.67	1.08	0.9	1.454	1.492	1.08
Gd	26.47	7.381	13.64		5.303	17.04		8.244	4.452	3.709	5.522	6.874	3.772
Tb	4.816	0.904	13.64	0.474	0.603	2.738	0.575	0.56	0.34	0.37	0.752	1.166	0.5584
Tm	2.473	0.376	1.717	0.334	0.322	1.236	1.094	0.16	0	0.22	0.203	0.634	0.1525
Yb	16.24	2.017	3.236	1.326	1.563	6.262	1.559	0.58	0.62	0.96	1.839	3.663	0.9228
Lu	2.451	0.312	0.474	0.245	0.244	0.843	0.2507	0.09	0.09	0.16	0.319	0.608	0.1446
Th	17.8	11.5	4.053	7.878	11.45	12.25	19.03	16.22	9.105	10.59	11.56	14.81	13.79
Ta	6.691	1.091	3.483	1.236	0.9071	4.038	0.3524	0.1363	0.6358	0.579	0.5231	1.305	0.166
Hf	26.36	7.735	7.078	3.333	5.31	7.652	7.224	5.813	5.345	5.13	4.4	6.714	3.76
Co	20.55	10.14	26.45	2.195	5.1	10.53	6.616	5.38	14.16	13.48	12.1	1.459	3.648
Sc	0.453	5.65	20.93	2.771	3.975	9.793	6.285	3.292	11.61	10.65	5.725	15.59	2.897
U	4.347	1.4	1.348	2.473	2.401	10.02	0.955	1.001	1.078			2.815	0.8891
Cs	2.862	2.005	3.045	1.052	1.408	4.785	0.4497	0.4339	2.169	1.986	0.9316	7.37	0.7499

	Standard WS	CAMPINAS RSM A21	Piritini RSM A64	Encruzilhada RSM A30	red beds RSM 24	RSM 44	RSM A41	RSM 27	Andesite RSM 31	basalt RS SM 23A	metased RS SM 23B	RSM C71	RSM 23E
La	25.76	7.427	33.83	122.3	41.77	12.16	22.47	36.74	32.29	49.22	57.54	47	50.02
Ce	54.96	13.72	65.68	220.9	83.37	22.86	35.47	73.96	64.91	103.4	119.9	97.64	104.9
Nd	33.33	5.889	28.53	90.17	37.23	14.2	18.84	23.62	34.41	54.08	60.89	53.81	53.7
Sm	7.116	1.491	5.117	14.28	7.152	3.112	3.743	3.831	7.03	10.07	12.48	10.13	10.13
Eu	2.239	0.358	1.307	1.155	0.958	0.65	0.848	0.735	1.716	3.211	3.574	3.142	3.493
Gd	10.56			10.68	21.07		3.799	4.716	7.915	10.48	34.82	10.93	35.69
Tb	1.074	0.184	0.376	1.67	1.143	0.544	0.468	0.689	1.051	1.348	1.515	1.32	1.334
Tm	0.4604	0.608	0.145	0.478	0.59	0.351	0.191	0.462	0.548	0.294	0	1.07	0.287
Yb	2.434	0.299	0.8488	3.529	4.32	1.786	1.623	3.024	3.19	2.597	2.821	2.574	2.457
Lu	0.394	0.089	0.14	0.549	0.675	0.3	0.299	0.498	0.5	0.396	0.476	0.42	0.402
Th	2.894	3.004	7.011	21.16	11.99	12.93	5.546	12.11	8.238	4.822	5.359	4.52	4.569
Ta	1.336	3.823	0.8467	1.308	1.228	1.103	0.5417	1.111	0.9314	3.875	4.501	3.883	3.811
Hf	4.796	1.352	5.378	10.95	4.188		11.92	13.75	5.171	7.653	8.901	7.647	7.898
Co	49.66	1.467	5.043	0.8646	2.784	6.206	4.604	1.546	33.97	34.1	33.9	26.63	34.27
Sc	29	1.639	4.452	3.902	6.621	7.261	2.421	3.805	34.23	16.97	19.38	17.03	17.65
U	0.8276	1.032	1.549	3.32	3.443	2.168	1.283	1.672	2.37	1.227	5.952	4.065	1.703
Cs	1.074	122.8	2.819	1.881	3.613	7.791	2.843	3.857	0.8127	3.654	0.989	2.288	0.7723

C.3 Normative data

vol%	Neph	Qtz	AFspar	Plag	An(wt%)	
Cascata Orthogneiss						
RSMX1	.0	29.8	20.8	49.3	35.9	Malm
RSMX2	.0	29.8	18.5	51.6	34.9	Malm
RSMX4	.0	25.8	34.7	39.5	32.2	Palm
RSMX7	.0	27.9	19.3	52.7	37.8	Malm
RSM3A	.0	10.6	8.3	81.0	43.5	Malm
RSM3B1	.0	28.9	24.3	46.8	38.0	Malm
RSM3B2	.0	21.6	15.0	63.5	35.3	Malm
RSM3B3	.0	29.0	23.7	47.2	36.5	Malm
RSM3C	.0	25.7	18.6	55.7	36.8	Malm
RSM3C2	.0	12.3	11.9	75.9	36.8	Malm
RSMA5A	.0	29.5	36.4	34.1	25.2	Palm
RSM A5D	.0	31.4	33.9	34.7	24.5	Palm
RSMA5F	.0	32.8	41.2	26.0	24.2	Palm
RSM A6B	.0	33.6	20.2	46.2	29.4	Palm
RSMX12	.0	9.6	4.0	86.4	53.1	Malm
RSM3F	2.1	.0	18.4	79.5	47.7	Malm
RSM2A	.0	32.0	29.8	38.2	37.5	Malm
RSM4A	.0	26.4	6.3	67.3	25.1	Malm
RSM4B	.0	24.8	56.5	18.6	19.5	Malm
RSM4C	.0	23.6	41.0	35.3	39.1	Malm
RSM5	.0	18.1	33.6	48.4	16.1	Malm
RSM6A	.0	27.9	14.8	57.4	36.4	Palm
RSM8	.0	30.8	19.0	50.2	32.6	Palm
Cascata Leucogranite						
RSMA34	.0	33.4	41.5	25.1	24.0	Palm
RSM3D	.0	38.7	47.7	13.6	37.4	Palm
RSM3D1	.0	33.9	36.8	29.3	32.9	Malm
RSMX11	.0	28.9	51.4	19.7	22.6	Palm
RSMA6A	.0	29.3	59.8	10.8	31.0	Palm
RSM2B	.0	34.8	35.6	29.6	32.7	Palm
RSMA54	.0	32.2	32.0	35.8	14.2	Palm
RSMA47	.0	34.7	41.3	23.9	26.2	Palm
RSMC62B	.0	33.4	41.7	24.9	27.2	Palm
RSM69A	.0	30.5	26.1	43.4	41.5	Palm
RSM69B	.0	30.4	23.4	46.3	43.0	Palm
Piritini Granite						
RSMA68	.0	30.2	41.8	28.0	32.2	Malm
RSMA69A	.0	30.0	43.5	26.4	30.2	Palm
RSMA64	.0	35.0	40.6	24.4	35.3	Palm
RSMA26II	.0	30.9	28.3	40.8	40.7	Palm
RSMA69B	.0	31.6	39.9	28.5	31.6	Palm
RSMA68B	.0	29.9	40.7	29.4	31.9	Malm
Pink Granite						
RSM23C	.0	33.2	38.4	28.4	33.8	Palm
RSMA17A	.0	31.0	39.1	29.9	23.7	Palm
RSMA17B	.0	32.1	39.9	28.1	24.1	Palm
RSMA16B1	.0	34.4	43.9	21.8	21.1	Palm
RSMC34	.0	34.5	37.5	28.0	19.0	Palm
RSMC12	.0	31.2	29.5	39.4	25.1	Palm
RSM11A	.0	39.5	45.8	14.7	23.1	Palm
RSM11B	.0	40.2	42.1	17.8	19.2	Palm
RSM11C	.0	37.5	46.5	15.9	22.3	Palm
RSM11D	.0	40.0	44.1	15.9	23.1	Palm
RSM11E	.0	38.9	48.6	12.4	24.6	Palm
RSM11F	.0	36.8	46.5	16.8	22.0	Palm
RSM11H	.0	28.4	42.0	29.6	23.7	Malm
Campinas Granite						
RSMA33	.0	39.8	41.8	18.3	10.4	Palm
RSMA31	.0	41.4	58.6	.0	.0	Palm
RSMA21	.0	56.3	43.7	.0	.0	Palm

Migmatitic Granite						
RSMC57	.0	37.1	8.0	54.9	26.6	Palm
RSMA58B	.0	41.1	46.9	12.0	17.3	Palm
RSM10B	.0	.1	45.9	54.0	57.0	Malm
RSM21	.0	57.8	9.8	32.4	30.1	Palm
RSM20	.0	51.0	14.3	34.7	36.3	Palm
RSMC46	.0	42.1	9.0	48.9	35.7	Palm
RSM11KI	.0	29.9	34.5	35.6	23.6	Palm
RSM11KII	.0	31.2	38.0	30.8	23.6	Palm
RSM11L	.0	35.2	34.4	30.4	24.6	Palm
RSM11M	.0	30.7	36.8	32.5	21.4	Palm
RSM11.5	.0	25.3	14.2	60.4	34.9	Palm
RSMC35B	.0	44.2	23.7	32.1	31.0	Palm
RSMC54	.0	31.5	38.1	30.3	32.4	Palm
RSM7	.0	25.5	4.2	70.3	29.8	Palm
RSM9	.0	29.0	34.8	36.2	32.3	Palm
RSM10	.0	34.0	24.9	41.2	35.4	Palm
Caçapava Granite						
RSM42A	.0	32.7	32.7	34.6	19.9	Palm
RSM42B	.0	34.0	36.2	29.9	21.3	Palm
RSM42C	.0	34.0	20.0	46.0	23.1	Palm
RSM42D	.0	32.8	21.5	45.7	23.6	Palm
RSM42G	.0	7.9	59.1	33.1	25.8	Palm
RSM42M	.0	34.1	17.7	48.2	24.3	Palm
RSM42N	.0	31.1	9.0	59.9	23.5	Palm
RSM15A	.0	23.6	23.0	53.4	35.6	Malm
Encruzilhada Granite						
RSMA71B	.0	30.1	46.5	23.4	21.0	Malm
RSMC31	.0	37.8	43.3	18.9	24.7	Palm
RSMA30	.0	31.5	51.3	17.2	28.1	Malm
RSMA28	.0	22.0	61.3	16.6	22.6	Malm
RSMA19	.0	32.1	49.3	18.6	27.5	Palm
RSMA72B	.0	33.1	47.9	19.0	13.5	Malm
RSMC3	.0	28.7	47.2	24.1	26.2	Malm
Capao do Leao Granite						
RSMA13	.0	36.7	32.0	31.3	23.5	Palm
RSMA12	.0	36.1	39.9	24.0	31.0	Palm
RSMA11	.0	36.1	39.8	24.1	30.8	Palm
RSMA56H	.0	32.8	50.0	17.2	24.7	Palm
RSMA56A	.0	33.7	40.9	25.4	10.5	Palm
RSMA56F	.0	36.3	40.0	23.6	9.8	Palm
RSMA56G	.0	34.8	39.8	25.4	9.6	Palm
Canguçu Red Granite						
RSM13	.0	36.2	43.2	20.6	12.7	Palm
RSM13B	.0	37.2	44.2	18.6	10.0	Palm
RSMC6	.0	40.0	44.3	15.7	8.1	Palm
Pink Granite						
RSMA17B	.0	31.6	40.3	28.1	23.9	Malm
RSMA16B1	.0	34.4	43.9	21.8	21.1	Palm
RSMA16C	.0	26.7	34.8	38.5	33.2	Malm
RSM12	.0	31.2	42.5	26.3	28.8	Malm
RSM12B	.0	29.2	45.9	24.9	25.9	Malm
RSMC67	.0	47.3	52.7	.0	.0	Palm
RSMA9A	.0	31.1	32.9	36.0	26.3	Malm
RSMA7A	.0	35.6	43.7	20.7	15.6	Malm
Pegmatites						
RSMA57A	.0	32.0	66.1	1.9	56.2	Palm
RSM3E	.0	30.3	56.6	13.1	37.0	Malm
Santana Granite						
RSM B36	.0	38.0	15.9	46.2	8.7	Palm

D. Calculations and Isotope Data

D.1 The Rb-Sr Age Equation

The Rb-Sr method of dating whole rocks is based on the ß-decay of 87Rb to 87Sr with a half-life of 48.8 x 10^9 years Jâger,1979). This half-life corresponds to the recommended decay constant of 1.42 x 10^{11}. The equation for determining the age of a sample from the decay of ^{87}Rb to ^{86}Sr is expressed as:

$$(^{87}Sr/^{86}Sr)_p = (^{87}Sr/^{86}Sr)_0 + {}^{87}Rb/^{86}Sr \ (e^{\lambda t}-1)$$

where t =intrusion age of the granite λ = decay constant

$(^{87}Sr/^{86}Sr)_p$ =measured ratio $(^{87}Sr/^{86}Sr)_0$ = initial ratio

D.2 Data representation

In several diagrams Sr and Nd data have been reported using the Ɛ notation of De Paulo and Wasserburg (1976).

$$\varepsilon Nd = \frac{^{143}Nd/^{144}Nd \text{ sample at time t}}{^{143}Nd/^{144}Nd \text{ Chur at time t}}$$

$^{143}Nd/^{144}Nd$ Chur = 0.51264 at t=0

$^{147}Sm/^{144}Nd$ Chur = 0.1967

$$\varepsilon Sr = \frac{^{87}Sr/^{86}Sr \text{ sample at time t}}{^{87}Sr/^{86}Sr \text{ UR at time t}}$$

$^{87}Sr/^{86}Sr$ UR =0.7047 at t=0

where

$^{87}Sr/^{86}Sr$ UR =0.7047 at t=0

$^{87}Rb/^{86}Sr$ UR=0.0847 at t=0

Model Nd ages are given by the intercept between two curves (Ben Othman et al (1984)).

$(^{143}Nd/^{144}Nd)_{sample}=(^{143}Nd/^{144}Nd)T+(^{147}Sm/^{144}Nd)_{sample}(e^{\lambda T}-1)$

and $(^{143}Nd/^{144}Nd)_{DM}= AT^2+BT+C$:

Depleted mantle with

A =1.53077 x 10-5

B =-0.22073 x 6.54 x 10-3

C = 0.513078

A,B,C are chosen to fit the evoltion curve of a depleted mantle defined by data on MORB, ophiolites, precambrian mafic volcanics, komatitites supracrustals and meteorites.

The model age is calculated using a program by D.Wright and the results are presented in table D3.

D.3 Isotope data

Standard data are presented in the form of a graph in figures D1 and D2. These also calculate standard deviations over the period 1987-1989 (pages 321-334). Two standards are regularly run with each batch of samples. NBS 987 for Sr samples and J+M std for Nd samples. The data for standards run in this study are presented here:

Standards

Date	8/4/88	11/7/88	16/9/88	18/11/88	10/1/88
NBS 987	0.710235	0.710101	0.710155	0.710157	0.710124
J+M std	0.511873	0.511906	0.511914	0.511916	0.511905
Date	13/3/89	5/5/89	8/7/89	10/8/89	
NBS 987	0.710148	0.710224	0.710320	0.710233	
J+M Std	0.511906	0.511916			

All isotopic data is presented in table D3 on pages 335-337.

Fig 01

Ave 0.7102228
std dev 0.00003

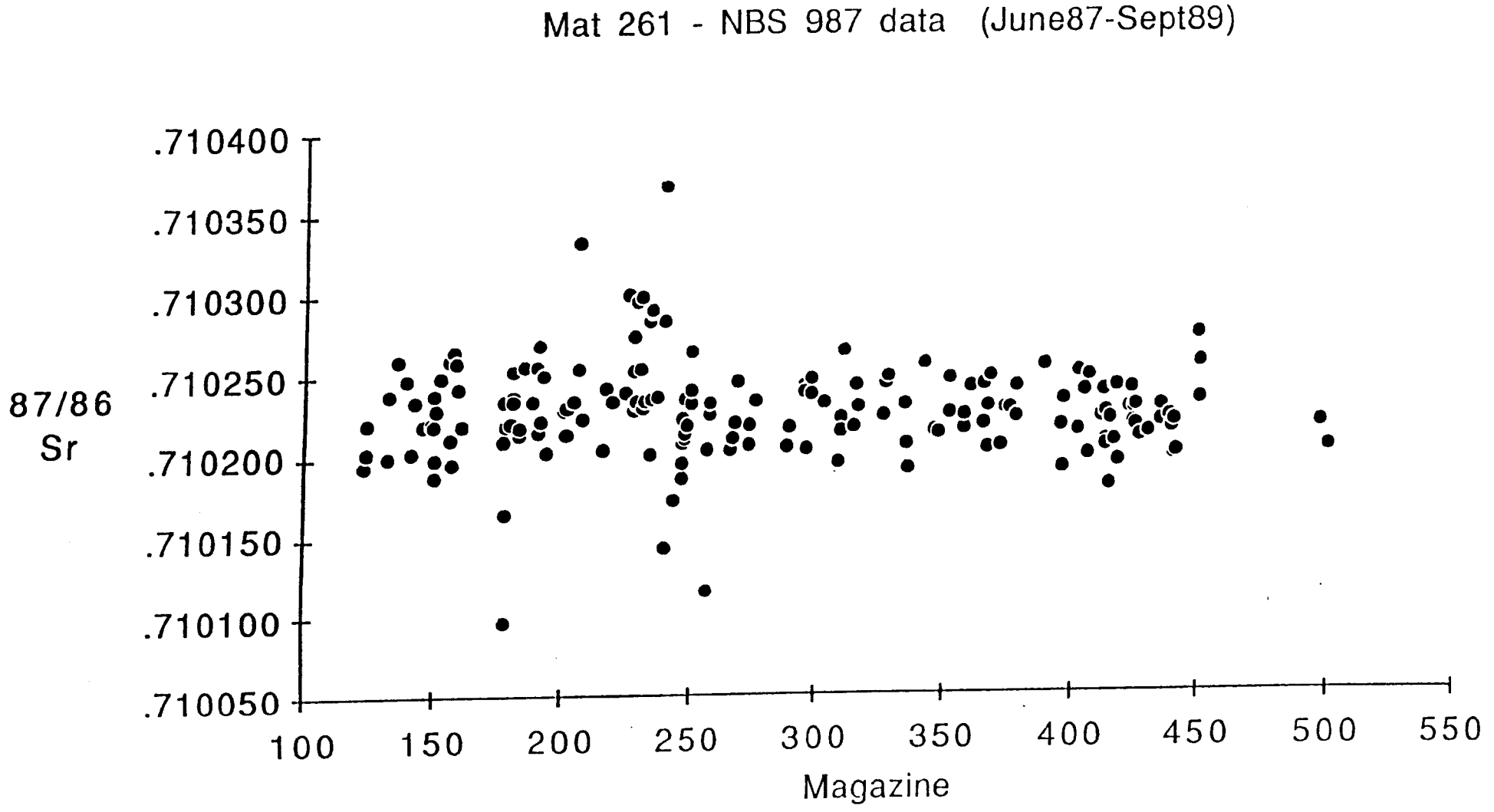

Date	Magazine	87/86 Sr	error
6/9/89	122.13	.710195	.000026
	123.01	.710221	.000023
	123.07	.710203	.000029
	132.01	.710200	.000026
	132.11	.710239	.000029
	135.01	.710260	.000026
	138.01	.710248	.000013
	141.09	.710203	.000023
	142.01	.710234	.000014
	145.01	.710220	.000019
	148.11	.710221	.000019
	149.01	.710238	.000025
	149.05	.710219	.000024
	150.01	.710199	.000026
	150.06	.710229	.000025
	150.11	.710189	.000024
	152.07	.710249	.000024
	155.01	.710260	.000020
	156.11	.710212	.000028
	157.01	.710196	.000025
	157.13	.710266	.000024
	158.01	.710259	.000023
	158.13	.710242	.000028
	160.01	.710220	.000020
	177.06	.710234	.000030
	177.07	.710210	.000027
	178.02	.710220	.000017
	178.03	.710165	.000022
	178.04	.710098	.000016
	179.05	.710221	.000024
	180.04	.710237	.000019
	180.07	.710234	.000021
	180.1	.710253	.000021
	183.09	.710214	.000023
	183.1	.710218	.000040
	184.06	.710256	.000018
	188.01	.710235	.000027
	189.13	.710256	.000013
	190.01	.710215	.000029
	190.13	.710270	.000023
	191.13	.710222	.000031
	192.06	.710251	.000029
	194.01	.710203	.000032
	200.09	.710229	.000027
	201.01	.710214	.000025
	201.13	.710230	.000029
	204.01	.710235	.000026
	205.01	.710334	.000021
	205.13	.710255	.000025
	207.01	.710224	.000035
	215.01	.710205	.000037
	216.01	.710242	.000018

	219.09	.710235	.000017
	224.13	.710240	.000019
	225.01	.710301	.000025
	227.01	.710253	.000016
	227.11	.710275	.000023
	227.12	.710233	.000020
	227.13	.710229	.000019
	228.01	.710297	.000017
	228.08	.710233	.000011
	228.13	.710234	.000016
6/11/88	230.01	.710255	.000019
	230.07	.710300	.000032
	230.13	.710230	.000017
	231.09	.710234	.000030
	233.11	.710284	.000019
	234.09	.710202	.000012
	234.1	.710290	.000014
	234.11	.710292	.000009
	234.12	.710236	.000010
	236.09	.710237	.000014
	239.01	.710368	.000014
	239.03	.710284	.000009
	240.08	.710143	.000013
	243.08	.710174	.000012
	246.01	.710187	.000012
	246.02	.710209	.000011
	246.12	.710197	.000015
	246.13	.710224	.000013
	247.01	.710212	.000011
	247.02	.710214	.000013
	247.13	.710236	.000010
	248.02	.710220	.000010
	250.01	.710233	.000009
	250.05	.710241	.000010
	250.08	.710266	.000008
	256.04	.710204	.000010
	256.13	.710116	.000010
	257.01	.710227	.000014
	257.11	.710233	.000013
	265.1	.710204	.000008
	265.9	.710212	.000010
	266.01	.710204	.000008
	266.02	.710204	.000010
	266.07	.710212	.000010
	267.01	.710221	.000009
	267.09	.710247	.000010
	267.1	.710221	.000009
	267.9	.710247	.000010
	273.01	.710220	.000010
	273.13	.710208	.000010
	276.02	.710235	.000010
	288.1	.710206	.000009
	288.8	.710218	.000012

	295.1	.710244	.000010
	295.2	.710240	.000012
	295.9	.710205	.000010
	297.1	.710238	.000010
	297.8	.710248	.000010
	302.8	.710233	.000009
	308.1	.710196	.000010
	308.8	.710223	.000010
	309.2	.710216	.000010
	310.01	.710266	.000009
	314.07	.710218	.000010
	315.12	.710244	.000005
	316.13	.710230	.000010
	326.13	.710225	.000010
	327.1	.710246	.000010
	328.03	.710249	.000010
	334.01	.710232	.000009
	335.01	.710207	.000016
	336.08	.710193	.000011
	342.05	.710259	.000011
	342.13	.710257	.000010
	346.01	.710215	.000009
	348.01	.710214	.000010
	352.01	.710226	.000009
	352.13	.710248	.000010
	358.01	.710217	.000010
	358.13	.710225	.000010
	360.06	.710243	.000011
	365.01	.710244	.000009
	365.08	.710219	.000010
	367.01	.710205	.000009
	367.08	.710231	.000010
	368.01	.710249	.000010
	372.01	.710206	.000010
	374.01	.710229	.000010
	375.1	.710229	.000011
	378.01	.710242	.000010
	378.08	.710224	.000011
	389.09	.710256	.000010
	395.01	.710218	.000010
	396.01	.710192	.000010
	396.13	.710234	.000011
	402.01	.710216	.000011
	402.13	.710252	.000010
	405.03	.710240	.000011
	406.01	.710250	.000010
	406.13	.710200	.000011
	411.01	.710224	.000110
	412.01	.710240	.000010
	413.05	.710209	.000010
	413.12	.710226	.000010
	413.13	.710206	.000011
	415.01	.710181	.000011

	415.07	.710222	.000010
	416.01	.710243	.000009
	416.111	.710209	.000009
	417.01	.710242	.000011
	418.13	.710196	.000010
	422.02	.710229	.000010
	423.13	.710241	.000010
	424.01	.710229	.000010
	424.1	.710220	.000011
	425.01	.710231	.000011
	425.13	.710218	.000011
	426.07	.710212	.000011
	430.06	.710214	.000011
	435.02	.710221	.000011
	435.06	.710231	.000010
	438.09	.710223	.000011
	439.08	.710217	.000010
	440.03	.710221	.000009
	440.08	.710201	.000010
	441.01	.710202	.000011
	449.01	.710275	.000012
8/8/89	450.01	.710257	.000010
	450.07	.710235	.000011
	497.07	.710219	.000010
10/14/89	500.07	.710205	.000011
	Average	0.710228	
	1 std dev	0.00003	

Period	Results	
21.11.86 to 7.5.88 (static runs)	Average	0.511859
	1 Std deviation	0.000026
	Sigma	0.000004
	Max	0.511933
	Min	0.511806
8.5.88 to 13.9.88 (static runs)	Average	0.511894
	1 Std deviation	0.000031
	Sigma	0.000006
	Max	0.511953
	Min	0.511833
14.9.88 to 14.3.89	Tests	No samples
15.3.89 to 12.10.89 (static runs)	Average	0.511914
	1 Std deviation	0.00002
	Sigma	0.000003
	Max	0.511957
	Min	0.511856
3.7.89 to 25.11.89 (dynamic runs)	Average	0.511811
	1 Std deviation	0.000021
	Sigma	0.000003
	Max	0.511856
	Min	0.511774

Fig D2

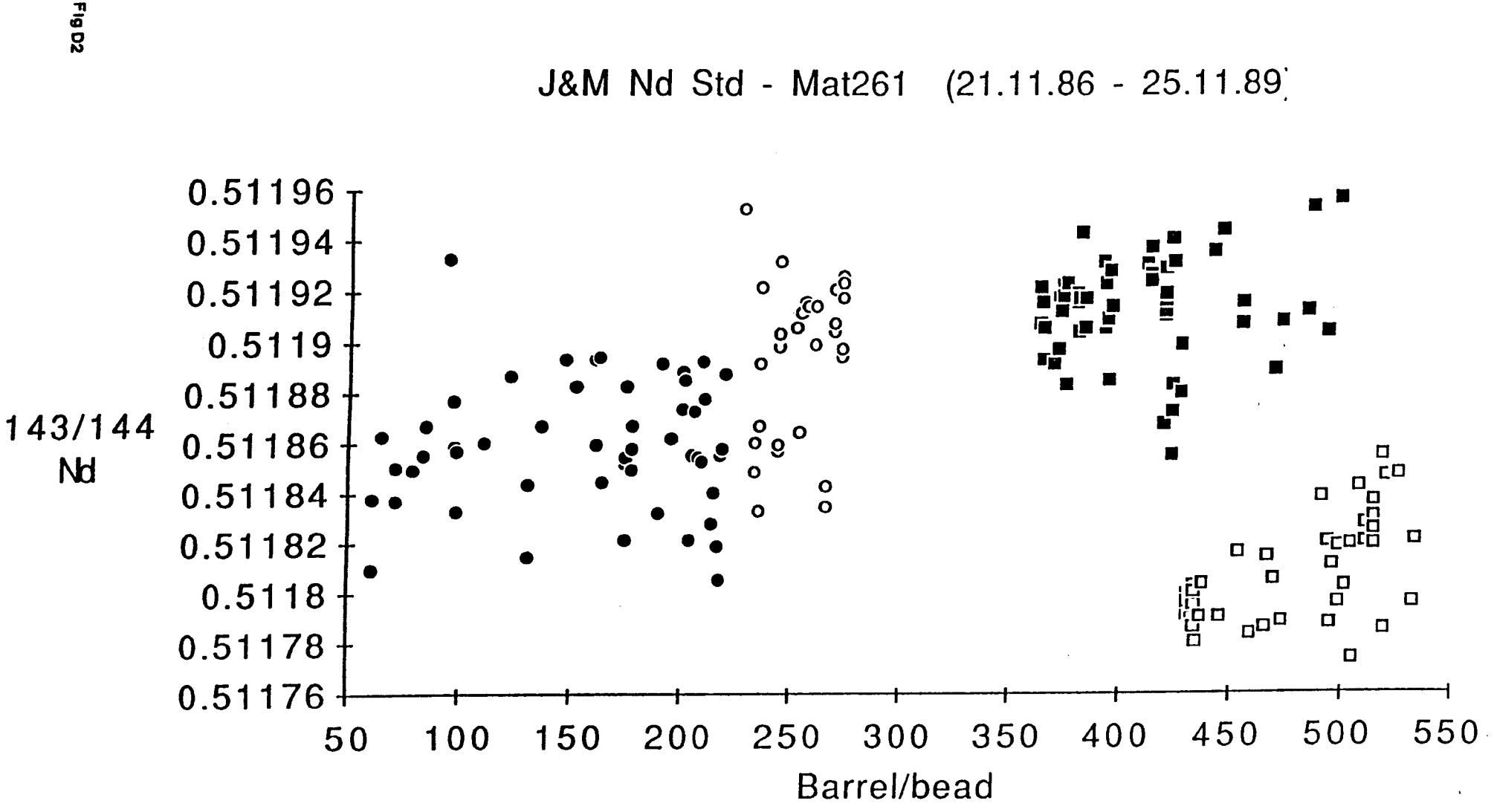
J&M Nd Std - Mat261 (21.11.86 - 25.11.89)
143/144 Nd
0.51196
0.51194
0.51192
0.5119
0.51188
0.51186
0.51184
0.51182
0.5118
0.51178
0.51176
50
100
150
200
250
300
350
400
450
500
550
Barrel/bead

261 J@M Nd standards - 21.11.86 to 25.11.89

Date	Barrel/bead	143/144 Nd	143/144 error
21.11.86	60.06	.511810	0.000019
	60.07	.511838	0.000011
	64.06	.511863	0.000019
23.12.86	71.01	.511851	0.000013
	71.08	.511837	0.000017
28.1.87	78.13	.511850	0.000022
	83.01	.511856	0.000018
	84.13	.511867	0.000023
18.3.87	93.08	.511933	0.000028
	96.09	.511877	0.000012
	97.01	.511859	0.000016
27.3.87	98.01	.511833	0.000018
	98.09	.511857	0.000029
	110.13	.511861	0.000025
8.6.87	121.12	.511887	0.000019
23.6.87	130.05	.511815	0.000018
	130.12	.511844	0.000016
5.8.87	136.01	.511867	0.000019
	146.11	.511894	0.000022
30.9.87	151.11	.511883	0.00002
23.10.87	159.01	.511894	0.00002
27.10.87	160.08	.511860	0.00002
28.10.87	161.01	.511895	0.000026
3.11.87	163.13	.511845	
	173.01	.511883	0.000018
	173.02	.511852	0.000019
	173.03	.511855	0.000015
	173.04	.511822	0.000014
27.1.88	176.01	.511867	0.000015
	176.02	.511858	0.000018
	176.04	.511850	0.000019
23.3.88	188.08	.511832	
24.3.88	189.06	.511892	0.000018
	194.01	.511862	0.00002
4.4.88	199.01	.511889	0.000023
	199.07	.511874	0.000015
5.4.88	200.01	.511886	0.000015
8.4.88	203.01	.511822	0.000024
	203.13	.511856	0.000017
9.4.88	204.07	.511873	0.000013
12.4.88	206.11	.511855	0.000014
17.4.88	208.01	.511853	0.00002
	208.08	.511893	0.000016
19.4.88	209.01	.511878	0.000018
25.4.88	213.01	.511828	0.000018
29.4.88	214.01	.511841	0.000018
4.5.88	216.08	.511819	0.000016
5.5.88	217.01	.511806	0.000016
	217.11	.511856	0.000017
6.5.88	218.01	.511858	0.000017
7.5.88	219.1	.511888	0.000019

	Ave	.511859	
	std dev	.000026	
	sigma	.000004	
	Max	.511933	
	Min	.511806	
30.5.88	226.02	.511953	0.000022
14.6.88	233.06	.511861	0.000007
	233.1	.511849	0.000011
24.6.88	235.01	.511867	0.000006
	235.06	.511922	0.000006
	235.1	.511833	0.000002
	235.13	.511892	0.000002
	243.01	.511932	0.000006
	243.02	.511857	0.000006
	243.03	.511857	0.000008
	243.04	.511899	0.000006
	243.05	.511903	0.000007
	243.06	.511904	0.000004
	243.07	.511860	0.000011
30.7.88	251.13	.511906	0.000003
1.8.88	252.01	.511912	0.000006
	252.13	.511865	0.000002
2.8.88	253.07	.511912	0.000005
3.8.88	254.01	.511916	0.000002
5.8.88	255.13	.511915	0.000004
15.8.88	259.01	.511900	0.000001
	259.02	.511915	0.000003
30.8.88	265.01	.511843	0.000003
	265.09	.511835	0.000003
8.9.88	268.01	.511905	0.000003
	268.08	.511921	0.000001
	268.13	.511908	0.000004
13.9.88	271.01	.511926	0.000004
	271.02	.511895	0.000004
	271.03	.511898	0.000001
	271.04	.511924	0.000001
	271.05	.511918	0.000003
	Ave	.511894	
	std dev	.000031	
	sigma	.000006	
	Max	.511953	
	Min	.511833	
	Beginning of	Test period	
	271.06	.511918	0.000002
18.9.88	274.02	.511894	0.000003
	274.09	.511922	0.000005
19.9.88	275.01	.511910	0.000002
22.9.88	276.05	.511908	0.000002

tests	276.13	.511934	0.000003
"	277.13	.511914	0.000003
25.9.88	280.04	.511878	0.000002
"	280.06	.511840	0.000002
"	280.1	.511877	0.000001
"	280.11	.511914	0.000001
11.11.88	298.01	.511880	0.000003
"	298.02	.511880	0.000003
"	298.04	.511900	0.000003
23.11.88	303.12	.511872	0.000004
"	305.01	.511889	0.000004
"	305.02	.511903	0.000005
"	305.03	.511909	0.000005
"	305.04	.511922	0.000004
"	305.05	.511896	0.000008
"	305.06	.511894	0.000005
"	305.07	.511908	0.000004
"	305.08	.511906	0.000005
14.12.88	312.1	.511838	0.000004
"	312.2	.511828	0.000003
"	312.4	.511841	0.000005
"	312.5	.511872	0.000003
"	312.6	.511855	0.000005
"	312.7	.511812	0.000007
"	314.1	.511829	0.000003
"	314.2	.511857	0.000005
"	316.1	.511866	0.000005
"	316.2	.511864	0.000003
"	316.3	.511900	0.000004
"	316.5	.511842	0.000005
"	316.6	.511901	0.000005
"	316.7	.511891	0.000005
"	316.8	.511893	0.000004
"	318.1	.511835	0.000006
"	318.2	.511902	0.000005
"	318.5	.511984	0.000006
"	318.6	.511868	0.000005
"	318.7	.511828	0.000005
"	318.8	.511843	0.000007
"	319.01	.511835	0.000012
"	319.02	.511852	0.000013
"	319.08	.511860	0.000004
"	320.01	.511895	0.000004
"	320.04	.511867	0.000006
"	320.06	.511861	0.000005
"	320.07	.511909	0.000005
"	320.08	.511872	0.000004
"	321.03	.511837	0.000024
"	321.04	.511883	0.000005
"	321.05	.511860	0.000006
"	321.06	.511926	0.000006
12.1.89	323.01	.511865	0.000003
"	323.02	.511891	0.000004

"	323.03	.511853	0.000002
"	323.04	.511886	0.000004
"	323.06	.511893	0.000004
"	323.07	.511915	0.000003
"	323.08	.511858	0.000003
"	326.01	.511866	0.000003
"	326.02	.511866	0.000003
"	326.03	.511861	0.000005
"	326.04	.511863	0.000004
"	326.05	.511864	0.000003
"	326.06	.511861	0.000002
"	326.07	.511866	0.000004
"	331.01	.511867	0.000004
"	331.02	.511868	0.000005
"	331.03	.511875	0.000005
"	331.04	.511862	0.000006
"	331.05	.511880	0.000004
"	331.06	.511875	0.000012
"	331.07	.511875	0.000005
"	331.08	.511877	0.000005
28.1.89	332.09	.511834	0.000005
29.1.89	333.12	.511840	0.000006
"	333.13	.511821	0.000004
1.2.89	335.08	.511853	0.000004
"	335.09	.511884	0.00001
"	335.1	.511859	0.000005
"	335.11	.511860	0.000005
"	335.13	.511875	0.000006
3.2.89	336.09	.511828	0.000005
"	336.1	.511836	0.000005
"	336.11	.511851	0.000002
"	336.12	.511817	0.000005
"	351.01	.511903	0.000003
"	351.02	.511919	0.000004
"	351.03	.511907	0.000002
"	351.04	.511924	0.000003
"	351.05	.511910	0.000004
"	351.06	.511907	0.000003
"	354.01	.511878	0.000003
"	354.02	.511921	0.000003
"	354.03	.511900	0.000003
"	354.04	.511910	0.000003
"	354.05	.511893	0.000003
"	354.06	.511920	0.000003
	Test period	finished	
15.3.89	362.08	.511922	0.000004
	362.11	.511908	0.000007
17.3.89	363.07	.511916	0.000003
19.3.89	364.01	.511894	0.000003
	364.05	.511906	0.000003
30.3.89	369.01	.511892	0.000002

1.4.89	370.01	.511918	0.000002
	370.13	.511898	0.000004
3.4.89	371.01	.511913	0.000006
4.4.89	372.08	.511923	0.000007
	372.09	.511919	0.000003
6.4.89	374.12	.511884	0.000005
	374.13	.511924	0.000001
13.4.89	379.01	.511920	0.000002
14.4.89	379.13	.511916	0.000004
	380.01	.511905	0.000002
	380.07	.511918	0.000005
15.4.89	381.07	.511944	0.000005
18.4.89	383.01	.511918	0.000004
	383.07	.511906	0.000004
27.4.89	391.13	.511932	0.000008
30.4.89	392.01	.511906	0.000004
	392.07	.511924	0.000003
1.5.89	393.13	.511910	0.000005
3.5.89	394.01	.511929	0.000003
	394.08	.511886	0.000003
8.5.89	395.07	.511915	0.000004
3.6.89	411.05	.511931	0.000002
5.6.89	413.01	.511928	0.000004
	413.02	.511938	0.000002
	413.03	.511927	0.000003
	413.04	.511925	0.000002
15.6.89	419.08	.511911	
	419.09	.511913	
	419.07	.511917	
	419.11	.511920	
	419.12	.511868	
	419.13	.511930	
19.6.89	422.8	.511931	0.000004
	422.9	.511932	0.000003
	422.01	.511941	0.000003
22.6.89	423.01	.511884	0.000004
	423.02	.511856	0.000004
	423.03	.511873	0.000004
27.6.89	427.06	.511900	0.000004
	427.07	.511881	0.000004
26.7.89	441.08	.511936	0.000004
31.7.89	445.01	.511945	0.000004
	454.01	.511908	0.000003
	454.13	.511916	0.000004
7.9.89	469.02	.511890	0.000004
11.9.89	472.01	.511909	0.000004
25.9.89	484.01	.511913	0.000003
27.9.89	485.02	.511954	0.000004
6.10.89	493.01	.511905	0.000006
12.10.89	498.13	.511957	0.000005
Nd static	Ave	.511914	
	std dev	.000020	

	sigma	.000003	
	Max	.511957	
	Min	.511856	
3.7.89	431.07	.511800	0.000004
	431.08	.511795	0.000004
	431.09	.511792	0.000004
	431.1	.511797	0.000004
6.7.89	433.01	.511791	0.000006
	433.02	.511799	0.000004
	433.04	.511800	0.000005
	433.06	.511800	0.000004
8.7.89	434.01	.511803	0.000004
	434.02	.511796	0.000003
	434.04	.511801	0.000002
	434.05	.511787	0.000007
	435.01	.511781	0.000005
18.7.89	436.01	.511791	0.000005
20.7.89	437.02	.511804	0.000006
31.7.89	445.07	.511791	0.000004
11.8.89	453.08	.511817	0.000002
	453.08	.511817	0.000002
22.8.89	459.05	.511784	0.000006
1.9.89	466.04	.511787	0.000005
4.9.89	467.1	.511815	0.000004
7.9.89	469.01	.511806	0.000004
12.9.89	473.01	.511789	0.000011
3.10.89	491.06	.511839	0.000005
7.10.89	494.11	.511821	0.000005
8.10.89	495.01	.511788	0.000006
10.10.89	496.01	.511812	0.000003
13.10.89	499.01	.511797	0.000002
	499.1	.511819	0.000005
15.10.89	501.01	.511804	0.000007
	501.06	.511803	0.000002
18.10.89	504.03	.511820	0.000003
20.10.89	505.13	.511774	0.000009
24.10.89	508.08	.511843	0.000006
27.10.89	511.07	.511828	0.000005
	511.1	.511821	0.000005
1.11.89	515.01	.511832	0.000008
	515.02	.511833	0.000005
	515.03	.511835	0.000002
	515.04	.511837	0.000005
	515.06	.511831	0.000005
	515.07	.511826	0.000002
	515.08	.511820	0.000005
7.11.89	518.1	.511856	0.000002
9.11.89	519.09	.511786	0.000009
10.11.89	520.06	.511847	0.000005
16.11.89	525.05	.511849	0.000005
17.11.89	526.07	.511848	0.000002
24.11.89	533.08	.511797	0.000009

25.11.89	534.01	.511822	0.000003
Nd DYN	Ave	.511811	
	std dev	.000021	
	sigma	.000003	
	Max	.511856	
	Min	.511774	

ISOTOPE DATA

Santana Metamorphic Belt														
Igneous	Ag	87/86 Sr	Rb/Sr	87Rb/86 Sr	(87Sr/86Sr) i	E Sri	Nd 143/144	Sm/Nd 147	Sm/144Nd	(143Nd/144Nd)i	ENd	TDM Nd (Ma)		
Basalts	*=assumed age													
RSM23D	*120	0.704418	0.037	0.107	0.70423	-4.6	0.512626	0.19	0.115	0.51254	1.0	663		
RSM23A	*120	0.707562	0.121	0.349	0.70697	34.2	0.512599	0.186	0.112	0.51251	0.5	683		
Andesites														
RSM31	*300	0.715169	0.385	1.115	0.71041	86.2	0.512258	0.204	0.123	0.51202	-4.6	1325		
RSM113A	*300	0.711144	0.039	0.113	0.71066	89.8	0.511895	0.19	0.115	0.51167	-11.4	1781		
RSM41B	*300	0.707812	0.126	0.365	0.70625	27.2	0.511978	0.19	0.115	0.51175	-9.8	1651		
Metagabbro														
RSM94	*800	0.708933	0.172	0.498	0.70324	-7.0	0.51188	0.19	0.115	0.51128	-6.5	1805		
RSM108A	*800	0.705436	0.098	0.284	0.70219	-21.9		0.19	0.101					
Santana Gr														
RSM836	*800	0.713669	0.095	0.276	0.71052	96.4								
Campinas Gr														
RSMA21	785	1.045440	12.580	37.615	0.72359	278.7		0.253	0.134					
Caçapava Gr														
RSM42A	474	0.710252	0.278	0.805	0.70482	9.8	0.511338	0.165	0.100	0.51103	-19.5	2307		
RSM 42B	474	0.713062	0.349	1.009	0.70624	30.1								
RSM 42C	474	0.709337	0.196	0.569	0.70550	19.4	0.511237	0.146	0.088	0.51096	-20.8	2207		
RSM 42D	474	0.710406	0.227	0.656	0.70598	26.2								
RSM 42 F	474	0.708592	0.167	0.484	0.70533	17.0								
RSM42N	474	0.709380	0.154	0.447	0.70636	31.8								
RSM 42Q	474	0.708849	0.171	0.496	0.70550	19.5								
Encruzilhada Gr														
RSMC31	*600	0.755742	2.126	6.182	0.70285	-16.0		0.158	0.084					
RSMA28	*600	0.798247	3.627	10.591	0.70762	51.8		0.16	0.085					
Sediments		87/86 Sr	Rb/Sr				Nd 143/144							
Encantada Gneisses														
RSM45A	2030	0.713693	0.119	0.346	0.70358	19.4	0.510885	0.132	0.080	0.50982	-3.8	2485		
RSM45B	2030	0.715965	0.141	0.409	0.70399	25.2								
RSM59A	2030	0.724142	0.225	0.652	0.70508	40.7	0.511206	0.144	0.087	0.51004	0.6			
RSM59B	2030	0.725262	0.214	0.621	0.70709	69.3	0.51157	0.18	0.109	0.51012	2.1			
RSM59C	2030	0.717794	0.134	0.387	0.70647	60.5	0.51133	0.19	0.115	0.50979	-4.3	2318		
RSM78D	2030	0.713706	0.104	0.302	0.70487	37.8								
RSM93	2030	0.774378	0.825	2.402	0.70413	27.2								
RSM40B	2030	0.711899	0.075	0.218	0.70552	47.0								
Amphibolite														
RSM95	*2030	0.715332	0.129	0.374	0.70441	31.1	0.511038	0.175	0.106	0.50962	-7.6	2889		
Encantada Schists														
RSM54	*1000	0.728175	0.358	1.037	0.71334	140.1	0.510965			0.51097	-7.5			
RSM48	*1000	0.000000	3.705	9.982			0.511924	0.206	0.125	0.51026	4.9	1935		
RSM96B	*1000	0.727908	0.486	1.408	0.70777	60.9		0.146	0.078					
RSM119B	*1000	0.726989	0.343	0.995	0.71276	131.7								
Metasediments														
RSM23B	*400	0.710887	0.155	0.449	0.70833	58.4		0.204	0.108					
RSM23E	*400	0.710252	0.091	0.262	0.70876	64.5	0.512626	0.188	0.114	0.51233	4.0	657		
RSMC71	*400	0.711846	0.185	0.537	0.70817	60.0	0.512614	0.188	0.114	0.51187	4.2	675		

RSMA41	*300		0.727895	1.015	2.942	0.71533	156.1	0.512161	0.198	0.120	0.51193	-6.4	1440
RSM44	*800		0.734931	0.634	1.841	0.71390	144.5	0.511938	0.219	0.132	0.51124	-7.1	2078

Pelotas Batholith Igneous Foliated		Age	87/86 Sr	Rb/Sr	87Rb/86 Sr	(87Sr/86Sr) i	E Sr	Nd 143/144	Sm/Nd 147	Sm/144Nd	(143Nd/144Nd)i	ENd	TDM Nd (Ma)
Cascata Orthogneiss													
RSMX1		572	0.724685	0.698	2.025	0.70817	59.2						
RSMX2		572	0.724096	0.675	1.957	0.70814	58.6						
RSMX3		572	0.725997	0.719	2.085	0.70899	70.8						
RSMX7		572	0.721475	0.495	1.436	0.70977	81.8						
RS SM 3A		572	0.713388	0.194	0.562	0.70881	68.2	0.511968	0.197	0.119	0.51152	-7.4	1738
RS SM 3B1		572	0.717531	0.338	0.979	0.70955	78.7	0.511913	0.178	0.108	0.51151	-7.7	1636
RS SM 3B2		572	0.716397	0.328	0.949	0.70866	66.0						
RS SM 3B3		572	0.718307	0.401	1.163	0.70882	68.3						
RS SM 3C		572	0.717671	0.425	1.231	0.70763	51.5						
RS SM 3C2		572	0.718142	0.355	1.030	0.70974	81.4						
RSM A5A		572	0.717831	0.439	1.271	0.70747	49.1	0.512082	0.19	0.115	0.51165	-4.9	1490
RSMA6B		572	0.723246	0.604	1.751	0.70896	70.4	0.51199	0.19	0.115	0.51156	-6.7	1632
RSM 2A		572		0.346	0.932			0.511956	0.19	0.115	0.51153	-7.4	1686
RSM 4A		572	0.722334	0.606	1.757	0.70801	56.8	0.511979	0.144	0.087	0.51165	-4.9	1286
RSM 5		572	0.719798	0.453	1.312	0.70910	72.3		0.19	0.101			
RSM 6A		572	0.715271	0.317	0.918	0.70779	53.6	0.511946	0.18	0.109	0.51154	-7.1	1603
RSM11.5		572	0.717065	0.306	0.885	0.70985	82.9						
RSMX12		572	0.724570	1.357	3.933	0.69249	-163.6						
Piritini Granite													
RSMA68	*560		0.721042	0.489	1.418	0.70972	80.9						
RSMA69A	*560		0.724809	0.645	1.871	0.70987	83.0						
RSMA64	*560		0.732974	0.757	2.198	0.71543	162.0						
RSMA26II	*560		0.736584	0.633	1.837	0.72192	254.1						
RSMA69B	*560		0.720790	0.604	1.749	0.70683	39.8						
Cangucu Phenocrystic Gr													
RSMA16C	*560		0.716451	0.362	1.049	0.70808	57.5	0.511952	0.19	0.115	0.51153	-7.6	1692
RSM12	*560		0.000000	0.973	2.622			0.512221	0.19	0.115	0.51180	-2.3	1275
Migmatitic Granite													
RSMC57		556	0.720416	0.451	1.307	0.71005	85.6						
RSM21		556	0.721204	0.395	1.144	0.71214	115.2	0.511966	0.184	0.111	0.51156	-7.1	1604
RSM20		556	0.734565	0.660	1.916	0.71938	218.0						
RSMC46		556	0.735799	0.875	2.539	0.71567	165.4	0.511897	0.19	0.115	0.51148	-8.7	1778
RSM11KI		556	0.723023	0.552	1.600	0.71034	89.7						
RSM11KII		556	0.729245	0.802	2.327	0.71080	96.2						
RSM11L		556	0.735581	1.081	3.137	0.71072	95.0						
RSM11M		556	0.735804	1.132	3.284	0.70977	81.6						
RSMC54		556	0.722114	0.545	1.580	0.70959	79.0	0.512057	0.19	0.115	0.51164	-5.6	1528
RS SM 7		556	0.726080	0.720	2.087	0.70954	78.2	0.511907	0.169	0.102	0.51153	-7.6	
RS SM 9		556	0.722925	0.456	1.322	0.71245	119.6						1556
RS SM 10		556		0.418	1.125			0.511907	0.155	0.094	0.51157	-7.0	1452
RSM 16A	*500		0.723232	0.641	1.857	0.71000	83.8						
RSM 16B	*500		0.708915	0.214	0.620	0.70450	5.7	0.512487	0.195	0.118	0.51210	2.1	898

RSM 5	*500		0.719798	0.453	1.312	0.71045	90.3						
								Nd 144/143					
Unfoliated		87/86 Sr											
Pink Granite													
RSM23C		465	0.730078	0.644	1.868	0.71810	198.1	0.512079	0.188	0.114	0.51174	-6.2	1479
RSMA17A		465		0.860	2.318			0.512012	0.19	0.115	0.51167	-7.6	1598
RSMA16BI		465	0.719955	0.519	1.504	0.71032	87.5	0.512141	0.19	0.115	0.51180	-5.0	1398
RSMC34		465	0.729973	0.901	2.613	0.71322	128.7						
RSM 11A		465	0.761678	2.397	6.973	0.71548	161.1	0.512063	0.146	0.088	0.51179	-4.8	1194
RSM 11C		465	0.755345	2.127	6.185	0.71437	145.3	0.512003	0.15	0.091	0.51173	-6.1	1297
RSM 11D		465	0.752403	1.921	5.584	0.71541	160.0						
RSM 11F		465	0.755013	2.015	5.859	0.71619	171.2	0.512041	0.15	0.091	0.51176	-5.4	1250
Cascata Leucogranite													
RSMA34	*465		0.776439	0.487	1.419	0.76704	893.3		0.19	0.101			
RSM 30	*465		0.720780	0.355	1.030	0.71396	139.4	0.511717	0.089	0.054	0.51155	-9.5	985
X11	*465		0.735731	2.814	8.168	0.68162		0.512109	0.235	0.142			
2B	*465		0.718958	3.506	10.157	0.65167			0.162	0.086			
RSMA54	*465		0.800210	0.831	2.427	0.78413	1136.0						
RSMA47	*465		0.755867	2.010	5.846	0.71714	184.6						
RSMC62B	*465		0.735479	1.076	3.122	0.71479	151.3	0.512375	0.19	0.115	0.51203	-0.3	1041
RSMA13	*465		0.752810	1.936	5.628	0.71552	161.7						
RSMA12	*465		0.733137	1.034	3.000	0.71326	129.6						
RSMA11	*465		0.732881	1.024	2.970	0.71321	128.8						
RSM A9A	*465		0.717418	0.402	1.166	0.70969	78.9						
Canguçu Granite													
RSM13	*500		1.276491	21.873	66.829	0.80031	1366.5	0.512221	0.279	0.169	0.51167	-6.4	2919
RSMC6	*500		1.016986	12.438	37.090	0.75271	690.4	0.512389	0.213	0.129	0.51197	-0.6	1184

Rock sample management/catalogue file guide - Page 1 - General Information

1	2	3	4	5	6	7	8
	Details of sample and origin						
Personal Sample Identifier	Rock/Spec. Type	Rock/Spec. Sub-type	Description/Special Features of sample	Place of Origin (location)	Description of Locality	Date Collected	Rock Storage (Box no.)
RSM A56A	Granite	Capao do Leoi	Medium grained white unfoliated	A56	Capao do Leon Quarry		RS1
RSM A56B	Granite	Capao do Leoi	Medium grained pink unfoliated	A56	Capao do Leon Quarry		RS1
RSM A56C	Granite	Capao do Leoi	Medium grained white unfoliated	A56	Capao do Leon Quarry	Nov-87	RS1
RSM A56D	Granite	Capao do Leoi	Medium grained white unfoliated	A56	Capao do Leon Quarry	Nov-87	RS1
RSM A56E	Granite	Capao do Leoi	Medium grained pink unfoliated	A56	Capao do Leon Quarry	Nov-87	RS1
RSM A56F	Granite	Capao do Leoi	Medium grained white unfoliated	A56	Capao do Leon Quarry	Nov-87	RS1
RSM A56G	Granite	Capao do Leoi	Medium grained white unfoliated	A56	Capao do Leon Quarry	Nov-87	RS1
RSM A56H	Granite	Capao do Leoi	Gt-Bi xenolith	A56	Capao do Leon Quarry	Nov-87	RS1
RSM A56I	Granite	Capao do Leoi	Medium grained white unfoliated	A56	Capao do Leon Quarry	Nov-87	RS1
RSM A9A	Granite	Capao do Leoi	Medium grained white unfoliated	A56	Capao do Leon Quarry	Nov-87	RS1
RSM A9B	Granite	Capao do Leoi	Medium grained white unfoliated	A56	Capao do Leon Quarry	Nov-87	RS1
RSM A9C	Granite	Capao do Leoi	Medium grained white unfoliated	A56	Capao do Leon Quarry	Nov-87	RS1
RSM A9D	Granite	Capao do Leoi	Medium grained white unfoliated	A56	Capao do Leon Quarry	Nov-87	RS1
RSM A9E	Granite	Capao do Leoi	Medium grained white unfoliated	A56	Capao do Leon Quarry	Nov-87	RS1
RSM A7A	Granite	Capao do Leoi	Medium grained pink unfoliated	A56	Capao do Leon Quarry	Nov-87	RS1
RSM A7B	Granite	Capao do Leoi	Coarse grained pink unfoliated	A56	Capao do Leon Quarry	Nov-87	RS1
RSM A7C	Granite	Capao do Leoi	Coarse grained pink unfoliated	A56	Capao do Leon Quarry	Nov-87	RS1
RSM A55A	Granite	Capao do Leoi	Medium grained white unfoliated	A56	Capao do Leon Quarry	Nov-87	RS1
RSM A55B	Granite	Capao do Leoi	Medium grained white unfoliated	A56	Capao do Leon Quarry	Nov-87	RS1
RSM A51	Granite	Capao do Leoi	Medium grained white unfoliated	A56	Capao do Leon Quarry	Nov-87	RS1
RSM X1	Orthogneiss	Cascata	Coarse foliated inhomogeneous	X	Quarry off BR392	Nov-87	RS2
RSM X2	Orthogneiss	Cascata	Coarse foliated inhomogeneous	X	Quarry off BR392	Nov-87	RS2
RSM X3	Orthogneiss	Cascata	Coarse foliated inhomogeneous	X	Quarry off BR392	Nov-87	RS2
RSM X4	Orthogneiss	Cascata	Coarse foliated inhomogeneous	X	Quarry off BR392	Nov-87	RS2
RSM X5	Orthogneiss	Cascata	Coarse foliated inhomogeneous	X	Quarry off BR392	Nov-87	RS2
RSM X6	Orthogneiss	Cascata	Coarse foliated inhomogeneous	X	Quarry off BR392	Nov-87	RS2
RSM X7	Orthogneiss	Cascata	Coarse foliated inhomogeneous	X	Quarry off BR392	Nov-87	RS2
RSM X8	Orthogneiss	Cascata	Coarse foliated inhomogeneous	X	Quarry off BR392	Nov-87	RS2
RSM X12	Orthogneiss	Cascata	Mafic Xenolith	X	Quarry off BR392	Nov-87	RS2
RSM A23	Leucogranite	Cascata	Fine grained white mgt bearing	A23	Roadside of BR392	Nov-87	RS2
RSM A69A	Leucogranite	Cascata	Fine grained white mgt bearing	A69	road to Quevidos	Nov-87	RS2
RSM A69B	Leucogranite	Cascata	Fine grained white mgt bearing	A69	road to Quevidos	Nov-87	RS2
RSM X11	Leucogranite	Cascata	Fine grained white mgt bearing	X	Quarry	Nov-87	RS2
RSM C62B	Leucogranite	Cascata	Fine grained white mgt bearing	C62	BR392	Sep-86	RS2
RSM C62B	Leucogranite	Cascata	Fine grained white mgt bearing	C62	BR392	Sep-86	RS2
RSM C54	Leucogranite	Cascata	Fine grained white mgt bearing	C54	BR392	Sep-86	RS2
RSM A47	Leucogranite	Cascata	Fine grained white mgt bearing	A47	road to Piritini	Sep-86	RS2
RSM 3D2	Leucogranite	Cascata	Fine grained white mgt bearing	'3	Quarry off Br392	Sep-86	RS2
RSM 11.5	Migmatite	Grey	Inhomogeneous grey with pink pods	'11	Quarry off Br392	Sep-86	RS2
RSM 11 K1	Migmatite	Grey	Inhomogeneous grey with pink pods	'11	Quarry off Br392	Sep-86	RS2
RSM 11K2	Migmatite	Grey	Inhomogeneous grey with pink pods	'11	Quarry off Br392	Sep-86	RS2
RSM 11I	Migmatite	Grey	Inhomogeneous grey with pink pods	'11	Quarry off Br392	Sep-86	RS2
RSM 11L	Migmatite	Grey	Inhomogeneous grey with pink pods	'11	Quarry off Br392	Sep-86	RS2
RSM 11M	Migmatite	Grey	Inhomogeneous grey with pink pods	'11	Quarry off Br392	Sep-86	RS2
RSM A15C	Migmatite	Grey	Inhomogeneous grey with pink pods	A15	Quarry off Br392	Sep-86	RS2
RSM C54	Migmatite	Grey	Inhomogeneous grey with pink pods	C54	BR392	Sep-86	RS2
RSM 42M	Cassapava	Grey	Inhomogeneous grey with pink pods	'42	Caçapava quarry	Sep-86	RS2
RSM 42Q	Cassapava	Grey	Inhomogeneous grey with pink pods	'42	Caçapava quarry	Sep-86	RS2

Rock sample management/catalogue file guide - Page 1 - General Information

1	2	3	4	5	6	7	8
RSM A48	Granite	Muscovite	Weathered two mica coarse grained	A48	Piritini road	Nov-87	RS3
RSM A51A	Granite	Muscovite	Weathered two mica coarse grained	A51	Piritini road	Nov-87	RS3
RSM A25	Granite	Muscovite	Weathered two mica coarse grained	A25	Piritini road	Nov-87	RS3
RSM A48	Granite	Muscovite	Weathered two mica coarse grained	A48	Piritini road	Nov-87	RS3
RSM A58A	Granite	Muscovite	Weathered two mica coarse grained	A58	BR392	Nov-87	RS3
RSM A79A	Granite	Muscovite	Weathered two mica coarse grained	A79	BR392	Nov-87	RS3
RSMA55A	Granite	Muscovite	Weathered two mica coarse grained	A55	BR392	Nov-87	RS3
RSM A78	Granite	Muscovite	Weathered two mica coarse grained	A78	BR392	Nov-87	RS3
RSM A71A	Granite	Muscovite	Weathered two mica coarse grained	A71	BR392	Nov-87	RS3
RSM A49B	Granite	Muscovite	Weathered two mica coarse grained	A49	BR392	Nov-87	RS3
RSM A52A	Granite	Muscovite	Weathered two mica coarse grained	A52	BR392	Nov-87	RS3
RSM A35	Granite	Muscovite	Weathered two mica coarse grained	A35	Campinas	Nov-87	RS3
RSM A21	Granite	Muscovite	Weathered two mica coarse grained	A21	Campinas	Nov-87	RS3
RSM 23C	Granite	Pink	Fine red hbl granite	'23	BR392	Sep-86	RS4
RSM 42I	Granite	Caçapava pink	Dark red medium grained granite	'42	Caçapava quarry	Sep-86	RS4
RSM 42J	Granite	Caçapava pink	Dark red medium grained granite	'42	Caçapava quarry	Sep-86	RS4
RSM C34	Granite	Canguçu Red	Red fine hbl bearing	C34	BR392	Sep-86	RS4
RSM 11G	Granite	Pink	Medium grained pink homogeneous	'11	Quarry	Sep-86	RS4
RSM 42 K2	Granite	Caçapava Pinl	Dark red medium grained granite	'42	Caçapava	Sep-86	RS4
RSM A17A	Granite	Pink	Coarse grained pink homogeneous	A17	BR392	Sep-86	RS4
RSM A72 A	Granite	Pink	Coarse grained pink homogeneous	A72	BR392	Sep-86	RS4
RSM C6	Granite	Red	Red fine hbl bearing	C6	Canguçu BR 392	Sep-86	RS4
RSM C61B	Granite	Pink	Coarse grained pink homogeneous	C61	BR392	Sep-86	RS4
RSM A72B	Granite	Pink	Coarse grained pink homogeneous	A72	BR392	Sep-86	RS4
RSM 42B	Granite	Cassapava Pin	Dark red medium grained granite	'42	Caçapava quarry	Sep-86	RS4
RSM 42K	Granite	Cassapava Pin	Dark red medium grained granite	'42	Caçapava quarry	Sep-86	RS4
RSM A20	Schist	Chlorite	Green finegrained schist	A20	Santana area	Nov-87	RS5
RSM A38	Schist	Graphite	Qz bearing graphitic schist	A38	Santana area	Nov-87	RS5
RSM A39	Schist	Quartzite	White quartzite	A39	Santana area	Nov-87	RS5
RSM A49	Schist	Mc schist	Fine-grained schist	A49	Santana area	Nov-87	RS5
RSM A27A	Schist	Graphitic	Fine-grained schist	A27	Santana area	Nov-87	RS5
RSM A27C	Schist	Graphitic	Fine-grained schist	A27	Santana area	Nov-87	RS5
RSM A40A	Schist	Pyroxenite	dark green coarse grained	A40	SE Santana area	Nov-87	RS5
RSM A40B	Schist	Amphibolite	Black with garnets	A40	SE Santana area	Nov-87	RS5
RSM A40C	Schist	Amphibolite	Black with garnets	A40	SE Santana area	Nov-87	RS5
RSM A40D	Schist	Gneisses	Banded qz gneiss	A40	SE Santana area	Nov-87	RS5
RSM A40E	Schist	Gneisses	Banded qz gneiss	A40	SE Santana area	Nov-87	RS5
RSM A24C	Schist	Blue grey	Fine-grained schist	A24	Santana area	Nov-87	RS5
RSM A57C	Xenolith	Mafic Biotite	Fine-grained schist	A57	Santana area	Nov-87	RS5
RSM A24ii	Schist	Graphitic	Fine-grained schist	A24	Santana area	Nov-87	RS5
RSM A30C	Schist	Limestone	Blue limestone	A30	Santana area	Nov-87	RS5
RSM A24i	Schist	Bi Schist	Fine-grained schist	A24	Santana area	Nov-87	RS5
RSM A5A	Granite	Grey	Possibly Cassapava type	A5	Camaqua quarry	Sep-86	RS6
RSM 42A	Granite	Caçapava	Medium grained grey migmatitic	'42	Caçapava Quarry	Sep-86	RS6
RSM 42B	Granite	Caçapava	Coarse red homogeneous	'42	Caçapava Quarry	Sep-86	RS6
RSM 42C	Granite	Caçapava	Medium grained grey migmatitic	'42	Caçapava Quarry	Sep-86	RS6
RSM 42E	Granite	Caçapava	Coarse red homogeneous	'42	Caçapava Quarry	Sep-86	RS6
RSM 42F	Granite	Caçapava	Medium grained grey migmatitic	'42	Caçapava Quarry	Sep-86	RS6
RSM 42H	Granite	Caçapava	Coarse red homogeneous	'42	Caçapava Quarry	Sep-86	RS6
RSM 11A	Granite	Pink	Medium grained pink homogeneous	'11	Quarry off BR392	Sep-86	RS6
RSM 11B	Granite	Pink	Medium grained pink homogeneous	'11	Quarry off BR392	Sep-86	RS6
RSM 11C	Granite	Pink	Medium grained pink homogeneous	'11	Quarry off BR392	Sep-86	RS6
RSM 11D	Granite	Pink	Medium grained pink homogeneous	'11	Quarry off BR392	Sep-86	RS6
RSM 11E	Granite	Pink	Medium grained pink homogeneous	'11	Quarry off BR392	Sep-86	RS6
RSM 11G	Granite	Pink	Medium grained pink homogeneous	'11	Quarry off BR392	Sep-86	RS6
RSM 5	Schist	Sheared gr	Very sheared granite mylonitized?	'5	BR392 roadside	Sep-86	RS6
RSM 4B	Granite	Porphyritic	Feldspar porphyroblasts grey matrix	'4	BR392 roadside	Sep-86	RS6

Rock sample management/catalogue file guide - Page 1 - General Information

1	2	3	4	5	6	7	8
RSM 3A	Xenolith	Mafic	Mafdic portion of gneiss	'3	BR392 roadside	Sep-86	RS6
RSM 23A	Basalt	dyke	Intruding granite	'23	BR392 roadside	Sep-86	RS6
RSM 23E	Metasediment	Blue green	Chlorite replacing cordierite	'23	BR392 roadside	Sep-86	RS6
RSM A1	Pyroxenite		Dark green coarse grained	A1	Barra Velha beach SC	Sep-86	RS6
RSM C12	Granite	Pink	Medium grained pink homogeneous	C12	BR392 roadside	Sep-86	RS6
RSM 11H	Migmatite	Grey	Migmatiticwith pink pods	'11	BR392 roadside	Sep-86	RS6
RSM A5C	Pegmatite	White	Very large crystals	A5	BR392 roadside	Sep-86	RS6
RSM 9	Migmatite	Grey	Coarse grained representative	'9	BR392 roadside	Sep-86	RS7
RSM 12	Granite	Porphyritic	Coarse grained phenocrystic	'12	BR392 roadside	Sep-86	RS7
RSM 2A	Granite	Micaceous	Weathered coarse grained	'2	BR392 roadside	Sep-86	RS7
RSM 4B	Granite	Porphyritic	Coarse grained phenocrystic	'4	BR392 roadside	Sep-86	RS7
RSM 4C	Granite	Porphyritic	Coarse grained phenocrystic weathered	'4	BR392 roadside	Sep-86	RS7
RSM 12B	Granite	Porphyritic	Coarse grained grey phenocrystic	'12	BR392 roadside	Sep-86	RS7
RSM A16C	Granite	Porphyritic	Coarse grained grey phenocrystic	A16	Quarry off BR392	Nov-87	RS7
RSM A19	Granite	Encruzilhada	Coarse grained grey phenocrystic	A19	Encruzilhada	Nov-87	RS7
RSM A28	Granite	Encruzilhada	Coarse grained grey phenocrystic	A28	Encruzilhada	Nov-87	RS7
RSM A30	Granite	Encruzilhada	Coarse grained grey phenocrystic	A30	Encruzilhada	Nov-87	RS7
RSM A77	Granite	Encruzilhada	Coarse grained grey phenocrystic	A77	Encruzilhada	Nov-87	RS7
RSM A70B	Granite	Encruzilhada	Coarse grained grey phenocrystic	A70	Encruzilhada	Nov-87	RS7
RSM C62A	Granite	Muscovite	Pale grey fine grained	C62	BR392	Sep-86	RS7
RSM A36	Granite	Encruzilhada	Coarse grained grey phenocrystic	A36	Encruzilhada	Nov-87	RS7
RSM A61	Granite	Encruzilhada	Coarse grained grey phenocrystic	A61	Encruzilhada	Nov-87	RS7
RSM A10	Granite	C dos Piegos	White fine grained Mgt bearing	A10	Piritini area	Nov-87	RS7
RSM A11	Granite	C dos Piegos	White fine grained Mgt bearing	A11	Piritini area	Nov-87	RS7
RSM A12	Granite	C dos Piegos	White fine grained Mgt bearing	A12	Piritini area	Nov-87	RS7
RSM A13	Granite	C dos Piegos	White fine grained Mgt bearing	A13	Piritini area	Nov-87	RS7
RSM A 26i	Granite	C dos Piegos	White fine grained Mgt bearing	A26	Piritini area	Nov-87	RS7
RSM A26ii	Granite	C dos Piegos	White fine grained Mgt bearing	A26	Piritini area	Nov-87	RS7
RSM A17B	Granite	Red	Fine grained homogeneous hbl	A17	BR 392	Nov-87	RS7
RSM 13B	Granite	Red	Fine grained homogeneous hbl	'13	BR 392	Nov-87	RS7
RSM A 33	Granite	Red	Fine grained homogeneous hbl	A33	BR 392	Nov-87	RS7
RSM A16Bi	Granite	Pink	Medium grained pink homogeneous	A16	BR 392	Nov-87	RS7
RSM A17A	Granite	Pink	Medium grained pink homogeneous	A17	BR 392	Nov-87	RS7
RSM A75	Granite	Leucogranite	White fine grained Mgt bearing	A75	BR 392	Nov-87	RS7
RSM A64	Granite	Piritini	Speckly biotite fine inhomogeneos	A64	Piritini	Nov-87	RS7
RSM A76	Granite	Piritini	Speckly biotite fine inhomogeneos	A76	Piritini	Nov-87	RS7
RSM A69A	Granite	Piritini	Speckly biotite fine inhomogeneos	A69	Piritini	Nov-87	RS7
RSM A69B	Granite	Piritini	Speckly biotite fine inhomogeneos	A69	Piritini	Nov-87	RS7
RSM A68B	Granite	Piritini	Speckly biotite fine inhomogeneos	A68	Piritini	Nov-87	RS7
RSM A26	Granite	Piritini	Speckly biotite fine inhomogeneos	A26	Piritini	Nov-87	RS7
RSM A31	Granite	Piritini	Speckly biotite fine inhomogeneos	A31	Piritini	Nov-87	RS7
RSM 1A	Schist	Muscovite	Fine grained schist	'1	BR392	Sep-86	RS8
RSM A5D	Granite	Leucogranite	White fine grained Mgt bearing	A5	BR116	Sep-86	RS8
RSM 4D	Granite	Leucogranite	White fine grained Mgt bearing	'4	BR392	Sep-86	RS8
RSM A5A	Granite	Leucogranite	White fine grained Mgt bearing	A5	BR116	Sep-86	RS8
RSM 3E	Pegmatite	Coarse	Large biotites and felspar	'3	BR392 quarry	Sep-86	RS8
RSM A5C	Pegmatite	Coarse	Large biotites and felspar	A5	BR116	Sep-86	RS8
RSM 3D	Granite	Leucogranite	White fine grained Mgt bearing	'3	BR392 quarry	Sep-86	RS8
RSM A5F	Granite	Fine grained	Dark red very fine homogeneous	A5	BR116	Sep-86	RS8
RSM A5E	Migmatite	mafic	Inhomogeneous grey with pink pods	A5	BR116	Sep-86	RS8
RSM A5G	Granite	Cassapava grey	Inhomogeneous grey with pink pods	A5	BR116	Sep-86	RS8
RSM 10	Migmatite	mafic	Inhomogeneous grey with pink pods	'10	BR392	Sep-86	RS8
RSM 23C	Granite	Encruzilhada	Coarse grained grey phenocrystic	'23	BR392	Sep-86	RS8
RSM 3B2	Gneiss	Cascata	Coarse foliated inhomogeneous	'3	BR392 quarry	Sep-86	RS8
RSM 3B3	Gneiss	Cascata	Coarse foliated inhomogeneous	'3	BR392 quarry	Sep-86	RS8
RSM 3F	Xenolith	Cascata	Biotite rich fine grained	'3	BR392 quarry	Sep-86	RS8
RSM 3C2	Gneiss	Cascata	Coarse foliated inhomogeneous	'3	BR392 quarry	Sep-86	RS8

Rock sample management/catalogue file guide - Page 1 - General Information

1	2	3	4	5	6	7	8
RSM 2B	Granite	Leuco	White fine grained Mgt bearing	'2	BR392	Sep-86	RS8
RSM 16A	Mylonite	Quartz	Work hardened Qz rich	'16	BR392	Sep-86	RS8
RSM 6B	Schist	Porphyritic	Foliated gneissose granite	'6	BR392	Sep-86	RS8
RSM 5	Schist	Sheared	Sediment like	'5	BR392	Sep-86	RS8
RSM 8	Migmatitre	Grey	Foliated with pink portions	'8	BR392	Sep-86	RS8
RSM 6A	Granite	Piritini	Speckly biotite fine inhomogeneos	'6	BR392	Sep-86	RS8
RSM A5G	Granite	Piritini	Speckly biotite fine inhomogeneos	A5	BR 116	Sep-86	RS8
RSM 15A	Granite	Piritini	Speckly biotite fine inhomogeneos	'15	BR392	Sep-86	RS8
RSM C2	Granite	Piritini	Speckly biotite fine inhomogeneos	C2	BR392	Sep-86	RS9
RSM C28A	Granite	Piritini	Speckly biotite fine inhomogeneos	C28	BR392	Sep-86	RS9
RSM C57	Granite	Piritini	Speckly biotite fine inhomogeneos	C57	BR392	Sep-86	RS9
RSM A34	Granite	Piritini	Speckly biotite fine inhomogeneos	A34	BR392	Sep-86	RS9
RSM C1	Granite	Piritini	Speckly biotite fine inhomogeneos	C1	BR392	Sep-86	RS9
RSM C61A	Granite	Cdo Leon ?	Coarse white homogeneous	C61	BR392	Sep-86	RS9
RSM 13	Granite	Red	Fine grained homogeneous hbl	'13	BR392	Sep-86	RS8
RSM C3	Granite	Encruzilhada	Coarse grained grey phenocrystic	C3	Encruzilhada	Sep-86	RS9
RSM C62A	Granite	Encruzilhada	Coarse grained grey phenocrystic	C62	Encruzilhada	Sep-86	RS9
RSM C24	Granite	Encruzilhada	Coarse grained grey phenocrystic	C24	Encruzilhada	Sep-86	RS9
RSM C31	Granite	Encruzilhada	Coarse grained grey phenocrystic	C31	Encruzilhada	Sep-86	RS9
RSM C48	Granite	Encruzilhada	Coarse grained grey phenocrystic	C48	Encruzilhada	Sep-86	RS9
RSM C67	Granite	Muscovite	Campinas type post tectonic	C67	BR392	Sep-86	RS9
RSM C22	Migmatite	Grey	Inhomogeneous grey with pink pods	C22	BR392	Sep-86	RS9
RSM C49	Breccia	Brown	angular clasts	C49	BR392	Sep-86	RS10
RSM C42	Schist	Fine grained		C42	BR392	Sep-86	RS10
RSM 21B	Dolerite	black	weathered	'21	BR392	Sep-86	RS10
RSM C20C	Basalt	fresh	large geochemical sample	C20	BR392	Sep-86	RS10
RSM C35A	Basalt	fresh	large geochemical sample	C35	BR392	Sep-86	RS10
RSM C20B	Basalt	fresh	large geochemical sample	C20	BR392	Sep-86	RS10
RSM A56H	Xenolith	Capao do Leac	Garnet-Biotite xenolith	A56	Capao do Leao quarry	Nov-87	RS10
RSM A70A	Basalt	Fresh	From dyke	A70	BR392	Nov-87	RS10
RSM B58	Schist	Chlorite	Fine grained	B58	Santana area (fig 2.2)	Nov-87	RS10
RSM 20	Migmatite	Grey	Inhomogeneous grey with pink pods	'20	BR392	Nov-87	RS10
RSM A57A	Migmatite	Grey	Inhomogeneous grey with pink pods	A57	BR392	Nov-87	RS10
RSM A57B	Pegmatite	Pink	Coarse grained	A57	BR392	Nov-87	RS10
RSM A32	Granite	Cassapava	Red medium grained	A32	BR392	Nov-87	RS11
RSM A83	Andesite	red	fine grained pillow andesites	A83	BR392	Nov-87	RS11
RSM A48A	Gneiss	Cascata	Orthogneiss	A48	BR392	Nov-87	RS11
RSM A65A	Quartzite	Cerro dos Bic	White quartzite	A65	Santana area	Nov-87	RS11
RSM A46	Pegmatite	Pink	Coarse grained	A46	BR392	Nov-87	RS11
RSM A79B	Pegmatite	Pink	Coarse grained	A79	BR392	Nov-87	RS11
RSM A29	Volcanic	Felsic	pale brown	A29	BR392 Triassic area	Nov-87	RS11
RSM A16A	Leucogranite	Coarse	Coarse white mgt bearing	A16	Pelotas Batholith	Nov-87	RS11
RSM A45	Leucogranite	Cascata	Fine grained white mgt bearing	A45	Pelotas Batholith	Nov-87	RS11
RSM A53	Orthogneiss	Cascata	Coarse foliated inhomogeneous	A53	Pelotas Batholith	Nov-87	RS11
RSM A65B	Migmatite	Grey	Inhomogeneous grey with pink pods	A65	Pelotas Batholith	Nov-87	RS11
RSM A63B	Volcanic	Felsic	Fine grained buff coloured	A63	Pelotas Batholith	Nov-87	RS11
RSM A70A	Migmatite	Grey	Inhomogeneous grey with pink pods	A70	Pelotas Batholith	Nov-87	RS11
RSM A63C	Basalt	Black	Fresh	A63	Pelotas Batholith	Nov-87	RS11
RSM A42	Pegmatite	Pink	Hornblende,feldspar	A42	Pelotas Batholith	Nov-87	RS11
RSM A 62	Granite	Encruzilhada	Weathered	A62	Pelotas Batholith	Nov-87	RS11
RSM A37	volcanics	Felsic	Weathered	A37	Pelotas Batholith	Nov-87	RS11
RSM A51B	volcanics	Felsic	Weathered	A51	Pelotas Batholith	Nov-87	RS11
RSM B50B	Schist	Graphite	Grey foliated	B50	Santana area	Nov-87	RS11
RSM A51C	Gabbro	Green	coarse plag,cpx	A51	Santana area	Nov-87	RS11
RSM C25	Granite	Leuco	Coarse white	C25	Pelotas Batholith	Nov-87	RS11
RSM A70	Granite	Red	Fine hbl weathered	A70	Pelotas Batholith	Nov-87	RS11
RSM A80	Granite	Red	Fine hbl weathered	A80	Pelotas Batholith	Nov-87	RS11

Rock sample management/catalogue file guide - Page 1 - General Information

1	2	3	4	5	6	7	8
RSM C69	Volcanic	Felsic	Pink	C69	Pelotas Batholith	Nov-87	RS11
RSM A74	Weathered	Cdo leon	White	A74	Pelotas Batholith	Nov-87	RS11
RSM A63A	Weathered	Cdo leon	White	A63	Pelotas Batholith	Nov-87	RS11
RSM A73	Weathered	Red	Fine grained	A73	Pelotas Batholith	Nov-87	RS11
RSM C2B	Weathered	Piritini	Speckly biotite granite	C2	Pelotas Batholith	Nov-87	RS11
RSM C21A	Weathered	Cdo leon	White	C21	Capao do Leao quarry	Nov-87	RS11
RSM 43	Marble	Cerro Canberra	pure white	'43	Santana area	Sep-86	RS12
RSM 126	Marble	Cerro Canberra	white	'126	Santana area	Sep-86	RS12
RSM 74	Marble	Cerro Canberra	grey with en echelon veins	'74	Santana area	Sep-86	RS12
RSM 81E	Mc schist	Arrio Arreio		'81	Santana area	Sep-86	RS12
RSM 18E	Granite	Encantschist		'18	Santana area	Sep-86	RS12
RSM 120	Amphibolite	Encantschist	Very weathered blue green	'120	Santana area	Sep-86	RS12
RSM 85A	Bi schist	Encantschist	2 samples of fold hinge	'85	Santana area	Sep-86	RS12
RSM 96	Amphibolite	Gneiss	Fold hinge	'96	Santana area	Sep-86	RS12
RSM 129	mc schist	Arrio Arreio		'129	Santana area	Sep-86	RS12
RSM 53	granitic sc	Encantadaschist		'53	Santana area	Sep-86	RS12
RSM 33	schist	Cerro Canberra	samples	'33	Santana area	Sep-86	RS12
RSM 119	gt schist	Encantschist	garnet bearing	'119	Santana area	Sep-86	RS12
RSM 77B	chl mc schist	Encant schist		'77	Santana area	Sep-86	RS12
RSM 122B	Basalt			'122	Santana area	Sep-86	RS12
RSM 91B	Graphite schis	Cerro Canberra		'91	Santana area	Sep-86	RS12
RSM 120B	Amphibolite			'120	Santana area	Sep-86	RS12
RSM 70A	Amphibolite	Tourmalinized	Associated with the Campinas granite	'70	Santana area	Sep-86	RS12
RSM 70B	Amphibolite	Tourmalinized	Associated with the Campinas granite	'70	Santana area	Sep-86	RS12
RSM 40B	Gneiss	Encantada	banded	'40	Santana area	Sep-86	RS12
RSM 134	Mc schist	Arrio Arreio	Gt bearing	'134	Santana area	Sep-86	RS12
RSm 120C	Chl schist	Encant schist	Mc bearing	'120	Santana area	Sep-86	RS12
RSM 92	Chl schist	Encant schist		'92	Santana area	Sep-86	RS12
RSM 75	Conglomerate	ArriodosNobre	Red sandstone	'75	Santana area	Sep-86	RS12
RSM 132	Graphiteschist	Cerro Canberra	Mc bearing	'132	Santana area	Sep-86	RS12
RSM 90A	Graphiteschist	Cerro Canberra	Mc bearing	'90	Santana area	Sep-86	RS12
RSM 66	Pink mylonite	Arrio Arreio	marked cleavage/chalky	'66	Santana area	Sep-86	RS12
RSM 129	Mc schist	Arrio Arreio		'129	Santana area	Sep-86	RS12
RSM 40C	Amphibolite	Green	Possibly Ex Gabbro	'40	Santana area	Sep-86	RS12
RSM 81D	Xenolith?	Green /Pink	Coarse grained weathered	'81	Santana area	Sep-86	RS12
RSM 64	Graphiteschist	CerroCanberra		'64	Santana area	Sep-86	RS12
RSM 58	Bi schist	Encant schist		'58	Santana area	Sep-86	RS12
RSM 52A	Qzite			'52	Santana area	Sep-86	RS12
RSM 78B	Bi schist	Encant schist		'78	Santana area	Sep-86	RS12
RSM 40A	Gneiss	Encantada	Biotite gneiss	'40	Santana area	Sep-86	RS12
RSM 40B	Gneiss	Encantada	Biotite gneiss	'40	Santana area	Sep-86	RS12
RSM 52B	Bi schist	Encant schist		'52	Santana area	Sep-86	RS12
RSM 36	Qzite	CdBicudos		'36	Santana area	Sep-86	RS12
RSM 90B	Schist	Cerro Canberra		'90	Santana area	Sep-86	RS12
RSM 77B	bi schist	Encant schist		'77	Santana area	Sep-86	RS12
RSM 40B	Granite	Syntectonic	Two mica pink qz granite	'40	Santana area	Sep-86	RS13
RSM B36	Granite	Syntectonic	Two mica pink qz granite	B36	Santana area	Sep-86	RS13
RSM 45A	Bi gneiss	Encantada	Banded biotite gneiss	'45	Santana area	Sep-86	RS13
RSM 59A	Bi gneiss	Encantada	Banded biotite gneiss	'59	Santana area	Sep-86	RS13
RSM 59B	Bi gneiss	Encantada	Banded biotite gneiss	'59	Santana area	Sep-86	RS13
RSM 59C	Bi gneiss	Encantada	Banded biotite gneiss	'59	Santana area	Sep-86	RS13
RSM 136	Bi gneiss	Encantada	Banded biotite gneiss	'136	Santana area	Sep-86	RS13
RSM 96B	Bi gneiss	Encantada	Banded biotite gneiss	'96	Santana area	Sep-86	RS13
RSM 78D	Gran gneiss	Encantada	Granitic gneiss banded	'78	Santana area	Sep-86	RS13
RSM 93	Gran gneiss	Encantada	Granitic gneiss banded	'93	Santana area	Sep-86	RS13
RSM 59C	Gran gneiss	Encantada	Granitic gneiss banded	'59	Santana area	Sep-86	RS13
RSM45B	Gran gneiss	Encantada	Granitic gneiss banded	'45	Santana area	Sep-86	RS13

Rock sample management/catalogue file guide - Page 1 - General Information

Originator: P.C.Webb

1	2	3	4	5	6	7	8
RSM 54	Chl schist	Encant schist		'54	Santana area	Sep-86	RS13
RSM 95	Amphibolite	Gneiss	Encantada gneiss fm	'95	Santana area	Sep-86	RS13
RSM 96	Amphibolite	Gneiss	Encantada gneiss fm	'96	Santana area	Sep-86	RS13
RSM 96C	Amphibolite	Gneiss	Encantada gneiss fm	'96	Santana area	Sep-86	RS13
RSM B47	Mc schist	Arrio Arreio	crenulated	B47	Santana area	Nov-87	RS14
RSM B40A	Bi schist	Encant schist		B40	Santana area	Nov-87	RS14
RSM B10	Volcanic	Felsic		B10	Santana area	Nov-87	RS14
RSM B61A	Qzite			B61	Santana area	Nov-87	RS14
RSM B71	Bi schist			B71	Santana area	Nov-87	RS14
RSM B72B	Qzite			B72	Santana area	Nov-87	RS14
RSM B12	Pink mylonite	ArrioArreio		B12	Santana area	Nov-87	RS14
RSM B4C	Graphiticschis	Cerro Canberra		B4	Santana area	Nov-87	RS14
RSM B17	Mc schist	Quartz rich	Quartz rods	B17	Santana area	Nov-87	RS14
RSM B1A	Granite	Syntectonic	Santana area	B1	Santana area	Nov-87	RS14
RSM B50A	graphite schist	Cerro Canberra		B50	Santana area	Nov-87	RS14
RSM B26	Gabbro			B26	Santana area	Nov-87	RS14
RSM B16A	Graphite schis	Cerro Canberra		B26	Santana area	Nov-87	RS14
RSM B16C	Mc schist	Arrio Arreio		B16	Santana area	Nov-87	RS14
RSM B58A	Graphite schis	Cerro Canberra		B58	Santana area	Nov-87	RS14
RSM B61B	Qzite	White		B61	Santana area	Nov-87	RS14
RSM B16D	mc schist	Arrio Arreio		B16	Santana area	Nov-87	RS14
RSM B72A	Tuff	Felsic		B72	Santana area	Nov-87	RS14
RSM B46	volcanic	White		B46	Santana area	Nov-87	RS14
RSM B34B	Pink mylonite	Arrio Arreio		B34	Santana area	Nov-87	RS14
RSM B4A	Graphite schis	Cerro Canberra		B4	Santana area	Nov-87	RS14
RSM B18A	Graphite schis	Cerro Canberra		B18	Santana area	Nov-87	RS14
RSM B5	Sandstone	Ados Nobres	Fine brown sandstone	B5	Santana area	Nov-87	RS14
RSM A46	Amphibolite		Pegmatite contact withthis	A46	Santana area	Nov-87	RS14
RSM B16B	Bi schist	Encant schist		B16	Santana area	Nov-87	RS14
RSM B18B	Graphite schis	Cerro Canberra		B18	Santana area	Nov-87	RS14
RSM B2	Pink mylonite	Arrio Arreio		B2	Santana area	Nov-87	RS14
RSM A24A	Graphite schis	Cerro Canberra		A24	Santana area	Nov-87	RS14
RSM B16C	Breccia			B16	Santana area	Nov-87	RS14
RSM 100	Mc schist	crenulatred	Blueish coloured	'100	Santana area	Sep-86	RS14
RSM 23B	Gabbro			'23	Santana area	Sep-86	RS14
RSM 83	Qzite	Banded	Brown and white	'83	Santana area	Sep-86	RS14
RSM 79	Tuff	White		'79	Santana area	Sep-86	RS14
RSM 81C	Chl schist	Encant schist		'81	Santana area	Sep-86	RS14
RSM B7B	Graphite schis	Cerro Canberra		B7	Santana area	Nov-87	RS14
RSM B29C	Qzite			B29	Santana area	Nov-87	RS14
RSM 76	Mc schist	Arrio Arreio	Crenulated	'76	Santana area	Sep-86	RS14
RSM C49	Breccia	Volcanic	Red with grey clasts	C49	Santana area	Sep-86	RS15
RSM 27	Sandstone	Fine red		'27	Santana area	Sep-86	RS15
RSM 92	Basalt	Boulder		'92	Santana area	Sep-86	RS15
RSM 94	Gabbro	Green	Coarse grained	'94	Santana area	Sep-86	RS15
RSM 108A	Pyroxenite	Green	Metacumuate	'108	Santana area	Sep-86	RS15
RSM 108B	Pyroxenite	Green	Metacumuate	'108	Santana area	Sep-86	RS15
RSM 41A	Andesite	Brown		'41	Santana area	Sep-86	RS15
RSM 41B	Andesite	Brown		'41	Santana area	Sep-86	RS15
RSM 113	Andesite	Red	Vesicle infillas of Cpx,zeolite	'113	Santana area	Sep-86	RS15
RSM 23E	Metasediment	Bleish	Cordierite replaced by chlorite	'23	Santana area	Sep-86	RS15
RSM 44	Sandstone	micaceous	Representitive of red sstone	'44	Santana area	Sep-86	RS15
RSM 23D	Basalt			'23	Santana area	Sep-86	RS15
RSM 121	Lava	Basaltic	Weathered	'121	Santana area	Sep-86	RS15
RSM 24	Breccia	Volcanic	Red	'24	Santana area	Sep-86	RS15
RSM 31	Andesite	Red		'31	Santana area	Sep-86	RS15
					Santana area	Sep-86	RS15